

Scale-free avalanches in arrays of FitzHugh–Nagumo oscillators

Cite as: Chaos 33, 093106 (2023); doi: 10.1063/5.0165778

Submitted: 30 June 2023 · Accepted: 14 August 2023 ·

Published Online: 6 September 2023



View Online



Export Citation



CrossMark

Max Contreras,^{1,a)}  Everton S. Medeiros,²  Anna Zakharova,^{1,3}  Philipp Hövel,^{4,b)}  and Igor Franović^{5,c)} 

AFFILIATIONS

¹Institut für Theoretische Physik, Technische Universität Berlin, Hardenbergstraße 36, 10623 Berlin, Germany

²Institute for Chemistry and Biology of the Marine Environment, Carl von Ossietzky University Oldenburg, 26111 Oldenburg, Germany

³Bernstein Center for Computational Neuroscience, Humboldt-Universität zu Berlin, Philippstraße 13, 10115 Berlin, Germany

⁴Theoretical Physics and Center for Biophysics, Saarland University, Campus E2 6, 66123 Saarbrücken, Germany

⁵Scientific Computing Laboratory, Center for the Study of Complex Systems, Institute of Physics Belgrade, University of Belgrade, Pregrevica 118, 11080 Belgrade, Serbia

Note: This paper is part of the Focus Issue on Nonlinear dynamics, synchronization and networks: Dedicated to Juergen Kurths' 70th birthday.

^{a)}Electronic mail: mecontrl@gmx.de

^{b)}Electronic mail: philipp.hoevel@uni-saarland.de

^{c)}Author to whom correspondence should be addressed: franovic@ipb.ac.rs

ABSTRACT

The activity in the brain cortex remarkably shows a simultaneous presence of robust collective oscillations and neuronal avalanches, where intermittent bursts of pseudo-synchronous spiking are interspersed with long periods of quiescence. The mechanisms allowing for such coexistence are still a matter of an intensive debate. Here, we demonstrate that avalanche activity patterns can emerge in a rather simple model of an array of diffusively coupled neural oscillators with multiple timescale local dynamics in the vicinity of a canard transition. The avalanches coexist with the fully synchronous state where the units perform relaxation oscillations. We show that the mechanism behind the avalanches is based on an inhibitory effect of interactions, which may quench the spiking of units due to an interplay with the maximal canard. The avalanche activity bears certain heralds of criticality, including scale-invariant distributions of event sizes. Furthermore, the system shows increased sensitivity to perturbations, manifested as critical slowing down and reduced resilience.

Published under an exclusive license by AIP Publishing. <https://doi.org/10.1063/5.0165778>

Cascading dynamics is a prominent feature of many complex systems, from information or disease spreading in social interactions to propagation of neuronal activity. Since the discovery of neuronal avalanches, it has been suggested that the brain cortex operates at criticality, leveraging this feature to maximize its dynamic range, information capacity, and dynamical repertoire. Nevertheless, in neuronal systems, the patterns of transient synchrony, such as avalanches, typically coexist and/or interact with robust collective rhythms, and the problem of generic mechanisms that give rise to avalanches and simultaneously allow for their coexistence with collective oscillations still remains unresolved. Here, we demonstrate that the avalanche activity can emerge and coexist with synchronous oscillations in a simple

model of diffusively coupled neural oscillators with multiple timescale local dynamics in the vicinity of a canard transition. The avalanches are characterized by scale-invariant distributions of event sizes and an analysis of laminar, that is, inter-event, times. The latter quantifies both cascading and non-successive avalanches. At the critical transition between the states of lower and higher spiking rates that facilitates the onset of avalanches, the system exhibits increased sensitivity to perturbations, manifested as critical slowing down and reduced resilience. The disclosed scenario for coexistence of a well-defined oscillation rhythm and patterns with scale-invariant features may open a new avenue of research concerning multistability (and metastability) in neuronal systems.

I. INTRODUCTION

The notions of criticality and phase transitions have gained a revived interest following the formulation of the concept of critical transitions and tipping,^{1–3} which essentially translate the ideas of bifurcation theory to the realm of complex systems. Naturally, the latter is not a straightforward process due to high-dimensional dynamics of complex systems. Moreover, in many applications, understanding the details of the states involved in a critical transition, as well as finding appropriate indicators of tipping, proves to be a difficult problem. Many complex systems exhibit multistability and metastability, an ample example being the brain activity. On the one hand, the functionality of the brain relies on generating robust collective rhythms based on synchronization at different levels of self-organization within the cortex.^{4,5} On the other hand, various types of experiments, both under *in vivo* and *in vitro* conditions, have revealed the presence of neuronal avalanches,^{6–9} that is, cascades of quasi-synchronous bursts of activity, whose main feature is scale invariance where the spatial and temporal distributions of events follow power-law behaviors. The discovery of neuronal avalanches has led to the brain criticality hypothesis,^{10–14} suggesting that the emergent cortical dynamics derive from being poised at the boundary of instability or at the edge of chaos. However, the precise character of the underlying continuous phase transition remains elusive.^{15–18} Moreover, a question that naturally arises is how can so different types of activity, in particular, those with a well-defined characteristic timescale (regular synchronous activity) and others where such timescales are absent (irregular transiently synchronous activity), coexist. Furthermore, what are the mechanisms that facilitate such coexistence?

Recalling the classical theory of phase transitions, power-law behaviors should naturally be expected in scenarios where critical transitions can be associated with supercritical bifurcations; for instance, it is typically stated that neuronal avalanches emerge in the vicinity of a critical transition between silent (absorbing) and active states from a critical branching process^{11,19} or at the synchronization transition.^{16–18,20,21} Nevertheless, power laws and other heralds of criticality, such as critical slowing down, have also been observed in relation to first-order phase transitions,^{22,23} where criticality involves multistable and metastable behaviors. This also applies to certain models of neuronal avalanches, which have indicated their onset in the vicinity of a discontinuous transition showing hysteresis between the low-activity (down) and the high-activity (up) state.²⁴ Nevertheless, the general mechanisms that can reconcile the emergence of avalanche-like patterns with collective rhythms in neuronal systems are still a subject of on-going research.^{17,19,25,26}

Motivated by the latter problem, we show in this paper that avalanche-like bursting patterns can emerge in a rather simple model of an array of non-locally coupled FitzHugh–Nagumo (FHN) units with attractive diffusive interactions, whereby such an intermittent, recurrent collective bursting activity coexists with a completely synchronous state. An important ingredient of local dynamics is that it conforms to relaxation oscillations close to a canard transition^{27–29} between subthreshold and relaxation oscillations. Blending a recently introduced concept of phase-sensitive excitability of a periodic orbit^{30–32} and the interaction-induced trapping of orbits,^{33–35} we explain the mechanism by which the interplay of interactions and the vicinity of a canard transition results in

quenching of relaxation oscillations. This gives rise to patterns of rare spiking, which under variation of coupling strength may self-organize into avalanche-like activity with scale-invariant features. We further show that avalanche patterns emerge in the vicinity of a transition between two collective regimes with lower and higher spiking rates, exhibiting classical indicators of criticality, such as decreased resilience to perturbations and critical slowing down.^{13,36–38}

This paper is organized as follows: Sec. II provides the details of the model and outlines the aspects of singular perturbation theory relevant to the explanation given in Sec. III on how the interplay of interactions and structures associated with local multiple timescale dynamics may quench the spiking activity. In Sec. IV, we investigate the statistical features of avalanche patterns and show that these patterns emerge at the transition where the system displays classical criticality features in response to external stimulation. Section V contains our concluding remarks and outlook.

II. ARRAY OF NON-LOCALLY COUPLED FITZHUGH-NAGUMO UNITS

Our model is an array of N identical FHN units³⁹ with a simple non-local interaction scheme where each unit is coupled to P of its neighbors to its left and to its right on a one-dimensional ring,

$$\begin{aligned}\epsilon \dot{u}_i &= u_i - \frac{u_i^3}{3} - v_i + \frac{\sigma}{2P} \sum_{j=i-P}^{i+P} (u_j - u_i), \\ \dot{v}_i &= u_i + \alpha + \frac{\sigma}{2P} \sum_{j=i-P}^{i+P} (v_j - v_i).\end{aligned}\quad (1)$$

All the indices are periodic modulo N . Due to the smallness of the parameter $\epsilon \ll 1$, here set to $\epsilon = 0.05$, the local dynamics feature a slow-fast structure with the fast (activator) variables u_i representing neuronal membrane potentials and the slow (recovery) variables v_i reproducing the coarse-grained behavior of ion-gating channels. The non-local interactions are assumed to be linear (diffusive) and act between the activator/recovery variables in the units' fast/slow subsystems;^{40–42} see the coupling scheme in Fig. 1. Apart from the coupling radius $p = P/N$, the interactions are characterized by the coupling strength σ and are considered to be attractive ($\sigma > 0$) and homogeneous over the array.

Local dynamics is controlled by the bifurcation parameter $\alpha > 0$ such that the singular Hopf bifurcation at $\alpha = 1$ mediates the transition between the excitable regime ($\alpha \gtrsim 1$), featuring a stable equilibrium $(u^*, v^*) = (-\alpha, -\alpha + \alpha^3/3)$, and the oscillatory regime ($\alpha < 1$).³⁹ Within the framework of singular perturbation theory,²⁹ which treats the limit $\epsilon \rightarrow 0$, an isolated FHN system has been shown to exhibit a special type of trajectories, called *canards*, which closely follow the repelling branch of the slow manifold for an appreciable time^{27–29} instead of rapidly departing from it. For small but finite ϵ , such trajectories form an exponentially thin layer, whereby there exists a so-called *maximal canard*⁴³ that follows the entire repelling branch of the slow manifold. The presence of such trajectories strongly impacts the behavior of the bifurcating limit cycle when decreasing α further below the bifurcation threshold $\alpha = 1$. In particular, the incipient limit cycle undergoes a *canard transition*,⁴⁴

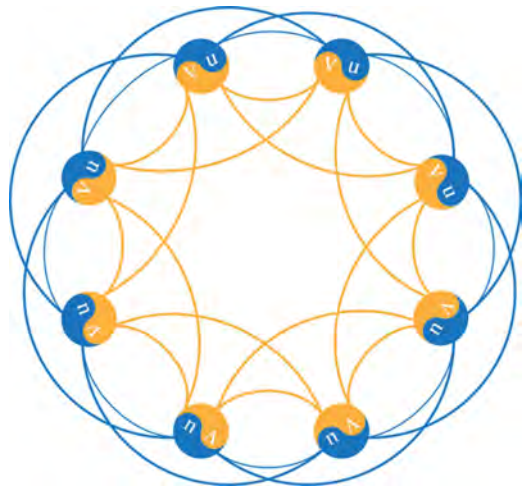


FIG. 1. An array of FHN neurons for $N = 8$ and $P = 2$. Fast variables u are represented in blue, while slow variables v are shown in yellow.

where its amplitude sharply increases within a narrow interval of α values exponentially small in ε . The canard transition mediates between small-amplitude harmonic oscillations of period $\mathcal{O}(\sqrt{\varepsilon})$ and large-amplitude relaxation oscillations of period $\mathcal{O}(1)$. In the language of neuroscience, this corresponds to a transition from sub-threshold oscillations to the regime of tonic spiking. A classical result from asymptotic expansion theory is that the canard transition occurs at $\alpha = \alpha_c = 1 - \varepsilon/8$; cf. Ref. 45.

Throughout this paper, the local bifurcation parameter is set to $\alpha = 0.99$, the value below α_c , such that it supports relaxation oscillations. Nonetheless, the vicinity of the canard transition still influences the way the system responds to perturbations, be it due to interactions and/or noise. In particular, while the subthreshold oscillations below the canard transition manifest excitability in the classical sense,⁴⁶ it has recently been reported that the relaxation oscillations show a specific type of excitable behavior called phase-sensitive excitability of a limit cycle.³⁰ The latter comprises a non-uniform response to perturbations along the orbit of relaxation oscillations such that the FHN system provides a nonlinear threshold-like response to perturbations during the passage close to the unstable equilibrium (u^*, v^*) . Then, perturbations of sufficient amplitude and acting in the appropriate direction are capable of inducing one or more subthreshold oscillations around the unstable equilibrium, whereby the maximal canard acts as the threshold manifold. The emergence of such subthreshold oscillations in response to interactions will later prove important for understanding the mechanism giving rise to nontrivial collective dynamics behind the activity avalanches.

Our primary interest concerns the impact of coupling strength σ on the system's dynamics, focusing on the case of weak interactions $\sigma \in [0, 0.1]$. All the numerical experiments have been performed for the system size $N = 50$ and coupling range $P = 10$ unless stated otherwise. The numerical integration has been performed using the Cash-Karp (4, 5) method with adaptive stepsize control

implemented via GNU Scientific Library (GSL).⁴⁷ The time series in the remainder of the paper illustrate the asymptotic system behavior after discarding a sufficiently long transient of, e.g., 5×10^3 time units. When illustrating the dependence on σ , the coupling strength increment is $\Delta\sigma = 10^{-3}$. For each value of σ , we consider a set of ten different random initial conditions $(\vec{u}_0, \vec{v}_0) \in [-2, 2]^N \times [-2, 2]^N$.

We find that a range of coupling strengths supports the onset of a regime where an irregular asynchronous rare spiking activity is interspersed with brief intervals of cascading pseudo-synchronous bursting activities, called avalanches. The described regime is bistable with the regime of a synchronous regular spiking activity, as we will demonstrate in Sec. III.

III. ARRAY DYNAMICS IN DEPENDENCE OF COUPLING STRENGTH

Given that the units are identical and interact by attractive diffusive couplings, the system (1) possesses an invariant synchronization manifold $u_1(t) = u_2(t) = \dots = u_N(t)$, $v_1(t) = v_2(t) = \dots = v_N(t)$. Since the isolated dynamics of neurons comprises relaxation oscillations, this manifold contains a limit cycle attractor where all the units perform identical relaxation oscillations. In the following, we will show that under a variation of the coupling strength σ , the system (1) may exhibit non-trivial emergent dynamics that unfolds off the invariant synchronization manifold. In other words, we find a range of σ values where due to non-local interactions, not all of the initial conditions converge to the invariant manifold, and the completely synchronized relaxation oscillations coexist with another type of collective dynamics.

To observe such emergent dynamics, we introduce a global order parameter μ that characterizes the synchronization of units' average spiking frequencies. Unlike the more classical synchronization parameters, involving synchronization error or average local variances from the mean variables, μ is not intended to quantify both frequency and phase synchronization of units, but rather to describe the quenching of units' average spiking frequencies due to non-local interactions. By construction, μ is introduced to indicate the relative persistence of units' trajectories in the neighborhood of the limit cycle S corresponding to relaxation oscillations of an uncoupled (isolated) unit. To define μ , we first denote by K the spike count of an uncoupled unit within a sufficiently long time interval ΔT . Then, for the system of coupled units (1), we consider J_i as the spike count of a unit i within the time interval ΔT . Using these two quantities, the global order parameter μ is given by

$$\mu = \frac{1}{NK} \sum_{i=1}^N J_i. \quad (2)$$

Qualitatively, μ compares the ensemble-averaged spiking frequency of coupled units to the spiking frequency of an uncoupled unit. Naturally, these two frequencies are equal, resulting in $\mu = 1$, when the system's state lies on the large-amplitude limit cycle on the invariant synchronization manifold. Nevertheless, note that $\mu = 1$ also corresponds to such states where the units are not on the synchronization manifold, but perform relaxation oscillations mutually shifted in phase. One expects the emergent dynamics with quenched spiking of individual units to be characterized by $\mu < 1$.

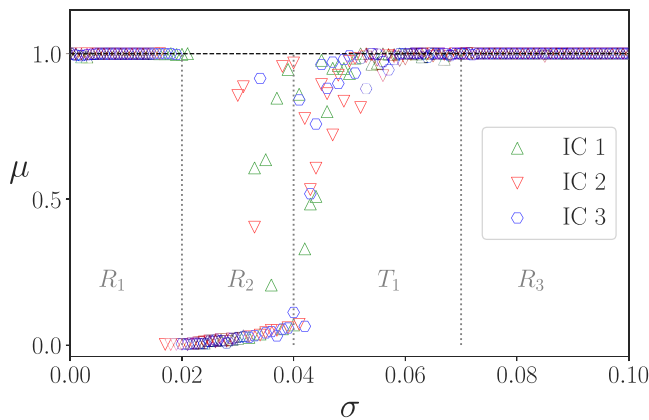


FIG. 2. Order parameter μ in dependence of coupling strength σ for three different sets of initial conditions (green up-triangles, red down-triangles, and blue circles). Intervals of σ denoted by R_1 and R_3 are characterized by the prevalence of relaxation oscillations ($\mu \approx 1$). Intervals R_2 and T_1 , respectively, support coexistence of asynchronous states $\mu \approx 0$ and $0 < \mu < 1$ with a completely synchronous state. The dashed line $\mu = 1$ corresponds to the case where all the units perform completely synchronous relaxation oscillations.

Figure 2 shows the order parameter μ in terms of the coupling strength σ for asymptotic dynamics obtained from three different sets of initial conditions (green up-triangles, red down-triangles, and blue circles) in the weak coupling regime ($\sigma \ll 1$). For sufficiently small σ , all the initial conditions lead to frequency synchronized relaxation oscillations of individual units; see the region R_1 . Nevertheless, when increasing σ , one observes an interval $\sigma \sim [0.02, 0.07]$ that supports asynchronous states characterized by the global order parameter $\mu < 1$. Such states emerge only for certain sets of initial conditions, and the synchronous state coexists throughout the entire σ interval. By the corresponding values of μ , one may distinguish between two types of asynchronous states: (i) the region R_2 where the global order parameter attains very small values $\mu \approx 0$ and (ii) an interval T_1 where μ values of asynchronous states are enhanced but still lie notably below the $\mu = 1$ level. For a stronger coupling strength σ , one finds region R_3 where the synchronous state is regained for all sets of initial conditions. The same physical picture qualitatively holds for a range of coupling radii p . Nevertheless, the width of the interval of intermediate σ values supporting asynchronous states reduces with p , eventually vanishing for interactions of sufficiently long-range.

To gain a deeper insight into the emergent dynamics typical for different σ intervals, we consider the corresponding state-space projections (u_i, v_i) for two representative units, indicated in blue solid and red dashed lines in Fig. 3. For $\sigma = 0.001$, which lies in the region R_1 , the neurons already perform relaxation oscillations along the same orbit but are shifted in phase; cf. the orbits and the time traces in Fig. 3(a). For this small coupling strength, the phases remain free along the limit cycles at the state space of different FHN units.⁴⁸ Within the region R_2 , represented by $\sigma = 0.02$ in Fig. 3(b), the units mostly perform small-amplitude oscillations around the unstable equilibrium (u^*, v^*) , and only a few or none

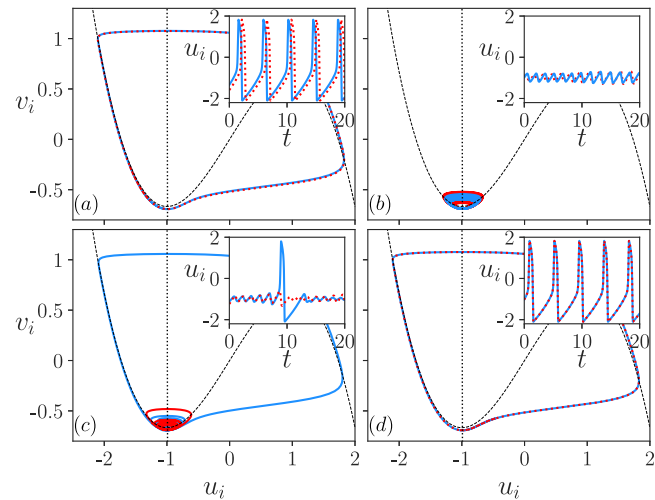


FIG. 3. Main frames: orbits $(u_i(t), v_i(t))$ of two units $i = 20$ (blue solid lines) and $i = 50$ (red dashed lines); insets: time traces $u_i(t)$ of the same two units for different system states. (a) $\sigma = 0.001$: phase-shifted synchronization of relaxation oscillations. (b) $\sigma = 0.02$: the feedback from local mean-fields causes trapping of orbits around the unstable equilibrium (u^*, v^*) . (c) $\sigma = 0.041$: the orbits eventually escape from the trapping region, generating rare spikes. (d) $\sigma = 0.1$: coupling strength is sufficient to induce complete synchronization of relaxation oscillations. The unstable equilibrium (u^*, v^*) of isolated dynamics lies at the intersection of nullclines (black dashed and dotted curves).

of the units occasionally escape the trapping region generating rare spikes. Trapping of the trajectories in the vicinity of the unstable equilibrium derives from the impact of local mean-fields, whose fluctuations are reflected in the amplitude variability of subthreshold oscillations around (u^*, v^*) . The localized excitations (spikes) become more prevalent for a larger $\sigma = 0.041$ that belongs to the interval T_1 ; see Fig. 3(c). By increasing σ within T_1 , one observes patterns comprising local mixed-mode oscillations⁴⁴ where units fire more frequently and more correlated. The statistical properties of such solutions are a key aspect of this study and will be elucidated in Sec. IV. Finally, for $\sigma = 0.1$ from the region R_3 , the system dynamics are characterized by completely (both frequency and phase) synchronized relaxation oscillations of individual units; cf. Fig. 3(d).

Now, let us focus on the mechanism causing the trapping of units' orbits in the vicinity of the unstable fixed point (u^*, v^*) . First, we recall the notion of phase-sensitive excitability of a periodic orbit invoked in Sec. II. At variance with,³⁰ which introduced this notion while analyzing the non-uniform response of relaxation oscillations to noise, a similar type of effect emerges due to non-local interactions. Specifically, the units whose isolated dynamics comprise relaxation oscillations become trapped and perform subthreshold oscillations around the unstable equilibrium. Then, the maximal canard establishes a state space threshold separating the transient small-amplitude oscillation from the limit cycle of relaxation oscillations. For deterministic networked systems, the trapping of trajectories has previously been observed in the vicinity of more complex invariant sets. In particular, in Refs. ^{33–35}, it has been

demonstrated that the couplings can trap units' trajectories in the vicinity of unstable chaotic sets. Then, the trapping mechanism is based on an interplay between interactions and the dynamics in the chaotic set, which creates random perturbations that prevent the trajectories from escaping the vicinity of the invariant set via its unstable manifold. The chaotic sets involved in the trapping occur in the state space of each unit. The latter is similar to the scenario here, but instead of chaotic sets, we consider the trapping mediated by unstable equilibria encircled by the maximal canards.

In the following, we propose a mechanism to explain the dynamics in the intervals R_2 and T_1 that contains the main ingredients of both phase-sensitive excitability of periodic orbits and the above described trapping phenomenon. We begin by revisiting the dynamics of an isolated FHN neuron where the maximal canard provides a threshold between different types of orbits, distinguished by the motion around the unstable fixed point (u^*, v^*) . The differences between the associated transients become apparent if one determines the corresponding *escapes time* t_e from the region enclosed by the maximal canard. This quantity expresses the dimensionless time required for trajectories starting from different initial conditions to reach the limit cycle of relaxation oscillations S . In Fig. 4(a), color coding indicates the escape times t_e for a large set of initial conditions (u_0, v_0) . Note the thin boundaries between the regions with different values of t_e that reflect the spiraling of the maximal canard around (u^*, v^*) , and the white line just below indicates a segment of the orbit of the limit cycle corresponding to relaxation oscillations. The subtlety of such boundaries makes the system highly sensitive to perturbations; for instance, a trajectory in the maximal canard region with a certain prescribed escape time, if perturbed, may change its current escape route and perform extra loops around (u^*, v^*) . The same applies to the orbit of relaxation oscillations, which, under the effect of an appropriate perturbation, may be injected into the maximal canard region when passing close to it so as to perform loops around the unstable fixed point.

Let us now focus on the case of FHN neurons embedded in an array. There, it is the non-local interactions that provide perturbations to local dynamics, sensitively affecting the units' orbits around the maximal canard. Depending on the character of perturbations, the trajectories of only a subset of neurons may undergo subthreshold oscillations due to trapping by the maximal canard, while the remaining neurons continue to perform relaxation oscillations. Such a scenario gives rise to an emergent asynchronous behavior. Since the coupling function is diffusive, its amplitude increases in a desynchronized network, contributing to larger perturbations to neuronal dynamics. Consequently, the interaction between the perturbation-sensitive dynamics around the maximal canard and the couplings, i.e., local mean-fields, constitutes a positive feedback loop. One may numerically assess the range of coupling strengths σ where such an impact of interactions is the strongest. Appreciating that the interactions introduce a parametric perturbation of local neuronal dynamics, we introduce an effective bifurcation parameter α_i for each neuron as

$$\alpha_i^{\text{eff}}(t) = \alpha + \frac{\sigma}{2P} \sum_{j=i-P}^{i+P} (v_j(t) - v_i(t)), \quad (3)$$

where $\alpha = 0.99$ is the unperturbed value defined in Sec. II.

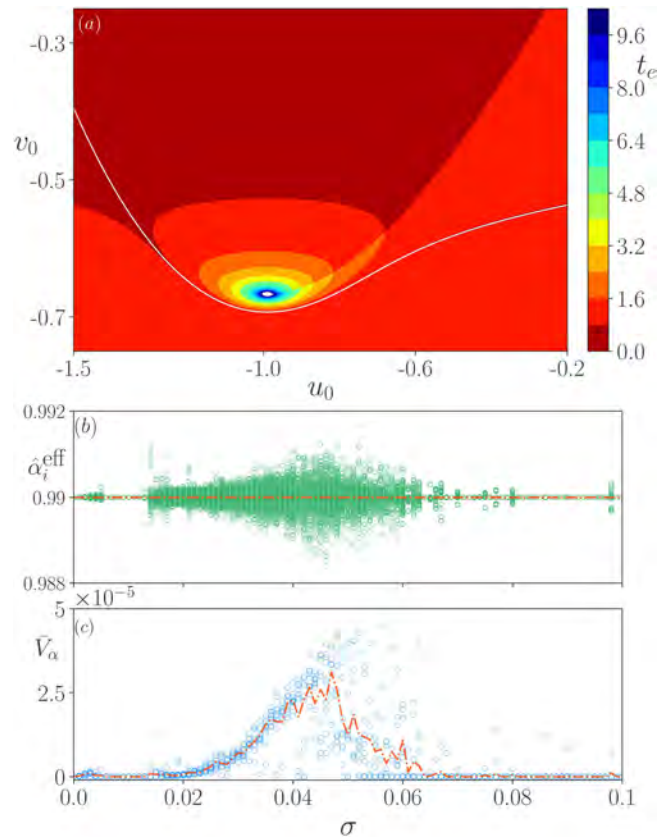


FIG. 4. (a) For an isolated FHN unit, i.e., Eq. (1) with $\sigma = 0$, the color scheme indicates escape times t_e from the maximal canard region for different initial conditions (u_0, v_0) ; white curve: segment of the limit-cycle S close to the maximal canard. (b) Time-averaged effective bifurcation parameters $\hat{\alpha}_i^{\text{eff}}$ as a function of σ . (c) Blue dots: local variances $V_{\alpha,i}$ of effective bifurcation parameters $\alpha_i^{\text{eff}}(t)$; red dashed-dotted curves in (b) and (c): population-averaged values for different σ .

Figure 4(b) depicts the time averages $\hat{\alpha}_i^{\text{eff}}$ of the effective parameter $\alpha_i^{\text{eff}}(t)$ as a function of σ . One observes that for $\sigma \lesssim 0.018$, the value of $\hat{\alpha}_i^{\text{eff}} \approx 0.99$ approximately equals that of an isolated unit. Here, the amplitude of perturbations from the local mean-fields is subthreshold and cannot induce small-amplitude oscillations around (u^*, v^*) . Consequently, all the units perform relaxation oscillations; cf. region R_1 in Fig. 2. However, for $\sigma \approx 0.018$, the couplings become capable of trapping the units within the canard region to generate small-amplitude oscillations. In parallel, one observes that the value of $\hat{\alpha}_i^{\text{eff}}$ begin to substantially depart from the unperturbed value $\alpha = 0.99$; cf. Fig. 4(b). Such increasing deviations are associated with the feedback from non-local interactions, whose impact on system dynamics grows as the desynchronization sets in. Enhancing σ further, the contribution from non-local interactions to $\hat{\alpha}_i^{\text{eff}}$ peaks around $\sigma \approx 0.04$. There, the parametric perturbation to units shows high variability over the array; cf. the increase in the corresponding variances $V_{\alpha,i}$ of effective bifurcation parameters in Fig. 4(c). The given value of σ approximately corresponds to the transition

between regions R_2 and T_1 from Fig. 2. As σ is further increased, the attractive nature of the couplings begins to dominate the dynamics, contributing to units' synchronization. This is accompanied by the decrease of the amplitudes of parametric perturbations affecting the units up to the point where they become subthreshold such that the units again perform relaxation oscillations; cf. region R_3 in Fig. 2.

In Sec. IV, we will explore the statistical properties of the network solutions. We pay special attention to the transition between R_2 and T_1 , where the non-local coupling and sensitive response to perturbations of relaxation oscillations in the vicinity of the maximal canard make the largest impact.

IV. AVALANCHE ACTIVITY

As elaborated in Sec. III, for a range of intermediate σ in Fig. 2, one finds activity patterns where the units spend much time trapped by the maximal canard in the vicinity of the unstable fixed point (u^*, v^*) , while being rarely released to perform spikes. In the following, we resolve the spatiotemporal structure of such emergent states showing that they conform to an avalanche-like activity, where intermittent pseudo-synchronous spiking, localized to various degrees, is separated by long periods of quiescence over the array. Note that the observed avalanches are not intended to model

classical neuronal avalanches,^{6–9} though a partial analogy may be drawn, as discussed in Sec. IV A.

Let us first consider the spatiotemporal evolution of local membrane potentials $u_i(t)$ described by Eq. (1); see Figs. 5(a) and 5(b). Indeed, the latter indicates that the typical activity patterns are self-organized into episodes of pseudo-synchronous spiking separated by silent episodes. Nevertheless, in terms of temporal organization, two types of avalanches may be distinguished, namely, *cascading* events, cf. the example of an avalanche beginning around $t \approx 30$ in Fig. 5(b), where the (spatially localized) spiking activity propagates forming temporal sequences; and *temporally localized* (isolated) events, where the (spatially localized) spiking occurs within a narrow time window. Note that the duration of the time window used to identify pseudo-synchronous spiking is specified in Sec. IV A. Qualitatively, the episodes of a spiking activity resemble self-localized excitations in excitable media.^{49,50} The cascading events have a step-pyramid-like space-time structure. This reflects the fact that at every next level, only the units closer to the center of the previous level perform a spike. The latter units remain active because they receive most of the input from the spiking rather than the silent units. Naturally, the units at the top level, e.g., unit $i = 68$ in Figs. 5(a) and 5(b), fire more spikes during a cascading event than the units whose spiking terminates at some of the lower levels. In contrast to cascading avalanches, each unit participating in a temporally localized event

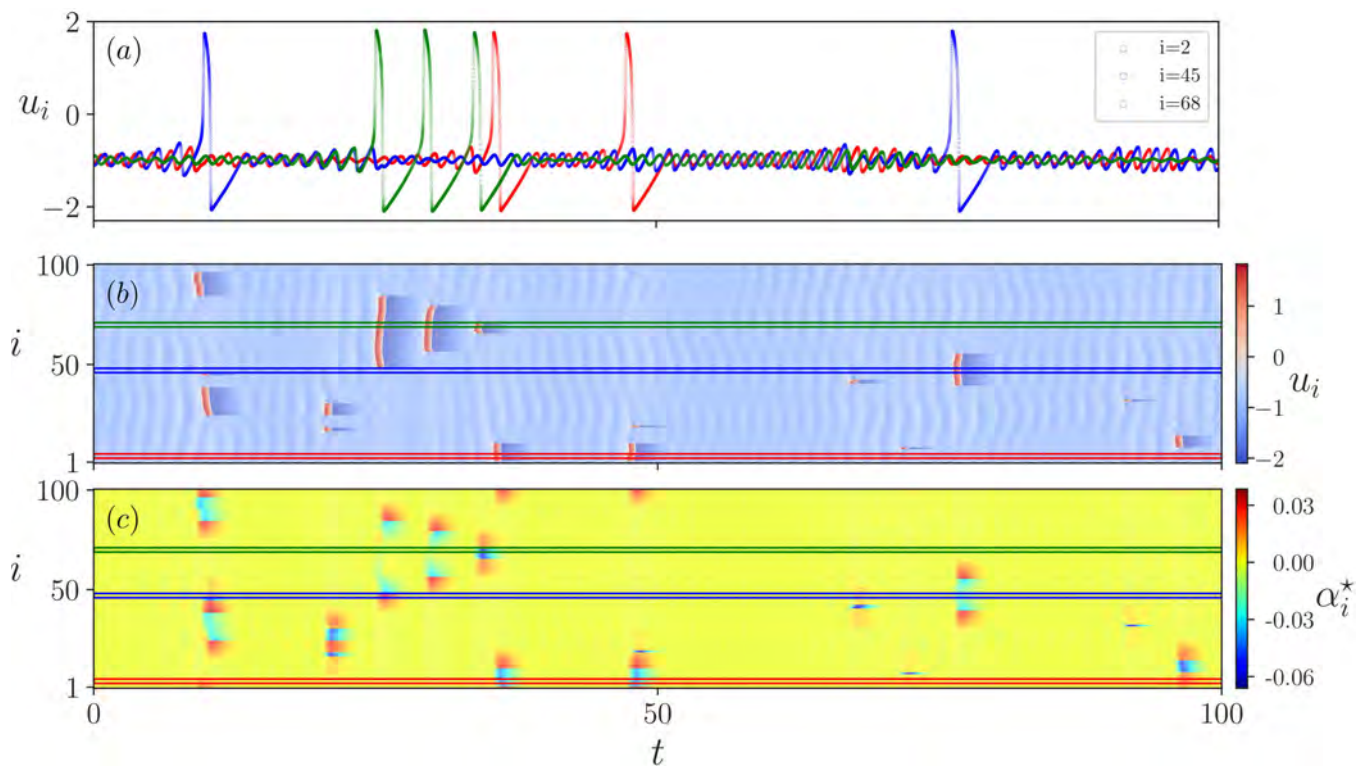


FIG. 5. Self-organization of avalanches. (a) Time traces $u_i(t)$ for three units $i = 2$, $i = 45$, and $i = 68$, indicated by green, blue, and red rectangles in panel (b), respectively. (b) Spatiotemporal evolution of fast variables $u_i(t)$. (c) Spatiotemporal evolution of the quantity $\alpha_i^*(t) = \alpha_i^{\text{eff}}(t) - \alpha_c$, which shows that the units spend most of the time in the vicinity of the canard transition. System parameters: $\sigma = 0.04$, $N = 100$, $p = 0.2$.

spikes only once. In terms of spatial organization, the units spiking within a given narrow time window can appear as connected clusters or may display a multi-cluster structure forming spatially disconnected clusters.

The intrinsic structure and self-organization of avalanche patterns can be described in more detail by looking into the spatiotemporal evolution of the quantity $\alpha_i^*(t) = \alpha_i^{\text{eff}}(t) - \alpha_c$ as shown in Fig. 5(c). In particular, one observes that units spend most of the time in the vicinity of the canard transition $\alpha_i^* \approx 0$, which underlies the important role of the canard transition in the self-organization of avalanches. Moreover, for the cascading events, one observes that the units around the excited region are furthest above the bifurcation threshold, i.e., have the largest values of $\alpha_i^*(t)$. This effectively facilitates the pattern confinement, making the avalanche events spatially localized.

The local dynamics comprise irregular mixed-mode oscillations, involving fast subthreshold oscillations interspersed with random rare spikes, cf. Fig. 5(a), which illustrates the time traces $u_i(t)$ of three units highlighted in Fig. 5(b). The irregularity of single units' interspike intervals is corroborated by Fig. 6(a) showing the temporal evolution of the return times $\Delta t_n(t)$ to the Poincaré cross section $u_k(t) = 1, \dot{u}_k(t) > 0$ for an arbitrary unit. Together with the corresponding first return map of successive return times $\Delta t_n(\Delta t_{n-1})$ in Fig. 6(b), it evinces that the units may sometimes fire spikes in close succession, but that there may also be long periods of quiescence. The spatial profile of average spiking frequencies $\omega_k = 2\pi M_k/T$, where M_k is the spike count within a macroscopic time interval T , is shown in Fig. 6(c). Expectedly, as the averaging time interval is increased, the ω_i profile becomes more uniform, indicating that it

should appear flat for very long T as the spiking excitations occur randomly in space. Qualitatively, our scenario involving rare and irregular recurrent spiking bears certain resemblance to the onset of extreme events in systems of diffusively coupled nonidentical FHN units with excitable local dynamics,^{51–54} as well as identical FHN oscillators with delayed diffusive couplings.^{40,42} However, in contrast to Ref. 51, we typically find spatially localized events, rather than the bursting events spanning the entire network.

A. Statistical features of avalanches

In this section, our goal is to address in detail how the statistical features of activity patterns, such as the one in Fig. 5(a), depend on the coupling strength σ . Let us first precisely define the avalanche events and the associated properties we are interested in. Starting from a set of random initial conditions $(\vec{u}_0, \vec{v}_0) \in [-2, 2]^N \times [-2, 2]^N$, we consider the evolution of an array Eq. (1) over the interval $\Delta T = 5 \times 10^4$. An individual avalanche event comprises a joint spiking activity of a cluster of a certain number of units k within the narrow time window $\Delta t = 100\delta t$, where δt is the integration step. The avalanche size, denoted by S_k , then refers to the number of units that have fired at least once during this small interval and is not related to the total number of spikes emitted by the units forming the cluster. In other words, S_1 denotes an event where only a single unit has fired within the given time window Δt , whereas S_N corresponds to an avalanche spanning the whole array. To elucidate how the avalanche properties depend on σ without a potential bias due to initial conditions; for each value of σ , we perform numerical experiments with ten different sets of random initial conditions.

Focusing on the σ interval associated with regimes R_2 and T_1 , Fig. 7(a) illustrates the σ dependence of the maximal avalanche sizes $\max(s_k)$ normalized over the array size N ; i.e., $s_k = S_k/N$. Multiple symbols for a given value of σ denote the results obtained for the different sets of initial conditions, and the red curve indicates the values averaged over the ensemble of initial conditions. For smaller σ , even the maximal avalanche sizes do not exceed the normalized coupling range $2p = 2P/N$, indicated by the horizontal green line. This implies that avalanches remain localized events focused around the initial excitation or, put differently, that the correlation length of spontaneous activity fluctuations remains short. However, for larger coupling strengths $\sigma \gtrsim 0.025$, the average values over different initial conditions exceed the coupling range, suggesting that the synchronous spiking activity typically propagates over the array, indicating an increase in the system's correlation length. Enhancing the coupling strength further into the T_1 regime ($\sigma > 0.04$), we observe that maximal avalanches indeed span the entire array.

To get an insight into the variability of avalanche cluster sizes, in Fig. 7(b), we show how the maximal number of different cluster sizes $\mathcal{C}(s_k)$ depends on σ . Multiple symbols for any given σ again correspond to results for different initial conditions. One observes that the variability of cluster sizes, reflected in the number of different recorded cluster sizes, reaches a maximum around $\sigma \approx 0.04$, the values near the transition between the regimes R_2 and T_1 from Fig. 2. Nonetheless, within the T_1 regime, another form of variability increases. Specifically, the diversity of cluster sizes recorded in

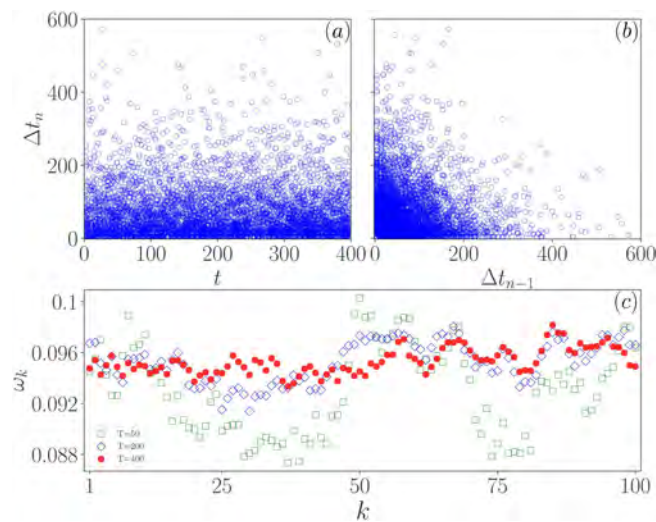


FIG. 6. (a) Temporal evolution of the return times $\Delta t_n(t)$ to the Poincaré cross section $u_k(t) = 1, \dot{u}_k(t) > 0$ of a single unit. (b) First return map $\Delta t_n(\Delta t_{n-1})$ of successive return times to the Poincaré cross-section. (c) Spatial distribution of average spiking frequencies ω_k over time periods $T = 5 \times 10^4$ (empty squares), $T = 2 \times 10^5$ (empty diamonds), and $T = 4 \times 10^5$ (solid circles). System parameters: $\sigma = 0.04$, $N = 100$, $p = 0.2$.

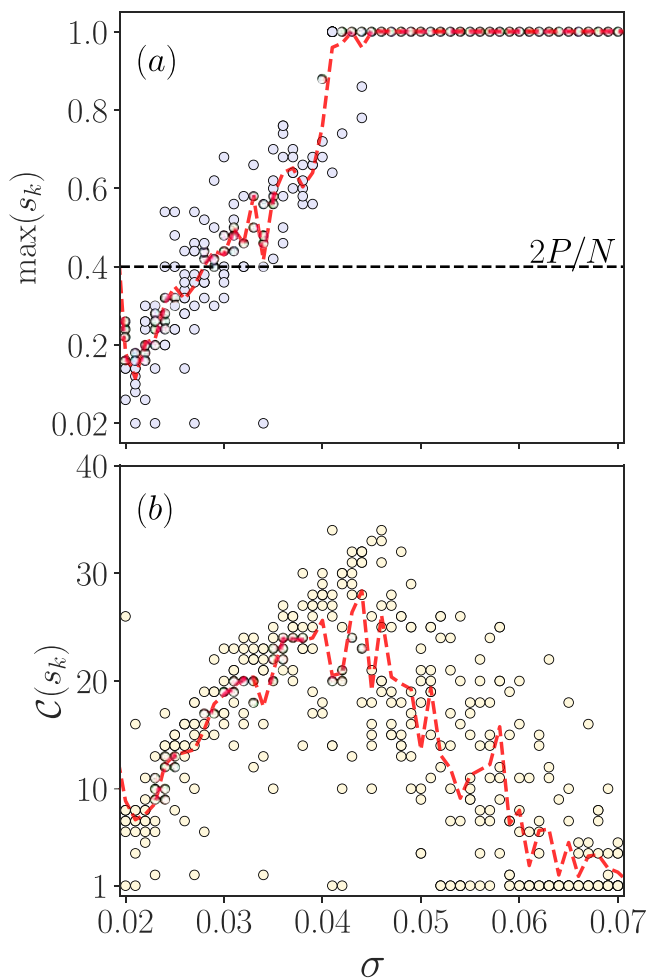


FIG. 7. Statistical properties of avalanches. (a) Largest, relative avalanche sizes $\max(s_k)$ in terms of σ . For each σ , dots indicate the results for ten different initial conditions. The average values (red curve) exceed the connectivity $2p = 2P/N$ (green dashed line) for $\sigma > 0.03$. (b) Number of different cluster sizes $C(s_k)$ as a function of σ . The average (red curve) shows a peak in the vicinity of the transition between regions R_2 and T_1 ; cf. Figs. 2 and 4.

simulations starting from different initial conditions becomes much more pronounced than in the R_2 regime.

Both the onset of avalanches that span the entire array in Fig. 7(a), and the highest variability of avalanche sizes observed in Fig. 7(b) for $\sigma \approx 0.04$, suggest that the change of regimes from R_2 to T_1 under increasing σ bears signatures of criticality. One may draw a partial analogy to observations on a resting state (spontaneous) activity in neuronal systems. There, the neuronal avalanches,^{6–9} found in electrophysiological recordings, both under *in vitro* and *in vivo* conditions, as well as by electroencephalography and functional magnetic resonance imaging, are known to show criticality features. Manifestations of criticality classically involve scale invariance in the distributions of relevant quantities, e.g., the size and

duration of neuronal avalanches, which is reflected in the power-law behaviors of the form $F(x) \propto x^{-\gamma}$, where γ is a critical exponent.^{55,56} Criticality features are generally associated with proximity to critical/phase transitions between ordered and disordered phases^{11,14,19,57} or in the case of neuronal avalanches, between an absorbing state with a quickly decaying spiking activity and an active state with runaway (exploding) activity propagation.⁵⁸ Nevertheless, the concept of phase transitions applies to systems in the thermodynamic limit $N \rightarrow \infty$; therefore, an observation of genuine power-laws cannot be expected for finite-size systems. To resolve this, one often invokes the point that the phase transitions in finite systems extend over a critical region called the Griffiths phase.^{59–61} There, the system is quasi-critical and maintains certain aspects of criticality, including the truncated power-law behaviors (power laws with exponential cutoffs) of relevant quantities.⁶² This also applies to neuronal avalanches, where the classically reported exponents for the avalanche size and duration are $3/2$ (with some exceptions) and 2 , respectively, while the cutoff typically matches the system size^{6,63} but may also deviate from it.^{64,65} One should further note that the power-law distributions of event sizes per se may not necessarily imply that the system is poised close to criticality.^{66,67} Conversely, there are instances, such as certain models of neuronal avalanches, where a critical system shows a scale-free distribution of event sizes that does not conform to a power-law.⁶⁸ Such results may partly derive from a potentially fuzzy relationship between the definition of observed events and the local dynamics behind them.

Given the arguments above, we focus on the properties of avalanches in the narrow range $\sigma \in [0.037, 0.043]$ around the transition between the regimes R_2 and T_1 from Fig. 2. In particular, fixing σ , we consider the probability distribution $\mathcal{P}(s)$ of relative avalanche cluster sizes $s = S/N$ and the probability distribution $\mathcal{P}(\tau)$ of time intervals τ between the successive avalanches; see the left and right column in Fig. 8, respectively. Both $\mathcal{P}(s)$ and $\mathcal{P}(\tau)$ are sampled for three different array sizes ($N = 50$, $N = 100$, and $N = 200$) maintaining the fixed coupling radius $p = P/N = 0.2$. For all three N values, the distributions $\mathcal{P}(s)$ show an approximate scaling regime for small and intermediate relative cluster sizes $s \leq p$, cf. the vertical dashed lines in Figs. 8(a), 8(c), and 8(e), followed by a cutoff due to finite system size. For the largest array size $N = 200$ in Fig. 8(e), we have included as a guideline the power-law scaling $\beta = 3/2$ (black dashed-dotted line) classically obtained for the distribution of neuronal avalanches.

The distributions $\mathcal{P}(\tau)$ of intervals between the successive avalanche events, also called the *laminar times*,^{69,70} indicate two different regimes that guide the avalanche recurrence processes; cf. Figs. 8(b), 8(d), and 8(f). In particular, very short laminar times describe the intrinsic dynamics of cascading avalanches, i.e., correspond to cascades' intra-event intervals between the successive bursts. For intermediate τ , one observes the peak that indicates the presence of a characteristic timescale in the avalanche recurrence process rather than the scale invariant behavior. Such traces of pseudo-regularity in avalanche recurrent times reflect an occasional degradation of the trapping mechanism associated with the maximal canard, which allows the system to intermittently evolve in the vicinity (not on) of the synchronization manifold, having the units generate spikes mutually shifted in phase.

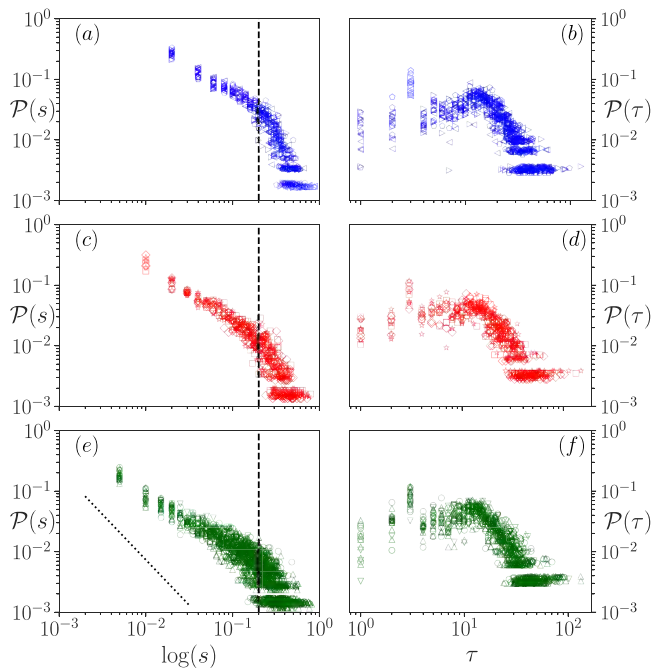


FIG. 8. Distributions of relative avalanche sizes $s = S/N$ and laminar times τ for (a) and (b) $N = 50$, (c) and (d) $N = 100$, and (e) and (f) $N = 200$. Different symbols indicate the results obtained for different sets of initial conditions. σ is chosen in the vicinity of the transition between the regions R_2 and T_1 . Coupling radius $p = P/N = 0.2$ (vertical dashed black lines in the left column) is kept fixed in all the simulations. Distributions $\mathcal{P}(s)$ in (a), (c), and (e) show power-law behavior for small and intermediate avalanches followed by a cutoff. The comparison with the power-law $\beta = 3/2$ (black dotted line) in panel (e) is provided as a guideline. Distributions of laminar times $\mathcal{P}(\tau)$ in (b), (d), and (f) show a peak indicating the presence of a characteristic timescale.

The results in this section suggest that our system in the vicinity of the transition between the regimes R_2 and T_1 from Fig. 2 shows certain aspects of critical behavior, such as the increase of correlation length compared to coupling radius (indirectly observed by the growth of maximal cluster sizes) and the enhanced variability of cluster sizes. To further this point, in the next section, we investigate the system’s response to perturbations, demonstrating evidence of *critical slowing down* and *decreased resilience* of the system’s dynamics in the vicinity of this transition.

B. Indicators of criticality

Approaching the critical transition, complex systems tend to show progressively less resilience to perturbations, taking increasingly longer times to recover.² Such slower recovery rates are classically described as a herald of a critical slowing down phenomenon.^{13,36–38} The latter also influences the relaxation processes and, hence, the statistics of fluctuations underlying the spontaneous activity of systems near criticality. Qualitatively, this increases their short-term memory and variability and is reflected in enhanced autocorrelation and variance of systems’ observables.

In terms of induced activity, systems at criticality are known to maximize their dynamic range.^{10,71,72}

In the following, our goal is to demonstrate that at the onset of the T_1 region, or rather for σ values close to the transition between regions R_2 and T_1 from Fig. 2, an array of FHN units exhibits two signature effects of criticality, namely, increased recovery times to small perturbations and reduced resilience. To do so, we introduce two types of stimulation protocols: one, called an *LC-shift*, where a small fraction M of units is triggered to spike, i.e., their orbits are kicked toward the orbit of a relaxation oscillation limit cycle; and the other, called an *FP-shift*, where the same fraction of units is injected into the vicinity of the unstable fixed point (u^*, v^*) . The described perturbations are applied at time $t = T_p$, after which the array spontaneously evolves until the moment $t = T$. To quantify the effect of perturbations, we compare the orbit of the system after introducing the stimulus to that of the unperturbed system and numerically determine the deviations $\zeta(t)$. As a measure of the impact of the stimulus, we take the variance $\text{Var}(\zeta(t))$ of the deviations calculated over the interval $T - T_p$.

In Fig. 9(a) are shown the time series of variances $\text{Var}(\zeta(t))$ for three different values of σ following an *FP-shift* at $T_p = 150$. The horizontal red dashed lines indicate the levels of the corresponding initial *FP-shifts*. We first point out that the post-stimulus amplitude variance (shown green) is much higher than the initial amplitude of the *FP-shift* for $\sigma = 0.04$ (middle panel), whereas it is lower for $\sigma = 0.024$ (top panel) and $\sigma = 0.043$ (bottom panel). This reflects the array’s reduced resilience, i.e., the decreased recovery capability for $\sigma = 0.04$, and also shows that the perturbations from external stimuli are amplified for this value of σ . Moreover, one observes that the post-stimulus interval of nonzero variance is much longer for $\sigma = 0.04$ than for the other two σ values. This evinces that the array’s recovery times T_R from a perturbation (see the blue dashed line with arrows) are much slower for $\sigma = 0.04$. Note that the values at the top and bottom panels are selected from regions R_2 and T_1 from Fig. 2, while the longest recovery time and the largest variance amplitude are found approximately at the transition boundary between these regions. In other words, in the vicinity of the latter transition, the system shows two prominent features of criticality, having the recovery time and signal variance following a perturbation substantially different compared to the system’s behavior below and above the transition.

To better characterize the described behavior, let us investigate the array’s recovery times and variances over the continuous interval of σ spanning between the regions R_2 and T_1 . Our aim is to show that the variability of the system’s response to perturbations is indeed the largest in the vicinity of the transition between these two regions. Hence, for each considered value of σ , we perform simulations of the array dynamics for ten different initial conditions and implement either the *FP-shift* or the *LC-shift* stimulation protocol. Then, we numerically estimate the cumulative variance per unit time ϕ^2 for each set of initial conditions,

$$\phi^2 = \frac{1}{T - T_p} \int_{T_p}^T \text{Var}(\zeta) dt. \tag{4}$$

The dependence of the quantity ϕ^2 on σ is illustrated in Fig. 9(b). Note that for a given value of σ , each symbol describes the

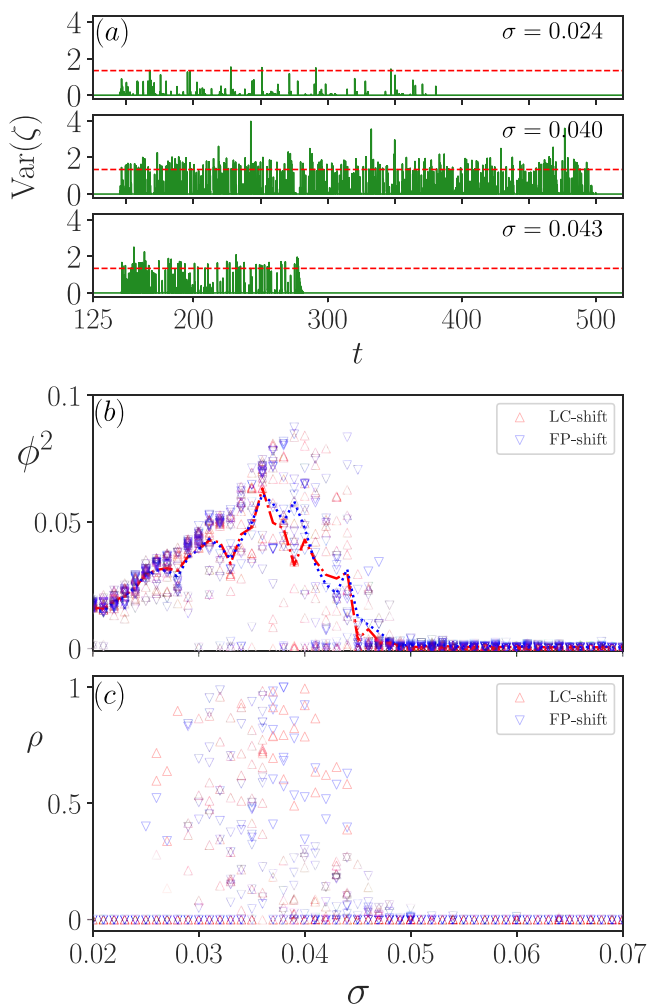


FIG. 9. Indicators of criticality at the transition between regions R_2 and T_1 from Fig. 2. (a) Time traces of variance $\text{Var}(\zeta)$ after an *FP-shift* introduced to a fraction of $M = 0.05$ units at $T_p = 150$ for $\sigma = 0.024$ (top panel), $\sigma = 0.04$ (middle panel), and $\sigma = 0.043$ (bottom panel); red dashed line: level of an initial *FP-shift*. (b) Cumulative variance ϕ^2 and (c) normalized recovery time ρ as a function of σ . Each symbol stands for a different set of initial conditions, and the color code refers to *LC-shift* (red) and *FP-shift* (blue) stimulation protocols. The dashed-dotted and dotted curves in panel (b) indicate the values of ϕ^2 averaged over an ensemble of initial conditions for *LC-shift* (red) and *FP-shift* (blue), respectively. System parameters: $N = 50$, $\rho = 0.2$.

system's response for a different set of initial conditions, whereas the responses to different types of stimulation protocols are indicated by red (*LC-shift*) and blue (*FP-shift*). The two dotted lines indicate the system's responses averaged over the ensemble of different initial conditions for the two types of stimulus. One finds that such averaged ϕ^2 quantities show peaks around the coupling strength $\sigma \approx 0.04$, indicating that the system is most sensitive to perturbations near the transition between the regions R_2 and T_1 . Nonetheless, for the same interval of σ , we examine the array's recovery times

after implementing both types of stimulation protocols. In particular, we collect the recovery times T_R [indicated in Fig. 9(a)] for ten different sets of initial conditions. To make the observed values of T_R comparable, we normalize them by the total observation time after the stimulus $T - T_p$, thus obtaining the normalized recovery time $\rho = T_R / (T - T_p)$. Figure 9(c) shows the observed values of ρ as a function of σ . One readily notes that indeed, the larger values of ρ occur near the transition between the regions R_2 and T_1 .

V. DISCUSSION

We have introduced a simple model of an array of diffusively coupled neural oscillators whose local dynamics are poised in the vicinity of a canard transition. This facilitates coexistence between completely synchronous oscillations and avalanche-like patterns of pseudo-synchronous bursting activities. The onset of avalanches is shown to be associated with an inhibitory effect of interactions. This effect is manifested at a range of small coupling strengths, where interactions quench local relaxation oscillations due to an interplay with a maximal canard, a structure that stems from local multiple timescale dynamics. The observed long-term trapping of orbits in the vicinity of an unstable fixed point derives from a combination of a recently introduced concept of phase-sensitive excitability of a periodic orbit³⁰ and the trapping mechanism from Refs. ^{33–35}. Essentially, each unit, as an oscillating system driven by a fluctuating local mean-field, provides a non-uniform response to perturbations along the orbit of a limit cycle, which leads to persistent strong deviations from the unperturbed orbit. Compared to Refs. ^{33–35}, the trapping phenomenon is here extended to a confinement of orbits to a region of maximal canard instead of the original confinement by a chaotic saddle. In terms of concept, one should note that distinct from the classical notion of excitability, the phase-sensitive excitability is not immediately related to the system being close to a bifurcation between stable stationary and oscillatory states, but is instead connected to a canard transition between subthreshold and relaxation oscillations. In a broader context, the important role of a canard transition in pattern formation has already been shown in the cases of alternating (leap-frog) dynamics in small motifs of units³¹ or the different types of coherence–incoherence patterns (solitary states and patched patterns) in non-locally coupled arrays with repulsive and attractive interactions,^{32,50} involving either coupled excitable units or self-oscillating units close to the bifurcation toward the excitable state. Complementing this, here, we have shown the impact of a canard transition on the self-organization and intrinsic structure of avalanche patterns.

We have further demonstrated that avalanches can emerge at the transition between two collective regimes featuring lower and higher spiking activity rates. The avalanches have been shown to satisfy power-law behaviors regarding avalanche cluster sizes and laminar times. Moreover, the system generating avalanches has been found to bear classical indicators of criticality under external perturbations, including reduced resilience and critical slowing down. So far, neuronal avalanches have primarily been suggested to arise in the vicinity of two very different types of continuous transitions, namely, the transition between absorbing and active phases or at the onset of synchronization. Also, implementing various adaptation rules, such as synaptic plasticity or excitability adaptation, it has

been indicated that models of neuronal networks may self-organize to a critical state facilitating avalanches, which has linked the onset of avalanches to self-organized criticality.^{23,73–75} On the other hand, it has been found that avalanches may emerge from critical dynamics in balanced excitatory–inhibitory networks, where they can be combined with different types of collective oscillation rhythms.^{76,77} The latter can involve two types of scenarios: one with collective rhythms and avalanches coexisting (either independently or with rhythms modifying the features of avalanches) and the other having the rhythms embedded in the avalanche activity.^{20,78} Finally, it has been reported that scale-invariant avalanches may also emerge without the neural network operating at criticality, but just due to a balanced input or its interaction with noise.^{76,77,79,80}

In light of the above studies, our findings apparently point to a possibility of independent coexistence between a synchronous oscillation rhythm and a transiently synchronous avalanche activity, whereby the mechanism facilitating such coexistence requires two ingredients: the non-local diffusive interactions and local dynamics in the vicinity of a canard transition between subthreshold and relaxation oscillations. In terms of the states involved, the character of the critical transition supporting avalanches is most similar to the one in Ref. 24, in the sense that it also mediates between the states with lower- and higher spiking rates. Nevertheless, in contrast to our study, the model in Ref. 24 has a more complex structure combining stochastic local dynamics with a quenched disorder in network topology, and criticality occurs in the vicinity of a spinodal line of a discontinuous transition. For future research, it would be important to gain insight into the switching dynamics between the coexisting regimes in our model, both under the impact of noise and when applying different types of external stimulation.

ACKNOWLEDGMENTS

M.C. thanks Javiera Contreras for the support and help with the design of the figures.

E.S.M. acknowledges the support by the Deutsche Forschungsgemeinschaft (DFG) via Project No. 454054251. This work was supported by the Deutsche Forschungsgemeinschaft (DFG, German Research Foundation)—Projektnummer—163436311—SFB 910.

A.Z. acknowledges support by the Deutsche Forschungsgemeinschaft (DFG, German Research Foundation)—Projektnummer—163436311—SFB 910.

P.H. acknowledges support by the Deutsche Forschungsgemeinschaft (DFG, German Research Foundation)—Project ID 434434223—SFB 1461.

I.F. acknowledges the funding from the Institute of Physics Belgrade through grant by the Ministry of Science, Technological Development and Innovation of the Republic of Serbia and the partial support by the ANSO—Alliance of International Science Organizations Collaborative Research Projects and Training Projects (Grant No. ANSO-CR-PP-2022-05).

AUTHOR DECLARATIONS

Conflict of Interest

The authors have no conflicts to disclose.

Author Contributions

Max Contreras: Conceptualization (equal); Data curation (equal); Formal analysis (equal); Funding acquisition (equal); Investigation (equal); Methodology (equal); Project administration (equal); Resources (equal); Software (equal); Supervision (equal); Validation (equal); Visualization (equal); Writing – original draft (equal); Writing – review & editing (equal). **Everton S. Medeiros:** Conceptualization (equal); Data curation (equal); Formal analysis (equal); Funding acquisition (equal); Investigation (equal); Methodology (equal); Project administration (equal); Resources (equal); Software (equal); Supervision (equal); Validation (equal); Visualization (equal); Writing – original draft (equal); Writing – review & editing (equal). **Anna Zakharova:** Conceptualization (equal); Data curation (equal); Formal analysis (equal); Funding acquisition (equal); Investigation (equal); Methodology (equal); Project administration (equal); Resources (equal); Software (equal); Supervision (equal); Validation (equal); Visualization (equal); Writing – original draft (equal); Writing – review & editing (equal). **Philipp Hövel:** Conceptualization (equal); Data curation (equal); Formal analysis (equal); Funding acquisition (equal); Investigation (equal); Methodology (equal); Project administration (equal); Resources (equal); Software (equal); Supervision (equal); Validation (equal); Visualization (equal); Writing – original draft (equal); Writing – review & editing (equal). **Igor Franović:** Conceptualization (equal); Data curation (equal); Formal analysis (equal); Funding acquisition (equal); Investigation (equal); Methodology (equal); Project administration (equal); Software (equal); Supervision (equal); Validation (equal); Visualization (equal); Writing – original draft (equal); Writing – review & editing (equal).

DATA AVAILABILITY

The data that support the findings of this study are available from the corresponding author upon reasonable request.

REFERENCES

- ¹M. Scheffer, *Critical Transitions in Nature and Society* (Princeton University Press, 2009).
- ²M. Scheffer, S. R. Carpenter, T. M. Lenton, J. Bascompte *et al.*, “Anticipating critical transitions,” *Science* **338**, 344 (2012).
- ³C. Kuehn, “A mathematical framework for critical transitions: Bifurcations, fast–slow systems and stochastic dynamics,” *Phys. D* **240**, 1020 (2011).
- ⁴G. Buzsáki and A. Draguhn, “Neuronal oscillations in cortical networks,” *Science* **304**, 1926 (2004).
- ⁵G. Buzsáki, *Rhythms of the Brain* (Oxford University Press, 2006).
- ⁶J. M. Beggs and D. Plenz, “Neuronal avalanches in neocortical circuits,” *J. Neurosci.* **23**, 11167 (2003).
- ⁷J. M. Beggs and D. Plenz, “Neuronal avalanches are diverse and precise activity patterns that are stable for many hours in cortical slice cultures,” *J. Neurosci.* **24**, 5216 (2004).
- ⁸D. Plenz and T. C. Thiagarajan, “The organizing principles of neuronal avalanches: Cell assemblies in the cortex?,” *Trends Neurosci.* **30**, 101 (2007).
- ⁹G. Hahn, T. Petermann, M. N. Havenith *et al.*, “Neuronal avalanches in spontaneous activity in vivo,” *J. Neurophysiol.* **104**, 3312 (2010).
- ¹⁰O. Kinouchi and M. Copelli, “Optimal dynamical range of excitable networks at criticality,” *Nat. Phys.* **2**, 348 (2006).
- ¹¹D. Chialvo, “Emergent complex neural dynamics,” *Nat. Phys.* **6**, 744 (2010).
- ¹²W. L. Shew and D. Plenz, “The functional benefits of criticality in the cortex,” *Neuroscientist* **19**, 88 (2013).

- ¹³L. Cocchi, L. L. Gollo, A. Zalesky, and M. Breakspear, "Criticality in the brain: A synthesis of neurobiology, models and cognition," *Prog. Neurobiol.* **158**, 132–152 (2017).
- ¹⁴M. A. Muñoz, "Colloquium: Criticality and dynamical scaling in living systems," *Rev. Mod. Phys.* **90**, 031001 (2018).
- ¹⁵B. Mariani, G. Nicoletti, M. Bisio *et al.*, "Disentangling the critical signatures of neural activity," *Sci. Rep.* **12**, 10770 (2022).
- ¹⁶A. J. Fontenele *et al.*, "Criticality between cortical states," *Phys. Rev. Lett.* **122**, 208101 (2019).
- ¹⁷L. Dalla Porta and M. Copelli, "Modeling neuronal avalanches and long-range temporal correlations at the emergence of collective oscillations: Continuously varying exponents mimic M/EEG results," *PLoS Comput. Biol.* **15**, e1006924 (2019).
- ¹⁸S. di Santo, P. Villegas, R. Burioni, and M. A. Muñoz, "Landau-Ginzburg theory of cortex dynamics: Scale-free avalanches emerge at the edge of synchronization," *Proc. Natl. Acad. Sci. U. S. A.* **115**, E1356 (2018).
- ¹⁹E. Niebur and D. Plenz, *Criticality in Neural Systems* (Wiley-VCH, 2014).
- ²⁰E. D. Gireesh and D. Plenz, "Neuronal avalanches organize as nested theta- and beta/gamma-oscillations during development of cortical layer 2/3," *Proc. Natl. Acad. Sci. U. S. A.* **105**, 7576 (2008).
- ²¹H. Yang, W. L. Shew, R. Roy, and D. Plenz, "Maximal variability of phase synchrony in cortical networks with neuronal avalanches," *J. Neurosci.* **32**, 1061 (2012).
- ²²A. Levina, J. M. Herrmann, and T. Geisel, "Phase transitions towards criticality in a neural system with adaptive interactions," *Phys. Rev. Lett.* **102**, 118110 (2009).
- ²³D. Millman, S. Mihalas, A. Kirkwood, and E. Niebur, "Self-organized criticality occurs in non-conservative neuronal networks during 'up' states," *Nat. Phys.* **6**, 801 (2010).
- ²⁴S. Scarpetta, I. Apicella, L. Minati, and A. de Candia, "Hysteresis, neural avalanches, and critical behavior near a first-order transition of a spiking neural network," *Phys. Rev. E* **97**, 062305 (2018).
- ²⁵S. R. Miller, S. Yu, and D. Plenz, "The scale-invariant, temporal profile of neuronal avalanches in relation to cortical gamma oscillations," *Sci. Rep.* **9**, 16403 (2019).
- ²⁶S. di Santo, P. Villegas, R. Burioni, and M. A. Muñoz, "Simple unified view of branching process statistics: Random walks in balanced logarithmic potentials," *Phys. Rev. E* **95**, 032115 (2017).
- ²⁷T. Vo and M. Wechselberger, "Canards of folded saddle-node type I," *SIAM J. Math. Anal.* **47**, 3235 (2015).
- ²⁸M. Wechselberger, J. Mitry, and J. Rinzel, "Canard theory and excitability," in *Nonautonomous Dynamical Systems in the Life Sciences*, edited by P. Kloeden and C. Pötzsche (Springer International Publishing, Cham, Switzerland, 2013), pp. 89–132.
- ²⁹C. Kuehn, *Multiple Time Scale Dynamics* (Springer International Publishing, Cham, Switzerland, 2015).
- ³⁰I. Franović, O. E. Omel'chenko, and M. Wolfrum, "Phase-sensitive excitability of a limit cycle," *Chaos* **28**, 071105 (2018).
- ³¹S. R. Eydám, I. Franović, and M. Wolfrum, "Leap-frog patterns in systems of two coupled FitzHugh-Nagumo units," *Phys. Rev. E* **99**, 042207 (2019).
- ³²I. Franović, S. Eydám, N. Semenova, and A. Zakharova, "Unbalanced clustering and solitary states in coupled excitable systems," *Chaos* **32**, 011104 (2022).
- ³³E. S. Medeiros, R. O. Medrano-T, I. L. Caldas, and U. Feudel, "Boundaries of synchronization in oscillator networks," *Phys. Rev. E* **98**, 030201 (2018).
- ³⁴E. S. Medeiros, R. O. Medrano-T, I. L. Caldas, T. Tél, and U. Feudel, "State-dependent vulnerability of synchronization," *Phys. Rev. E* **100**, 052201 (2019).
- ³⁵E. S. Medeiros, R. O. Medrano-T, I. L. Caldas, and U. Feudel, "The impact of chaotic saddles on the synchronization of complex networks of discrete-time units," *J. Phys. Complex.* **2**, 035002 (2021).
- ³⁶C. Meisel, A. Klaus, C. Kuehn, and D. Plenz, "Critical slowing down governs the transition to neuron spiking," *PLoS Comput. Biol.* **11**, e1004097 (2015).
- ³⁷T. Wilkat, T. Rings, and K. Lehnertz, "No evidence for critical slowing down prior to human epileptic seizures," *Chaos* **29**, 091104 (2019).
- ³⁸M. I. Maturana, C. Meisel, K. Dell *et al.*, "Critical slowing down as a biomarker for seizure susceptibility," *Nat. Commun.* **11**, 2172 (2020).
- ³⁹E. M. Izhikevich, *Dynamical Systems in Neuroscience: The Geometry of Excitability and Bursting* (The MIT Press, Cambridge, MA, 2007).
- ⁴⁰A. Saha and U. Feudel, "Riddled basins of attraction in systems exhibiting extreme events," *Chaos* **28**, 033610 (2018).
- ⁴¹A. Saha and U. Feudel, "Characteristics of in-out intermittency in delay-coupled FitzHugh-Nagumo oscillators," *Eur. Phys. J. Spec. Top.* **227**, 1205 (2018).
- ⁴²A. Saha and U. Feudel, "Extreme events in FitzHugh-Nagumo oscillators coupled with two time delays," *Phys. Rev. E* **95**, 062219 (2017).
- ⁴³M. Krupa and P. Szmolyan, "Extending geometric singular perturbation theory to nonhyperbolic points—Fold and canard points in two dimensions," *SIAM J. Math. Anal.* **33**, 286 (2001).
- ⁴⁴M. Desroches, J. Guckenheimer, B. Krauskopf, C. Kuehn, H. M. Osinga, and M. Wechselberger, "Mixed-mode oscillations with multiple time scales," *SIAM Rev.* **54**, 211 (2012).
- ⁴⁵S. M. Baer and T. Erneux, "Singular Hopf bifurcation to relaxation oscillations," *SIAM J. Appl. Math.* **46**, 721 (1986).
- ⁴⁶V. A. Makarov, V. I. Nekorkin, and M. G. Velarde, "Spiking behavior in a noise-driven system combining oscillatory and excitatory properties," *Phys. Rev. Lett.* **86**, 3431 (2001).
- ⁴⁷M. Galassi *et al.*, *GNU Scientific Library Reference Manual*, 3rd ed. (Free Software Foundation, Inc., 2009), ISBN: 0954612078.
- ⁴⁸A. Pikovsky, M. Rosenblum, and J. Kurths, *Synchronization: A Universal Concept in Nonlinear Sciences*, Cambridge Nonlinear Science Series (Cambridge University Press, 2001).
- ⁴⁹M. Wolfrum, O. E. Omel'chenko, and J. Sieber, "Regular and irregular patterns of self-localized excitation in arrays of coupled phase oscillators," *Chaos* **25**, 053113 (2015).
- ⁵⁰I. Franović and S. Eydám, "Patched patterns and emergence of chaotic interfaces in arrays of nonlocally coupled excitable systems," *Chaos* **32**, 091102 (2022).
- ⁵¹G. Ansmann, R. Karnatak, K. Lehnertz, and U. Feudel, "Extreme events in excitable systems and mechanisms of their generation," *Phys. Rev. E* **88**, 052911 (2013).
- ⁵²R. Karnatak, G. Ansmann, U. Feudel, and K. Lehnertz, "Route to extreme events in excitable systems," *Phys. Rev. E* **90**, 022917 (2014).
- ⁵³S. Bialowski, G. Ansmann, and H. Kantz, "Data-driven prediction and prevention of extreme events in a spatially extended excitable system," *Phys. Rev. E* **92**, 042910 (2015).
- ⁵⁴G. Ansmann, K. Lehnertz, and U. Feudel, "Self-induced switchings between multiple space-time patterns on complex networks of excitable units," *Phys. Rev. X* **6**, 011030 (2016).
- ⁵⁵H. Nishimori and G. Ortiz, *Elements of Phase Transitions and Critical Phenomena* (Oxford University Press, 2010).
- ⁵⁶C. T. Kello, G. D. A. Brown *et al.*, "Scaling laws in cognitive sciences," *Trends Cognit. Sci.* **14**, 223 (2010).
- ⁵⁷J. Wilting and V. Priesemann, "25 years of criticality in neuroscience—Established results, open controversies, novel concepts," *Curr. Opin. Neurobiol.* **58**, 105–111 (2019).
- ⁵⁸S. Scarpetta and A. de Candia, "Neural avalanches at the critical point between replay and non-replay of spatiotemporal patterns," *PLoS One* **8**, e64162 (2013).
- ⁵⁹P. Moretti and M. Muñoz, "Griffiths phases and the stretching of criticality in brain networks," *Nat. Commun.* **4**, 2521 (2013).
- ⁶⁰V. Zimmern, "Why brain criticality is clinically relevant: A scoping review," *Front. Neural Circuits* **14**, 54 (2020).
- ⁶¹N. Gutjahr, P. Hövel, and A. Viol, "Controlling extended criticality via modular connectivity," *J. Phys. Complex.* **2**, 035023 (2021).
- ⁶²S. Yu, A. Klaus, H. Yang, and D. Plenz, "Scale-invariant neuronal avalanche dynamics and the cut-off in size distributions," *PLoS One* **9**, e99761 (2014).
- ⁶³O. Shriki, J. Alstott, F. Carver *et al.*, "Neuronal avalanches in the resting MEG of the human brain," *J. Neurosci.* **33**, 7079 (2013).
- ⁶⁴A. Klaus, S. Yu, and D. Plenz, "Statistical analyses support power law distributions found in neuronal avalanches," *PLoS One* **6**, e19779 (2011).
- ⁶⁵A. Bellay, T. Klaus, S. Seshadri, and D. Plenz, "Irregular spiking of pyramidal neurons organizes as scale-invariant neuronal avalanches in the awake state," *eLife* **4**, e07224 (2015).
- ⁶⁶J. Touboul and A. Destexhe, "Can power-law scaling and neuronal avalanches arise from stochastic dynamics?," *PLoS One* **5**, e8982 (2010).

- ⁶⁷J. Touboul and A. Destexhe, “Power-law statistics and universal scaling in the absence of criticality,” *Phys. Rev. E* **95**, 012413 (2017).
- ⁶⁸T. J. Taylor, C. Hartley, P. L. Simon *et al.*, “Identification of criticality in neuronal avalanches: I. A theoretical investigation of the non-driven case,” *J. Math. Neurosci.* **3**, 5 (2013).
- ⁶⁹G. Boffetta, V. Carbone, P. Giuliani, P. Veltri, and A. Vulpiani, “Power laws in solar flares: Self-organized criticality or turbulence?,” *Phys. Rev. Lett.* **83**, 4662–4665 (1999).
- ⁷⁰M. Bartolozzi, D. Leinweber, and A. Thomas, “Self-organized criticality and stock market dynamics: An empirical study,” *Phys. A* **350**, 451–465 (2005).
- ⁷¹W. L. Shew, H. Yang, T. Petermann, R. Roy, and D. Plenz, “Neuronal avalanches imply maximum dynamic range in cortical networks at criticality,” *J. Neurosci.* **29**, 15595 (2009).
- ⁷²D. B. Larremore, W. L. Shew, and J. G. Restrepo, “Predicting criticality and dynamic range in complex networks: Effects of topology,” *Phys. Rev. Lett.* **106**, 058101 (2011).
- ⁷³A. Levina, J. Herrmann, and T. Geisel, “Dynamical synapses causing self-organized criticality in neural networks,” *Nat. Phys.* **3**, 857 (2007).
- ⁷⁴M. Rybarsch and S. Bornholdt, “Avalanches in self-organized critical neural networks: A minimal model for the neural SOC universality class,” *PLoS One* **9**, e93090 (2014).
- ⁷⁵S. Landmann, L. Baumgarten, and S. Bornholdt, “Self-organized criticality in neural networks from activity-based rewiring,” *Phys. Rev. E* **103**, 032304 (2021).
- ⁷⁶S. S. Poil, R. Hardstone, H. D. Mansvelder, and K. Linkenkaer-Hansen, “Critical-state dynamics of avalanches and oscillations jointly emerge from balanced excitation/inhibition in neuronal networks,” *J. Neurosci.* **32**, 9817 (2012).
- ⁷⁷J. Liang, T. Zhou, and C. Zhou, “Hopf bifurcation in mean field explains critical avalanches in excitation-inhibition balanced neuronal networks: A mechanism for multiscale variability,” *Front. Syst. Neurosci.* **14**, 580011 (2020).
- ⁷⁸F. Lombardi, H. J. Herrmann, D. Plenz, and L. De Arcangelis, “On the temporal organization of neuronal avalanches,” *Front. Syst. Neurosci.* **8**, 204 (2014).
- ⁷⁹F. Lombardi, H. J. Herrmann, C. Perrone-Capano, D. Plenz, and L. De Arcangelis, “Balance between excitation and inhibition controls the temporal organization of neuronal avalanches,” *Phys. Rev. Lett.* **108**, 228703 (2012).
- ⁸⁰S. H. Gautam, T. T. Hoang, K. McClanahan, S. K. Grady, and W. L. Shew, “Maximizing sensory dynamic range by tuning the cortical state to criticality,” *PLoS Comput. Biol.* **11**, e1004576 (2015).

Perspectives on adaptive dynamical systems



Cite as: Chaos 33, 071501 (2023); doi: 10.1063/5.0147231

Submitted: 20 February 2023 · Accepted: 24 May 2023 ·

Published Online: 24 July 2023



View Online



Export Citation



CrossMark

Jakub Sawicki,^{1,2,a)} Rico Berner,^{3,a)} Sarah A. M. Loos,^{4,a)} Mehrnaz Anvari,^{1,5} Rolf Bader,⁶ Wolfram Barfuss,^{7,8} Nicola Botta,^{1,9} Nuria Brede,^{1,10} Igor Franović,¹¹ Daniel J. Gauthier,^{1,2,13} Sebastian Goldt,¹⁴ Aida Hajizadeh,¹⁵ Philipp Hövel,^{16,17} Omer Karin,¹⁸ Philipp Lorenz-Spreen,¹⁹ Christoph Miehl,^{20,21} Jan Mölter,²² Simona Olmi,^{23,24} Eckehard Schöll,^{1,25,26} Alireza Seif,²⁷ Peter A. Tass,²⁸ Giovanni Volpe,²⁹ Serhiy Yanchuk,^{1,30} and Jürgen Kurths^{1,3}

AFFILIATIONS

¹Potsdam Institute for Climate Impact Research, Telegrafenberg, 14473 Potsdam, Germany

²Akademie Basel, Fachhochschule Nordwestschweiz FHNW, Leonhardsstrasse 6, 4009 Basel, Switzerland

³Department of Physics, Humboldt-Universität zu Berlin, Newtonstraße 15, 12489 Berlin, Germany

⁴DAMTP, University of Cambridge, Wilberforce Road, Cambridge CB3 0WA, United Kingdom

⁵Fraunhofer Institute for Algorithms and Scientific Computing, Schloss Birlinghoven, 53757 Sankt-Augustin, Germany

⁶Institute of Systematic Musicology, University of Hamburg, Hamburg, Germany

⁷Transdisciplinary Research Area: Sustainable Futures, University of Bonn, 53113 Bonn, Germany

⁸Center for Development Research (ZEF), University of Bonn, 53113 Bonn, Germany

⁹Department of Computer Science and Engineering, Chalmers University of Technology, 412 96 Göteborg, Sweden

¹⁰Department of Computer Science, University of Potsdam, An der Bahn 2, 14476 Potsdam, Germany

¹¹Scientific Computing Laboratory, Center for the Study of Complex Systems, Institute of Physics Belgrade, University of Belgrade, Pregrevica 118, 11080 Belgrade, Serbia

¹²Department of Physics and Electrical and Computer Engineering, The Ohio State University, 191 West Woodruff Ave., Columbus, Ohio 43210, USA

¹³ResCon Technologies, LLC, 1275 Kinnear Rd., Suite 239, Columbus, Ohio 43212, USA

¹⁴Department of Physics, International School of Advanced Studies (SISSA), Trieste, Italy

¹⁵Research Group Comparative Neuroscience, Leibniz Institute for Neurobiology, Magdeburg, Germany

¹⁶Theoretical Physics, Saarland University, 66123 Saarbrücken, Germany

¹⁷Center for Biophysics, Saarland University, 66123 Saarbrücken, Germany

¹⁸Department of Mathematics, Imperial College London, London SW7 2AZ, United Kingdom

¹⁹Center for Adaptive Rationality, Max Planck Institute for Human Development, Lentzeallee 94, 14195 Berlin, Germany

²⁰Max Planck Institute for Brain Research, Max-von-Laue-Straße 4, 60438 Frankfurt am Main, Germany

²¹School of Life Sciences, Technical University of Munich, Alte Akademie 8, 85354 Freising, Germany

²²Department of Mathematics, School of Computation, Information and Technology, Technical University of Munich, Boltzmannstraße 3, 85748 Garching bei München, Germany

²³CNR - Consiglio Nazionale delle Ricerche - Istituto dei Sistemi Complessi, via Madonna del Piano 10, I-50019 Sesto Fiorentino, Italy

²⁴INFN, Sezione di Firenze, Via Sansone 1, I-50019 Sesto Fiorentino (FI), Italy

²⁵Institut für Theoretische Physik, Technische Universität Berlin, Hardenbergstraße 36, 10623 Berlin, Germany

²⁶Bernstein Center for Computational Neuroscience Berlin, Humboldt-Universität, 10115 Berlin, Germany

²⁷Pritzker School of Molecular Engineering, The University of Chicago, Chicago, Illinois 60637, USA

²⁸Department of Neurosurgery, Stanford University School of Medicine, Stanford, California 94304, USA

²⁹Department of Physics, University of Gothenburg, Gothenburg, Sweden

³⁰Department of Mathematics, Humboldt-Universität zu Berlin, Rudower Chaussee 25, 12489 Berlin, Germany

^{a)}Authors to whom correspondence should be addressed: zergon@gmx.net; rico.berner@physik.hu-berlin.de; and s12127@cam.ac.uk

ABSTRACT

Adaptivity is a dynamical feature that is omnipresent in nature, socio-economics, and technology. For example, adaptive couplings appear in various real-world systems, such as the power grid, social, and neural networks, and they form the backbone of closed-loop control strategies and machine learning algorithms. In this article, we provide an interdisciplinary perspective on adaptive systems. We reflect on the notion and terminology of adaptivity in different disciplines and discuss which role adaptivity plays for various fields. We highlight common open challenges and give perspectives on future research directions, looking to inspire interdisciplinary approaches.

© 2023 Author(s). All article content, except where otherwise noted, is licensed under a Creative Commons Attribution (CC BY) license (<http://creativecommons.org/licenses/by/4.0/>). <https://doi.org/10.1063/5.0147231>

Charles Darwin taught us that it is not the strongest of a species that survive, but the ones who are most *adaptable* to change. Likewise, the process of learning can be considered to be “any change in a system that produces a more or less permanent change in its capacity for adapting to its environment.”¹ These two statements clearly underline the importance of adaptivity for life. Simply speaking, one could say: “To live means to adapt.” At the same time, adaptive mechanisms are also the essential features of (“intelligent”) artificial systems, from state-of-the-art control techniques for complex systems, to machine learning approaches and robotic systems. Perhaps the most basic notion of adaptivity is the ability to adjust to condition or change over time. This ability is an essential component of various natural and artificial processes considered in different research fields. It is also the key property of the human mind to perceive and enjoy music and visual arts and to create and invent and, thus, is the driving force behind all cultural achievements. Adaptive mechanisms take place on a wide range of spatial and temporal scales, from the adaptation of a single neuron, over the ability of a social system to adjust to a changing environment, up to the adaptation of the Earth system’s climate. Over the last few decades, substantial know-how to describe and control complex systems has been developed in different scientific areas. With the increasing potential of modern technology, on the one hand, and the enormous challenges facing humanity as a large social system, on the other hand, there is a renewed interest to take an interdisciplinary approach to adaptivity. This article gives an overview of the role of adaptive systems in different scientific fields and highlights prospects for future research directions on adaptivity.

I. INTRODUCTION

A widespread feature of natural and artificial complex systems is their adaptivity. There is lively interest in modeling and understanding the various forms of adaptive mechanisms appearing in real-world systems and to develop new control strategies based on adaptive mechanisms.

Such control strategies play an essential role, especially in *complex systems science*, as they reflect to some extent the understanding we have of a complex system. Because of their interactions, relationships, dependencies, nonlinearities, and high-dimensionalities, the behavior of complex systems is inherently difficult to model. Machine learning tools are often used to solve predictions about complex systems. However, applying machine

learning to complex systems is quite challenging because the training data set has to reflect the diverse dynamics. This usually results in the data set being very large, making such methods well suited for so-called big data.

Moreover, the focus today is not only on complex systems consisting of many interacting components, but as an interdisciplinary field, complex systems actually attract contributions from many different fields. Despite the strong drive for innovation and application of adaptive complex systems in various scientific fields, as conceptualized in Fig. 1, cross-fertilization between different disciplines is hardly promoted. A partial answer toward a mathematical theory of adaptive systems has been developed since the 1960s for control and optimization problems,^{2–6} including stochastic systems,⁷ a systematic exposition of the interrelations and interplay between adaptation and learning,⁷ as well as the use of the speed gradient



FIG. 1. Adaptivity across different scientific disciplines (blue) and applications (yellow) as well as its strong interlinking and interlocking, similar to a system of gears.

method⁸ in adaptive control of network topology.⁹ In this review, we discuss recent interdisciplinary applications of adaptive dynamical systems and focus on collecting ideas that would allow for including modern research fields, such as complex network theory, power grid modeling, or climate systems where a full mathematical theory is still elusive.

This Perspective article aims to make a first step in opening a dialogue between different scientific communities and the diverse formalism of their languages. It summarizes different perspectives on the concept of adaptivity and shows which open challenges are waiting to be taken up. To this end, it brings together the viewpoints on the topic of adaptivity of researchers from a wide range of backgrounds, including physics, biology, mathematics, computer and social science, and musicology. This Perspective article features a collection of contributions from experts representing various scientific disciplines. The individual contributions are guided by the following questions:

1. What role do adaptive mechanisms play in their respective field? How can one *define* adaptivity? What *methods* are related to adaptivity? What *applications* are related to adaptivity?
2. Which *challenges* can be solved by using adaptive mechanisms? Are there *open research questions* related to adaptivity? What are the *future perspectives*?

The article consists of four main topical parts: Network Perspective and Models of Adaptivity (Sec. II), Perception and Neural Adaptivity (Sec. III), Adaptivity and Artificial Learning (Sec. IV), and Adaptivity in Socio-Economic Systems (Sec. V). Each part contains perspectives from several specialists active in the respective area of research.

In Sec. II, we discuss different ideas on the definition of adaptivity from the perspective of nonlinear dynamics, control theory, and network science, and how adaptive systems can be used to understand real-world systems of interacting units (networks). In the beginning, a generic viewpoint on adaptivity with regard to the interplay of structure and function in dynamical network theory is introduced (Sec. II A). Building upon this idea, adaptation is discussed as a slowly evolving feedback mechanism (Sec. II B). Further highlighted are the interplay of adaptivity and noise as well as the role of adaptive control mechanisms in inducing critical transitions. Complementing the discussion on the notion of adaptivity, the question is raised: Is adaptivity in nonlinear dynamics, neuroscience, artificial intelligence, and socio-economic dynamics instances of the same abstract notion? To answer this question, the framework of dependent type theory is introduced and suggested to be utilized for comparing different notions of adaptivity (Sec. II C). Section II D summarizes the first part from the complex networks perspective where the interplay between dynamics and network topology is in the center of interest. Here, various connections between models featuring adaptivity are shown, and adaptive network models are highlighted as a powerful modeling approach toward real-world dynamical systems.

Section III focuses on the important role of adaptation in physiology, especially in the form of perception mechanisms and neuronal plasticity. Evolution tends to come up with similar solutions to related problems. The physiological properties of biological systems can be seen as complex networks of interactions, which are

known as regulatory networks. Under similar contexts, such regulatory networks of distinct systems share similarities—these are so-called adaptation motifs, where specific adaptation motifs have distinct functional significance (Sec. III A). Organisms, and, hence, their brains, have developed strategies to adapt to modifications in the environment across timescales, from adaptation to sudden changes in sensory stimuli to long timescales of evolutionary processes. Also, learning and memory formation can be viewed as adaptive processes, where learning in neuronal circuits relies on short- and specifically long-term synaptic plasticity (Sec. III B). Neuronal systems often consist of millions of neurons whose individual dynamics are often not accessible with mathematical methods. However, for the macroscopic collective dynamics emerging in such systems, several methodologies have been developed. A powerful method is the next generation neural mass approach, which allows for a low-dimensional reduction of neuronal populations equipped with frequency adaptation and short-term plasticity (Sec. III C). Computational models have proven to be useful for understanding the mechanisms underlying adaptation mechanisms in the brain. In medicine, for example, deep brain stimulation is the gold standard for treating medically refractory Parkinson's patients who suffer from various motor and non-motor-symptoms and display an abnormal neuronal synchrony. Considering synaptic plasticity in computational modeling enables to design appropriate therapeutic stimulation (Sec. III D). Music is a constant adaptation process, where adaptations are active processes, including changing strategies, emotional reactions, or the development of new abilities. A physical culture theory is assuming music as an adaptive system to be represented by spatiotemporal electric fields in the brain, consisting of impulses, physical energy bursts, sent out, returning with certain damping, thereby causing new impulses (Sec. III E). In experiments, the magnitude of the neural response in the auditory cortex is decreasing if the same stimulus is presented repetitively with a constant stimulus onset interval. The gradual reduction of the magnitude is termed adaptation and is suggested to be due to modulations of synaptic coupling between neurons (Sec. III F).

Another wide field where adaptivity plays a key role is artificial intelligence and machine learning. We illuminate this field in Sec. IV. Indeed, at its very heart, “learning” means “adapting” to input data. The adapting system can, therefore, be, for example, a real or “artificial brain,” such as a neural network, and the adaptation rules may depend on the learning task, network architecture, and learning algorithm. Section IV provides a variety of perspectives on adaptivity in artificial learning, discussing current research, new applications, and open challenges. The methods span from deep neural networks (Sec. IV A), recurrent neural networks (Sec. IV B), and reinforcement learning (Sec. IV D) to reservoir computing (Sec. IV C). A common focus throughout Sec. IV is the two-way relationship between natural sciences and machine learning. On the one hand, tools from theoretical physics may provide insights into the functionality of machine learning algorithms, pushing our understanding beyond the “black box” paradigm. In particular, concepts from statistical physics are explored to address fundamental questions, such as reconciling the success of artificial learning with the curse of dimensionality (see Sec. IV A). Second, simple models inspired from physics are used to generate training data to probe specific features of machine learning algorithms, such as their

ability to extract and utilize memory of a given input sequence (see Sec. IV B). On the other hand, the usage of machine learning tools to investigate (Secs. IV B and IV D) or to control (Secs. IV C and IV E) complex physical systems is a field of rapidly growing relevance. A sticking example is how reservoir-computing techniques open up new strategies to control chaotic nonlinear dynamics (Sec. IV C). In this context, another major challenge concerns the exploration of the rules of (and the control of) the collective or cooperative behavior of self-organizing multi-agent systems; from the design of new algorithms (Sec. IV D) to the control of real-world microscopic “biomimetic” intelligent particles and swarms of robots (Sec. IV E).

Section V is devoted to the large field of a socio-economic system. Here, adaptive mechanisms appear naturally and play an important role for their modeling. Adaptive networks also play a central role not only for realistic investigations of spreading dynamics but can help to study and design interventions for disease containment, mitigation, and eradication. Elaborating on this, in the last section of this fourth part, an overview on adaptivity in epidemiology is provided (Sec. V A). Another interesting topic is the interaction of social and epidemic systems where also the coevolutionary (adaptive) dynamics of the interaction structure and the dynamical units is in the focus of recent research (Sec. V B). Apart from the connection to epidemiology, social systems themselves are adaptive. Here, adaptivity can be regarded as the process of changing social systems through external influences. In this context, understanding these changes induced by increasing connectivity through online platforms or increasing availability of information are driving research questions (Sec. V C). The human factor is also considerably important for the (adaptive) control of power grids, e.g., considering a temporally changing energy consumption (Sec. V D). The challenges in order to be compatible with new circumstances are discussed from different viewpoints. In power grid systems, we find the adaptation of both the topology and dynamics of the grid. On the other side, there is an anthropogenic influence on the Earth system (Sec. V E). Here, we can learn much from the past about adaptive mechanisms in this complex system and the perturbations to which it is subjected. With this, Sec. VI of this article provides challenging open research questions that could be solved by using adaptivity one or the other way.

II. NETWORK PERSPECTIVE AND MODELS OF ADAPTIVITY

In this section, different ideas are discussed on how adaptivity can be defined in the context of nonlinear dynamics, control theory, and network science, and how adaptive systems could be used to understand real-world systems of interacting units (networks). Perspectives are provided on how different dynamical models featuring adaptive mechanisms are related and how these models can be used to investigate the dynamics of natural or man-made systems.

A. Structural adaptivity in dynamical networks—By Serhiy Yanchuk

Adaptivity is a general concept commonly understood as a process or ability of a system to adjust itself to changing (external)

conditions. Thus, when speaking of adaptivity, one implicitly distinguishes the “conditions” (X) and the adaptation property (Y). In the following, an attempt is made to define these two variables (components) with a special reference to the theory of adaptive dynamical networks.

- **The structure** Y is the adaptation matter, the part of the system responsible for the adaptation properties. In adaptive dynamical networks, this is usually understood as a network structure represented by connectivity and/or connection weights. By analogy with dynamical networks and neuroscience in general, we refer to this variable as a *structure*.
- **The function** X represents the conditions that trigger the adaptation. In adaptive dynamical networks, this is usually the dynamic state of the network, i.e., the collective and individual dynamics of the nodes. This factor may also include stochastic or external perturbations. These variables usually change with time, i.e., $X(t)$ in the case of temporal adaptation. Following the terminology of the dynamical networks, we generally refer to this variable as *function*.

The non-adaptive systems correspond to a constant structure $Y = Y_0$, which is independent of the function $X(t)$. By assuming that X is governed by a system of differential equations, a general representation of a *non-adaptive* system is

$$\dot{X}(t) = f(X, Y), \quad (1)$$

$$\dot{Y} = 0. \quad (2)$$

We assume here the general case that the structure Y influences the function X . Systems (1) and (2) are often used for modeling neural networks with fixed connectivity Y . An example of a *non-adaptive* dynamical network is the coupled system

$$\dot{x}_i = f_i(x_i, t) + \sum_{j=1}^N \kappa_{ij} g_{ij}(x_i, x_j),$$

where $x_i(t)$ determines the state of node $i = 1, \dots, N$ and κ_{ij} is the connection weight ($\kappa_{ij} = 0$ if there is no connection). The absence of network adaptivity is indicated by the fixed structure κ_{ij} . The function variable in this example is $X = (x_1, \dots, x_N)$, while the structure variable is $Y = \{\kappa_{ij}\}_{i,j=1,\dots,N}$ and it is constant. The class of non-adaptive networks is extremely useful for modeling many processes and phenomena in nature and technology;^{10–12} see also Secs. II D and V A–V C.

When the structure depends on the function, we obtain an adaptive system

$$\dot{X}(t) = f(X, Y), \quad (3)$$

$$\dot{Y}(t) = g(X, Y), \quad (4)$$

with a mutual structure–function interaction.¹³

An example of an adaptive dynamical network is

$$\dot{x}_i = f_i(x_i, t) + \sum_{j=1}^N \kappa_{ij} g(x_i, x_j), \quad (5)$$

$$\dot{\kappa}_{ij} = h(x_i, x_j, \kappa_{ij}), \quad (6)$$

where the rule (6) is responsible for the adaptation and the temporal changes of the structure Y . The rule (6) is the case when the connection weight between node i and node j depends only on the function of these nodes $x_i(t)$ and $x_j(t)$. Of course, this is not the only possible adaptation rule. Particular realizations of the adaptation rule (6) are neuronal systems with plasticity. Specifically, when the plasticity is long-term, i.e., the structural changes act on a slower timescale than the functional dynamics (neuronal spiking),^{14–18} this leads to systems with multiple timescales. As a representative system, the paradigmatic adaptive network of phase oscillators,

$$\dot{\phi}_i = \omega_i - \sum_{j=1}^N \kappa_{ij} \sin(\phi_i - \phi_j + \alpha), \quad (7)$$

$$\dot{\kappa}_{ij} = -\varepsilon (\kappa_{ij} + \sin(\phi_i - \phi_j + \beta)), \quad (8)$$

appears to be very useful to study various phenomena in adaptive networks, such as synchronization, frequency clustering, recurrent synchronization, adaptivity-induced resistance to noise, and others.^{17,19–24} Equations (7) and (8) are a special case of the more general equations (9) and (10) in Sec. II D; see also the examples discussed there. All of these phenomena are also revealed in more realistic and complex models, such as Hodgkin–Huxley neurons with spike-timing-dependent plasticity.^{17,25} Thus, paradigmatic models of the type (7) and (8) have demonstrated their effectiveness in studying and predicting novel phenomena characteristic for large classes of adaptive networks.

The main challenges in studying the above classes of adaptive dynamical networks are as follows:

- High dimensionality. If the number of nodes in the network is N , the number of possible connections is N^2 . Thus, the dimensionality of the model increases dramatically compared to dynamical networks with a fixed structure.
- If the adaptation is slow, i.e., $\varepsilon \ll 1$ in Eq. (8), the system becomes multi-scale with the slow manifold of dimension N^2 . This additional multiscale structure provides opportunities for analysis,²⁶ but for large networks, it goes far beyond the standard results employing geometric singular perturbation theory.

Despite recent advances in the study of dynamical adaptive networks, many challenging problems remain unsolved. These problems include mean-field theory, application to climate network modeling, understanding the role of adaptivity in machine learning, developing dimensionality reduction techniques, particularly methods for dealing with extremely high-dimensional slow manifolds. Besides large networks, small networks with adaptivity appear to have a highly nontrivial bifurcation structure compared to their non-adaptive counterparts. Studying and finding typical bifurcation scenarios in such systems (also known as Eckhaus instability or Busse-balloons in PDEs) is another open and challenging problem.

B. Adaptation, slow feedback, and noise—By Igor Franović

Adaptation is often qualitatively described as a slow evolution of network connectivity patterns due to a feedback from the nodal dynamics, drawing comparison to synaptic plasticity in neuronal systems;²⁷ see also Sec. II A. Nevertheless, one should bear in mind that adaptation may also directly impact the features of nodal dynamics, with examples ranging from frequency adaptation in clapping audiences or flashing fireflies²⁸ to scenarios where the limited availability of metabolic resources modulates neuronal excitability^{29,30} or contributes to maintaining neuronal systems near criticality.³¹ A detailed discussion concerning the two latter effects in relation to spike-frequency adaptation and short-term synaptic plasticity can be found in Sec. III C. While these two types of adaptation, affecting the coupling or nodal dynamics, may appear independently, it is also not uncommon that they act in concert guiding the system's self-organization.^{32,33} So far, most of the systematic insights on the role of adaptation have been gained regarding its impact on synchronization, including how it gives rise to different states of (partial) synchrony,^{16,21,34–37} or the way it modifies the order of synchronization transition²⁸ and the associated nucleation process.³⁸ Another active branch of research concerns adaptation as a general control mechanism, establishing its role in inducing critical transitions^{30,31} and triggering of alternating or cyclic activity patterns.^{39–41} Moreover, unfolding studies employing reservoir computing for design of controllers for nonlinear, and, in particular, chaotic systems, also hold great promise; see Sec. IV C.

1. Interaction of adaptation and noise

An important, but still insufficiently understood problem concerns the interaction between adaptation and noise, an issue naturally arising in applications to neuroscience. In spite of an apparently desynchronizing effect of noise, it has been shown that adaptation and noise may give rise to a self-organized network activity that promotes growth of overall synaptic strength,¹⁷ thereby canceling the potentially desynchronizing stochastic effects. While this may seem counterintuitive, one should recall that classical synaptic plasticity rules, such as spike-timing-dependent plasticity,²⁷ support synaptic potentiation if coupled neurons are approximately (but not identically) synchronized and maintain their relative order of firing.⁴² However, such self-organized resilience of synchronization to noise is so far evinced for coupled oscillators rather than coupled excitable or mixed excitable-oscillatory populations. Addressing the two latter cases would be highly relevant for applications in neuroscience where local dynamics typically involves excitability and diversity.^{43–45}

Apart from the mean effect on the overall coupling strength, an additional subtlety from the interaction of adaptation and noise concerning stochastic fluctuations so far addressed mostly at the microscopic level. For motifs of coupled stochastic excitable units, such an interaction may induce switching dynamics, i.e., slow stochastic fluctuations between coexisting metastable states. The switching is naturally reflected both at the level of nodal dynamics and the effective motif coupling configuration, given by the coupling strengths.⁴⁶ In particular, for the example of a system of two identical excitable

units, the noise can induce two different oscillatory modes with a different prevailing order of firing between the units. In the presence of slow adaptation, such metastable states engage in an alternating dynamics, accompanied by an alternation of coupling configurations characterized by a strong coupling in one direction and a strongly depressed one in the opposite direction. Translated to the language of neuroscience, the latter effect corresponds to switching between two functional neuronal motifs with directed couplings on the same structural motif.⁴⁷

Concerning stochastic fluctuations at the level of a single excitable system, it has been shown that a slowly adapting feedback, acting as a low pass filter to affect the unit's excitability,⁴⁰ may in an interaction with noise induce a novel form of behavior called stochastic bursting, an alternating activity involving episodes of relative silence interspersed with irregular spiking. Such stochastic bursting occurs in the parameter region that in the limit of an infinite scale separation between the units' dynamics and adaptation supports bistability between noise-induced and noise-perturbed spiking. Apart from inducing a novel type of behavior, adaptation may also provide for a control mechanism of coherence resonance⁴⁰ or may make the noise-induced suppression of spiking frequency within inverse stochastic resonance more efficient.^{41,48}

2. Impact of an adaptation rate

An often overlooked feature of adaptation when elaborating its impact on emergent dynamics is the adaptation rate. Classically, an adaptation rate is considered to be sufficiently slow such that the overall dynamics may be treated within the framework of singular perturbation theory,²⁶ separating between the fast local dynamics of units and the slow evolution of adaptation variables. However, the impact of an adaptation rate has not been investigated systematically, mostly due to a lack of an appropriate analytical method. In certain examples, it has numerically been shown that intermediate adaptation rates can substantially deviate the system's behavior from the predictions of singular perturbation theory,⁴⁶ and finding appropriate means to address this issue remains an open problem.

3. Mathematical approaches to adaptation

From a broader perspective, developing mathematical approaches to study adaptive networks is challenging because it requires reconciling different aspects of system behavior, such as criticality, feedback, multiple timescale dynamics, diversity, and noise. So far, an extension of a master stability function approach⁴⁹ has proven effective in reducing the synchronization problem by separating for dynamical and topological features, allowing for a classification of system states with respect to synchronization properties. For coupled phase or neural oscillators, such an approach has revealed that adaptation may induce a desynchronization transition²¹ and support different multi-frequency hierarchical cluster states and chimera-like states of partial synchronization. Nevertheless, the general problem of the impact of adaptation on system's multistability remains open. In certain cases, such as the Kuramoto phase oscillators with an asymmetric spike-timing-dependent plasticity-like plasticity rule, adaptation has been shown to induce multistability between the synchronized, desynchronized,

and multiple partially synchronous states.¹⁶ Also, for adaptively coupled identical phase oscillators, multicluster states have been shown to exhibit a high degree of multistability.^{34,35} Apart from understanding the impact on synchronization problems, an important issue concerns the role of adaptation in inducing cyclic activity patterns by controlling critical transitions of the adaptation-free system. Treating such problems, such as the onset of collective activity bursts in heterogeneous systems adaptively coupled to a pool of resources,³⁹ requires combining different reduction approaches^{50–52} and multiple timescale methods. Nevertheless, developing rigorous mathematical approaches where mean-field methods apply to layer dynamics while adaptation is treated by a reduced system is a vibrant field of investigation. In parallel, a hybrid approach for treating the interaction of adaptation and noise by combining the Fokker–Planck formalism with multiple timescale methods has recently been derived.⁴⁰ Further generalization of an adaptation concept to cases where an adaptation rate itself varies in time may additionally require including methods from nonequilibrium thermodynamics and information theory. This naturally applies to sensory adaptation,^{53,54} where information transmission is optimized under different constraints, including metabolic costs, dynamic range, and intrinsic stochasticity.⁵⁵ From the perspective of nonequilibrium thermodynamics, sensory adaptation is a dissipative process ruled by an energy–speed–accuracy tradeoff,⁵³ where one may exploit the relation between adaptation and irreversibility,⁵⁴ quantified by the entropy production.

C. Adaptivity: A shared notion?—By Nuria Brede and Nicola Botta

This article discusses notions of *adaptivity* from the perspective of different disciplines, ranging from non-linear dynamics to psychology, neuroscience, and computer science. Yet, while most authors would agree that adaptivity is a *property*, their answers to the question “A property of **what?**” presented in the various contributions seem to differ. This is not accidental, but simply a consequence of the exploratory nature of the paper, and it poses a challenge for future work: Can we find a framework that is sufficiently generic to formulate and compare the notions of *adaptivity* in different research areas, understand their differences and similarities, identify shared concepts and computational methods, and facilitate the communication between disciplines?

We argue in this section that *dependent type theory* would be an ideal candidate for (formulating) such a framework. What do we mean by this? The reader who is unfamiliar with dependent type theory should for the moment think of it as a mathematical logic fused with a programming language (we will explain more in Sec. II C 2). Ionescu *et al.*⁵⁶ argue that type theory fits most of the requirements for frameworks for *modeling* and *programming* put forward by Broy *et al.*⁵⁷ In a research program originally initiated by Ionescu, type theory has been applied to understand notions of *vulnerability*, *viability*, *reachability*, *avoidability* (discrete dynamical systems), *optimality* (control theory), *climate sensitivity*, *commitment*, and *responsibility* (climate policy).^{58–61} The largest study of the above is Ionescu *et al.*⁵⁸ where various notions of *vulnerability*, stemming from domains such as climate change, food security, or natural hazard studies, are compared.

1. Notions of adaptivity

A key idea commonly put forward is that adaptivity is a “feature of natural and artificial complex systems.” Thus, from this perspective, adaptivity is a *property of a system*. However, in their 1992 seminal paper “Reinforcement learning is direct adaptive optimal control,”⁶² Sutton *et al.* argue that what is *adaptive* is a *method* for controlling a system, rather than the system itself. This suggests to see adaptivity as a *property of optimal control methods*.

It is worth noticing that optimal control methods do not need to be adaptive. At least since 1957,⁶³ we know that many deterministic and stochastic sequential decision problems can be solved for optimal *policies* via dynamic programming. Dynamic programming can indeed be applied to also solve non-deterministic, fuzzy, and, more generally, *monadic* sequential decision problems,⁶⁴ as long as the uncertainty monads and the *measures of uncertainty* (for example, for stochastic uncertainty, the expected value measure) satisfy certain *compatibility* conditions.⁶⁵ However, when the transition function (or the reward function) of a sequential decision problem is not given, optimal policies have to be learned by interacting, step by step, with an *environment*: for example, via Q-learning.⁶⁶ This is *learning to act optimally* rather than *optimal planning*.

Even if we share the intuition that adaptivity is a property of a *system*, or of a *method* for controlling a system that interacts *sequentially* with an *environment*, it remains to clarify whether the notions of adaptivity in different domains arise as instances of the same abstract notion or whether they are genuinely different, potentially even incompatible. Such a clarification requires *specifying* and comparing different notions of adaptivity in a common framework. As mentioned above, in prior work, we have employed type theory for this purpose.

2. Logic and type theory

Most scientists are well trained in applying elementary mathematics and first-order logic to formulate properties in specific *domains*; e.g., in mathematics, you might define what it means for a function to be *injective*, or in dynamical systems theory, what it means for a function to be the *flow* of a dynamical system. Therefore, for a mathematically trained people, logic is a well-suited language to make precise and develop a shared understanding of concepts. Indeed, this purpose is at the heart of a modern mathematical logic, at least going back to Leibniz’ vision of a universal language that would not suffer from the ambiguities of natural language.

Dependent type theory⁶⁷ takes the advantages of a mathematical logic one step further. It is a theory that may be seen both as a higher-order logic and as a pure functional programming language with a static type system. It was developed as a foundational theory for constructive mathematics by the Swedish mathematician and philosopher Per Martin-Löf.⁶⁸ Dependent type theory has solid implementations^{69–73} and impeccable mathematical credentials^{74–77} (see also Refs. 78 and 79 for popular science accounts, including the voices of mathematicians who have turned to computer-aided formalization).

Due to its double role as logic and programming language, dependent type theory is well-suited as a framework for both formulating and machine checking mathematical specifications. Because

types can represent propositions and well-typed programs correspond to proofs,⁸⁰ dependent type theory is also the key for writing programs that are correct “by construction,” bridging the gap between the mathematical model and implementation. This is crucial for safety-critical applications^{81–85} but also in research areas in which testing model implementations is nearly impossible or too expensive.⁸⁶

3. Monadic dynamical systems

The vulnerability study of Ionescu *et al.*⁵⁸ led to the introduction of *monadic dynamical systems*, combining ideas from generic programming^{87,88} and category theory⁸⁹ with dynamical systems theory. Monadic dynamical systems are sufficiently general to capture various different definitions of vulnerability as instances of a common abstract schema. The framework for vulnerability was later extended by Botta *et al.*^{59,64,65} to a framework for specifying and solving *sequential decision problems* within dependent type theory. We think that this framework could also be applied and suitably extended to study different notions of adaptivity.

D. Partial synchronization patterns in adaptive networks—By Eckehard Schöll

This subsection explores the applications of network models as outlined in Sec. II A in different domains. From a complex networks perspective, the interplay between dynamics and network topology is in the center of interest. Collective dynamics in networks of nonlinear oscillators is often characterized by synchronization phenomena,^{10,11} as already studied by Christiaan Huygens in 1656. Among these, partial synchronization patterns have become a major focus of research recently.⁹⁰ Examples are provided by cluster or group synchronization (where within each cluster, all elements are completely synchronized, but between the clusters, there is a phase lag, or even a difference in frequency), and many other forms. A particularly intriguing example of partial synchronization patterns, which has recently gained much attention, is *chimera states*, i.e., symmetry-breaking states of partially coherent and partially incoherent behavior; for recent reviews, see Refs. 91–93. Chimera states in dynamical networks consist of spatially separated, coexisting domains of synchronized (spatially coherent) and desynchronized (spatially incoherent) dynamics. They are a manifestation of spontaneous symmetry-breaking in systems of identical oscillators and occur in a variety of physical, chemical, biological, neuronal, ecological, technological, or socio-economic systems. Other examples of partial synchronization include solitary states,^{94–96} where one single or a few elements behave differently compared with the behavior of the background group, i.e., the neighboring elements or hierarchical multifrequency clusters.²⁰

In adaptive networks, the coupling weights are not fixed but are continuously adapted by feedback of the dynamics, and both the local dynamics and the coupling weights evolve in time as co-evolutionary processes; compare with discussions in Secs. II A or II B. Adaptive networks have been reported for chemical,⁹⁷ epidemic⁹⁸ (see also Secs. V A and V B), biological, and social systems⁹⁹ (see also Sec. V C). A paradigmatic example of adaptively coupled phase oscillators has recently attracted much attention^{20,21,34,35,100–107} and it appears to be useful for

predicting and describing phenomena in more realistic and detailed models.^{18,25,108,109} It describes N adaptively coupled phase oscillators^{20,34} [as a general case of Eqs. (7) and (8) in Sec. II A],

$$\dot{\phi}_i = \omega_i + \sum_{j=1}^N a_{ij} \kappa_{ij} f(\phi_i - \phi_j), \quad (9)$$

$$\dot{\kappa}_{ij} = -\epsilon (\kappa_{ij} + g(\phi_i - \phi_j)), \quad (10)$$

where $\phi_i \in [0, 2\pi)$ represents the phase of the i th oscillator ($i = 1, \dots, N$), ω_i is its natural frequency, and κ_{ij} is the coupling weight of the connection from node j to i . Furthermore, f and g are 2π -periodic functions where f is the coupling function, g is the adaptation rule, and $\epsilon \ll 1$ is the adaptation time constant. The connectivity between the oscillators is described by the entries $a_{ij} \in \{0, 1\}$ of the adjacency matrix A . In particular, for the Kuramoto phase oscillator,¹¹⁰ the coupling function is $f(\phi) = -\sin \phi$, and synaptic neuronal plasticity may be described by $g(\phi) = -\cos(\phi + \beta)$ where the parameter β describes different adaptivity rules.

One purpose of this section is to provide a new perspective by demonstrating that a wide range of models ranging from neuronal networks with synaptic plasticity via power grids to physiological networks modeling tumor disease and sepsis can be viewed as adaptive oscillator networks, and partial synchronization patterns can be described on equal footing. This modeling approach allows one to transfer methods and results from one system to the other.

A common class of network models describing power grids is given by N coupled phase oscillators with inertia,¹¹¹ also known as a swing equation. It has been widely used in works on synchronization of complex networks and as a paradigm for the dynamics of modern power grids,^{112–122}

$$M\ddot{\phi}_i + \gamma\dot{\phi}_i = P_i + \sum_{j=1}^N a_{ij} h(\phi_i - \phi_j), \quad (11)$$

where M is the inertia coefficient, γ is the damping constant, P_i is the power of the i th oscillator (related to the natural frequency $\omega_i = P_i/\gamma$), h is the coupling function, and a_{ij} is the adjacency matrix as defined in Eq. (9). Another view on the role of adaptivity for power grid systems can also be found in Sec. V D.

It has been shown¹²³ that the class of phase oscillator models with inertia is a natural subclass of systems with adaptive coupling weights where the weights denote the power flows between the corresponding nodes. We first write Eq. (11) in the form

$$\dot{\phi}_i = \omega_i + \psi_i, \quad (12)$$

$$\dot{\psi}_i = -\frac{\gamma}{M} \left(\psi_i - \frac{1}{\gamma} \sum_{j=1}^N a_{ij} h(\phi_i - \phi_j) \right), \quad (13)$$

where ψ_i is the deviation of the instantaneous phase velocity from the natural frequency ω_i . We observe that this is a system of N phase oscillators (12) augmented by the adaptation (13) of the frequency deviation ψ_i . Similar systems with a direct frequency adaptation have been studied in Refs. 28 and 124–126. Note that the coupling between the phase oscillators is realized in the frequency

adaptation, which is different from the classical Kuramoto system.¹¹⁰ In order to introduce coupling weights into system (12) and (13), we express the frequency deviation ψ_i as the sum $\psi_i = \sum_{j=1}^N a_{ij} \chi_{ij}$ of the dynamical power flows χ_{ij} from the nodes j that are coupled with node i . The power flows are governed by the equation $\dot{\chi}_{ij} = -\epsilon (\chi_{ij} + g(\phi_i - \phi_j))$, where $g(\phi_i - \phi_j) \equiv -h(\phi_i - \phi_j)/\gamma$ are their stationary values¹²⁷ and $\epsilon = \gamma/M$. It is straightforward to check that ψ_i , defined in such a way, satisfies the dynamical equation (13).

As a result, the swing equations (12) and (13) can be written as the following system of adaptively coupled phase oscillators:

$$\dot{\phi}_i = \omega_i + \sum_{j=1}^N a_{ij} \chi_{ij}, \quad (14)$$

$$\dot{\chi}_{ij} = -\epsilon (\chi_{ij} + g(\phi_i - \phi_j)). \quad (15)$$

The obtained system corresponds to (9) and (10) with coupling weights χ_{ij} and coupling function $f(\phi_i - \phi_j) \equiv 1$. The coupling weights form a pseudocoupling matrix χ describing the power flow between the nodes. Note that the base network topology a_{ij} of the phase oscillator system with inertia equation (11) is unaffected by the transformation.

In adaptive phase oscillator networks, there exists a diversity of multifrequency cluster states,^{20,35,107} including chimera states²⁰ and solitary states.¹²⁸ In a multifrequency cluster state, all oscillators split into M groups (called clusters), each of which is characterized by a common cluster frequency Ω_μ . In particular, the temporal behavior of the i th oscillator of the μ th cluster ($\mu = 1, \dots, M$) is given by $\phi_i^\mu(t) = \Omega_\mu t + \rho_i^\mu + s_i^\mu(t)$ where $\rho_i^\mu \in [0, 2\pi)$ and $s_i^\mu(t)$ are bounded functions describing different types of phase clusters characterized by the phase relation within each cluster.³⁴

As an example, in Figs. 2(a) and 2(c), we present a four-cluster state of in-phase synchronous clusters on a globally coupled network. Hierarchical multicluster states are built out of single cluster states whose frequency scales approximately with the number N_μ of elements in the cluster. The coupling matrix displayed in Fig. 2(e) shows the characteristic block diagonal shape known for adaptive networks. In particular, the oscillators within each cluster are more strongly connected than the oscillators between different clusters.

A second example, which uses a splay state with $\phi_i = 2\pi k j/N$ and wavenumber $k \in \mathbb{N}$ as the building block for multiclusters, is shown in Figs. 2(b), 2(d), and 2(f). Splay states are characterized by the vanishing local order parameter $R_j = |\sum_{k=1}^N a_{jk} \exp(i\phi_k)| = 0$. Figures 2(b), 2(d), and 2(f) present a hierarchical mixed-type multicluster on a nonlocally coupled ring of phase oscillators. It consists of one large splay cluster with wavenumber $k = 2$ and a small in-phase cluster consisting of three solitary states.

In summary, the findings for partial synchronization of adaptively coupled phase oscillators can be transferred to networks of phase oscillators with inertia. This holds not only for simple homogeneous systems, but also for heterogeneous real-world networks, such as the German ultrahigh voltage power grid.¹²³

In recent years, studies on both types of models, oscillators with inertia and adaptively coupled oscillators, have revealed a plethora of common dynamical scenarios, including solitary states,^{118,119,128,130} multifrequency clusters,^{34,35,117,131} chimera states,^{20,103,132} hysteretic

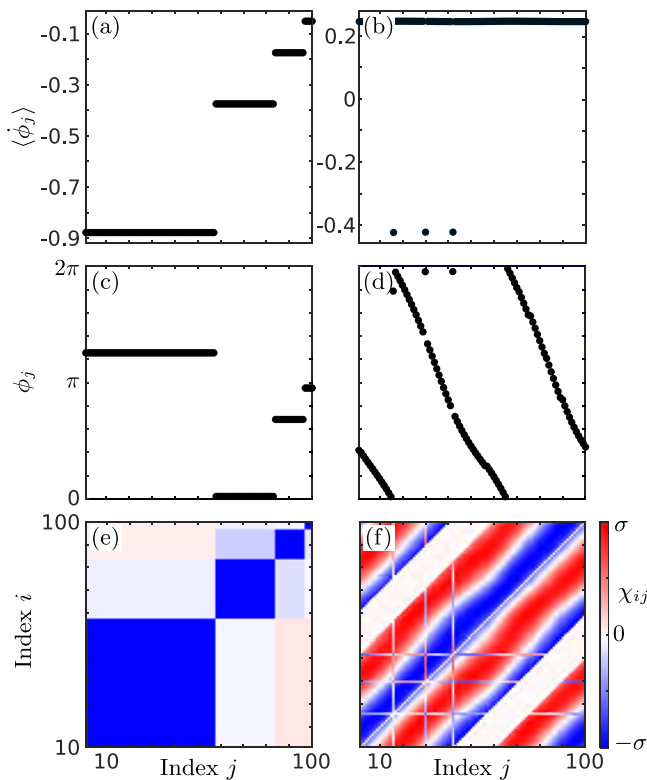


FIG. 2. Hierarchical multicluster states in networks of coupled phase oscillators with inertia. Panels (a) and (b), (c) and (d), and (e) and (f) show the temporally averaged phase velocities $\langle \dot{\phi}_j \rangle$, phase snapshots $\phi_j(t)$, and the pseudocoupling matrices $\chi_{ij}(t)$, respectively, at $t = 10\,000$. In (e), the oscillator indices are sorted in an increasing order of their mean phase velocity. The states were found by numerical integration of (11) with identical oscillators $P_i = 0$, $h(\phi) = -\sigma\gamma \sin(\phi + \alpha)$, and uniform random initial conditions $\phi_i(0) \in (0, 2\pi)$, $\psi_i(0) \in (-0.5, 0.5)$. The parameter α is a phase lag of the interaction.¹²⁹ Parameters: (a), (c), and (e) globally coupled networks, $M = 1$, $\gamma = 0.05$, $\sigma = 0.016$, $\alpha = 0.46\pi$ and (b), (d), and (f) nonlocally coupled ring networks with coupling radius $P = 40$, $M = 1$, $\gamma = 0.3$, $\sigma = 0.033$, $\alpha = 0.8\pi$; $N = 100$. After Berner *et al.*, Phys. Rev. E **103**, 042315 (2021). Copyright 2021 American Physical Society.¹²³

behavior, and non-smooth synchronization transitions.^{38,101,116,133,134} Power grids, as well as neuronal networks with synaptic plasticity, and other adaptive networks describe real-world systems of tremendous importance for our daily life, which exhibit partial synchronization patterns that may be important for the understanding of the onset of instability. Neural systems and power grid networks are also discussed in Secs. III and V, respectively. A particularly intriguing example and a future perspective is the functional modeling of physiological two-layer networks of the immune system and the parenchyma coupled adaptively by cytokines.^{135,136} This can be used for the modeling of tumor disease and sepsis with the immune layer as a reference point, where the healthy state is characterized by complete frequency synchronization and the pathological state is a multifrequency cluster state.

III. PERCEPTION AND NEURAL ADAPTIVITY

In this section, the focus is on adaptive mechanisms in physiological systems. Here, basic regulatory principles are highlighted, fundamental concepts for a physical culture theory are developed, mechanisms and modeling of perception are described, and concrete medical applications on neural networks are presented.

A. Design principles for adaptation in physiological systems—By Omer Karin

Here, we will explore motifs for adaptation in physiological regulatory networks. The physiological properties of biological systems arise from the myriad of interactions of their underlying components. As an example, the production rate of proteins from a gene depends on the abundance of other proteins, known as transcription factors, whose production depends on the abundance of other transcription factors. Similarly, the secretion of a hormone to the bloodstream depends on the concentrations of other blood factors, which are themselves affected by the levels of other hormones. These complex networks of interactions are known as regulatory networks.

To study regulatory networks, it is useful to notice that evolution tends to come up with similar solutions to related problems. It is often the case that, under similar contexts, the regulatory networks of distinct systems share mathematical similarities—these are so-called regulatory motifs or design principles.^{137–139} By identifying such *design principles*, one can extract a deeper understanding of the functional significance of the regulatory interactions. We may, therefore, ask what are the design principles that support adaptation—the ability of the system to adjust itself to function properly, despite uncertainty in internal parameters or the external environment.

Consider the problem of maintaining homeostasis of a blood factor, such as glucose (denoted x). Blood glucose needs to be maintained within a narrow range (around 5 mM) with deviations being detrimental or even life-threatening. Our bodies have a natural mechanism to lower blood glucose—we have specialized cells called β -cells, which can sense blood glucose and secrete the hormone insulin, which causes remote cells (fat cells, skeletal muscle cells, and liver cells) to reduce glucose levels. This mechanism can maintain glucose around some steady state, which would depend sensitively on many parameters, including the abundances β -cells, plasma volume, and the responses of cells to insulin. These can (and do) vary greatly between individuals; yet, we know that most individuals can maintain blood glucose within a narrow range.¹⁴⁰

A related problem occurs in bacterial chemotaxis. The bacteria *E. coli* navigates with a strategy resembling a random walk, where it moves and reorients with some set rate ϕ (typically once every few seconds). This is known as the tumbling rate. Navigation is achieved by adjusting ϕ according to sensed ligand molecules known as attractors and repellants. A step increase in an attractant molecule transiently decreases ϕ , leading to a net drift toward areas with higher attractant concentration. However, at fixed attractant concentration u , over a wide sensed range, ϕ is constant and independent of u .^{141,142} How is ϕ maintained constant, despite variations in the input activity of the circuit?

It has long been suggested that both problems are closely related to the engineering problem of disturbance rejection.^{143–145}

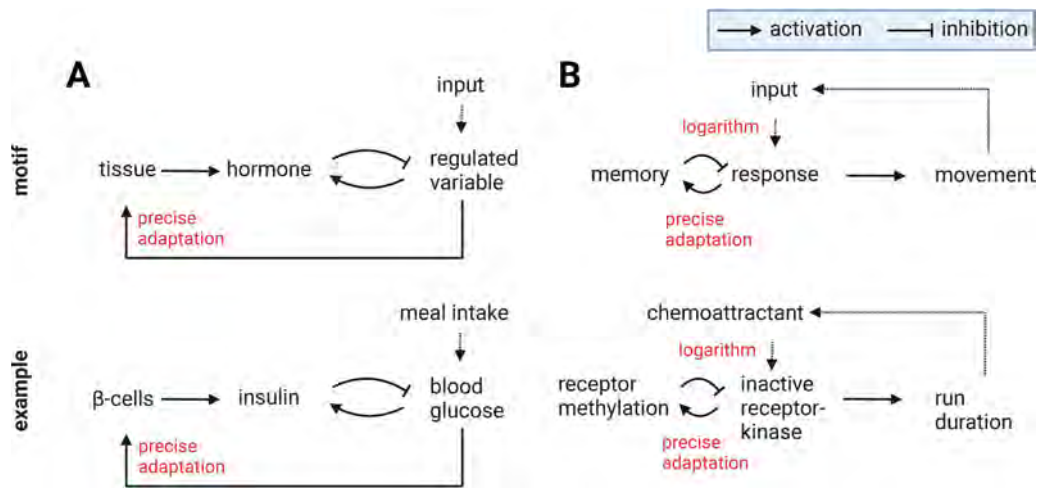


FIG. 3. Motifs for adaptation in physiological systems. (a) In hormone circuits, a hormone-regulated variable governs the growth rate of the tissue responsible for its secretion, enabling precise adaptation. This adaptation mechanism ensures that the dynamics of the regulated variable remain robust in the face of physiological variations. (b) Organisms employ a combination of logarithmic sensing, precise adaptation, coupled to movement regulation, to achieve robust sampling of an input field. This motif is observed in chemotaxis and potentially in the mammalian dopamine system.

This problem is exemplified by how a cruise-control system of a car maintains a fixed speed on varying slopes, or how a thermostat maintains a fixed temperature in uncertain operating conditions. The solution requires integral feedback: the controller feedback increases with the error (it integrates the error); therefore, at a steady state, the error is zero.

How is integral feedback implemented in biological circuits? In hormone circuits, there appears to be a simple answer [Fig. 3(a)]. Let x be the regulated variable and y be its regulating hormone, with Z being the mass of the tissue that secretes the hormone. In the blood glucose system, x is the blood glucose, y is the blood insulin, and Z is the β -cell mass. The following motif is observed across hormone systems: there is a slow negative feedback where the main regulator of the growth dynamics of Z is x ; that is, x adjusts the death-, growth-, and replication-rates of the cells of Z . Thus,

$$\dot{Z} = f(x)Z, \tag{16}$$

where $f(x)$ is the x -dependent growth rate. The system will settle at the steady state where $f(x) = 0$ (denoted x_0) regardless of variation in the other physiological parameters, including plasma volume, secretion rate, and the responses of remote cells.

The ubiquity of the motif suggests that it is uniquely advantageous. Why is it so prevalent? Beyond integral feedback, another intriguing phenomena occur. Consider, for example, the following simple model for the glucose system:

$$\begin{aligned} \dot{u} &= u - sxy, \\ \dot{y} &= pZ - \gamma y, \end{aligned} \tag{17}$$

where s is the sensitivity to the response of the hormone and p is the product of the per-cell secretion and (inverse) plasma volume. u is the time-dependent input, incorporating, e.g., meal intake. Equation (16) not only sets the steady state of x to $x = x_0$, it makes

the entire dynamics in response to any input u invariant of s, p .¹⁴⁶ These scale-invariant dynamics are evident in clinical data from distinct hormonal systems.^{146–149} Thus, in hormone systems, negative feedback from the regulated variable to its controlling tissue allows the system to adapt its dynamics to variability in key system parameters, which are uncertain and may be highly variable.

Scale invariance also occurs in bacterial chemotaxis; in this case, the dynamics of the tumbling rate $\phi(t)$ are modulated by the attractant input $u(t)$ in a manner, which depends only on relative, rather than absolute, changes in $u(t)$, a phenomenon known as *fold-change detection*.¹⁵⁰ Fold-change detection is documented in the navigation systems of other simple organisms, including in worms and slime molds.^{151,152}

What about more complex organisms? In vertebrates, including mice and humans, movement is controlled by the transmission of dopamine in the mid-brain. Dopamine is secreted in response to surprise (or *prediction error*) about rewards, such as food or drink; better outcomes than expected cause dopaminergic neurons to fire above their baseline rate, while worse outcomes transiently inhibit dopaminergic firing.¹⁵³ The responses are also scale-invariant.¹⁵⁴ Finally, when the animal moves, dopamine changes in a way that is consistent with a response to the temporal derivative of a spatial input field.¹⁵⁵

Upon closer examination, the dopamine system shares key similarities with the chemotaxis system, where in the case of dopamine, the input field corresponds to expectations about rewards.¹⁵⁶ This input field decays spatially from actual locations where rewards are provided, similar to the decay of a chemical attractant from its source. Dopamine also invigorates movements in a manner analogous to the effect of attractants on bacterial movement.

We, therefore, identified another regulatory motif: fold-change detection of an input field, which modulates movement statistics [Fig. 3(b)]. What is the function of this motif? From the perspective

of sensing, scale invariance allows us to remove uncertainty and retain sensitivity over a wide dynamic input range. An additional distinct advantage is apparent when we consider the coupling between sensing and movement. The fold-change detection circuit calculates the temporal logarithmic derivative of the input $u(t)$. In a spatial setting, we can consider a spatial input field $U(x)$; the movement dynamics of the organism over long time- and length- scales are captured by the stochastic dynamics,

$$dx = \beta v^2 \phi \nabla \log U \, dt + v^2 \sqrt{2\phi} \, dW, \quad (18)$$

where v is the typical movement speed, and β depends on circuit parameters. The steady-state distribution of the organism location is $P(x) = U(x)^\beta$, which only depends on circuit parameters (rather than movement parameters); the motif, thus, provides a robust mechanism for sampling a power of the input field. This is again consistent with experimental observations on both chemotaxis and the dopamine system.¹⁵⁶ Thus, in these systems, a motif that appears to support adaptation of sensing in the background of uncertain input levels, in fact, provides a mechanism for robust sampling of uncertain environments.

The examples considered here suggest that adaptation motifs that allow for scale-invariant dynamics are prevalent, and that specific adaptation regulatory motifs, which recur in similar contexts, have distinct functional significance. Identifying these motifs, and comparing their behavior in different contexts, is due to improve our understanding of how adaptation is achieved by complex regulatory networks.

B. Adaptation and neuronal coding—By Christoph Miehl

“To live is to adapt to the world around us.”¹⁵⁷ The environment of an organism can change on vastly different timescales, ranging from, e.g., a change in lighting to climate change. Organisms, and hence their brains, have developed strategies to adapt to these modifications in the environment across timescales, from adaptation to sudden changes in sensory stimuli to long timescales of evolutionary processes. In the following, some key adaptive mechanisms in the brain on short timescales are highlighted.

In principle, single neurons can adapt to changes in the environment based on two strategies, either by modifying their intrinsic or extrinsic properties. Intrinsic changes include, e.g., increase or decrease in the excitability of a neuron.¹⁶⁰ Extrinsic changes are related to updates in the strength of the synaptic connections onto the neuron. An extrinsic mechanism that has been linked to adaptation on short timescales (tens to hundreds of milliseconds) is short-term synaptic plasticity. Input spikes that occur within short timescales can cause a transient decrease (short-term depression) or an increase (short-term facilitation) of the synaptic efficacy¹⁶¹ (see Sec. III C). The mechanism leading to a permanent increase or decrease in synaptic strength is long-term synaptic plasticity. In experiments, long-term changes in the synaptic strength can be induced via a “pairing protocol,” a prominent example being spike-timing-dependent plasticity.¹⁶² Repeatedly triggering a spike in the postsynaptic neuron following a spike in the presynaptic neuron within approx. 10 ms leads to long-term potentiation, while presynaptic spikes following postsynaptic spikes within ≈ 10 –100 ms leads

to long-term depression.^{163,164} Both short- and long-term plasticities have not only been identified at synapses between excitatory neurons but also at inhibitory-to-excitatory synapses (for more information, see Refs. 158 and 165).

A prominent experimental paradigm to test adaptation on short timescales is the “oddball paradigm.”¹⁶⁶ In this paradigm, one (usually visual or auditory) stimulus is presented many times, the standard (or familiar, predictable) stimulus. The second stimulus is only presented rarely, the deviant (or novel, unpredictable) stimulus. On the whole-brain level, electroencephalogram measurements reveal that presenting the deviant stimulus leads to a strong negative deflection in the EEG signal compared to the signal following from a standard stimulus presentation, termed “mismatch negativity.”^{167,168} Similarly, measurements of either single neurons or neuronal populations in sensory cortices reveal elevated neuronal responses for deviant compared to the standard stimuli^{169–171} [Fig. 4(a)]. Computational models have proven to be useful for understanding the mechanisms underlying short-term adaptation in the brain (see also Secs. III C and III F). Multiple studies suggest that short-term plasticity is a critical mechanism underlying adaptation to familiar stimuli,^{172–174} and short-term plasticity at inhibitory synapses is important for controlling temporal context-dependent neuronal responses.^{175,176} In a complementary approach, it has been suggested that long-term plasticity at inhibitory-to-excitatory synapses underlies the difference in responses to familiar and novel stimuli.¹⁷⁷ In this work, increase of inhibitory-to-excitatory synapses via long-term plasticity leads to a decrease in excitatory responses to familiar stimuli, while novel stimuli still lead to elevated responses.

Many functional implications have been suggested for the role of reduced neuronal activity for familiar stimuli compared to elevated activity for novel stimuli, ranging from efficient coding and redundancy reduction, fast detection of unexpected events, to Bayesian inference.^{157,166} Another highly considered implication is predictive coding. In this framework, it is thought that the goal of the brain is to minimize the difference between its internal prediction about the world and the sensory input.¹⁷⁸ High responses to novel stimuli can be thought of as the prediction error. However, how exactly these computations are implemented in the brain and how they are related to short- and long-term plasticity mechanisms are largely unresolved.

Neuronal circuits also need to be robust against perturbations. In experimental studies, disrupting the sensory inputs in the developing brain by performing deprivation experiments (e.g., closing the eye of an animal) leads to homeostatic adjustments of the respective neuronal circuits.¹⁷⁹ A related question is how tightly neuron intrinsic properties, such as conductance densities, need to be regulated to maintain a proper circuit function.¹⁸⁰ For example, computational models and machine learning tools reveal that similar circuit dynamics can be found even for vastly different ion channel conductance densities and that this degeneracy allows one to dynamically compensate perturbations on very fast timescales.^{181–183} Neuromodulators (such as serotonin, dopamine, etc.) are the chemicals that control the neuron’s intrinsic properties.¹⁸⁴ Further computational studies have started investigating the combined effects of intrinsic and extrinsic neuron properties on neuronal activity and robust formation of switches between activity states, as found, e.g., in the sleep-wake cycle.¹⁸⁵

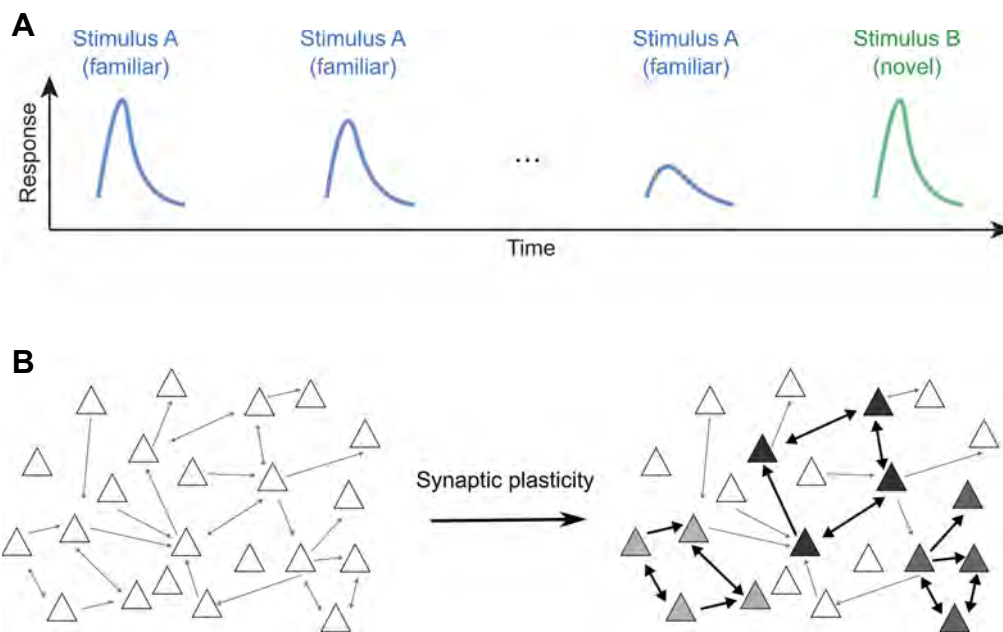


FIG. 4. (a) Oddball paradigm. Presenting a stimulus repeatedly (stimulus A) leads to a decrease of the neuronal response, while the deviant stimulus (stimulus B) leads to a high neuronal response. Panel adapted from Wu *et al.*, *Trends Neurosci.* **45**, 884–898 (2022). Copyright 2022 Elsevier, Inc.¹⁵⁸ (b) Synaptic plasticity leading to strongly recurrently connected structures (assemblies). Panel adapted from Miehl *et al.*, *J. Physiol.* (published online) (2023). Copyright 2023 John Wiley & Sons, Inc.¹⁵⁹

Furthermore, learning and memory formation can be viewed as adaptive processes. Interestingly, it is suggested that learning in neuronal circuits relies on the same mechanisms as described above, short- and specifically long-term synaptic plasticity. While short-term plasticity might underlie working memory,¹⁸⁶ long-term plasticity has been hypothesized as the basis for long-term memory storage.¹⁴ One prominent idea is that groups of strongly interconnected neurons, so-called assemblies, are the basic unit of representation in the brain, and long-term plasticity has proven key for learning these connectivity structures in computational models^{159,187} [Fig. 4(b)]. Neuronal circuits face the problem of “stability-flexibility tradeoff,” meaning that on the one hand, synaptic connectivity should remain stable to allow for long-term memory storage and be robust against perturbations, while on the other hand, circuits should remain flexible allowing re-learning or learning of new representations.¹⁸⁸ Computational studies modeling neuronal networks have suggested different solutions, such as reverberate neuronal activity,¹⁸⁹ inhibitory-to-excitatory plasticity,¹⁹⁰ or a combination of multiple synaptic plasticity and homeostatic mechanisms.¹⁹¹

Despite recent promising developments, experimental and computational studies have only scratched the surface of understanding the role of intrinsic, short-, and long-term plasticity mechanisms in sensory adaptation. This endeavor is specifically important because deficits of information processing in neuropsychiatric diseases have been linked to disruptions in excitatory and inhibitory local circuits,^{192,193} and mismatch negativity has been suggested as a biomarker for psychotic disorders.¹⁹⁴ Therefore, uncovering the

role of different cellular dynamics can have positive therapeutical impacts (see Sec. III D).

C. A next generation neural mass approach to spike-frequency adaptation and short-term plasticity—By Simona Olmi

Neural mass models are mean-field models developed to mimic the dynamics of homogenous populations of neurons. These models range from purely heuristic ones (as the well-known Wilson–Cowan model¹⁹⁵), to more refined versions obtained by considering the eigenfunction expansion of the Fokker–Planck equation for the distribution of the membrane potentials.^{196,197} However, quite recently, a *next generation neural mass model* has been derived in an exact manner for heterogeneous populations of spiking neurons.^{198–200} This exact derivation is possible for networks of quadratic integrate and fire (QIF) neurons, representing the normal form of Hodgkin’s class I excitable membranes,²⁰¹ thanks to the analytical techniques developed for coupled phase oscillators.⁵⁰ Specifically, next generation neural mass models describe the dynamics of networks of spiking neurons in terms of macroscopic variables, such as the population firing rate and the mean membrane potential, and they have already found various applications in many neuroscientific contexts.^{202–211} Resuming the terminology introduced in Sec. III B, here, we investigate the dynamics emergent in next generation neural mass models when populations of neurons adapt to changes in the environment by modifying their intrinsic or extrinsic properties. In particular, we present an overview of the emergence of

collective dynamics (e.g., synchronous, bursting neural dynamics) in next generation neural mass models that arise from spike-frequency adaptation or post-synaptic plasticity.

Spike-frequency adaptation is a widespread neurobiological phenomenon, exhibited by almost any type of neuron that generates action potentials. It occurs in vertebrates as well as in invertebrates, in peripheral as well as in central neurons, and may play an important role in neural information processing. As it will be clarified in the following, all biophysical mechanisms that can cause spike-frequency adaptation include a form of slow negative feedback to the excitability of the cell; therefore, spike-frequency adaptation represents an intrinsic mechanism to adaptation. More in detail, experimental work suggests that it is a result of different balancing currents triggered at a single cell after it generates a spike.^{212,213} Three main types of ionic adaptation currents that influence spike generation are known: voltage-gated potassium currents, which are caused by voltage-dependent, high-threshold potassium channels;²¹⁴ the interplay of calcium currents and intracellular calcium dynamics with calcium-gated potassium channels;²¹⁵ and the slow recovery from inactivation of the fast sodium channel.²¹⁶ As a result of these cellular mechanisms, many neurons show a reduction in the firing frequency of their spike response following an initial increase when stimulated with a square pulse or step.

Short-term plasticity^{161,217–220} refers to a phenomenon in which synaptic efficacy changes over time in a way that reflects the history of presynaptic activity, thus resulting to be an extrinsic mechanism of adaptation (see Sec. III B). Two types of short-term plasticity, with opposite effects on synaptic efficacy, have been observed in experiments: short-term depression and short-term facilitation. On one hand, synaptic depression is caused by the depletion of neurotransmitters consumed during the synaptic signaling process at the axon terminal of a pre-synaptic neuron, and it has been linked to various mechanisms, such as receptor desensitization,^{221,222} receptor density reduction,^{223,224} or resource depletion at glial cells involved in synaptic transmission.^{32,225} On the other hand, synaptic facilitation is caused by the influx of calcium into the axon terminal after spike generation, which increases the release probability of neurotransmitters. Short-term plasticity has been found in various cortical regions and exhibits great diversity in properties.^{226–228}

In the context of spike-frequency adaptation, first efforts in the direction of applying a neural mass model were made in a network of coupled linear integrate and fire neurons, employing the Fokker–Planck formalism and an adiabatic approximation given long spike-frequency adaptation timescales.²²⁹ Analyzing this mean-field description, Gigante *et al.* were able to identify different types of collective bursting. Recently, it has been shown that an excitatory next generation neural mass equipped with different short-term mechanisms of global adaptation can give rise to bursting behaviors.²⁰⁹ Moreover, in Ref. 230, the authors have studied the effect of this adaptation mechanism on the macroscopic dynamics of excitatory and inhibitory next generation neural mass models by including in the original neural mass model proposed in Ref. 200 an additional collective afterhyperpolarization current, which temporarily hyperpolarizes the cell upon spike emission. In a single population spike-frequency, adaptation favors the emergence of population bursts in excitatory networks, while it hinders tonic

population spiking for inhibitory ones. When considering two neural masses, symmetrically coupled in the absence of adaptation, it is possible to observe the emergence of macroscopic solutions with broken symmetry: namely, chimera-like solutions in the inhibitory case and anti-phase population spikes in the excitatory one. Here, the addition of spike-frequency adaptation leads to new collective dynamical regimes exhibiting cross-frequency coupling among the fast synaptic time scale and the slow adaptation one, ranging from anti-phase slow–fast nested oscillations to symmetric and asymmetric bursting phenomena.

In the context of short-term plasticity, a fundamental implementation has been first done by Mongillo *et al.* in Ref. 186 to explain the mechanisms underlying *working memory*. Working memory is the ability to temporarily store and manipulate stimuli representations that are no longer available to the senses. In particular, in the model suggested by Mongillo and co-authors, synaptic facilitation allows the system to maintain an item stored for a certain period in working memory, without the need for an enhanced spiking activity. Furthermore, synaptic depression is responsible for the emergence of population bursts, which correspond to a sub-population of neurons firing almost synchronously within a short time window.^{231,232} In this context, the bursting activity allows for item retrieval. The working memory mechanism is investigated in Ref. 186 by means of a recurrent network of spiking neurons, while a simplified heuristic firing rate model is employed to gain some insight into the population dynamics. A next generation neural mass model encompassing short-term synaptic facilitation and depression has been recently developed to revise the synaptic theory of working memory with a specific focus on the emergence of neural oscillations and their relevance for working memory operations.²⁰⁷ In particular, Taher and co-authors in Ref. 207 consider multiple coupled excitatory populations, each coding for one item, and a single inhibitory population connected to all the excitatory neurons. This architecture is justified by recent experimental results indicating that GABAergic (i.e., inhibitory) interneurons in mouse frontal cortex are not arranged in sub-populations and that they densely innervate all pyramidal (i.e., excitatory) cells.²³³ The role of inhibition is to avoid abnormal synchronization and to allow for a competition of different items once stored in the excitatory population activity. Furthermore, in order to mimic synaptic-based working memory, only the excitatory–excitatory synapses are assumed to be plastic displaying short-term depression and facilitation (at the contrary with what is shown in Sec. III B where examples of short-term plasticity in inhibitory-to-excitatory synapses are also considered). As a result, memory operations are joined to sustained or transient oscillations emerging in different frequency bands, in accordance with experimental results for primate and humans performing working memory tasks.^{234–237} Due to the possibility of reproducing working memory operations associated with population bursts delivered at different frequencies, the neural mass model with short-term plasticity presented in Ref. 207 can represent a first building block for the development of a unified control mechanism for working memory, relying on the frequencies of deliverance of the self-emerging trains of population bursts. However, a development toward realistic neural architectures would require to design a multi-layer network topology to reproduce the interactions among superficial and deep cortical layers.²³⁸

Spike-frequency adaptation and post-synaptic plasticity can be modeled, respectively, as an additive and a multiplicative term in the evolution equation of the mean membrane potential in the exact neural mass model. The novelty of this neural mass model, besides not being heuristic, but derived in an exact manner from the microscopic underlying dynamics, is that it reproduces the evolution of the population firing rate as well as of the mean membrane potential. This allows us to get insight not only on the synchronized spiking activity, but also on the sub-threshold dynamics and to extract information correlated to local field potentials and electroencephalographic signals, which are usually measured to characterize the activity of the brain at a mesoscopic/macroscale. Even though these adaptation mechanisms can express tremendously different timescales, ranging from a few hundred milliseconds (e.g., spike-frequency adaptation²¹²) to days (e.g., postsynaptic receptor density reduction²²⁴), the mean-field descriptions remain applicable. However, note that a macroscopic model of synaptic plasticity cannot express vesicle depletion at the presynaptic site,²¹¹ as introduced for single cell models in Ref. 239. Finally, thanks to the fact that adding spike-frequency adaptation leads to new collective dynamical regimes exhibiting cross-frequency coupling among the fast synaptic time scale and the slow adaptation one, the adaptive mechanisms in the framework of exact neural mass models could be useful to develop new models of self-organizing biological neural circuits that produce rhythmic outputs even in the absence of rhythmic input. An example could be the central pattern generators, which are responsible for the generation of rhythmic movements, since these models are often based on two interacting oscillatory populations with adaptation, as reported for the spinal cord²⁴⁰ and the respiratory system.²⁴¹

D. Therapeutic reshaping of plastic networks—By Peter A. Tass

Regular deep brain stimulation is the gold standard for treating medically refractory Parkinson's patients.^{242–246} In patients with advanced Parkinson's disease, it was shown that regular deep brain stimulation plus medication was superior to medication alone.²⁴⁷ Notwithstanding its therapeutic efficacy,^{248,249} side effects are an issue.^{250–253} In fact, regular deep brain stimulation may cause characteristic side effects denoted as deep brain stimulation-induced movement disorders.^{254,255} Treatment efficacy is another limitation. Regular deep brain stimulation administered to the standard targets, subthalamic nucleus, or globus pallidus internus is not effective for the therapy of gait and other so-called axial symptoms, e.g., balance and posture impairment, and hardly improves or even worsens speech as well as affective and cognitive symptoms.^{256–259}

Abnormal neuronal synchrony is a hallmark of Parkinson's disease.²⁶⁰ Based on computational modeling, it was suggested to specifically counteract abnormal neuronal synchrony by desynchronizing stimulation with phase-dependent stimulus delivery²⁶¹ or by administering compound stimuli, which cause desynchronization irrespective of the initial dynamic condition.^{262,263} By design, coordinated reset stimulation employs comparably weak, phase resetting stimuli and does not require sophisticated calibration procedures.²⁶³ Accordingly, it was selected for pre-clinical studies (animal experiments) and clinical studies. Initially, coordinated reset stimuli were

suggested to be delivered in a demand-controlled manner in a closed-loop setting, e.g., by delivering coordinated reset stimuli whenever a neuronal population gets resynchronized or by adapting the amplitude of the coordinated reset stimuli to the amount of synchrony.²⁶³ At that time, no implantable pulse generators for coordinated reset stimulation were available for clinical tests.^{246,264} Engineering-based concepts led to the development of closed-loop brain stimulation devices that recorded muscular or neuronal activity to suppress unwanted neuronal activity whenever detected.^{265,266} Routine clinical applications of closed-loop deep brain stimulation still require a number of issues to be resolved.²⁶⁷

In contrast, based on principles of adaptive dynamical systems, a qualitatively different stimulation approach was computationally developed.²⁶⁸ Adaptivity is a fundamental feature of the nervous system and, in fact, the entire body to cope with complex physiological processes subjected to environmental changes; see Secs. III A–III C, III E, and III F. By the same token, adaptive as well as maladaptive, i.e., less favorable responses to pathological changes, are key to disease mechanisms. For instance, in Parkinson's disease, a lack of dopamine initiates a cascade of functional and structural changes.²⁶⁹ To specifically counteract disease-related adaptive changes, synaptic plasticity^{159,191} (see also Secs. III B and III C), specifically spike-timing-dependent plasticity,^{14,27,162,163} was incorporated in neuronal network models used to design therapeutic stimulation, giving rise to a radically new stimulation and treatment concept.²⁶⁸

It was observed that coordinated reset stimulation can shift a network from an unfavorable, synchronized attractor to a more favorable, desynchronized attractor (Fig. 5).²⁶⁸ From then on, coordinated reset stimulation and further variants were computationally developed and optimized to robustly cause an “unlearning” of pathological synchrony and synaptic connectivity, in this way causing long-lasting therapeutic effects.^{268,270–277} A series of computational studies revealed *novel stimulus response characteristics* of neural networks with spike-timing-dependent plasticity:

- *Rebound of synchrony after cessation of stimulation:* Directly after cessation of coordinated reset stimulation, synchrony may reemerge and then spontaneously fade while further approaching the desynchronized attractor.²⁷⁰
- *Cumulative effects:* Effects of coordinated reset stimulation may accumulate over time,²⁷⁸ and stimulation pauses may even improve the outcome.¹⁰⁸
- *Acute vs long-term effects:* Acute stimulation effects (observed during stimulation) and long-term effects (emerging when the system relaxes into a stable state after cessation of stimulation) may differ substantially.^{272,274} One can even decouple neurons, i.e., reduce their synaptic weights, without desynchronization during stimulation.²⁷⁴ In fact, acute effects do not necessarily serve as predictive markers for a long-term outcome.^{272,274}
- *Transition to non-invasive stimulation:* Long-term effects are favorable because they enable to reduce stimulation time and, hence, potentially reduce side effects. However, a profound advantage of this type of stimulation is that it does not require implants to permanently deliver stimulation. Rather, as predicted theoretically,^{279,280} non-invasive stimulation can be delivered occasionally or regularly for a few hours. Non-invasive

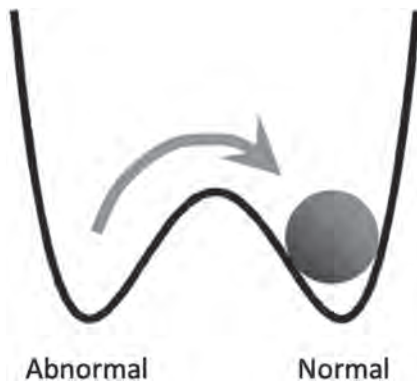


FIG. 5. Schematic illustrating how desynchronizing stimulation induces long-lasting therapeutic effects by leveraging plasticity. Spike-timing-dependent plasticity is a fundamental plasticity mechanism of the nervous system, which adapts the synaptic strengths based on the relative timings of post- and presynaptic spikes.^{14,27,163} Neural networks with spike-timing-dependent plasticity typically display bi- or multi-stability of stable states with stronger synchrony and synaptic connectivity and stable desynchronized states with weaker synaptic connectivity,^{16,268,270,272,274,278} as illustrated by a simple double-well potential here. These states serve as models for pathological and physiological conditions. Coordinated reset stimulation may shift the network into the basin of attraction of a stable desynchronized state, in this way causing a long-lasting desynchronization.²⁶⁸

therapies are typically less risky and more appropriate for larger patient populations.

- **Functional restoration:** Not only stimulation-induced unlearning of abnormal synaptic connectivity and neuronal synchronization,²⁶⁸ but also reshaping network connectivity by differentially up- or downregulating different synaptic connections²⁷⁶ may contribute to restoration of function.
- **Different plasticity mechanisms:** In Parkinson's disease pathophysiology, both spike-timing-dependent plasticity and structural plasticity^{281,282} are important²⁶⁹ and may induce different stimulation responses.^{283,284}

These computationally derived predictions and results enabled to design appropriate protocols for pre-clinical and clinical studies.

Invasive coordinated reset studies: Coordinated reset deep brain stimulation was successfully tested in Parkinsonian monkeys.^{280,285–287} For instance, a few hours of coordinated reset deep brain stimulation led to therapeutic effects lasting for one month.²⁸⁰ In addition, cumulative and long-lasting desynchronizing and therapeutic effects were observed in Parkinson's patients treated with coordinated reset deep brain stimulation.²⁶⁴

Non-invasive coordinated reset studies: Vibrotactile coordinated reset fingertip stimulation was developed to provide patients with a non-surgical and non-pharmacological treatment option.²⁸⁸ To this end, instead of administering electrical bursts through depth electrodes, weak, non-painful vibratory bursts were non-invasively delivered in a coordinated reset mode to patients' fingertips.²⁸⁸ A first in human study²⁸⁹ as well as pilot studies²⁹⁰ showed that vibrotactile coordinated reset stimulation is safe and tolerable and

revealed a statistically and clinically significant reduction of Parkinson's disease symptoms off medication together with a significant reduction of high beta (21–30 Hz) power in the sensorimotor cortex. Remarkably, also, axial symptoms, difficult to treat with regular deep brain stimulation, responded well to vibrotactile coordinated reset in these studies.^{289,290} For illustration, see patient videos in Ref. 290. Of note, Parkinson's disease patients improved during a month-long vibrotactile coordinated reset treatment when evaluated after medication withdrawal, indicating a substantial improvement of the patients' conditions.²⁹⁰ These findings indicate that a vibrotactile coordinated reset treatment might even have an impact on metabolic and degenerative processes,^{290,291} e.g., by slowing or even counteracting degeneration-related processes, e.g., vicious circles giving rise to oxidant stress and mitochondrial impairment, causing a bioenergetic crisis and the death of dopamine neurons in the substantia nigra.^{292–294}

In summary, instead of simply suppressing unwanted neuronal activity, based on principles of adaptive dynamical systems, appropriately designed stimulation techniques intend to induce sustained therapeutic effects by moving affected neural systems to more favorable attractors (Fig. 5).

E. Music and adaptivity—A physical culture theory—By Rolf Bader

Understanding music is an interdisciplinary task.²⁹⁵ Musical instruments are built such that we can listen to them, actively play them, use them in social contexts, or use them in terms of individual demands and tasks. Therefore, scientific disciplines, such as the physics of musical instruments, music psychology and neuromusicology, music sociology, or political science, must interact to arrive at a holistic understanding of music. Furthermore, the role of music in culture, technology, economy, ethnicity, or its interactions with natural resources, such as wood or alternative material for musical instrument building, needs to be considered.

Therefore, music is a constant adaptation process. Listeners adapt to new musical pieces. Musicians adapt to audiences, new musical instruments available, or new ideas of compositional techniques. Instrument builders adapt to contemporary sound and performance demands, new materials, or new technologies. Society adapts to new musical pieces, genres, or ways of music presentations, such as mass media or streaming platforms. Such adaptations are processes, including changing strategies, emotional reactions, or the development of new abilities. The participants of such adaptations might welcome and deal with or might try to reject and oppose new developments.

In contemporary research, each scientific discipline uses its own methods for understanding and predicting music.²⁹⁵ Music psychology often uses statistics or Bayesian methods. Musical acoustics involves mainly analytical equations and discretization methods, such as finite-element or finite-difference methods. Music ethnology is still dominated by heuristic and historical methodology, while computational or analytical ethnomusicology also includes mathematical modeling, e.g., of tonal systems. In all fields, machine learning methods have become more and more important like connectionist models are nearly always used for composition (see, e.g.,

Briot *et al.*²⁹⁶ for an overview) or self-organizing Kohonen maps²⁹⁷ are often used for the analytical purpose.^{298–300}

The methodologies used, therefore, strongly depend on the subfields, but some also intertwine, e.g., in the field of psychoacoustics, relating physics to perception, using algorithms calculating loudness, brightness, pitch, spatial audio, or the like. Still, to arrive at a common, robust, suitable algorithm able to model music in a global, holistic way in the future, also including extra-musical players, such as ecology, economy, or politics, a common ground is needed, not debatable among the very diverse disciplines involved. For example, a physical culture theory suggests music as an adaptive system to consist of impulses, physical energy bursts sent out, returning with a specific damping, thereby causing new impulses.³⁰¹ In its most general form, the impulse pattern formulation can be written as a system parameter g representing an impulse sent out by one subsystem. This impulse is reflected at n other subsystems with damping parameters α and β_k for each reflection point k , such as^{302,303}

$$g_+ = g - \ln \left(\frac{1}{\alpha} \left(g - \sum_{k=1}^n \beta_k e^{g-g_{k-}} \right) \right). \quad (19)$$

The system parameter g is updated at each iteration step to g_+ , taking the most recent g and the previous g_{k-} into consideration. The logarithm reflects the exponential damping found in most systems. Adaptation is present for $g_+ = g$; e.g., with musical instruments, g can be taken as a periodicity of a musical tone. During the initial transient phase, $g_+ \neq g$, and the system struggles, leading to a complex initial transient sound. After the initial phase, a stable periodicity is reached, and a musical pitch is heard. For example, with a guitar, two subsystems are present, the string and the guitar body, both with their own eigenfrequencies. Still, when playing a note, the string's vibration takes over the guitar body's vibration; i.e., the body adapts to the string's pitch. Therefore, the impulse pattern formulation is able to model the guitar tone very precisely, which is especially reflected in the length and complexity of the initial sound phase.³⁰²

Such an impulse pattern formulation algorithm is scale-free and, therefore, able to model and predict very small networks as well as overall or general behavior fast and precise in musical acoustics^{303,304} or music perception and action.³⁰⁵ Such a self-organizing system is found as a basis for all musical instrument families. Moreover, it is the basis of brain dynamics³⁰⁶ and all interactions in society or politics.

For such a system to work for aesthetic and artistic matters, consciousness and conscious content, such as experiencing sound, vision, emotion, or any kind of cognition, need to be incorporated. The physical culture theory assumes conscious content to be spatiotemporal electric fields in the brain, complex enough to arrive at experiences of all kinds. Such a spatiotemporal field again is nothing but a complex impulse pattern. Brain dynamics is, therefore, no longer taken as an interplay of bottom-up and top-down processes but as a complex, self-organizing system. Localization of brain regions processing certain tasks, such as audition, vision, or thinking, is still evident in this picture, as auditory input enters the brain through the ear, cochlear, and auditory pathway to end in the auditory cortex (as, e.g., in the auditory oddball paradigm; see Fig. 4 and

Secs. III B and III F). Still, already within this brain network, circular neural processing is often present, nearly directly connecting the cortex to the cochlear in the inner ear and back up to the cortex. Therefore, adaptation of the brain to an external input is an active process involving the whole brain, although the input of sensory information can clearly be located.

In such global musical networks, stable, bi-stable, bifurcating, complex, or chaotic scenarios occur.³⁰² In terms of musical instrument sounds, a stable musical pitch is only established after a complex initial transient sound phase. Each new tone of a melody needs to undergo such changes. This also holds for brain activity.³⁰⁷ In ensemble playing, the interaction of musicians reacting to co-musicians' performances is also undergoing such complex changes. Therefore, the whole system is a constant interplay of surprise and adaptation to changing scenarios. Although such adaptation might work, leading to a steady state, it also might fail to arrive at more extended times of chaos, noise, or bifurcating sounds. Adaptation and disruption are, therefore, two essential and ever-repeating sides of music on all levels, with sound, musical pieces, musical genre formation, or music history.

F. Adaptation in auditory cortex explained by modulations of synaptic coupling—By Aida Hajizadeh

Most sounds, such as speech and music, evolve and unfold in time, and yet, the brain perceives them as one whole continuous entity (see also Sec. III E). For this, the brain needs to exhibit a memory mechanism whereby incoming stimuli are represented and integrated with the trace of the stimuli extending to the immediate past. This ability is termed temporal integration. While source localization and spectral analysis are suggested to be the task of subcortical areas, temporal integration of sounds is proposed to occur in the auditory cortex.³⁰⁸ In an attempt to understand how auditory cortex performs temporal binding, it was shown by intracranial and extracranial measurements that neural responses in auditory cortex are context sensitive.^{309,310} That is, the neural response to a stimulus is modified when the same stimulus is presented in the context of different stimuli where this sensitivity is a function of both temporal occurrence and spectral content of the preceding stimuli.^{311–313} The simplest form of context sensitivity in the auditory cortex occurs when the same stimulus is presented repetitively with a constant stimulus onset interval. The result is a gradual reduction of the magnitude of the neural responses and is termed adaptation. Adaptation is stimulus specific and a function of the interval between the stimulus onset interval.³¹⁴

The stimulus-specificity of adaptation was shown in oddball paradigms, where the repetitive presentation of a frequent standard stimulus is interrupted by an infrequent deviant stimulus (see also Fig. 4 in Sec. III B). The magnitude of the neural responses to the standards is smaller than the magnitude of the responses to the deviants.^{309,312} This is known as stimulus-specific adaptation and the mismatch responses in invasive and noninvasive measurements, respectively.^{311,312} Despite decades of research on adaptation and its relevance for stimulus-specific adaptation and mismatch responses, understanding how adaptation takes place in auditory cortex remains challenging. Already single neurons, due to

their intrinsic properties, show adaptation, which is termed spike-frequency adaptation (see also Sec. III C).³¹⁴ Adaptation is observed in the auditory nerve fibers of the cochlea as well as in the inferior colliculus and thalamus, which act as relay stations between the cochlea and the auditory cortex. There are reasons why adaptation in auditory cortex is neither only the result of single neurons adapting to the stimulus statistics nor just inherited from the sub-cortical regions.^{157,314} The time scales at which single neurons in different stations along the auditory pathway exhibit adaptation are different from those occurring in the auditory cortex.^{314,315} Unlike in the nonlemniscal pathway, adaptation does not occur in those subdivisions of the inferior colliculus and thalamus in the lemniscal pathway, which target the primary auditory cortex (i.e., the core area).^{312,314} Along the auditory pathway, adaptation manifests itself in more complex ways with its time scales in the auditory cortex adapting to the time scales of the stimulation.^{312,314}

Neurons in the brain form networks and do not appear in isolation. The contact points between neurons are synapses whose dynamics are highly plastic. One prevailing view on the underlying mechanisms of adaptation in auditory cortex is that it is due to modulations of synaptic coupling between neurons. However, what accounts for modulations of synaptic coupling is an ongoing debate.^{316,317} Short-term synaptic depression has been hypothesized to be one plausible physiological mechanism^{176,318–320} (see also Secs. III B and III C). This type of synaptic plasticity, which occurs due to the repetitive stimulation of the pre-synaptic neurons, is mainly based on vesicle depletion and desensitization of release sites and calcium channels on the synapses of the pre-synaptic neurons.¹⁶¹ Short-term synaptic depression occurs at time scales that are similar to the time scales of context sensitive responses, and it has a high functional relevance for temporal filtering,³²¹ gain control,²¹⁹ and, although counterintuitively, efficient information transfer between neurons.³²²

In our research, we implemented dynamics of short-term synaptic depression in a computational model whose network structure is based on the anatomy of the mammalian auditory cortex.^{323–325} The auditory cortex of mammals is characterized by the hierarchical core-belt-parabelt structure, where each of these three areas is subdivided into tonotopically organized fields.^{326,327} The model comprises mean-field excitatory and mean-field inhibitory cell populations, which are characterized by nonlinear firing rates. The interconnection between cell populations is modulated by short-term synaptic depression according to the spectrotemporal pattern of the stimulation. The linearized form of the state equations together with the slow-fast approximation of the equation for short-term synaptic depression allows for the analysis of the model dynamics in terms of damped harmonic oscillators, i.e., normal modes.^{324,325} We could show that the properties of the normal modes (i.e., frequency, phase, initial amplitude, spatial wave pattern, and decay rate) are functions of the macro- (gross anatomy) and micro-structure (synaptic weight values) of the auditory cortex network as well as of the spectrotemporal pattern of the stimulation. In this approach, the auditory cortex is viewed as a spatially extended structure, and the activity elicited by an external stimulus propagates in time and space. The dynamics of short-term synaptic depression, which locally traces the stimulus history at the synapses, determine the oscillations that are spread over the entire auditory cortex. In

this view, local and global population activities that are revealed by intracranial and extracranial recordings, respectively, emerge from the constructive and destructive interference patterns of superimposed normal modes. This contrasts with the traditional view where, for example, an electromagnetic activity in the brain measured by means of magnetoencephalography reflects the summed activity of discrete local generators distributed over the auditory cortex. In the normal-mode view, adaptation in the auditory cortex can be described as modulations of the properties of these normal modes due to the modulations of synaptic coupling, where the reduction of a response magnitude is just a by-product.³²⁵

IV. ADAPTIVITY AND ARTIFICIAL LEARNING

In this section, different authors reflect on the meaning of adaptivity in the context of artificial learning. Among other topics, fundamental open problems in machine learning are discussed, as well as some perspectives on how machine learning can be used to solve physics problems and to create new control strategies for nonlinear (chaotic) systems are given. Toward the end of this section, the role of artificial learning to understand and control complex many-body systems and cooperative behavior is discussed.

A. Adaptivity is the key to success of neural networks—By Sebastian Goldt

Deep neural networks have powered a series of breakthroughs in machine learning over the last ten years. Since their early success in computer vision,^{328–332} they have set new standards in natural language processing^{333–336} and the playing of complex games, such as Go^{337,338} or Poker.^{339–341} Deep learning also increasingly impacts the natural sciences,³⁴² for example, deep neural networks recently helped predict the 3D-structure of a nearly every human protein³⁴³ in a breakthrough for structural biology. Further applications of machine learning to solve physics problems are also given in Sec. IV B.

While neural networks used in machine learning are inspired by biological neural circuits, such as the ones described in Secs. III B and III C, the neurons in machine learning are much simpler than biological neurons. Yet, it turns out that a different form of adaptivity is behind the success of deep learning. We illustrate this point using the classic machine learning task of recognizing whether a given image shows a cat or a dog. Given an image x , represented by an array of pixel values, the classical approach was to compute a vector \tilde{x} of features^{344–346} that represents the image, which is then fed into a classifier. Features could be the location of edges in an image or the correlations between patches of the same image. These features were designed *a priori* and required extensive domain knowledge.

The key idea of deep learning is instead to learn the relevant features directly from data. Therefore, rather than computing a feature vector using a predefined set of transformations, we try to learn a function $f_\theta(x)$ that maps the raw images x directly to a “label” $y = \pm 1$, indicating whether the image shows a cat or a dog. A neural network is a particular functional form for $f_\theta(x)$, usually consisting of a series of alternating linear transformations and pointwise non-linear functions.³⁴⁷ The adjustable parameters θ , called

weights, determine what the transformations compute exactly. They are found by maximizing the prediction accuracy of the network on a given set of images, which is called “training” the network.³⁴⁸ In practice, simple first-order optimization methods, such as stochastic gradient descent, work best.^{349,350} Training a neural network is, thus, a general-purpose procedure to obtain features that are well-adapted to the input data and the task at hand.

From a theoretical point of view, the success of this approach is surprising for several reasons. For example, fitting a function in a high-dimensional space, such as the space of natural images, suffers from the curse of dimensionality: the number of samples required to estimate such a function accurately scales exponentially in the input dimension.³⁵¹ Many current research activities, for example, in statistical physics,^{342,352–354} are currently working to reconcile the success of neural networks with the curse of dimensionality.

One key to this puzzle is that images are not as high-dimensional as they seem. Most of the points in the high-dimensional input space do not represent images (at least not to a human observer) and instead look like random noise. The points that do represent real images tend to concentrate on a lower-

dimensional *manifold* in input space, sketched as a two-dimensional curved surface in Fig. 6. While the manifold is not easily defined, it is tangible: its dimension has been estimated numerically^{355–359} and found to be 10–100 times smaller than the image dimension.

It is difficult to analyze the impact of the low intrinsic dimension of images on neural networks theoretically, because we lack the mathematical tools to reason about real-world data. A series of works, therefore, introduced models of data with low intrinsic dimension, such as object manifolds,³⁶² the hidden manifold,^{360,363} or the spiked covariate model.^{364,365} Each of these models offers a controlled environment in which the adaptivity of neural networks can be studied, using tools from statistics or statistical physics. One result of these studies is that neural networks can indeed adapt to lower-dimensional manifolds in their data better than classical methods of machine learning, such as kernel methods.^{364,366–371}

These results set the blueprint for a research program that aims to understand the interplay of neural networks and the data on which they operate. What are the (potentially) low-dimensional structures in other data modalities, such as the human language or amino acid sequences, that neural networks can exploit?

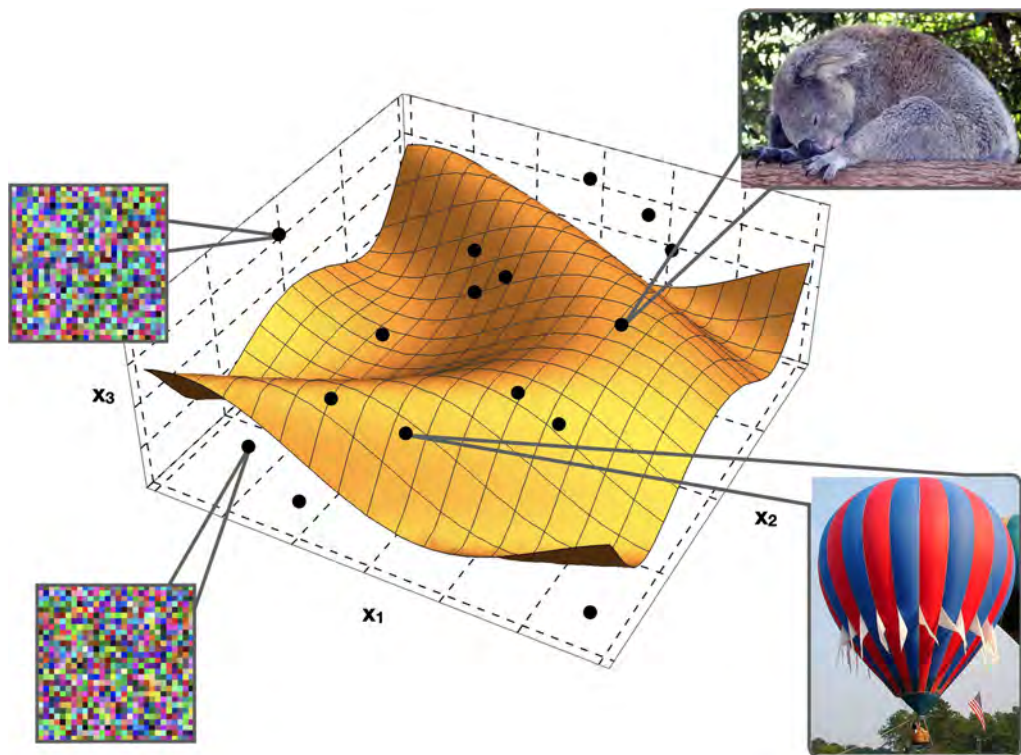


FIG. 6. The manifold structure of realistic images. Each black dot indicates a point in a high-dimensional space, which could be an input for neural networks. In the eye of a human observer, most inputs in this space resemble random noise, such as the “images” shown on the left. Neural networks exploit the fact that realistic images tend to concentrate on a lower-dimensional manifold in input space, sketched here as a two-dimensional curved surface. Figure adapted from Goldt *et al.*, *Phys. Rev. X* **10**, 041044 (2020). Copyright 2020 American Physical Society.³⁶⁰ Images are taken from the ImageNet³⁶¹ data set [Deng *et al.*, “ImageNet: A large-scale hierarchical image database,” in *2009 IEEE Conference on Computer Vision and Pattern Recognition* (IEEE, 2009), pp. 248–255. Copyright 2009 IEEE.].

B. Machine learning applications in physics—By Alireza Seif

Machine learning tools have found extensive use in the study of physical problems.³⁴² While it is not possible to provide an exhaustive list of these applications in this Perspective, we highlight a few examples related to statistical physics, namely, learning and sampling from equilibrium distributions,³⁷² classifying phases of matter,^{373,374} estimating free energy differences,³⁷⁵ identifying the direction of time's arrow,³⁷⁶ and estimating entropy production.³⁷⁷ For a comprehensive review of machine learning in physical sciences, readers may refer to Ref. 342. However, the relationship between physics and machine learning is not one-sided. Tools from theoretical physics have illuminated how machine learning tools function³⁵² (see also Sec. IV A). In the following, we examine these two directions through the lens of adaptivity.

First, we examine how machine learning can be applied to solve physics problems, with a focus on the role of adaptivity. In particular, we consider supervised learning tasks where input–output pairs are provided, and the objective is to train a neural network to accurately predict the target output value given an input. As discussed in Sec. IV A, adaptivity plays a crucial role in training the networks. In the optimization process, the network's weights are adjusted to minimize the difference between the predicted and target output values so that the network can make accurate predictions. However, as we discuss in this section, the network's prediction can be further enhanced by adapting to the history of previous inputs. This additional degree of adaptivity is particularly useful when working with sequential data. Recurrent neural networks allow for this type of adaptive inference by using an internal state that depends on the input at the previous step. Given a sequence of input tokens $\mathbf{x}_t \in \mathbb{R}^{n_v}$ and the hidden state $\mathbf{h}_t \in \mathbb{R}^{n_h}$ at time step t , this dependency can be captured as³⁷⁸

$$\mathbf{h}_t = f(\mathbf{x}_t, \mathbf{h}_{t-1}; \theta), \quad (20)$$

where f represents a neural network parameterized by θ . In the most basic form, the output of the network \mathbf{y}_t can be calculated by applying another parameterized function to \mathbf{h}_t . While in principle, these networks can capture long-term dependencies in a sequence, it has been shown that training them can be challenging due to vanishing or exploding gradients.³⁷⁹ More complicated constructions of recurrent neural networks, such as long short-term memory networks, solve this problem using a self-loop that allows the gradient to flow for longer.³⁸⁰ Modern machine translation tools build on these networks to map sequences in one language to sequences in another (seq2seq).³³⁴

Among many applications of these models in physics, we briefly discuss inferring force fields from the trajectory of particles³⁸¹ and chaotic time-series forecasting.³⁸² Reference 381 considers the problem of inferring the force field in overdamped Brownian motion. Specifically, the input \mathbf{x}_t represents the position of the Brownian particle, and the output is the parameter(s) that describe the functional form of the potential. For example, in the case of a harmonic potential $U(x) = \frac{1}{2}kx^2$, the output of the network at the final step represents the inferred value of k . The recurrent neural network is shown to outperform conventional methods with limited data and can remarkably infer non-conservative time-dependent force

fields, which conventional methods cannot handle. Reference 382 focuses on forecasting the dynamics of chaotic systems following the Kuramoto–Sivashinsky equation.^{383–385} The input is a discretized scalar field in space at step t , and the desired output is the value of the field at step $t + 1$. The authors use the framework of reservoir computing³⁸⁶ (a recurrent neural network with an untrainable input-to-internal-state mapping) to forecast the dynamics far beyond the Lyapunov time. In addition, see Sec. IV C for a discussion on using reservoir computing to control chaotic dynamical systems. In both of these examples, the network's internal state is adjusted based on the input history [see Eq. (20)], allowing it to capture temporal dependencies in the input data sequence.

The two examples discussed earlier demonstrate applications of recurrent neural networks in solving physics problems. However, it is also important to examine the reverse direction, where physics problems can be used to better understand recurrent neural networks. Reference 387 provides a case study of this approach, where a simple model for seq2seq tasks is used to investigate the impact of the data distribution in learning using a physical problem. Specifically, it considers the stochastic switching–Ornstein–Uhlenbeck process, which is a latent variable model that describes the trajectories of a Brownian particle in a harmonic potential with a time-dependent center that stochastically alternates between two values. The non-Markovianity of the input sequence is controlled by varying the distributions of waiting times between these alternations. The goal is to infer the current location of the center from the particle's past trajectory. The authors use several machine learning models for this task and demonstrate that increasing the memory of the learning model always improves the accuracy of the predictions, whereas increasing the non-Markovianity of the input sequences can either improve or degrade performance. They also identify an intriguing relationship between the performance of a learning model and distinct phases in the stationary state of the stochastic switching–Ornstein–Uhlenbeck process. In this case, as the memory of the learning model is increased, the network becomes more adaptable to longer-term dependencies in the input sequence, which in turn leads to improved performance.

The two-sided relationship between physics and machine learning is still in its early stages of development, leaving plenty of opportunities for further exploration. On the one hand, artificial intelligence can aid in discovering and explaining scientific phenomena, with emerging techniques, such as natural language processing models, potentially facilitating communication between users and algorithms.³⁸⁸ On the other hand, statistical physics has already been used to provide theoretical insights into the behavior of deep learning,³⁵² and the theory of adaptive systems could prove particularly valuable in understanding the role of data structures and the dynamics of learning in recurrent neural networks.

C. Controlling dynamical systems—By Daniel Gauthier

In this section, we consider controlling complex dynamical systems using a closed-loop feedback based on a machine learning approach known as reservoir computing. Here, the concept of adaptivity appears in at least two guises: the dynamical system being controlled, often call the *plant*, and the controller. For a plant to be controlled to desired behavior, we need to have access to some

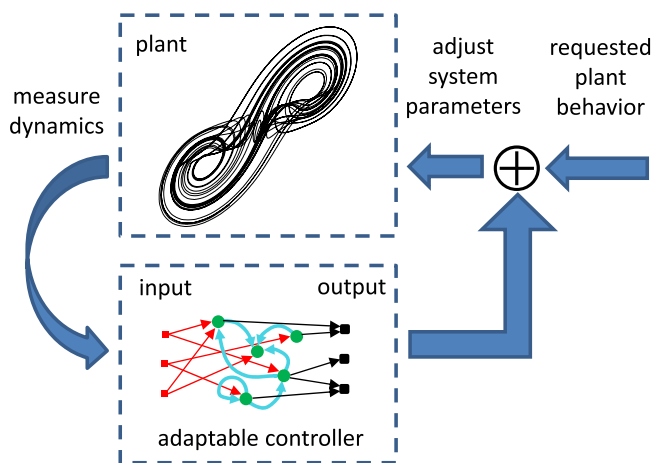


FIG. 7. A complex dynamical system controlled using a closed-loop feedback. The controller is designed using an adaptive machine learning approach.

signals generated by transducers attached to the plant that can be used to infer its dynamical state and have access to one or more parameters that adjust the state of the plant as illustrated in Fig. 7.

The controller needs to process plant signals and perform inference to estimate the state, compare this to the requested plant behavior, and generate control perturbations that are applied to the adjustable system parameters. For complex dynamical systems, especially those that display chaos, the control perturbations are a nonlinear function of the plant's state and requested behavior and, therefore, fall in the category of a nonlinear controller. Traditionally, nonlinear controllers require an accurate model of the plant, which often entails substantial effort from expert control engineers and mathematical model builders.

One highly successful alternative that was developed decades ago for controlling chaotic systems is to take advantage of unstable sets that are the backbone of the chaotic system in phase space, such as unstable periodic orbits.^{389,390} A chaotic system naturally visits these unstable sets, and control perturbations are designed using a linear algorithm that is valid in a local neighborhood of these sets. Controlling other behaviors, however, requires a fully nonlinear controller.

One approach for realizing a fully nonlinear controller is to use machine learning to learn a model of the plant,³⁹¹ referred to as nonlinear system identification in the control engineering literature. Artificial deep neural networks in a feed-forward geometry are known to be universal approximators of functions (see Sec. IV A) and, hence, should be able to learn how to map measurements and requested state to control perturbations. Here, a multi-layer network of artificial neurons with nonlinear input-output functions is trained by adjusting the network link weights using supervised learning. While there has been good success using this approach, the amount of data needed to train the network can be substantial, making it difficult for the controller to adapt to changes in the plant.

Reservoir computing is a fast and low-data machine learning approach especially well suited for learning models of dynamical

systems³⁹² because it is also a dynamical system and it holds great promise for controlling dynamical systems. As seen in the lower dashed box of Fig. 7, the reservoir computer consists of an input layer (red squares), a pool of neurons (green dots, the “reservoir”), and an output layer (black squares). The neuron dynamics are described by a differential equation that is driven by a nonlinear function of the signals from the input layer and the output of other neurons in the reservoir and has a simple exponential time constant. Thus, it has short-term memory that can be matched to the plant dynamics. The link weights on the input layer and the internal “reservoir” of neurons are not trained; they are assigned randomly at the outset, and only the weights of the output layer are trained. This dramatically reduces the size of the training data as well as the training computation time. Furthermore, the neural network can perform multiple tasks by combining a single reservoir with different trained output layers. One approach for controlling dynamical systems with a reservoir computer is to train it to learn the inverse of a dynamical system in the presence of control;³⁹³ that is, we train it to learn the perturbations required to guide the system to the desired state sometime in the future. This approach works well for systems, such as a robotic arm, that display constrained low-dimensional behavior, but a parallel deep architecture appears to be required for controlling complex systems that display chaos.³⁹⁴ The training data required for reservoir-computing inverse control appear to be on the order of 10 000 data points and modest computation time, suggesting that it can be used for real-time adaption of the controller as the underlying plant changes its dynamics because of non-stationarity or a damage event.

An open question is whether the data requirements can be reduced further so that a small microprocessor typically found on internet-of-things devices can be used to retrain the controller. Our recent work³⁹⁵ that reformulates the reservoir computer as delay lines of the measured plant signals followed by a nonlinear output layer may be promising for this application because it reduces the amount of training data by a factor of ten or more. However, it is not yet clear whether this new approach gives up some adaptivity. We are working on extensions of this work to balance the desire for fast training with wide adaptivity.

D. Modeling complex adaptive human-environment systems with multi-agent reinforcement learning dynamics—By Wolfram Barfuss

Rapid and large-scale collective action is required to enter sustainable development pathways in coupled human-environment systems safely away from dangerous tipping elements³⁹⁶ (also, see Sec. V E). The question, however, of how *collective* or *cooperative* behavior—in which agents seek ways to improve their welfare jointly—emerges is unresolved.³⁹⁷ Evolutionary game theory has produced a sound equation-based analytical understanding of the mechanisms for the evolution of cooperation.³⁹⁸ Yet, this was primarily done with highly simplified models, lacking environmental context and cognitive processes.³⁹⁹ These elements are the center of artificial intelligence and cognitive neuroscience research,^{400,401} which only recently emphasized the need for developing cooperative intelligence.^{402,403} Moreover, analyzing systems composed of multiple intelligent agents typically requires expensive computer

simulations, which are not straightforward to understand.^{404–407} Thus, little is known about how cooperative behavior emerges from and influences a collective of individually intelligent agents in complex environments.

There is a unique opportunity for *adaptivity* in non-linear dynamical systems to help solve this challenge. Based on the link between evolutionary game theory and reinforcement learning,^{408,409} we can model a collective of reinforcement learning agents as a dynamical system. Doing so provides improved, qualitative insights into the emerging collective learning dynamics,⁴¹⁰ enabling equation-based analytical tractability of agent-based simulations.

Here, reinforcement learning is the central adaptive mechanism (cf. “Reinforcement learning is direct adaptive optimal control”;⁶² also, see Sec. II C). Reinforcement learning is a trial-and-error method of mapping observations to actions in order to maximize a numerical reward signal. The challenge is that those actions can change the environment’s state, and rewards may be delayed. Reinforcement learning is not only an artificial learning algorithm,⁴⁰¹ it also has wide empirical support from neuroscience,^{153,411} psychology,⁴¹² and economics.^{413–416} It is, therefore, ideally suited to model coupled human-nature systems.

In their seminal work, Börgers and Sarin showed how one of the most basic reinforcement learning update schemes, cross-learning,⁴¹³ can converge to the deterministic replicator dynamics of evolutionary games theory.⁴¹⁷ The relationship between the two fields is as follows: one population with a frequency over phenotypes in the evolutionary setting corresponds to one agent with a frequency over actions in the learning setting.⁴⁰⁸ Since then, this analogy has been extended to other reinforcement learning variants, such as stateless Q-learning,^{418,419} regret-minimization,⁴²⁰ and fictitious play.⁴²¹ Of particular relevance to modeling coupled human-nature systems is the dynamic formulation of the general and widely used class of temporal-difference learning,⁴²² which is able to learn in changing state-full environments.

Typically, the learning dynamics are derived by performing a mathematical separation of timescales of the interacting process with the other agents and the environment and the process of adapting the agents’ policy to gain more reward over time.⁴²³ Under the complete separation of timescales, the dynamics become deterministic. One can understand such learning dynamics as an idealized model of the multi-agent learning process, in which agents learn as if they have a perfect model of the current environment, including the other agents’ current behavior.⁴²⁴

This learning-dynamic approach offers a formal yet practical, lightweight, and deterministically reproducible way to uncover the principles of collective cooperation emerging from intelligent agents in changing environments. We briefly highlight three examples; for instance, it was found that, in contrast to non-changing static environments, no social reciprocity is required for cooperation to emerge in changing environments.⁴²⁵ The individual attitude of how much the agents care for the future alone can adjust the setting from a tragedy of the commons to a comedy, where agents predominantly learn to cooperate. However, for this mechanism to work, the severity of an environmental collapse must be sufficiently severe. Another work showed how the agents’ irreducible uncertainty about the actual environmental state can induce a tipping point toward mutually high-rewarding cooperation. However, this is only valid

when all agents are equally uncertain about the environment.⁴²⁶ The last example highlights how the same temporal-difference learning dynamics can be used to model agents that not only learn to react to their physical but also to their social environment, which is likewise a pathway to mutually high-rewarding cooperation.⁴²⁷

Such learning-dynamic studies focus on understanding the underlying principles of collective cooperation from intelligent agents in complex environments. Therefore, these models are reduced as much as possible to capture only the most essential features. However, evidence from deep multi-agent reinforcement learning studies shows that sustainable and cooperative behavior can likewise emerge from intelligent agents in high-dimensional environments.^{428–430}

The advantage of the learning-dynamics approach is that it opens up all the tools of dynamical systems theory to the study of collective learning; for instance, the learning dynamics have been found to exhibit multiple dynamic regimes, such as the convergence to fixed points, limit cycles, and chaos,^{419,422} critical transitions with a slowing down of the learning processes at the tipping point,⁴²⁶ and the separation of the learning dynamics into fast and slow eigendirections.⁴²⁶

Future work in many directions is required to build this approach of *adaptivity* in non-linear dynamical systems into a new way of modeling human–environment interactions and socio-economic systems (see Sec. V). First, the presented learning dynamics need to become applicable to the system with many agents, using various types of mean-field approaches.^{431–433} Second, the learning dynamics need to consider the effect of intrinsic noise, which can substantially alter their collective behavior^{427,434} (see also Sec. II B). Third, the learning dynamics needs to be advanced to be able to model more refined notions of cognition, such as representation learning, learning and using intrinsic world models, and intrinsic motivations (see also Sec. III). A social-ecological resilience paradigm of multi-agent environment interactions, in turn, can benefit such endeavors.^{435,436}

E. Biomimetic intelligence for active matter—By Giovanni Volpe

Over billions of years of evolution, motile micro-organisms have developed complex strategies to survive and thrive in their environment by integrating three components (Fig. 8): *sensors*, *actuators*, and *information processing*. Their biochemical networks and sensory systems are optimized to excel at specific tasks, such as to climb chemical gradients,⁴³⁸ to cope with ocean turbulence,⁴³⁹ and to efficiently forage for food.^{440,441} They have also acquired complex strategies to interact with their environment and with other micro-organisms, leading to the emergence of macroscopic collective patterns⁴⁴² (also, see Sec. IV D). These patterns are driven by energy conversion from the smallest to the largest scales and permit micro-organisms to break free some of their physical limits; for example, dense systems of bacteria develop “active turbulence” at length scales where only laminar flows are expected from the underlying physical laws.^{443,444}

There are both scientific and technological reasons that are driving the quest toward biomimetic artificial active matter. Scientifically, biomimetic systems capable of harnessing energy and

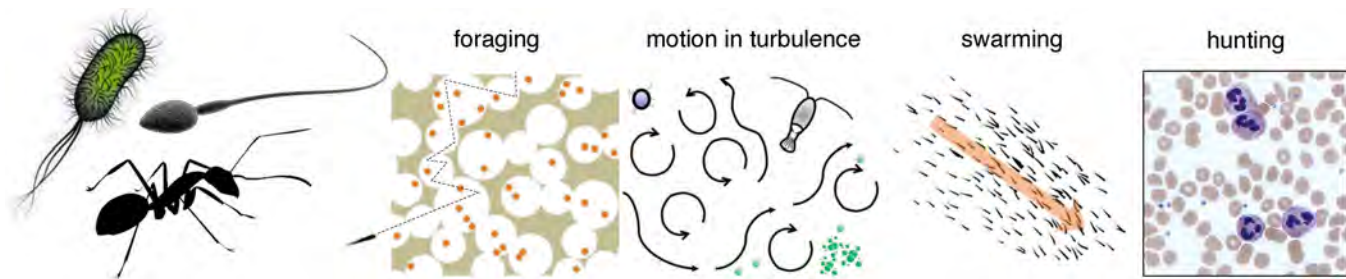


FIG. 8. Active matter with embodied intelligence. Bacteria, sperm cells, and ants are biological examples of active particles with embodied intelligence. They feature intelligent behaviors that permit them to survive and thrive in their ecosystem thanks to the integration of sensors, actuators, and information processing. Their behaviors also adapt to complex environments (e.g., foraging for food), and their dynamic interactions lead to collective emerging behaviors (e.g., swarming and hunting). The challenge is now to draw inspiration from nature to create microscopic artificial active particles with embodied intelligence that mimic these adaptive and dynamic emerging behaviors. Adapted from Cichos *et al.*, *Nat. Mach. Intell.* **2**, 94–103 (2020). Copyright 2020 Springer Nature.⁴³⁷

information flows are ideal model systems to investigate and test physics far from equilibrium, which is one of the greatest challenges for physics in the twenty-first century. Technologically, biomimetic active particles hold tremendous potential as autonomous agents for healthcare, sustainability, and security applications: for example, enabling the targeted localization, pick-up and delivery of microscopic objects in bioremediation, catalysis, chemical sensing, and drug delivery.⁴⁴⁵

In the last two decades, the active-matter research field has tried to replicate the evolutionary success of micro-organisms in artificial systems.⁴⁴⁵ Researchers have replicated the actuators by developing artificial active particles that extract energy from their environment to perform mechanical work.^{446,447} Albeit to a lesser extent, they have also been able to replicate the sensors by making these active particles adjust their motion properties (e.g., their speed) to chemical, thermal, or illumination stimuli.^{448,449} However, these artificial particles are still largely incapable of autonomous information processing, which is dramatically limiting the potential of artificial microscopic active matter to provide scientific insight and technological applications.⁴³⁷ Thus, the active-matter research field is now confronted with several open challenges to create truly autonomous active particles.

1. Make active particles capable of autonomous information processing

Currently available active particles lack the complexity necessary for autonomous information processing. In fact, active particles are still rather simple in shape and behavior.⁴⁴⁵ They are often Janus microspheres or microrods with different materials on their two sides, which can self-propel and sterically interact with each other. This physical simplicity is a consequence of the relative simplicity of the employed design and fabrication processes, which in turn limits the range of behaviors achievable by the active particles. Despite this simplicity, the study of active particles has already led to major breakthroughs, such as to understand how plankton copes with turbulence^{439,450,451} and to program self-assembling robotic swarms.^{452,453}

Motile micro-organisms exhibit more powerful and flexible strategies to survive and thrive in their environment. Even the simplest motile bacteria have evolved intelligent behaviors by following powerful adaptive strategies encoded in their shape, biophysical properties, and signal-processing networks: not only can they extract energy from their environment to move and interact with other bacteria, but they can also extract information by sensing their environment and adjust their behavior accordingly.⁴³⁸ The challenge is now to make active particles capable of autonomous information processing, such as living motile micro-organisms. This can be addressed by pushing the boundaries of design and micro-fabrication techniques to build microscopic active particles with embodied intelligence (*microbots*).⁴⁵⁴ These microbots will be able to sense their environment, to differentiate stimuli, and to adapt their behavior toward determinate goals.

2. Optimize the behavioral strategies adopted by individual active particles

The behavioral strategies that can be adopted by active particles are still very limited. There have been several studies on the behaviors of active particles in response to the properties of their environment;^{445,455–457} for example, the presence of periodic arrays of static obstacles alters the preferential swimming direction of self-propelling active particles, a fact that permits one to sort microswimmers on the basis of their swimming style.⁴⁵⁶ However, these behaviors are still rather simple and rely on in-built properties of the active particles that cannot be changed at will or adapted to different environmental conditions. This is a consequence of their limited capability of gaining information about their environment and reacting accordingly.

More complex behaviors have been achieved using micro-organisms instead of active particles; for example, the presence of obstacles in the environment has permitted to alter the pathway toward the formation of multicellular colonies of bacteria.⁴⁵⁸ Also, genetically modified bacteria whose speed is controllable by light have been arranged into complex and re-configurable density patterns using a digital light projector.^{459,460} The optimal behaviors in complex environments are often not obvious; for example,

let us consider the foraging problem,^{440,441} where an active particle performs a blind search to catch some sparse targets. When the environment does not present spatial features, the number of caught targets is maximum for a Lévy-search strategy^{440,441} (even though this is still an active research field⁴⁶¹). Surprisingly, in a porous medium, the optimal strategy mixes Lévy runs and Brownian diffusion.⁴⁶²

The challenge is now to discover, understand, and engineer intelligent behavioral strategies that can be autonomously adopted by active particles with embodied intelligence. This can be addressed by designing and engineering the behavior of microbots to enable them to autonomously perform directed tasks in complex environments, such as efficient navigation, target localization, environment monitoring, and conditional execution of actions.

3. Optimize the interactions between active particles

Currently, active particles cannot communicate with each other beyond interacting through some simple physical interactions. Natural systems, such as swarms of midges, schools of fish, and flocks of birds, have evolved powerful sensing capabilities to gain information about their environments and to communicate.^{463,464} The underlying behavioral rules are often hard to identify.^{437,442,465,466} Active-matter studies provide the testing grounds for new non-equilibrium descriptions, which are by necessity often computational.⁴⁶⁷ They are either based on hypothesized mechanistic models for local interactions,⁴⁴² upon coarse-grained hydrodynamic approximations,⁴⁶⁸ or on basic fluctuation theorems.⁴⁶⁹ The question is often how local energy input and physical interactions determine the macroscopic spatiotemporal patterns. Answers may be sought, e.g., by computational techniques.^{470–473}

Differently from computational studies, most active-matter experiments rely on very simple steric and short-range physical interactions. Even these simple interactions can lead to interesting complex behaviors and self-organization whose onset is often observed in artificial systems where increased energy input above a threshold density drives a phase transition to an aggregated state. An example of such behaviors is the formation of “living crystals,” which are metastable clusters of active particles.^{474,475}

Much more interesting behaviors are observed when the interactions between the active particles can be tuned at will. This can be achieved by externally imposing interaction rules on the active particles; for example, external feedback control loops have been used to create information-based individual dynamical behavior⁴⁷⁶ or interactions⁴⁷⁷ between active particles, which explicitly depends on the information about the position of other particles. Such complex forms of interaction can also be achieved using macroscopic robots. In fact, the field of robotics can serve as a major source of inspiration for the development of active matter at the microscale;^{453,478,479} for example, some robots (5 cm in diameter) have been programmed to respond to sensorial inputs with a delay and have shown that, by controlling the delay, we can control the aggregation vs dispersion of the robots.^{480–482}

The challenge is now to identify and engineer optimal interaction rules that can be embodied in active particles interacting with other particles and with their environment. This can be addressed by programming microbots with embodied interaction strategies beyond the simple steric and short-range interactions employed

by current active particles. This will permit researchers to realize microscopic swarms of artificial active particles capable of collective intelligent behaviors and to engineer microscopic ecosystems where multiple species of microbots and particles interact.

V. ADAPTIVITY IN SOCIO-ECONOMIC SYSTEMS

In this section, we provide a perspective on adaptivity from socio-economic systems, including topics, such as the conception of modern power grids, adaptive social interactions, and the role of adaptive mechanisms in epidemiological and climatic models.

A. Adaptive networks and their importance for epidemiology—By Philipp Hövel

Network epidemiology is a prime example of adaptive networks at work. Many infectious diseases spread via direct contacts. These contacts can be captured by social, transportation, and other logistic networks. They provide a mathematical framework to formalize the interaction of individuals (humans or animals) and, hence, potential paths of disease transmission. Locally, e.g., within a population or between group individuals, the dynamics of pathogens are often described by compartment models, such as the widely used susceptible–infected–recovered model originally introduced by Kermack and McKendrick.⁴⁸³ Adaptivity must be considered if the state of the networked system, say, the number of infected, triggers an adjustment of the network structure with the aim to mitigate an outbreak and to contain the disease. This closes the mutually influencing feedback loop of the dynamics on and of networks as depicted in Fig. 9: (i) The network structure governs the spreading of the disease (*dynamics*). (ii) In turn, the current state of the system leads to changes in the structure of interactions (*networks*).

The dynamics-induced changes to the network are often akin to control schemes that involve minimizing a goal function to reach a target state.⁹ Similarly, non-pharmaceutical containment protocols, which demand a reduction of social contacts or restriction of movement, can be based on, for instance, the number of new infections. Prominent cases, where such applications of adaptive networks have been successfully implemented, include the H1N1 pandemics in 2009,^{484,485} the Ebola epidemic in 2014,⁴⁸⁶ and—of course—the on-going SARS-CoV-2 pandemic.^{487–490} In these examples, one prominent path of transmission was the global airline transportation network, which has been accounted for in many studies.^{491–493}

Extensive numerical simulations are able to explore possible interventions and quantify their impact. Key findings might be

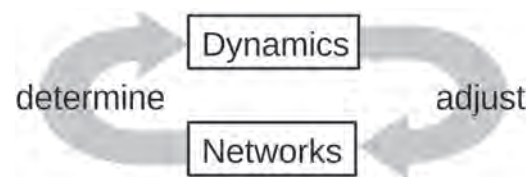


FIG. 9. Schematics of the interplay between dynamics and networks.

that international travel bans yield a limited delay of spreading as demonstrated for Ebola in 2014⁴⁸⁶ or the feasibility of *zero-COVID* or *low-incidence* strategies.^{494,495} They are also able to provide insight into less than optimal adherence to containment measures.⁴⁹⁰ In any case, these studies are valuable tools for policy makers to reach evidence-based and data-driven decisions and to inform the public about their potential impact.

The concept of adaptive networks for the study of epidemic spreading of infectious diseases has a long history and dates back beyond the most recent examples of public health emergency of international concern. Rewiring of susceptibles to avoid contact with infected has been studied, for instance, by Gross *et al.*^{98,99} They employed a low-dimensional compartment model, which allowed an exhaustive bifurcation analysis, and identified dynamical patterns, such as first-order transitions and hysteresis. In short, as long as a node remained healthy, its network neighborhood evolved gradually. However, the moment an infection occurs, the degree of a node drops rapidly, and the node finds itself isolated until recovery. Note that due to the small-worldness of many social networks,⁴⁹⁶ there could be situations, where rewiring would potentially deteriorate the situation because it might create new shortcuts through the network that could—unintentionally—bring nodes closer to other, distant regions of infection.

Besides travel restrictions, surveillance and monitoring of incidence numbers are key ingredients for a rapid identification of an outbreak. For that purpose, the introduction of *sentinel nodes* on temporal networks has proven to be insightful and demonstrated in the case of animal diseases.^{90,497} These nodes should be monitored because of their position in the network that allows early detection and reliable identification of the origin of the outbreak for many different initial conditions. Therefore, they provide helpful and detailed clues where the network could be best adjusted. Similarly, screening a fraction of incoming patients has been shown to be effective as potential control measure nosocomial infectious diseases and the spread via hospital-referral networks.^{498,499} The impact of a rapid response has been exemplified during the early stages of the COVID-19 pandemic, where—in mainland China—containment policies effectively depleted the susceptible population and resulted in a subexponential growth of infection cases.⁴⁸⁸ Upon successful containment, restriction can be relaxed again, and the network returns to its original state.

Adaptive networks are a special case of time-varying or temporal networks, where every edge has a time stamp and is active for a certain amount of time.^{500,501} In epidemiology, in particular, the sequence of contacts is crucially important. Only time-respecting paths contribute to the transmission of a pathogen and the spreading of a disease. Any interaction with contacts/neighbors in the social network before their infection carries no risk of transmission. Luckily, concepts, such as network controllability,⁵⁰² can be easily extended for temporal and multiplex networks.^{503,504} From a mathematical point of view, the temporal nature of networks—including changes of their structure due to adaptation—can be implemented by time-dependent adjacency matrices, which give rise to modeling frameworks for the spreading of epidemics, such as the individual-based and pair-based models.^{505–508}

To sum up, adaptive networks play a central role not only for realistic investigations of spreading dynamics but can help to study

and design interventions for disease containment, mitigation, and eradication. With a further increase of data availability (often in real time), models of network epidemiology become more and more realistic and informative in their predictive power. Future challenges include the integration of purely epidemiological models and a mathematical framework for the dynamics of social behavior and opinion formation. This would lead the way for a holistic description of disease spreading on adaptive networks.

B. Coevolutionary network dynamics in social and epidemic systems—By Jan Mölter

In the context of dynamical systems on networks, one manifestation of adaptivity is in so-called adaptive or coevolutionary networks.^{99,509}

A network is a collection of entities together with a relation between these entities that are generally represented as nodes and links, respectively. In a dynamical setting, every node is a dynamical system that not only depends on its internal dynamics but also on the dynamics of its neighborhood in the network, i.e., the set of nodes it is linked to. Constituting for an adaptive network is the idea that the topology of the network and, therefore, the interactions between the individual nodes of the network are not static but rather also dynamic, coupled to the dynamics of the nodes. As such, we have a closed feedback loop in which the topology of the network influences the dynamics of the nodes and the state of the nodes influences the dynamics of the topology.⁹⁹ Combining the so-called dynamics on the network with the dynamics of the network in that way is what makes the system *fully adaptive* (see Fig. 9 in Sec. V A).

To make this more concrete, let us consider the paradigmatic example of the adaptive voter model,^{511,512} which is an extension of classical models of opinion or consensus formation.^{513,514} In this model, one considers a population in which every individual subscribes to one of two contradictory opinions and in which the social relationships are encoded in some social network. As for the dynamics, one assumes that at each time step, individuals either adapt their opinion to the opinion of individuals in their neighborhood or that they break off their relationship with individuals of opposing opinions and rather connect with others of the same opinion. While the former corresponds to the dynamics on the network, the latter corresponds to the dynamics of the network. Depending on the relative strength of these two processes, in expectation, the population eventually reaches either a dynamic equilibrium characterized by non-vanishing prevalence of pairs of connected individuals with opposing opinions or a static equilibrium where the underlying social network fragments so that in every component, only one opinion prevails.^{511,515,516}

Another paradigmatic example besides the adaptive voter model is that of an adaptive susceptible–infected–susceptible (SIS) epidemic.⁹⁸ One considers again a population on an underlying social network that encodes the relationship between individuals. Every individual is then exposed to an SIS epidemic, meaning that individuals start off as susceptible, become infected at some rate when individuals in their neighborhood are infected, and upon recovery at another rate are susceptible again.⁵¹⁷ In addition to these epidemic transitions, one allows, similar to the adaptive

voter model, that susceptible individuals can break off the relationship with infected individuals and instead connect to a susceptible individual.⁹⁸ Now, for the SIS epidemic and in expectation, it is well-known that at a critical infection rate, the system exhibits a supercritical transcritical bifurcation and beyond which the system eventually reaches an endemic dynamic equilibrium as opposed to the epidemic dying out. In contrast, due to the adaptivity, this bifurcation can turn from supercritical to subcritical, the consequence being that a region of bistability emerges and the transition to an endemic equilibrium is not continuous anymore.^{98,518}

While these examples both illustrate the idea behind adaptive or coevolutionary networks in the sense that dynamics on the network and of the network depend on each other, they also highlight the fact that adaptivity can induce fundamental changes in the phenomenology. This suggests that, when developing models of the natural world, it can be paramount to take adaptive dynamics into account.

Recognizing the importance of adaptive networks, many research studies have been done focused on different aspects of the phenomenology that comes with adaptivity or extending existing models by introducing adaptivity. Hence, in the following, we are going to highlight some works from the last decade—without any claim to comprehensiveness.

In relation to the adaptive voter model that we have introduced before, it has been reported that if one considers directed as opposed to undirected networks in an adaptive voter model, fragmentation might occur far below the critical value due to the formation of self-stabilizing structure.^{519,520} Moreover, there has also been work extending the model to allow for a continuum of opinions (see also Sec. V C), which in many cases is a more realistic assumption, demonstrating the emergence of communities with diverse opinions rather than leading to fragmentation.^{521,522}

Further investigations in the adaptive SIS epidemic and adaptive epidemics, in general, have led to studies about the bifurcation behavior⁵²³ and the epidemic threshold itself⁵²⁴ as well as the dynamics near this threshold with an emphasis on early-warnings signs.⁵²⁵ In the context of a pandemic (see also Sec. V A), adaptive epidemics have also been studied to assess the relationship between containment strategies of quarantining and social distancing.⁵²⁶ Besides rewiring as a mechanism for adaptivity,^{98,527} others have considered network growth due to birth and death processes,⁵²⁸ the latter in response to the epidemic upon being infected, and activation and deactivation of links following an adaptive strategy.⁵²⁹

Apart from the adaptive voter model and adaptive epidemics, another frequently studied model system is that of coupled phase oscillators^{110,530} with adaptive coupling strengths (see also Secs. II A and II D). The main feature one is interested in these systems is the emergence of fully or partly synchronous states. Importantly, it has been shown that certain adaptivity rules promote the explosive transitions into synchrony.⁵³¹ Moreover, others have reported that adaptivity can be used to control cluster synchronization⁹ or that slow adaptation leads to the emergence of frequency clusters.^{34,35}

In recent years, there has been an increasing interest in generalizing the notion of networks to higher-order networks, i.e., simplicial complexes or more generally hypergraphs. Instead of only dyadic relations, these structures can also capture higher-order interactions. Consequently, evolutionary games⁵³² as well

as consensus formation in the form of an adaptive voter model have been investigated on simplicial complexes as well as hypergraphs.^{533,534} Due to their much more complex topology, these structures promise a much richer phenomenology while at the same time being considerably more complicated to handle so that it will be interesting to see what the coming years will bring.

C. How social dynamics and networks adapt to growing connectivity—By Philipp Lorenz-Spreen

Online communication can be understood as an adaptive, non-linear system, all the more so because it increasingly involves many-to-many interactions and is, thus, a highly coupled system. In my research on self-organized online discourse, I interpret adaptivity as the process of changing social systems through external influences, such as technological developments. Information technology has made various aspects of our lives more dynamic, both in spatial and temporal dimensions. Connections with others can be made across spatial and sociodemographic constraints, and messages can be recorded and spread across the globe in seconds.

However, these increased dynamics and the resulting adaptations do not happen without values: As old boundaries are overcome, new ones emerge, if only because of finite amounts of available attention resulting from very simple limits on human processing capabilities, but also because of the implementation and commercial incentive structure of the technology. Here, I will present two mechanisms we have recently proposed for how social systems adapt to these changes and how online platforms shape this process along commercial interests since there is no apparent, neutral status quo in which social systems would evolve. To this end, I want to focus on two key questions that an individual decision maker faces online and their downstream consequences for macroscopic dynamics and the shape of public discourse.

First, connectivity is increasing through online platforms, and new connections can and are easily made. Since the famous six degrees of separation⁵³⁵ on the U.S. social network, networks seem much better connected; Facebook reports 3.5 degrees of separation on its friendship graph.⁵³⁶ Nevertheless, there are consistent reports of segregated, homophilic network structures on nearly all online platforms, as well as related trends of increasing polarization (see Ref. 537 for a recent overview). The mechanism that might resolve this apparent paradox may lie behind the question of whether we change our opinions according to our friends or whether we change our friends according to our opinions. In classical models of opinion dynamics, the network structure is fixed and the core assumption is a constructive process of an opinion change in a social interaction.⁵³⁸ In the long run, this process would predict convergence to a global consensus opinion with increasing connectivity; only under the assumption of disconnected networks or limited trust are disconnected opinions conceivable, let alone an outward or distancing movement of these clusters possible. We have recently proposed an alternative mechanism that describes the dynamics of an agent's opinion $o_i(t)$,⁵³⁹

$$\dot{o}_i = -o_i + K \sum_{j=1}^N A_{ij}(t) \tanh(\alpha o_j), \quad (21)$$

which describes a process of mutual reinforcement of opinions within groups of shared stance [i.e., if $\text{sgn}(o_i) = \text{sgn}(o_j)$]. The additive term $\tanh(\alpha o_j)$ moves both opinions in the same direction if they have the same sign and moves them toward the neutral state 0 if they have a different sign. Who is interacting with whom is governed by the time-dependent adjacency matrix $A_{ij}(t)$, which only has a non-zero entry if an interaction happens between i and j at time t . Its structure dynamically adapts to changing opinions, hence co-evolving and following a probability distribution ruled by homophily,⁵⁴⁰

$$P_{ij} = \frac{|o_i(t) - o_j(t)|^{-\beta}}{\sum_j |o_i(t) - o_j(t)|^{-\beta}}, \quad (22)$$

which is a term that might be partly driven by algorithmic recommendations suggesting like-minded others as interaction partners on social media. This combination helps to explain the potential emergence of growing polarization dynamics even under increasing connectivity [i.e., if the average path length of $A_{ij}(t)$ decreases, at least for controversial topics (i.e., high α)]. For more details, please see Ref. 539, and an extension into multi-dimensional opinion spaces, see Ref. 541.

Second, the increasing availability of information poses a challenge to the allocation of attention. So how does public discussion adapt to the increasing speed of available information? To describe this process, we quantified and modeled the dynamics of public interest for individual topics in various domains.⁵⁴² The main result can be described as an acceleration of the dynamics of public interest in a topic and a narrowing of the amount of time spent on each topic, while the overall amount of attention spent on a topic remained stable over the years. For a mechanistic understanding of these dynamics, we modeled them as an adaptation of a Lotka–Volterra process for species competing for a common resource, with finite memory,

$$\dot{a}_i = r_p a_i \left(1 - r_c \int_{-\infty}^t e^{-\alpha(t-t')} a_i(t') dt' - c \sum_{j=1, j \neq i}^N a_j \right), \quad (23)$$

where $a_i(t)$ describes the dynamics of the collective attention or public interest to a topic i . It depends on a growth term $r_p a_i$ with an exponential growth rate r_p if it is undisturbed. However, two terms are slowing and eventually reversing the growth process. That is, $r_c \int_{-\infty}^t e^{-\alpha(t-t')} a_i(t') dt'$, which grows proportionally with the attention to the topic itself by exhausting the available resources at rate r_c , and $c \sum_{j=1, j \neq i}^N a_j$, which describes the constantly ongoing competition with all other topics j for that common resource. This we believe captures the essence of the idea of competitive attention economy originally formulated by Ref. 543 and describes well the empirical observations. It also captures the economic incentive structures to produce information faster in this competitive situation to have an advantage for gaining public interest.

In summary, I believe that these mechanisms may capture two adaptive mechanisms of social systems in response to increasing interconnectedness and information availability that are driven by fundamental limits of human cognition, namely, the ability to maintain a certain number of social contacts as well as to process a finite

amount of information in parallel, as well as economic incentives to capture those. Future research in this area should aim to put those assumptions of mechanism of social dynamics on an empirical, probably experimental, footing to understand the causal drivers of how social systems adapt to changes in our world, e.g., technological and political changes.

D. Energy transition and moving toward the CO₂-neutral power grid—By Mehrnaz Anvari

The important role played by electricity in the daily life and activities causes a serious dependency of modern society on the reliable functionality of the power grid. Moreover, because of the interconnection of the power grid to other societal networks and systems, such as transportation,⁵⁴⁴ telecommunication,⁵⁴⁵ and health systems,⁵⁴⁶ it is of great importance that the power grid adjusts itself to changing conditions or, indeed, mitigates any internal and external perturbations and fluctuations, as generally discussed in Sec. II A for dynamic networks. Any failure in the power grid can quickly spread not only within the grid itself, but can set off a chain of failures, as a domino effect, in other social networks and systems. During energy transition and moving toward a CO₂-neutral power grid, fossil fuels sources should be replaced by renewable energy sources, such as wind, sunlight, water, and geothermal heat. The need for rapid CO₂ reduction is comprehensively discussed in Sec. V E. Among renewable energy sources, wind and solar power are sources inherently time-varying. This means that a constant generator power in Eq. (11) in Sec. II D will be replaced by irregular, hardly predictable wind and solar power that may constitute serious threats for power grid stability. Furthermore, the pattern of electricity consumption is changing due to the exploitation of green energy sources in other sectors, such as transportation⁵⁴⁷ and heating.⁵⁴⁸ Therefore, for being able to plan and operate future-compliant electricity grids with a continuously increasing share of renewable energy sources, it is vital to recognize the new origins of fluctuations in both supply and demand side, along with their statistical and stochastic characteristics to be able to adapt the power grid or to mitigate these fluctuations and, thus, maintain the energy balance in the grid.

The identification of these characteristics, along with the empirical data, enables us to develop valid data-driven models to describe the underlying system dynamics. Last, the combination of data-driven models and the complex network science empowers us to indicate the impact of new sources of both supply and demand on the current power grid and, therefore, to determine how the power grid structure and control systems should be adapted in the future to keep the energy balance and, consequently, the stability in the system.

In the following, we will review briefly some recent works related to the data analysis and data-driven models as well as their combination with the complex network science leading to a deep understanding of power grid dynamics.

1. Data analysis

Wind and solar power are highly dependent on weather conditions and, therefore, can ramp up or down in just a few seconds. In a power grid with a high integration of variable energy sources, these

extreme short-time fluctuations not only influence the energy availability, but also the stability of the power grid. The analysis of the data of wind and solar power recorded in different regions around the world demonstrates multiple universal types of variability and nonlinearity in the short-time scales.^{549–552} Importantly, considering the aggregated variable energy sources of even country-wide installation of wind and solar fields shows that the data are still non-Gaussian and includes intermittent fluctuations.⁵⁴⁹ Indeed, this is the direct consequence of the long-range correlations of the wind velocity and the cloud size distribution that are approximately 600 and 1200 km, respectively.^{553,554} The footprint of these short-time intermittent fluctuations has been recently monitored in the power grid frequency variations.⁵⁵⁵

The analysis of the highly resolved electricity consumption data of households that consume 29% of all electricity in European Union⁵⁵⁶ shows that these data are highly intermittent. The intermittent fluctuations of electricity consumption cannot be captured from the data with a resolution of 1 h or even 15 min.^{557–559} The variability of energy sources, along with the uncertainty of the electricity consumption, can make it more difficult to balance supply and demand. Therefore, as the share of feed-in is increasing, a deeper understanding of the variable energy source dynamics as well as the advanced approach of balancing demand and supply by load shifting is required.^{560,561}

2. Data-driven models

Identifying the stochastic behavior of the short-time variable energy sources and electricity consumption fluctuations allows us to construct a dynamic equation that governs these stochastic processes. The dynamic equation should include two main terms as follows:

$$\dot{X}(t) = F(X, t) + G(X, t), \quad (24)$$

where $F(X, t)$ is the deterministic term showing the trend of a stochastic process $X(t)$ (which is here a variable source of energy or electricity consumption) vs time, and $G(X, t)$ is the stochastic term modeling the extreme fluctuations and, indeed, non-Gaussianity in the considered process. Equation (24) is known as a stochastic differential equation, which is a non-parametric model. With the term “non-parametric,” we mean that all of the functions and parameters in the model can be found directly from the empirical time series. Recently, the *jump-diffusion* process^{562,563} and the *superstatistics* method⁵⁶⁴ have been introduced to model short-term variable energy sources and electricity consumption fluctuations, respectively. Moreover, in Ref. 564, a data-driven load profile that is consistent with high-resolution electricity consumption data is obtained. This data-driven load profile outperforms the standard load profile used by the energy supplier,⁵⁶⁵ and it does not require microscopic parameters for consumer behavior, consumer appliances, house infrastructures, or other features that other models depend on.⁵⁶⁶

The data-driven models allow us not only to generate time series with identical statistics to empirical ones, but also by adjusting the parameters in the stochastic models, to consider the response of the power grid and control systems to different circumstances.

3. Complex network science

From a structural view point, the power grid is a complex network consisting of many units and agents that interact in a nonlinear way. Due to economic factors, power grids often run near their operational limits. The nature of renewable energies will add more and more fluctuations to this complex system, causing concerns about the reliability and stability of the power supply.^{567–569} Therefore, the probability of having grid instabilities will increase, which may result in more frequent occurrences of extreme events, such as cascading failures resulting in large blackouts. Any strategy under discussion, such as upgrading the existing power grid, the formation of virtual power plants combining different power sources, introducing new storage capacities, intelligent “smart grid” concepts, etc., will further increase the complexity of the existing systems and have to be based on the detailed knowledge of the dynamics of variable energy sources and consumer variable sources of energy. The data-driven models and the generation of data sets imitating the characteristics of the real data sets empower us to consider accurately the interplay of the network structure and features with supply and demand fluctuations and, therefore, resulting in deep insight into how the future structure and control systems should be designed to mitigate the intermittent fluctuations and allows us to increase the share of variable sources of energy in the power grid without any restriction.

E. Adaptability of the Earth system: Past success and present challenges—By Jürgen Kurths

The Earth system is a highly complex system with various interactions, including positive and negative feedbacks. Its representation is sometimes even called a horrendogram. However, it is also an open system that corresponds with its closer and farther surrounding. All these properties are crucial for the ability to *adapt* in response to external as well as intrinsic changes and perturbations.

There are outstanding examples of adaptive behavior in the history of the Earth system: About 66 000 000 years ago, a rather large asteroid struck Earth and formed the Chicxulub impactor crater with a diameter of about 180 km in the peninsular Yucatan in Mexico.⁵⁷⁰ This external shock induced titanic changes on the surface and in the atmosphere as megatsunamis, giant wildfires and a rapid strong decrease of the temperature. More importantly, it is now well accepted that it was the main cause of the *Cretaceous–Paleogene extinction event*, a mass extinction of 75% of plant and animal species on Earth, including all non-avian dinosaurs. However, it is important to emphasize that the Earth system was not destroyed due to this giant event, but it adapted and reached another stable regime after some time whose global climate was rather similar to the former one.⁵⁷¹ Another example of a shock-like but intrinsic event was the Toba supervolcanic eruption about 74 000 years back in Sumatra.⁵⁷² It changed the climate situation drastically and, in particular, induced a strong temperature decrease 3–5°C. However, the Earth system again adapted and reached via rather large fluctuations a stable climate regime whose global temperature was, however, clearly below the former one.⁵⁷³

There are also recurrent-like strong influences on the Earth system over broad scales in time. On the one end, we have as long-term factors the Milankovic cycles, which are due to complex variations in eccentricity, axial tilt, and precession of the Earth’s motion in the

solar system leading to main components of 41 000 years, 95 000 years, and others. These orbital forcing components have a strong influence on long-range climate dynamics, as the occurrence of glacials and interglacials. On the other end, recurrent patterns, such as El Niño Southern Oscillations (ENSO) in the range of 3–7 years, have a powerful impact on the onset and intensity of monsoons and the formation of extreme climate events. However, the Earth system has been able to adapt to all these recurrent events and acts in stable regimes, which can even become different, e.g., switching from glacial to interglacial.

However, one component of the Earth system has substantially increased its impact in the more recent past, the humans. The huge amount of greenhouse gas emissions, such as CO₂ and methane, is the most striking expression of this tremendous *anthropogenic activity*. There is clear evidence and broad acceptance that this has already caused distinct global warming and various other strong changes in the Earth system.⁵⁷⁵ Due to several reasons, the kind of adaptation of the Earth system in response to these emissions is hard to evaluate. One crucial uncertainty is the future development of these emissions despite the immense efforts for their serious reduction, e.g., via the UN Climate Change Conferences of the Parties (COP).

Therefore, typical scenarios of future Earth system's adaptation in dependence on different emission amounts are estimated based on combined models and measured data. However, there are challenging problems in modeling of the corresponding processes and data acquisition. A very promising approach to treat these tasks is based on the study of *tipping elements* because the Earth system comprises a number of such large-scale subsystems,

which are vulnerable and can undergo large and possibly irreversible changes in response to anthropogenic perturbations beyond a critical threshold.^{574,576} The whole system of tipping elements, including their interactions, can be well described as a complex network in order to understand the spreading of tipping; i.e., will the tipping of one element exert only local effects or will it induce a cascading-like dynamics?⁵⁷⁷ This is a typical multistable system where phenomena, such as partial synchronization, are typical (see also Sec. II D). Additionally, intrinsic and external noise may strongly influence the dynamics of the Earth system (see also Sec. II B). We know the main elements of this network because they have been identified and described, such as dieback of the Amazon forest or melting of poles (see Fig. 10). However, the kind of interactions as well as the intrinsic dynamics at each tipping area are only very partly known.

To treat the first problem, connections between the Amazon forest area and other tipping points have been recently uncovered quantitatively by analyzing near-surface air temperature fields.⁵⁷⁸ This way, teleconnections between the Amazon forest area and the Tibetan plateau as well as the West Antarctic ice sheet have been identified. In other studies based on conceptual models for selected tipping elements with complex structure–function interrelations as treated in Sec. II A of this Perspective, it has been shown that the polar ice sheets could be typically the initiators of tipping cascades, while the Atlantic Meridional overturning circulation acts as a mediator.⁵⁷⁷ However, these studies are in the beginning, and there are several crucial problems to solve until getting a reliable predictability of tipping dynamics and, hence, on evaluating in detail the adaptability of the Earth system, in particular, to anthropogenic

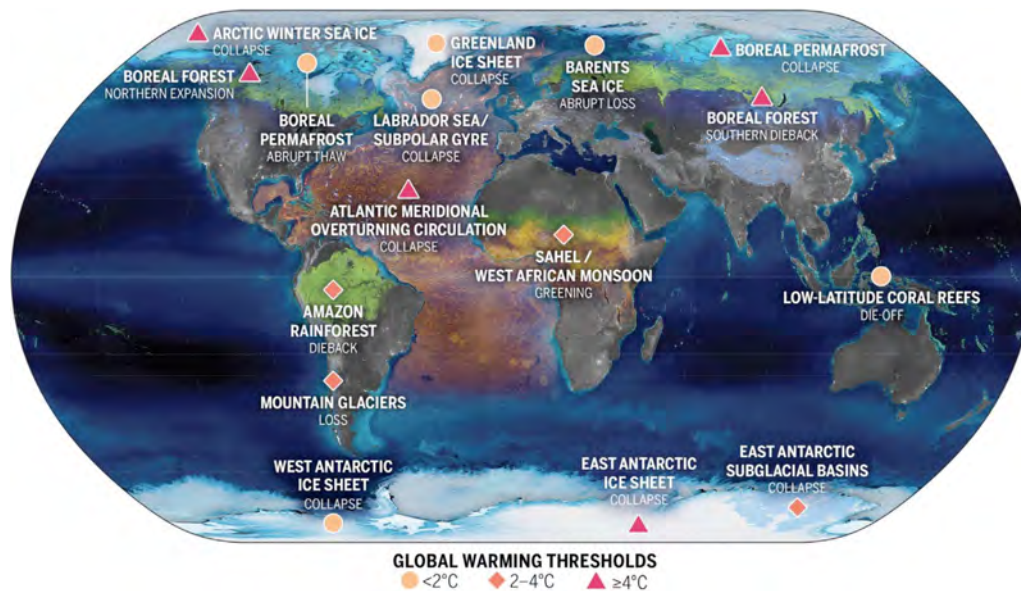


FIG. 10. The location of climate tipping elements in the cryosphere (blue), biosphere (green), and ocean/atmosphere (orange), and global warming levels at which their tipping points will likely be triggered. Pins are colored according to our central global warming threshold estimate being below 2°C, i.e., within the Paris Agreement range (light orange, circles); between 2 and 4°C, i.e., accessible with current policies (orange, diamonds); and 4°C and above (red, triangles). Figure from Armstrong McKay *et al.*, *Science* **377**, eabn7950 (2022). Copyright 2022 American Association for the Advancement of Science.⁵⁷⁴

influences. A promising way to retrieve these interactions will be the application of modern machine learning methods (see Sec. IV).

However, it is evident that the greenhouse gas emissions have to be strongly reduced. In Sec. V D of this Perspective paper, problems and approaches for reaching this ambitious goal are discussed.

To summarize, the Earth system is an adaptive one as is obvious from the past. We have now clear evidence that the huge anthropogenic influences create a new kind of perturbation, which has the power to induce a novel pathway of adaptation. This will end for sure in some stable regime, but it is very questionable whether we can live there.

VI. CONCLUDING REMARKS

The notion of *adaptivity* is used in a variety of contexts, from nonlinear dynamics over socioeconomic systems to cognitive science and musicology. This article presents various viewpoints on adaptive systems and the notion of adaptivity itself from different research disciplines aiming to open the dialogue between communities.

The article shows that the terminology and definition of “adaptivity” may vary among the communities. While “adaptability” refers generally to the ability of a system to amend its properties according to dynamic (external or intrinsic) changes, the specific details of adaptive mechanisms depend on the context and the community, for example, how and which part of a system can amend (adaptation rules) or what strategies enable the perception (or sensing) of such changes. In addition, the mathematical framework for describing adaptive mechanisms and adaptive systems also varies across communities.

On the other hand, various commonalities become apparent throughout this article. For example, a common starting point in many contexts is descriptions based on *networks*, where the notion of adaptivity is well established. Adaptive networks are applied in numerous fields, such as power grids, neural systems, and machine learning. Another commonality across disciplines is the link between adaptivity and *feedback* mechanisms, which are ubiquitous in both natural systems and engineering.

We believe that the similarities and differences provide opportunities for further cross-fertilization between the research communities centered around the concept of adaptivity as a common mechanism; for example, adaptive networks can serve as a powerful modeling paradigm for realistic dynamical systems, possibly applicable to even more systems, e.g., in the context of cognitive sciences, musicology, or active matter. Furthermore, a great opportunity lies in utilizing the mechanisms that have emerged in nature as inspiration and guiding principles to engineer artificial (intelligent, cooperative) systems and to develop control strategies. In this spirit, for example, the cooperative behavior of animals may guide the way to engineer robots capable to perform collective motion reminiscent of swarms of insects or schools of fish or the development of new machine learning algorithms may potentially profit from a deeper understanding of the brain provided by the field of neuroscience. Indeed, it has long been recognized that “The adaptiveness of the human organism, the facility with which it acquires new representations and strategies and becomes adept in dealing with highly

specialized environments, makes it an elusive and fascinating target of our scientific inquiries and the very prototype of the artificial.”¹

This article follows the workshop on “Adaptivity in nonlinear dynamical systems,” which brought together specialists from various disciplines to share their views on the abstract concept of *adaptivity*. During the presentations and the coffee breaks, there was a lively exchange of ideas that highlighted the great interest in this topic. We hope that this Perspective article will be a first step in promoting knowledge transfer between disciplines.

In order to conclude this Perspective article, we collect the current open research questions for each section to stimulate future research on adaptivity in the different fields represented in this collection of perspectives and beyond.

- How does a mathematical theory of adaptive systems, which includes cutting-edge applications, such as, e.g., adaptive networks, look like?
- How can knowledge about adaptive mechanisms be used to better understand and influence processes in neuronal, physiological, and socio-economic systems?
- Can the knowledge about neural plasticity of the human brain be used to inspire the development of new artificial learning algorithms?
- What are the capabilities of modeling real-world dynamical systems by using adaptivity?

ACKNOWLEDGMENTS

J.S., R.B., and S.A.M.L. thank the Joachim Herz Foundation for funding an interdisciplinary and international workshop on “Adaptivity in nonlinear dynamical systems,” which was held from 20 to 23 September 2022 and provided a platform for discussions that resulted in this article. We further thank the Potsdam Institute for Climate Impact Research for supporting and hosting the workshop. J.S. acknowledges funding support by the Deutsche Forschungsgemeinschaft (DFG, German Research Foundation)—through the project 429685422. R.B. acknowledges funding support by the Deutsche Forschungsgemeinschaft (DFG, German Research Foundation)—through the project 440145547. S.A.M.L. acknowledges funding support by the Deutsche Forschungsgemeinschaft (DFG, German Research Foundation)—through the project 498288081. I.F. acknowledges funding from the Institute of Physics Belgrade through a grant by the Ministry of Education, Science and Technological Development of Republic of Serbia. P.H. acknowledges further support by the Deutsche Forschungsgemeinschaft (DFG, German Research Foundation) under project ID 434434223—SFB 1461. J.M. acknowledges funding support by the Deutsche Forschungsgemeinschaft (DFG, German Research Foundation)—through the project 458548755. P.L.-S. acknowledges financial support from the Volkswagen Foundation (grant “Reclaiming individual autonomy and democratic discourse online: How to rebalance human and algorithmic decision-making”). P.A.T. acknowledges funding support by the John A. Blume Foundation and the Vaughn and Nancy Bryson fund. G.V. would like to acknowledge funding from the H2020 European Research Council (ERC) Starting Grant ComplexSwimmers (Grant No. 677511), the Horizon Europe ERC Consolidator Grant MAPEI

(Grant No. 101001267), and the Knut and Alice Wallenberg Foundation (Grant No. 2019.0079). S.G. acknowledges co-funding from Next Generation EU, in the context of the National Recovery and Resilience Plan, Investment PE1 - Project FAIR “Future Artificial Intelligence Research”, co-financed by the Next Generation EU [DM 1555 del 11.10.22].

AUTHOR DECLARATIONS

Conflict of Interest

The authors have no conflicts to disclose.

Author Contributions

Jakub Sawicki, Rico Berner, and Sarah A. M. Loos contributed equally to this paper.

Jakub Sawicki: Conceptualization (equal); Writing – original draft (equal); Writing – review & editing (equal). **Rico Berner:** Conceptualization (equal); Writing – original draft (equal); Writing – review & editing (equal). **Sarah A. M. Loos:** Conceptualization (equal); Writing – original draft (equal); Writing – review & editing (equal). **Mehrnaz Anvari:** Writing – original draft (equal). **Rolf Bader:** Writing – original draft (equal). **Wolfram Barfuss:** Writing – original draft (equal). **Nicola Botta:** Writing – original draft (equal). **Nuria Brede:** Writing – original draft (equal). **Igor Franović:** Writing – original draft (equal). **Daniel J. Gauthier:** Writing – original draft (equal). **Sebastian Goldt:** Writing – original draft (equal). **Aida Hajizadeh:** Writing – original draft (equal). **Philipp Hövel:** Writing – original draft (equal). **Omer Karin:** Writing – original draft (equal). **Philipp Lorenz-Spreen:** Writing – original draft (equal). **Christoph Miehl:** Writing – original draft (equal). **Jan Mölter:** Writing – original draft (equal). **Simona Olmi:** Writing – original draft (equal). **Eckehard Schöll:** Writing – original draft (equal). **Alireza Seif:** Writing – original draft (equal). **Peter A. Tass:** Writing – original draft (equal). **Giovanni Volpe:** Writing – original draft (equal). **Serhiy Yanchuk:** Writing – original draft (equal). **Jürgen Kurths:** Writing – original draft (equal); Writing – review & editing (equal).

DATA AVAILABILITY

The data that support the findings of this study are available within the article.

REFERENCES

- H. A. Simon, “The sciences of the artificial,” in *Karl Taylor Compton Lectures* (MIT Press, Cambridge, MA, 1969).
- V. Yakubovich, “Theory of adaptive systems,” *Sov. Phys.-Dokl.* **13**, 852–855 (1968).
- V. Yakubovich, “Adaptive systems with multistep goal conditions,” *Sov. Phys.-Dokl.* **13**, 1096–1099 (1968).
- V. Fomin, A. Fradkov, and V. Yakubovich, *Adaptive Control of Dynamical Systems* (Nauka, Moscow, 1981).
- A. M. Annaswamy and A. L. Fradkov, “A historical perspective of adaptive control and learning,” *Annu. Rev. Control* **52**, 18–41 (2021).
- A. L. Fradkov and A. I. Shepeljavyi, “The history of cybernetics and artificial intelligence: A view from Saint Petersburg,” *Cybern. Phys.* **11**, 253–263 (2022).

⁷Y. Z. Tsyppin, “Adaptation and learning in automatic systems,” in *Mathematics in Science and Engineering* (Academic Press, 1971).

⁸A. Fradkov, *Cybernetical Physics: From Control of Chaos to Quantum Control* (Springer, Berlin, 2007).

⁹J. Lehnert, P. Hövel, A. A. Selivanov, A. L. Fradkov, and E. Schöll, “Controlling cluster synchronization by adapting the topology,” *Phys. Rev. E* **90**, 042914 (2014).

¹⁰A. Pikovsky, M. Rosenblum, and J. Kurths, *Synchronization: A Universal Concept in Nonlinear Sciences*, 1st ed. (Cambridge University Press, Cambridge, 2001).

¹¹S. Boccaletti, A. N. Pisarchik, C. I. del Genio, and A. Amann, *Synchronization: From Coupled Systems to Complex Networks* (Cambridge University Press, Cambridge, 2018).

¹²S. Yanchuk, A. C. Roque, E. E. N. Macau, and J. Kurths, “Dynamical phenomena in complex networks: Fundamentals and applications,” *Eur. Phys. J. Spec. Top.* **230**, 2711–2716 (2021).

¹³J. Cabral, V. Jirsa, O. Popovych, A. Torcini, and S. Yanchuk, “Editorial: From structure to function in neuronal networks: Effects of adaptation, time-delays, and noise,” *Front. Syst. Neurosci.* **16**, 871165 (2022).

¹⁴L. F. Abbott and S. B. Nelson, “Synaptic plasticity: Taming the beast,” *Nat. Neurosci.* **3**, 1178–1183 (2000).

¹⁵Y. Dan and M.-M. Poo, “Spike timing-dependent plasticity of neural circuits,” *Neuron* **44**, 23–30 (2004).

¹⁶Y. L. Maistrenko, B. Lysyansky, C. Hauptmann, O. Burylko, and P. A. Tass, “Multistability in the Kuramoto model with synaptic plasticity,” *Phys. Rev. E* **75**, 066207 (2007).

¹⁷O. V. Popovych, S. Yanchuk, and P. A. Tass, “Self-organized noise resistance of oscillatory neural networks with spike timing-dependent plasticity,” *Sci. Rep.* **3**, 2926 (2013).

¹⁸L. Lücken, O. V. Popovych, P. A. Tass, and S. Yanchuk, “Noise-enhanced coupling between two oscillators with long-term plasticity,” *Phys. Rev. E* **93**, 032210 (2016).

¹⁹T. Aoki and T. Aoyagi, “Co-evolution of phases and connection strengths in a network of phase oscillators,” *Phys. Rev. Lett.* **102**, 034101 (2009).

²⁰D. V. Kasatkin, S. Yanchuk, E. Schöll, and V. I. Nekorkin, “Self-organized emergence of multi-layer structure and chimera states in dynamical networks with adaptive couplings,” *Phys. Rev. E* **96**, 062211 (2017).

²¹R. Berner, S. Vock, E. Schöll, and S. Yanchuk, “Desynchronization transitions in adaptive networks,” *Phys. Rev. Lett.* **126**, 028301 (2021).

²²R. Berner, V. Mehrmann, E. Schöll, and S. Yanchuk, “The multiplex decomposition: An analytic framework for multilayer dynamical networks,” *SIAM J. Appl. Dyn. Syst.* **20**, 1752–1772 (2021).

²³R. Berner and S. Yanchuk, “Synchronization in networks with heterogeneous adaptation rules and applications to distance-dependent synaptic plasticity,” *Front. Appl. Math. Stat.* **7**, 714978 (2021).

²⁴M. Thiele, R. Berner, P. A. Tass, E. Schöll, and S. Yanchuk, “Asymmetric adaptivity induces recurrent synchronization in complex networks,” *Chaos* **33**, 023123 (2023).

²⁵V. Röhr, R. Berner, E. L. Lameu, O. V. Popovych, and S. Yanchuk, “Frequency cluster formation and slow oscillations in neural populations with plasticity,” *PLoS One* **14**, e0225094 (2019).

²⁶C. Kuehn, *Multiple Time Scale Dynamics* (Springer International Publishing, Switzerland, 2015).

²⁷N. Caporale and Y. Dan, “Spike timing-dependent plasticity: A hebbian learning rule,” *Annu. Rev. Neurosci.* **31**, 25 (2008).

²⁸D. Taylor, E. Ott, and J. G. Restrepo, “Spontaneous synchronization of coupled oscillator systems with frequency adaptation,” *Phys. Rev. E* **81**, 046214 (2010).

²⁹T. Fardet and A. Levina, “Simple models including energy and spike constraints reproduce complex activity patterns and metabolic disruptions,” *PLoS Comput. Biol.* **16**, e1008503 (2020).

³⁰G. Bonvento and J. P. Bolaños, “Astrocyte-neuron metabolic cooperation shapes brain activity,” *Cell Metab.* **33**, 1546 (2021).

³¹J. A. Roberts, K. K. Iyer, S. Vanhatalo, and M. Breakspear, “Critical role for resource constraints in neural models,” *Front. Syst. Neurosci.* **8**, 154 (2014).

- ³²Y. S. Virkar, W. L. Shew, J. G. Restrepo, and E. Ott, "Feedback control stabilization of critical dynamics via resource transport on multilayer networks: How glia enable learning dynamics in the brain," *Phys. Rev. E* **94**, 042310 (2016).
- ³³A. Levina, J. M. Herrmann, and T. Geisel, "Dynamical synapses causing self-organized criticality in neural networks," *Nat. Phys.* **3**, 857 (2007).
- ³⁴R. Berner, E. Schöll, and S. Yanchuk, "Multiclusters in networks of adaptively coupled phase oscillators," *SIAM J. Appl. Dyn. Syst.* **18**, 2227–2266 (2019).
- ³⁵R. Berner, J. Fialkowski, D. V. Kasatkin, V. I. Nekorkin, S. Yanchuk, and E. Schöll, "Hierarchical frequency clusters in adaptive networks of phase oscillators," *Chaos* **29**, 103134 (2019).
- ³⁶K. A. Kroma-Wiley, P. J. Mucha, and D. S. Bassett, "Synchronization of coupled Kuramoto oscillators under resource constraints," *Phys. Rev. E* **104**, 014211 (2021).
- ³⁷S. Thamizharasan, V. K. Chandrasekar, M. Senthilvelan, R. Berner, E. Schöll, and D. V. Senthilkumar, "Exotic states induced by coevolving connection weights and phases in complex networks," *Phys. Rev. E* **105**, 034312 (2021).
- ³⁸J. Fialkowski, S. Yanchuk, I. M. Sokolov, E. Schöll, G. A. Gottwald, and R. Berner, "Heterogeneous nucleation in finite size adaptive dynamical networks," *Phys. Rev. Lett.* **130**, 067402 (2022).
- ³⁹I. Franović, S. R. Eydum, S. Yanchuk, and R. Berner, "Collective activity bursting in a population of excitable units adaptively coupled to a pool of resources," *Front. Netw. Physiol.* **2**, 841829 (2022).
- ⁴⁰I. Franović, S. Yanchuk, S. R. Eydum, I. Bačić, and M. Wolfrum, "Dynamics of a stochastic excitable system with slowly adapting feedback," *Chaos* **30**, 083109 (2020).
- ⁴¹I. Bačić, V. Klinshov, V. I. Nekorkin, M. Perc, and I. Franović, "Inverse stochastic resonance in a system of excitable active rotators with adaptive coupling," *EPL* **124**, 40004 (2018).
- ⁴²A. Knoblauch, F. Hauser, M.-O. Gewaltig, E. Körner, and G. Palm, "Does spike-timing-dependent synaptic plasticity couple or decouple neurons firing in synchrony?," *Front. Comput. Neurosci.* **6**, 55 (2012).
- ⁴³D. Pazo and E. Montbrío, "Universal behavior in populations composed of excitable and self-oscillatory elements," *Phys. Rev. E* **73**, 055202 (2006).
- ⁴⁴L. F. Lafuerza, P. Colet, and R. Toral, "Nonuniversal results induced by diversity distribution in coupled excitable systems," *Phys. Rev. Lett.* **105**, 084101 (2010).
- ⁴⁵V. Klinshov and I. Franović, "Two scenarios for the onset and suppression of collective oscillations in heterogeneous populations of active rotators," *Phys. Rev. E* **100**, 062211 (2019).
- ⁴⁶I. Bačić, S. Yanchuk, M. Wolfrum, and I. Franović, "Noise-induced switching in two adaptively coupled excitable systems," *Eur. Phys. J. Spec. Top.* **227**, 1077 (2018).
- ⁴⁷O. Sporns and R. Kötter, "Motifs in brain networks," *PLoS Biol.* **2**, e369 (2004).
- ⁴⁸I. Bačić and I. Franović, "Two paradigmatic scenarios for inverse stochastic resonance," *Chaos* **30**, 033123 (2020).
- ⁴⁹L. M. Pecora and T. L. Carroll, "Master stability functions for synchronized coupled systems," *Phys. Rev. Lett.* **80**, 2109–2112 (1998).
- ⁵⁰E. Ott and T. M. Antonsen, "Low dimensional behavior of large systems of globally coupled oscillators," *Chaos* **18**, 037113 (2008).
- ⁵¹E. Ott and T. M. Antonsen, "Long time evolution of phase oscillator systems," *Chaos* **19**, 023117 (2009).
- ⁵²C. Bick, M. Goodfellow, C. R. Laing, and E. A. Martens, "Understanding the dynamics of biological and neural oscillator networks through exact mean-field reductions: A review," *J. Math. Neurosci.* **10**, 9 (2020).
- ⁵³G. Lan, P. Sartori, S. Neumann, V. Sourjik, and Y. Tu, "The energy–speed–accuracy trade-off in sensory adaptation," *Nat. Phys.* **8**, 422 (2012).
- ⁵⁴D. Conti and T. Mora, "Nonequilibrium dynamics of adaptation in sensory systems," *Phys. Rev. E* **106**, 054404 (2022).
- ⁵⁵G. Tkačik and W. Bialek, "Information processing in living systems," *Annu. Rev. Condens. Matter Phys.* **7**, 89 (2016).
- ⁵⁶C. Ionescu, P. Jansson, and N. Botta, "Type theory as a framework for modelling and programming," in *Leveraging Applications of Formal Methods, Verification and Validation. Modeling*, edited by T. Margaria and B. Steffen (Springer International Publishing, Cham, 2018), pp. 119–133.
- ⁵⁷M. Broy, K. Havelund, and R. Kumar, "Towards a unified view of modeling and programming," in *Leveraging Applications of Formal Methods, Verification and Validation: Discussion, Dissemination, Applications*, edited by T. Margaria and B. Steffen (Springer International Publishing, Cham, 2016), pp. 238–257.
- ⁵⁸C. Ionescu, R. J. T. Klein, J. Hinkel, K. S. Kavi Kumar, and R. Klein, "Towards a formal framework of vulnerability to climate change," *Environ. Model. Assess.* **14**, 1–16 (2009).
- ⁵⁹N. Botta, P. Jansson, and C. Ionescu, "Contributions to a computational theory of policy advice and avoidability," *J. Funct. Program.* **27**, e23 (2017).
- ⁶⁰N. Brede (2021). "Toward a DSL for sequential decision problems with tipping point uncertainties," Zenodo.
- ⁶¹N. Botta, N. Brede, M. Crucifix, C. Ionescu, P. Jansson, Z. Li, M. Martínez, and T. Richter, "Responsibility under uncertainty: Which climate decisions matter most?," *Environ. Model. Assess.* **28**, 337–365 (2023).
- ⁶²R. Sutton, A. Barto, and R. Williams, "Reinforcement learning is direct adaptive optimal control," *IEEE Control Syst. Mag.* **12**, 19–22 (1992).
- ⁶³R. Bellman, *Dynamic Programming* (Princeton University Press, 1957).
- ⁶⁴N. Botta, P. Jansson, C. Ionescu, D. R. Christiansen, and E. Brady, "Sequential decision problems, dependent types and generic solutions," *Log. Methods Comput. Sci.* **13**, 1–23 (2017).
- ⁶⁵N. Brede and N. Botta, "On the correctness of monadic backward induction," *J. Funct. Program.* **31**, e26 (2021).
- ⁶⁶C. J. C. H. Watkins and P. Dayan, "Q-learning," *Mach. Learn.* **8**, 279–292 (1992).
- ⁶⁷B. Nordström, K. Petersson, and J. Smith, *Programming in Martin-Löf's Type Theory* (Oxford University Press, 1990).
- ⁶⁸P. Martin-Löf, *Intuitionistic Type Theory* (Bibliopolis, 1984).
- ⁶⁹S. Allen, M. Bickford, R. Constable, R. Eaton, C. Kreitz, L. Lorigo, and E. Moran, "Innovations in computational type theory using NuPrL," *J. Appl. Log.* **4**, 428–469 (2006).
- ⁷⁰The Coq Development Team, "The Coq proof assistant," Zenodo, latest version.
- ⁷¹U. Norell, "Towards a practical programming language based on dependent type theory," Ph.D. thesis (Chalmers University of Technology, 2007).
- ⁷²E. Brady, *Type-Driven Development in Idris* (Manning Publications Co., 2017).
- ⁷³L. de Moura, S. Kong, J. Avigad, F. van Doorn, and J. von Raumer, "The lean theorem prover (system description)," in *Automated Deduction—CADE-25* (Springer International Publishing, Cham, 2015), pp. 378–388.
- ⁷⁴V. Voevodsky, "Univalent foundations of mathematics," in *Logic, Language, Information and Computation: 18th International Workshop, WoLLIC 2011, Philadelphia, PA. Proceedings 18* (Springer, 2011), 4 pp.
- ⁷⁵G. Gonthier, "Formal proof—the four-color theorem," *Not. AMS* **55**, 1382–1393 (2008), <https://community.ams.org/journals/notices/200811/tx081101382p.pdf>.
- ⁷⁶G. Gonthier, A. Asperti, J. Avigad, Y. Bertot, C. Cohen, F. Garillot, S. Le Roux, A. Mahboubi, R. O'Connor, S. Ould Biha, and I. Pasca, "A machine-checked proof of the odd order theorem," in *Interactive Theorem Proving: 4th International Conference, ITP 2013, Rennes, France, 22–26 July 2013. Proceedings 4* (Springer, 2013), pp. 163–179.
- ⁷⁷K. Buzzard, J. Commelin, and P. Massot, "Formalising perfectoid spaces," in *Proceedings of the 9th ACM SIGPLAN International Conference on Certified Programs and Proofs* (Association for Computing Machinery, 2020), pp. 299–312.
- ⁷⁸K. Hartnett, "Building the mathematical library of the future," <https://www.quantamagazine.org/building-the-mathematical-library-of-the-future-20201001/> (2020).
- ⁷⁹S. Ornes, "How close are computers to automating mathematical reasoning," <https://www.quantamagazine.org/how-close-are-computers-to-automating-mathematical-reasoning-20200827/> (2020).
- ⁸⁰P. Wadler, "Propositions as types," *Commun. ACM* **58**, 75–84 (2015).
- ⁸¹X. Leroy, "Formal verification of a realistic compiler," *Commun. ACM* **52**, 107–115 (2009).
- ⁸²N. Swamy, J. Chen, C. Fournet, P.-Y. Strub, K. Bhargavan, and J. Yang, "Secure distributed programming with value-dependent types," in *Proceedings of ICFP 2011* (Association for Computing Machinery, 2011), pp. 266–278.
- ⁸³J. Morgenstern and D. Licata, "Security-typed programming within dependently-typed programming," in *International Conference on Functional Programming* (ACM, 2010).

- ⁸⁴E. Brady and K. Hammond, "Resource-safe systems programming with embedded domain specific languages," in *Practical Aspects of Declarative Languages* (Springer, 2012), pp. 242–257.
- ⁸⁵A. Chlipala, *Certified Programming with Dependent Types: A Pragmatic Introduction to the Coq Proof Assistant* (MIT Press, 2022).
- ⁸⁶C. Ionescu and P. Jansson, "Testing versus proving in climate impact research," in *Proc. TYPES 2011, Leibniz International Proceedings in Informatics (LIPIcs)* (Schloss Dagstuhl–Leibniz-Zentrum fuer Informatik, Dagstuhl, Germany, 2013), Vol. 19, pp. 41–54.
- ⁸⁷R. S. Bird and O. de Moor, *Algebra of Programming*, Prentice Hall International Series in Computer Science (Prentice Hall, 1997).
- ⁸⁸E. Moggi, "Computational lambda-calculus and monads," in *Proceedings of the Fourth Annual Symposium on Logic in Computer Science (LICS '89)* (IEEE, 1989), pp. 14–23; P. Wadler and M. Broy, "Monads for functional programming," in *Program Design Calculi, Proceedings of the NATO Advanced Study Institute on Program Design Calculi*, NATO ASI Series (Springer, 1992), Vol. 118, pp. 233–264.
- ⁸⁹S. MacLane, *Categories for the Working Mathematician*, 2nd ed., Graduate Texts in Mathematics (Springer, 1978).
- ⁹⁰E. Schöll, "Partial synchronization patterns in brain networks," *Europhys. Lett.* **136**, 18001 (2021).
- ⁹¹E. Schöll, "Chimeras in physics and biology: Synchronization and desynchronization of rhythms," *Nova Acta Leopoldina* **425**, 67–95 (2020). invited contribution.
- ⁹²J. Sawicki, *Delay Controlled Partial Synchronization in Complex Networks*, Springer Theses (Springer, Heidelberg, 2019).
- ⁹³A. Zakharova, "Chimera patterns in networks: Interplay between dynamics, structure, noise, and delay," in *Understanding Complex Systems* (Springer, Cham, 2020).
- ⁹⁴Y. Maistrenko, B. Penkovsky, and M. Rosenblum, "Solitary state at the edge of synchrony in ensembles with attractive and repulsive interactions," *Phys. Rev. E* **89**, 060901 (2014).
- ⁹⁵P. Jaros, Y. Maistrenko, and T. Kapitaniak, "Chimera states on the route from coherence to rotating waves," *Phys. Rev. E* **91**, 022907 (2015).
- ⁹⁶V. Semenov, A. Zakharova, Y. Maistrenko, and E. Schöll, "Delayed-feedback chimera states: Forced multicusters and stochastic resonance," *Europhys. Lett.* **115**, 10005 (2016).
- ⁹⁷S. Jain and S. Krishna, "A model for the emergence of cooperation, interdependence, and structure in evolving networks," *Proc. Natl. Acad. Sci. U.S.A.* **98**, 543–547 (2001).
- ⁹⁸T. Gross, C. J. Dommar D'Lima, and B. Blasius, "Epidemic dynamics on an adaptive network," *Phys. Rev. Lett.* **96**, 208701 (2006).
- ⁹⁹T. Gross and B. Blasius, "Adaptive coevolutionary networks: A review," *J. R. Soc. Interface* **5**, 259–271 (2008).
- ¹⁰⁰R. Gutiérrez, A. Amann, S. Assenza, J. Gómez-Gardeñes, V. Latora, and S. Boccaletti, "Emerging meso- and macroscales from synchronization of adaptive networks," *Phys. Rev. Lett.* **107**, 234103 (2011).
- ¹⁰¹X. Zhang, S. Boccaletti, S. Guan, and Z. Liu, "Explosive synchronization in adaptive and multilayer networks," *Phys. Rev. Lett.* **114**, 038701 (2015).
- ¹⁰²M. Madadi Asl, A. Valizadeh, and P. A. Tass, "Dendritic and axonal propagation delays may shape neuronal networks with plastic synapses," *Front. Physiol.* **9**, 1849 (2018).
- ¹⁰³D. V. Kasatkin and V. I. Nekorkin, "Synchronization of chimera states in a multiplex system of phase oscillators with adaptive couplings," *Chaos* **28**, 093115 (2018).
- ¹⁰⁴D. V. Kasatkin and V. I. Nekorkin, "The effect of topology on organization of synchronous behavior in dynamical networks with adaptive couplings," *Eur. Phys. J. Spec. Top.* **227**, 1051 (2018).
- ¹⁰⁵R. Berner, J. Sawicki, and E. Schöll, "Birth and stabilization of phase clusters by multiplexing of adaptive networks," *Phys. Rev. Lett.* **124**, 088301 (2020).
- ¹⁰⁶P. Feketa, A. Schaum, and T. Meurer, "Synchronization and multi-cluster capabilities of oscillatory networks with adaptive coupling," *IEEE Trans. Autom. Control* **66**, 3084–3096 (2020).
- ¹⁰⁷R. Berner, *Patterns of Synchrony in Complex Networks of Adaptively Coupled Oscillators*, Springer Theses (Springer, Cham, 2021).
- ¹⁰⁸O. V. Popovych, M. N. Xenakis, and P. A. Tass, "The spacing principle for unlearning abnormal neuronal synchrony," *PLoS One* **10**, e0117205 (2015).
- ¹⁰⁹S. Chakravartula, P. Indic, B. Sundaram, and T. Killingback, "Emergence of local synchronization in neuronal networks with adaptive couplings," *PLoS One* **12**, e0178975 (2017).
- ¹¹⁰Y. Kuramoto, *Chemical Oscillations, Waves and Turbulence* (Springer-Verlag, Berlin, 1984).
- ¹¹¹G. Filatrella, A. H. Nielsen, and N. F. Pedersen, "Analysis of a power grid using a Kuramoto-like model," *Eur. Phys. J. B* **61**, 485–491 (2008).
- ¹¹²F. Dörfler and F. Bullo, "Synchronization and transient stability in power networks and nonuniform Kuramoto oscillators," *SIAM J. Control Optim.* **50**, 1616–1642 (2012).
- ¹¹³M. Rohden, A. Sorge, M. Timme, and D. Witthaut, "Self-organized synchronization in decentralized power grids," *Phys. Rev. Lett.* **109**, 064101 (2012).
- ¹¹⁴A. E. Motter, S. A. Myers, M. Anghel, and T. Nishikawa, "Spontaneous synchrony in power-grid networks," *Nat. Phys.* **9**, 191–197 (2013).
- ¹¹⁵F. A. Rodrigues, T. K. D. M. Peron, P. Ji, and J. Kurths, "The Kuramoto model in complex networks," *Phys. Rep.* **610**, 1–98 (2016).
- ¹¹⁶L. Tumash, S. Olmi, and E. Schöll, "Effect of disorder and noise in shaping the dynamics of power grids," *Europhys. Lett.* **123**, 20001 (2018).
- ¹¹⁷L. Tumash, S. Olmi, and E. Schöll, "Stability and control of power grids with diluted network topology," *Chaos* **29**, 123105 (2019).
- ¹¹⁸H. Taher, S. Olmi, and E. Schöll, "Enhancing power grid synchronization and stability through time delayed feedback control," *Phys. Rev. E* **100**, 062306 (2019).
- ¹¹⁹F. Hellmann, P. Schultz, P. Jaros, R. Levchenko, T. Kapitaniak, J. Kurths, and Y. Maistrenko, "Network-induced multistability through lossy coupling and exotic solitary states," *Nat. Commun.* **11**, 592 (2020).
- ¹²⁰C. Kuehn and S. Thom, "Power network dynamics on graphons," *SIAM J. Appl. Math.* **79**, 1271–1292 (2019).
- ¹²¹C. H. Totz, S. Olmi, and E. Schöll, "Control of synchronization in two-layer power grids," *Phys. Rev. E* **102**, 022311 (2020).
- ¹²²X. Zhang, C. Ma, and M. Timme, "Vulnerability in dynamically driven oscillatory networks and power grids," *Chaos* **30**, 063111 (2020).
- ¹²³R. Berner, S. Yanchuk, and E. Schöll, "What adaptive neuronal networks teach us about power grids," *Phys. Rev. E* **103**, 042315 (2021).
- ¹²⁴J. A. Acebrón and R. Spigler, "Adaptive frequency model for phase-frequency synchronization in large populations of globally coupled nonlinear oscillators," *Phys. Rev. Lett.* **81**, 2229 (1998).
- ¹²⁵J. A. Acebrón, L. L. Bonilla, C. J. Pérez Vicente, F. Ritort, and R. Spigler, "The Kuramoto model: A simple paradigm for synchronization phenomena," *Rev. Mod. Phys.* **77**, 137–185 (2005).
- ¹²⁶P. S. Skardal, D. Taylor, and J. G. Restrepo, "Complex macroscopic behavior in systems of phase oscillators with adaptive coupling," *Physica D* **267**, 27–35 (2013).
- ¹²⁷B. Schäfer, D. Witthaut, M. Timme, and V. Latora, "Dynamically induced cascading failures in power grids," *Nat. Commun.* **9**, 1975 (2018).
- ¹²⁸R. Berner, A. Polanska, E. Schöll, and S. Yanchuk, "Solitary states in adaptive nonlocal oscillator networks," *Eur. Phys. J. Spec. Top.* **229**, 2183–2203 (2020).
- ¹²⁹H. Sakaguchi and Y. Kuramoto, "A soluble active rotator model showing phase transitions via mutual entertainment," *Prog. Theor. Phys.* **76**, 576–581 (1986).
- ¹³⁰P. Jaros, S. Brezetsky, R. Levchenko, D. Dudkowski, T. Kapitaniak, and Y. Maistrenko, "Solitary states for coupled oscillators with inertia," *Chaos* **28**, 011103 (2018).
- ¹³¹I. V. Belykh, B. N. Brister, and V. N. Belykh, "Bistability of patterns of synchrony in Kuramoto oscillators with inertia," *Chaos* **26**, 094822 (2016).
- ¹³²S. Olmi, "Chimera states in coupled Kuramoto oscillators with inertia," *Chaos* **25**, 123125 (2015).
- ¹³³S. Olmi, A. Navas, S. Boccaletti, and A. Torcini, "Hysteretic transitions in the Kuramoto model with inertia," *Phys. Rev. E* **90**, 042905 (2014).
- ¹³⁴J. Barré and D. Métivier, "Bifurcations and singularities for coupled oscillators with inertia and frustration," *Phys. Rev. Lett.* **117**, 214102 (2016).
- ¹³⁵J. Sawicki, R. Berner, T. Löser, and E. Schöll, "Modelling tumor disease and sepsis by networks of adaptively coupled phase oscillators," *Front. Netw. Physiol.* **1**, 730385 (2022).

- ¹³⁶R. Berner, J. Sawicki, M. Thiele, T. Löser, and E. Schöll, "Critical parameters in dynamic network modeling of sepsis," *Front. Netw. Physiol.* **2**, 904480 (2022).
- ¹³⁷J. J. Tyson, K. C. Chen, and B. Novak, "Sniffers, buzzers, toggles and blinkers: Dynamics of regulatory and signaling pathways in the cell," *Curr. Opin. Cell Biol.* **15**, 221–231 (2003).
- ¹³⁸U. Alon, *An Introduction to Systems Biology*, 2nd ed., Chapman & Hall/CRC Computational Biology Series (Taylor & Francis, Philadelphia, PA, 2019).
- ¹³⁹J. Ferrell, *Systems Biology of Cell Signaling* (CRC Press, Boca Raton, FL, 2021).
- ¹⁴⁰S. E. Kahn, R. L. Prigeon, D. K. McCulloch, E. J. Boyko, R. N. Bergman, M. W. Schwartz, J. L. Neifing, W. K. Ward, J. C. Beard, and J. P. Palmer, "Quantification of the relationship between insulin sensitivity and beta-cell function in human subjects. Evidence for a hyperbolic function," *Diabetes* **42**, 1663–1672 (1993).
- ¹⁴¹R. M. Macnab and D. E. J. Koshland, "The gradient-sensing mechanism in bacterial chemotaxis," *Proc. Natl. Acad. Sci. U.S.A.* **69**, 2509–2512 (1972).
- ¹⁴²H. C. Berg and P. M. Tedesco, "Transient response to chemotactic stimuli in *Escherichia coli*," *Proc. Natl. Acad. Sci. U.S.A.* **72**, 3235–3239 (1975).
- ¹⁴³T. M. Yi, Y. Huang, M. I. Simon, and J. Doyle, "Robust perfect adaptation in bacterial chemotaxis through integral feedback control," *Proc. Natl. Acad. Sci. U.S.A.* **97**, 4649–4653 (2000).
- ¹⁴⁴H. El-Samad, J. P. Goff, and M. Khammash, "Calcium homeostasis and parturient hypocalcemia: An integral feedback perspective," *J. Theor. Biol.* **214**, 17–29 (2002).
- ¹⁴⁵C. Briat, A. Gupta, and M. Khammash, "Antithetic integral feedback ensures robust perfect adaptation in noisy biomolecular networks," *Cell Syst.* **2**, 15–26 (2016).
- ¹⁴⁶O. Karin, A. Swisa, B. Glaser, Y. Dor, and U. Alon, "Dynamical compensation in physiological circuits," *Mol. Syst. Biol.* **12**, 886 (2016).
- ¹⁴⁷O. Karin, M. Raz, A. Tendler, A. Bar, Y. Korem Kohanim, T. Milo, and U. Alon, "A new model for the hpa axis explains dysregulation of stress hormones on the timescale of weeks," *Mol. Syst. Biol.* **16**, e9510 (2020).
- ¹⁴⁸Y. Korem Kohanim, T. Milo, M. Raz, O. Karin, A. Bar, A. Mayo, N. Mendelson Cohen, Y. Toledano, and U. Alon, "Dynamics of thyroid diseases and thyroid-axis gland masses," *Mol. Syst. Biol.* **18**, e10919 (2022).
- ¹⁴⁹A. Tendler, A. Bar, N. Mendelsohn-Cohen, O. Karin, Y. K. Kohanim, L. Maimon, T. Milo, M. Raz, A. Mayo, A. Tanay, and U. Alon, "Hormone seasonality in medical records suggests circannual endocrine circuits," *Proc. Natl. Acad. Sci. U.S.A.* **118**, e2003926118 (2021).
- ¹⁵⁰M. D. Lazova, T. Ahmed, D. Bellomo, R. Stocker, and T. S. Shimizu, "Response rescaling in bacterial chemotaxis," *Proc. Natl. Acad. Sci. U.S.A.* **108**, 13870–13875 (2011).
- ¹⁵¹J. Larsch, S. W. Flavell, Q. Liu, A. Gordus, D. R. Albrecht, and C. I. Bargmann, "A circuit for gradient climbing in *C. elegans* chemotaxis," *Cell Rep.* **12**, 1748–1760 (2015).
- ¹⁵²K. Kamino, Y. Kondo, A. Nakajima, M. Honda-Kitahara, K. Kaneko, and S. Sawai, "Fold-change detection and scale invariance of cell–cell signaling in social amoeba," *Proc. Natl. Acad. Sci. U.S.A.* **114**, E4149–E4157 (2017).
- ¹⁵³W. Schultz, P. Dayan, and P. R. Montague, "A neural substrate of prediction and reward," *Science* **275**, 1593–1599 (1997).
- ¹⁵⁴P. N. Tobler, C. D. Fiorillo, and W. Schultz, "Adaptive coding of reward value by dopamine neurons," *Science* **307**, 1642–1645 (2005).
- ¹⁵⁵H. R. Kim, A. N. Malik, J. G. Mikhael, P. Bech, I. Tsutsui-Kimura, F. Sun, Y. Zhang, Y. Li, M. Watabe-Uchida, S. J. Gershman, and N. Uchida, "A unified framework for dopamine signals across timescales," *Cell* **183**, 1600–1616 (2020).
- ¹⁵⁶O. Karin and U. Alon, "The dopamine circuit as a reward-taxis navigation system," *PLoS Comput. Biol.* **18**, e1010340 (2022).
- ¹⁵⁷C. J. Whitmire and G. B. Stanley, "Rapid sensory adaptation redux: A circuit perspective," *Neuron* **92**, 298–315 (2016).
- ¹⁵⁸Y. K. Wu, C. Miehl, and J. Gjorgjieva, "Regulation of circuit organization and function through inhibitory synaptic plasticity," *Trends Neurosci.* **45**, 884–898 (2022).
- ¹⁵⁹C. Miehl, S. Onasch, D. Festa, and J. Gjorgjieva, "Formation and computational implications of assemblies in neural circuits," *J. Physiol.* (published online) (2023).
- ¹⁶⁰D. Debanne, Y. Inglebert, and M. Russier, "Plasticity of intrinsic neuronal excitability," *Curr. Opin. Neurobiol.* **54**, 73–82 (2019).
- ¹⁶¹R. S. Zucker and W. G. Regehr, "Short-term synaptic plasticity," *Annu. Rev. Physiol.* **64**, 355–405 (2002).
- ¹⁶²D. E. Feldman, "The spike-timing dependence of plasticity," *Neuron* **75**, 556–571 (2012).
- ¹⁶³H. Markram, J. Lübke, M. Frotscher, and B. Sakmann, "Regulation of synaptic efficacy by coincidence of postsynaptic APs and EPSPs," *Science* **275**, 213–215 (1997).
- ¹⁶⁴G.-G. Bi and M.-M. Poo, "Synaptic modifications in cultured hippocampal neurons: Dependence on spike timing, synaptic strength, and postsynaptic cell type," *J. Neurosci.* **18**, 10464–10472 (1998).
- ¹⁶⁵H. Motanis, M. J. Seay, and D. V. Buonomano, "Short-term synaptic plasticity as a mechanism for sensory timing," *Trends Neurosci.* **41**, 701–711 (2018).
- ¹⁶⁶A. I. Weber, K. Krishnamurthy, and A. L. Fairhall, "Coding principles in adaptation," *Annu. Rev. Vis. Sci.* **5**, 427–449 (2019).
- ¹⁶⁷R. Näätänen, M. Simpson, and N. E. Loveless, "Stimulus deviance and evoked potentials," *Biol. Psychol.* **14**, 53–98 (1982).
- ¹⁶⁸J. M. Ross and J. P. Hamm, "Cortical microcircuit mechanisms of mismatch negativity and its underlying subcomponents," *Front. Neural Circuits* **14**, 13 (2020).
- ¹⁶⁹N. Ulanovsky, L. Las, and I. Nelken, "Processing of low-probability sounds by cortical neurons," *Nat. Neurosci.* **6**, 391–398 (2003).
- ¹⁷⁰R. G. Natan, J. J. Briguglio, L. Mwilambwe-Tshilobo, S. I. Jones, M. Aizenberg, E. M. Goldberg, and M. N. Geffen, "Complementary control of sensory adaptation by two types of cortical interneurons," *eLife* **4**, e09868 (2015).
- ¹⁷¹J. Homann, S. Ann, K. S. Chen, D. W. Tank, and M. J. Berry, "Novel stimuli evoke excess activity in the mouse primary visual cortex," *Proc. Natl. Acad. Sci. U.S.A.* **119**, e2108882119 (2022).
- ¹⁷²R. Mill, M. Coath, T. Wennekers, and S. L. Denham, "Abstract stimulus-specific adaptation models," *Neural Comput.* **23**, 435–476 (2011).
- ¹⁷³R. Mill, M. Coath, T. Wennekers, and S. L. Denham, "Characterising stimulus-specific adaptation using a multi-layer field model," *Brain Res.* **1434**, 178–188 (2012).
- ¹⁷⁴I. Hershenhoren, N. Taaseh, F. M. Antunes, and I. Nelken, "Intracellular correlates of stimulus-specific adaptation," *J. Neurosci.* **34**, 3303–3319 (2014).
- ¹⁷⁵Y. Park and M. N. Geffen, "A circuit model of auditory cortex," *PLoS Comput. Biol.* **16**, e1008016 (2020).
- ¹⁷⁶M. J. Seay, R. G. Natan, M. N. Geffen, and D. V. Buonomano, "Differential short-term plasticity of PV and SST neurons accounts for adaptation and facilitation of cortical neurons to auditory tones," *J. Neurosci.* **40**, 9224–9235 (2020).
- ¹⁷⁷A. Schulz, C. Miehl, M. J. Berry II, and J. Gjorgjieva, "The generation of cortical novelty responses through inhibitory plasticity," *eLife* **10**, e65309 (2021).
- ¹⁷⁸R. P. N. Rao and D. H. Ballard, "Predictive coding in the visual cortex: A functional interpretation of some extra-classical receptive-field effects," *Nat. Neurosci.* **2**, 79–87 (1999).
- ¹⁷⁹G. G. Turrigiano and S. B. Nelson, "Homeostatic plasticity in the developing nervous system," *Nat. Rev. Neurosci.* **5**, 97–107 (2004).
- ¹⁸⁰E. Marder and J.-M. Goaillard, "Variability, compensation and homeostasis in neuron and network function," *Nat. Rev.* **7**, 563–574 (2006).
- ¹⁸¹S. Onasch and J. Gjorgjieva, "Circuit stability to perturbations reveals hidden variability in the balance of intrinsic and synaptic conductances," *J. Neurosci.* **40**, 3186–3202 (2020).
- ¹⁸²P. J. Gonçalves, J. M. Lueckmann, M. Deistler, M. Nonnenmacher, K. Öcal, G. Bassetto, C. Chintaluri, W. F. Podlaski, S. A. Haddad, T. P. Vogels, D. S. Greenberg, and J. H. Macke, "Training deep neural density estimators to identify mechanistic models of neural dynamics," *eLife* **9**, e56261 (2020).
- ¹⁸³M. Deistler, J. H. Macke, and P. J. Gonçalves, "Energy efficient network activity from disparate circuit parameters," *Proc. Natl. Acad. Sci. U.S.A.* **119**, e2207632119 (2022).
- ¹⁸⁴E. Marder, T. O'Leary, and S. Shruti, "Neuromodulation of circuits with variable parameters: Single neurons and small circuits reveal principles of state-dependent and robust neuromodulation," *Annu. Rev. Neurosci.* **37**, 329–346 (2014).
- ¹⁸⁵K. Jacquerie and G. Drion, "Robust switches in thalamic network activity require a timescale separation between sodium and T-type calcium channel activations," *PLoS Comput. Biol.* **17**, e1008997 (2021).

- ¹⁸⁶G. Mongillo, O. Barak, and M. Tsodyks, "Synaptic theory of working memory," *Science* **319**, 1543–1546 (2008).
- ¹⁸⁷R. Yuste, "From the neuron doctrine to neural networks," *Nat. Rev. Neurosci.* **16**, 487–497 (2015).
- ¹⁸⁸S. Fusi, "Computational models of long term plasticity and memory," [arXiv:1706.04946](https://arxiv.org/abs/1706.04946) (2017).
- ¹⁸⁹A. Litwin-Kumar and B. Doiron, "Formation and maintenance of neuronal assemblies through synaptic plasticity," *Nat. Commun.* **5**, 5319 (2014).
- ¹⁹⁰C. Miehl and J. Gjorgjieva, "Stability and learning in excitatory synapses by nonlinear inhibitory plasticity," *PLoS Comput. Biol.* **18**, e1010682 (2022).
- ¹⁹¹F. Zenke, E. J. Agnes, and W. Gerstner, "Diverse synaptic plasticity mechanisms orchestrated to form and retrieve memories in spiking neural networks," *Nat. Commun.* **6**, 6922 (2015).
- ¹⁹²J. P. Hamm, D. S. Peterka, J. A. Gogos, and R. Yuste, "Altered cortical ensembles in mouse models of schizophrenia," *Neuron* **94**, 153–167 (2017).
- ¹⁹³R. Batista-Brito, E. Zagha, J. M. Ratliff, and M. Vinck, "Modulation of cortical circuits by top-down processing and arousal state in health and disease," *Curr. Opin. Neurobiol.* **52**, 172–181 (2018).
- ¹⁹⁴G. A. Light and R. Näätänen, "Mismatch negativity is a breakthrough biomarker for understanding and treating psychotic disorders," *Proc. Natl. Acad. Sci. U.S.A.* **110**, 15175–15176 (2013).
- ¹⁹⁵H. R. Wilson and J. D. Cowan, "A mathematical theory of the functional dynamics of cortical and thalamic nervous tissue," *Kybernetik* **13**, 55–80 (1973).
- ¹⁹⁶M. Mattia and P. Del Giudice, "Population dynamics of interacting spiking neurons," *Phys. Rev. E* **66**, 051917 (2002).
- ¹⁹⁷E. S. Schaffer, S. Ostoic, and L. F. Abbott, "A complex-valued firing-rate model that approximates the dynamics of spiking networks," *PLoS Comput. Biol.* **9**, e1003301 (2013).
- ¹⁹⁸T. B. Luke, E. Barreto, and P. So, "Complete classification of the macroscopic behavior of a heterogeneous network of theta neurons," *Neural Comput.* **25**, 3207–3234 (2013).
- ¹⁹⁹C. R. Laing, "Derivation of a neural field model from a network of theta neurons," *Phys. Rev. E* **90**, 010901 (2014).
- ²⁰⁰E. Montbrió, D. Pazó, and A. Roxin, "Macroscopic description for networks of spiking neurons," *Phys. Rev. X* **5**, 021028 (2015).
- ²⁰¹G. B. Ermentrout and N. Kopell, "Parabolic bursting in an excitable system coupled with a slow oscillation," *SIAM J. Appl. Math.* **46**, 233–253 (1986).
- ²⁰²A. Byrne, M. J. Brookes, and S. Coombes, "A mean field model for movement induced changes in the beta rhythm," *J. Comput. Neurosci.* **43**, 143–158 (2017).
- ²⁰³H. Schmidt, D. Avitabile, E. Montbrió, and A. Roxin, "Network mechanisms underlying the role of oscillations in cognitive tasks," *PLoS Comput. Biol.* **14**, e1006430 (2018).
- ²⁰⁴Á. Byrne, R. D. O'Dea, M. Forrester, J. Ross, and S. Coombes, "Next-generation neural mass and field modeling," *J. Neurophysiol.* **123**, 726–742 (2020).
- ²⁰⁵A. Ceni, S. Olmi, A. Torcini, and D. Angulo-García, "Cross frequency coupling in next generation inhibitory neural mass models," *Chaos* **30**, 053121 (2020).
- ²⁰⁶H. Bi, M. Segneri, M. Di Volo, and A. Torcini, "Coexistence of fast and slow gamma oscillations in one population of inhibitory spiking neurons," *Phys. Rev. Res.* **2**, 013042 (2020).
- ²⁰⁷H. Taher, A. Torcini, and S. Olmi, "Exact neural mass model for synaptic-based working memory," *PLoS Comput. Biol.* **16**, e1008533 (2020).
- ²⁰⁸M. Segneri, H. Bi, S. Olmi, and A. Torcini, "Theta-nested gamma oscillations in next generation neural mass models," *Front. Comput. Neurosci.* **14**, 47 (2020).
- ²⁰⁹R. Gast, H. Schmidt, and T. R. Knösche, "A mean-field description of bursting dynamics in spiking neural networks with short-term adaptation," *Neural Comput.* **32**, 1615–1634 (2020).
- ²¹⁰M. Gerster, H. Taher, A. Škoch, J. Hlinka, M. Guye, F. Bartolomei, V. Jirsa, A. Zakharaova, and S. Olmi, "Patient-specific network connectivity combined with a next generation neural mass model to test clinical hypothesis of seizure propagation," *Front. Syst. Neurosci.* **15**, 79 (2021).
- ²¹¹R. Gast, T. R. Knösche, and H. Schmidt, "Mean-field approximations of networks of spiking neurons with short-term synaptic plasticity," *Phys. Rev. E* **104**, 044310 (2021).
- ²¹²G. Fuhrmann, H. Markram, and M. Tsodyks, "Spike frequency adaptation and neocortical rhythms," *J. Neurophysiol.* **88**, 761–770 (2002).
- ²¹³J. Benda and A. V. Herz, "A universal model for spike-frequency adaptation," *Neural Comput.* **15**, 2523–2564 (2003).
- ²¹⁴D. Brown and P. Adams, "Muscarinic suppression of a novel voltage-sensitive K⁺ current in a vertebrate neurone," *Nature* **283**, 673–676 (1980).
- ²¹⁵D. Madison and R. Nicoll, "Control of the repetitive discharge of rat CA 1 pyramidal neurones in vitro," *J. Physiol.* **354**, 319–331 (1984).
- ²¹⁶I. A. Fleidervish, A. Friedman, and M. J. Gutnick, "Slow inactivation of Na⁺ current and slow cumulative spike adaptation in mouse and guinea-pig neocortical neurones in slices," *J. Physiol.* **493**, 83–97 (1996).
- ²¹⁷C. F. Stevens and Y. Wang, "Facilitation and depression at single central synapses," *Neuron* **14**, 795–802 (1995).
- ²¹⁸H. Markram and M. Tsodyks, "Redistribution of synaptic efficacy between neocortical pyramidal neurons," *Nature* **382**, 807–810 (1996).
- ²¹⁹L. F. Abbott, J. Varela, K. Sen, and S. Nelson, "Synaptic depression and cortical gain control," *Science* **275**, 221–224 (1997).
- ²²⁰L. Abbott and W. G. Regehr, "Synaptic computation," *Nature* **431**, 796–803 (2004).
- ²²¹M. V. Jones and G. L. Westbrook, "The impact of receptor desensitization on fast synaptic transmission," *Trends Neurosci.* **19**, 96–101 (1996).
- ²²²A. Y. Wong, B. P. Graham, B. Billups, and I. D. Forsythe, "Distinguishing between presynaptic and postsynaptic mechanisms of short-term depression during action potential trains," *J. Neurosci.* **23**, 4868–4877 (2003).
- ²²³G. G. Turrigiano, "The self-tuning neuron: Synaptic scaling of excitatory synapses," *Cell* **135**, 422–435 (2008).
- ²²⁴K. Pozo and Y. Goda, "Unraveling mechanisms of homeostatic synaptic plasticity," *Neuron* **66**, 337–351 (2010).
- ²²⁵Y.-T. Huang, Y.-L. Chang, C.-C. Chen, P.-Y. Lai, and C. Chan, "Positive feedback and synchronized bursts in neuronal cultures," *PLoS One* **12**, e0187276 (2017).
- ²²⁶H. Markram, Y. Wang, and M. Tsodyks, "Differential signaling via the same axon of neocortical pyramidal neurons," *Proc. Natl. Acad. Sci. U.S.A.* **95**, 5323–5328 (1998).
- ²²⁷J. S. Dittman, A. C. Kreitzer, and W. G. Regehr, "Interplay between facilitation, depression, and residual calcium at three presynaptic terminals," *J. Neurosci.* **20**, 1374–1385 (2000).
- ²²⁸Y. Wang, H. Markram, P. H. Goodman, T. K. Berger, J. Ma, and P. S. Goldman-Rakic, "Heterogeneity in the pyramidal network of the medial prefrontal cortex," *Nat. Neurosci.* **9**, 534–542 (2006).
- ²²⁹G. Gigante, M. Mattia, and P. Del Giudice, "Diverse population-bursting modes of adapting spiking neurons," *Phys. Rev. Lett.* **98**, 148101 (2007).
- ²³⁰A. Ferrara, D. Angulo-García, A. Torcini, and S. Olmi, "Population spiking and bursting in next-generation neural masses with spike-frequency adaptation," *Phys. Rev. E* **107**, 024311 (2023).
- ²³¹M. Tsodyks, A. Uziel, and H. Markram, "Synchrony generation in recurrent networks with frequency-dependent synapses," *J. Neurosci.* **20**, RC50 (2000).
- ²³²S. Luccioli, E. Ben-Jacob, A. Barzilay, P. Bonifazi, and A. Torcini, "Clique of functional hubs orchestrates population bursts in developmentally regulated neural networks," *PLoS Comput. Biol.* **10**, e1003823 (2014).
- ²³³E. Fino and R. Yuste, "Dense inhibitory connectivity in neocortex," *Neuron* **69**, 1188–1203 (2011).
- ²³⁴C. Tallon-Baudry, O. Bertrand, F. Peronnet, and J. Pernier, "Induced γ -band activity during the delay of a visual short-term memory task in humans," *J. Neurosci.* **18**, 4244–4254 (1998).
- ²³⁵M. W. Howard, D. S. Rizzuto, J. B. Caplan, J. R. Madsen, J. Lisman, R. Aschenbrenner-Scheibe, A. Schulze-Bonhage, and M. J. Kahana, "Gamma oscillations correlate with working memory load in humans," *Cereb. Cortex* **13**, 1369–1374 (2003).
- ²³⁶M. K. Van Vugt, A. Schulze-Bonhage, B. Litt, A. Brandt, and M. J. Kahana, "Hippocampal gamma oscillations increase with memory load," *J. Neurosci.* **30**, 2694–2699 (2010).
- ²³⁷F. Roux, M. Wibral, H. M. Mohr, W. Singer, and P. J. Uhlhaas, "Gamma-band activity in human prefrontal cortex codes for the number of relevant items maintained in working memory," *J. Neurosci.* **32**, 12411–12420 (2012).
- ²³⁸E. K. Miller, M. Lundqvist, and A. M. Bastos, "Working memory 2.0," *Neuron* **100**, 463–475 (2018).

- ²³⁹M. Tsodyks, K. Pawelzik, and H. Markram, "Neural networks with dynamic synapses," *Neural Comput.* **10**, 821–835 (1998).
- ²⁴⁰H. Lindén and R. W. Berg, "Why firing rate distributions are important for understanding spinal central pattern generators," *Front. Hum. Neurosci.* **15**, 504 (2021).
- ²⁴¹J. E. Rubin, B. J. Bacak, Y. I. Molkov, N. A. Shevtsova, J. C. Smith, and I. A. Rybak, "Interacting oscillations in neural control of breathing: Modeling and qualitative analysis," *J. Comput. Neurosci.* **30**, 607–632 (2011).
- ²⁴²A. Benabid, P. Pollak, C. Gross, D. Hoffmann, A. Benazzouz, D. Gao, A. Laurent, M. Gentil, and J. Perret, "Acute and long-term effects of subthalamic nucleus stimulation in Parkinson's disease," *Stereotact. Funct. Neurosurg.* **62**, 76–84 (1994).
- ²⁴³M. Pinter, F. Alesch, M. Murg, M. Seiwald, R. Hetscher, and H. Binder, "Deep brain stimulation of the subthalamic nucleus for control of extrapyramidal features in advanced idiopathic Parkinson's disease: One year follow-up," *J. Neural Transm.* **106**, 693–709 (1999).
- ²⁴⁴M. C. Rodriguez-Oroz, J. A. Obeso, A. E. Lang, J.-L. Houeto, P. Pollak, S. Rehncrona, J. Kulisevsky, A. Albanese, J. Volkmann, M. I. Hariz, N. P. Quinn, J. D. Speelman, J. Guridi, I. Zambalde, A. Gironell, J. Molet, B. Pascual-Sedano, B. Pidoux, A. M. Bonnet, Y. Agid, J. Xie, A.-L. Benabid, A. M. Lozano, J. Saint-Cyr, L. Romito, M. F. Contarino, M. Scerrati, V. Fraix, and N. Van Blercom, "Bilateral deep brain stimulation in Parkinson's disease: A multicentre study with 4 years follow-up," *Brain* **128**, 2240–2249 (2005).
- ²⁴⁵A. L. Benabid, S. Chabardes, J. Mitrofanis, and P. Pollak, "Deep brain stimulation of the subthalamic nucleus for the treatment of Parkinson's disease," *Lancet Neurol.* **8**, 67–81 (2009).
- ²⁴⁶A. M. Lozano, N. Lipsman, H. Bergman, P. Brown, S. Chabardes, J. W. Chang, K. Matthews, C. C. McIntyre, T. E. Schlaepfer, M. Schulder, Y. Temel, J. Volkmann, and J. K. Krauss, "Deep brain stimulation: Current challenges and future directions," *Nat. Rev. Neurol.* **15**, 148–160 (2019).
- ²⁴⁷G. Deuschl, C. Schade-Brittinger, P. Krack, J. Volkmann, H. Schäfer, K. Bötzel, C. Daniels, A. Deuschländer, U. Dillmann, W. Eisner, D. Gruber, W. Hamel, J. Herzog, R. Hilker, S. Klebe, M. Kloss, J. Koy, M. Krause, A. Kupsch, D. Lorenz, S. Lorenzl, H. M. Mehdorn, J. R. Moringlane, W. Oertel, M. O. Pinsker, H. Reichmann, A. Reuss, G.-H. Schneider, A. Schnitzler, U. Steude, V. Sturm, L. Timmermann, V. Tronnier, T. Trottenberg, L. Wojtecki, E. Wolf, W. Poewe, and J. Voges, "A randomized trial of deep-brain stimulation for Parkinson's disease," *N. Engl. J. Med.* **355**, 896–908 (2006).
- ²⁴⁸F. M. Weaver, K. Follett, M. Stern, K. Hur, C. Harris, W. J. Marks, J. Rothlind, O. Sagher, D. Reda, C. S. Moy, and R. Pahwa, "Bilateral deep brain stimulation vs best medical therapy for patients with advanced parkinson disease: A randomized controlled trial," *JAMA* **301**, 63–73 (2009).
- ²⁴⁹K. A. Follett, F. M. Weaver, M. Stern, K. Hur, C. L. Harris, P. Luo, W. J. J. Marks, J. Rothlind, O. Sagher, C. Moy, R. Pahwa, K. Burchiel, P. Hogarth, E. C. Lai, J. E. Duda, K. Holloway, A. Samii, S. Horn, J. M. Bronstein, G. Stoner, P. A. Starr, R. Simpson, G. Baltuch, A. De Salles, G. D. Huang, and D. J. Reda, "Pallidal versus subthalamic deep-brain stimulation for Parkinson's disease," *N. Engl. J. Med.* **362**, 2077–2091 (2010).
- ²⁵⁰A. Beric, P. J. Kelly, A. Rezaei, D. Sterio, A. Mogilner, M. Zonenshayn, and B. Kopell, "Complications of deep brain stimulation surgery," *Stereotact. Funct. Neurosurg.* **77**, 73–78 (2001).
- ²⁵¹M. Y. Oh, A. Abosch, S. H. Kim, A. E. Lang, and A. M. Lozano, "Long-term hardware-related complications of deep brain stimulation," *Neurosurgery* **50**, 1268–1276 (2002).
- ²⁵²D. K. Binder, G. Rau, and P. A. Starr, "Hemorrhagic complications of microelectrode-guided deep brain stimulation," *Stereotact. Funct. Neurosurg.* **80**, 28–31 (2003).
- ²⁵³K. E. Lyons, S. B. Wilkinson, J. Overman, and R. Pahwa, "Surgical and hardware complications of subthalamic stimulation: A series of 160 procedures," *Neurology* **63**, 612–616 (2004).
- ²⁵⁴E. Y. Uc and K. A. Follett, "Deep brain stimulation in movement disorders," *Semin. Neurol.* **27**, 170–182 (2007).
- ²⁵⁵J. Baizabal-Carvalho and J. Jankovic, "Movement disorders induced by deep brain stimulation," *Parkinsonism Relat. Disord.* **25**, 1–9 (2016).
- ²⁵⁶V. Voon and S. H. Fox, "Medication-related impulse control and repetitive behaviors in Parkinson disease," *Arch. Neurol.* **64**, 1089–1096 (2007).
- ²⁵⁷S. A. Eisenstein, W. B. Dewispelaere, M. C. Campbell, H. M. Lugar, J. S. Perlmutter, K. J. Black, and T. Hershey, "Acute changes in mood induced by subthalamic deep brain stimulation in Parkinson disease are modulated by psychiatric diagnosis," *Brain Stimul.* **7**, 701–708 (2014).
- ²⁵⁸A. Merola, A. Romagnolo, L. Rizzi, M. G. Rizzone, M. Zibetti, M. Lanotte, G. Mandybur, A. P. Duker, A. J. Espay, and L. Lopiano, "Impulse control behaviors and subthalamic deep brain stimulation in Parkinson disease," *J. Neurol.* **264**, 40–48 (2017).
- ²⁵⁹S. Healy, H. Shepherd, N. Mooney, A. D. Costa, J. Osman-Farah, and A. Macerollo, "The effect of deep brain stimulation on impulse control related disorders in Parkinson's disease – a 10-year retrospective study of 137 patients," *J. Neurol. Sci.* **440**, 120339 (2022).
- ²⁶⁰C. Hammond, H. Bergman, and P. Brown, "Pathological synchronization in Parkinson's disease: Networks, models and treatments," *Trends Neurosci.* **30**, 357–364 (2007).
- ²⁶¹P. A. Tass, *Phase Resetting in Medicine and Biology: Stochastic Modelling and Data Analysis* (Springer-Verlag, Berlin, 1999).
- ²⁶²P. A. Tass, "Desynchronizing double-pulse phase resetting and application to deep brain stimulation," *Biol. Cybern.* **85**, 343–354 (2001).
- ²⁶³P. A. Tass, "A model of desynchronizing deep brain stimulation with a demand-controlled coordinated reset of neural subpopulations," *Biol. Cybern.* **89**, 81–88 (2003).
- ²⁶⁴I. Adamchic, C. Hauptmann, U. B. Barnikol, N. Pawelczyk, O. V. Popovych, T. T. Barnikol, A. Silchenko, J. Volkmann, G. Deuschl, W. G. Meissner, M. Maarouf, V. Sturm, H.-J. Freund, and P. A. Tass, "Coordinated reset neuromodulation for Parkinson's disease: Proof-of-concept study," *Mov. Disord.* **29**, 1679–1684 (2014).
- ²⁶⁵W. Bouthour, P. Mégevand, J. Donoghue, C. Lüscher, N. Birbaumer, and P. Krack, "Biomarkers for closed-loop deep brain stimulation in Parkinson disease and beyond," *Nat. Rev. Neurol.* **15**, 343–352 (2019).
- ²⁶⁶K. B. Hoang and D. A. Turner, "The emerging role of biomarkers in adaptive modulation of clinical brain stimulation," *Neurosurgery* **85**, E430–E439 (2019).
- ²⁶⁷M. Beudel and P. Brown, "Adaptive deep brain stimulation in Parkinson's disease," *Parkinsonism Relat. Disord.* **22 Suppl 1**, S123–S126 (2016).
- ²⁶⁸P. A. Tass and M. Majtanik, "Long-term anti-kindling effects of desynchronizing brain stimulation: A theoretical study," *Biol. Cybern.* **94**, 58–66 (2006).
- ²⁶⁹M. Madadi Asl, A.-H. Vahabie, A. Valizadeh, and P. A. Tass, "Spike-timing-dependent plasticity mediated by dopamine and its role in Parkinson's disease pathophysiology," *Front. Netw. Physiol.* **2**, 817524 (2022).
- ²⁷⁰P. A. Tass and C. Hauptmann, "Therapeutic modulation of synaptic connectivity with desynchronizing brain stimulation," *Int. J. Psychophysiol.* **64**, 53–61 (2007).
- ²⁷¹M. Zeitler and P. A. Tass, "Augmented brain function by coordinated reset stimulation with slowly varying sequences," *Front. Syst. Neurosci.* **9**, 49 (2015).
- ²⁷²T. Manos, M. Zeitler, and P. A. Tass, "How stimulation frequency and intensity impact on the long-lasting effects of coordinated reset stimulation," *PLoS Comput. Biol.* **14**, e1006113 (2018).
- ²⁷³D. Tyulmankov, P. A. Tass, and H. Bokil, "Periodic flashing coordinated reset stimulation paradigm reduces sensitivity to on and off period durations," *PLoS One* **13**, e0203782 (2018).
- ²⁷⁴J. A. Kromer and P. A. Tass, "Long-lasting desynchronization by decoupling stimulation," *Phys. Rev. Res.* **2**, 033101 (2020).
- ²⁷⁵A. Khaleedi-Nasab, J. A. Kromer, and P. A. Tass, "Long-lasting desynchronization of plastic neural networks by random reset stimulation," *Front. Physiol.* **11**, 622620 (2021).
- ²⁷⁶J. A. Kromer and P. A. Tass, "Synaptic reshaping of plastic neuronal networks by periodic multichannel stimulation with single-pulse and burst stimuli," *PLoS Comput. Biol.* **18**, e1010568 (2022).
- ²⁷⁷M. Madadi Asl, A. Valizadeh, and P. A. Tass, "Decoupling of interacting neuronal populations by time-shifted stimulation through spike-timing-dependent plasticity," *PLoS Comput. Biol.* **19**, e1010853 (2023).
- ²⁷⁸C. Hauptmann and P. A. Tass, "Cumulative and after-effects of short and weak coordinated reset stimulation: A modeling study," *J. Neural Eng.* **6**, 016004 (2009).

- ²⁷⁹O. V. Popovych and P. A. Tass, “Desynchronizing electrical and sensory coordinated reset neuromodulation,” *Front. Hum. Neurosci.* **6**, 58 (2012).
- ²⁸⁰P. A. Tass, L. Qin, C. Hauptmann, S. Dovero, E. Bezdard, T. Boraud, and W. G. Meissner, “Coordinated reset has sustained aftereffects in Parkinsonian monkeys,” *Ann. Neurol.* **72**, 816–820 (2012).
- ²⁸¹M. Butz, F. Wörgötter, and A. van Ooyen, “Activity-dependent structural plasticity,” *Brain Res. Rev.* **60**, 287 (2009).
- ²⁸²M. Butz and A. van Ooyen, “A simple rule for dendritic spine and axonal bouton formation can account for cortical reorganization after focal retinal lesions,” *PLoS Comput. Biol.* **9**, e1003259 (2013).
- ²⁸³T. Manos, S. Diaz-Pier, and P. A. Tass, “Long-term desynchronization by coordinated reset stimulation in a neural network model with synaptic and structural plasticity,” *Front. Physiol.* **12**, 716556 (2021).
- ²⁸⁴K. Chauhan, A. Khaledi-Nasab, A. B. Neiman, and P. A. Tass, “Dynamics of phase oscillator networks with synaptic weight and structural plasticity,” *Sci. Rep.* **12**, 15003 (2022).
- ²⁸⁵J. Wang, S. Nebeck, A. Muralidharan, M. D. Johnson, J. L. Vitek, and K. B. Baker, “Coordinated reset deep brain stimulation of subthalamic nucleus produces long-lasting, dose-dependent motor improvements in the 1-methyl-4-phenyl-1,2,3,6-tetrahydropyridine non-human primate model of parkinsonism,” *Brain Stimul.* **9**, 609–617 (2016).
- ²⁸⁶J. Wang, S. P. Fergus, L. A. Johnson, S. D. Nebeck, J. Zhang, S. Kulkarni, H. Bokil, G. F. Molnar, and J. L. Vitek, “Shuffling improves the acute and carryover effect of subthalamic coordinated reset deep brain stimulation,” *Front. Neurol.* **13**, 716046 (2022).
- ²⁸⁷J. Chelangat Bore, B. A. Campbell, H. Cho, F. Pucci, R. Gopalakrishnan, A. G. Machado, and K. B. Baker, “Long-lasting effects of subthalamic nucleus coordinated reset deep brain stimulation in the non-human primate model of parkinsonism: A case report,” *Brain Stimul.* **15**, 598–600 (2022).
- ²⁸⁸P. A. Tass, “Vibrotactile coordinated reset stimulation for the treatment of neurological diseases: Concepts and device specifications,” *Cureus* **9**, e1535 (2017).
- ²⁸⁹J. Syrkin-Nikolau, R. Neuville, J. O’Day, C. Anidi, M. Miller Koop, T. Martin, P. A. Tass, and H. Bronte-Stewart, “Coordinated reset vibrotactile stimulation shows prolonged improvement in Parkinson’s disease,” *Mov. Disord.* **33**, 179–180 (2018).
- ²⁹⁰K. J. Pfeifer, J. A. Kromer, A. J. Cook, T. Hornbeck, E. A. Lim, B. J. P. Mortimer, A. S. Fogarty, S. S. Han, R. Dhall, C. H. Halpern, and P. A. Tass, “Coordinated reset vibrotactile stimulation induces sustained cumulative benefits in Parkinson’s disease,” *Front. Physiol.* **12**, 624317 (2021).
- ²⁹¹P. A. Tass, “Vibrotactile coordinated reset stimulation for the treatment of Parkinson’s disease,” *Neural Regen. Res.* **17**, 1495–1497 (2021).
- ²⁹²E. Esposito, V. Di Matteo, and G. Di Giovanni, “Death in the substantia nigra: A motor tragedy,” *Expert Rev. Neurother.* **7**, 677–697 (2007).
- ²⁹³N. A. Haelterman, W. H. Yoon, H. Sandoval, M. Jaiswal, J. M. Shulman, and H. J. Bellen, “A mitocentric view of Parkinson’s disease,” *Annu. Rev. Neurosci.* **37**, 137–159 (2014).
- ²⁹⁴M. M. McGregor and A. B. Nelson, “Circuit mechanisms of Parkinson’s disease,” *Neuron* **101**, 1042–1056 (2019).
- ²⁹⁵*Springer Handbook of Systematic Musicology*, Springer Handbooks, edited by R. Bader (Springer, Berlin, 2019).
- ²⁹⁶J.-P. Briot, G. Hadjeres, and F.-D. Pachet, *Deep Learning Techniques for Music Generation* (Springer International Publishing, 2020).
- ²⁹⁷T. Kohonen, *Self-Organizing Maps* (Springer, Berlin, 1995).
- ²⁹⁸M. Bläß, J. L. Fischer, and N. Plath, “Computational phonogram archiving,” *Phys. Today* **73**(12), 50–55 (2020).
- ²⁹⁹*Computational Phonogram Archiving*, 1st ed., Current Research in Systematic Musicology, edited by R. Bader (Springer Nature, Cham, Switzerland, 2019).
- ³⁰⁰M. Leman and F. Carreras, “Schema and gestalt: Testing the hypothesis of psychoneural isomorphism by computer simulation,” in *Music, Gestalt, and Computing* (Springer, Berlin, 1997), pp. 144–168.
- ³⁰¹R. Bader, *How Music Works* (Springer International Publishing, 2021).
- ³⁰²R. Bader, *Nonlinearities and Synchronization in Musical Acoustics and Music Psychology* (Springer, Berlin, 2013).
- ³⁰³S. Linke, R. Bader, and R. Mores, “The impulse pattern formulation (IPF) as a model of musical instruments—investigation of stability and limits,” *Chaos* **29**, 103109 (2019).
- ³⁰⁴S. Linke, R. Bader, and R. Mores, “Influence of the supporting table on initial transients of the fretted zither: An impulse pattern formulation model,” in *Proceedings of Meetings on Acoustics* (ASA, 2021).
- ³⁰⁵S. Linke, R. Bader, and R. Mores, “Modeling synchronization in human musical rhythms using impulse pattern formulation (IPF),” *arXiv:2112.03218* (2021).
- ³⁰⁶R. Bader, “Impulse pattern formulation (IPF) brain model,” *arXiv:2212.11021* (2022).
- ³⁰⁷R. Kozma and W. J. Freeman, *Cognitive Phase Transitions in the Cerebral Cortex—Enhancing the Neuron Doctrine by Modeling Neural Fields* (Springer International Publishing, 2016).
- ³⁰⁸I. Nelken, “Processing of complex stimuli and natural scenes in the auditory cortex,” *Curr. Opin. Neurobiol.* **14**, 474–480 (2004).
- ³⁰⁹R. A. Butler, “Effect of changes in stimulus frequency and intensity on habituation of the human vertex potential,” *J. Acoust. Soc. Am.* **44**, 945–950 (1968).
- ³¹⁰M. Brosch and C. E. Schreiner, “Sequence sensitivity of neurons in cat primary auditory cortex,” *Cereb. Cortex* **10**, 1155–1167 (2000).
- ³¹¹R. Näätänen, A. W. Gaillard, and S. Mäntysalo, “Early selective-attention effect on evoked potential reinterpreted,” *Acta Psychol.* **42**, 313–329 (1978).
- ³¹²N. Ulanovsky, L. Las, D. Farkas, and I. Nelken, “Multiple time scales of adaptation in auditory cortex neurons,” *J. Neurosci.* **24**, 10440–10453 (2004).
- ³¹³N. Zacharias, R. König, and P. Heil, “Stimulation-history effects on the M100 revealed by its differential dependence on the stimulus onset interval,” *Psychophysiology* **49**, 909–919 (2012).
- ³¹⁴D. Pérez-González and M. S. Malmierca, “Adaptation in the auditory system: An overview,” *Front. Integr. Neurosci.* **8**, 19 (2014).
- ³¹⁵M. S. Malmierca, L. A. Anderson, and F. M. Antunes, “The cortical modulation of stimulus-specific adaptation in the auditory midbrain and thalamus: A potential neuronal correlate for predictive coding,” *Front. Syst. Neurosci.* **9**, 19 (2015).
- ³¹⁶K. Friston, “A theory of cortical responses,” *Philos. Trans. R. Soc.* **360**, 815–836 (2005).
- ³¹⁷P. J. C. May, “The adaptation model offers a challenge for the predictive coding account of mismatch negativity,” *Front. Hum. Neurosci.* **15**, 721574 (2021).
- ³¹⁸P. J. C. May and H. Tiitinen, “Mismatch negativity (MMN), the deviance-elicited auditory deflection, explained,” *Psychophysiology* **47**, 66–122 (2010).
- ³¹⁹P. Wang and T. R. Knösche, “A realistic neural mass model of the cortex with laminar-specific connections and synaptic plasticity-evaluation with auditory habituation,” *PLoS One* **8**, e77876 (2013).
- ³²⁰P. Kudela, D. Boatman-Reich, D. Beeman, and W. S. Anderson, “Modeling neural adaptation in auditory cortex,” *Front. Neural Circuits* **12**, 72 (2018).
- ³²¹E. S. Fortune and G. J. Rose, “Short-term synaptic plasticity as a temporal filter,” *Trends Neurosci.* **24**, 381–385 (2001).
- ³²²M. Salmasi, A. Loebel, S. Glasauer, and M. Stemmler, “Short-term synaptic depression can increase the rate of information transfer at a release site,” *PLoS Comput. Biol.* **15**, e1006666 (2019).
- ³²³P. J. C. May and H. Tiitinen, “Temporal binding of sound emerges out of anatomical structure and synaptic dynamics of auditory cortex,” *Front. Comput. Neurosci.* **7**, 152 (2013).
- ³²⁴A. Hajizadeh, A. Matysiak, P. J. C. May, and R. König, “Explaining event-related fields by a mechanistic model encapsulating the anatomical structure of auditory cortex,” *Biol. Cybern.* **113**, 321–345 (2019).
- ³²⁵A. Hajizadeh, A. Matysiak, M. Wolfrum, P. J. C. May, and R. König, “Auditory cortex modelled as a dynamical network of oscillators: Understanding event-related fields and their adaptation,” *Biol. Cybern.* **116**, 475–499 (2022).
- ³²⁶J. H. Kaas and T. A. Hackett, “Subdivisions of auditory cortex and processing streams in primates,” *Proc. Natl. Acad. Sci. U.S.A.* **97**, 11793–11799 (2000).
- ³²⁷T. A. Hackett, “Anatomic organization of the auditory cortex,” in *Handbook of Clinical Neurology* (Elsevier, 2015), Vol. 129, pp. 27–53.
- ³²⁸A. Krizhevsky, I. Sutskever, and G. Hinton, “ImageNet classification with deep convolutional neural networks,” in *Advances in Neural Information Processing Systems* (Curran Associates, Inc., 2012), pp. 1097–1105.

- ³²⁹Y. LeCun, Y. Bengio, and G. Hinton, “Deep learning,” *Nature* **521**, 436–444 (2015).
- ³³⁰K. Simonyan and A. Zisserman, “Very deep convolutional networks for large-scale image recognition,” presented at the 3rd International Conference on Learning Representations (ICLR 2015), San Diego, CA, May 7–9, 2015.
- ³³¹K. He, X. Zhang, S. Ren, and J. Sun, “Deep residual learning for image recognition,” in *Proceedings of the IEEE Conference on Computer Vision and Pattern Recognition* (IEEE, 2016), pp. 770–778.
- ³³²A. Dosovitskiy, L. Beyer, A. Kolesnikov, D. Weissenborn, X. Zhai, T. Unterthiner, M. Dehghani, M. Minderer, G. Heigold, S. Gelly, J. Uszkoreit, and N. Houlsby, “An image is worth 16x16 words: Transformers for image recognition at scale,” presented at the 9th International Conference on Learning Representations, virtual, 3–7 May 2021.
- ³³³G. Hinton, L. Deng, D. Yu, G. E. Dahl, A.-R. Mohamed, N. Jaitly, A. Senior, V. Vanhoucke, P. Nguyen, T. N. Sainath, and B. Kingsbury, “Deep neural networks for acoustic modeling in speech recognition: The shared views of four research groups,” *IEEE Signal Process. Mag.* **29**, 82–97 (2012).
- ³³⁴I. Sutskever, O. Vinyals, and Q. Le, “Sequence to sequence learning with neural networks,” in *Advances in Neural Information Processing Systems 27*, edited by Z. Ghahramani, M. Welling, C. Cortes, N. D. Lawrence, and K. Q. Weinberger (Curran Associates, Inc., 2014), pp. 3104–3112.
- ³³⁵A. Vaswani, N. Shazeer, N. Parmar, J. Uszkoreit, L. Jones, A. N. Gomez, Ł. Kaiser, and I. Polosukhin, “Attention is all you need,” in *Advances in Neural Information Processing Systems* (Curran Associates, Inc., 2017), pp. 5998–6008.
- ³³⁶J. Devlin, M.-W. Chang, K. Lee, and K. Toutanova, “BERT: Pre-training of deep bidirectional transformers for language understanding,” in *Proceedings of NAACL-HLT* (Association for Computational Linguistics, 2019), pp. 4171–4186.
- ³³⁷D. Silver, A. Huang, C. J. Maddison, A. Guez, L. Sifre, G. van den Driessche, J. Schrittwieser, I. Antonoglou, V. Panneershelvam, M. Lanctot, S. Dieleman, D. Grewe, J. Nham, N. Kalchbrenner, I. Sutskever, T. Lillicrap, M. Leach, K. Kavukcuoglu, T. Graepel, and D. Hassabis, “Mastering the game of go with deep neural networks and tree search,” *Nature* **529**, 484–489 (2016).
- ³³⁸D. Silver, J. Schrittwieser, K. Simonyan, I. Antonoglou, A. Huang, A. Guez, T. Hubert, L. Baker, M. Lai, A. Bolton, Y. Chen, T. Lillicrap, F. Hui, L. Sifre, G. van den Driessche, T. Graepel, and D. Hassabis, “Mastering the game of go without human knowledge,” *Nature* **550**, 354–359 (2017).
- ³³⁹M. Bowling, N. Burch, M. Johanson, and O. Tammelin, “Heads-up limit hold’em poker is solved,” *Science* **347**, 145–149 (2015).
- ³⁴⁰N. Brown and T. Sandholm, “Superhuman ai for heads-up no-limit poker: Libratus beats top professionals,” *Science* **359**, 418–424 (2018).
- ³⁴¹N. Brown and T. Sandholm, “Superhuman ai for multiplayer poker,” *Science* **365**, 885–890 (2019).
- ³⁴²G. Carleo, I. Cirac, K. Cranmer, L. Daudet, M. Schuld, N. Tishby, L. Vogt-Maranto, and L. Zdeborová, “Machine learning and the physical sciences,” *Rev. Mod. Phys.* **91**, 045002 (2019).
- ³⁴³K. Tunyasuvunakool, J. Adler, Z. Wu, T. Green, M. Zielinski, A. Židek, A. Bridgland, A. Cowie, C. Meyer, A. Laydon, S. Velankar, G. J. Kleywegt, A. Bateman, R. Evans, A. Pritzel, M. Figurnov, O. Ronneberger, R. Bates, S. A. A. Kohl, A. Potapenko, A. J. Ballard, B. Romera-Paredes, S. Nikolov, R. Jain, E. Clancy, D. Reiman, S. Petersen, A. W. Senior, K. Kavukcuoglu, E. Birney, P. Kohli, J. Jumper, and D. Hassabis, “Highly accurate protein structure prediction for the human proteome,” *Nature* **596**, 590–596 (2021).
- ³⁴⁴A. Oliva and A. Torralba, “Modeling the shape of the scene: A holistic representation of the spatial envelope,” *Int. J. Comput. Vis.* **42**, 145–175 (2001).
- ³⁴⁵N. Dalal and B. Triggs, “Histograms of oriented gradients for human detection,” in *2005 IEEE Computer Society Conference on Computer Vision and Pattern Recognition (CVPR’05)* (IEEE, 2005), Vol. 1, pp. 886–893.
- ³⁴⁶H. Bay, T. Tuytelaars, and L. Van Gool, “SURF: Speeded up robust features,” in *Computer Vision—ECCV 2006*, edited by A. Leonardis, H. Bischof, and A. Pinz (Springer, Berlin, 2006), pp. 404–417.
- ³⁴⁷There are different architectures that are appropriate for certain types of data or certain tasks; for an overview, cf. Ref. 380.
- ³⁴⁸D. J. MacKay, *Information Theory, Inference and Learning Algorithms* (Cambridge University Press, 2003).
- ³⁴⁹M. Hardt, B. Recht, and Y. Singer, “Train faster, generalize better: Stability of stochastic gradient descent,” in *Proceedings of the 33rd International Conference on Machine Learning, Proceedings of Machine Learning Research*, Vol. 48, edited by M. F. Balcan and K. Q. Weinberger (PMLR, New York, 2016), pp. 1225–1234.
- ³⁵⁰A. C. Wilson, R. Roelofs, M. Stern, N. Srebro, and B. Recht, “The marginal value of adaptive gradient methods in machine learning,” in *Advances in Neural Information Processing Systems* Vol. 30, edited by I. Guyon, U. V. Luxburg, S. Bengio, H. Wallach, R. Fergus, S. Vishwanathan, and R. Garnett (Curran Associates, Inc., 2017).
- ³⁵¹U. von Luxburg and O. Bousquet, “Distance-based classification with Lipschitz functions,” *J. Mach. Learn. Res.* **5**, 669–695 (2004).
- ³⁵²Y. Bahri, J. Kadmon, J. Pennington, S. Schoenholz, J. Sohl-Dickstein, and S. Ganguli, “Statistical mechanics of deep learning,” *Annu. Rev. Condens. Matter Phys.* **11**, 501–528 (2020).
- ³⁵³L. Zdeborová, “Understanding deep learning is also a job for physicists,” *Nat. Phys.* **16**, 602–604 (2020).
- ³⁵⁴M. Geiger, L. Petrini, and M. Wyart, “Landscape and training regimes in deep learning,” *Phys. Rep.* **924**, 1–18 (2021).
- ³⁵⁵P. Grassberger and I. Procaccia, “Measuring the strangeness of strange attractors,” *Phys. D: Nonlinear Phenom.* **9**, 189–208 (1983).
- ³⁵⁶J. Costa and A. Hero, “Learning intrinsic dimension and intrinsic entropy of high-dimensional datasets,” in *2004 12th European Signal Processing Conference* (IEEE, 2004), pp. 369–372.
- ³⁵⁷E. Levina and P. Bickel, “Maximum likelihood estimation of intrinsic dimension,” in *Advances in Neural Information Processing Systems 17* (Curran Associates, Inc., 2004).
- ³⁵⁸S. Spigler, M. Geiger, and M. Wyart, “Asymptotic learning curves of kernel methods: Empirical data versus teacher–student paradigm,” *J. Stat. Mech.: Theory Exp.* **2020**, 124001.
- ³⁵⁹P. Pope, C. Zhu, A. Abdelkader, M. Goldblum, and T. Goldstein, “The intrinsic dimension of images and its impact on learning,” presented at the 9th International Conference on Learning Representations, virtual, 3–7 May 2021.
- ³⁶⁰S. Goldt, M. Mézard, F. Krzakala, and L. Zdeborová, “Modeling the influence of data structure on learning in neural networks: The hidden manifold model,” *Phys. Rev. X* **10**, 041044 (2020).
- ³⁶¹J. Deng, W. Dong, R. Socher, L.-J. Li, K. Li, and L. Fei-Fei, “ImageNet: A large-scale hierarchical image database,” in *2009 IEEE Conference on Computer Vision and Pattern Recognition* (IEEE, 2009), pp. 248–255.
- ³⁶²S. Chung, D. Lee, and H. Sompolinsky, “Classification and geometry of general perceptual manifolds,” *Phys. Rev. X* **8**, 031003 (2018).
- ³⁶³S. Goldt, B. Loureiro, G. Reeves, F. Krzakala, M. Mézard, and L. Zdeborová, “The Gaussian equivalence of generative models for learning with shallow neural networks,” in *Proceedings of the 2nd Mathematical and Scientific Machine Learning Conference*, Proceedings of Machine Learning Research Vol. 145, edited by J. Bruna, J. Hesthaven, and L. Zdeborová (PMLR, 2022), pp. 426–471.
- ³⁶⁴B. Ghorbani, S. Mei, T. Misiakiewicz, and A. Montanari, “When do neural networks outperform kernel methods?,” in *Advances in Neural Information Processing Systems* (Curran Associates, Inc., 2020), Vol. 33.
- ³⁶⁵D. Richards, J. Mourada, and L. Rosasco, “Asymptotics of ridge(less) regression under general source condition,” in *Proceedings of the 24th International Conference on Artificial Intelligence and Statistics*, Proceedings of Machine Learning Research Vol. 130, edited by A. Banerjee and K. Fukumizu (PMLR, 2021), pp. 3889–3897.
- ³⁶⁶F. Bach, “Breaking the curse of dimensionality with convex neural networks,” *J. Mach. Learn. Res.* **18**, 629–681 (2017).
- ³⁶⁷B. Ghorbani, S. Mei, T. Misiakiewicz, and A. Montanari, “Limitations of lazy training of two-layers neural network,” in *Advances in Neural Information Processing Systems* (Curran Associates, Inc., 2019), Vol. 32, pp. 9111–9121.
- ³⁶⁸L. Chizat and F. Bach, “Implicit bias of gradient descent for wide two-layer neural networks trained with the logistic loss,” in *Conference on Learning Theory* (PMLR, 2020), pp. 1305–1338.
- ³⁶⁹M. Geiger, S. Spigler, A. Jacot, and M. Wyart, “Disentangling feature and lazy training in deep neural networks,” *J. Stat. Mech.: Theory Exp.* **2020**, 113301.
- ³⁷⁰A. Daniely and E. Malach, “Learning parities with neural networks,” in *Advances in Neural Information Processing Systems* (Curran Associates, Inc., 2020), Vol. 33.

- ³⁷¹M. Refinetti, S. Goldt, F. Krzakala, and L. Zdeborova, "Classifying high-dimensional Gaussian mixtures: Where kernel methods fail and neural networks succeed," in *Proceedings of the 38th International Conference on Machine Learning*, Proceedings of Machine Learning Research Vol. 139, edited by M. Meila and T. Zhang (PMLR, 2021), pp. 8936–8947.
- ³⁷²G. Torlai and R. G. Melko, "Learning thermodynamics with Boltzmann machines," *Phys. Rev. B* **94**, 165134 (2016).
- ³⁷³J. Carrasquilla and R. G. Melko, "Machine learning phases of matter," *Nat. Phys.* **13**, 431–434 (2017).
- ³⁷⁴E. P. Van Nieuwenburg, Y.-H. Liu, and S. D. Huber, "Learning phase transitions by confusion," *Nat. Phys.* **13**, 435–439 (2017).
- ³⁷⁵P. Wirnsberger, A. J. Ballard, G. Papamakarios, S. Abercrombie, S. Racanière, A. Pritzel, D. Jimenez Rezende, and C. Blundell, "Targeted free energy estimation via learned mappings," *J. Chem. Phys.* **153**, 144112 (2020).
- ³⁷⁶A. Seif, M. Hafezi, and C. Jarzynski, "Machine learning the thermodynamic arrow of time," *Nat. Phys.* **17**, 105–113 (2021).
- ³⁷⁷D.-K. Kim, Y. Bae, S. Lee, and H. Jeong, "Learning entropy production via neural networks," *Phys. Rev. Lett.* **125**, 140604 (2020).
- ³⁷⁸I. Goodfellow, Y. Bengio, and A. Courville, *Deep Learning* (MIT Press, 2016).
- ³⁷⁹Y. Bengio, P. Simard, and P. Frasconi, "Learning long-term dependencies with gradient descent is difficult," *IEEE Trans. Neural Netw.* **5**, 157–166 (1994).
- ³⁸⁰S. Hochreiter and J. Schmidhuber, "Long short-term memory," *Neural Comput.* **9**, 1735–1780 (1997).
- ³⁸¹A. Argun, T. Thalheim, S. Bo, F. Cichos, and G. Volpe, "Enhanced force-field calibration via machine learning," *Appl. Phys. Rev.* **7**, 041404 (2020).
- ³⁸²J. Pathak, B. Hunt, M. Girvan, Z. Lu, and E. Ott, "Model-free prediction of large spatiotemporally chaotic systems from data: A reservoir computing approach," *Phys. Rev. Lett.* **120**, 024102 (2018).
- ³⁸³Y. Kuramoto, "Diffusion-induced chaos in reaction systems," *Prog. Theor. Phys. Suppl.* **64**, 346–367 (1978).
- ³⁸⁴G. I. Sivashinsky, "Nonlinear analysis of hydrodynamic instability in laminar flames—I. Derivation of basic equations," *Acta Astronaut.* **4**, 1177–1206 (1977).
- ³⁸⁵G. I. Sivashinsky, "On flame propagation under conditions of stoichiometry," *SIAM J. Appl. Math.* **39**, 67–82 (1980).
- ³⁸⁶M. Lukoševičius and H. Jaeger, "Reservoir computing approaches to recurrent neural network training," *Comput. Sci. Rev.* **3**, 127–149 (2009).
- ³⁸⁷A. Seif, S. A. M. Loos, G. Tucci, É. Roldán, and S. Goldt, "The impact of memory on learning sequence-to-sequence tasks," [arXiv:2205.14683](https://arxiv.org/abs/2205.14683) (2022).
- ³⁸⁸M. Krenn, R. Pollice, S. Y. Guo, M. Aldeghi, A. Cervera-Lierta, P. Friederich, G. dos Passos Gomes, F. Häse, A. Jimich, A. Nigam, and Z. Yao, "On scientific understanding with artificial intelligence," *Nat. Rev. Phys.* **4**, 761–769 (2022).
- ³⁸⁹E. Ott, C. Grebogi, and J. A. Yorke, "Controlling chaos," *Phys. Rev. Lett.* **64**, 1196–1199 (1990).
- ³⁹⁰F. Romeiras, C. Grebogi, E. Ott, and W. Dayawansa, *Physica D* **58**, 165–192 (1992).
- ³⁹¹J. Sarangapani, *Neural Network Control of Nonlinear Discrete-Time Systems* (Taylor & Francis, Boca Raton, FL, 2006).
- ³⁹²H. Jaeger and H. Haas, "Harnessing nonlinearity: Predicting chaotic systems and saving energy in wireless communication," *Science* **304**, 78–80 (2004).
- ³⁹³T. Waegeman, F. Wyffels, and B. Schrauwen, "Feedback control by online learning an inverse model," *IEEE Trans. Neural Netw. Learn. Syst.* **23**, 1637–1648 (2012).
- ³⁹⁴D. Canaday, A. Pomerance, and D. J. Gauthier, "Model-free control of dynamical systems with deep reservoir computing," *J. Phys. Complex.* **2**, 035025 (2021).
- ³⁹⁵D. J. Gauthier, E. Bollt, A. Griffith, and W. A. S. Barbosa, "Next generation reservoir computing," *Nat. Commun.* **12**, 5564 (2021).
- ³⁹⁶W. Steffen, J. Rockström, K. Richardson, T. M. Lenton, C. Folke, D. Liverman, C. P. Summerhayes, A. D. Barnosky, S. E. Cornell, M. Crucifix, J. F. Donges, I. Fetzer, S. J. Lade, M. Scheffer, R. Winkelmann, and H. J. Schellnhuber, "Trajectories of the Earth system in the anthropocene," *Proc. Natl. Acad. Sci. U.S.A.* **115**, 8252–8259 (2018).
- ³⁹⁷S. A. Levin, "Collective cooperation: From ecological communities to global governance and back," in *Collective Cooperation: From Ecological Communities to Global Governance and Back* (Princeton University Press, 2020), pp. 311–317.
- ³⁹⁸M. A. Nowak, *Evolutionary Dynamics: Exploring the Equations of Life* (Harvard University Press, 2006).
- ³⁹⁹J. M. McNamara, "Towards a richer evolutionary game theory," *J. R. Soc. Interface* **10**, 20130544 (2013).
- ⁴⁰⁰M. Botvinick, J. X. Wang, W. Dabney, K. J. Miller, and Z. Kurth-Nelson, "Deep reinforcement learning and its neuroscientific implications," *Neuron* **107**, 603–616 (2020).
- ⁴⁰¹R. S. Sutton and A. G. Barto, *Reinforcement Learning: An Introduction*, 2nd ed., Adaptive Computation and Machine Learning Series (The MIT Press, Cambridge, MA, 2018).
- ⁴⁰²A. Dafoe, E. Hughes, Y. Bachrach, T. Collins, K. R. McKee, J. Z. Leibo, K. Larson, and T. Graepel, "Open problems in cooperative AI," preprint [arXiv:2012.08630](https://arxiv.org/abs/2012.08630) (2020).
- ⁴⁰³A. Dafoe, Y. Bachrach, G. Hadfield, E. Horvitz, K. Larson, and T. Graepel, "Cooperative AI: Machines must learn to find common ground," *Nature* **593**, 33–36 (2021).
- ⁴⁰⁴J. H. Holland, "Studying complex adaptive systems," *J. Syst. Sci. Complex.* **19**, 1–8 (2006).
- ⁴⁰⁵J. Schulze, B. Müller, J. Groeneveld, and V. Grimm, "Agent-based modelling of social-ecological systems: Achievements, challenges, and a way forward," *J. Artif. Soc. Econ. Simul.* **20**, 8 (2017).
- ⁴⁰⁶N. M. Gots, G. A. K. van Voorn, J. G. Polhill, E. de Jong, B. Edmonds, G. J. Hofstede, and R. Meyer, "Agent-based modelling of socio-ecological systems: Models, projects and ontologies," *Ecol. Complex.* **40**, 100728 (2019).
- ⁴⁰⁷P. Hernandez-Leal, B. Kartal, and M. E. Taylor, "A survey and critique of multiagent deep reinforcement learning," *Auton. Agents Multi-Agent Syst.* **33**, 750–797 (2019).
- ⁴⁰⁸K. Tuyls and A. Nowé, "Evolutionary game theory and multi-agent reinforcement learning," *Knowl. Eng. Rev.* **20**, 63–90 (2005).
- ⁴⁰⁹K. Tuyls and S. Parsons, "What evolutionary game theory tells us about multiagent learning," *Artif. Intell.* **171**, 406–416 (2007).
- ⁴¹⁰D. Bloembergen, K. Tuyls, D. Hennes, and M. Kaisers, "Evolutionary dynamics of multi-agent learning: A survey," *J. Artif. Intell. Res.* **53**, 659–697 (2015).
- ⁴¹¹P. Dayan and Y. Niv, "Reinforcement learning: The good, the bad and the ugly," *Curr. Opin. Neurobiol.* **18**, 185–196 (2008).
- ⁴¹²R. R. Bush and F. Mosteller, "A mathematical model for simple learning," *Psychol. Rev.* **58**, 313–323 (1951).
- ⁴¹³J. G. Cross, "A stochastic learning model of economic behavior," *Q. J. Econ.* **87**, 239–266 (1973).
- ⁴¹⁴T. Erev and A. E. Roth, "Predicting how people play games: Reinforcement learning in experimental games with unique, mixed strategy equilibria," *Am. Econ. Rev.* **88**, 848–881 (1998), <https://www.jstor.org/stable/117009>.
- ⁴¹⁵W. Schultz, W. R. Stauffer, and A. Lak, "The phasic dopamine signal maturing: From reward via behavioural activation to formal economic utility," *Curr. Opin. Neurobiol.* **43**, 139–148 (2017).
- ⁴¹⁶M. N. Burton-Chellew and S. A. West, "Payoff-based learning best explains the rate of decline in cooperation across 237 public-goods games," *Nat. Hum. Behav.* **5**, 1330–1338 (2021).
- ⁴¹⁷T. Börgers and R. Sarin, "Learning through reinforcement and replicator dynamics," *J. Econ. Theory* **77**, 1–14 (1997).
- ⁴¹⁸K. Tuyls, K. Verbeeck, and T. Lenaerts, "A selection-mutation model for q-learning in multi-agent systems," in *Proceedings of the Second International Joint Conference on Autonomous Agents and Multiagent Systems—AAMAS '03* (ACM Press, Melbourne, Australia, 2003), p. 693.
- ⁴¹⁹Y. Sato and J. P. Crutchfield, "Coupled replicator equations for the dynamics of learning in multiagent systems," *Phys. Rev. E* **67**, 015206 (2003).
- ⁴²⁰T. Klos, G. J. van Ahee, and K. Tuyls, "Evolutionary dynamics of regret minimization," in *Machine Learning and Knowledge Discovery in Databases*, Vol. 6322, edited by D. Hutchison, T. Kanade, J. Kittler, J. M. Kleinberg, F. Mattern, J. C. Mitchell, M. Naor, O. Nierstrasz, C. Pandu Rangan, B. Steffen, M. Sudan, D. Terzopoulos, D. Tygar, M. Y. Vardi, G. Weikum, J. L. Balcázar, F. Bonchi, A. Gionis, and M. Sebag (Springer, Berlin, 2010), pp. 82–96.
- ⁴²¹E. Hopkins, "Two competing models of how people learn in games," *Econometrica* **70**, 2141–2166 (2002).

- ⁴²²W. Barfuss, J. F. Donges, and J. Kurths, “Deterministic limit of temporal difference reinforcement learning for stochastic games,” *Phys. Rev. E* **99**, 043305 (2019).
- ⁴²³W. Barfuss, “Reinforcement learning dynamics in the infinite memory limit,” in *Proceedings of the 19th International Conference on Autonomous Agents and MultiAgent Systems, AAMAS '20* (International Foundation for Autonomous Agents and Multiagent Systems, Richland, SC, 2020), pp. 1768–1770.
- ⁴²⁴W. Barfuss, “Dynamical systems as a level of cognitive analysis of multi-agent learning,” *Neural Comput. Appl.* **34**, 1653–1671 (2021).
- ⁴²⁵W. Barfuss, J. F. Donges, V. V. Vasconcelos, J. Kurths, and S. A. Levin, “Caring for the future can turn tragedy into comedy for long-term collective action under risk of collapse,” *Proc. Natl. Acad. Sci. U.S.A.* **117**, 12915–12922 (2020).
- ⁴²⁶W. Barfuss and R. P. Mann, “Modeling the effects of environmental and perceptual uncertainty using deterministic reinforcement learning dynamics with partial observability,” *Phys. Rev. E* **105**, 034409 (2022).
- ⁴²⁷W. Barfuss and J. M. Meylahn, “Intrinsic fluctuations of reinforcement learning promote cooperation,” *Sci. Rep.* **13**, 1309 (2023).
- ⁴²⁸F. M. Strnad, W. Barfuss, J. F. Donges, and J. Heitzig, “Deep reinforcement learning in World-Earth system models to discover sustainable management strategies,” *Chaos* **29**, 123122 (2019).
- ⁴²⁹J. Perolat, J. Z. Leibo, V. Zambaldi, C. Beattie, K. Tuyls, and T. Graepel, “A multi-agent reinforcement learning model of common-pool resource appropriation,” in *Proceedings of the 31st International Conference on Neural Information Processing Systems, NIPS'17* (Curran Associates, Inc., Red Hook, NY, 2017), pp. 3646–3655.
- ⁴³⁰S. Zheng, A. Trott, S. Srinivasa, N. Naik, M. Gruesbeck, D. C. Parkes, and R. Socher, “The AI economist: Improving equality and productivity with AI-driven tax policies,” [arXiv:2004.13332](https://arxiv.org/abs/2004.13332) (2020).
- ⁴³¹Y. Yang, R. Luo, M. Li, M. Zhou, W. Zhang, and J. Wang, “Mean field multi-agent reinforcement learning,” in *Proceedings of the 35th International Conference on Machine Learning* (PMLR, 2018), pp. 5571–5580.
- ⁴³²S. Hu, C.-W. Leung, and H.-F. Leung, “Modelling the dynamics of multiagent q-learning in repeated symmetric games: A mean field theoretic approach,” in *Proceedings of the 33rd International Conference on Neural Information Processing Systems* (NeurIPS, 2019), pp. 12134–12144.
- ⁴³³S. Perrin, M. Laurière, J. Pérolat, R. Élie, M. Geist, and O. Pietquin, “Generalization in mean field games by learning master policies,” *Proc. AAAI Conf. Artif. Intell.* **36**(9), 9413–9421 (2022).
- ⁴³⁴T. Galla, “Intrinsic noise in game dynamical learning,” *Phys. Rev. Lett.* **103**, 198702 (2009).
- ⁴³⁵J. F. Donges and W. Barfuss, “From math to metaphors and back again: Social-ecological resilience from a multi-agent-environment perspective,” *GAIA* **26**, 182–190 (2017).
- ⁴³⁶W. Barfuss, J. F. Donges, S. J. Lade, and J. Kurths, “When optimization for governing human-environment tipping elements is neither sustainable nor safe,” *Nat. Commun.* **9**, 2354 (2018).
- ⁴³⁷F. Cichos, K. Gustavsson, B. Mehlig, and G. Volpe, “Machine learning for active matter,” *Nat. Mach. Intell.* **2**, 94–103 (2020).
- ⁴³⁸H. C. Berg, *E. coli in Motion* (Springer, 2004).
- ⁴³⁹A. Sengupta, F. Carrara, and R. Stocker, “Phytoplankton can actively diversify their migration strategy in response to turbulent cues,” *Nature* **543**, 555–558 (2017).
- ⁴⁴⁰G. M. Viswanathan, M. G. Da Luz, E. P. Raposo, and H. E. Stanley, *The Physics of Foraging: An Introduction to Random Searches and Biological Encounters* (Cambridge University Press, 2011).
- ⁴⁴¹O. Bénichou, C. Loverdo, M. Moreau, and R. Voituriez, “Intermittent search strategies,” *Rev. Mod. Phys.* **83**, 81 (2011).
- ⁴⁴²T. Vicsek and A. Zafeiris, “Collective motion,” *Phys. Rep.* **517**, 71–140 (2012).
- ⁴⁴³J. M. Yeomans, “Nature’s engines: Active matter,” *Europhys. News* **48**, 21–25 (2017).
- ⁴⁴⁴J. Urzay, A. Doostmohammadi, and J. M. Yeomans, “Multi-scale statistics of turbulence motorized by active matter,” *J. Fluid Mech.* **822**, 762–773 (2017).
- ⁴⁴⁵C. Bechinger, R. Di Leonardo, H. Löwen, C. Reichhardt, G. Volpe, and G. Volpe, “Active particles in complex and crowded environments,” *Rev. Mod. Phys.* **88**, 045006 (2016).
- ⁴⁴⁶S. J. Ebbens and J. R. Howse, “In pursuit of propulsion at the nanoscale,” *Soft Matter* **6**, 726–738 (2010).
- ⁴⁴⁷J. L. Moran and J. D. Posner, “Phoretic self-propulsion,” *Annu. Rev. Fluid Mech.* **49**, 511–540 (2017).
- ⁴⁴⁸K. Villa and M. Pumera, “Fuel-free light-driven micro/nanomachines: Artificial active matter mimicking nature,” *Chem. Soc. Rev.* **48**, 4966–4978 (2019).
- ⁴⁴⁹S. Palagi and P. Fischer, “Bioinspired microrobots,” *Nat. Rev. Mater.* **3**, 113–124 (2018).
- ⁴⁵⁰K. Gustavsson, F. Berglund, P. Jonsson, and B. Mehlig, “Preferential sampling and small-scale clustering of gyrotactic microswimmers in turbulence,” *Phys. Rev. Lett.* **116**, 108104 (2016).
- ⁴⁵¹G. Reddy, A. Celani, T. J. Sejnowski, and M. Vergassola, “Learning to soar in turbulent environments,” *Proc. Natl. Acad. Sci. U.S.A.* **113**, E4877–E4884 (2016).
- ⁴⁵²M. Rubenstein, A. Cornejo, and R. Nagpal, “Programmable self-assembly in a thousand-robot swarm,” *Science* **345**, 795–799 (2014).
- ⁴⁵³L. Bayindir, “A review of swarm robotics tasks,” *Neurocomputing* **172**, 292–321 (2016).
- ⁴⁵⁴D. Andrén, D. G. Baranov, S. Jones, G. Volpe, R. Verre, and M. Käll, “Microscopic metavehicles powered and steered by embedded optical metasurfaces,” *Nat. Nanotechnol.* **16**, 970–974 (2021).
- ⁴⁵⁵P. Galajda, J. Keymer, P. Chaikin, and R. Austin, “A wall of funnels concentrates swimming bacteria,” *J. Bacteriol.* **189**, 8704–8707 (2007).
- ⁴⁵⁶G. Volpe, I. Buttinoni, D. Vogt, H.-J. Kümmerer, and C. Bechinger, “Microswimmers in patterned environments,” *Soft Matter* **7**, 8810–8815 (2011).
- ⁴⁵⁷J. Simmchen, J. Katuri, W. E. Uspal, M. N. Popescu, M. Tasinkevych, and S. Sánchez, “Topographical pathways guide chemical microswimmers,” *Nat. Commun.* **7**, 10598 (2016).
- ⁴⁵⁸C. H. Ramos, E. Rodríguez-Sánchez, J. A. A. Del Angel, A. V. Arzola, M. Benítez, A. E. Escalante, A. Franci, G. Volpe, and N. Rivera-Yoshida, “The environment topography alters the way to multicellularity in *Myxococcus xanthus*,” *Sci. Adv.* **7**, eabh2278 (2021).
- ⁴⁵⁹G. Frangipane, D. Dell’Arciprete, S. Petracchini, C. Maggi, F. Saglimbeni, S. Bianchi, G. Vizsnyiczai, M. L. Bernardini, and R. Di Leonardo, “Dynamic density shaping of photokinetic *E. coli*,” *eLife* **7**, e36608 (2018).
- ⁴⁶⁰J. Arlt, V. A. Martinez, A. Dawson, T. Pilizota, and W. C. Poon, “Painting with light-powered bacteria,” *Nat. Commun.* **9**, 768 (2018).
- ⁴⁶¹N. Levernier, J. Textor, O. Bénichou, and R. Voituriez, “Inverse square Lévy walks are not optimal search strategies for $d \geq 2$,” *Phys. Rev. Lett.* **124**, 080601 (2020).
- ⁴⁶²G. Volpe and G. Volpe, “The topography of the environment alters the optimal search strategy for active particles,” *Proc. Natl. Acad. Sci. U.S.A.* **114**, 11350–11355 (2017).
- ⁴⁶³H. J. Charlesworth and M. S. Turner, “Intrinsically motivated collective motion,” *Proc. Natl. Acad. Sci. U.S.A.* **116**, 15362–15367 (2019).
- ⁴⁶⁴A. Strandburg-Peshkin, C. R. Twomey, N. W. Bode, A. B. Kao, Y. Katz, C. C. Ioannou, S. B. Rosenthal, C. J. Torney, H. S. Wu, S. A. Levin, and I. D. Couzin, “Visual sensory networks and effective information transfer in animal groups,” *Curr. Biol.* **23**, R709–R711 (2013).
- ⁴⁶⁵S. A. M. Loos and S. H. L. Klapp, “Irreversibility, heat and information flows induced by non-reciprocal interactions,” *New J. Phys.* **22**, 123051 (2020).
- ⁴⁶⁶S. A. M. Loos, S. H. L. Klapp, and T. Martynek, “Long-range order and directional defect propagation in the nonreciprocal XY model with vision cone interactions,” *Phys. Rev. Lett.* **130**, 198301 (2023).
- ⁴⁶⁷A. Argun, A. Callegari, and G. Volpe, *Simulation of Complex Systems* (IOP Publishing, 2021).
- ⁴⁶⁸M. C. Marchetti, J.-F. Joanny, S. Ramaswamy, T. B. Liverpool, J. Prost, M. Rao, and R. A. Simha, “Hydrodynamics of soft active matter,” *Rev. Mod. Phys.* **85**, 1143 (2013).
- ⁴⁶⁹G. Falasco, R. Pfaller, A. P. Bregulla, F. Cichos, and K. Kroy, “Exact symmetries in the velocity fluctuations of a hot Brownian swimmer,” *Phys. Rev. E* **94**, 030602 (2016).
- ⁴⁷⁰D. Frenkel and B. Smit, *Understanding Molecular Simulation: From Algorithms to Applications* (Elsevier, 2001), Vol. 1.
- ⁴⁷¹M. N. Rosenbluth, “Genesis of the Monte Carlo algorithm for statistical mechanics,” *AIP Conf. Proc.* **690**, 22–30 (2003).

- ⁴⁷²S. Wolfram, "Cellular automata as models of complexity," *Nature* **311**, 419–424 (1984).
- ⁴⁷³E. Lauga and T. R. Powers, "The hydrodynamics of swimming microorganisms," *Rep. Prog. Phys.* **72**, 096601 (2009).
- ⁴⁷⁴J. Palacci, S. Sacanna, A. P. Steinberg, D. J. Pine, and P. M. Chaikin, "Living crystals of light-activated colloidal surfers," *Science* **339**, 936–940 (2013).
- ⁴⁷⁵I. Buttinoni, J. Bialké, F. Kümmel, H. Löwen, C. Bechinger, and T. Speck, "Dynamical clustering and phase separation in suspensions of self-propelled colloidal particles," *Phys. Rev. Lett.* **110**, 238301 (2013).
- ⁴⁷⁶F. A. Lavergne, H. Wendehenne, T. Bäuerle, and C. Bechinger, "Group formation and cohesion of active particles with visual perception-dependent motility," *Science* **364**, 70–74 (2019).
- ⁴⁷⁷U. Khadka, V. Holubec, H. Yang, and F. Cichos, "Active particles bound by information flows," *Nat. Commun.* **9**, 3864 (2018).
- ⁴⁷⁸S. Doncieux, N. Bredeche, J. B. Mouret, and A. E. G. Eiben, "Evolutionary robotics: What, why, and where to," *Front. Robot. AI* **2**, 4 (2015).
- ⁴⁷⁹S. Jones, A. F. Winfield, S. Hauert, and M. Studley, "Onboard evolution of understandable swarm behaviors," *Adv. Intell. Syst.* **1**, 1900031 (2019).
- ⁴⁸⁰M. Mijalkov, A. McDaniel, J. Wehr, and G. Volpe, "Engineering sensorial delay to control phototaxis and emergent collective behaviors," *Phys. Rev. X* **6**, 011008 (2016).
- ⁴⁸¹G. Volpe and J. Wehr, "Effective drifts in dynamical systems with multiplicative noise: A review of recent progress," *Rep. Prog. Phys.* **79**, 053901 (2016).
- ⁴⁸²M. Leyman, F. Ogemarck, J. Wehr, and G. Volpe, "Tuning phototactic robots with sensorial delays," *Phys. Rev. E* **98**, 052606 (2018).
- ⁴⁸³W. O. Kermack and A. G. McKendrick, "A contribution to the mathematical theory of epidemics," *Proc. R. Soc. A* **115**, 700–721 (1927).
- ⁴⁸⁴D. Balcan, H. Hu, B. Gonçalves, P. Bajardi, C. Poletto, J. J. Ramasco, D. Paolotti, N. Perra, M. Tizzoni, W. Van den Broeck, V. Colizza, and A. Vespignani, "Seasonal transmission potential and activity peaks of the new influenza A(H1N1): A Monte Carlo likelihood analysis based on human mobility," *BMC Med.* **7**, 45 (2009).
- ⁴⁸⁵L. H. Chung, "Impact of pandemic control over airport economics: Reconciling public health with airport business through a streamlined approach in pandemic control," *J. Air Transp. Manag.* **44**, 42–53 (2015).
- ⁴⁸⁶C. Poletto, M. Gomes, A. P. Y. Piontti, L. Rossi, L. Bioglio, D. L. Chao, I. Longini, Jr., M. E. Halloran, V. Colizza, and A. Vespignani, "Assessing the impact of travel restrictions on international spread of the 2014 West African Ebola epidemic," *Eurosurveillance* **19**, 20936 (2014).
- ⁴⁸⁷Y. N. Kyrychko, K. B. Blyuss, and I. Brovchenko, "Mathematical modelling of the dynamics and containment of COVID-19 in Ukraine," *Sci. Rep.* **10**, 19662 (2020).
- ⁴⁸⁸B. F. Maier and D. Brockmann, "Effective containment explains subexponential growth in recent confirmed COVID-19 cases in China," *Science* **368**, 742–746 (2020).
- ⁴⁸⁹K. Prem, Y. Liu, T. W. Russell, A. J. Kucharski, R. M. Eggo, N. Davies, S. Flasche, S. Clifford, C. A. Pearson, J. D. Munday, and S. Abbott, "The effect of control strategies to reduce social mixing on outcomes of the COVID-19 epidemic in Wuhan, China: A modelling study," *Lancet Public Health* **5**, e261–e270 (2020).
- ⁴⁹⁰R. Humphries, M. Spillane, K. Mulchrone, S. Wiczorek, M. O'Riordain, and P. Hövel, "A metapopulation network model for the spreading of SARS-CoV-2: Case study for Ireland," *Infect. Dis. Model.* **6**, 420–437 (2021).
- ⁴⁹¹D. Brockmann and D. Helbing, "The hidden geometry of complex, network-driven contagion phenomena," *Science* **342**, 1337–1342 (2013).
- ⁴⁹²F. Iannelli, A. Koher, D. Brockmann, P. Hövel, and I. M. Sokolov, "Effective distances for epidemics spreading on complex networks," *Phys. Rev. E* **95**, 012313 (2017).
- ⁴⁹³L. Gold, E. Balal, T. Horak, R. L. Cheu, T. Mehmetoglu, and O. Gurbuz, "Health screening strategies for international air travelers during an epidemic or pandemic," *J. Air Transp. Manag.* **75**, 27–38 (2019).
- ⁴⁹⁴S. Cousins, "New Zealand eliminates COVID-19," *Lancet* **395**, 1474 (2020).
- ⁴⁹⁵T. Czipionka, E. N. Iftekhar, B. Prainsack, V. Priesemann, S. Bauer, A. C. Valdez, S. Cuschieri, E. Glaab, E. Grill, J. Krutzinna, and C. Lionis, "The benefits, costs and feasibility of a low incidence COVID-19 strategy," *Lancet Reg. Health Eur.* **13**, 100294 (2022).
- ⁴⁹⁶D. J. Watts and S. H. Strogatz, "Collective dynamics of "small-world" networks," *Nature* **393**, 440–442 (1998).
- ⁴⁹⁷P. Bajardi, A. Barrat, L. Savini, and V. Colizza, "Optimizing surveillance for livestock disease spreading through animal movements," *J. R. Soc. Interface* **9**, 2814–2825 (2012).
- ⁴⁹⁸V. Belik, R. Mikolajczyk, and P. Hövel, "Control of epidemics on hospital networks," in *Control of Self-Organizing Nonlinear Systems*, edited by E. Schöll, S. H. L. Klapp, and P. Hövel (Springer, Berlin, 2016), Chap. 22, pp. 431–440.
- ⁴⁹⁹V. Belik, A. Karch, P. Hövel, and R. Mikolajczyk, "Leveraging topological and temporal structure of hospital referral networks for epidemic control," in *Temporal Network Epidemiology*, Theoretical Biology, edited by N. Masuda and P. Holme (Springer, Singapore, 2017), Chap. 9, pp. 199–214.
- ⁵⁰⁰N. Masuda and P. Holme, *Temporal Network Epidemiology* (Springer, Singapore, 2017).
- ⁵⁰¹P. Holme and J. Saramäki, *Temporal Network Theory* (Springer, 2019), Vol. 2.
- ⁵⁰²Y. Y. Liu, J. J. Slotine, and A. L. Barabási, "Controllability of complex networks," *Nature* **473**, 167–173 (2011).
- ⁵⁰³M. Pósfai and P. Hövel, "Structural controllability of temporal networks," *New J. Phys.* **16**, 123055 (2014).
- ⁵⁰⁴M. Pósfai, J. Gao, S. P. Cornelius, A.-L. Barabási, and R. M. D'Souza, "Controllability of multiplex, multi-time-scale networks," *Phys. Rev. E* **94**, 032316 (2016).
- ⁵⁰⁵E. Valdano, L. Ferreri, C. Poletto, and V. Colizza, "Analytical computation of the epidemic threshold on temporal networks," *Phys. Rev. X* **5**, 021005 (2015).
- ⁵⁰⁶M. Frasca and K. J. Sharkey, "Discrete-time moment closure models for epidemic spreading in populations of interacting individuals," *J. Theor. Biol.* **399**, 13–21 (2016).
- ⁵⁰⁷A. Koher, H. H. K. Lentz, J. P. Gleeson, and P. Hövel, "Contact-based model for epidemic spreading on temporal networks," *Phys. Rev. X* **9**, 031017 (2019).
- ⁵⁰⁸R. Humphries, K. Mulchrone, J. Tratalos, S. J. More, and P. Hövel, "A systematic framework of modelling epidemics on temporal networks," *Appl. Netw. Sci.* **6**, 23 (2021).
- ⁵⁰⁹"Adaptive networks," in *Understanding Complex Systems*, 1st ed., edited by T. Gross and H. Sayama (Springer, 2009).
- ⁵¹⁰P. Holme and M. E. J. Newman, "Nonequilibrium phase transition in the coevolution of networks and opinions," *Phys. Rev. E* **74**, 056108 (2006).
- ⁵¹¹G. Demirel, F. Vazquez, G. A. Böhme, and T. Gross, "Moment-closure approximations for discrete adaptive networks," *Physica D* **267**, 68–80 (2014).
- ⁵¹²G. Zschaler, "Adaptive-network models of collective dynamics," *Eur. Phys. J. Spec. Top.* **211**, 1–101 (2012).
- ⁵¹³P. Clifford and A. Sudbury, "A model for spatial conflict," *Biometrika* **60**, 581–588 (1973).
- ⁵¹⁴R. A. Holley and T. M. Liggett, "Ergodic theorems for weakly interacting infinite systems and the voter model," *Ann. Probab.* **3**, 643–663 (1975).
- ⁵¹⁵F. Vazquez, V. M. Eguiluz, and M. S. Miguel, "Generic absorbing transition in coevolution dynamics," *Phys. Rev. Lett.* **100**, 108702 (2008).
- ⁵¹⁶R. Durrett, J. P. Gleeson, A. L. Lloyd, P. J. Mucha, F. Shi, D. Sivakoff, J. E. S. Socolar, and C. Varghese, "Graph fission in an evolving voter model," *Proc. Natl. Acad. Sci. U.S.A.* **109**, 3682–3687 (2012).
- ⁵¹⁷L. Z. Kiss, J. Miller, and P. L. Simon, *Mathematics of Epidemics on Networks*, 1st ed., Interdisciplinary Applied Mathematics (Springer, 2017).
- ⁵¹⁸C. Kuehn and C. Bick, "A universal route to explosive phenomena," *Sci. Adv.* **7**, eabe3824 (2021).
- ⁵¹⁹G. Zschaler, G. A. Böhme, M. Seifinger, C. Huepe, and T. Gross, "Early fragmentation in the adaptive voter model on directed networks," *Phys. Rev. E* **85**, 046107 (2012).
- ⁵²⁰G. A. Böhme and T. Gross, "Analytical calculation of fragmentation transitions in adaptive networks," *Phys. Rev. E* **83**, 035101 (2011).
- ⁵²¹B. Kozma and A. Barrat, "Consensus formation on adaptive networks," *Phys. Rev. E* **77**, 016102 (2008).
- ⁵²²Y. Yu, G. Xiao, G. Li, W. P. Tay, and H. F. Teoh, "Opinion diversity and community formation in adaptive networks," *Chaos* **27**, 103115 (2017).
- ⁵²³X. Zhang, C. Shan, Z. Jin, and H. Zhu, "Complex dynamics of epidemic models on adaptive networks," *J. Differ. Equ.* **266**, 803–832 (2019).

- 524 M. Ogura and V. M. Preciado, "Epidemic processes over adaptive state-dependent networks," *Phys. Rev. E* **93**, 062316 (2016).
- 525 L. Horstmeyer, C. Kuehn, and S. Thurner, "Network topology near criticality in adaptive epidemics," *Phys. Rev. E* **98**, 042313 (2018).
- 526 L. Horstmeyer, C. Kuehn, and S. Thurner, "Balancing quarantine and self-distancing measures in adaptive epidemic networks," *Bull. Math. Biol.* **84**, 79 (2022).
- 527 L. B. Shaw and I. B. Schwartz, "Fluctuating epidemics on adaptive networks," *Phys. Rev. E* **77**, 066101 (2008).
- 528 G. Demirel, E. Barter, and T. Gross, "Dynamics of epidemic diseases on a growing adaptive network," *Sci. Rep.* **7**, 42352 (2017).
- 529 K. Clauß and C. Kuehn, "Self-adapting infectious dynamics on random networks," *arXiv:2203.16949* (2022).
- 530 S. H. Strogatz, "From Kuramoto to Crawford: Exploring the onset of synchronization in populations of coupled oscillators," *Physica D* **143**, 1–20 (2000).
- 531 V. Avalos-Gaytán, J. A. Almendral, I. Leyva, F. Battiston, V. Nicosia, V. Latora, and S. Boccaletti, "Emergent explosive synchronization in adaptive complex networks," *Phys. Rev. E* **97**, 042301 (2018).
- 532 D. Schlager, K. Clauß, and C. Kuehn, "Stability analysis of multiplayer games on adaptive simplicial complexes," *Chaos* **32**, 053128 (2022).
- 533 L. Horstmeyer and C. Kuehn, "Adaptive voter model on simplicial complexes," *Phys. Rev. E* **101**, 022305 (2020).
- 534 N. Papanikolaou, G. Vaccario, E. Hormann, R. Lambiotte, and F. Schweitzer, "Consensus from group interactions: An adaptive voter model on hypergraphs," *Phys. Rev. E* **105**, 054307 (2022).
- 535 S. Milgram, "The small world problem," *Psychol. Today* **2**, 60–67 (1967).
- 536 See <https://research.fb.com/blog/2016/02/three-and-a-half-degrees-of-separation/> for "Three and a half degrees of separation."
- 537 P. Lorenz-Spreen, L. Oswald, S. Lewandowsky, and R. Hertwig, "A systematic review of worldwide causal and correlational evidence on digital media and democracy," *Nat. Hum. Behav.* **7**, 74–101 (2022).
- 538 G. Deffuant, D. Neau, F. Amblard, and G. Weisbuch, "Mixing beliefs among interacting agents," *Adv. Complex Syst.* **3**, 87–98 (2000).
- 539 F. Baumann, P. Lorenz-Spreen, I. M. Sokolov, and M. Starnini, "Modeling echo chambers and polarization dynamics in social networks," *Phys. Rev. Lett.* **124**, 048301 (2020).
- 540 M. McPherson, L. Smith-Lovin, and J. M. Cook, "Birds of a feather: Homophily in social networks," *Annu. Rev. Sociol.* **27**, 415–444 (2001).
- 541 F. Baumann, P. Lorenz-Spreen, I. M. Sokolov, and M. Starnini, "Emergence of polarized ideological opinions in multidimensional topic spaces," *Phys. Rev. X* **11**, 011012 (2021).
- 542 P. Lorenz-Spreen, B. M. Mønsted, P. Hövel, and S. Lehmann, "Accelerating dynamics of collective attention," *Nat. Commun.* **10**, 1759 (2019).
- 543 H. A. Simon, "Designing organizations for an information-rich world," in *Computers, Communications, and the Public Interest* (The Johns Hopkins Press, 1971), Vol. 72, p. 37.
- 544 J. Bialek, "What does the GB power outage on 9 August 2019 tell us about the current state of decarbonised power systems?," *Energy Policy* **146**, 111821 (2020).
- 545 S. V. Buldyrev, R. Parshani, G. Paul, H. E. Stanley, and S. Havlin, "Catastrophic cascade of failures in interdependent networks," *Nature* **464**, 1025–1028 (2010).
- 546 C. Klinger, O. Landeg, and V. Murray, "Power outages, extreme events and health: A systematic review of the literature from 2011–2012," *PLoS Curr.* **6**, ecurrnts.dis (2014), <https://www.ncbi.nlm.nih.gov/pmc/articles/PMC3879211/>.
- 547 DW, "High price and range anxiety stops Germans from buying e-cars," (2021); see <https://www.dw.com/en/germany-cars-e-cars-e-mobility-charging-stations-electric-cars-emissions/a-57921124>.
- 548 R. Ferroukhi, P. Frankl, and R. Adib, *Renewable Energy Policies in a Time of Transition: Heating and Cooling* (Hydrogen Knowledge Centre, 2020), https://www.irena.org/-/media/Files/IRENA/Agency/Publication/2020/Nov/IRENA_JEA_REN21_Policies_Heating_Cooling_2020.pdf.
- 549 M. Anvari, G. Lohmann, M. Wächter, P. Milan, E. Lorenz, D. Heinemann, M. R. R. Tabar, and J. Peinke, "Short term fluctuations of wind and solar power systems," *New J. Phys.* **18**, 063027 (2016).
- 550 J. Apt, "The spectrum of power from wind turbines," *J. Power Sources* **169**, 369–374 (2007).
- 551 A. E. Curtright and J. Apt, "The character of power output from utility-scale photovoltaic systems," *Prog. Photovolt.: Res. Appl.* **16**, 241–247 (2008).
- 552 C. Luo and B.-T. Ooi, "Frequency deviation of thermal power plants due to wind farms," *IEEE Trans. Energy Convers.* **21**, 708–716 (2006).
- 553 R. Baile and J.-F. Muzy, "Spatial intermittency of surface layer wind fluctuations at mesoscale range," *Phys. Rev. Lett.* **105**, 254501 (2010).
- 554 R. Wood and P. R. Field, "The distribution of cloud horizontal sizes," *J. Clim.* **24**, 4800–4816 (2011).
- 555 H. Haehne, J. Schottler, M. Waechter, J. Peinke, and O. Kamps, "The footprint of atmospheric turbulence in power grid frequency measurements," *Europhys. Lett.* **121**, 30001 (2018).
- 556 S. Schilling, "Final energy consumption by sector and fuel," Technical Report, European Environment Agency, 2021; see <https://www.eea.europa.eu/ims/primary-and-final-energy-consumption>.
- 557 A. Monacchi, D. Egarter, W. Elmenreich, S. D'Alessandro, and A. M. Tonello, "GREEND: An energy consumption dataset of households in Italy and Austria," in *2014 IEEE International Conference on Smart Grid Communications (SmartGridComm)* (IEEE, 2014), pp. 511–516.
- 558 A. Wright and S. Firth, "The nature of domestic electricity-loads and effects of time averaging on statistics and on-site generation calculations," *Appl. Energy* **84**, 389–403 (2007).
- 559 A. Marszal-Pomianowska, P. Heiselberg, and O. K. Larsen, "Household electricity demand profiles—A high-resolution load model to facilitate modelling of energy flexible buildings," *Energy* **103**, 487–501 (2016).
- 560 M. A. López, S. De La Torre, S. Martín, and J. A. Aguado, "Demand-side management in smart grid operation considering electric vehicles load shifting and vehicle-to-grid support," *Int. J. Electr. Power Energy Syst.* **64**, 689–698 (2015).
- 561 T. Logenthiran, D. Srinivasan, and T. Z. Shun, "Demand side management in smart grid using heuristic optimization," *IEEE Trans. Smart Grid* **3**, 1244–1252 (2012).
- 562 M. Anvari, B. Werther, G. Lohmann, M. Wächter, J. Peinke, and H.-P. Beck, "Suppressing power output fluctuations of photovoltaic power plants," *Sol. Energy* **157**, 735–743 (2017).
- 563 M. Anvari, M. Tabar, J. Peinke, and K. Lehnertz, "Disentangling the stochastic behavior of complex time series," *Sci. Rep.* **6**, 35435 (2016).
- 564 M. Anvari, E. Proedrou, and B. E. A. Schäfer, "Data-driven load profiles and the dynamics of residential electricity consumption," *Nat. Commun.* **13**, 4593 (2022).
- 565 R. Bitterer and B. Schieferdecker, "Repräsentative VDEW-Lastprofile Aktionsplan Wettbewerb, M-32/99," Technical Report (VDEW, Stresemannallee 23 D-60596 Frankfurt/M, 2001).
- 566 M. Parti and C. Parti, "The total and appliance-specific conditional demand for electricity in the household sector," *Bell J. Econ.* **11**, 309–321 (1980).
- 567 M. Anvari, F. Hellmann, and X. Zhang, "Introduction to Focus Issue: Dynamics of modern power grids," *Chaos* **30**, 063140 (2020).
- 568 S. Auer, F. Hellmann, M. Krause, and J. Kurths, "Stability of synchrony against local intermittent fluctuations in tree-like power grids," *Chaos* **27**, 127003 (2017).
- 569 W. Li, G. Joós, and C. Abbey, "Wind power impact on system frequency deviation and an ESS based power filtering algorithm solution," in *2006 IEEE PES Power Systems Conference and Exposition* (IEEE, 2006), pp. 2077–2084.
- 570 L. W. Alvarez, W. Alvarez, F. Asaro, and H. V. Michel, "Extraterrestrial cause for the Cretaceous-Tertiary extinction," *Science* **208**, 1095–1108 (1980).
- 571 J. Brugger, G. Feulner, and S. Petri, "Baby, it's cold outside: Climate model simulations of the effects of the asteroid impact at the end of the Cretaceous," *Geophys. Res. Lett.* **44**, 419–427, <https://doi.org/10.1002/2016GL072241> (2017).
- 572 R. Sparks, "Gas release rates from pyroclastic flows: A assessment of the role of fluidisation in their emplacement," *Bull. Volcanol.* **41**, 1–9 (1978).
- 573 M. A. Williams, S. H. Ambrose, S. van der Kaars, C. Ruehlemann, U. Chatopadhyaya, J. Pal, and P. R. Chauhan, "Environmental impact of the 73 ka Toba super-eruption in South Asia," *Palaeogeogr. Palaeoclimatol. Palaeoecol.* **284**, 295–314 (2009).
- 574 D. I. Armstrong McKay, A. Staal, J. F. Abrams, R. Winkelmann, B. Sakschewski, S. Loriani, I. Fetzter, S. E. Cornell, J. Rockström, and T. M. Lenton, "Exceeding 1.5°C global warming could trigger multiple climate tipping points," *Science* **377**, eabn7950 (2022).

⁵⁷⁵V. Masson-Delmotte *et al.*, “Climate change 2021: The physical science basis,” Contribution of Working Group I to the Sixth Assessment Report of the Intergovernmental Panel on Climate Change, IPCC, 2021.

⁵⁷⁶T. M. Lenton, H. Held, E. Kriegler, J. W. Hall, W. Lucht, S. Rahmstorf, and H. J. Schellnhuber, “Tipping elements in the Earth’s climate system,” *Proc. Natl. Acad. Sci. U.S.A.* **105**, 1786–1793 (2008).

⁵⁷⁷N. Wunderling, J. F. Donges, J. Kurths, and R. Winkelmann, “Interacting tipping elements increase risk of climate domino effects under global warming,” *Earth Syst. Dyn.* **12**, 601–619 (2021).

⁵⁷⁸T. Liu, D. Chen, L. Yang, J. Meng, Z. Wang, J. Ludescher, J. Fan, S. Yang, D. Chen, J. Kurths, X. Chen, S. Havlin, and H. J. Schellnhuber, “Teleconnections among tipping elements in the Earth system,” *Nat. Clim. Change* **13**, 67–74 (2023).



A non-autonomous mega-extreme multistable chaotic system

Atefeh Ahmadi^a, Sriram Parthasarathy^b, Hayder Natiq^{c,d}, Sajad Jafari^{a,e}, Igor Franović^{f,*}, Karthikeyan Rajagopal^g

^a Department of Biomedical Engineering, Amirkabir University of Technology (Tehran Polytechnic), Tehran, Iran

^b Centre for Computational Modelling, Chennai Institute of Technology, Chennai 600069, Tamil Nadu, India

^c Ministry of Higher Education and Scientific Research, Baghdad 10024, Iraq

^d Department of Computer Technology Engineering, College of Information Technology, Imam Ja'afar Al-Sadiq University, Baghdad 10001, Iraq

^e Health Technology Research Institute, Amirkabir University of Technology (Tehran Polytechnic), Tehran, Iran

^f Scientific Computing Laboratory, Center for the Study of Complex Systems, Institute of Physics Belgrade, University of Belgrade, Pregrevica 118, 11080 Belgrade, Serbia

^g Centre for Nonlinear Systems, Chennai Institute of Technology, Chennai 600069, Tamil Nadu, India

ARTICLE INFO

Keywords:

Megastability

Extreme multistability

Coexisting attractors

Connecting curves

Analog circuit design

ABSTRACT

Megastable and extreme multistable systems comprise two major new branches of multistable systems. So far, they have been studied separately in various chaotic systems. Nevertheless, to the best of our knowledge, no chaotic system has so far been reported that possesses both types of multistability. This paper introduces the first three-dimensional non-autonomous chaotic system that displays megastability and extreme multistability, jointly called mega-extreme multistability. Our model shows extreme multistability for a variation of an initial condition associated with one system variable and megastability concerning another variable. The different types of coexisting attractors are characterized by the corresponding phase portraits and first return maps, as well as by constructing the appropriate bifurcation diagrams, calculating the Lyapunov spectra, the Kaplan-Yorke dimension and the connecting curves, and by determining the corresponding basins of attraction. The system is explicitly shown to be dissipative, with the dissipation being state-dependent. We demonstrate the feasibility and applicability of our model by designing and simulating an appropriate analog circuit.

1. Introduction

The foundation stone of chaos theory was laid by Edward Lorenz in 1963, having introduced a simplified model of atmospheric convection whose evolution, surprisingly at that point, turned out to sensitively depend on initial conditions [1]. Since then, concepts from chaos theory have permeated almost every branch of science and engineering, triggering profound changes of paradigm in physics, chemistry, climate and environmental sciences, optics, electronics, pharmacology, medicine, economy, and sociology, to name but a few [2]. Chaos theory describes complex nonlinear systems such as the earth's atmosphere, animal populations, lasers, fluid flows, pathological heartbeat and brain activity patterns, and geological processes [3–5], whose long-term dynamics are intrinsically unpredictable despite their deterministic nature [6,7]. The global stability of dynamics on a chaotic attractor counteracts the local instability in the sense that statistical (average) properties can be predictable even if the detailed dynamics are not [7].

Another type of nonlinear systems whose dynamics critically

depends on initial conditions are multistable systems [8–10], which possess multiple coexisting attractors for a given set of parameters. Examples of multistable behavior have been found in various fields, from biology, ecology, climatology, and neuroscience to laser and semiconductor physics, chemical reactions, and social systems [11–13]. Multistability emerges generically in several classes of systems, including weakly dissipative systems, coupled systems and systems with time-delayed feedback and/or interactions [8–10]. The problems of constructing multistable systems with desired properties and controlling the switching dynamics between the coexisting states have catalyzed intense research in theory and applications [9]. Specific methods have been developed to discover and generate coexisting attractors in dynamical systems, like amplitude control [14], offset boosting [15,16], and offset parameter cancellation [17]. While multistability has classically been associated with the coexistence of a finite number of attractors, within the last decade, it has come to light that there is indeed an entirely new realm of dissipative systems that feature infinitely many coexisting attractors [18–21]. Moreover, two distinct classes of such

* Corresponding author.

E-mail address: franovic@ipb.ac.rs (I. Franović).

systems have been discovered: on the one hand, systems with *extreme multistability* [22–28] possess *uncountable* infinitely many attractors, such that a continuous variation of initial conditions may induce bifurcations [29–31]; at the other hand, *megastable systems* [32–34] exhibit *countable* many nested coexisting attractors, and the corresponding initial conditions cannot act as additional bifurcation parameters [35–37].

In the present paper, we introduce the first system exhibiting mega and extreme multistability features. The model comprises a non-autonomous three-dimensional system that can present chaotic, torus, and periodic attractors. We show how the mega and extreme multistability features manifest themselves with respect to the variation of initial conditions corresponding to two different state variables. To the best of our knowledge, such a system has previously not been reported in the literature.

The paper is organized as follows. Section 2 introduces our model of a non-autonomous chaotic system and studies its dynamical regimes by providing the relevant phase portraits and first return maps. Also, the dissipative character of system dynamics is explicitly demonstrated, and the connecting curves are calculated to illustrate the underlying attractors' structure better. Section 3 addresses the extreme multistability feature of the system dynamics, involving the appropriate bifurcation diagrams, calculation of the Lyapunov exponents spectra and Kaplan-Yorke dimension, and an analysis of the basins of attraction. The applicability of the proposed model is demonstrated by analog circuit simulations in Section 4. Section 5 provides a summary of our main results.

2. The non-autonomous chaotic system

The model we introduce is a three-dimensional non-autonomous system given by

$$\begin{cases} \dot{x} = y \\ \dot{y} = z + y\cos(x) \\ \dot{z} = -by + A\omega\cos(\omega t) \end{cases}, \quad (1)$$

where $A\omega\cos(\omega t)$ is the forcing term with an amplitude A and frequency ω , while b is another control parameter.

Having fixed the forcing and intrinsic system parameters to $A = 0.8$, $b = 0.1$, $\omega = 0.7$, we observe three different types of attractors of System (1) under variation of initial conditions, see Fig. 1. In the top row are shown the phase portrait projections in the $Y - Z$ plane, whereas in the bottom row are provided the corresponding first return maps obtained by collecting the successive maxima of the Y signal. The initial conditions are given by $(x_0, y_0, z_0) = (0, 0, z_0)$ whereby z_0 is respectively set to zero, -0.3 , and 2.2 in the left, middle, and right columns of Fig. 1. It turns out that System (1) can exhibit three different types of dynamics by varying the initial condition z_0 . In particular, the solutions in Fig. 1(a)–(c) display chaotic, periodic (period 3), and torus attractors, respectively. The number of points in Fig. 1(e) corresponds to the period of the attractor in Fig. 1(b). The general pattern of the return maps in Fig. 1(d) and (f) are similar, although the one for the torus attractor in Fig. 1(f) shows a more ordered structure. The areas of phase space occupied by the chaotic and torus attractors are approximately the same, but the sequences of points in the return maps are entirely different.

Fig. 1 demonstrates that the continuous variation of the initial condition z_0 can indeed give rise to bifurcations, which is a signature of the extreme multistability of System (1).

To show the megastability of this system, two different values of z_0 are chosen, and the megastability feature under varying y_0 is demonstrated separately for each of the two given z_0 values. The phase portraits of System (1) with $A = 0.8$, $b = 0.1$, $\omega = 0.7$ and initial conditions $x_0 = 0, y_0 \in \{0, 5, 7\}, z_0 \in \{0, -0.9\}$ are shown in Fig. 2(a) and (b), z_0 is set to zero and -0.9 , respectively. In both panels, the blue, orange, and yellow attractors correspond to $y_0 = 0, y_0 = 5$, and $y_0 = 7$, respectively. All coexisting attractors are chaotic in Fig. 2(a), whereas in Fig. 2(b), two are periodic, and the outermost one is chaotic. It should be noted that only three of the coexisting attractors are plotted in this figure, and changing y_0 leads to an infinite but countable number of coexisting attractors, which conforms to the megastability property. On the other hand, variation of z_0 gives rise to an infinite and uncountable

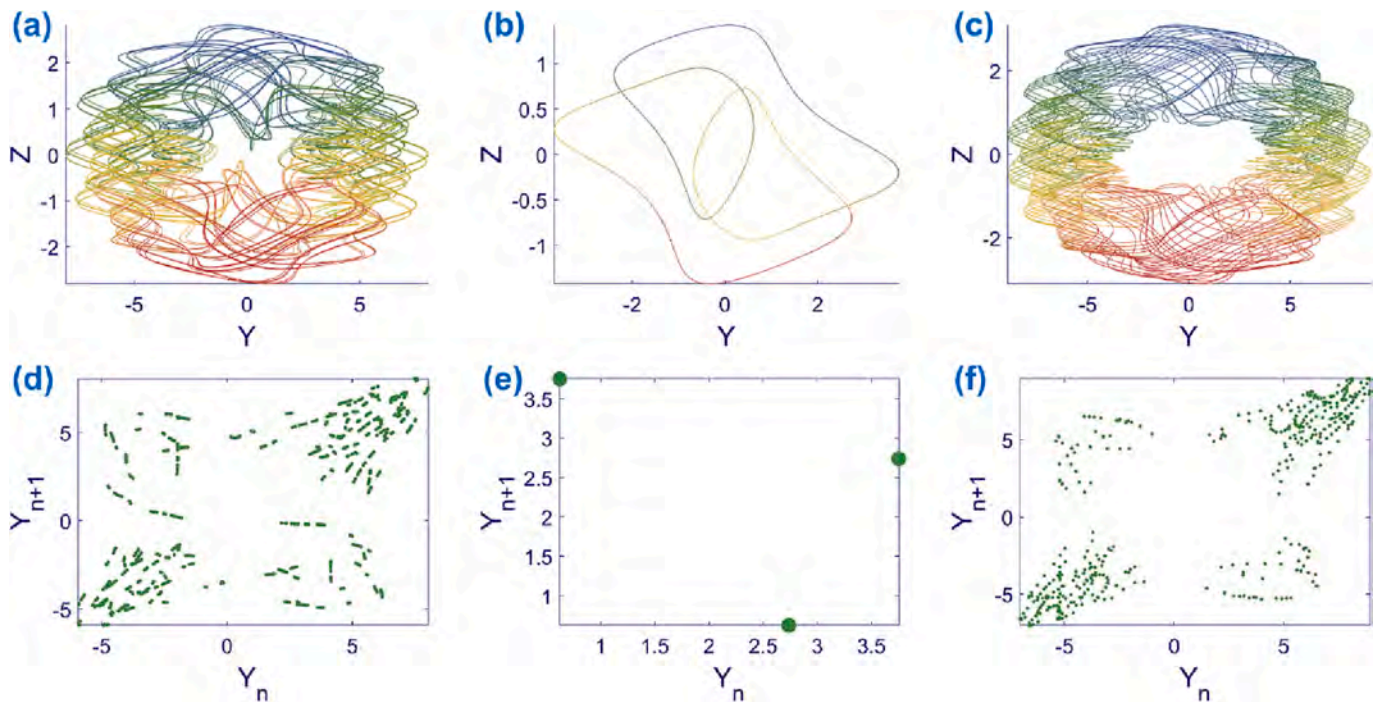


Fig. 1. Phase portrait projections in the $Y - Z$ plane and return maps of System (1) for fixed $A = 0.8, b = 0.1, \omega = 0.7$ and initial conditions $(x_0, y_0, z_0) = (0, 0, z_0)$. By changing z_0 , three different types of behaviors are observed. (a) and (d): chaotic dynamics with $z_0 = 0$, (b) and (e): periodic dynamics with $z_0 = -0.3$, and (c) and (f): torus-like dynamic with $z_0 = 2.2$. The corresponding first return maps are constructed by collecting the maximum values of the Y signal.

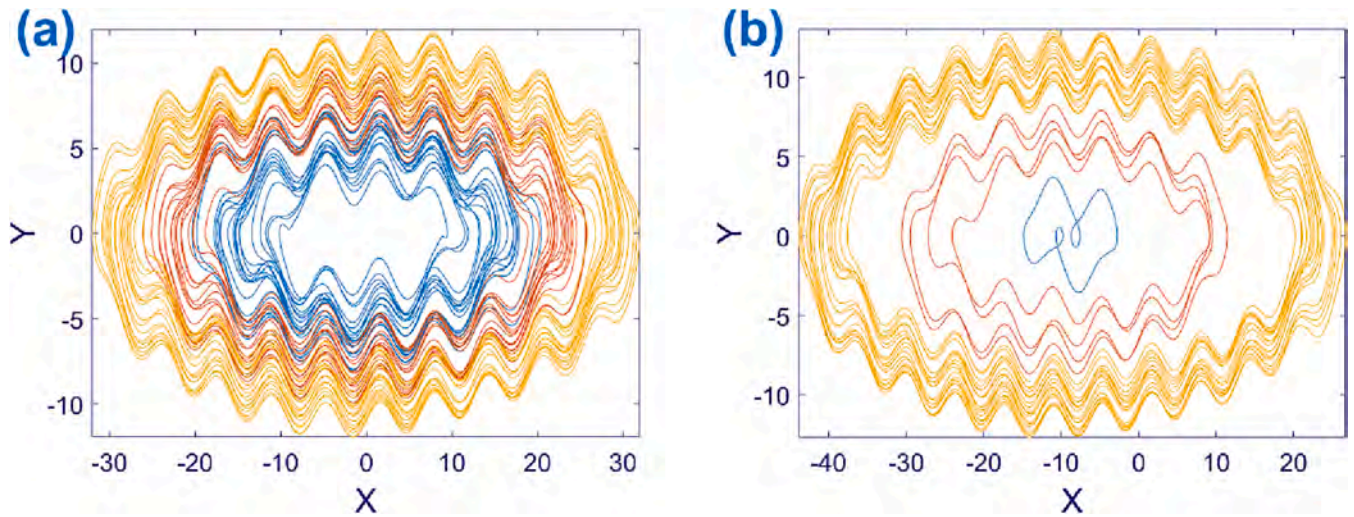


Fig. 2. Phase portrait projections in the $X - Y$ plane of **System (1)** with fixed $A = 0.8, b = 0.1, \omega = 0.7$ and initial conditions $(x_0, y_0, z_0) = (0, y_0, z_0)$ where $y_0 \in \{0, 5, 7\}$. **(a)** Coexisting chaotic attractors with $z_0 = 0$ and **(b)** coexisting periodic and chaotic attractors for $z_0 = -0.9$. Blue, orange, and yellow attractors correspond to $y_0 = 0, y_0 = 5$, and $y_0 = 7$, respectively. For each given value of z_0 , **System (1)** exhibits an infinite but countable number of coexisting attractors under the variation of y_0 , which confirms its megastability. (For interpretation of the references to color in this figure legend, the reader is referred to the web version of this article.)

number of coexisting attractors, a hallmark of extreme multistability. In summary, **System (1)** shows extreme multistability concerning the variation of z_0 , but for any arbitrary value of z_0 , it is megastable under the variation of y_0 . Therefore, **System (1)** can be called a mega-extreme multistable system.

2.1. Dissipative character of system dynamics

The energy dissipation of a dynamical system is calculated by the trace of the system's Jacobian matrix, which is equal to the divergence of the system. The Jacobian matrix and divergence of **System (1)** are calculated as

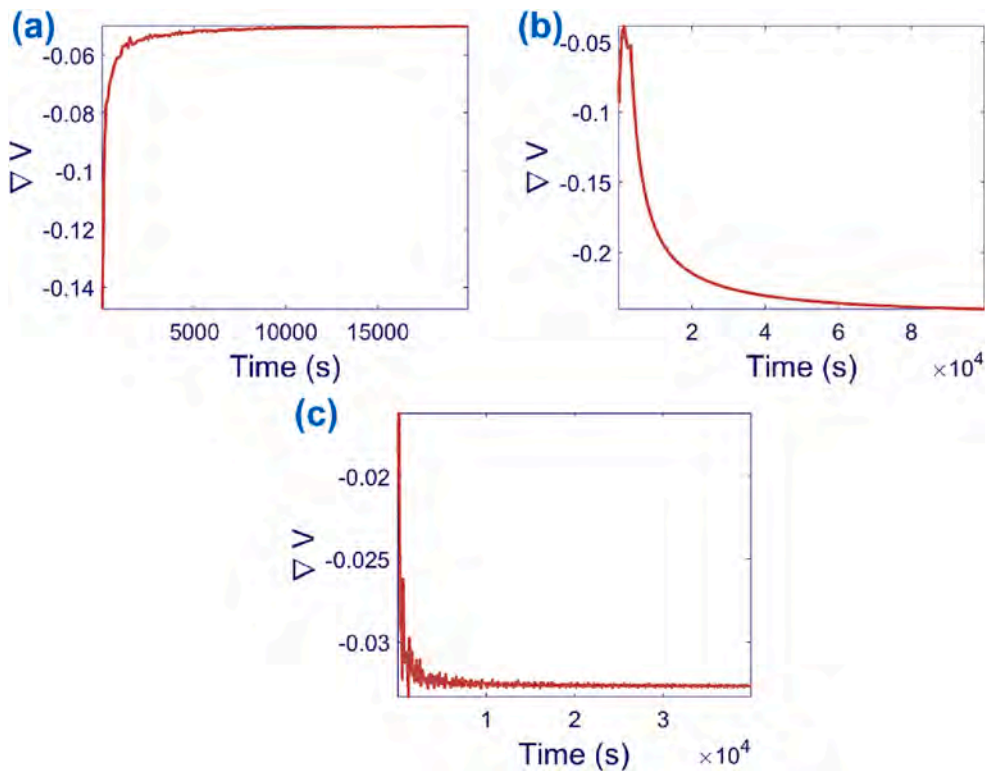


Fig. 3. The average divergence for **System (1)** with $A = 0.8, b = 0.1, \omega = 0.7$ and initial conditions $(x_0, y_0, z_0) = (0, 0, z_0)$: **(a)** $z_0 = 0$ (chaotic behavior), **(b)** $z_0 = -0.3$ (periodic behavior), and **(c)** $z_0 = 2.2$ (quasiperiodic dynamics). Note that all three average divergences converge to a negative value, indicating that all three types of dynamics are indeed system attractors.

$$J = \begin{bmatrix} 0 & 1 & 0 \\ -y\sin(x) & \cos(x) & 1 \\ 0 & -b & 0 \end{bmatrix} \rightarrow \nabla V = \text{Tr}(J) = \cos(x) \quad (2)$$

Eq. (2) implies that the energy dissipation depends on the value of the x state variable. For such a scenario, one should calculate the average value of the divergence ∇V , whereby the negative, zero, and positive values conform to dissipative, conservative, and explosive dynamics, respectively. The divergence is calculated for each system attractor separately and does not determine the overall system's behavior.

The average value of divergence for System (1) with $A = 0.8, b = 0.1, \omega = 0.7$ and initial conditions $(x_0, y_0, z_0) = (0, 0, z_0)$ is plotted in Fig. 3. The value of z_0 is set to zero, -0.3 , and 2.2 in panels (a)–(c). The runtimes in each simulation are adapted to ensure the convergence of the average dissipation. Note that Fig. 3 corroborates that for each of the three previously discussed examples of system dynamics, one finds a negative average divergence, implying the existence of genuine attractors.

2.2. Connecting curves

While the equilibrium points of a dynamical system can help determine the position of attractors locally, the connecting curves can provide information on a more global landscape [38]. In particular, the connecting curves highlight the direction in which the attractor swirls [39]. While the fixed points are classically called zero-dimensional invariant sets, the connecting curves are nevertheless one-dimensional invariant sets [40]. Consider the flow $\vec{S} = (x(t), y(t), z(t))^T$ that includes all three state variables. The velocity field $\vec{V}(t)$ is then given by $\frac{d\vec{S}}{dt} = \vec{V}(t) = (f_1, f_2, f_3)$ where f_1, f_2, f_3 are the right-hand side expressions in a set of ordinary differential equations. The acceleration field $\vec{A}(t)$ is calculated as

$$\frac{d\vec{V}}{dt} = \vec{A}(t) = \frac{\partial \vec{V}}{\partial \vec{S}} \frac{d\vec{S}}{dt} \rightarrow \vec{A}(t) = J\vec{V}(t) = \lambda\vec{V}(t) \rightarrow J\vec{V}(t) - \lambda\vec{V}(t) = 0 \quad (3)$$

Applying the chain rule in Eq. (3), the acceleration field is shown to be proportional to the velocity field. Finally, the connecting curves satisfy the condition $J\vec{V}(t) - \lambda\vec{V}(t) = 0$ [41].

System (3) leads to an equation for each state variable. Nevertheless, the number of unknowns is four (three state variables and λ). To solve these equations, a state variable must be selected as the principal state variable: in our case, variable y is selected. Afterward, all other state variables (here x and z) and λ should be written in terms of the principal state variable. The principal state variable should be chosen to simplify the calculations. Next, considering the attractor's position in space, a desired interval is selected for the state variable y , and for each point in that interval, the value of λ and other state variables are calculated. In the case of System (1), λ is independent of y and is always zero. Consequently, x and z only depend on y , so there can be four different

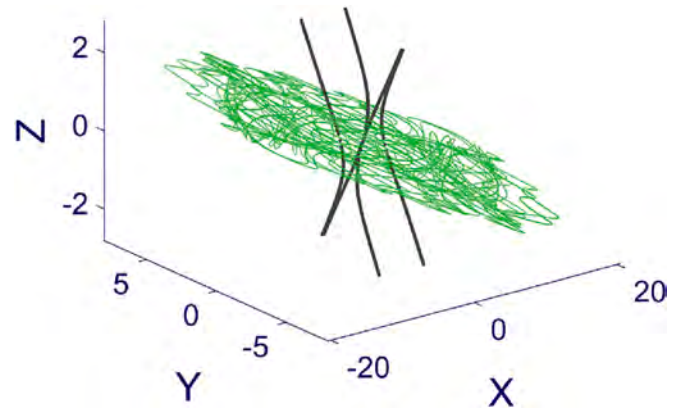


Fig. 4. Chaotic attractor and connecting curves of System (1) with $A = 0.8, b = 0.1, \omega = 0.7$ and initial conditions $(x_0, y_0, z_0) = (0, 0, 0)$. The black lines are the connecting curves showing the direction around which the attractor swirls. Four black lines correspond to four pairs of x and z in Table 1.

solutions for different combinations of x and z , see Table 1. The corresponding connecting curves of System (1) with its chaotic attractor are depicted in Fig. 4. The system parameters are $A = 0.8, b = 0.1, \omega = 0.7$ and the initial conditions are $(x_0, y_0, z_0) = (0, 0, 0)$. The connecting curves (black lines) provide global information about the attractor position and curvature.

3. Extreme multistability

To study the extreme multistability of System (1), we consider its initial conditions-dependent dynamics via the bifurcation diagram, Lyapunov exponents, Kaplan-Yorke dimension and attraction basins. The bifurcation diagram and the corresponding Kaplan-Yorke dimension of System (1) are shown in Fig. 5 using the initial condition z_0 as a control parameter that varies within the interval $[-3, 3]$. The system parameters are set to $A = 0.8, b = 0.1, \omega = 0.7$, whereas the remaining initial conditions are fixed to $(x_0, y_0) = (0, 0)$. The bifurcation diagram in Fig. 5(a) is constructed by plotting the local maxima of the Z state variable. One observes that System (1) continuously switches between the periodic and chaotic behaviors within the selected z_0 interval. The Kaplan-Yorke dimension D_{KY} shown in Fig. 5(b) is defined as [42,43]

$$D_{KY} = j + \frac{\sum_{i=1}^j \lambda_i}{|\lambda_{j+1}|}, \sum_{i=1}^j \lambda_i \geq 0, \sum_{i=1}^{j+1} \lambda_i < 0, \quad (4)$$

where λ_i are Lyapunov exponents. Note that in order to calculate D_{KY} , all Lyapunov exponents should be sorted in descending order, whereby j in Eq. (4) denotes the index of the Lyapunov exponent up to which the sum of Lyapunov exponents is non-negative. The latter implies that the D_{KY} of chaotic, torus, and periodic attractors are larger than two, equal to

Table 1

x and z state variables in terms of y for solving Eq. (3). The value of λ is not related to y and is always zero. y state variable is treated as the principal state variable to simplify the mathematical operations. Four different pairs of x and z can be considered in calculating the connecting curves.

λ	x	z
0	$2 \tan^{-1} \left(\frac{\sqrt{(5y-4)(10y+7)(50y^2+5y+28)} - 50y^2}{5y+28} \right)$	$-\frac{\sqrt{(5y-4)(10y+7)(50y^2+5y+28)}}{50y}$
0	$-2 \tan^{-1} \left(\frac{\sqrt{(5y-4)(10y+7)(50y^2+5y+28)} + 50y^2}{5y+28} \right)$	$\frac{\sqrt{(5y-4)(10y+7)(50y^2+5y+28)}}{50y}$
0	$2 \tan^{-1} \left(\frac{\sqrt{(5y+4)(10y-7)(50y^2-5y+28)} - 50y^2}{5y-28} \right)$	$-\frac{\sqrt{(5y+4)(10y-7)(50y^2-5y+28)}}{50y}$
0	$-2 \tan^{-1} \left(\frac{\sqrt{(5y+4)(10y-7)(50y^2-5y+28)} + 50y^2}{5y-28} \right)$	$\frac{\sqrt{(5y+4)(10y-7)(50y^2-5y+28)}}{50y}$

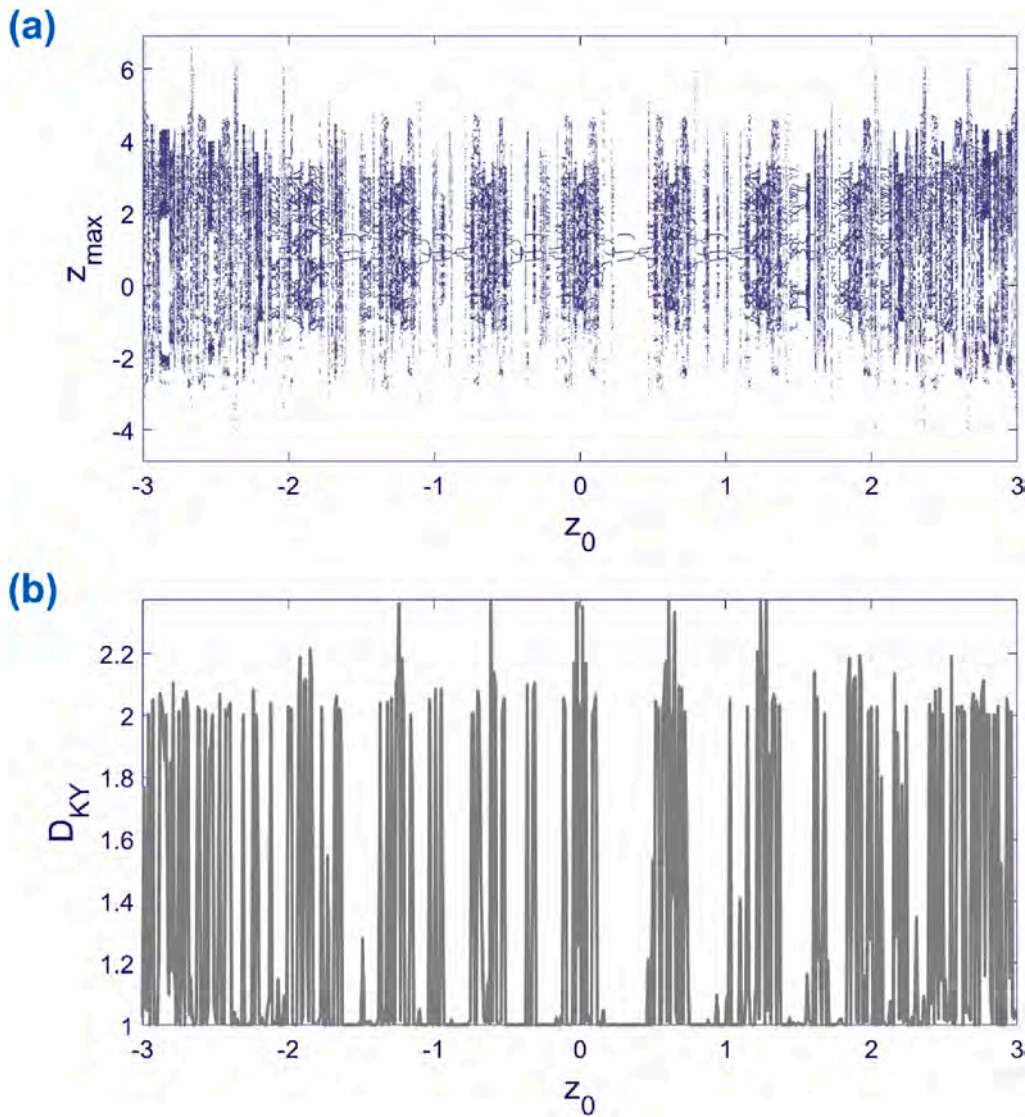


Fig. 5. Bifurcation diagram and D_{KY} of **System (1)** with $A = 0.8, b = 0.1, \omega = 0.7$ for fixed initial conditions $(x_0, y_0) = (0, 0)$ while varying z_0 in the $[-3, 3]$ interval. **(a)** Bifurcation diagram showing the local maxima of Z state variable and **(b)** the corresponding D_{KY} . **System (1)** exhibits chaotic or periodic attractors in the selected interval. D_{KY} matches the bifurcation diagram because its value is more than two in chaotic regions and one within periodic windows.

two, and equal to one, respectively. The variation of D_{KY} in **Fig. 5(b)** is indeed consistent with the bifurcation diagram from **Fig. 5(a)**.

The Lyapunov exponents of **System (1)** with the same parameters as in **Fig. 5(a)** and z_0 as the control parameter are provided in **Fig. 6**. **Fig. 6(a)** shows the variation of the first two largest Lyapunov exponents with z_0 , while **Fig. 6(b)** indicates the changes of the smallest one. The smallest Lyapunov exponent is always zero, but the exponents can have different values according to the system's dynamics. For chaotic attractors of a three-dimensional system, the Lyapunov spectrum contains one positive, one negative, and one zero exponent, whereby the value of the positive exponent is less than the absolute value of the negative one. On the other hand, the Lyapunov spectrum of a periodic attractor contains one zero and two negative exponents. Finally, one observes one negative and two zero exponents for torus attractors. The changes between the system attractors with z_0 reflected in the Lyapunov spectra from **Fig. 6** are consistent with the results from **Fig. 5**.

Another important tool to investigate the multistable systems is to identify the corresponding attraction basins. **Fig. 7** shows the attraction basins for the dynamics of **System (1)** with $A = 0.8, b = 0.1, \omega = 0.7$, obtained by fixing one initial condition to zero and varying the other two. The attraction basins are plotted in (a) $x_0 - y_0$ plane with $x_0 \in [2, 5]$

and $y_0 \in [-4, 2]$, (b) $x_0 - z_0$ plane with $x_0 \in [-3, 3], z_0 \in [-1, 1]$, and (c) $y_0 - z_0$ plane with $y_0 \in [-4, 4]$ and $z_0 \in [-1, 1]$. The intervals of initial conditions are chosen to avoid the torus attractors. Yellow and blue-green colors represent chaotic and periodic solutions, respectively. For periodic solutions, the representing color encodes the period. In **Fig. 7(b)** and (c), where the initial condition z_0 is varied, one may observe the same transitions between the different periodic and chaotic attractors, as illustrated in the bifurcation diagram in **Fig. 5(a)**.

4. Analog circuit design

To corroborate the previous numerical simulations, we have designed an analog circuit of **System (1)** given by

$$\begin{cases} \dot{X} = \frac{1}{R_1 C_1} Y \\ \dot{Y} = \frac{1}{R_2 C_2} Z + \frac{1}{R_3 C_2} Y \cos(X) \\ \dot{Z} = -\frac{1}{R_4 C_3} Y + \frac{1}{R_5 C_3} \cos(0.7t) \end{cases} \quad (5)$$

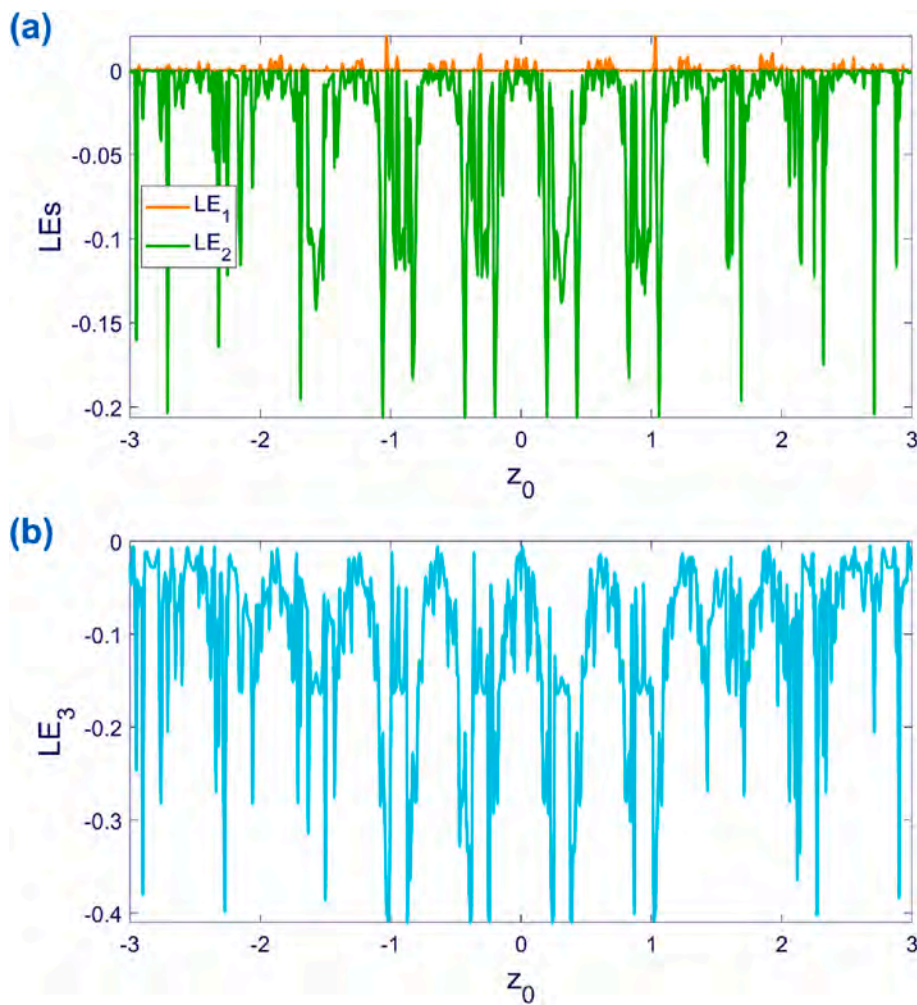


Fig. 6. Lyapunov exponents of System (1) with $A = 0.8, b = 0.1, \omega = 0.7$ and for fixed initial conditions $(x_0, y_0) = (0, 0)$ under variation of z_0 within the $[-3, 3]$ interval. (a) Two largest Lyapunov exponents and (b) the smallest Lyapunov exponent. While the smallest Lyapunov exponent is always zero, the other two exponents in (a) can have different values. If the latter are one positive and one zero (the positive exponent is less than the absolute value of the negative one), the attractor is chaotic. The attractor is periodic with one zero and one negative exponent in (a). The Lyapunov exponents corroborate the type of solutions from the bifurcation diagram in Fig. 5.

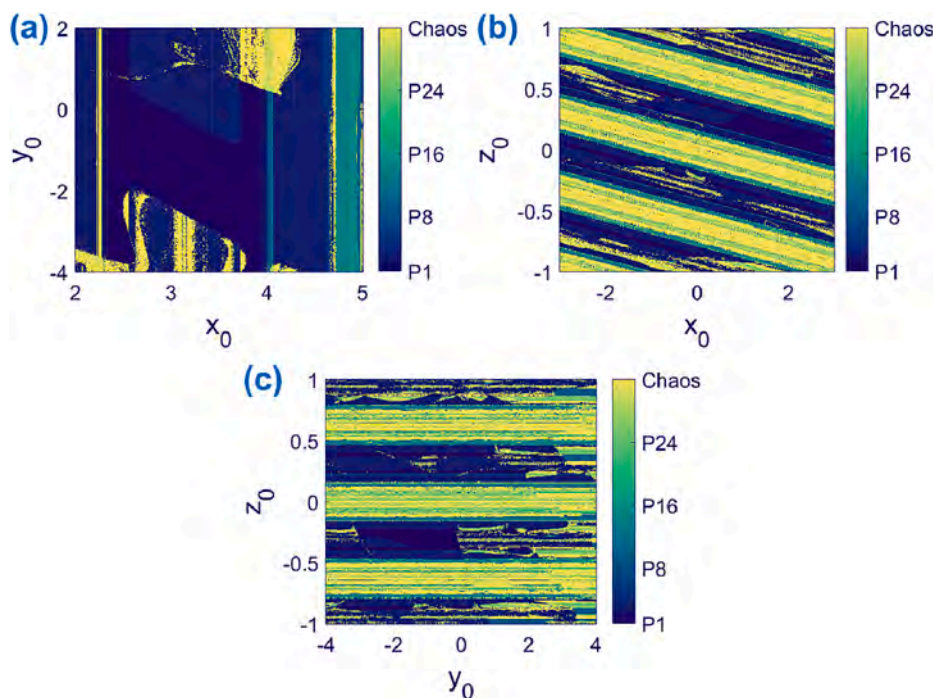


Fig. 7. Attraction basins of System (1) with $A = 0.8, b = 0.1, \omega = 0.7$. (a) On $x_0 - y_0$ plane with $x_0 \in [2, 5], y_0 \in [-4, 2]$, and $z_0 = 0$, (b) on $x_0 - z_0$ plane with $x_0 \in [-3, 3], z_0 \in [-1, 1]$, and $y_0 = 0$ and, and (c) on $y_0 - z_0$ plane with $y_0 \in [-4, 4], z_0 \in [-1, 1]$, and $x_0 = 0$. A 300×300 grid of initial conditions is used to obtain each basin of attraction. Yellow and blue-green colors represent the chaotic and periodic solutions, respectively. As the period of the periodic attractor increases, its representative color changes from blue to green. The transitions between the different types of attractors from Fig. 5 (a) are recovered in (b) and (c), where one of the variable initial conditions is z_0 .

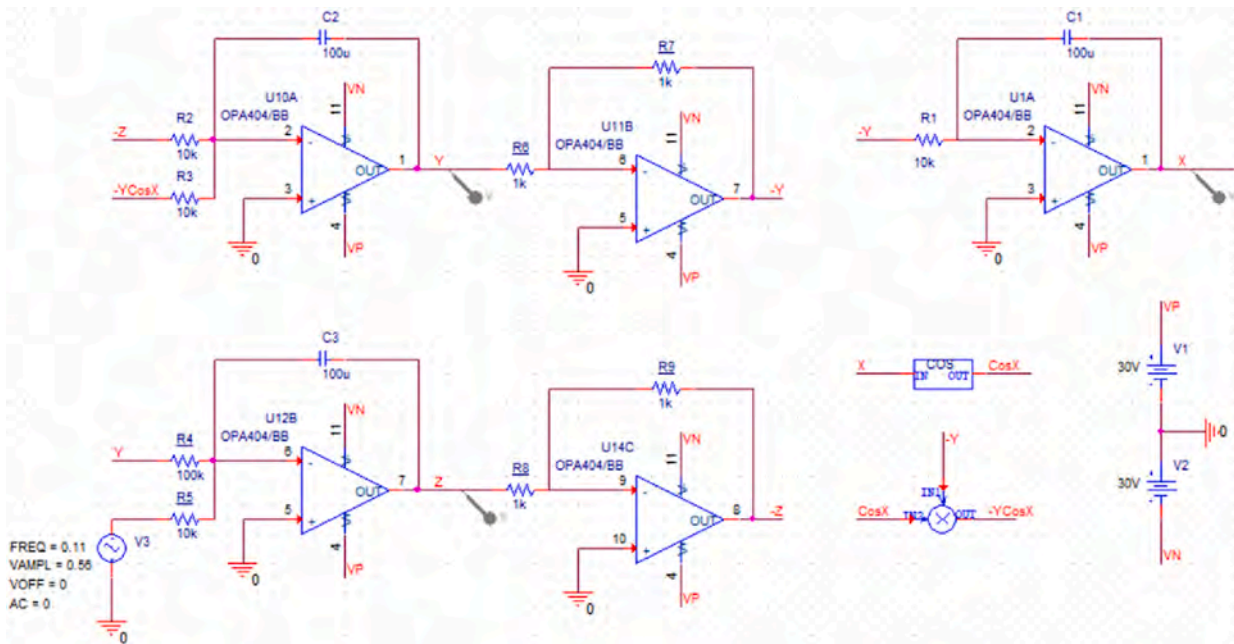


Fig. 8. The analog circuit following System (5) is implemented in OrCAD. The particular circuit elements are $C_1 = C_2 = C_3 = 100\mu F$ and $R_1 = R_2 = R_3 = R_5 = 10k\Omega, R_4 = 100k\Omega, R_6 = R_7 = R_8 = R_9 = 1k\Omega$. The supply voltages of the OpAmps are set to $V_p = 30V, V_N = -30V$. Three integrator and two inverter circuits are implemented based on OpAmps. Also, one multiplier, one cosine function block, and one cosine (sine with a $\frac{\pi}{2}rad$ phase shift) voltage generator are required.

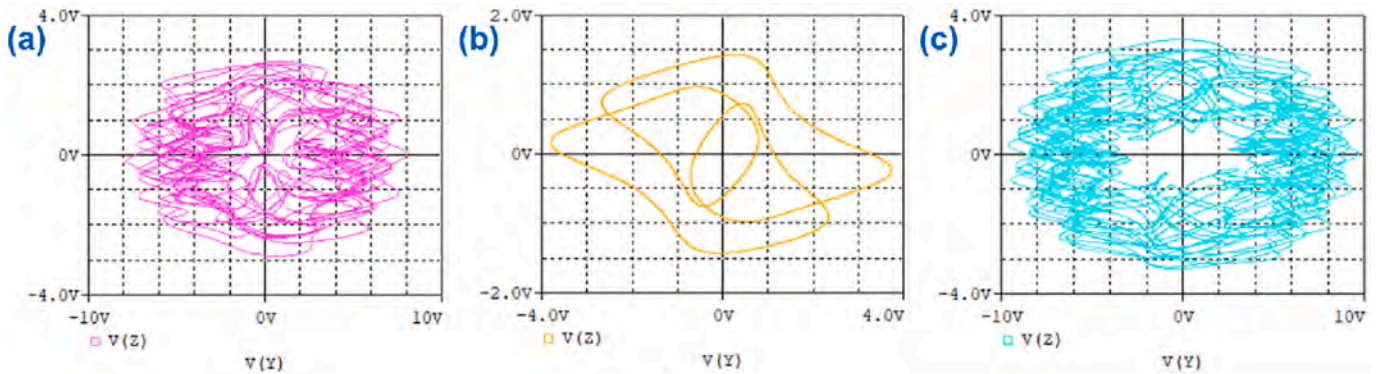


Fig. 9. The simulation results of the circuit from Fig. 8 in $Y - Z$ plane. Projection of (a) chaotic attractor with $z_0 = 0$, (b) periodic attractor with $z_0 = -0.3$, and (c) torus attractor with $z_0 = 2.2$. The dynamics of an analog circuit agrees with the numerical results from Fig. 1.

The schematic of the designed circuit in the OrCAD simulation environment is provided in Fig. 8. Three integrators are used to implement the three state variables. Also, two inverters, a multiplier, a cosine function block, and a sinusoidal voltage generator are employed. The integrator and inverter circuits are designed based on operational amplifiers (OpAmps). The value of capacitors is $C_1 = C_2 = C_3 = 100\mu F$, and the resistors' values are set as $R_1 = R_2 = R_3 = R_5 = 10k\Omega, R_4 = 100k\Omega, R_6 = R_7 = R_8 = R_9 = 1k\Omega$. Moreover, the supply voltages of the OpAmps are $V_p = 30V, V_N = -30V$.

The cosine signal in the last line of System (5) is implemented by applying a $\frac{\pi}{2} rad$ phase shift to the generated sine function. The frequency in the cosine signal is measured in $\frac{rad}{s}$, but the frequency measurement unit in OrCAD is Hz, so the frequency in Fig. 8 is set to 0.11 Hz according to

$$\omega = 2\pi f \rightarrow f = \frac{\omega}{2\pi} = \frac{0.7}{2\pi} \approx 0.11 Hz \tag{6}$$

The results of the simulation of the designed circuit from Fig. 8 are demonstrated in Fig. 9. To allow for a comparison with the previous numerical results, the attractors are projected on $Y - Z$ plane with initial

conditions $(x_0, y_0, z_0) = (0, 0, z_0)$ and (a) $z_0 = 0$, (b) $z_0 = -0.3$, and (c) $z_0 = 2.2$. The circuit's behavior matches the numerical results, recovering all chaotic, periodic, and torus attractors from Fig. 1.

5. Conclusion

In the present paper, we have provided the first example of a mega-extreme multistable chaotic system. The introduced three-dimensional non-autonomous system shows extreme and megastability under the variation of initial conditions corresponding to two different state variables. The megastability of our system has been corroborated by phase portrait projections demonstrating an infinite but countable number of coexisting attractors. The latter can conform to the same or different types of dynamics. To verify that the model exhibits genuine attractors, we have investigated the dissipative character of the system's dynamics by explicitly calculating the divergence, which turned out to be state-dependent. Nevertheless, the numerically determined average divergences for all the relevant regimes showed convergence to negative values, indicating that the system dynamics is indeed dissipative. Also, the connecting curves have been determined to better characterize the

system attractors.

Concerning the extreme multistability feature of the novel system, we have constructed the bifurcation diagram under the variation of the appropriate initial condition and have numerically determined the corresponding Lyapunov spectra and the Kaplan-Yorke dimension. The transitions between periodic and chaotic attractors observed in the bifurcation diagram have been corroborated by constructing the attraction basins in three planes of initial conditions. Finally, we have confirmed the validity of the numerical results by designing and simulating an analog circuit in the OrCAD environment. The circuit was designed using simply available components like OpAmps, resistors, capacitors, multipliers, and signal generators. We have shown that the circuit dynamics agrees well with the numerical results for the original system, demonstrating that the mega-extreme multistability feature is reproducible and flexible in applications. This is especially important given that there may be instances where the realization of solely extreme multistable or megastable systems may be difficult. We believe that discovering a new class of mega-extreme multistable systems will catalyze new research directions concerning the origin, design, and control of multistable nonlinear systems.

Declaration of competing interest

The authors have no relevant financial or non-financial interests to disclose.

Data availability

The authors admit that the data supporting the findings of this study are accessible through the paper.

Acknowledgments

This work was supported by the Centre for Nonlinear Systems, Chennai Institute of Technology (CIT), India (Grant number [CIT/CNS/2023/RP/005]). I.F. acknowledges the funding provided by the Institute of Physics Belgrade through a grant by the Ministry of Science, Technological Development, and Innovations of the Republic of Serbia.

References

- [1] Lorenz EN. Deterministic nonperiodic flow. *J Atmos Sci* 1963;20:130.
- [2] Strogatz SH. *Nonlinear dynamics and chaos: with applications to physics, biology, chemistry, and engineering*. Westview Press; 2014.
- [3] Degn H, Holden AV, Olsen LF. *Chaos in biological systems*. Springer Science & Business Media; 2013.
- [4] Lin H, Wang C, Cui L, Sun Y, Zhang X, Yao W. Hyperchaotic memristive ring neural network and application in medical image encryption. *Nonlinear Dyn* 2022;110:841.
- [5] Lin H, Wang C, Yu F, Sun J, Du S, Deng Z, et al. A review of chaotic systems based on Memristive Hopfield neural networks. *Mathematics* 2023;11:1369.
- [6] Chen G, Dong X. *From chaos to order: methodologies, perspectives and applications*. World Scientific; 1998.
- [7] Boccaletti S, Grebogi C, Lai Y-C, Mancini H, Maza D. The control of chaos: theory and applications. *Phys Rep* 2000;329:103.
- [8] Feudel U. Complex dynamics in multistable systems. *Int J Bifurcation Chaos* 2008;18:1607.
- [9] Pisarchik AN, Feudel U. Control of multistability. *Phys Rep* 2014;540:167.
- [10] Feudel U, Pisarchik AN, Showalter K. Multistability and tipping: from mathematics and physics to climate and brain—minireview and preface to the focus issue. *Chaos* 2018;28:033501.
- [11] Xu Q, Lin Y, Bao B, Chen M. Multiple attractors in a non-ideal active voltage-controlled Memristor based Chua's circuit. *Chaos, Solitons Fractals* 2016;83:186.
- [12] Xu Q, Cheng S, Ju Z, Chen M, Wu H. Asymmetric coexisting bifurcations and multistability in an asymmetric Memristive diode-bridge-based jerk circuit. *Chin J Phys* 2021;70:69.
- [13] Wang Z, Moroz I, Wei Z, Ren H. Dynamics at infinity and a Hopf bifurcation arising in a quadratic system with coexisting attractors. *Pramana* 2018;90:1.
- [14] Li C, Sprott J. Finding coexisting attractors using amplitude control. *Nonlinear Dyn* 2014;78:2059.
- [15] Li C, Wang X, Chen G. Diagnosing multistability by offset boosting. *Nonlinear Dyn* 2017;90:1335.
- [16] Wang Q, Yan S, Wang E, Ren Y, Sun X. A simple Hamiltonian conservative chaotic system with extreme multistability and offset-boosting. *Nonlinear Dyn* 2023;111:7819.
- [17] Li C, Lei T, Liu Z. Offset parameter cancellation produces countless coexisting attractors. *Chaos* 2022;32:121104.
- [18] Deng Z, Wang C, Lin H, Sun Y. A Memristive spiking neural network circuit with selective supervised attention algorithm. In: *IEEE transactions on computer-aided design of integrated circuits and systems*; 2022.
- [19] Liao M, Wang C, Sun Y, Lin H, Xu C. Memristor-based affective associative memory neural network circuit with emotional gradual processes. *Neural Comput & Applic* 2022;34:13667.
- [20] Lin H, Wang C, Tan Y. Hidden extreme multistability with hyperchaos and transient chaos in a Hopfield neural network affected by electromagnetic radiation. *Nonlinear Dyn* 2020;99:2369.
- [21] Zhang H, Sun K, He S. A fractional-order ship power system with extreme multistability. *Nonlinear Dyn* 2021;106:1027.
- [22] Hens C, Banerjee R, Feudel U, Dana S. How to obtain extreme multistability in coupled dynamical systems. *Phys Rev E* 2012;85:035202.
- [23] Ngonghala CN, Feudel U, Showalter K. Extreme multistability in a chemical model system. *Phys Rev E* 2011;83:056206.
- [24] Jin M, Sun K, Wang H. Hyperchaos, extreme multistability, and hidden attractors in the novel complex nonlinear system and its adaptive hybrid synchronization. *Nonlinear Dyn* 2022;110:3853.
- [25] Fossi JT, Deli V, Njitacke ZT, Mendimi JM, Kemwoue FF, Atangana J. Phase synchronization, extreme multistability and its control with selection of a desired pattern in hybrid coupled neurons via a Memristive synapse. *Nonlinear Dyn* 2022;109:925.
- [26] Zhang S, Zheng J, Wang X, Zeng Z. A novel no-equilibrium HR neuron model with hidden homogeneous extreme multistability. *Chaos, Solitons Fractals* 2021;145:110761.
- [27] Bao H, Gu Y, Xu Q, Zhang X, Bao B. Parallel bi-memristor hyperchaotic map with extreme multistability. *Chaos, Solitons Fractals* 2022;160:112273.
- [28] Zhang Y, Liu Z, Wu H, Chen S, Bao B. Two-memristor-based chaotic system and its extreme multistability reconstitution via dimensionality reduction analysis. *Chaos, Solitons Fractals* 2019;127:354.
- [29] Patel MS, Patel U, Sen A, Sethia GC, Hens C, Dana SK, et al. Experimental observation of extreme multistability in an electronic system of two coupled Rössler oscillators. *Phys Rev E* 2014;89:022918.
- [30] Hens C, Dana SK, Feudel U. Extreme multistability: attractor manipulation and robustness. *Chaos* 2015;25:053112.
- [31] Chen M, Luo X, Suo Y, Xu Q, Wu H. Hidden extreme multistability and synchronicity of memristor-coupled non-autonomous Memristive Fitzhugh–Nagumo models. *Nonlinear Dyn* 2023;111:7773.
- [32] Sprott JC, Jafari S, Khalaf AJM, Kapitaniak T. Megastability: coexistence of a countable infinity of nested attractors in a periodically-forced oscillator with spatially-periodic damping. *Eur Phys J Spec Top* 2017;226:1979.
- [33] Prakash P, Rajagopal K, Singh JP, Roy BK. Megastability, multistability in a periodically forced conservative and dissipative system with Signum nonlinearity. *Int J Bifurcation Chaos* 2018;28:1830030.
- [34] Jafari S, Rajagopal K, Hayat T, Alsaedi A, Pham V-T. Simplest megastable chaotic oscillator. *Int J Bifurcation Chaos* 2019;29:1950187.
- [35] Leutcho GD, Jafari S, Hamarash II, Kengne J, Njitacke ZT, Hussain I. A new Megastable nonlinear oscillator with infinite attractors. *Chaos, Solitons Fractals* 2020;134:109703.
- [36] Zhang K, Vijayakumar M, Jamal SS, Natiq H, Rajagopal K, Jafari S, et al. A novel Megastable oscillator with a strange structure of coexisting attractors: design, analysis, and FPGA implementation. *Complexity* 2021;2021:2594965.
- [37] Li R, Dong E, Tong J, Du S. A new autonomous Memristive megastable oscillator and its Hamiltonian-energy-dependent Megastability. *Chaos* 2022;32:013127.
- [38] Gilmore R, Ginoux J-M, Jones T, Letellier C, Freitas U. Connecting curves for dynamical systems. *J Phys A Math Theor* 2010;43:255101.
- [39] López-Rentería JA, Aguirre-Hernández B, González F Verdúco. On Hurwitz and Schur connecting-curves and dense trajectories. In: *Advances in Mathematical and Computational Methods: Addressing Modern Challenges of Science, Technology, and Society*. 1368; 2011. p. 271.
- [40] Byrne G, Gilmore R, Cebral J. Connecting curves in higher dimensions. *J Phys A Math Theor* 2014;47:215101.
- [41] Guan X, Xie Y. Connecting curve: a new tool for locating hidden attractors. *Chaos* 2021;31:113143.
- [42] Frederickson P, Kaplan JL, Yorke ED, Yorke JA. The Liapunov dimension of strange attractors. *J Differ Equ* 1983;49:185.
- [43] Kaplan JL, Mallet-Paret J, Yorke JA. The Lyapunov dimension of a nowhere differentiable attracting torus. *Ergodic Theory Dynam Syst* 1984;4:261.

Patched patterns and emergence of chaotic interfaces in arrays of nonlocally coupled excitable systems

Cite as: Chaos 32, 091102 (2022); doi: 10.1063/5.0111507

Submitted: 19 July 2022 · Accepted: 19 August 2022 ·

Published Online: 16 September 2022





View Online



Export Citation



CrossMark

Igor Franović^{1,a)}  and Sebastian Eydam^{2,b)} 

AFFILIATIONS

¹Scientific Computing Laboratory, Center for the Study of Complex Systems, Institute of Physics Belgrade, University of Belgrade, Pregrevica 118, 11080 Belgrade, Serbia

²Neural Circuits and Computations Unit, RIKEN Center for Brain Science, 2-1 Hirosawa, 351-0198 Wako, Japan

^{a)}Author to whom correspondence should be addressed: franovic@ipb.ac.rs

^{b)}Electronic mail: richard.eydam@riken.jp

ABSTRACT

We disclose a new class of patterns, called patched patterns, in arrays of non-locally coupled excitable units with attractive and repulsive interactions. The self-organization process involves the formation of two types of patches, majority and minority ones, characterized by uniform average spiking frequencies. Patched patterns may be temporally periodic, quasiperiodic, or chaotic, whereby chaotic patterns may further develop interfaces comprised of units with average frequencies in between those of majority and minority patches. Using chaos and bifurcation theory, we demonstrate that chaos typically emerges via a torus breakup and identify the secondary bifurcation that gives rise to chaotic interfaces. It is shown that the maximal Lyapunov exponent of chaotic patched patterns does not decay, but rather converges to a finite value with system size. Patched patterns with a smaller wavenumber may exhibit diffusive motion of chaotic interfaces, similar to that of the incoherent part of chimeras.

Published under an exclusive license by AIP Publishing. <https://doi.org/10.1063/5.0111507>

While coherence–incoherence patterns have been exhaustively explored both for spatially discrete systems of coupled oscillators and in the continuum limit, much less is known about the generic mechanisms of onset and the finite-size effects associated with such patterns in coupled excitable systems. Recently discovered supercritical scenario for the onset of bumps in coupled excitable active rotators with nonlocal attraction and global repulsion, as well as the two types of solitary states unveiled in arrays of excitable FitzHugh–Nagumo units with nonlocal attractive and repulsive interactions, already suggests that the coherence–incoherence patterns in coupled excitable systems may defy the common intuition based on coupled oscillators. Here, we introduce a new class of patterns, called patched patterns, in non-locally coupled arrays of excitable units with attractive and repulsive interactions. These patterns involve splitting of an array into spatially continuous domains, called patches, comprised of units locked by their average spiking frequencies. Patched patterns may be temporally periodic, quasiperiodic, or chaotic, and depending on the prevalence of attraction vs repulsion, chaotic patterns

can develop interfaces with frequencies intermediate between the majority and minority patches. Distinct from chimeras, chaos in patched patterns is not spatially localized, but is of different character for the units in the patches and at the interfaces: the latter show more variability and resemble chaotic itinerancy. We demonstrate the typical bifurcation scenario giving rise to chaos for smaller and intermediate coupling ranges. We also show that adjusting the coupling range to reduce the pattern wavenumber may result in a transition to chaos accompanied by a diffusive motion of interfaces.

I. INTRODUCTION

Combining different approaches and methods from pattern formation, finite dimensional chaos, and bifurcation theory, as well as statistical physics, has in recent years allowed for some deep insights into the coherence–incoherence patterns in systems of coupled oscillators. The two most important aspects concern

understanding their mechanisms of onset and the dependence of their behavior on system size. For example, it has become clear that chimeras^{1–8} constitute inhomogeneous equilibria of certain macroscopic averaged quantities in the continuum limit,^{9–11} while in spatially discrete systems, they are characterized by a self-localized, spatially extensive weak hyperchaos where the positive part of the Lyapunov spectrum decays to zero with system size.¹² The interplay of local nonlinearity and interactions, at least for the two classical scenarios admitting chimeras,^{1,3} results in nontrivial finite-size effects, such as the pattern collapse to a uniform coherent state¹³ and the Brownian-like diffusion of the incoherent domain.¹⁴

Nevertheless, an intriguing question is what happens to coherence–incoherence patterns if a system is not comprised of oscillators, but rather of excitable units.^{15–19} When isolated, excitable systems remain in a stable stationary state, but may be triggered to oscillate by a sufficiently strong perturbation via interactions and/or noise. Excitability is one of the cornerstones for the physics of life; underpinning the local dynamics of neuronal, cardiac, and endocrine systems;^{15,20–23} and is also important for understanding many other natural and synthetic systems, from chemical reactions²⁴ and climate dynamics²⁵ to lasers²⁶ and machine learning.²⁷ Self-organization in coupled excitable systems cannot be described in terms of a simple mutual adjustment of local oscillations, and even the very onset of a collective mode requires the presence of inhibitory/repulsive couplings,^{28,29} defying the common intuition developed for coupled oscillators. With the full analogy to coupled oscillators missing, the basic questions on coherence–incoherence patterns in coupled excitable systems, such as the potential working definition, classification, generic mechanisms of onset, and the contribution from finite-size effects still remain open.

Currently, it seems likely that the extension of the concept of weak chimeras,³⁰ classically associated with small systems of coupled oscillators, provides an effective framework for characterization of coherence–incoherence patterns in finite systems of coupled excitable units. By this concept, coherence–incoherence patterns can be described in terms of frequency locking/unlocking, typically involving a majority of units that are coherent, i.e., frequency locked, and a minority of units unlocked from the bulk (and possibly mutually unlocked). In these terms, bump states,^{10,31–33} a common type of pattern associated in neuroscience with spatial working memory³⁴ and the head direction system³⁵ can be described as a set of units with an elevated firing rate self-localized on a continuous spatial domain and appearing on top of an inactive background. Using the model of excitable active rotators with a short-range attraction and long-range repulsion, it has recently been shown that the bumps may emerge from Turing patterns via a supercritical scenario that involves unlocking of a single unit from the bulk and a subsequent sequence of bifurcations to a fully developed extensive chaos.³⁶ Such an onset mechanism turned out to be completely independent on system size. In contrast to classical chimeras, no pattern collapse was observed in small systems, and while typically being static, bumps could also exhibit a lateral diffusive motion depending on the parameters. Also quite recently, applying the model of an array of FitzHugh–Nagumo units with nonlocal attractive and repulsive interactions, it has been shown that coupled excitable systems may display two types of solitary states³⁷ with a different finite-size behavior, namely, either size-independent periodic solutions

closely associated with unbalanced cluster states in globally coupled networks or weakly chaotic solutions where a few isolated oscillators split off from the background alternating (modulated traveling) wave. Finally, for the same model, it has been shown that the noise may play a facilitatory role allowing for the onset of the so-called coherence–resonance chimeras,^{38,39} whereby instead of the diffusion drift of classical chimeras, the interplay of local noise and the intrinsic noise due to finite size gives rise to switching of positions between the coherent and the incoherent domains.

In the present paper, we introduce a new class of patterns in non-locally coupled excitable systems, called *patched patterns*. The basic pattern structure is such that the units self-organize into spatially continuous domains, called patches, comprised of units that are mutually frequency locked. Our model is the same as in Refs. 40 and 37 and comprises an array of N non-locally coupled identical FitzHugh–Nagumo units described by

$$\begin{aligned}\varepsilon \dot{u}_k &= u_k - \frac{u_k^3}{3} - v_k + \frac{\kappa}{2R} \sum_{l=k-R}^{k+R} [g_{uu}(u_l - u_k) + g_{uv}(v_l - v_k)], \\ \dot{v}_k &= u_k + a + \frac{\kappa}{2R} \sum_{l=k-R}^{k+R} [g_{vu}(u_l - u_k) + g_{vv}(v_l - v_k)].\end{aligned}\quad (1)$$

The local slow-fast dynamics is paradigmatic of type II excitability¹⁵ and involves activator variables u_k and recovery variables v_k with a timescale separation $\varepsilon = 0.05$. For an isolated unit, variation of the bifurcation parameter $a > 0$ gives rise to a singular Hopf bifurcation at $a = 1$, mediating between excitable ($a \gtrsim 1$) and oscillatory regimes ($a < 1$). Above the canard transition at $a \approx 1 - \varepsilon/8$,⁴¹ harmonic subthreshold (low-amplitude) oscillations give way to large-amplitude relaxation oscillations. Here, we fix $a = 1.01$ such that the isolated units are in the excitable regime. Each unit is coupled to R nearest neighbors to its left and to its right, with all the indices being periodic modulo N . Coupling strength κ is assumed to be homogeneous and is fixed to $\kappa = 0.4$. Interactions between units involve direct terms including only activator or only recovery variables, as well as the mixing terms, which is compactly described by the rotational coupling matrix⁴⁰

$$G = \begin{pmatrix} g_{uu} & g_{uv} \\ g_{vu} & g_{vv} \end{pmatrix} = \begin{pmatrix} \cos \varphi & \sin \varphi \\ -\sin \varphi & \cos \varphi \end{pmatrix}.$$

Note that the parameter φ impacts the prevalence of attractive vs repulsive interactions by affecting the sign of the interaction terms.³⁷

The paper is organized as follows. In Sec. II, we first make a basic description of patched patterns and then focus on static chaotic patched patterns with interfaces to characterize the local switching dynamics of interface units, showing that it consists of laminar and turbulent epochs consistent with chaotic itinerancy.^{42–44} In Sec. III, we use chaos and bifurcation theory to demonstrate the typical scenario for the onset of chaos with increasing coupling parameter φ , where the torus bifurcation mediates the transition from periodic to quasiperiodic patterns, and chaos emerges via torus breakup. It is also shown that the maximal Lyapunov exponent converges to a finite value rather than decaying with the system size, demonstrating the persistence of chaos. In Sec. IV, we demonstrate how varying the coupling range to reduce the pattern wavenumber may give

rise to the diffusion of interfaces. Section V provides a summary, discussion, and outlook concerning our findings.

II. PATCHED PATTERNS

As already announced, patched patterns involve the formation of coherent spatial domains of frequency locked units. One may distinguish between two types of domains, here called majority and minority patches. The majority patches maintain a 1:2 resonant frequency locking to the minority patches. Patched patterns can be temporally periodic, quasiperiodic, or chaotic. The basic spatial profile of average spiking frequencies $\omega_k = 2\pi M_k/T$, where M_k is the spike count within a macroscopic time interval T , is piecewise constant, as in Fig. 1(a), which illustrates a periodic solution with an additional reflection symmetry. In terms of local dynamics, the patches are heterogeneous such that the units closer to the patch center show a more similar dynamics than those at the patches' boundaries. In contrast to periodic solutions, the chaotic solutions may further develop *interfaces* comprised of incoherent units with *switching* dynamics, whose frequencies are intermediate between majority and minority patches, see Fig. 1(b). Depending on the system parameters, in particular, the coupling range that controls the pattern wavenumber, i.e., the number of minority patches, these interfaces may be static, as in Fig. 1(b), or may display Brownian-like diffusive motion we analyze later on in the paper. Within the

entire range supporting the patched patterns, the coupling parameter φ favors repulsive over attractive interactions since three out of four interaction terms (g_{uu}, g_{vu}, g_{vv}) between any two coupled units have a negative sign.

A. Switching dynamics at the interfaces

Let us analyze in more detail the self-organization of local dynamics for an example of a static chaotic pattern with interfaces, whose spatial profile of average spiking frequencies is illustrated in Fig. 1(b). Such wavenumber-4 pattern emerges from the corresponding periodic solution with a piecewise constant profile of average frequencies, illustrated in Figs. 1(a) and 1(c), via a sequence of bifurcations described in Sec. III. The typical time series of a fast variable of a majority unit $k = 62$ [see the red arrow in Fig. 1(b)] indicates mixed mode oscillations with each pair of successive spikes separated by a subthreshold oscillation, whereas the time trace of a typical minority unit $k = 58$, denoted by the blue arrow in Fig. 1(b), primarily shows successive spiking, cf. Figs. 1(e) and 1(f). On the other hand, a short time trace of an interface unit $k = 60$ in Fig. 1(g) indicates mixed-mode oscillations with a switching dynamics between the episodes where it approaches either the adjacent majority or the minority patch.

To further elucidate the switching dynamics at the interfaces, we construct the diagrams comparing the time evolution of the first return times $\Delta t_n(t)$ to the Poincaré cross section $u_k(t) = 1.5, \dot{u}_k$

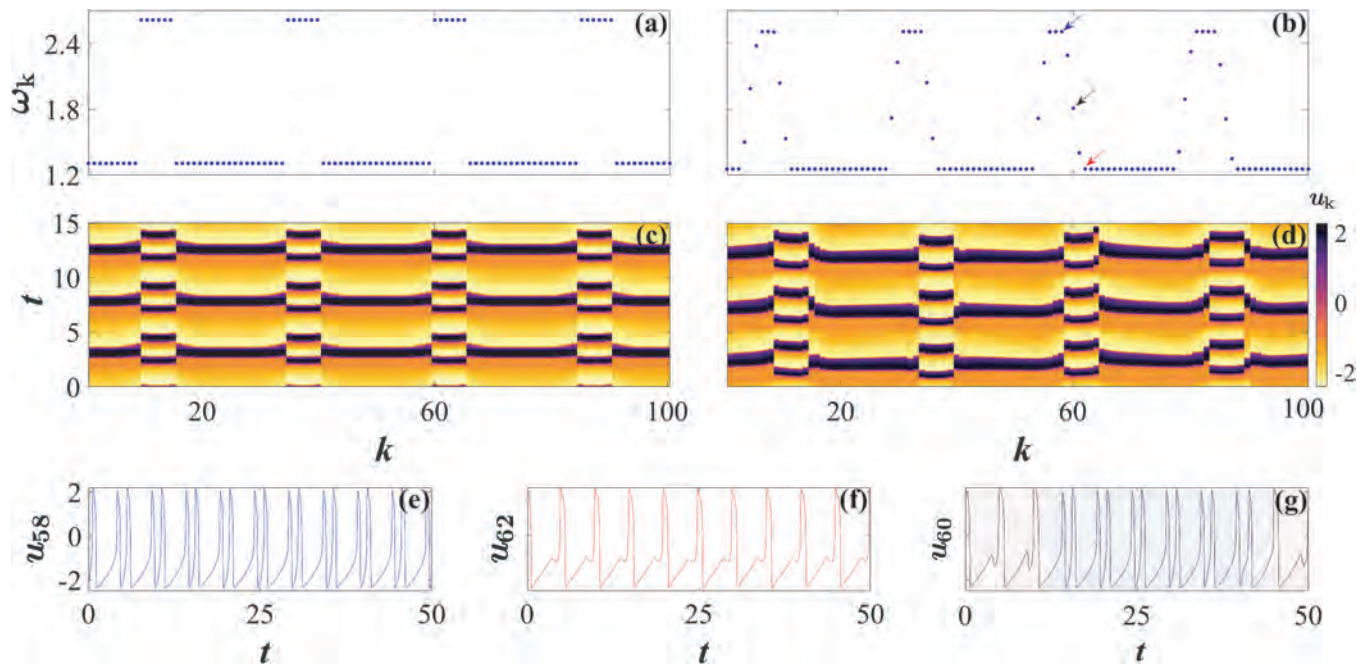


FIG. 1. Patched patterns without and with chaotic interfaces. (a) and (c) Spatial profile of average spiking frequencies and spatiotemporal evolution of fast variables $u_k(t)$ for a periodic patched pattern at $\varphi = 2$; (b) and (d) show the same, but for a chaotic patched pattern with interfaces ($\varphi = 2.2$). (e)–(g) Typical time traces $u_k(t)$ of units from a majority patch [$k = 62$, red arrow in (b)], minority patch ($k = 58$, blue arrow), and from the interface ($k = 60$, black arrow). Red and blue shading in (g) indicates transient episodes where the interface unit attaches to one of the patches. Remaining parameters: $N = 100$, $a = 1.01$, $\varepsilon = 0.05$, $\kappa = 0.4$, $R = 20$. The time horizon used to obtain average spiking frequencies is $T = 10^8$ t.u.

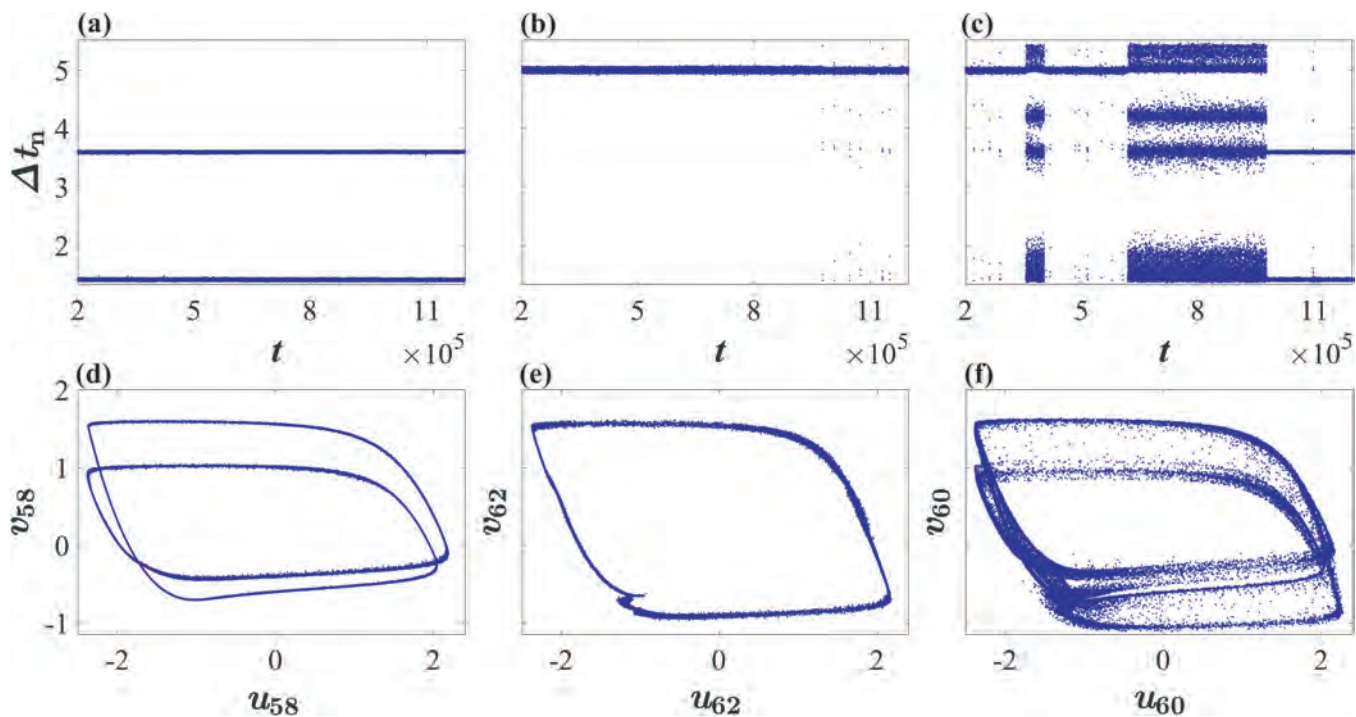


FIG. 2. Local fluctuations within patches and at interfaces. (a)–(c) Temporal evolution of the first return times to the Poincaré cross section $u_k(t) = 1.5$, $\dot{u}_k(t) > 0$ for the representative minority, majority, and interface units from Fig. 1(b), respectively. (d)–(f) Corresponding phase portraits in the $u_k - v_k$ plane. System parameters are the same as in Fig. 1(b).

($t > 0$ for the representative majority, minority and interface units from Fig. 1, see Figs. 2(a)–2(c). For a minority unit, one typically observes small variations around two basic levels, which are just induced by fluctuations of the local mean-field, also see the phase portrait in Fig. 2(d). The similar holds for the representative majority unit, cf. Figs. 2(b) and 2(e), though here one also finds larger fluctuations in the first return times derived from rare sub-threshold excitations. The most peculiar behavior is manifested by the representative interface unit in Figs. 2(c) and 2(f), where the dependence $\Delta t_n(t)$ involves a slow alternation between two types of epochs: the laminar ones, when the unit is approximately frequency locked to the adjacent majority or minority patch, and turbulent ones, when the unit displays a high variability due to fast fluctuations between the orbits resembling those of units in majority and minority patches. Such slow alternating dynamics is considered a fingerprint of chaotic itinerancy,^{42–44} ubiquitous in high-dimensional state spaces. As opposed to the units within minority and majority patches whose typical dynamics is illustrated in Figs. 2(d) and 2(e), respectively, the units at the interfaces are subjected to highly variable local mean-fields which act as sources of intrinsic noise. Due to such variability, under increasing parameter φ , the chaotic attractor undergoes transformation into a chaotic saddle by acquiring unstable directions associated with the subspaces of interface units. This is why the time evolution of the Poincaré cross section of the interface unit in Fig. 2(c) contains the “levels”

associated with the laminar epochs, as well as additional structure related to the turbulent epochs. Similarly, the phase portrait of the interface unit in Fig. 2(e) combines the typical dynamics of the patches but shows additional complexity reflecting the switching process.

The mechanism giving rise to switching between the epochs, as well as the fast fluctuations between the episodes within turbulent epochs, appears to be qualitatively the same. It is associated with the interface unit performing small-amplitude oscillations around the ghost of an unstable fixed point derived from the stable equilibrium of an isolated unit, as illustrated in Fig. 3 for the fast fluctuations within a turbulent epoch. Successive subthreshold oscillations are also the reason of why the turbulent epochs contain Δt_n levels absent in the case of units within the patches, see Fig. 2(c). Relaxation oscillations both within laminar and turbulent epochs are susceptible to perturbations in a way similar to the phenomenon of phase-sensitive excitability of a limit cycle,^{45,46} in the sense that a strong enough perturbation due to fluctuations in the local mean-field may induce a large deviation from the relaxation oscillation orbit, giving rise to one or more successive subthreshold oscillations.

Pattern formation is based on two self-organization mechanisms classically observed in coupled excitable systems, namely, *self-localized excitations*⁴⁷ and *propagation of excitation*.^{38,48} The activity within an array consists of sequentially repeating excitation episodes, where the majority (minority) patches fire once (twice).

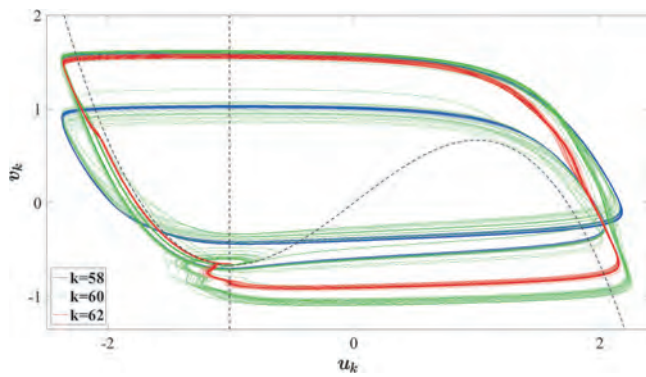


FIG. 3. Superimposed orbits of a representative minority unit ($k = 58$, blue), majority unit ($k = 62$, red), and an interface unit ($k = 60$, green) for the pattern in Fig. 1(b). Black dashed lines: isolated unit's fast and slow nullclines, whose intersection determines the position of the corresponding stable equilibrium. Fast switching between episodes within the turbulent epoch of an interface unit is due to subthreshold oscillations around the ghost of the isolated unit's equilibrium.

Within the patches, spiking is typically organized in such a way that the units closer to the center fire before those at the patches' boundaries. The excitation episodes are initiated at the minority patches, see Figs. 4(a) and 4(d) that show the space-time evolution of \hat{u}_k , $k \in [1, N]$ for the periodic and the chaotic patched pattern with interfaces from Figs. 1(a) and 1(b), respectively. For the periodic pattern, the excitation of the minority patches, see, e.g., black regions for $t \approx 1$ occurs simultaneously as the solution carries a reflection space-time symmetry. Contrasting that, the reflection symmetry is broken for the chaotic pattern, cf. Fig. 4(d). The localized excitation elicited within a minority patch becomes a source of two counterpropagating excitation waves emanating to its left and right. Each majority patch is embedded between two minority patches and, hence, receives from them two counterpropagating excitation waves that collide and annihilate. In their wake, another excitation is born and induced by the described paradigm a second spike of units within the minority patches. The latter cannot induce further excitation at the majority patches because the units there feature longer spikes and subsequently also have longer refractory periods, see Figs. 4(b) and 4(e).

The temporal organization of activity within and between the patches may further be examined by constructing the corresponding cross-correlation matrix

$$C_{kl} = \frac{\langle \hat{u}_k(t) \hat{u}_l(t) \rangle_T}{\sqrt{\langle \hat{u}_k(t)^2 \rangle_T \langle \hat{u}_l(t)^2 \rangle_T}},$$

where $\langle \cdot \rangle_T$ denotes the time averaging, while $\hat{u}_k(t) = u_k(t) - \langle u_k(t) \rangle_T$ are the deviations of $u_k(t)$ from their means, see Figs. 4(c) and 4(f). One immediately realizes that C_{kl} for the periodic pattern has a clear-cut structure with a strong correlation within and between a given type of patches (majority or minority), while the correlation of activities between patches of different type is rather weak. The intrinsic structure of C_{kl} for the chaotic pattern is more

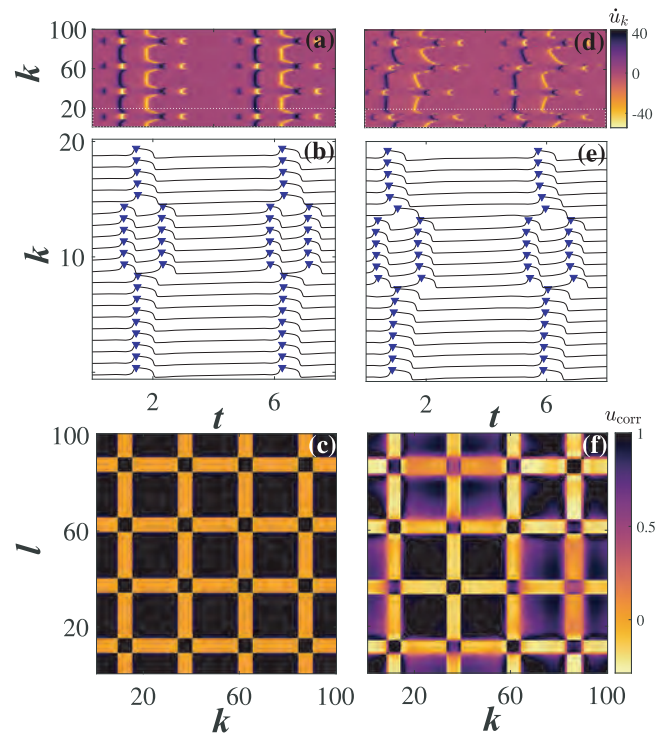


FIG. 4. Intrinsic structure of typical periodic (left column) and chaotic pattern with interfaces (right column). (a) Spatiotemporal evolution $\hat{u}_k(t)$; white dotted rectangle: segment of an array whose dynamics is extracted in (b); (b) bottom-up: time traces $u_k(t)$, $k = 1, 2, \dots, 20$ (black lines) shown shifted by a constant increment; blue triangles: spike times of units; (c) cross-correlation matrix C_{kl} ; (d)–(f) same as (a)–(c) but for chaotic pattern with interfaces. Respective parameters are identical to those in Figs. 1(a) and 1(b).

smearred, reflecting the existence of interface units, and in contrast to the periodic solution, there are also pairs of units with an anti-correlated behavior.

III. EMERGENCE OF CHAOS

Having explained the structure of local dynamics underpinning chaotic patched patterns with interfaces, we investigate the bifurcation scenario that gives rise to chaos as the coupling parameter φ is increased. Note that the features of the transition to chaos with φ depend on the wavenumber of the primary periodic solution, which is ultimately controlled by the coupling range R . We first elaborate on a generic scenario where periodic patterns follow the route to chaos via quasiperiodicity, focusing on the example of a wavenumber-4 pattern. For this generic scenario, which holds for smaller and intermediate coupling ranges R , the onset of chaos *per se* is not immediately associated with the formation of turbulent interfaces, and the latter emerge separately via a secondary bifurcation on a chaotic attractor.

The bifurcation diagram in Fig. 5(a) is constructed considering an array of $N = 100$ units, performing a forward sweep in φ to collect the first return times Δt_n of local dynamics to the Poincaré cross

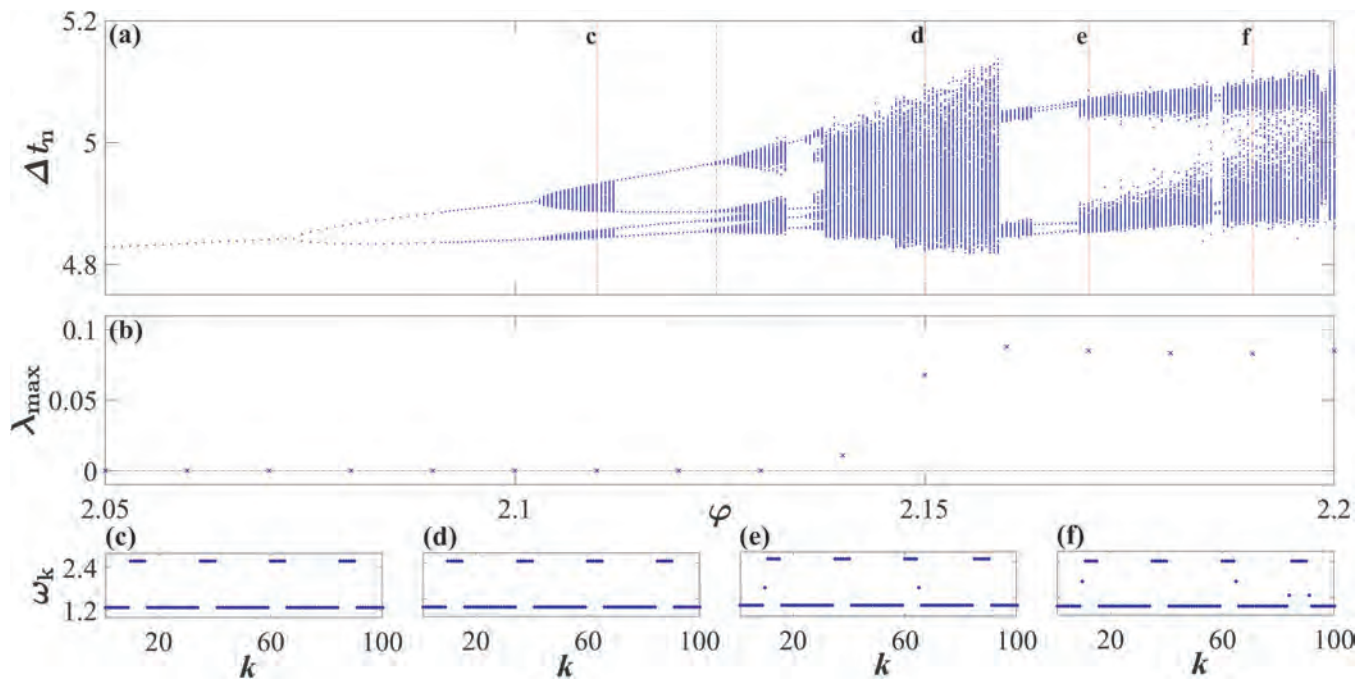


FIG. 5. Emergence of chaos and formation of turbulent interfaces. (a) Bifurcation diagram of local dynamics: first return times Δt_n to the cross section $u_k(t) = 1.5, \dot{u}_k(t) > 0$ in dependence of ϕ for the unit $k = 45$; black dash-dotted line: ϕ value where the solution loses reflection symmetry. (b) Variation of the maximal Lyapunov exponent λ_{\max} with ϕ . (c)–(f) Spatial profiles of average local spiking frequencies ω_k for the set of ϕ values indicated by the red dashed lines in (a). Remaining parameters are the same as in Fig. 1.

section $u_k(t) = 1.5, \dot{u}_k(t) > 0$. In the provided example, the selected unit remains within one of the majority frequency patches over the whole considered ϕ interval. The red dashed lines indicate the ϕ values associated with the spatial profiles of average spiking frequencies ω_k in Figs. 5(c)–5(f). The latter are calculated by averaging over an interval $T = 10^6$ t.u. having discarded a transient of additional 5×10^5 t.u. The bifurcation diagram is supplemented by the dependence of the maximal Lyapunov exponent $\lambda_{\max}(\phi)$,^{49,50} see Fig. 5(b), sampled for the solutions observed at a fixed increment $\Delta\phi = 0.01$.

The initial state at $\phi = 2.0$ is the periodic patched pattern with a reflection symmetry, already illustrated in Figs. 1(a) and 1(c). Following a period doubling at $\phi \approx 2.073$, the period two pattern is transformed into a stable quasiperiodic solution via a torus bifurcation at $\phi \approx 2.103$. Further increasing ϕ , there is a locking on the torus at $\phi \approx 2.112$, which is followed by a subsequent transition to chaos via a *torus breakup* around $\phi \approx 2.128$. The primary pattern, corresponding to a relative periodic orbit with the period four in the Poincaré section, as well as the incipient chaotic pattern, is illustrated by the respective first return maps $\Delta t_{n+1}(\Delta t_n)$ in Fig. 6. For $\phi \approx 2.125$ just below the transition, cf. the black dash-dotted line in Fig. 5(a), the solution loses the reflection symmetry, which we have verified by calculating the L2-norm of the difference between the solution and its counterpart obtained under reflection transformation. The onset of chaos under increasing ϕ is corroborated by the fact that the maximal Lyapunov exponent in Fig. 5(b) first exhibits a non-negligible positive value $\lambda_{\max} = 1.4 \times 10^{-4}$ at $\phi = 2.13$. Note

that in contrast to the onset of a localized extensive chaos, typical for chimeras or bumps, where a certain subset of units unlocks from the coherent background, the transition to chaos here is a collective instability in the sense that all the units within an array immediately exhibit chaotic behavior while the spiking frequencies remain locked within the respective patches. Above the transition, the emerging chaotic patterns do not immediately involve interface units and still feature the piecewise-constant profile of local average spiking frequencies, see Fig. 5(d). The creation of chaotic patterns featuring interface units with frequencies in-between those of majority and minority patches is rather associated with the reappearance of chaos around $\phi \approx 2.169$ following a period-four window. In terms of ω_k profiles, this transition may be understood as a “slope bifurcation” of patched patterns’ spatial frequency profile where the sharp transition between the majority and minority patches is replaced by a smoother one, see Fig. 5(e). Further increasing ϕ , the chaotic patterns gain complexity due to a growing number of turbulent interface units, showing the alternating dynamics described in Sec. II A, cf. Fig. 5(f). Meanwhile, the corresponding maximal Lyapunov exponent remains approximately constant, cf. Fig. 5(b).

Next, we address the two issues concerning how the system dynamics varies with system size. In particular, we first consider whether and how the observed sequence of bifurcations to chaos depends on N and then examine how the complexity of the solutions changes with N . In reply to the former, one notes that for

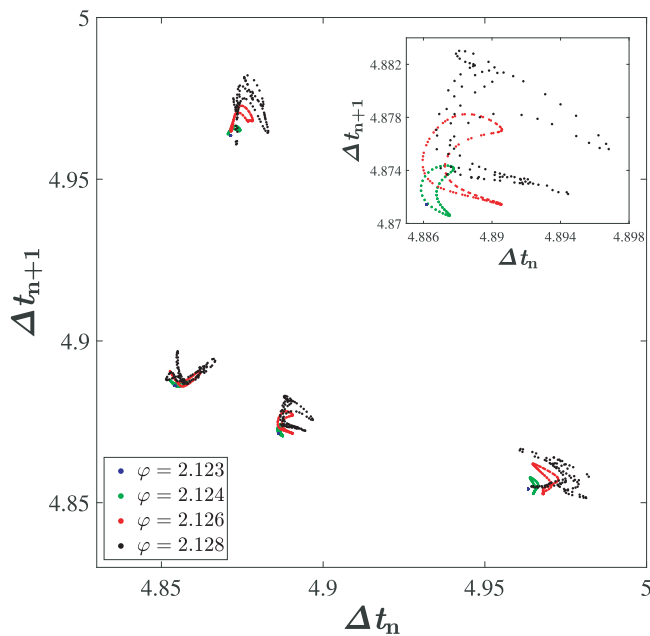


FIG. 6. Focus on the breakup of torus bifurcation: first return maps $\Delta t_{n+1}(\Delta t_n)$ indicate the disappearance of an invariant curve with increasing ϕ . Inset: an enlarged view of one of the segments of the relative period-four orbits in the Poincaré section. Remaining parameters are the same as in Fig. 1.

the given coupling strength κ and range R , the described bifurcation route to chaos qualitatively does not change with N when the initial periodic pattern is constructed by replicating the initial solution for $N = 100$. Nevertheless, our simulations indicate that the ϕ values where the particular bifurcations take place shift with increasing N , and the threshold for the emergence of chaos apparently reduces with system size. As for the solution complexity, one typically observes that the number of turbulent interface units grows with N when all the remaining parameters are kept fixed. Finally, chaos is found to persist with increasing N , as corroborated by the dependence of the maximal Lyapunov exponent λ_{\max} on system size in Fig. 7. There, the coupling parameter is fixed to $\phi = 2.13$, the value just above the transition to chaos for the system size $N = 100$, see Figs. 5(a) and 6. As expected, λ_{\max} for $N = 100$ is quite small, but the values calculated for the corresponding solutions at larger N indicate a convergence to a finite value $\lambda_{\max} \approx 0.06$ with increasing system size. This is distinct from the classical result for chimeras,¹² where the maximal Lyapunov exponent decays as $N^{-1/2}$.

IV. PATTERN DEPINNING AND DIFFUSION OF INTERFACES

So far, we have considered only static patched patterns that undergo the transition to chaos that is not accompanied by an immediate onset of turbulent interfaces. While this is typical for smaller and intermediate coupling ranges, one finds a rather different scenario if the coupling range R is further increased. Increasing the coupling range affects the primary pattern by reducing its

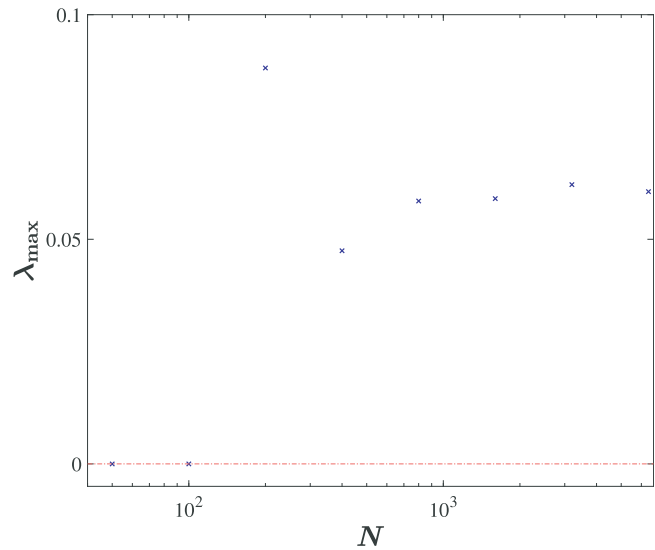


FIG. 7. Dependence of maximal Lyapunov exponent with system size $\lambda_{\max}(N)$. Note the convergence to a finite value $\lambda_{\max} \approx 0.06$ for large N . Parameters: $\phi = 2.13$, and the remaining ones are the same as in Fig. 1.

wavenumber, similar to Ref. 40 and 51. For such patterns, the transition to chaos coincides with the formation of turbulent interfaces, which moreover engage in lateral diffusive motion, similar to the random walk of the incoherent part of chimeras. As an example of this scenario, we have considered the onset of chaos for a periodic patched pattern with the wavenumber two, a solution analogous to that in Fig. 1(a), but obtained for $R = 40$ with all the other parameters preserved. About $\phi \approx 2.213$, one observes the transition to chaos, as corroborated by the dependence of the maximal Lyapunov exponent with ϕ , see Fig. 8(a). Below the transition, there is just a static periodic pattern, illustrated in Fig. 8(b) by the spatiotemporal evolution $u_k(t)$, plotting its local time averages within windows of 100 t.u. over a long time horizon of 10^6 t.u. In contrast to the scenario described in Sec. III, the interfaces emerge immediately at the transition, and instead of being pinned to the neighboring patches, rather display a Brownian-like motion, see Fig. 8(c). Due to this, just like in the case of chimeras,³⁰ the spatial profiles of average spiking frequencies for such diffusive patched patterns should be flat when considered over sufficiently long time intervals. The diffusive motion becomes more pronounced as ϕ is further increased, cf. Fig. 8(d).

To demonstrate that the motion of interfaces indeed conforms to a Brownian one, we explicitly show that the mean square displacement of the pattern position for example in Fig. 8(d) grows linearly with time. The position of the pattern at the given moment is determined following the procedure described in Ref. 14, which essentially entails comparing the vector $u_k(t), k \in [1, N]$ to a suitably chosen periodic reference function $f(x, \xi)$ so that the position of the pattern is given by the ξ value that minimizes the distance between $u_k(t)$ and the reference profile. The results of the procedure are shown in Fig. 9(a), where white dots, indicating the pattern

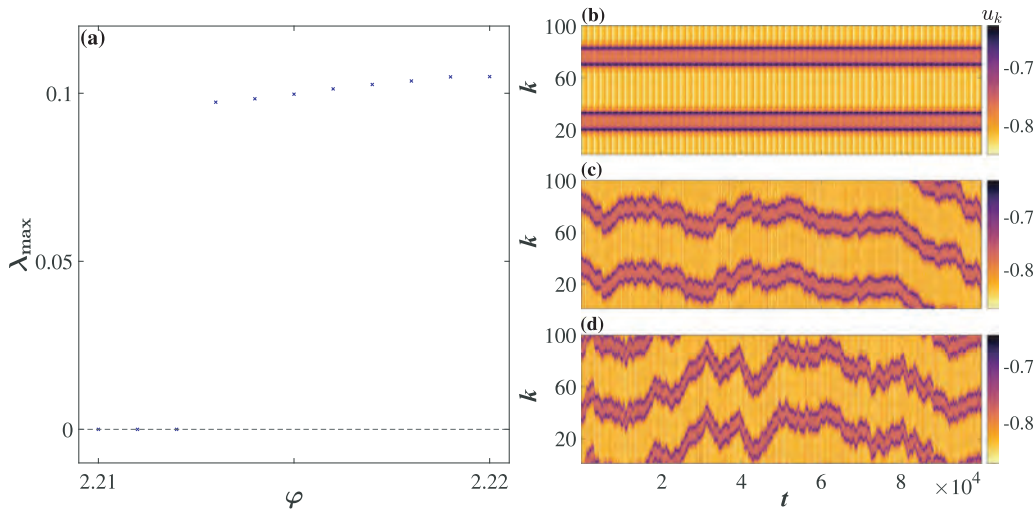


FIG. 8. Emergence of chaos and diffusion of interfaces for a wavenumber-2 pattern. (a) Dependence of maximal Lyapunov exponent with ϕ indicates the onset of chaos for $\phi \approx 2.213$. (b)–(d) Spatiotemporal evolution of $u_k(t)$ for a periodic pattern at $\phi = 2.21$ and chaotic patterns at $\phi = 2.22$ and $\phi = 2.23$, respectively. System parameters: $R = 40, \kappa = 0.4, a = 1.01, \varepsilon = 0.05, N = 100$.

position $\xi(t)$ after every $\tau = 400$ t.u., are plotted on top of the $u_k(t)$ heatmap. Note that the local time averages $\xi(t)$ are used to eliminate fast oscillations. In Fig. 9(b) are extracted the long-term (main-frame) and short-term (inset) motion of a single incoherent region, corresponding to a minority patch of the primary pattern bounded on both sides by the turbulent interface units. Similar to chimeras, the motion of interfaces providing the boundary of a minority region remains correlated such that the domain does not grow or shrink

with time. For a fixed sufficiently large time step τ , the histogram of the corresponding shifts in position $\Delta\xi$ can readily be fitted to a Gaussian distribution

$$p(\Delta\xi) = \frac{1}{\sqrt{2\pi}\sigma(\tau)} e^{-\frac{\Delta\xi^2}{2\sigma(\tau)^2}}, \quad (2)$$

see Fig. 9(c) for the case $\tau = 400$. Extracting in this way the variances $\sigma(\tau)$ for several values of τ , we demonstrate that they indeed follow

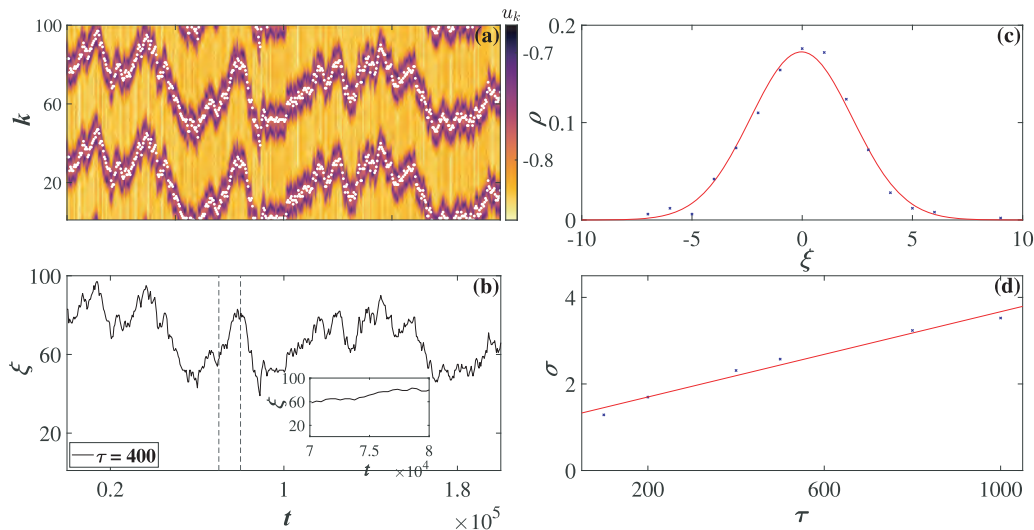


FIG. 9. (a) White dots: position of the pattern at every time step $\tau = 400$ t.u.; (b) shifts in position of a single incoherent region bounded by interfaces $\xi(t)$ over a long time horizon of 10^6 t.u. (mainframe) and over a short timescale (inset); (c) fit of a histogram of displacements $\Delta\xi$ to a Gaussian distribution for $\tau = 400$; (d) variance of Gaussian distributions σ as a function of time step τ . System parameters: $\phi = 2.23, R = 40, \kappa = 0.4, a = 1.01, \varepsilon = 0.05, N = 100$.

a linear dependence of the form $\sigma(\tau) = 2D\tau$, see Fig. 9(d), which can be used to determine the diffusion coefficient $D \approx 1.4 \times 10^{-4}$ of the corresponding Fokker–Planck equation.

V. SUMMARY AND DISCUSSION

We have presented patched patterns as a new class of self-organized patterns in coupled excitable systems with nonlocal attractive and repulsive interactions. Pattern formation involves a symmetry breaking, where an assembly of identical units with symmetrical interactions spontaneously splits into patches of frequency locked units, with the majority and minority patches displaying a 1:2 frequency resonance. We have demonstrated that in terms of temporal organization, patched patterns can be classified as periodic, quasiperiodic, or chaotic, whereby the former two are always static, while the latter may also show lateral diffusive motion. Apart from patches, chaotic patterns may also include interface units and feature chaotic itinerancy, characterized by a slow alternating activity between laminar epochs, where the unit is approximately locked to either of the neighboring patches, and turbulent epochs, with a fast switching between the orbits similar to local dynamics within the patches. We have explained the basic mechanism of self-organization of patched patterns as an interplay between self-localized excitations and propagation of excitations, the two phenomena classically observed in coupled excitable systems. Using standard chaos and bifurcation theory in finite-dimensional systems, we have disclosed the typical transition route from periodic solutions to chaos via quasiperiodicity as the coupling parameter φ is increased. There, chaos emerges from the torus breakup, and the onset of turbulent interfaces is associated with a secondary bifurcation. Nevertheless, the transition to chaos is further found to depend on the wavenumber of the primary pattern, which can be controlled by the coupling range. For sufficiently large coupling ranges admitting wavenumber-2 patterns, we have identified the second scenario of transition to chaos, where its emergence coincides with the formation of diffusive interfaces, explicitly shown to exhibit Brownian-like motion.

Patched patterns we have discovered bear a certain resemblance to coherence–incoherence patterns observed so far in coupled oscillators or coupled excitable systems, but also display considerable differences. In particular, patched patterns are different from bumps^{10,32,33,36} because the extensive chaos is spatially localized and the bulk units are stationary (inactive). Also, our patched patterns with interfaces are distinct from classical solitary states because the interface units are not isolated and randomly distributed, but rather form a spatially continuous profile. Distinct from the classical chimeras¹² in coupled phase oscillators, the maximal Lyapunov exponent for the patched patterns converges to a finite value instead of decaying with the system size, and at variance with the multi-headed chimeras,^{40,52} the frequency profile within all the patches is piecewise constant. Still, we note a certain similarity to some of the less conspicuous types of coherence–incoherence patterns observed in coupled oscillators. First, we recall the so-called chimera Ising walls in non-locally coupled Ginzburg–Landau oscillators with a parametric forcing.⁵³ There, the incoherent units also form interfaces connecting frequency-locked domains, but in contrast to our patched patterns, the domains at two sides of an interface are 1:1

frequency locked. Second, our class of solutions may be compared to oscillons,⁵⁴ which also involve a temporally modulated localized spiking activity, as in our minority patches, but such an activity is embedded on an inactive rather than a spiking background. The emergence of spatially incoherent interfaces has also been observed for the so-called mosaic or skeleton patterns in coupled maps,^{40,51,57} but the onset of spatial incoherence is not associated with temporal chaos in local dynamics. We note that the onset of an alternating activity similar to our interface units has been found for the so-called itinerant chimeras.⁵⁵ While this is also not a finite-size effect, it involves all the units within an array, rather than remaining spatially localized. Finally, a recent paper on theta-neuron oscillators mentions non-stationary patterns with the frequency profile similar to ours,³⁶ but instead of spiking, the majority units there are in the state of oscillation death.

The relation between the patched patterns and other types of coherence–incoherence patterns along the path from complete coherence to incoherence in coupled excitable systems requires further study. So far, there is only a partial result suggesting that the patched patterns coexist with solitary states in non-locally coupled arrays of FitzHugh–Nagumo units³⁷ and that the noise promotes patched patterns at the expense of solitary states. Such robustness of patched type of solutions relative to solitary states derives from their comparably larger basins of attraction. In terms of system's multistability, one also notes that the patched patterns per se may have different symmetry properties and that patterns with different wavenumbers and fractions of minority vs majority units may stably coexist. The patched patterns may further coexist with other types of solutions, such as rotating waves and modulated waves.

The presented results, together with Refs. 36 and 37, indicate that the study of self-organized coherence–incoherence patterns in coupled excitable systems opens up interesting new directions of research, revealing types of solutions that bear only a partial resemblance to those in coupled oscillators. An interesting problem would be to investigate these new types of solutions for models amenable to a rigorous analysis of the system behavior in the continuum limit. Also, in order to extend the comparison with coherence–incoherence patterns in coupled phase oscillators, it would be important to explicitly demonstrate the potentially extensive character of chaos for patched patterns with interfaces by calculating the corresponding Lyapunov spectrum. Another important problem for future research would be to understand in detail the scenario giving rise to primary periodic patched patterns with increasing coupling parameter φ . What makes this problem difficult to address is that their onset is not immediately related to the destabilization of the homogeneous stationary state, where all the units lie in the stable equilibrium of local dynamics. Under increasing φ , this state is destabilized around $\varphi = \pi/2$ because there the prevalence of attractive vs repulsive interactions changes such that the repulsive interactions begin to dominate.³⁷ Nevertheless, this factor alone does not give rise to patched patterns, and their onset is apparently related with the more complex patterns emerging from the secondary canard transitions. Therefore, disclosing the scenario by which solutions gain complexity under increasing coupling parameter φ , beginning from the initial homogeneous stationary state over intermediate spatially inhomogeneous states up to primary periodic patched patterns, would be an important step toward a more general

understanding of how the interplay between the repulsive interactions and canard transitions impacts pattern formation in coupled excitable systems.

ACKNOWLEDGMENTS

I.F. acknowledges funding from the Institute of Physics Belgrade through a grant by Ministry of Education, Science and Technological Development of Republic of Serbia.

AUTHOR DECLARATIONS

Conflict of Interest

The authors have no conflicts to disclose.

Author Contributions

Igor Franović: Conceptualization (equal); Data curation (equal); Formal analysis (equal); Funding acquisition (equal); Investigation (equal); Methodology (equal); Project administration (equal); Resources (equal); Software (equal); Supervision (equal); Validation (equal); Visualization (equal); Writing – original draft (equal). Writing – review & editing (equal). **Sebastian Eydam:** Conceptualization (equal); Data curation (equal); Formal analysis (equal); Funding acquisition (equal); Investigation (equal); Methodology (equal); Project administration (equal); Resources (equal); Software (equal); Supervision (equal); Validation (equal); Visualization (equal); Writing – review & editing (equal).

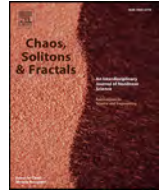
DATA AVAILABILITY

The data that support the findings of this study are available from the corresponding author upon reasonable request.

REFERENCES

- ¹Y. Kuramoto and D. Battogtokh, *Nonlinear Phenom. Complex Syst.* **5**, 380 (2002), available at <http://www.j-npcs.org/abstracts/vol2002/v5no4/v5no4p380.html>.
- ²D. M. Abrams and S. H. Strogatz, *Phys. Rev. Lett.* **93**, 174102 (2004).
- ³D. M. Abrams, R. Mirollo, S. H. Strogatz, and D. A. Wiley, *Phys. Rev. Lett.* **101**, 084103 (2008).
- ⁴A. Zakharova, *Chimera Patterns in Networks: Interplay Between Dynamics, Structure, Noise, and Delay—Understanding Complex Systems* (Springer Nature, Switzerland, 2020).
- ⁵F. Parastesh, S. Jafari, H. Azarnoush, Z. Shahriari, Z. Wang, S. Boccaletti, and M. Perc, *Phys. Rep.* **898**, 1 (2021).
- ⁶M. J. Panaggio and D. M. Abrams, *Nonlinearity* **28**, R67 (2015).
- ⁷S. W. Haugland, *J. Phys.: Complexity* **2**, 032001 (2021).
- ⁸O. E. Omel'chenko and E. Knobloch, *New J. Phys.* **21**, 093034 (2019).
- ⁹O. E. Omel'chenko, *Nonlinearity* **31**, R121 (2018).
- ¹⁰C. R. Laing, *Physica D* **240**, 1960 (2011).
- ¹¹O. E. Omel'chenko, *Nonlinearity* **26**, 2469 (2013).
- ¹²M. Wolfrum, O. E. Omel'chenko, S. Yanchuk, and Y. L. Maistrenko, *Chaos* **21**, 013112 (2011).
- ¹³M. Wolfrum and O. E. Omel'chenko, *Phys. Rev. E* **84**, 015201(R) (2011).
- ¹⁴O. E. Omel'chenko, M. Wolfrum, and Y. L. Maistrenko, *Phys. Rev. E* **81**, 065201(R) (2010).

- ¹⁵E. M. Izhikevich, *Dynamical Systems in Neuroscience: The Geometry of Excitability and Bursting* (MIT Press, Cambridge, MA, 2007).
- ¹⁶B. Lindner, J. García-Ojalvo, A. Neiman, and L. Schimansky-Geier, *Phys. Rep.* **392**, 321 (2004).
- ¹⁷I. Franović, S. Yanchuk, S. Eydam, I. Bačić, and M. Wolfrum, *Chaos* **30**, 083109 (2020).
- ¹⁸I. Franović, K. Todorović, M. Perc, N. Vasović, and N. Burić, *Phys. Rev. E* **92**, 062911 (2015).
- ¹⁹I. Franović, K. Todorović, N. Vasović, and N. Burić, *Phys. Rev. Lett.* **108**, 094101 (2012).
- ²⁰S. Alonso and M. Bär, *Phys. Rev. Lett.* **110**, 158101 (2013).
- ²¹S. Scialla, A. Loppini, M. Patriarca, and E. Heinsalu, *Phys. Rev. E* **103**, 052211 (2021).
- ²²J. P. Keener and J. Sneyd, *Mathematical Physiology* (Springer, New York, 2009).
- ²³Z. Wang, Z. Rostami, S. Jafari, F. E. Alsaadi, M. Slavinec, and M. Perc, *Chaos, Solitons Fractals* **128**, 229 (2019).
- ²⁴A. S. Mikhailov and K. Showalter, *Phys. Rep.* **425**, 79 (2006).
- ²⁵D. V. Alexandrov, I. A. Bashkirtseva, M. Crucifix, and L. B. Ryashko, *Phys. Rep.* **902**, 1 (2021).
- ²⁶S. Terrien, V. A. Pammi, B. Krauskopf, N. G. R. Broderick, and S. Barbay, *Phys. Rev. E* **103**, 012210 (2021).
- ²⁷A. Ceni, P. Ashwin, and L. Livi, *Cogn. Comput.* **12**, 330 (2019).
- ²⁸R. Rongge and M. A. Zaks, *Phys. Rev. E* **103**, 012206 (2021).
- ²⁹R. Rongge and M. A. Zaks, *Eur. Phys. J. Spec. Top.* **230**, 2717 (2021).
- ³⁰P. Ashwin and O. Burylko, *Chaos* **25**, 013106 (2015).
- ³¹M. Owen, C. Laing, and S. Coombes, *New J. Phys.* **9**, 378 (2007).
- ³²C. R. Laing, *Front. Comput. Neurosci.* **10**, 53 (2016).
- ³³C. R. Laing and O. E. Omel'chenko, *Chaos* **30**, 043117 (2020).
- ³⁴P. C. Bressloff, *J. Phys. A Math. Theor.* **45**, 033001 (2012).
- ³⁵K. Zhang, *J. Neurosci.* **16**, 2112 (1996).
- ³⁶I. Franović, O. E. Omel'chenko, and M. Wolfrum, *Phys. Rev. E* **104**, L052201 (2021).
- ³⁷I. Franović, S. R. Eydam, N. Semenova, and A. Zakharova, *Chaos* **32**, 011104 (2022).
- ³⁸N. Semenova, A. Zakharova, V. Anishchenko, and E. Schöll, *Phys. Rev. Lett.* **117**, 014102 (2016).
- ³⁹A. Zakharova, N. Semenova, V. Anishchenko, and E. Schöll, *Chaos* **27**, 114320 (2017).
- ⁴⁰I. Omelchenko, O. E. Omel'chenko, P. Hövel, and E. Schöll, *Phys. Rev. Lett.* **110**, 224101 (2013).
- ⁴¹S. M. Baer and T. Erneux, *SIAM J. Appl. Math.* **46**, 721 (1986).
- ⁴²I. Tsuda, *Chaos* **19**, 015113 (2009).
- ⁴³K. Kaneko and I. Tsuda, *Chaos* **13**, 926 (2003).
- ⁴⁴I. Tsuda and T. Umemura, *Chaos* **13**, 937 (2003).
- ⁴⁵I. Franović, O. E. Omel'chenko, and M. Wolfrum, *Chaos* **28**, 071105 (2018).
- ⁴⁶S. R. Eydam, I. Franović, and M. Wolfrum, *Phys. Rev. E* **99**, 042207 (2019).
- ⁴⁷M. Wolfrum, O. E. Omel'chenko, and J. Sieber, *Chaos* **25**, 053113 (2015).
- ⁴⁸T. Nomura and L. Glass, *Phys. Rev. E* **53**, 6353 (1996).
- ⁴⁹A. Pikovsky and A. Politi, *Lyapunov Exponents: A Tool to Explore Complex Dynamics* (Cambridge University Press, Cambridge, 2016).
- ⁵⁰G. Benettin, L. Galgani, and J.-M. Strelcyn, *Phys. Rev. A* **14**, 2338 (1976).
- ⁵¹I. Omelchenko, A. Zakharova, P. Hövel, J. Siebert, and E. Schöll, *Chaos* **25**, 083104 (2015).
- ⁵²Y. L. Maistrenko, A. Vasylenko, O. Sudakov, R. Levchenko, and V. L. Maistrenko, *Int. J. Bifurcat. Chaos* **24**, 1440014 (2014).
- ⁵³Y. Kawamura, *Phys. Rev. E* **75**, 056204 (2007).
- ⁵⁴H. Schmidt and D. Avitabile, *Chaos* **30**, 033133 (2020).
- ⁵⁵D. V. Kasatkin, V. V. Klinshov, and V. I. Nekorkin, *Phys. Rev. E* **99**, 022203 (2019).
- ⁵⁶O. Omel'chenko and C. R. Laing, *Proc. R. Soc. A* **478**, 20210817 (2022).
- ⁵⁷I. Omelchenko, Y. Maistrenko, P. Hövel, and E. Schöll, *Phys. Rev. Lett.* **106**, 234102 (2011).



Rate chaos and memory lifetime in spiking neural networks

Vladimir V. Klinshov^{a,b,**}, Andrey V. Kovalchuk^a, Igor Franović^c, Matjaž Perc^{d,e,f,g,*}, Milan Svetec^d

^a Institute of Applied Physics of the Russian Academy of Sciences, 46 Ulyanova Street, 603950 Nizhny Novgorod, Russia

^b Lobachevsky State University of Nizhny Novgorod, 23 Gagarin Avenue, 603022 Nizhny Novgorod, Russia

^c Scientific Computing Laboratory, Center for the Study of Complex Systems, Institute of Physics Belgrade, University of Belgrade, Pregrevica 118, 11080 Belgrade, Serbia

^d Faculty of Natural Sciences and Mathematics, University of Maribor, Koroška cesta 160, 2000 Maribor, Slovenia

^e Department of Medical Research, China Medical University Hospital, China Medical University, Taichung 404332, Taiwan

^f Alma Mater Europaea, Slovenska ulica 17, 2000 Maribor, Slovenia

^g Complexity Science Hub Vienna, Josefstädterstraße 39, 1080 Vienna, Austria

ARTICLE INFO

Article history:

Received 21 February 2022

Accepted 14 March 2022

Available online 25 March 2022

Keywords:

Rate chaos

Memory lifetime

Neural network

Spiking

Collective dynamics

ABSTRACT

Rate chaos is a collective state of a neural network characterized by slow irregular fluctuations of firing rates of individual neurons. We study a sparsely connected network of spiking neurons which demonstrates three different scenarios for the emergence of rate chaos, based either on increasing the synaptic strength, increasing the synaptic integration time, or clustering of the excitatory synaptic connections. Although all the scenarios lead to collective dynamics with similar statistical features, it turns out that the implications for the computational capability of the network in performing a simple delay task are strongly dependent on the particular scenario. Namely, only the scenario involving slow dynamics of synapses results in an appreciable extension of the network's dynamic memory. In other cases, the dynamic memory remains short despite the emergence of long timescales in the neuronal spike trains.

© 2022 The Authors. Published by Elsevier Ltd. This is an open access article under the CC BY license (<http://creativecommons.org/licenses/by/4.0/>).

1. Introduction

Patterns of spontaneous activity of cortical neurons are typically highly irregular [1–3], showing Poisson-like statistics of inter-spike intervals on short timescales [4,5] and firing rate fluctuations over longer timescales [5–11]. The classical theory accounting for the origin of neuronal irregular behavior invokes the paradigm of an approximate balance between strong excitation and inhibition which for the most time cancel each other out, leaving the network activity to be driven by fluctuations which intermittently interrupt the balanced conditions [12–20]. Asynchronous balanced states with irregular weakly correlated local activity have been observed in networks of realistic spiking neurons [21–24]. These states may be referred to as *homogeneous*, since the firing rates of all the neurons are approximately equal and stationary.

Nevertheless, introducing the balanced excitation-inhibition paradigm by itself does not resolve the second part of the variability problem, since it still does not explain how the networks of fast spiking

neurons may generate rate fluctuations over slow timescales. These fluctuations are a hallmark of the state typically called *rate chaos* or *heterogeneous state* [25,26] to describe both the temporal rate variability and the nonuniform distribution of rates over the neurons. The rate chaos was first observed in models of networks of rate neurons [27], having explicitly demonstrated the transition from regular to chaotic dynamics [28]. In contrast to that, the networks of spiking neurons in the thermodynamic limit are expected to be always chaotic [12]. Nevertheless, the question concerning the transition from the homogeneous to heterogeneous chaotic regime in spiking networks is still debated, and a potential physical explanation may be that above the transition, both the fluctuations in neuronal inputs and outputs become strongly colored [29]. Recently, much efforts have been made to understand the precise dynamical mechanisms underlying the rate chaos and its possible functional role for neural computations. Several scenarios leading to the onset of rate chaos in realistic networks of spiking neurons have been revealed. In particular, high variability and slow rate dynamics has been demonstrated in networks with clustered excitatory connections [15,30]. Highly heterogeneous chaotic states were shown to emerge in a sparse random network for strong synaptic couplings [25, 29]. Finally, a transition to rate chaos has been observed when the synaptic integration time becomes large compared to the characteristic times of neuronal dynamics [16,17].

Rate chaos is believed to play an important part in facilitating the complex computations unfolding in the brain [31–36], since it has

* Correspondence to: M. Perc, Faculty of Natural Sciences and Mathematics, University of Maribor, Koroška cesta 160, 2000 Maribor, Slovenia.

** Correspondence to: V.V. Klinshov, Institute of Applied Physics of the Russian Academy of Sciences, 46 Ulyanova Street, 603950 Nizhny Novgorod, Russia.

E-mail addresses: vladimir.klinshov@ipfran.ru (V.V. Klinshov), franovic@ipb.ac.rs (I. Franović), matjaz.perc@gmail.com (M. Perc).

been shown to support fluctuations over longer timescales, giving rise to slow neural activity associated with behavior, learning and memory. Chaotic spiking networks have already been successfully trained to perform computational tasks such as generating signals, classifying inputs or predicting nonlinear dynamics [37,60,61]. With this in mind, it is reasonable to assume that using heterogeneous rather than homogeneous chaotic states can improve the computational capabilities of the network. Indeed, many applications involve accumulating data over the timescales of seconds, which requires a comparatively long dynamic memory. In the present study we address the problem of whether the slow rate fluctuations observed in the heterogeneous chaotic state may provide the basis for such a dynamic memory.

As our basic model, in Section 2 we introduce a network of theta neurons with random sparse connectivity which is initially is set to a homogeneous state with stationary local firing rates and the Poisson-like uncorrelated spike trains of individual neurons. In Section 3, we demonstrate that by varying certain macroscopic control parameters, one may induce the transition to a heterogeneous chaotic regime (rate chaos) featuring slowly fluctuating firing rates. In particular, we consider three generic scenarios for such a transition, involving i) strengthening of the synapses, ii) slowing the dynamics of synapses and iii) clustering of excitatory connections. Remarkably, the spike trains and their statistics appear quite similar for all three scenarios. In Section 4, we investigate whether our system in the state of rate chaos may be applied as a dynamic memory network [38,39], intended to perform a simple delay task by preserving the input history within its internal state. The network is considered in a reservoir setting [40,41], whereby its dynamical state serves as a representation of the input stimuli and the desired response is extracted via a linear readout of output nodes. The maximal delay for which the task is fulfilled with satisfactory precision is used to estimate the dynamic memory lifetime. Surprisingly, the network performance shows a striking dependence on the method by which the transition to heterogeneous state is induced. We will show that the network's dynamic memory extends appreciably only for the scenario based on slow synapses, but remains virtually unchanged compared to that in a homogeneous state if the rate chaos is induced by strong synapses or clustered connections.

2. Model

Our main model is a network of N theta neurons [42,43] whose dynamics is given by

$$\frac{d\theta_j}{dt} = (1 - \cos \theta_j) + (1 + \cos \theta_j)I_j, \quad (1)$$

where $\theta_j \in S^1, j = 1, 2, \dots, N$ are the local phase variables related to the respective membrane voltages by $V_j = \tan(\theta_j/2)$. The input currents I_j comprise of two terms $I_j = I_b + s_j$, whereby I_b denotes the constant bias current and s_j is the synaptic current. The SNIPER bifurcation at $I_j = 0$ mediates between the excitable ($I_j < 0$) and oscillatory regime ($I_j > 0$). A neuron j is said to have fired a spike when its phase crosses the value $\theta_j = \pi$. The spikes are filtered by double exponential synapses of the form

$$\frac{dr_j}{dt} = -\frac{r_j}{\tau_d} + h_j, \quad (2)$$

$$\frac{dh_j}{dt} = -\frac{h_j}{\tau_r} + \frac{1}{\tau_r \tau_d} \sum_p \delta(t - t_j^p), \quad (3)$$

which can account for the separate timescales of the rapid neurotransmitter binding followed by their slow unbinding [44]. The parameters τ_r and τ_d denote the synaptic rise and decay times, respectively, r_j is the synaptic output current, and t_j^p denote the firing times of neuron j . The total synaptic current received by neuron j is given by

$$s_j = g \sum_{k=1}^N A_{jk} r_k, \quad (4)$$

where g is the coupling strength and A_{jk} are the elements of the adjacency matrix determining the structure of the synaptic connections. Note that the described model (1)–(4) with some modifications will provide for the reservoir within the computational framework elaborated in Section 4.

First we consider a sparse random network with the connectivity probability $p = 0.1$. For simplicity, we do not divide the neurons into excitatory and inhibitory pools and draw the coupling strength of each nonzero connection from the Gaussian distribution with a zero mean and a variance $(Np)^{-1}$. Together with a slightly negative bias current $I_b = -0.001$, this ensures the balance between excitation and inhibition [12,45], such that the overall network activity is fluctuation-driven rather than mean-driven [46].

To study the collective dynamics of the network, we have excited 10 arbitrary neurons and have simulated the network activity for $t = 20$ s. The synaptic rise and decay time constants are fixed to $\tau_r = 2$ ms and $\tau_d = 20$ ms, and the coupling strength g is used as the control parameter. One finds that if the coupling strength exceeds a certain critical value g_c , the chaotic self-sustained activity emerges from the quiescent state. Indeed, for weak couplings $g < g_c$, an elevated network activity observed upon stimulation is only transient and dies out in several seconds. The precise value of critical coupling strength g_c depends on the bias current and equals $g_c \approx 0.27$ for the chosen parameter set. For the coupling strengths slightly above the threshold, the network activity is sparse, irregular and weakly correlated, as illustrated in Fig. 1 for $g = 0.3$. The spike trains of individual neurons are sub-Poissonian with the assembly-averaged firing rate 3.74 ± 1.24 Hz, and the respective distributions of inter-spike intervals characterized by the mean coefficient of variation 0.81 ± 0.13 , see Fig. 1d) and e). Weak correlation between the outputs of different neurons is evinced by the average cross-correlation coefficient 0.002 ± 0.047 , see Fig. 1f). The assembly-averaged autocorrelation function of individual neurons quickly decays at time lags ~ 50 ms that are of the order of the characteristic synaptic time, cf. Fig. 1c), indicating an absence of any longer timescales in local neuronal dynamics.

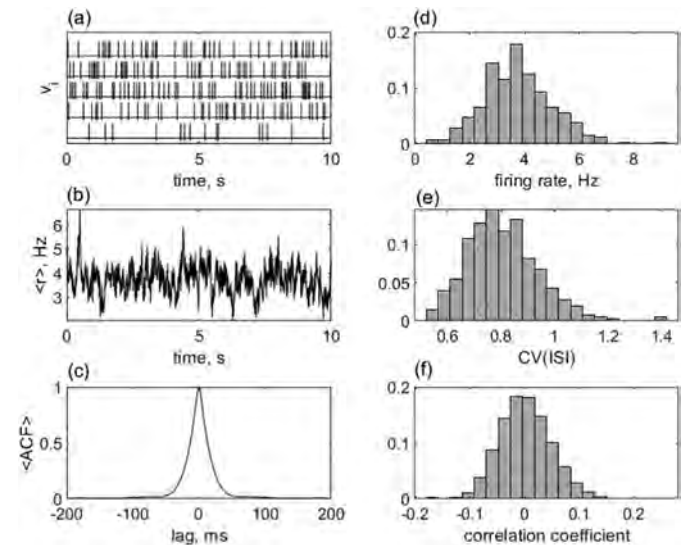


Fig. 1. Homogeneous state of the network. (a) Spike trains of five randomly selected neurons; (b) Average activity of the network $\langle r \rangle = 1/N \sum_{j=1}^N r_j$; (c) Averaged autocorrelation function of neurons; (d) Distribution of the local firing rates. (e) Distribution of coefficients of variation of neuronal inter-spike intervals. (f) Distribution of cross-correlation coefficients between neuronal inter-spike intervals. Network parameters: $N = 400, p = 0.1, \tau_r = 2$ ms, $\tau_d = 20$ ms, $g = 0.3$.

3. Three scenarios for transition to rate chaos

Further increase of the coupling strength results in the significant changes of the network state which is illustrated in Fig. 2 for $g = 1$. The stronger coupling not only increases the mean firing rate to 18.14 ± 6.96 Hz, but also induces a transition to the so-called rate chaos or heterogeneous state [25,29], where the firing rates of neurons exhibit slow fluctuations. At the level of spiking dynamics, the signature effect is that the neurons tend to generate bursts of spikes alternating with long periods of quiescence. Strong variability of spike trains is corroborated in Fig. 2e), which indicates large coefficients of variation of the inter-spike intervals, whose mean value 1.63 ± 0.30 is substantially supra-Poissonian. The emergence of bursting dynamics is also reflected in the shape of the assembly-averaged autocorrelation function, which now decays at longer lags ~ 400 ms, corresponding to a typical duration of a burst, see Fig. 2c). Also note that in the heterogeneous regime, the dynamics of individual neurons becomes more correlated compared to the homogeneous state, cf. Fig. 2f), as corroborated by the value 0.002 ± 0.16 for the mean correlation coefficient of individual spike trains.

In Fig. 3 are provided the dependencies of certain characteristics of the network dynamics on the coupling strength g . Although for $g = g_c$ the onset of chaotic spiking from quiescence is sudden, the transition from the homogeneous to heterogeneous irregular activity is a rather smooth one. In particular, the average firing rates illustrated in Fig. 3a) show a steady growth, and the coefficient of variation of neuronal inter-spike intervals increases almost linearly with coupling strength, see Fig. 3b). Similarly, the average correlation time displays small values $\sim \tau_d$ for weak coupling and increases to hundreds of milliseconds in case of strong coupling, cf. Fig. 3c). Note that the activity always remains non-uniform over the neurons with the standard deviation of local firing rates being of the same order as their mean values.

Apart from increasing the coupling strength, another scenario previously reported to induce transition to rate chaos is based on increasing the characteristic synaptic time [16,17]. To test for such a scenario in our model, we keep the coupling strength fixed at $g = 0.5$ and vary the synapse decay time τ_d . The results in Fig. 4 reveal that slowing down the synapses indeed induces the transition to heterogeneous irregular activity. Although the average firing rate does not change appreciably and equals ≈ 8 Hz for any $\tau_d > 20$ ms, see Fig. 4a), the mean coefficient of variation for the inter-spike intervals in Fig. 4b) visibly grows with synaptic time. The correlation time also shows a significant increase, reaching values larger than 600 ms for $\tau_d > 60$ ms, see Fig. 4c). The features of heterogeneous irregular activity observed for

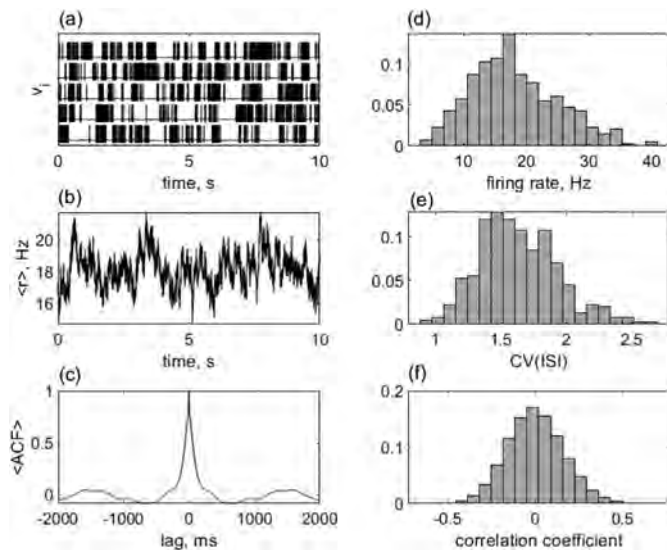


Fig. 2. Heterogeneous state of the network with strong synapses. Presentation style and the network parameters are the same as in Fig. 1, except for the coupling strength $g = 1$.

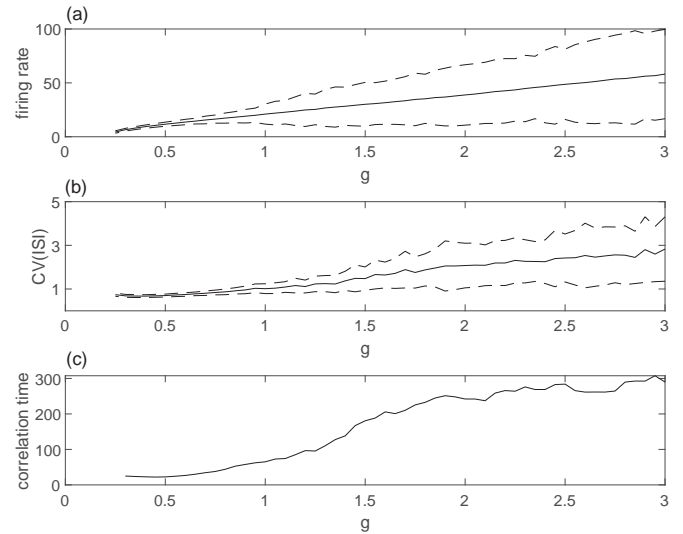


Fig. 3. Statistical features of network dynamics in dependence of coupling strength g . (a) Average firing rate of neurons (solid line) plus/minus its standard deviation (dashed lines). (b) Average coefficient of variation (solid line) plus/minus its standard deviation (dashed lines). (c) Average correlation time of the spike trains.

slow synapses are similar to those in case of strong couplings except that the overall network activity $r = \langle r_i \rangle$ shows slower fluctuations, see Fig. S1 of the Supplementary material.

So far we have considered only networks with a random connection topology. However, real cortical microcircuits are highly non-random [47–49], and the statistically nonuniform network structure may itself induce heterogeneous activity. For example, clustering of synaptic connections was shown to give rise to slow fluctuations of firing rates and high variability of spike trains [15,30,50,51]. In our model, it turns out that clustering of *all* connections does not result in a significant change of the network activity. However, clustering of *excitatory* (positive) connections alone yields a notable effect. To introduce clustering, we divide the network into $M = 5$ equal groups and rewire the excitatory connections in such a way that the connectivity inside each group p_{in} becomes larger than the connectivity between the groups p_{out} . The clustering coefficient $R = p_{in}/p_{out}$ is introduced to measure the degree of clustering, whereby the value $R = 1$ corresponds to a homogeneous

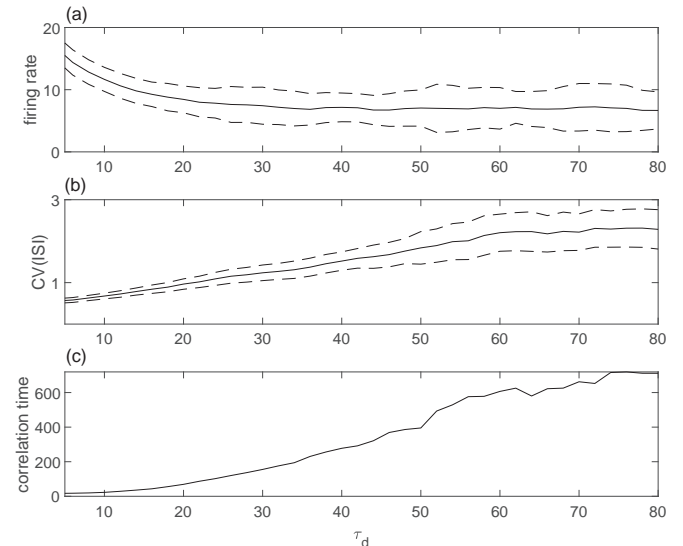


Fig. 4. Statistical features of network dynamics in terms of the synaptic decay time τ_d . Presentation style is the same as in Fig. 3.

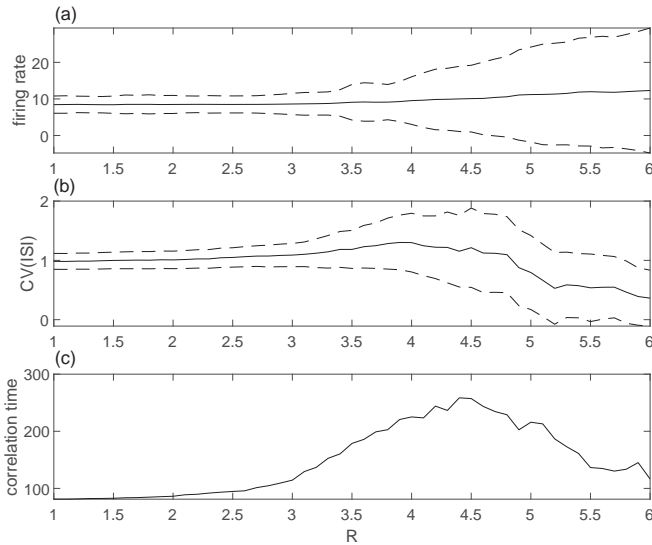


Fig. 5. Statistical features of network dynamics in terms of clustering coefficient R . Presentation style is the same as in Fig. 3.

random network. Note that the described rewiring scheme preserves the total network connectivity $p = p_{in}/M + p_{out}(1 - 1/M)$.

Fig. 5 shows the characteristics of the network dynamics depending on the clustering degree R . Note that due to the small size of clusters, the network dynamics significantly depends on the particular realization of the connectivity matrix, and the results we present were obtained by averaging over 20 different network configurations. Though the average firing rates in Fig. 5a) do not show much variation with R , one still notes the onset of heterogeneous activity and the highest variability at an intermediate clustering degree $R \sim 4$. While the mean coefficient of variation exceeds 1 only slightly, its standard deviation is about the same, see Fig. 5b), which indicates that there is a significant number of neurons with $CV \approx 2$ and larger. The mean correlation time also peaks at intermediate clustering degrees and reaches several hundreds of milliseconds, see Fig. 5c). The manifestation of heterogeneous irregular activity for networks with intermediate clustering is similar to the two previous scenarios. Namely, the neurons tend to generate bursts of spikes rather than isolated spikes, while the spike trains of different neurons remain weakly correlated. Note however that the local spiking rates, as coarse-grained quantities, tend to become correlated within the clusters, which induces pronounced slow fluctuations of the cluster activities, see Fig. S2 of the Supplementary material.

For larger clustering degrees, the local imbalance between the excitation and inhibition becomes too strong and one of the clusters typically settles into a regime of mean-driven activity with fast and regular spiking, cf. Fig. S3 of the Supplementary material. At the same time, this cluster tends to inhibit and synchronize other clusters, suppressing the irregular activity. Note that the time-averaged activity of neurons becomes quite diverse in this regime because of the high firing rate of the active cluster and low firing rates of the other ones.

4. Computational capabilities of the network

After the detailed study of the network dynamics, we investigate the relation between its intrinsic activity and computational capabilities, in particular its ability to serve as a dynamic memory network [38,39]. This recently introduced concept involves creating of networks optimized for question-answering problems, whereby the network processes the input, forms an episodic memory and generates the relevant output. Here, we train the network to perform a simple computational delay task defined as follows: the network receives a single input in the form of a spike train and has to indicate whether it has received or not

a spike within the period of a given duration. In particular, the network should respond by “1” if it has received at least one spike within the last τ milliseconds and by “0” otherwise. The maximum value of the delay τ at which the network shows a sufficient accuracy provides a reasonable estimate for its dynamic memory lifetime.

As an input signal, we use a Poisson spike train with the rate $\lambda = 1$ Hz. To feed the input into the network, the signal (4) received by each neuron is modified to

$$S_j = g \sum_{k=1}^N A_{jk} r_k + g_{inp} u_j r_{inp}, \quad (5)$$

where g_{inp} is the input gain, the weights u_j are drawn independently from a uniform random distribution $[-1; 1]$, and r_{inp} is the input synaptic current given by the same set of equations as Eqs. (2) and (3). The output of the network is calculated as

$$r_{out} = \sum_{j=1}^N w_j r_j, \quad (6)$$

having tuned the output weights w_j to train the network to perform the required task. The network response counts as “1” if its output exceeds $1/2$ and as “0” otherwise.

The described approach conforms to the classical computational framework of reservoir computing [40,52], a machine learning method derived from liquid-state and echo-state machines [53,54] to solve tasks using the response of a dynamical system, called a reservoir, to a certain input, having the output generated by linearly combining the states of the readout nodes. Reservoir computing has the advantage of an efficient training process, since only the readout weights affecting the output are trained, while the input weights and the weights within the reservoir remain unchanged [41]. In training the output weights w_j , we have used the method of least squares or the recursive least square algorithm [55]. Both methods turned out to provide similar results, and we preferred the least squares method for being the faster of the two. After a certain training period t_{train} , the network’s performance was estimated during the test period $t_{test} = 100$ s, see Fig. 6. To characterize the network performance, we have measured the error

$$\varepsilon = \varepsilon_0 \nu_0 + \varepsilon_1 \nu_1, \quad (7)$$

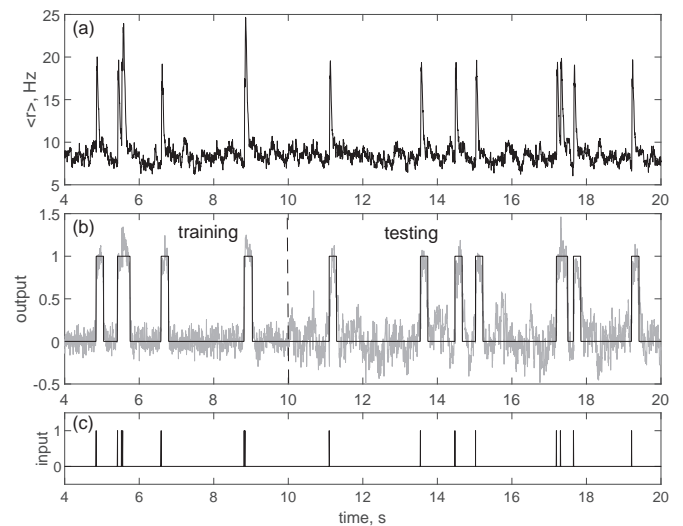


Fig. 6. Training the network and testing its performance. (a) Time trace of the average network activity; (b) Network output (gray) and the desired output (black); (c) The input signal.

where ν_0 and ν_1 are the rates of the false output being equal to zero or one, respectively, and ε_0 and ε_1 are the error weights set such that a constant output of either zero or one leads to a total error $\varepsilon = 1$. The network performance P is then estimated as the inverse of the error $P = 1/\varepsilon$.

One observes that the resulting performance improves with the increase of the training time and reaches maximum after several tens of seconds, see Fig. S4 of the Supplementary material. In our numerical experiments, we have used the training time of $t_{train} = 100$ s which warrants an optimal network performance. One also notes an important role of the input gain g_{inp} for the network performance. In particular, if g_{inp} is too small, the input signal fails to suppress the chaotic activity, resulting in a poor network performance. Thus, the input gain has to be sufficiently strong, but at the other hand, its excessive increase does not further a significant improvement in the network performance, see Fig. S5 of the Supplementary material. With this in mind, we have fixed $g_{inp} = 10$ in all the numerical experiments considered below.

To address the problem of enhancing the dynamic memory lifetime of the network, we have trained it to perform the delay task for different values of the delay τ and have analyzed the performance P . The results presented in Fig. 7 show the performance in terms of delay for several different network configurations. In particular, we have started from the network with weak and fast synapses and no clustering of connections ($g = 0.5$, $\tau_d = 20$, $R = 1$), which admits a *homogeneous* state. The optimal performance $P \approx 15$ is reached for the delay $\tau \approx 200$ ms. For small delays $\tau < 100$ ms, the network performance is poor since it does not have enough time to respond to the stimulus. For large delays, the performance quickly drops and reaches a half of the maximal value at $\tau \approx 500$ ms. This indicates that the dynamic memory of the network lasts about 0.2 s.

Next, we increased the strength of the synapses to $g = 2$ and checked whether it would improve the network performance. For such a strong coupling, the spike trains demonstrate a much longer correlation time of about 250 ms, see Fig. 3b), which would intuitively suggest a much longer dynamic memory. Surprisingly, however, the strengthening of the synapses changed the network performance only by a small margin, and the observed dynamic memory was still about 0.25 s. We have also studied the influence of clustering with $R = 4$, the value corresponding to the maximal correlation time of about 230

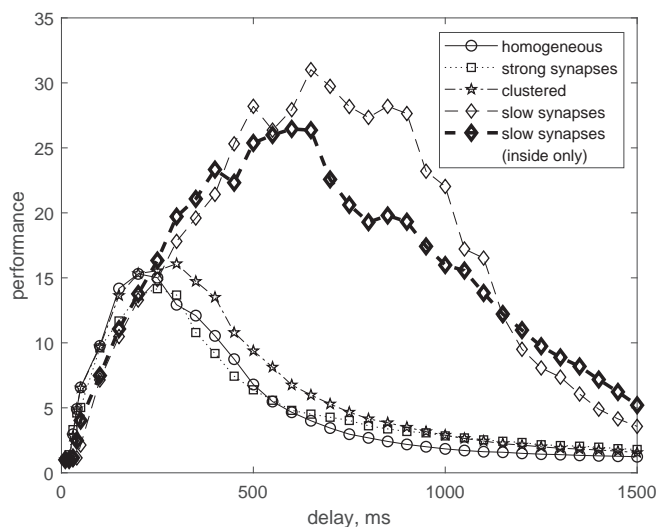


Fig. 7. Performance of the network P in terms of the delay τ . Solid line with circles: network in a homogeneous state; dotted line with squares: network with strong synapses ($g = 2$); dash-dotted line with stars: network with clustered connections ($R = 4$); dashed line with diamonds: network with slow synapses ($\tau_d = 60$ ms); thick dashed line with diamonds: network with slow internal synapses ($\tau_d = 60$ ms) but fast input synapses ($\tau_{d,inp} = 20$ ms).

ms, see Fig. 4b). This has led to a slightly improved network performance, which becomes optimal for $\tau = 300$ ms and drops twice at $\tau = 600$ ms. Thus, the dynamic memory lifetime in a clustered network increases only slightly compared to the network in the homogeneous state and reaches 0.3 s.

Finally, we have considered the scenario involving slow synapses by having increased the synaptic decay time to $\tau_d = 60$ ms. This approach has impacted most profoundly on the dynamic memory of the network. We have found that the network performance has indeed substantially improved, with the flat maximum $P \approx 30$ reached at the wide interval $\tau = 500 - 1000$ ms. For larger delays, the network performance quickly deteriorates, such that the network's dynamic memory can be estimated as 1 s. We have also checked whether the extension of dynamic memory may be caused by the change of stimulus itself, since for longer synaptic times it comprises longer pulses. To do so, we have decreased the decay time of the *input* synapses only to $\tau_d = 20$ ms and kept the *internal* synapses with $\tau_d = 60$ ms, observing that the network performance has marginally decreased but has still substantially outperformed the network with fast synapses. Indeed, the dynamic memory lifetime in this case is still about 1 s.

5. Discussion and conclusions

We have considered three different scenarios for the onset of rate chaos in a sparse network of spiking neurons and have examined their implications for the computational capability of the network to perform a simple dynamic memory task. The signature of rate chaos are the slow rate fluctuations of individual neurons, which introduce characteristic timescales longer than the one associated with the spike timing dynamics. Three generic scenarios of transition to rate chaos were considered. The first scenario involves strengthening of the synaptic coupling, the second one relies on slowing the dynamics of synapses, whereas the third one is observed when a certain degree of clustering is applied to synaptic connections. Though all three scenarios have been reported previously, they were still considered separately for different network models, and the present study provides for the first time a universal model where all the scenarios can be observed and compared by changing different system parameters, such as the coupling strength, the synaptic decay time and the clustering degree.

At the microscopic level of individual neuronal spike trains, all the three scenarios have been shown to yield very similar features. Nevertheless, the computational capabilities of the underlying regimes turned out to be quite different, at least in performing simple delay-related tasks. We have demonstrated that the dynamic memory of the network in the heterogeneous state depends significantly on the mechanism giving rise to this state. Namely, for scenarios involving strong synapses or clustering of connections, the duration of dynamic memory remains approximately the same as in the homogeneous state. Contrasting that, the scenario involving the slow synapses leads to a substantial increase in the duration of dynamic memory, found to reach values above 1 s.

Identifying mechanisms that allow cortical networks to perform computational tasks on the timescales of seconds while the local neuronal activity unfolds on the timescales of milliseconds has been a long-standing problem in neuroscience [10,29,56–58]. It has already been shown that merely increasing the network size has very little impact on the memory lifetime since it scales only as the logarithm of the network size [59]. Thus, the underlying problem has to be resolved in terms of finding an appropriate mechanism that endows the network dynamics with long timescales. Our study nevertheless indicates an additional subtlety in the sense that the mere presence of longer timescales in the spike trains may not warrant longer memory lifetimes.

We emphasize that our findings should by no means be interpreted as questioning the general usefulness of heterogeneous chaotic states as a substrate for computation in networks of spiking neurons. Such states have already been shown beneficial for complex computational tasks including decision-making, categorization or associative memory [25,

32,33,35,36]. Our results rather imply that spiking networks in a state of rate chaos are not optimal candidates for dynamic memory networks, so that finding a more suitable paradigm is required to carry out computations involving an extended temporal memory.

CRedit authorship contribution statement

V.V.K., A.V.K., I.F., M.P., and M.S. designed and performed the research as well as wrote the paper.

Declaration of competing interest

The authors declare that they have no known competing financial interests or personal relationships that could have appeared to influence the work reported in this paper.

Acknowledgment

The research was supported by the Russian Science Foundation (Grant No. 19-72-10114). The authors thank Oleg Maslennikov for fruitful discussions during the various stages of the study.

Appendix A. Supplementary data

Supplementary data to this article can be found online at <https://doi.org/10.1016/j.chaos.2022.112011>.

References

- [1] Abeles M. *Corticonics: neural circuits of the cerebral cortex*. Cambridge University Press; 1991.
- [2] Bair W, Koch C, Newsome W, Britten K. Power spectrum analysis of bursting cells in area MT in the behaving monkey. *J Neurosci*. 1994;14(5 Pt 1):2870–92. <https://doi.org/10.1523/jneurosci.14-05-02870.1994>.
- [3] Softky WR, Koch C. The highly irregular firing of cortical cells is inconsistent with temporal integration of random EPSPs. *J Neurosci*. 1993;13(1):334–50. <https://doi.org/10.1523/jneurosci.13-01-00334.1993>.
- [4] Churchland MM, Yu BM, Ryu SI, Santhanam G, Shenoy KV. Neural variability in premotor cortex provides a signature of motor preparation. *J Neurosci*. 2006;26:3697–712. <https://doi.org/10.1523/JNEUROSCI.3762-05.2006>.
- [5] Churchland MM, Byron MY, Cunningham JP, et al. Stimulus onset quenches neural variability: a widespread cortical phenomenon. *Nat Neurosci*. 2010;13:369–78. <https://doi.org/10.1038/nn.2501>.
- [6] Kohn A, Smith MA. Stimulus dependence of neuronal correlation in primary visual cortex of the macaque. *J Neurosci*. 2005;25(14):3661–73. <https://doi.org/10.1523/JNEUROSCI.5106-04.2005>.
- [7] Churchland AK, Kiani R, Chaudhuri R, Wang X-J, Pouget A, Shadlen MN. Variance as a signature of neural computations during decision making. *Neuron*. 2011;69(4):818–31. <https://doi.org/10.1016/j.neuron.2010.12.037>.
- [8] Smith M, Kohn A. Spatial and temporal scales of neuronal correlation in primary visual cortex. *J Neurosci*. 2008;28:12591–603. <https://doi.org/10.1523/JNEUROSCI.2929-08.2008>.
- [9] Churchland M, Abbott L. Two layers of neural variability. *Nat Neurosci*. 2012;15:1472–4. <https://doi.org/10.1038/nn.3247>.
- [10] Murray J, Bernacchia A, Freedman D, et al. A hierarchy of intrinsic timescales across primate cortex. *Nat Neurosci*. 2014;17:1661–3. <https://doi.org/10.1038/nn.3862>.
- [11] Klinshov V, Franović I. Slow rate fluctuations in a network of noisy neurons with coupling delay. *EPL*. 2016;116(4):48002. <https://doi.org/10.1209/0295-5075/116/48002>.
- [12] van Vreeswijk C, Sompolinsky H. Chaos in neuronal networks with balanced excitatory and inhibitory activity. *Science*. 1996;274(5293):1724–6. <https://doi.org/10.1126/science.274.5293.1724>.
- [13] Hansel D, Mato G. Asynchronous states and the emergence of synchrony in large networks of interacting excitatory and inhibitory neurons. *Neural Comput*. 2003;15(1):1–56. <https://doi.org/10.1162/089976603321043685>.
- [14] Renart A, De La Rocha J, Bartho P, Hollender L, Parga N, Reyes A, Harris KD. The asynchronous state in cortical circuits. *Science*. 2010;327(5965):587–90. <https://doi.org/10.1126/science.1179850>.
- [15] Litwin-Kumar A, Doiron B. Slow dynamics and high variability in balanced cortical networks with clustered connections. *Nat Neurosci*. 2012;15(11):1498–505. <https://doi.org/10.1038/nn.3220>.
- [16] Kadmon J, Sompolinsky H. Transition to chaos in random neuronal networks. *Phys Rev X*. 2015;5:041030. <https://doi.org/10.1103/PhysRevX.5.041030>.
- [17] Harish O, Hansel D. Asynchronous rate chaos in spiking neuronal circuits. *PLoS Comput Biol*. 2015;11(7):1–38. <https://doi.org/10.1371/journal.pcbi.1004266>.
- [18] Ullner E, Politi A, Torcini A. Ubiquity of collective irregular dynamics in balanced networks of spiking neurons. *Chaos*. 2018;28(8):81106. <https://doi.org/10.1063/1.5049902>.
- [19] Hayakawa T, Fukai T. Spontaneous and stimulus-induced coherent states of critically balanced neuronal networks. *Phys Rev Res*. 2020;2(1):013253. <https://doi.org/10.1103/PhysRevResearch.2.013253>.
- [20] Di Volo M, Segneri M, Goldobin D, Politi A, Torcini A. Coherent oscillations in balanced neural networks driven by endogenous fluctuations. *Chaos*. 2022;32:023120. <https://doi.org/10.1063/5.0075751>.
- [21] Amit DJ, Brunel N. Dynamics of a recurrent network of spiking neurons before and following learning. *Netw Comput Neural Syst*. 1997;8(4):373–404. https://doi.org/10.1088/0954-898X_8_4_003.
- [22] Amit DJ, Brunel N. Model of global spontaneous activity and local structured activity during delay periods in the cerebral cortex. *Cereb Cortex*. 1997;7(3):237–52. <https://doi.org/10.1093/cercor/7.3.237>.
- [23] Brunel N. Dynamics of sparsely connected networks of excitatory and inhibitory spiking neurons. *J Comput Neurosci*. 2000;8(3):183–208. <https://doi.org/10.1023/A:1008925309027>.
- [24] Teramae J-N, Tsubo Y, Fukai T. Optimal spike-based communication in excitable networks with strong-sparse and weak-dense links. *Sci Rep*. 2012;2:485. <https://doi.org/10.1038/srep00485>.
- [25] Ostojic S. Two types of asynchronous activity in networks of excitatory and inhibitory spiking neurons. *Nat Neurosci*. 2014;17(4):594–600. <https://doi.org/10.1038/nn.3658>.
- [26] Mastrogiuseppe F, Ostojic S. Intrinsically-generated fluctuating activity in excitatory-inhibitory network. *PLoS Comput Biol*. 2017;13:e1005498. <https://doi.org/10.1371/journal.pcbi.1005498>.
- [27] Sompolinsky H, Crisanti A, Sommers H-J. Chaos in random neural networks. *Phys Rev Lett*. 1988;61(3):259. <https://doi.org/10.1103/PhysRevLett.61.259>.
- [28] Crisanti A, Sompolinsky H. Path integral approach to random neural networks. *Phys Rev E*. 2018;98:062120. <https://doi.org/10.1103/PhysRevE.98.062120>.
- [29] Wieland S, Bernardi D, Schwalger T, Lindner B. Slow fluctuations in recurrent networks of spiking neurons. *Phys Rev E*. 2015;92:040901. <https://doi.org/10.1103/PhysRevE.92.040901>.
- [30] Doiron B, Litwin-Kumar A. Balanced neural architecture and the idling brain. *Front Comput Neurosci*. 2014;82:011903. <https://doi.org/10.3389/fncom.2014.00056>.
- [31] Jaeger H, Haas H. Harnessing nonlinearity: predicting chaotic systems and saving energy in wireless communication. *Science*. 2004;304(5667):78–80. <https://doi.org/10.1126/science.1091277>.
- [32] Sussillo D, Abbott LF. Generating coherent patterns of activity from chaotic neural networks. *Neuron*. 2009;63(4):544–57. <https://doi.org/10.1016/j.neuron.2009.07.018>.
- [33] Toyozumi T, Abbott LF. Beyond the edge of chaos: amplification and temporal integration by recurrent networks in the chaotic regime. *Phys Rev E*. 2011;84(5):51908. <https://doi.org/10.1103/PhysRevE.84.051908>.
- [34] Laje R, Buonomano DV. Robust timing and motor patterns by taming chaos in recurrent neural networks. *Nat Neurosci*. 2013;16(7):925–33. <https://doi.org/10.1038/nn.3405>.
- [35] Buonomano D, Maass W. State-dependent computations: spatiotemporal processing in cortical networks. *Nat Rev Neurosci*. 2009;10:113–25. <https://doi.org/10.1038/nrn2558>.
- [36] Rubin R, Abbott LF, Sompolinsky H. Balanced excitation and inhibition are required for high-capacity, noise-robust neuronal selectivity. *PNAS*. 2017;114:E9366–75. <https://doi.org/10.1073/pnas.1705841114>.
- [37] Nicola W, Clopath C. Supervised learning in spiking neural networks with FORCE training. *Nat Commun*. 2017;8(1):1–15. <https://doi.org/10.1038/s41467-017-01827-3>.
- [38] Kumar A, Irsay O, Ondruska P. Ask me anything: dynamic memory networks for natural language processing. In: Balcan MF, Weinberger KQ, editors. Proceedings of the 33rd international conference on machine learning, New York, USA; 2016. p. 1378–87.
- [39] Xiong C, Merity S, Socher R. Dynamic memory networks for visual and textual question answering. In: Balcan MF, Weinberger KQ, editors. Proceedings of the 33rd international conference on machine learning, New York, USA; 2016. p. 2397–406.
- [40] Nakajima K, Fischer I. Reservoir computing: theory, physical implementations, and applications. New York, USA: Springer; 2001.
- [41] Tanaka G, Yamane T, Héroux JB, et al. Recent advances in physical reservoir computing: a review. *Neural Netw*. 2019;115:100–23. <https://doi.org/10.1016/j.neunet.2019.03.005>.
- [42] Luke TB, Barreto E, So P. Complete classification of the macroscopic behavior of a heterogeneous network of theta neurons. *Neural Comput*. 2013;25(12):3207–34. https://doi.org/10.1162/NECO_a_00525.
- [43] Laing CR. Derivation of a neural field model from a network of theta neurons. *Phys Rev E*. 2014;90. <https://doi.org/10.1103/PhysRevE.90.010901>, 010901(R).
- [44] Roth A, van Rossum MC. Modeling synapses. In: Schutter E De, editor. Computational modeling methods for neuroscientists. Cambridge, Massachusetts: MIT Press; 2010. p. 139–60.
- [45] van Vreeswijk C, Sompolinsky H. Chaotic balanced state in a model of cortical circuits. *Neural Comput*. 1998;10(6):1321–71. <https://doi.org/10.1162/089976698300017214>.
- [46] Renart A, Moreno-Bote R, Wang X-J, Parga N. Mean-driven and fluctuation-driven persistent activity in recurrent networks. *Neural Comput*. 2007;19(1):1–46. <https://doi.org/10.1162/neco.2007.19.1.1>.
- [47] Song S, Sjöström PJ, Reigl M, Nelson S, Chklovskii DB. Highly nonrandom features of synaptic connectivity in local cortical circuits. *PLoS Biol*. 2005;3(3):e68. <https://doi.org/10.1371/journal.pbio.0030068>.

- [48] Perin R, Berger TK, Markram H. A synaptic organizing principle for cortical neuronal groups. *PNAS*. 2011;108(13):5419–24. <https://doi.org/10.1073/pnas.1016051108>.
- [49] Klinshov VV, Teramae J-N, Nekorkin VI, Fukai T. Dense neuron clustering explains connectivity statistics in cortical microcircuits. *PLoS ONE*. 2014;9(4):e94292. <https://doi.org/10.1371/journal.pone.0094292>.
- [50] Franović I, Klinshov V. Clustering promotes switching dynamics in networks of noisy neurons. *Chaos*. 2018;28(2):023111. <https://doi.org/10.1063/1.5017822>.
- [51] Franović I, Klinshov V. Stimulus-evoked activity in clustered networks of stochastic rate-based neurons. *Eur Phys J - Spec Top*. 2018;227(2):1063–76. <https://doi.org/10.1140/epjst/e2018-800080-6>.
- [52] Maslennikov OV, Pugavko MM, Shchapin DS, Nekorkin VI. Nonlinear dynamics and machine learning of recurrent spiking neural networks. *Phys Usp*. 2022. <https://doi.org/10.3367/UFNe.2021.08.039042>.
- [53] Jaeger H. The “echo state” approach to analysing and training recurrent neural networks—with an erratum note. Bonn, Germany: German National Research Center for Information Technology GMD Technical Report; 2001. p. 13.
- [54] Maass W, Natschl T, Markram H. Real-time computing without stable states: a new framework for neural computation based on perturbations. *Neural Comput*. 2002; 2560:2531–60. <https://doi.org/10.1523/JNEUROSCI.5446-11.2012>.
- [55] Haykin S. Adaptive filter theory. Upper Saddle River, NJ: Prentice Hal; 2002.
- [56] Ho ECY, Strüber M, Bartos M, Zhang L, Skinner FK. Inhibitory networks of fast-spiking interneurons generate slow population activities due to excitatory fluctuations and network multistability. *J Neurosci*. 2012;32(29):9931–46. <https://doi.org/10.1523/JNEUROSCI.5446-11.2012>.
- [57] Lim S, Goldman M. Balanced cortical microcircuitry for maintaining information in working memory. *Nat Neurosci*. 2013;16:1306–14. <https://doi.org/10.1038/nn.3492>.
- [58] Okun M, Steinmetz NA, Lak A, Dervinis M, Harris KD. Distinct structure of cortical population activity on fast and infraslow timescales. *Cereb Cortex*. 2019;29(5): 2196–210. <https://doi.org/10.1093/cercor/bhz023>.
- [59] Wallace E, Maei HR, Latham PE. Randomly connected networks have short temporal memory. *Neural Comput*. 2013;25(6):1408–39. https://doi.org/10.1162/NECO_a_00449.
- [60] Gilra A, Gerstner W. Predicting non-linear dynamics by stable local learning in a recurrent spiking neural network. *Elife*. 2017;6:e28295. <https://doi.org/10.7554/eLife.28295.001>.
- [61] Andreev AV, Ivanchenko MV, Pisarchik AN, Hramov AE. Stimulus classification using chimera-like states in a spiking neural network. *Chaos Solit Fractals*. 2020; 139:110061. <https://doi.org/10.1016/j.chaos.2020.110061>.

Unbalanced clustering and solitary states in coupled excitable systems

Cite as: Chaos 32, 011104 (2022); doi: 10.1063/5.0077022

Submitted: 29 October 2021 · Accepted: 28 December 2021 ·

Published Online: 11 January 2022



View Online



Export Citation



CrossMark

Igor Franović,^{1,a)} Sebastian Eydam,^{2,b)} Nadezhda Semenova,^{3,4,c)} and Anna Zakharova^{5,d)}

AFFILIATIONS

¹Scientific Computing Laboratory, Center for the Study of Complex Systems, Institute of Physics Belgrade, University of Belgrade, Pregrevica 118, 11080 Belgrade, Serbia

²Neural Circuits and Computations Unit, RIKEN Center for Brain Science, 2-1 Hirosawa, 351-0106 Wako, Japan

³Institute of Physics and Department of Fundamental Medicine and Medical Technology, Saratov State University, Astrakhanskaya str. 83, Saratov 410012, Russia

⁴Département d'Optique P. M. Duffieux, Institut FEMTO-ST, Université Bourgogne-Franche-Comte, CNRS UMR 6174, Besançon, France

⁵Institut für Theoretische Physik, Technische Universität Berlin, Hardenbergstr. 36, 10623 Berlin, Germany

^{a)} Author to whom correspondence should be addressed: franovic@ipb.ac.rs

^{b)} Electronic mail: sebastian.eydam@gmail.com

^{c)} Electronic mail: nadya.i.semenova@gmail.com

^{d)} Electronic mail: anna.zakharova@tu-berlin.de

ABSTRACT

We discover the mechanisms of emergence and the link between two types of symmetry-broken states, the unbalanced periodic two-cluster states and solitary states, in coupled *excitable* systems with attractive and repulsive interactions. The prevalent solitary states in non-locally coupled arrays, whose self-organization is based on successive (order preserving) spiking of units, derive their dynamical features from the corresponding unbalanced cluster states in globally coupled networks. Apart from the states with successive spiking, we also find cluster and solitary states where the interplay of excitability and local multiscale dynamics gives rise to so-called *leap-frog* activity patterns with an alternating order of spiking between the units. We show that the noise affects the system dynamics by suppressing the multistability of cluster states and by inducing pattern homogenization, transforming solitary states into patterns of patched synchrony.

Published under an exclusive license by AIP Publishing. <https://doi.org/10.1063/5.0077022>

With the remarkable discovery of chimera states, the research of self-organization in coupled oscillators witnessed a change of focus from the synchronization transition and the onset of the collective mode toward the emergence and the relationship between the states with symmetry breaking of synchrony (cluster states, chimeras, solitary states), where assemblies of indistinguishable oscillators with symmetric couplings split into groups with different dynamics. Currently, these problems remain widely open for a class of coupled *excitable* systems, which have a linearly stable rest state but may be triggered to oscillate by strong enough perturbations due to interactions and/or noise. We address the mechanisms of emergence and the link between two types of symmetry-broken states in coupled excitable FitzHugh–Nagumo systems, namely, the unbalanced periodic two-cluster states in globally coupled networks, characterized by an uneven partition between the clusters comprising identically

synchronized units, and solitary states in non-locally coupled arrays, where small groups of units display an average frequency distinct from the typical units forming the synchronized cluster. The prevalent solitary states, where the self-organization is based on successive (order preserving) spiking of units, are found to appear in the same parameter range as the corresponding unbalanced cluster states, inheriting the ratio of average frequencies of solitary and typical units and the form of corresponding units' orbits. Apart from the states displaying successive spiking, we also find the states involving leap-frog (leader-switching) dynamics, where the units from different clusters, or even within the same cluster, exchange their relative order of spiking. We further demonstrate that the noise reduces the multistability of cluster and solitary states by the effect of noise-induced preference of attractors, promoting the attractors with a larger basin of attraction at the expense of those with a smaller one.

I. INTRODUCTION

The discovery of chimera states^{1,2} spurred a profound change of paradigm in understanding of self-organization in assemblies of coupled oscillators. Instead of the synchronization transition and the onset of the collective mode,³ attention has shifted to states emerging via symmetry breaking of synchrony,⁴ where assemblies of indistinguishable oscillators with symmetric couplings split into groups with different dynamics. Classical examples of symmetry breaking of synchrony include cluster states,^{5–8} chimeras,^{9–12} and solitary states.^{13–22} In contrast to low-dimensional dynamics of cluster states, where the units within each group are identically synchronized, chimeras are self-organized patterns that are comprised of coexisting domains of coherence and incoherence.¹¹ A similar coexistence of locked and unlocked units underlies solitary states, where a single or a small subset of *solitary* units display an average frequency different from the synchronized cluster. However, distinct to the structure of chimeras, the solitary units spread randomly instead of forming spatially localized domains. Another difference is that solitary states involve spatial chaos,²³ reflecting sensitive dependence of the dynamics on spatial coordinates, which gives rise to extensive multistability. Regardless of these differences, both chimeras and solitary states satisfy the definition of weak chimeras.²⁴

For coupled oscillators, much progress has been made in resolving the two fundamental problems, namely, the mechanisms of onset and potential links between symmetry-broken states along the path from complete coherence to incoherence. In particular, emergence of cluster states from complete synchrony has been explained by unfolding of a so-called cluster singularity, revealing cascade transitions from a synchronous state to a balanced two-cluster partition, characterized by an equal number of oscillators within each cluster, via different unbalanced cluster states.^{5,25} Also, clustering has been identified as a prerequisite for the onset of chimeras.²⁶ Self-organization of strong chimeras, where coherent domains comprise identically (in-phase) synchronized oscillators, was shown to involve stabilization of the coherent cluster by the incoherent one,²⁷ while solitary states were found to mediate transition from complete coherence to chimeras.¹⁶

However, in a myriad of examples, from neural and cardiac tissue to chemical reactions, system components are not intrinsic oscillators, but are rather *excitable* units,^{28,29} nonlinear threshold elements that in the absence of input lie at rest, but may be triggered to oscillate by sufficiently strong perturbations. There is no reason to expect *a priori* that results for coupled oscillators translate to excitable systems, where even the onset of collective oscillations requires repulsive rather than attractive interactions.^{30–32} Apart for theoretical relevance, resolving fundamental questions on emergence and relation between periodic cluster states, chimeras, and solitary states in coupled excitable systems may be important for applications, e.g., for treating in neuroscience the problems of cluster synchronization during information transmission and processing,^{33,34} localized activity associated with working memory,^{35–38} or inducing desynchronization to control pathological states.^{39–41}

In this paper, we reveal mechanisms of onset and links between different types of unbalanced periodic two-cluster states and solitary states in systems with excitable local dynamics on multiple

timescales, typical for but not confined to neuroscience,^{29,42–45} and varying attractive/repulsive⁴⁶ type of interactions. We show that the prevalent solitary states in non-locally coupled arrays, having a self-organization based on successive spiking of units, derive their dynamical features, such as the frequency locking between typical and solitary units and the form of corresponding orbits, from the unbalanced two-cluster states in globally coupled networks, characterized by a permutation symmetry $\mathcal{S}_{N_A} \otimes \mathcal{S}_{N_B}$ with $N_A \neq N_B$ being the cluster sizes. However, we also discover cluster and solitary states where such a correspondence cannot be established. The self-organization of these peculiar cluster and solitary states is based on so-called *leap-frog* dynamics,^{47–51} characterized by an alternating order of spiking (leader-switching) between the units. Leap-frog dynamics was initially observed as a near-synchrony state in models of phase oscillators or type I relaxation neural oscillators supplied by strong nonlinear couplings with finite time constants.^{48,50,51} Nevertheless, it has recently been shown that leap-frogging can also occur in repulsively coupled type II excitable systems, considering an example of binary motifs of FitzHugh–Nagumo units poised close to (above or below) the bifurcation threshold.⁴⁷ There, leap-frog solutions of different complexity emerge from a slow–fast dynamics in vicinity of a canard transition and beyond a small coupling limit represent a particular type of mixed-mode oscillations at a folded node singularity.^{52,53} Given a strong sensitivity of excitable systems to noise,²⁸ we also investigate the resilience of the observed unbalanced cluster states and solitary states to noise. While noise has already been known to facilitate spontaneous clustering⁵⁴ and emergence of chimeras^{55,56} in coupled FitzHugh–Nagumo systems, here, we demonstrate the effect of noise-induced preference of attractors,^{57–59} where the noise suppresses the system's multistability by promoting only certain types of cluster states or by favoring patched patterns at the expense of solitary states.

Our system is an array of N identical FitzHugh–Nagumo units²⁹ whose dynamics obeys

$$\begin{aligned} \varepsilon \dot{u}_k &= u_k - \frac{u_k^3}{3} - v_k + \frac{\kappa}{2R} \sum_{l=k-R}^{k+R} [g_{uu}(u_l - u_k) + g_{uv}(v_l - v_k)] \\ &\quad + \sqrt{\varepsilon} \sigma \xi_k(t), \\ \dot{v}_k &= u_k + a + \frac{\kappa}{2R} \sum_{l=k-R}^{k+R} [g_{vu}(u_l - u_k) + g_{vv}(v_l - v_k)], \end{aligned} \quad (1)$$

where local slow–fast dynamics is governed by activator variables u_k and recovery variables v_k with timescale separation $\varepsilon = 0.05$. All indices are periodic modulo N . Local bifurcation parameter a , fixed to $a = 1.001$, mediates the transition from excitable ($|a| > 1$) to oscillatory regime ($|a| < 1$). Due to a singular character of Hopf bifurcation at $a = 1$, onset of oscillations is followed by a *canard transition* ($a \approx 1 - \varepsilon/8$) from small-amplitude (subthreshold) to large-amplitude relaxation oscillations.⁶⁰ Non-local interactions have coupling strength $\kappa = 0.4$, with each unit coupled to R neighbors on both sides, yielding a coupling radius $r = R/N$. Impact of direct and cross-coupling terms in u_k and v_k is compactly described via a rotational coupling

matrix⁶¹ $G = \begin{pmatrix} g_{uu} & g_{uv} \\ g_{vu} & g_{vv} \end{pmatrix} = \begin{pmatrix} \cos \phi & \sin \phi \\ -\sin \phi & \cos \phi \end{pmatrix}$. Parameter ϕ modifies prevalence of attractive and repulsive interactions. Spiking can also emerge due to noise, which here affects the fast variables similar to synaptic noise in neuronal systems,⁶² having each unit influenced by independent Gaussian white noise $\xi_k(t)$ of intensity σ : $\langle \xi_i(t) \rangle = 0$, $\langle \xi_i(t)\xi_j(t') \rangle = \delta_{ij}\delta(t-t')$. Note that the systems of ordinary (stochastic) differential equations were integrated by the standard adaptive ODE45 solver (SDETools toolbox available at <https://github.com/horchler/SDETools>).

We first focus on how the stability of unbalanced two-cluster states in globally connected networks ($r = 1/2$) changes with ϕ and then analyze the onset of solitary states in non-locally coupled arrays ($r < 1/2$) of excitable elements.

II. TWO-CLUSTER STATES IN GLOBALLY COUPLED NETWORKS

To gain insight into the structure of unbalanced periodic two-cluster states, their stability domains, and underlying bifurcations, we implement a twofold approach, combining the semi-analytical method of *evaporation exponents* and the numerical path-following method based on introducing *probe oscillators*. Since our interest is in solutions where both clusters emit spikes, the splitting scenario by which clusters emerge from a collective rest state is beyond our current scope. We remark that for stable local dynamics ($|a| > 1$), interaction-induced destabilization of a stationary state at $\phi^* = \arccos\left(\frac{1-a^2}{2\kappa}\right)$ is a highly degenerate point where $2(N-1)$ Jacobian eigenvalues with real parts $1 - a^2 - 2\kappa\cos(\phi)$ simultaneously become critical, giving rise to a large number of different cluster partitions featuring subthreshold oscillations, which in an exponentially small ϕ region start to display spikes via secondary canard transitions. Stability of a stationary state is regained at $\bar{\phi} = \phi^* + \pi$. Onsets of cluster instability and periodic cluster states for type I excitable units were addressed in Refs. 30 and 63.

Unlike Lyapunov exponents, evaporation exponents⁶⁴⁻⁶⁶ can describe perturbations that destroy cluster partitions. They characterize stability of clusters to emanation of elements, induced by perturbations transversal to invariant subspace of certain partition. Negative evaporation exponents indicate assembly's attractors, while their positive values imply instability. We consider a two-cluster state with partition parameter $p \in (0, 1)$ such that $N_A = pN$ units are in cluster A and $N_B = (1-p)N$ units in B. Its dynamics is independent of N and is governed by the reduced system

$$\begin{aligned} \varepsilon \dot{u}_i &= u_i - \frac{1}{3}u_i^3 - v_i + \kappa w_i(g_{uu}(u_j - u_i) + g_{uv}(v_j - v_i)), \\ \dot{v}_i &= u_i + a + \kappa w_i(g_{vu}(u_j - u_i) + g_{vv}(v_j - v_i)), \end{aligned} \quad (2)$$

with $i, j \in \{A, B\}$, $i \neq j$, and $(w_A, w_B) = (1-p, p)$ being additional coupling weights derived from particular partition. For $p \neq 1/2$, system (2) is equivalent to a pair of nonidentical excitable units. Different p values specify invariant subspaces in complete phase space that intersect only in the full synchrony plane. To introduce evaporation exponents, we consider symmetric small perturbations to two units, 1 and 2, in each cluster: $u_{i,1/2} = u_i \pm \delta u_i$, $v_{i,1/2} = v_i \pm \delta v_i$. Due to permutation symmetry, they can be applied to an arbitrary

pair of elements, leaving the cluster mean-fields unchanged. Linearized equations for deviations $[\delta u_i(t), \delta v_i(t)]$ transversal to cluster dynamics read

$$\begin{aligned} \varepsilon \delta \dot{u}_i &= (1 - u_i^2 - \kappa g_{uu})\delta u_i - (1 + \kappa g_{uv})\delta v_i, \\ \delta \dot{v}_i &= (1 - \kappa g_{vu})\delta u_i - \kappa g_{vv}\delta v_i. \end{aligned} \quad (3)$$

Evaporation exponents $\lambda_{ev,i} = \lim_{T \rightarrow \infty} \frac{1}{2} \ln \frac{\delta u_i^2(T) + \delta v_i^2(T)}{\delta u_i^2(0) + \delta v_i^2(0)}$ are obtained by integrating the system (2) and (3).

Bifurcations of particular cluster states are determined by numerical continuation using probe oscillators, indicating whether a unit added to the cluster asymptotically remains in it or leaves it. Probes are introduced at the cluster coordinates without affecting the mean-fields such that their dynamics $[\tilde{u}_i(t), \tilde{v}_i(t)]$ obeys

$$\begin{aligned} \varepsilon \dot{\tilde{u}}_i &= \tilde{u}_i - \tilde{u}_i^3 - \tilde{v}_i + \kappa [w_i(g_{uu}(u_i - \tilde{u}_i) + g_{uv}(v_i - \tilde{v}_i)) \\ &\quad + w_j(g_{uu}(u_j - \tilde{u}_i) + g_{uv}(v_j - \tilde{v}_i))], \\ \dot{\tilde{v}}_i &= \tilde{u}_i + a + \kappa [w_i(g_{vu}(u_i - \tilde{u}_i) + g_{vv}(v_i - \tilde{v}_i)) \\ &\quad + w_j(g_{vu}(u_j - \tilde{u}_i) + g_{vv}(v_j - \tilde{v}_i))]. \end{aligned} \quad (4)$$

Numerical continuation of solutions of (2) together with (4) was performed by the software package AUTO.⁶⁷

Figure 1(a) shows the stability diagram for system (2) and (3) in the (ϕ, p) plane, combining the results obtained by methods of evaporation exponents and probe oscillators. Regions supporting stable solutions are indicated in orange, with black and green lines at their boundaries denoting period-doubling bifurcations and curves of branching points, respectively. The latter are typically pitchfork bifurcations of the reduced system but correspond to unfolding of highly degenerate bifurcation points⁵ of system (1), where p becomes a solution parameter. System (2) supports six characteristic regimes with 1:1 (regions IV, V, and VI), 1:2 (I, II), or 2:3 (III) frequency locking, all conforming to *mixed-mode oscillations*^{52,53} with interspersed large- and small-amplitude oscillations; cf. Figs. 1(b)-1(e). Note that the partition parameter p for certain types of solutions can become small but still does not approach zero, indicating that only those periodic two-cluster states with a sufficiently balanced partition can exist. This is similar to the scenario recently described for coupled type I excitable systems.³⁰ Nevertheless, these results for coupled excitable systems are different from those for globally coupled networks of Kuramoto oscillators with inertia,¹⁹ where a stable existence of solitary states with a single or just few oscillators isolated from the synchronized cluster has been reported. Also note that some authors tend to refer to states characterized by a finite fraction of units (up to $p = 1/2$) split from the synchronized bulk cluster as solitary states.^{19,68} Nevertheless, here, we prefer to call the states with an uneven partition to two groups of *identically* synchronized units unbalanced cluster states, as opposed to the solitary states described later on for non-locally arrays, where the units are split into majority and minority groups of *frequency locked* but not *identically* synchronized units.

Apart from solutions I-III and V with a successive spiking between clusters, where the spiking order of clusters is preserved, one also observes mixed-mode solutions IV characterized by leap-frog dynamics⁴⁷⁻⁵⁰ of clusters. There, switching of leadership

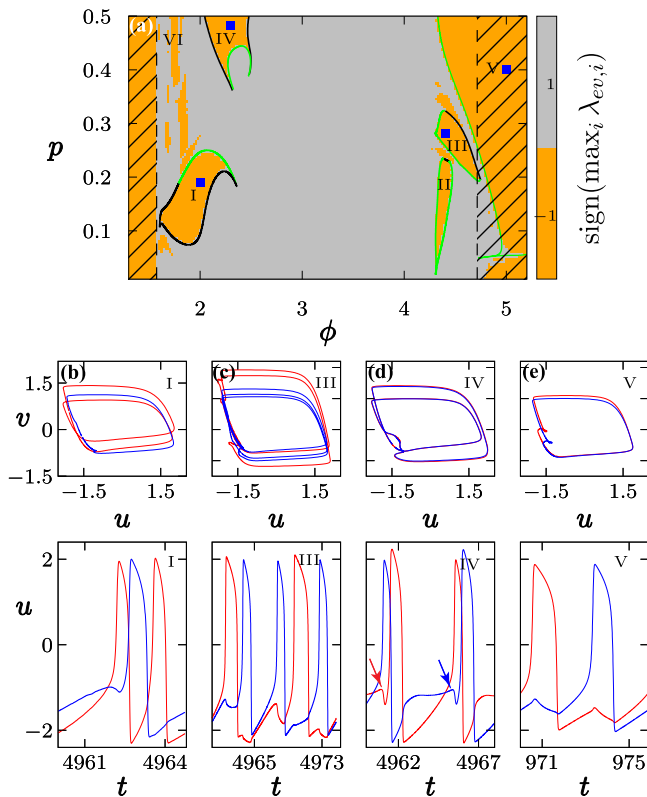


FIG. 1. Unbalanced periodic two-cluster states. (a) Stability diagram in the (ϕ, p) plane. Stable and unstable solutions are indicated in orange and gray, respectively. Black solid lines: period-doubling bifurcations. Green lines: curves of branching points. Black dashed lines: destabilization of rest state ($\phi = \phi^* \approx 1.573$) and its reappearance ($\phi = \bar{\phi} \approx 4.715$). (b)–(e) Time traces $u_i(t)$, $i \in \{A, B\}$ and phase portraits corresponding to (ϕ, p) values (blue squares) from (a).

between the clusters occurs via subthreshold oscillations such that the current leader performs an extra small oscillation allowing it to be overtaken by the lagging cluster; see the arrows in Fig. 1(d). Leap-frog solutions at $p = 1/2$ may acquire additional antiphase symmetry $u_A(t) = u_B(t + P/2)$, $v_A(t) = v_B(t + P/2)$, where P denotes the oscillation period. Note that different types of leap-frog patterns and their underlying mechanisms in binary motifs of repulsively coupled FitzHugh–Nagumo units were shown to be a consequence of phase-sensitive excitability of periodic orbits,⁴⁷ a recently introduced concept⁴⁹ referring to a non-uniform sensitivity to perturbations of both relaxation and subthreshold oscillations in the FitzHugh–Nagumo system.

Evaporation exponents can also be used to approximate impact of small noise to stability of two-cluster partitions. For (1) with $r = 1/2, \sigma > 0$, we find that the noise may cause transition to another type of two-cluster state or may reorganize the state’s structure by inducing migration of units between clusters without qualitatively affecting their mean-fields. Reorganization process eventually settles to a partition where the net transport between the

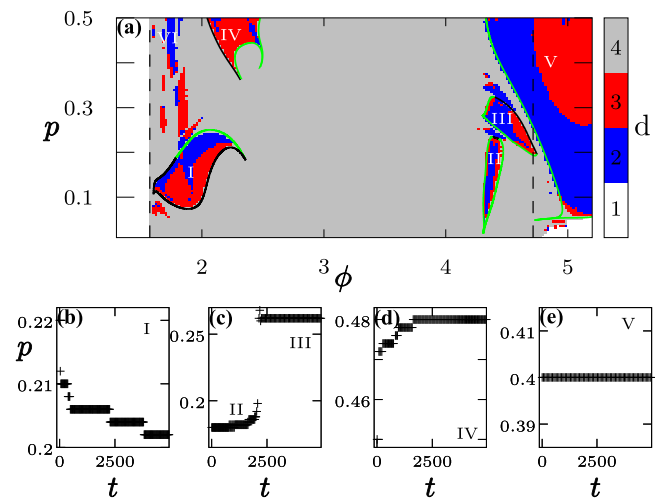


FIG. 2. Persistence of unbalanced two-cluster states under noise. (a) Quantity $d(\phi, p)$ distinguishes between four cases: cluster states reorganize to the partition with smaller (blue, $\lambda_{ev,A} > \lambda_{ev,B}$) or larger p values (red, $\lambda_{ev,B} > \lambda_{ev,A}$); two-cluster states are unstable (gray, $d = 4$); only synchronous stationary state is stable (white, $d = 1$). (b)–(e) Examples of evolution of partition parameter $p(t)$ under noise. Left to right: $\phi = 2, 4.4, 2.3, 5.0$ and $\sigma = 5, 0.6, 0.6, 5 \times 10^{-3}$, respectively.

clusters reaches a dynamical balance so that the partition parameter $p(t)$ becomes stationary. Splitting of a unit from a cluster and migration to another cluster may involve nonlinear effects of perturbations that cannot be captured by methods involving linearization around a certain solution, such as evaporation exponents. Still, at the linear level, “potential barrier” that has to be overcome when a unit leaves the cluster is proportional to $\lambda_{ev,i}$. This is used to characterize resilience of two-cluster states to noise in Fig. 2(a). We distinguish between the cases where noise is more likely to shift a two-cluster partition toward smaller ($0 > \lambda_{ev,A} > \lambda_{ev,B}$; blue regions) or a larger p value ($0 > \lambda_{ev,B} > \lambda_{ev,A}$; red regions), depending on the dominant stable exponent. There are also domains where unbalanced two-cluster states are unstable ($\lambda_{ev,A/B} > 0$, shown gray) or where only synchronous stationary state is stable (white). For convenience, each case is assigned with a discrete variable $d \in \{1, 2, 3, 4\}$. Evolution of cluster partition $p(t)$ under noise is illustrated in Figs. 2(b)–2(e) for solutions from regions I to VI. While states from I and V display persistence under noise, representative state from II migrates to region III. Interestingly, asymmetric leap-frog solution from IV evolves toward balanced partition $p = 1/2$.

III. SOLITARY STATES IN NON-LOCALLY COUPLED ARRAYS

The intrinsic dynamics of the prevalent solitary states in non-locally coupled arrays, called SS1 and SS2, is based on successive spiking of units. In the following, we show that they derive their dynamical features from the corresponding unbalanced cluster states from Fig. 1(a). In particular, state SS1 in Fig. 3 is a dynamical counterpart of a two-cluster state from region I, whereas SS2

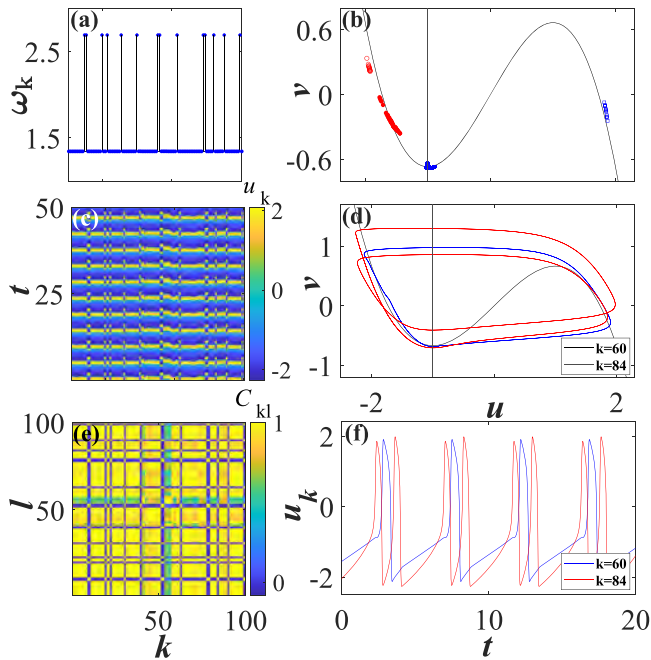


FIG. 3. Solitary state SS1 ($N = 100$, $\phi = 1.85$, $r = 0.2$). (a) Spatial profile of ω_k ; (b) red and blue: two snapshots of local variables (u_k, v_k), black: nullclines of isolated unit; (c) spatiotemporal evolution of $u_k(t)$; (d) phase portraits [$u_k(t), v_k(t)$] for solitary ($k = 84$) and typical unit ($k = 60$); (e) cross-correlation matrix C_{kl} ; and (f) time traces $u_k(t)$ for two units from (d).

(not shown) derives from the cluster state from region V. These solitary states occur within the same ϕ intervals as the corresponding cluster states and preserve the respective frequency locking of clusters, but due to nonlocal interactions and associated fluctuations of the local mean-fields, clusters of solitary and typical units are fuzzy^{13,16} rather than exact; see Fig. 3(b). In other words, introducing a nonlocal coupling $r < 1/2$ results in breaking of the permutation symmetry of the unbalanced cluster states observed for $r = 1/2$ such that the solitary and typical clusters consist of frequency locked but not identically synchronized units. The spatial profile of the average local frequencies $\omega_k = 2\pi M_k/\Delta$, where M_k is the spike count within interval Δ , shows a 2:1 frequency ratio between solitary and typical units. The analogy with the two-cluster state from region I in Fig. 1(a) in terms of local phase portraits and time traces $u_k(t)$ is illustrated in Figs. 3(d) and 3(f). Intrinsic dynamics of SS1 is characterized by a cross-correlation matrix $C_{kl} = \frac{\langle \hat{u}_k(t) \hat{u}_l(t) \rangle_T}{\sqrt{\langle \hat{u}_k(t)^2 \rangle_T \langle \hat{u}_l(t)^2 \rangle_T}}$, where $\langle \cdot \rangle_T$ denotes time averaging, while $\hat{u}_k(t) = u_k(t) - \langle u_k(t) \rangle_T$ are deviations of $u_k(t)$ from their means; cf. Fig. 3(e).

Nevertheless, we also find solitary states without two-cluster state counterparts. A typical example is a state SS3 illustrated in Fig. 4, which, unlike SS1 and SS2, is maintained by leap-frog dynamics of pairs of solitary-typical, only solitary or only typical units; cf. Figs. 4(b), 4(d), and 4(f). States of SS3 type emerge due to non-local interactions, which induce self-localized excitations⁷¹ at interfaces separating domains with distinct dynamics. Frequency profile

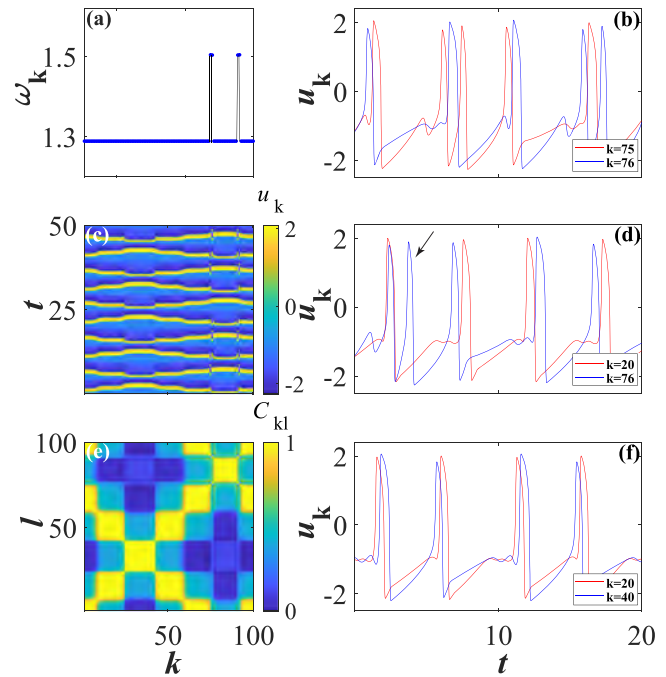


FIG. 4. Solitary state SS3 ($N = 100$, $\phi = 1.788$, $r = 0.2$). (a) Spatial profile of ω_k . (b) Time traces $u_k(t)$ for solitary units $k = 75$ and $k = 76$. (c) Spatiotemporal evolution of $u_k(t)$. (d) Time traces $u_k(t)$ for solitary unit $k = 76$ and typical unit $k = 20$. (e) Cross-correlation matrix C_{kl} . (f) Time traces $u_k(t)$ show leap-frog dynamics within majority cluster (units $k = 20$ and $k = 40$).

ω_k shows two clusters with a frequency ratio distinct from SS1; cf. Fig. 3(a). The difference in ω_k derives from events where solitary units emit two successive spikes rather than a spike followed by subthreshold oscillation; see the arrow in Fig. 4(d). SS3 involves a more complex correlation structure compared to SS1, cf. Figs. 4(e) and 3(e), and the corresponding maximal Lyapunov exponent⁷⁰ is 1.78×10^{-5} .

Contrasting with locally coupled excitable systems where the noise may strongly influence pattern formation by inducing, enhancing or controlling wave propagation, spiral dynamics, and pacemaking,²⁸ the deterministic dynamics of non-locally coupled arrays here features extensive multistability, and the main impact of noise is qualitatively different. We find that the noise reduces system's multistability, suppressing solitary states. This reflects the effect called noise-induced preference of attractors,⁵⁷ which may be understood as follows: in highly multistable systems, stability boundaries of attractors become smeared by noise, and only those with sufficiently large basins of attraction remain visible. This may be seen as a highly biased switching^{72,73} to a coexisting state without returning to the initial one. For small noise, unbalanced splitting into frequency clusters is preserved, but the preferred spatial distribution of minority units is localized rather than random. This gives rise to patched patterns with 1:2 subharmonic frequency locking. A typical example is shown in Fig. 5, where an initial SS1 state transforms under small noise into a state of patched synchrony.⁶¹ Note

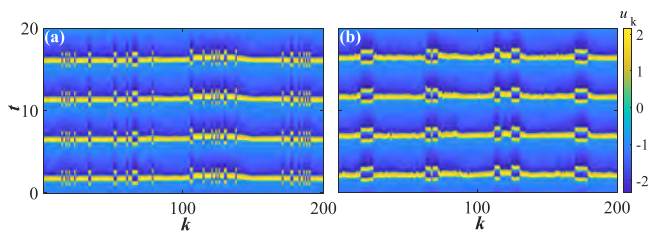


FIG. 5. Transformation of an SS1 state under noise. (a) Typical SS1 dynamics without noise. (b) Patched pattern developed from SS1 at $\sigma = 0.0011$. Parameters are $N = 200$, $\phi = 2.0$, $r = 0.2$.

that introducing intermediate noise favors rotating waves instead of patched synchrony, while an even larger noise leads to turbulence.

IV. CONCLUSION AND OUTLOOK

We have discovered the mechanisms of onset and links between unbalanced periodic two-cluster states and solitary states, as a form of weak chimeras, in coupled excitable systems. The fact that the prevalent solitary states SS1 and SS2 in non-locally coupled arrays, characterized by self-organization based on successive spiking of units, derive their dynamical features from unbalanced cluster states in globally coupled networks is to a certain extent qualitatively similar to the finding for globally coupled Stuart–Landau oscillators, where clustering has been identified as a symmetry-breaking step required for emergence of chimeras.²⁶ Distinct from the physical picture reported for the systems of Kuramoto oscillators with inertia,¹⁹ we have not observed states with a single or just a few units split from the synchronized cluster that can be continued for an arbitrary range of couplings from global via nonlocal to local. A peculiar finding associated with the interplay of local excitability and nonlocal interactions concerns the solitary states SS3 that have no cluster states counterparts and whose structure involves leap-frog activity patterns. Leap-frog dynamics derives from multiscale character of the system, and, in particular, the phase-sensitive excitability of relaxation oscillations, underlying their strong sensitivity to perturbations in the vicinity of a canard transition.^{47,69} Current results, together with Refs. 47 and 74, indicate the importance of this concept to pattern formation in multiscale systems, both in regard to coupled type II excitable units and oscillators. A question that remains open is whether a similar type of unbalanced cluster states and solitary states based on leap-frog dynamics can be observed in coupled type I excitable systems. Since leap-frogging in type I neural oscillators has so far only been found in the presence of strong nonlinear couplings,^{50,51} we suspect that they are also required for the onset of leap-frog states in type I excitable systems.

Regarding the impact of noise, we have found that it affects the cluster and solitary states by suppressing the multistability of system dynamics. This is a manifestation of noise-induced preference of attractors, an effect previously corroborated in coupled oscillators,⁵⁸ Hénon maps,⁷⁵ and multistable fiber lasers.⁵⁹ An additional subtlety is that the small noise influences pattern formation by promoting homogeneous patched patterns at the expense of solitary states. Since solitary states in coupled oscillators may mediate the

transition from complete synchrony to chimeras,¹⁶ it would be interesting to investigate whether a similar scenario applies to coupled excitable systems.

ACKNOWLEDGMENTS

I.F. acknowledges funding from the Institute of Physics Belgrade through a grant by the Ministry of Education, Science and Technological Development of Republic of Serbia. A.Z. acknowledges the support from the Deutsche Forschungsgemeinschaft (DFG) within the framework of the SFB 910 (Projektnummer 163436311). N.S. is supported by scholarship of the President of the Russian Federation (SP-749.2022.5).

AUTHOR DECLARATIONS

Conflict of Interest

The authors have no conflicts of interest to disclose.

DATA AVAILABILITY

The data that support the findings of this study are available from the corresponding author upon reasonable request.

REFERENCES

- Y. Kuramoto and D. Battogtokh, *Nonlinear Phenom. Complex Syst.* **5**, 380 (2002); available at <http://www.j-npcs.org/abstracts/vol2002/v5no4/v5no4p380.html>.
- D. M. Abrams and S. H. Strogatz, *Phys. Rev. Lett.* **93**, 174102 (2004).
- A. Pikovsky, M. Rosenblum, and J. Kurths, *Synchronization: A Universal Concept in Nonlinear Sciences* (Cambridge University Press, Cambridge, 2003).
- A. E. Motter, *Nat. Phys.* **6**(3), 164 (2010).
- F. P. Kemeth, S. W. Haugland, and K. Krischer, *Chaos* **29**, 023107 (2019).
- W. L. Ku, M. Girvan, and E. Ott, *Chaos* **25**, 123122 (2015).
- A. Ismail and P. Ashwin, *Dyn. Syst.* **30**, 122 (2015).
- D. Hansel, G. Mato, and C. Meunier, *Phys. Rev. E* **48**, 3470 (1993).
- M. J. Panaggio and D. M. Abrams, *Nonlinearity* **28**, R67 (2015).
- O. E. Omel'chenko, *Nonlinearity* **31**, R121 (2018).
- A. Zakharova, *Chimera Patterns in Networks: Interplay Between Dynamics, Structure, Noise, and Delay—Understanding Complex Systems* (Springer Nature, Cham, Switzerland, 2020).
- F. Parastesh, S. Jafari, H. Azarnoush, Z. Shahriari, Z. Wang, S. Boccaletti, and M. Perc, *Phys. Rep.* **898**, 1 (2021).
- Y. Maistrenko, B. Penkovsky, and M. Rosenblum, *Phys. Rev. E* **89**, 060901 (2014).
- V. Maistrenko, O. Sudakov, and O. Osiv, *Chaos* **30**, 063113 (2020).
- V. Maistrenko, O. Sudakov, and Y. Maistrenko, *Eur. Phys. J. Spec. Top.* **229**, 2327 (2020).
- P. Jaros, Y. Maistrenko, and T. Kapitaniak, *Phys. Rev. E* **91**, 022907 (2015).
- E. Rybalova, V. S. Anishchenko, G. I. Strelkova, and A. Zakharova, *Chaos* **29**, 071106 (2019).
- R. Berner, A. Polanska, E. Schöll, and S. Yanchuk, *Eur. Phys. J. Spec. Top.* **229**, 2183 (2020).
- P. Jaros, S. Brezetsky, R. Levchenko, D. Dudkowski, T. Kapitaniak, and Y. Maistrenko, *Chaos* **28**, 011103 (2018).
- M. Mikhaylenko, L. Ramlow, S. Jalan, and A. Zakharova, *Chaos* **29**, 023122 (2019).
- L. Schülen, D. A. Janzen, E. S. Medeiros, and A. Zakharova, *Chaos, Solitons Fractals* **145**, 110670 (2021).
- E. V. Rybalova, A. Zakharova, and G. I. Strelkova, *Chaos, Solitons Fractals* **148**, 111011 (2021).

- ²³I. Omelchenko, Y. Maistrenko, P. Hövel, and E. Schöll, *Phys. Rev. Lett.* **106**, 234102 (2011).
- ²⁴P. Ashwin and O. Burylko, *Chaos* **25**, 013106 (2015).
- ²⁵F. P. Kemeth, B. Fiedler, S. W. Haugland, and K. Krischer, *J. Phys. Complex.* **2**, 025005 (2021).
- ²⁶L. Schmidt and K. Krischer, *Phys. Rev. Lett.* **114**, 034101 (2015).
- ²⁷Y. Zhang and A. Motter, *Phys. Rev. Lett.* **126**, 094101 (2021).
- ²⁸B. Lindner, J. García-Ojalvo, A. Neiman, and L. Schimansky-Geier, *Phys. Rep.* **392**, 321 (2004).
- ²⁹E. M. Izhikevich, *Dynamical Systems in Neuroscience: The Geometry of Excitability and Bursting* (MIT Press, Cambridge, MA, 2007).
- ³⁰R. Rongge and M. A. Zaks, *Phys. Rev. E* **103**, 012206 (2021).
- ³¹E. Teichmann and M. Rosenblum, *Chaos* **29**, 093124 (2019).
- ³²R. Rongge and M. A. Zaks, *Eur. Phys. J. Spec. Top.* **230**, 2717 (2021).
- ³³G. Buzsáki, *Rhythms of the Brain* (Oxford University Press, New York, 2006).
- ³⁴P. A. Tass, *Phase Resetting in Medicine and Biology: Stochastic Modelling and Data Analysis* (Springer, Berlin, 2007).
- ³⁵K. Wimmer, D. Q. Nykamp, C. Constantinidis, and A. Compte, *Nat. Neurosci.* **17**, 431 (2014).
- ³⁶S. Kim, H. Rouault, S. Druckmann, and V. Jayaraman, *Science* **356**, 849 (2017).
- ³⁷Á. Byrne, D. Avitabile, and S. Coombes, *Phys. Rev. E* **99**, 012313 (2019).
- ³⁸C. R. Laing, W. C. Troy, B. Gutkin, and G. B. Ermentrout, *SIAM J. Appl. Math.* **63**, 62 (2002).
- ³⁹C. Lainscsek, N. Rungratsameetaweemana, S. S. Cash, and T. J. Sejnowski, *Chaos* **29**, 121106 (2019).
- ⁴⁰R. G. Andrzejak, C. Rummel, F. Mormann, and K. Schindler, *Sci. Rep.* **6**, 23000 (2016).
- ⁴¹R. Berner, S. Vock, E. Schöll, and S. Yanchuk, *Phys. Rev. Lett.* **126**, 028301 (2021).
- ⁴²S. Scialla, A. Loppini, M. Patriarca, and E. Heinsalu, *Phys. Rev. E* **103**, 052211 (2021).
- ⁴³W.-Y. Chiang, P.-Y. Lai, and C. K. Chan, *Phys. Rev. Lett.* **106**, 254102 (2011).
- ⁴⁴S. I. Shima and Y. Kuramoto, *Phys. Rev. E* **69**, 036213 (2004).
- ⁴⁵M. Heinrich, T. Dahms, V. Flunkert, S. W. Teitsworth, and E. Schöll, *New J. Phys.* **12**, 113030 (2010).
- ⁴⁶I. Belykh, R. Reimbayev, and K. Zhao, *Phys. Rev. E* **91**, 062919 (2015).
- ⁴⁷S. R. Eydám, I. Franović, and M. Wolfrum, *Phys. Rev. E* **99**, 042207 (2019).
- ⁴⁸P. Goel and G. B. Ermentrout, *Physica D* **163**, 191 (2002).
- ⁴⁹C. D. Acker, N. Kopell, and J. A. White, *J. Comput. Neurosci.* **15**, 71 (2003).
- ⁵⁰M. Oh and V. Matveev, *J. Comput. Neurosci.* **26**, 303 (2009).
- ⁵¹S. K. Maran and C. C. Canavier, *J. Comput. Neurosci.* **24**, 37 (2008).
- ⁵²M. Desroches, J. Guckenheimer, B. Krauskopf, C. Kuehn, H. M. Osinga, and M. Wechselberger, *SIAM Rev.* **54**, 211 (2012).
- ⁵³C. Kuehn, *Multiple Time Scale Dynamics* (Springer International Publishing, Switzerland, 2015).
- ⁵⁴I. Franović, K. Todorović, N. Vasović, and N. Burić, *Phys. Rev. Lett.* **108**, 094101 (2012).
- ⁵⁵A. Zakharova, N. Semenova, V. Anishchenko, and E. Schöll, *Chaos* **27**, 114320 (2017).
- ⁵⁶N. Semenova, A. Zakharova, V. Anishchenko, and E. Schöll, *Phys. Rev. Lett.* **117**, 014102 (2016).
- ⁵⁷A. N. Pisarchik and U. Feudel, *Phys. Rep.* **540**, 167 (2014).
- ⁵⁸K. Kaneko, *Phys. Rev. Lett.* **78**, 2736 (1997).
- ⁵⁹A. N. Pisarchik, R. Jaimes-Reátegui, R. Sevilla-Escoboza, G. Huerta-Cuillar, and M. Taki, *Phys. Rev. Lett.* **107**, 274101 (2011).
- ⁶⁰S. M. Baer and T. Erneux, *SIAM J. Appl. Math.* **46**, 721 (1986).
- ⁶¹I. Omelchenko, O. E. Omel'chenko, P. Hövel, and E. Schöll, *Phys. Rev. Lett.* **110**, 224101 (2013).
- ⁶²A. Destexhe and M. Rudolph-Lilith, *Neuronal Noise* (Springer, New York, 2012).
- ⁶³M. A. Zaks and P. Tomov, *Phys. Rev. E* **93**, 020201 (2016).
- ⁶⁴A. Pikovsky and A. Politi, *Lyapunov Exponents: A Tool to Explore Complex Dynamics* (Cambridge University Press, Cambridge, 2016).
- ⁶⁵A. Pikovsky, O. Popovych, and Y. Maistrenko, *Phys. Rev. Lett.* **87**, 044102 (2001).
- ⁶⁶M. Zaks and A. Pikovsky, *Sci. Rep.* **7**, 4648 (2017).
- ⁶⁷E. J. Doedel and B. E. Oldeman, *AUTO-07P: Continuation and Bifurcation Software for Ordinary Differential Equations* (Concordia University, Montreal, 2012).
- ⁶⁸N. Kruk, Y. Maistrenko, and H. Koepl, *Chaos* **30**, 111104 (2020).
- ⁶⁹I. Franović, O. E. Omel'chenko, and M. Wolfrum, *Chaos* **28**, 071105 (2018).
- ⁷⁰G. Benettin, L. Galgani, and J.-M. Strelcyn, *Phys. Rev. A* **14**, 2338 (1976).
- ⁷¹M. Wolfrum, O. E. Omel'chenko, and J. Sieber, *Chaos* **25**, 053113 (2015).
- ⁷²I. Bačić and I. Franović, *Chaos* **30**, 033123 (2020).
- ⁷³I. Franović, S. Yanchuk, S. R. Eydám, I. Bačić, and M. Wolfrum, *Chaos* **30**, 083109 (2020).
- ⁷⁴H. G. Rotstein and H. Wu, *Phys. Rev. E* **86**, 066207 (2012).
- ⁷⁵B. E. Martínez-Zérega and A. N. Pisarchik, *Commun. Nonlinear Sci. Numer. Simul.* **17**, 4023 (2012).

Bumps, chimera states, and Turing patterns in systems of coupled active rotatorsIgor Franović^{1,*}, Oleh E. Omel'chenko^{2,†} and Matthias Wolfrum^{3,‡}¹Scientific Computing Laboratory, Center for the Study of Complex Systems, Institute of Physics Belgrade, University of Belgrade, Pregrevica 118, 11080 Belgrade, Serbia²University of Potsdam, Institute of Physics and Astronomy, Karl-Liebknecht-Strasse 24/25, 14476 Potsdam-Golm, Germany³Weierstrass Institute, Mohrenstrasse 39, 10117 Berlin, Germany

(Received 7 April 2021; accepted 20 October 2021; published 4 November 2021)

Self-organized coherence-incoherence patterns, called *chimera states*, have first been reported in systems of Kuramoto oscillators. For coupled excitable units, similar patterns where coherent units are at rest are called *bump states*. Here, we study bumps in an array of active rotators coupled by nonlocal attraction and global repulsion. We demonstrate how they can emerge in a *supercritical* scenario from completely coherent Turing patterns: a single incoherent unit appears in a homoclinic bifurcation, undergoing subsequent transitions to quasiperiodic and chaotic behavior, which eventually transforms into extensive chaos with many incoherent units. We present different types of transitions and explain the formation of coherence-incoherence patterns according to the classical paradigm of short-range activation and long-range inhibition.

DOI: [10.1103/PhysRevE.104.L052201](https://doi.org/10.1103/PhysRevE.104.L052201)

Since their discovery in 2002 by Kuramoto and Battogtokh [1] chimera states have attracted remarkable attention. They represent a type of self-organization phenomenon where identical units in a system with symmetric couplings develop a stable pattern with regions of qualitatively different behavior. In their original work, Kuramoto and Battogtokh found such patterns with self-organized domains of synchronized (coherent) and nonsynchronized (incoherent) oscillators in systems of phase oscillators in a one-dimensional array with nonlocal coupling. After the term *chimera state* was coined by Abrams and Strogatz [2], it has been used for similar phenomena in a large variety of theoretical models [3,4] and has also been demonstrated in various experiments [5–8]. In spite of the abundance of examples of chimera states [9–16], sometimes even only loosely related to the original phenomenon from phase oscillator systems, an understanding of a principal mechanism leading to their formation is still missing [17]. In [2], it has been pointed out as an intriguing property of chimera states that they “cannot be ascribed to a supercritical instability” since they always stably coexist with the uniform locked state. Since then, no supercritical scenario leading to the emergence of chimera states has been presented. Some recent progress has been made only for the case of Stuart-Landau oscillators with global nonlinear coupling, where clustering has been identified as a prerequisite for chimera states in such systems [18].

In this Letter, we show that the solution to this outstanding problem can be found by applying the classical paradigm [19,20] of short-range activation and long-range inhibition

to the synchrony in an array of coupled excitable or oscillatory units. We demonstrate that the coherence-incoherence patterns can emerge in a *supercritical* scenario via a Turing instability of completely coherent states and a secondary homoclinic bifurcation, creating a *single* incoherent oscillator, a state which can be seen as a *weak chimera* in the sense of [21]. Subsequent transitions via periodic, quasiperiodic, and chaotic states with an increasing number of incoherent oscillators finally lead to a fully developed coherence-incoherence pattern with localized extensive chaos in the incoherent region. Remarkably, this scenario is essentially independent on the system size. We achieve this by introducing two modifications to the original phase oscillator system. In addition to the nonlocal attractive coupling, we introduce a global repulsive coupling, and the uniformly rotating phase oscillators are replaced by so-called *active rotators*, which can be in an oscillatory or excitable regime. Coupled units of this type can be seen as a simplified version of neuronal oscillators similar to *theta neurons* [22,23], and under excitatory and/or inhibitory coupling they are known to display various types of localized or propagating spiking patterns. In particular, they can display localized states of activity, so-called *bump states* [24–28], which have also been extensively studied in continuum models for neuronal mean-field activity [29–37]. With these additions, our system shows a variety of self-organized patterns; see Fig. 1. Already completely coherent states, where all active rotators have identical average frequencies ω_k , can be locked ($\omega_k = 0$) or unlocked ($\omega_k \neq 0$), and in both cases they can be spatially uniform or spatially modulated; see Figs. 1(a) and 1(b), respectively. Incoherent regions, where average frequencies ω_k are gradually varying, can occur interspersed with locked coherent regions, as in bump states; see Figs. 1(c) and 1(d), or with unlocked coherent regions, as observed in chimera states. The point that bumps and chimeras are related by a collective unlocking of the coherent region has

*franovic@ipb.ac.rs

†omelchenko@uni-potsdam.de

‡wolfrum@wias-berlin.de

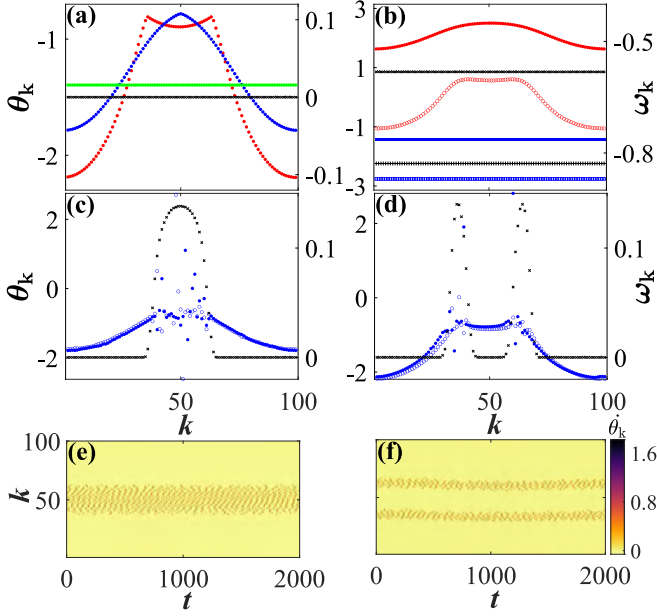


FIG. 1. Dynamical regimes of (1) with $N = 100$, $P = 35$, $\alpha = 0.6$, and different choices of K_1 , K_2 , a . All the solutions were obtained from coherent spatially modulated initial conditions, and are plotted centered at $k = 50$ using translational invariance. Snapshots of phases θ_k (colored symbols) and average frequencies ω_k (black) in (a)–(d). (a) Completely coherent locked states for $a = 1.2$: homogeneous (green) at $K_1 = 1.4$, $K_2 = 1.8$, spatially modulated (red, blue) at $K_1 = 1.4$, $K_2 = 1.983$, and $K_1 = 2$, $K_2 = 2.495$. (b) Time-periodic (unlocked) completely coherent states for $a = 0.5$, $K_2 = 1.8$: homogeneous (blue) at $K_1 = 3.4$, spatially modulated (red) at $K_1 = 3.3$; different symbols of the same color indicate snapshots at different time moments. Bump states: (c) Single-headed for $K_1 = 1.4$, $K_2 = 2$, $a = 1.2$, (d) two-headed for $K_1 = 2$, $K_2 = 2.52$, $a = 1.2$. Corresponding space-time plots of phase velocities $\dot{\theta}_k(t)$ in (e) and (f).

previously been described in a system of active rotators even without global repulsion, having a classical chimera subjected to a global periodic forcing [38].

Along with a mechanism of emergence, a related puzzling aspect is that in their original form, chimeras cannot be observed in small systems. In [39], it has been shown that even for large system size, they are in fact chaotic transients collapsing to the completely coherent state after a lifetime that is exponentially increasing with the system size. There is of course no reason to believe that both these properties are necessarily true for any chimeralike phenomenon in systems other than Kuramoto's original phase oscillators. Indeed, Kuramoto's simple phase oscillator system allows for variations only in the phase lag parameter and the shape of the non-local coupling. The introduction of a more general coupling function has led to a discovery of weak chimera states [21] which can also occur in rather small systems. However, they share only some of the properties of the classical chimeras, and it remained unclear to which extent the mechanisms of their emergence could serve as a general explanation of the original chimera phenomenon. In the case of bump states, our results demonstrate that they can stably exist in small systems without eventually collapsing to a completely coherent state.

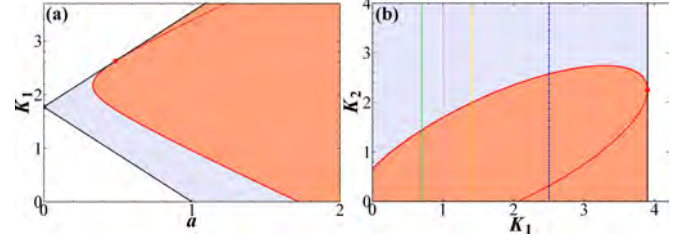


FIG. 2. Instabilities of the homogeneous locked state: fold (4) with $\kappa = 0$ (black), existence region (gray); Turing instability (4) for the mode with wave number $\kappa = 1$ (red), stability region (orange); dashed parts of the curves lie on the unstable sheet. (a) Locking cone in the (a, K_1) plane for fixed $K_2 = 1.4$; (b) locking region in the (K_1, K_2) plane for fixed $a = 1.2$. Other parameters: $\alpha = 0.6$, $N = 100$, $P = 35$. Vertical lines in (b) indicate choices of K_1 in Fig. 3.

We start with an array of N oscillators where the dynamics of phases $\theta_j \in S^1$, $j = 1, \dots, N$ is given by

$$\frac{d\theta_j}{dt} = 1 - a \cos \theta_j - \frac{K_1}{2P+1} \sum_{k=j-P}^{j+P} \sin(\theta_j - \theta_k + \alpha) + \frac{K_2}{N} \sum_{k=1}^N \sin(\theta_j - \theta_k), \quad j = 1, \dots, N, \quad (1)$$

where $K_1 > 0$ denotes the strength of the nonlocal attractive coupling and $K_2 > 0$ is the global repulsive coupling. For $a = 0$, $K_2 = 0$, and an appropriate choice of the phase lag parameter $0 < \alpha < \pi/2$ and the coupling range $1 < P < N$, this system is known to give rise to chimera states; see, e.g., [40–42]. Below $|a| = 1$ the dynamics of individual units changes from oscillatory to excitable.

The system (1) admits completely coherent homogeneous locked states,

$$\theta_j(t) \equiv \theta^\pm = \pm \arccos \left[\frac{1 - K_1 \sin \alpha}{a} \right], \quad 1 \leq j \leq N, \quad (2)$$

which come in pairs within a locking cone,

$$(K_1 \sin \alpha - 1)^2 < a^2, \quad (3)$$

with its tip located at $a = 0$, $K_1 = 1/\sin \alpha$; cf. Fig. 2(a). Note that the locking cone does not depend on the global coupling K_2 , since there is no phase lag in the corresponding coupling function. However, K_2 strongly affects the stability of the homogeneous locked states. Their Jacobian is a symmetric circulant matrix with real spectrum and discrete Fourier modes as eigenfunctions. The bifurcation condition for the mode with wave number κ is given by

$$a^2 = [K_1(1 - R_\kappa) \cos \alpha + (\delta_{\kappa 0} - 1)K_2]^2 + (1 - K_1 \sin \alpha)^2, \quad (4)$$

where

$$R_\kappa = \frac{1}{2P+1} \sum_{m=-P}^P \cos(2\pi \kappa m/N)$$

is the corresponding discrete Fourier component of the non-local coupling term. Note that inserting $\kappa = 0$ into (4) we recover the fold bifurcations outlining the locking cone

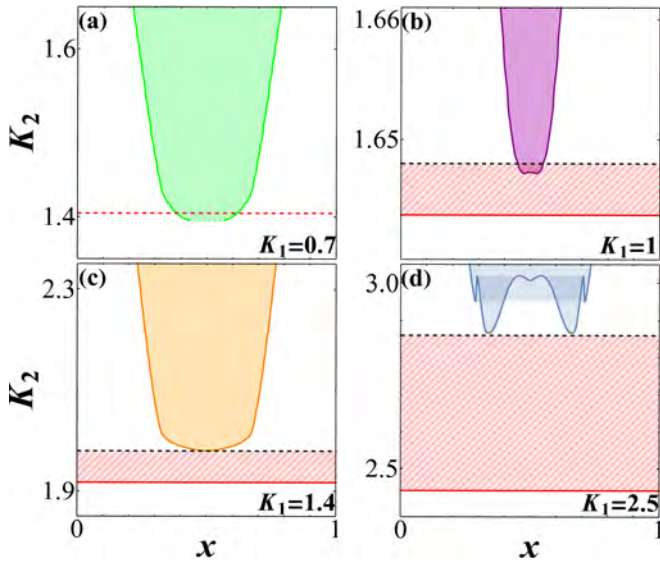


FIG. 3. Colored regions indicate increasing width of incoherent regions of bump states for varying K_2 and $K_1 \in \{0.7, 1, 1.4, 2.5\}$. Spatial parameter $x = k/N$ (k -oscillator index). Other parameters: $a = 1.2$, $\alpha = 0.6$. Turing instability of the homogeneous locked state (horizontal red line), where stable branches of modulated coherent locked states emerge (hatched region), ending at a saddle node (black dashed line). If the saddle node is a SNIC [cases (c) and (d)], there is a supercritical transition to bump states. In case (b) a saddle node of the modulated coherent state induces a subcritical transition to a fully developed bump. In case (a), the Turing instability is subcritical (red dashed line) and the solution jumps from the homogeneous coherent state to a bump.

(3), while $\kappa = 1, \dots, N$ leads to a discrete Turing instability [43,44] with wave number κ . In Fig. 2 we show the regions of existence and stability of the coherent uniform locked states. For $K_2 = 0$, the homogeneous locked state θ^- is stable within the whole locking region. Increasing K_2 , the system undergoes a discrete Turing instability with the leading mode $\kappa = 1$. If this bifurcation is supercritical, we obtain a stable spatially modulated completely coherent state (Turing pattern); see also [45,46]. We analyze now in detail four different destabilization scenarios of the homogeneous locked state induced by increasing the repulsive coupling K_2 along the vertical lines in Fig. 2(b), which all finally lead to the onset of a bump state.

Sub- and supercritical transitions to bump states. In Fig. 3 are illustrated different scenarios for the emergence of bump states showing how the incoherent region grows with increasing global repulsion K_2 for different choices of K_1 . For larger values of K_1 , see panels (b)–(d), the Turing bifurcation is supercritical and a branch of stable spatially modulated coherent states appears (hatched region). In (c) and (d), the stable branch of modulated coherent states extends to a SNIC (saddle-node on invariant circle) bifurcation. This instability represents the supercritical transition from a classical Turing pattern to a coherence-incoherence pattern. Remarkably, it is characterized by unlocking of single localized oscillators, independent on the system size N . Further increasing K_2 leads to the subsequent unlocking of neighboring oscillators and the coherence-incoherence pattern gradually attains temporal and

spatial complexity. In Fig. 3(d) is shown a scenario where the modulated coherent state develops two maxima, such that two incoherent regions emerge simultaneously. Increasing K_2 further, the two incoherent regions merge into a single one. During this process, the branch folds over and a region of coexistence of two different bump solutions appears. Fixing $K_1 = 1.4$, we observe a single monotonically growing incoherent region, as shown in Fig. 3(c). This transition will be investigated in more detail below. For $K_1 = 1.0$, shown in panel (b), the saddle node of the stable branch of modulated coherent states is a classical saddle-node bifurcation, which does not involve an invariant circle and is not localized to a single unlocking oscillator. Such a *collective instability* can induce a subcritical transition to a coexisting fully developed bump state, with incoherent region of finite size. This transition shows a hysteretic behavior when the coupling parameter K_2 is reduced again, whereby the bump state disappears in a chaotic saddle before the size of the incoherent region completely vanishes. For small values of K_1 the Turing instability becomes subcritical, and there is a direct transition from the homogeneous coherent state to a fully developed bump, shown in panel (a), displaying the same hysteretic behavior as described above.

Microscopic structure of the supercritical transition to bump states. Directly after the SNIC bifurcation, when the number of incoherent oscillators in the bump states is small, one can observe an intricate scenario of increasing spatial and temporal complexity, which finally leads to high dimensional extensive chaos. For large N , this transition is confined to a small parameter interval and one observes the almost immediate emergence of a small region of extensive chaos. In Fig. 4 we chose $N = 20$ such that we can study in detail an example of such a transition. The resulting dynamics can be characterized by the spatiotemporal pattern of the single excitation events of the individual oscillators, which manifest themselves as localized peaks in the phase velocity. A selection of such patterns is given in Figs. 4(c)–4(h), while in Figs. 4(a) and 4(b) we show a full parameter scan with respect to K_2 where we sampled the return times Δt_n between two consecutive peaks performed by any of the oscillators [42]. Starting from the simple periodic pattern with one incoherent oscillator that emerges from the SNIC of the modulated coherent state, we see multiple transitions between regular and chaotic states of increasing complexity. The transitions to chaos are mostly of intermittency type, but also torus breakup, illustrated in Fig. 5, and period-doubling cascades can be observed. The shadings of different colors in panels (a) and (b) indicate the increasing number of incoherent oscillators. Note that for $K_2 \approx 2.0255$ the chaotic lateral motion of the incoherent region, which was described in [39] for classical chimera states, sets in. Obviously, the specific shape of the transition scenario depends crucially on even small variations of the system parameters, in particular the number of oscillators N . However, a similar global scenario has been reported in [42], where the classical chimera system of [1] has been extended by a control term, such that also chimera states with a small number of incoherent oscillators became visible.

Outlook and discussion. Our system of excitable or oscillatory units with attractive and repulsive coupling, as given

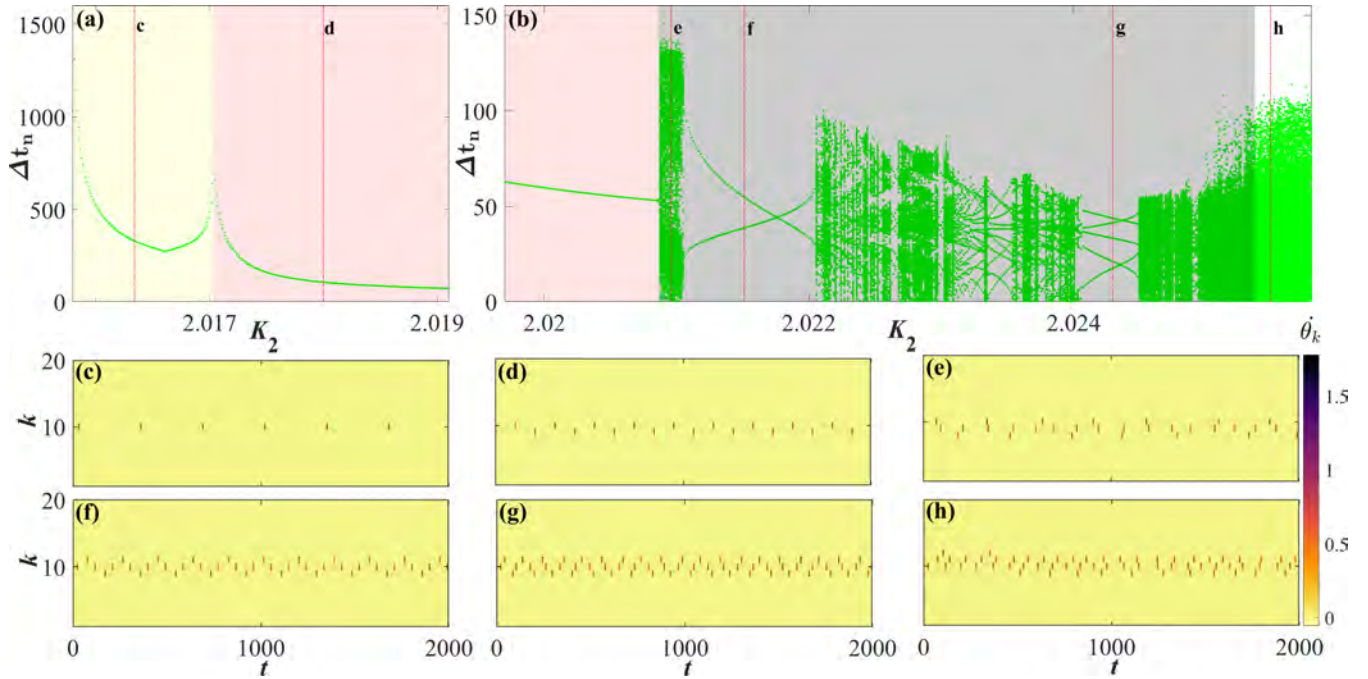


FIG. 4. (a),(b) Bifurcation diagrams in K_2 : time intervals Δt_n between successive velocity peaks. Space-time plots of phase velocities: periodic patterns in (c), (d), (f), and (g); chaotic patterns without (e) and with drift instability (h) for K_2 values indicated by dash-dotted lines in (a) and (b). Other parameters are $K_1 = 1.4$, $a = 1.2$, $\alpha = 0.6$, $N = 20$, $P = 7$.

in (1), shows an extremely rich variety of dynamics. Here we have focused on the emergence of coherence-incoherence patterns and demonstrated how the classical paradigm of pattern formation by Turing [19] and Gierer and Meinhardt [20] in terms of local activation and long-range inhibition leads to the formation of coherence-incoherence patterns in a *supercritical*

transition scenario. In the spatially extended discrete medium of active rotators the attractive and repulsive coupling with different spatial ranges does not activate or inhibit the local activity, as in neural field models, but acts on the local synchrony and in this way induces a pattern of qualitatively different behavior, rather than inducing quantitatively different levels of local activity as in the classical examples of pattern formation in neural field models. In this way, also the classical chimera states, which are related to the bump states discussed here by a simple collective unlocking of the coherent region as described in [38], are no longer an isolated phenomenon in the family of patterns, as stated in [2], but can be seen as a specific type of a Turing pattern, where a spatial modulation results in a self-localized unlocking that emerges gradually from a smooth coherent profile. We have further explained how this transition depends on the coupling strengths $K_{1,2}$. Moreover, we have shown that the coherence-incoherence patterns can be found for a large range of other parameters: in particular, the fine tuning of the phase lag α slightly below $\pi/2$ that was necessary to obtain chimera states in the classical setting [4,40] is no longer needed. Also, another puzzling aspect of chimera states in their original form could be resolved in our modified system. In [39], it was shown that chimeras cannot be observed in small systems, and that even for large system size, they behave as chaotic transients which collapse to the completely coherent state. With our extension of Kuramoto's simple phase oscillator system, coherence-incoherence patterns no longer need to coexist with the stable homogeneous state but, as we demonstrated, can be found as stable attractors even for small system size. In this way, sophisticated control schemes, which have been constructed for their observation [47,48], become no longer necessary. Instead, our model is universal in the sense that the transition between the classical

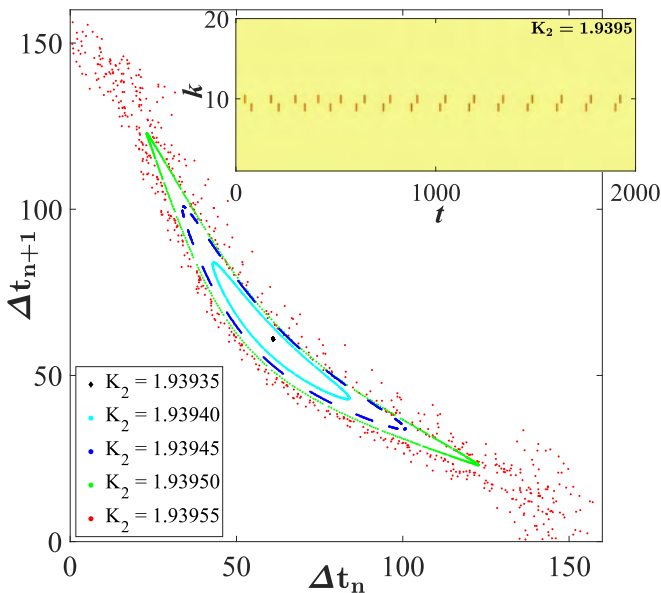


FIG. 5. Emergence of chaos under increasing K_2 . Torus bifurcation from periodic to quasiperiodic pattern at $K_2 \approx 1.9394$, onset of chaos via torus breakup at $K_2 \approx 1.9395$. Inset: space-time plots of phase velocities for quasiperiodic pattern at $K_2 = 1.9395$. Remaining parameters: $K_1 = 1.3$, $a = 1.2$, $\alpha = 0.6$, $N = 20$, $P = 7$.

subcritical scenario and the new supercritical scenario for the onset of coherence-incoherence patterns is achieved by the coupling parameters.

I.F. acknowledges funding from the Institute of Physics Belgrade through the grant by the Ministry of Education,

Science and Technological Development of the Republic of Serbia. The work of O.O. was supported by the Deutsche Forschungsgemeinschaft under Grant No. OM 99/2-1. The work of M.W. was supported by the Deutsche Forschungsgemeinschaft (DFG, German Research Foundation)–Projektnummer 163436311–SFB 910.

-
- [1] Y. Kuramoto and D. Battogtokh, *Nonlinear Phenom. Complex Syst.* **5**, 380 (2002).
- [2] D. M. Abrams and S. H. Strogatz, *Phys. Rev. Lett.* **93**, 174102 (2004).
- [3] F. Parastesh, S. Jafari, H. Azarnoush, Z. Shahriari, Z. Wang, S. Boccaletti, and M. Perc, *Phys. Rep.* **898**, 1 (2021).
- [4] M. J. Panaggio and D. M. Abrams, *Nonlinearity* **28**, R67 (2015).
- [5] J. F. Tetzlaff, J. Rode, M. R. Tinsley, K. Showalter, and H. Engel, *Nat. Phys.* **14**, 282 (2018).
- [6] A. M. Hagerstrom, T. E. Murphy, R. Roy, P. Hövel, I. Omelchenko, and E. Schöll, *Nat. Phys.* **8**, 658 (2012).
- [7] C. Lainscek, N. Rungratsameetaweemana, S. S. Cash, and T. J. Sejnowski, *Chaos* **29**, 121106 (2019).
- [8] R. G. Andrzejak, C. Rummel, F. Mormann, and K. Schindler, *Sci. Rep.* **6**, 23000 (2016).
- [9] O. E. Omel'chenko and E. Knobloch, *New J. Phys.* **21**, 093034 (2019).
- [10] D. M. Abrams, R. Mirollo, S. H. Strogatz, and D. A. Wiley, *Phys. Rev. Lett.* **101**, 084103 (2008).
- [11] E. A. Martens, C. Bick, and M. J. Panaggio, *Chaos* **26**, 094819 (2016).
- [12] M. Mikhaylenko, L. Ramlow, S. Jalan, and A. Zakharova, *Chaos* **29**, 023122 (2019).
- [13] A. Zakharova, *Chimera Patterns in Networks: Interplay Between Dynamics, Structure, Noise, and Delay* (Springer Nature, Switzerland, 2020).
- [14] I. Omelchenko, O. E. Omel'chenko, P. Hövel, and E. Schöll, *Phys. Rev. Lett.* **110**, 224101 (2013).
- [15] N. Semenova, A. Zakharova, V. S. Anishchenko, and E. Schöll, *Phys. Rev. Lett.* **117**, 014102 (2016).
- [16] K. Höhlein, F. P. Kemeth, and K. Krischer, *Phys. Rev. E* **100**, 022217 (2019).
- [17] Y. Zhang and A. E. Motter, *Phys. Rev. Lett.* **126**, 094101 (2021).
- [18] L. Schmidt and K. Krischer, *Phys. Rev. Lett.* **114**, 034101 (2015).
- [19] A. M. Turing, *Phil. Trans. R. Soc. Lond. B* **237**, 37 (1952).
- [20] A. Gierer and H. Meinhardt, *Kybernetik* **12**, 30 (1972).
- [21] P. Ashwin and O. Burylko, *Chaos* **25**, 013106 (2015).
- [22] C. R. Laing, *Phys. Rev. E* **90**, 010901(R) (2014).
- [23] T. B. Luke, E. Barreto, and P. So, *Neural Comput.* **25**, 3207 (2013).
- [24] M. Owen, C. Laing, and S. Coombes, *New J. Phys.* **9**, 378 (2007).
- [25] C. R. Laing, *Phys. D (Amsterdam, Neth.)* **240**, 1960 (2011).
- [26] C. R. Laing, *Frontiers Comput. Neurosci.* **10**, 53 (2016).
- [27] C. R. Laing and O. E. Omel'chenko, *Chaos* **30**, 043117 (2020).
- [28] H. Schmidt and D. Avitabile, *Chaos* **30**, 033133 (2020).
- [29] C. Bick, M. Goodfellow, C. R. Laing, and E. A. Martens, *J. Math. Neurosci.* **10**, 9 (2020).
- [30] Á. Byrne, D. Avitabile, and S. Coombes, *Phys. Rev. E* **99**, 012313 (2019).
- [31] S. Coombes, *Biol. Cybern.* **93**, 91 (2005).
- [32] P. C. Bressloff, *J. Phys. A: Math. Theor.* **45**, 033001 (2012).
- [33] C. R. Laing, W. C. Troy, B. Gutkin, and G. B. Ermentrout, *SIAM J. Appl. Math.* **63**, 62 (2002).
- [34] C. R. Laing and C. Chow, *Neural Comput.* **13**, 1473 (2001).
- [35] K. Wimmer, D. Q. Nykamp, C. Constantinidis, and A. Compte, *Nat. Neurosci.* **17**, 431 (2014).
- [36] E. Montbrió, D. Pazó, and A. Roxin, *Phys. Rev. X* **5**, 021028 (2015).
- [37] J. M. Esnaola-Acebes, A. Roxin, D. Avitabile, and E. Montbrió, *Phys. Rev. E* **96**, 052407 (2017).
- [38] M. I. Bolotov, L. A. Smirnov, G. V. Osipov, and A. Pikovsky, *Phys. Rev. E* **102**, 042218 (2020).
- [39] M. Wolfrum and O. E. Omel'chenko, *Phys. Rev. E* **84**, 015201(R) (2011).
- [40] O. E. Omel'chenko, *Nonlinearity* **31**, R121 (2018).
- [41] O. E. Omel'chenko, *Nonlinearity* **26**, 2469 (2013).
- [42] M. Wolfrum, O. E. Omel'chenko, and J. Sieber, *Chaos* **25**, 053113 (2015).
- [43] M. Wolfrum, *Phys. D (Amsterdam, Neth.)* **241**, 1351 (2012).
- [44] T. Carletti and H. Nakao, *Phys. Rev. E* **101**, 022203 (2020).
- [45] C.-U. Choe, R.-S. Kim, and J.-S. Ri, *Phys. Rev. E* **98**, 012210 (2018).
- [46] R.-S. Kim and C.-U. Choe, *Phys. Rev. E* **98**, 042207 (2018).
- [47] J. Sieber, O. E. Omel'chenko, and M. Wolfrum, *Phys. Rev. Lett.* **112**, 054102 (2014).
- [48] I. Omelchenko, O. E. Omel'chenko, A. Zakharova, and E. Schöll, *Phys. Rev. E* **97**, 012216 (2018).

Dynamics of a stochastic excitable system with slowly adapting feedback

Cite as: Chaos 30, 083109 (2020); doi: 10.1063/1.5145176

Submitted: 15 January 2020 · Accepted: 15 July 2020 ·

Published Online: 3 August 2020



View Online



Export Citation



CrossMark

Igor Franović,^{1,a)} Serhiy Yanchuk,^{2,b)} Sebastian Eydam,^{3,c)} Iva Bačić,^{1,d)} and Matthias Wolfrum^{3,e)}

AFFILIATIONS

¹Scientific Computing Laboratory, Center for the Study of Complex Systems, Institute of Physics Belgrade, University of Belgrade, Pregrevica 118, 11080 Belgrade, Serbia

²Institut für Mathematik, Technische Universität Berlin, Straße des 17. Juni 136, 10623 Berlin, Germany

³Weierstrass Institute, Mohrenstrasse 39, 10117 Berlin, Germany

^{a)}Author to whom correspondence should be addressed: franovic@ipb.ac.rs

^{b)}Electronic mail: yanchuk@math.tu-berlin.de

^{c)}Electronic mail: sebastian.eydam@gmail.com

^{d)}Electronic mail: iva@scl.rs

^{e)}Electronic mail: wolfrum@wias-berlin.de

ABSTRACT

We study an excitable active rotator with slowly adapting nonlinear feedback and noise. Depending on the adaptation and the noise level, this system may display noise-induced spiking, noise-perturbed oscillations, or stochastic bursting. We show how the system exhibits transitions between these dynamical regimes, as well as how one can enhance or suppress the coherence resonance or effectively control the features of the stochastic bursting. The setup can be considered a paradigmatic model for a neuron with a slow recovery variable or, more generally, as an excitable system under the influence of a nonlinear control mechanism. We employ a multiple timescale approach that combines the classical adiabatic elimination with averaging of rapid oscillations and stochastic averaging of noise-induced fluctuations by a corresponding stationary Fokker–Planck equation. This allows us to perform a numerical bifurcation analysis of a reduced slow system and to determine the parameter regions associated with different types of dynamics. In particular, we demonstrate the existence of a region of bistability, where the noise-induced switching between a stationary and an oscillatory regime gives rise to stochastic bursting.

Published under license by AIP Publishing. <https://doi.org/10.1063/1.5145176>

Recent years have witnessed a rapid expansion of stochastic models for a wide variety of important physical and biological phenomena, from sub-cellular processes and tissue dynamics, over large-scale population dynamics and genetic switching to optical devices, Josephson junctions, fluid mechanics, and climatology. These studies have demonstrated that the effects of noise manifest themselves on a broad range of scales but, nevertheless, display certain universal features. In particular, the effects of noise may generically be cast into two groups. On the one hand, the noise may enhance or suppress the features of deterministic dynamics, while on the other hand, it may give rise to novel forms of behavior, associated with the crossing of thresholds and separatrices or with stabilization of deterministically unstable states. The constructive role of noise has been evinced in diverse applications, from neural networks and chemical reactions to lasers and electronic circuits. Classical examples of stochastic facilitation in

neuronal systems concern resonant phenomena, such as coherence resonance, where an intermediate level of noise may trigger coherent oscillations in excitable systems, as well as spontaneous switching between the coexisting metastable states. In the present study, we show how the interaction of noise and multiscale dynamics, induced by slowly adapting feedback, may affect an excitable system. It gives rise to a new mode of behavior based on switching dynamics, namely, the stochastic bursting and allows for an efficient control of the properties of coherence resonance.

I. INTRODUCTION

Multiscale dynamics is ubiquitous in real-world systems. In neuron models, for instance, the evolution of recovery or gating variables is usually much slower than the changes of the

membrane potential.^{1,2} At the level of neural networks, certain mechanisms of synaptic adaptation, such as the spike timing-dependent plasticity,^{3–5} are slower than the spiking dynamics of individual neurons. When modeling the dynamics of semiconductor lasers,^{6–8} one similarly encounters at least two different timescales, one related to the carriers' and the other to the photons' lifetime, whereby their ratio can span several orders of magnitude. Investigating the dynamics of such multiscale systems has led to the development of a number of useful asymptotic and geometric methods, see Refs. 9–13, to name just a few.

Another ingredient inevitable in modeling real-world systems is noise, which may describe the intrinsic randomness of the system and the fluctuations in the embedding environment or may derive from coarse-graining over the degrees of freedom associated with small spatial or temporal scales.^{14,15} For instance, neuronal dynamics is typically influenced by intrinsic sources of noise, such as the random opening of ion channels, and by external sources, like the synaptic noise.¹⁶ In chemical reactions, noise comprises finite-size effects, while the stochasticity in laser dynamics reflects primarily quantum fluctuations. In general, the impact of noise can manifest itself by modification of the deterministic features of the system or by the emergence of qualitatively novel types of behavior, induced by the crossing of thresholds or separatrices.¹⁷

In the present paper, we study the effects of slowly adapting feedback and noise on an excitable system. Excitability is a general nonlinear phenomenon based on a threshold-like response of a system to perturbation.^{1,15,18,19} An excitable system features a stable “rest” state intermitted by excitation events (firing), elicited by perturbations. In the absence of a perturbation, such a system remains in the rest state and a small perturbation induces a small-amplitude linear response. If the perturbation is sufficiently strong, an excitable system reacts by a large-amplitude nonlinear response, such as a spike of a neuron. When an excitable system receives additional feedback or a stochastic input or is coupled to other such systems, new effects may appear due to the self- or noise-induced excitations, as well as excitations from the neighboring systems. Such mechanisms can give rise to different forms of oscillations, patterns, propagating waves, and other phenomena.^{15,20–28}

Our focus is on a stochastic excitable system subjected to a slow control via a low-pass filtered feedback

$$\dot{v}(t) = f(v(t), \mu(t)) + \sqrt{D}\xi(t), \quad (1)$$

$$\dot{\mu}(t) = \varepsilon(-\mu(t) + \eta g(v(t))), \quad (2)$$

where $\varepsilon \gtrsim 0$ is a small parameter that determines the timescale separation between the fast variable $v(t)$ and the slow feedback variable $\mu(t)$. The fast dynamics $\dot{v}(t) = f(v(t), 0)$ is excitable and is influenced by the Gaussian white noise $\xi(t)$ of variance D . Moreover, the slow feedback variable μ controls its excitability properties. The parameter η is the control gain such that for $\eta = 0$, one recovers a classical noise-driven excitable system.¹⁵ An important example of a system conforming to (1) and (2) for $\eta \neq 0$ is the Izhikevich neuron model,²⁹ where the stochastic input to the fast variable would describe the action of synaptic noise.

Here, we analyze a simple paradigmatic example from the class of systems (1) and (2), where the excitable local dynamics is

represented by an active rotator

$$\dot{\varphi}(t) = I - \sin \varphi(t) \quad \text{with} \quad \varphi \in [0, 2\pi).$$

The latter undergoes a saddle-node infinite period (SNIPER, sometimes also called SNIC – saddle node on invariant circle) bifurcation at $|I| = 1$, turning from excitable ($|I| \lesssim 1$) to oscillatory regime $|I| > 1$, see Ref. 30. The adaptation is represented by a positive periodic function $g(\varphi) = 1 - \sin \varphi$ such that the complete model reads

$$\dot{\varphi}(t) = I_0 + \mu(t) - \sin \varphi(t) + \sqrt{D}\xi(t), \quad (3)$$

$$\dot{\mu}(t) = \varepsilon(-\mu(t) + \eta(1 - \sin \varphi(t))). \quad (4)$$

In the presence of feedback, the noiseless dynamics of the active rotator depends now on $I = I_0 + \mu(t)$ involving the control variable $\mu(t)$, which can induce switching between the excitable equilibrium and the oscillatory regime. This adaptation rule provides a positive feedback for the spikes and oscillations, since $\mu(t)$ increases when $\varphi(t)$ is oscillating and drives the system toward the oscillatory regime, while in the vicinity of the equilibrium ($\sin \varphi \approx 1$) the control signal effectively vanishes.

We examine how the behavior of (3) and (4) is influenced by the noise level D and the control gain η , determining the phase diagram of dynamical regimes in terms of these two parameters. The first part of our results in Sec. II concerns the noise-free system $D = 0$, where we employ a combination of two multiscale methods, namely, adiabatic elimination in the regime where the fast subsystem has stable equilibrium and the averaging approach when the fast subsystem is oscillatory. As a result, we obtain a reduced slow system that is capable of describing both the slowly changing fast oscillations and the slowly drifting equilibrium, as well as the transitions between these regimes. The bifurcation analysis of this slow system reveals the emergence of bistability between the fast oscillations and the equilibrium for sufficiently large η .

The second part of our results, presented in Sec. III, addresses the multiscale analysis of the dynamics in the presence of noise ($D \neq 0$). Instead of deterministic averaging, we apply the method of *stochastic averaging*,^{25,31–34} where the distribution density for the fast variable obtained from a stationary Fokker–Planck equation is used to determine the dynamics of the slow flow. In this way, we obtain a deterministic slow dynamics for which one can perform a complete numerical bifurcation analysis with respect to D and η . In Sec. IV, we investigate the effects of stochastic fluctuations on the slow dynamics, which vanish in the limit of infinite timescale separation $\varepsilon \rightarrow 0$ employed in Sec. III. The effect of a slowly adapting feedback on the coherence resonance is shown by extracting from numerical simulations the coefficient of variation of the spike time distribution in the excitable regime. In particular, we compare the results for small positive ε with the case of infinite time scale separation, where we use the stationary but noise dependent μ obtained in Sec. III. The noise-induced switching dynamics in the bistability region is demonstrated by numerical simulations showing an Eyring–Kramers type of behavior.

In terms of the different dynamical regimes, our study of stochastic dynamics reveals three characteristic (D, η) regions featuring noise-induced spiking, noise-perturbed spiking, and stochastic bursting (see Fig. 1). We show that by varying the control gain

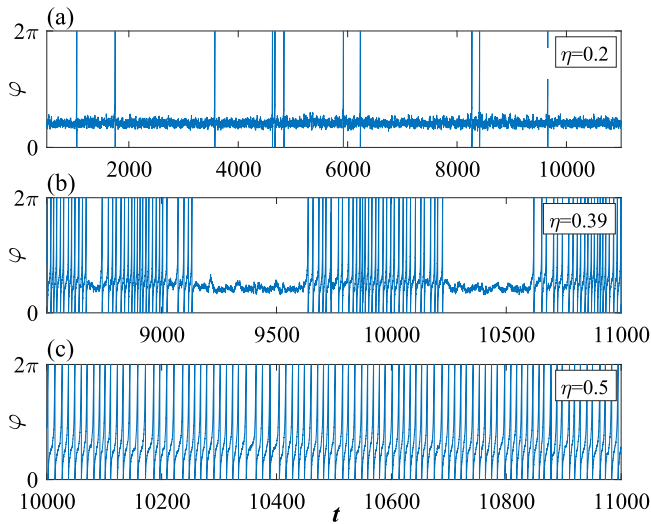


FIG. 1. Different dynamical regimes in the stochastic excitable system subjected to a slow control via a low-pass filtered feedback (3) and (4) with $\varepsilon = 0.005$, $D = 0.008$ and different choices of the control gain η : noise-induced spiking (a), stochastic bursting (b), and noise-perturbed spiking (c).

within the region of noise-induced spiking, one can enhance or suppress the coherence resonance, while within the bistability region, one can efficiently control the properties of stochastic bursting. Sections II–IV provide a detailed analysis of the described phenomena.

II. SLOW-FAST ANALYSIS OF THE DETERMINISTIC DYNAMICS

In this section, we analyze the systems (3) and (4) in the absence of noise ($D = 0$)

$$\dot{\varphi}(t) = I_0 - \sin \varphi(t) + \mu(t), \quad (5)$$

$$\dot{\mu}(t) = \varepsilon(-\mu(t) + \eta(1 - \sin \varphi(t))), \quad (6)$$

considering the limit $\varepsilon \rightarrow 0$ within the framework of singular perturbation theory. The fast subsystem

$$\dot{\varphi}(t) = I_0 + \mu - \sin \varphi(t), \quad (7)$$

often called a “layer equation” describes the dynamics on the fast timescale and is obtained from (5) and (6) by setting $\varepsilon = 0$, whereby μ acts as a parameter.

A. Dynamics for $\mu < 1 - I_0$: Adiabatic elimination

In the case $\mu < 1 - I_0$, the fast subsystem (7) possesses two equilibria

$$\varphi_+(\mu) = \arcsin(I_0 + \mu), \quad \varphi_-(\mu) = \pi - \varphi_+(\mu), \quad (8)$$

where φ_+ is stable and φ_- is unstable. Considering them as functions of the parameter μ , the equilibria give rise to two branches, which

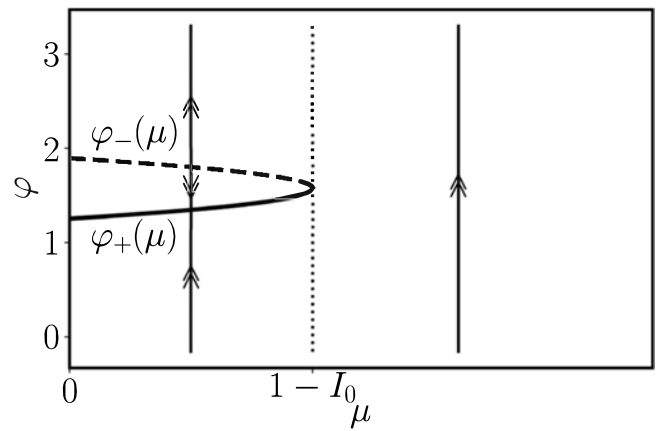


FIG. 2. Critical manifold and fast dynamics of systems (5) and (6). For $\mu < 1 - I_0$, the fast dynamics converges to the stable branch of the critical manifold, while for $\mu > 1 - I_0$, it is oscillatory with periodic rotation of the phase φ .

merge in a fold at $\mu = 1 - I_0$ (see Fig. 2). Equivalently, the set of equilibria of the fast subsystem

$$\{(\varphi, \mu) : \sin \varphi = I_0 + \mu\} \quad (9)$$

comprises the critical manifold of (5) and (6), with the stable part $\varphi_+(\mu)$ and the unstable part $\varphi_-(\mu)$.

Hence, for $\mu < 1 - I_0$, the trajectories are rapidly attracted toward the stable branch of the critical manifold, along which for positive ε they slowly drift. In order to describe this slow dynamics, we rescale time $T = \varepsilon t$ and obtain

$$\varepsilon \varphi'(T) = I_0 + \mu(T) - \sin \varphi(T), \quad (10)$$

$$\mu'(T) = -\mu(T) + \eta(1 - \sin \varphi(T)), \quad (11)$$

where the prime denotes the derivative with respect to the slow time T . Setting $\varepsilon = 0$, we can directly eliminate the term $\sin \varphi(T) = I_0 + \mu(T)$ and obtain the equation for the slow dynamics on the critical manifold

$$\mu'(T) = -\mu(T) + \eta(1 - I_0 - \mu(T)). \quad (12)$$

B. Dynamics for $\mu > 1 - I_0$: Averaging fast oscillations

For $\mu > 1 - I_0$, there is no stable equilibrium of the fast subsystem (7) (see Fig. 2). Instead, one finds periodic oscillations

$$\varphi_\mu(t) = 2 \arctan \frac{1 + \Omega(\mu) \tan \frac{t}{2} \Omega(\mu)}{I_0 + \mu}, \quad (13)$$

with the μ -dependent frequency

$$\Omega(\mu) = \sqrt{(I_0 + \mu)^2 - 1}.$$

In this case, the fast oscillations $\varphi_\mu(t)$ should be averaged in order to obtain the dynamics of the slow variable $\mu(T)$, see Refs 35

and 36. A rigorous formal derivation is provided in Appendix A, finally arriving at

$$\mu'(T) = -\mu(T) + \eta(1 - I_0 - \mu(T) + \Omega(\mu(T))). \quad (14)$$

Here, we give a simplified explanation of the averaging procedure. First, we substitute the fast-oscillating solution $\varphi = \varphi_\mu(t)$ of the fast subsystem into the equation for the slow variable (11),

$$\mu'(T) = -\mu(T) + \eta(1 - \sin \varphi_\mu(t)).$$

Since the term $\sin(\cdot)$ is fast oscillating, the last equation can be averaged over the fast timescale t , which leads to

$$\mu'(T) = -\mu(T) + \eta(1 - \langle \sin \varphi_\mu(t) \rangle_t). \quad (15)$$

The average $\langle \sin \varphi_\mu(t) \rangle_t$ can be found by integrating (7) over the period, which gives

$$\langle \dot{\varphi}(t) \rangle_t = \Omega(\mu) = I_0 + \mu - \langle \sin \varphi_\mu(t) \rangle_t. \quad (16)$$

Hence, by substituting

$$\langle \sin \varphi_\mu(t) \rangle_t = I_0 + \mu(T) - \Omega(\mu(T))$$

into (15), we obtain the slow averaged dynamics (14).

C. Combined dynamics of the slow variable

Summarizing the results so far, Eq. (12) describes the dynamics of the slow variable for $\mu < 1 - I_0$, while Eq. (14) holds for $\mu > 1 - I_0$. These two equations can be conveniently combined into a single equation of the form (14) by extending the definition of the frequency $\Omega(\mu)$ as follows:

$$\Omega(\mu) = \begin{cases} 0, & \mu < 1 - I_0, \\ \sqrt{(I_0 + \mu)^2 - 1}, & \mu > 1 - I_0. \end{cases} \quad (17)$$

Hence, the slow dynamics is described by the scalar ordinary differential equation on the real line (14), and, as a result, the only possible attractors are fixed points, which are given by the zeros of the right-hand side as

$$\Omega(\mu) = \frac{\eta + 1}{\eta} \mu + I_0 - 1. \quad (18)$$

Geometrically, they are points of intersection of the frequency profile $\Omega(\mu)$ with the line $\frac{\eta+1}{\eta}\mu + I_0 - 1$ [see Fig. 3(a)]. In particular, one can check that there is always one fixed point

$$\mu_1 = \frac{\eta(1 - I_0)}{1 + \eta} < 1 - I_0, \quad (19)$$

for which $\Omega(\mu_1) = 0$ such that it corresponds to a pair of equilibria on the critical manifold (9). Since μ_1 is stable for the slow dynamics, the point $(\varphi_+(\mu_1), \mu_1)$ is also a stable equilibrium for original systems (5) and (6) with small ε . The other two fixed points of the slow

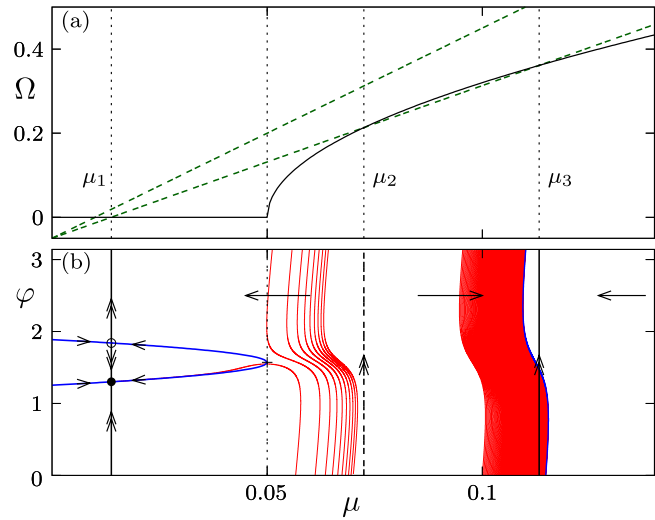


FIG. 3. (a) Graphical solution of the fixed point Eq. (18): $\Omega(\mu)$ according to (17) (black) and the right-hand side of (18) for different choices of η . One finds from one to three fixed points depending on η . (b) Scheme of the slow-fast dynamics of systems (5) and (6) with parameters $I_0 = 0.95$ and $\eta = 0.38$ and the numerical sample trajectories for $\varepsilon = 0.005$ (red). For $\mu < 1 - I_0$, trajectories are attracted to the stable branch of the slow manifold (blue curve) and subsequently slowly drift toward the stable fixed point $(\varphi_+(\mu_1), \mu_1)$ (black dot). For $\mu > 1 - I_0$, the sample trajectories show fast oscillations in φ with a slow average drift in μ in the direction indicated by the arrows.

equation

$$\mu_{2,3} = \frac{\eta(1 + \eta - I_0 \mp \sqrt{(\eta + I_0)^2 - 1 - 2\eta})}{1 + 2\eta}, \quad (20)$$

with $\Omega(\mu_{2,3}) > 0$ appear in a saddle-node bifurcation at

$$\eta_{sn} = 1 - I_0 + \sqrt{2(1 - I_0)} \quad (21)$$

and correspond to a pair of periodic orbits of fast subsystem (7).

In Fig. 3(b) we show schematically the results of our slow-fast analysis for $I_0 = 0.95$ and $\eta = 0.38$. For the chosen parameter values there are two stable regimes: the fixed point $(\varphi_+(\mu_1), \mu_1)$ and a fast oscillation with $\langle \mu(t) \rangle_t \approx \mu_3$.

Finally, Fig. (4) presents the bifurcation diagram of the fixed points of the slow dynamics with respect to the control gain η . One observes that there is always one branch of stable fixed points corresponding to the steady state and two stable fixed points corresponding to fast oscillations for $\eta > \eta_{sn}$. For our choice of $I_0 = 0.95$, we obtain $\eta_{sn} \approx 0.3662$.

III. SLOW-FAST ANALYSIS OF THE DYNAMICS WITH NOISE

In this section, we consider the dynamics of systems (3) and (4) in the presence of noise ($D > 0$). In analogy to the noise-free case,

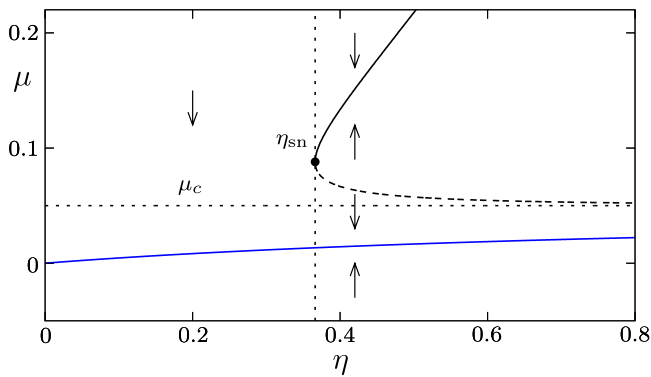


FIG. 4. Fixed points of the slow dynamics (14) for varying control gain η . The values $\mu_{2,3}$ on the upper branch (black curve) correspond to periodic orbits of the fast subsystem (7), while μ_1 (blue curve) is the branch of fixed points; solid and dashed lines indicate stable and unstable solutions, respectively. The direction of the motion in $\mu(T)$ is indicated by the arrows. The dotted lines indicate the onset of bistability for $\eta = \eta_{sn}$ and the transition at $\mu_c = 1 - I_0$ from equilibria to periodic orbits.

one can use the limit $\varepsilon \rightarrow 0$ and employ the *stochastic average*

$$\langle \sin \varphi(t) \rangle_t = \lim_{t \rightarrow \infty} \frac{1}{t} \int_0^t \sin \varphi(t') dt',$$

for solutions of the stochastic fast equation

$$\dot{\varphi}(t) = I_0 + \mu - \sin \varphi(t) + \sqrt{D} \xi(t) \quad (22)$$

to approximate the slow dynamics in (11) by

$$\mu'(T) = -\mu(T) + \eta(1 - \langle \sin \varphi(t) \rangle_t). \quad (23)$$

To this end, we consider the *stationary probability density distribution* $\rho(\varphi; \mu, D)$ for the fast noisy dynamics (3), which for fixed control μ and noise intensity D is given as a solution to the stationary Fokker–Planck equation

$$\frac{D}{2} \partial_{\varphi\varphi} \rho - \partial_{\varphi} [(I_0 + \mu - \sin \varphi) \rho] = 0, \quad (24)$$

together with the periodic boundary conditions $\rho(0) = \rho(2\pi)$ and the normalization

$$\int_0^{2\pi} \rho(\varphi; \mu, D) d\varphi = 1. \quad (25)$$

From this, we can calculate the average

$$\langle \sin \varphi(t) \rangle_t = \int_0^{2\pi} \rho(\varphi; \mu, D) \sin \varphi d\varphi \quad (26)$$

and obtain the mean frequency

$$\Omega_D(\mu) = I_0 + \mu - \langle \sin \varphi(t) \rangle_t, \quad (27)$$

which depends via (26) both on D and μ . Taking into account (23) and (27), the equation for the slow dynamics of $\mu(T)$ reads

$$\mu'(T) = -\mu(T) + \eta(1 - I_0 - \mu + \Omega_D(\mu(T))), \quad (28)$$

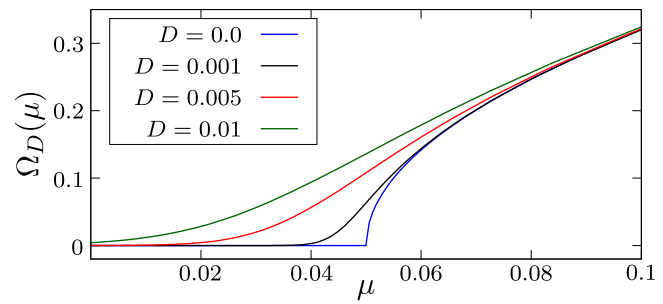


FIG. 5. Average frequency of the fast dynamics (3) given by (26) and (27) using numerical solutions of the stationary Fokker–Planck Eq. (24), where μ acts as a time independent parameter and fixed $I_0 = 0.95$.

i.e., it is of the same form as in the deterministic case (14). The corresponding fixed point equation for the stationary values of μ with respect to the slow dynamics is given by (18).

The stationary Fokker–Planck Eq. (24) can be solved directly by integral expressions [see Appendix B]. In particular, for $D = 0$, we readily recover the results for periodic averaging from Sec. II. However, for small non-vanishing D , the integrals become difficult to evaluate numerically, and we preferred to solve (24) as a first-order ODE boundary value problem with software AUTO,³⁷ which provides numerical solutions to boundary value problems by collocation methods together with continuation tools for numerical bifurcation analysis.

In Fig. 5 are shown the numerically obtained effective frequencies $\Omega_D(\mu)$ for different noise levels D . Solving the stationary Fokker–Planck Eq. (24) together with the fixed point equation for $\mu(T)$ (18), we obtain for fixed values of D and varying control gain η branches of stationary solutions $(\mu^*, \rho(\varphi; \mu^*, D))$ [see Fig. 6(a)]. For small noise intensities, these branches are folded, which indicates the coexistence of up to three stationary solutions, similarly as in the noise-free case. Alternatively, we can also fix η and obtain branches for varying D [see Fig. 6(c)]. For small η they are monotonically increasing, while for larger η they are folded. For $\eta_{sn} < \eta$ there are two separate branches, emanating from the three solutions of (18) at $D = 0.6$

Numerical continuation of the folds in the (η, D) parameter plane provides the curves outlining the boundaries of the bistability region. Figure 6(b) shows that the two branches of folds meet at a cusp point (η_{cu}, D_{cu}) . One of the branches approaches for $D \rightarrow 0$ the value $\eta = \eta_{sn}$, which we have calculated in (21), while the other one diverges to infinite values of η . From our numerics for different values of I_0 , we observe that closer to the critical value $I_0 = 1$, the cusp point shifts to a smaller noise intensity D such that the region of bistability decreases.

Note that for $D > 0$, all the average frequencies satisfy $\Omega_D > 0$ such that a clear distinction between the stationary and the oscillatory regime of the fast dynamics is no longer possible. However, one can compare the critical value of the deterministic fast dynamics

$$\mu_c = 1 - I_0, \quad (29)$$

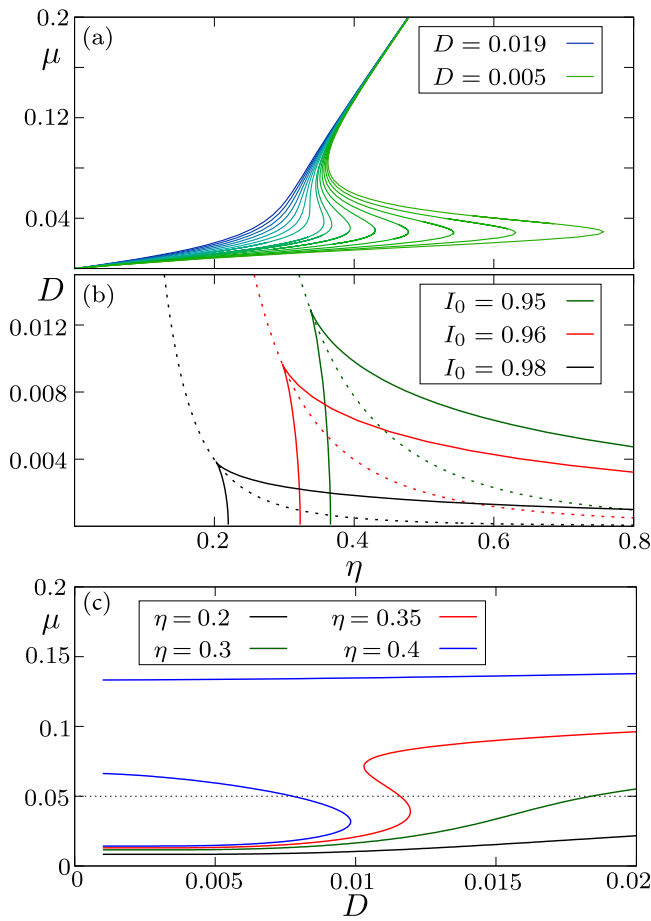


FIG. 6. Panels (a) and (c): Branches of fixed points μ^* of the slow dynamics (28) calculated at $l_0 = 0.95$ from (18) together with the stationary Fokker–Planck Eq. (24). (a) Branches $\mu^*(\eta)$ for noise values $D = 0.005, 0.006, \dots, 0.019$ and (b) two-dimensional bifurcation diagrams in terms of η and D for three different values of l_0 show the curves of fold bifurcations, which meet at the cusp point. Dashed curves indicate the case where $\mu^* = \mu_c = 1 - l_0$. (c) Branches $\mu^*(D)$ for control gain values $\eta \in \{0.2, 0.3, 0.35, 0.4\}$.

with the corresponding stationary value μ^* of the slow variable from (28) to distinguish between the regime of $\mu^* < \mu_c$, where the oscillations are induced by the noisy fluctuations of $\mu(t)$ and have the form of rare spikes [see Fig. 1(a)], and the regime $\mu^* > \mu_c$ where the oscillatory behavior is already induced by the stationary value of μ^* [see Fig. 1(c)].

Our numerical bifurcation analysis shows that the curves where the stationary values of μ satisfy the condition $\mu = \mu_c$, shown as dashed line in Fig. 6(b), pass exactly through the corresponding cusp points and inside the bistability region refer to the unstable solutions given by the middle part of the S-shaped curves in Fig. 6(a). From this, we conclude that changing the parameters across this line outside the bistability region results in a gradual transition between the regime of fluctuation-induced oscillations and the oscillations induced by the stationary value of μ^* , while at the boundary of the

bistability region, a hysteretic transition between the two regimes is obtained. Moreover, for finite timescale separation $\varepsilon > 0$, there can also be transitions between the two stable regimes within the bistability region, which are induced as well by the stochastic fluctuations. In Sec. IV, we study in detail how the region of bistability found for the singular limit $\varepsilon \rightarrow 0$ also affects the dynamics of the original system in the case of finite timescale separation.

IV. EFFECTS OF FLUCTUATIONS AND FINITE TIMESCALE SEPARATION

The two basic deterministic regimes of the fast dynamics, which are the excitable equilibrium, and the oscillations induce in a natural way the two corresponding states of the system with noise and small $\varepsilon > 0$, namely,

- noise-induced spiking, characterized by a Poisson-like distribution of inter-spike intervals (ISIs) [see Fig. 7(a)] and
- noisy oscillations, involving a Gaussian-like distribution of the ISIs, centered around the deterministic oscillation period [see Fig. 7(b)].

These states are found for sufficiently small or large values of η , respectively, where only a corresponding single branch of the deterministic system is available and the fluctuations of μ around its average value have no substantial impact on the dynamics, cf. the blue and orange distributions in Fig. 7. For sufficiently large noise levels above the cusp ($D > D_{cu}$) and intermediate values of η , one observes a gradual transition between these two regimes. However, for smaller noise $D < D_{cu}$, allowing for the existence of the region

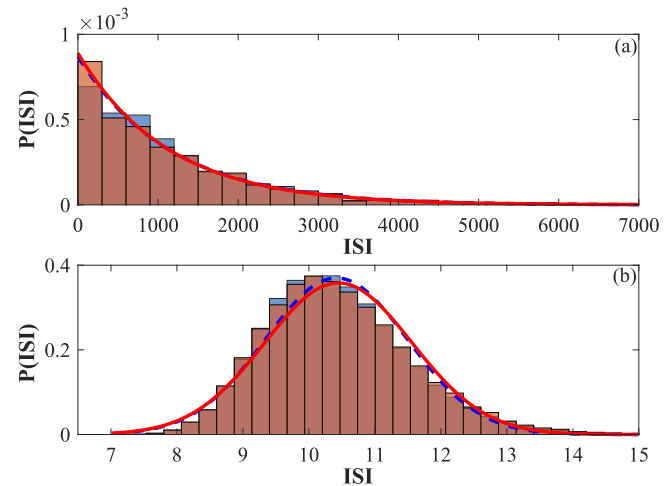


FIG. 7. Histograms of inter-spike intervals of the phase variable for control gain $\eta = 0.2$ (top panel) and $\eta = 0.5$ (bottom panel) obtained from numerical simulations of full systems (3) and (4) with $\varepsilon = 0.005$ (orange) and in the limit of infinite timescale separation (blue), using (22) with the stationary $\mu(T) \equiv \mu_D$ determined from the stationary Fokker–Planck Eq. (24). Solid red and dashed blue curves represent fits to an exponential decay (a) and a Gaussian (b) for the histograms concerning the full system and the limit of infinite scale separation, respectively.

of bistability [cf. Fig. 6(b)], new regimes of stochastic dynamics can emerge, namely,

- enhanced coherence resonance, where a noise-induced dynamical shift of the excitability parameter $I_0 + \mu_D$ is self-adjusted close to criticality and
- noise-induced switching between the two coexisting regimes in the bistability region [see Fig. 1(b)].

A. Enhanced coherence resonance

The phenomenon of coherence resonance,^{20,38,39} where the regularity of noise-induced oscillations becomes maximal at an intermediate noise level, is well-known for noisy excitable systems such as the fast Eq. (22) without adaptation, i.e., for $\eta = 0$ and therefore also $\mu = 0$. For values of the control gain $0 < \eta < \eta_{cu}$ below the region of bistability, the control leads to a substantially enhanced coherence resonance. This effect can be quantified by studying the noise dependence of the coefficient of variation of the inter-spike intervals. For a given noisy trajectory of (22), the spiking times t_k are defined as the first passage times $\varphi(t_k) = 2\pi k, k \in \mathbb{N}$ with corresponding inter-spike intervals $\tau_k = t_k - t_{k-1}$. The coefficient of variation of their distribution is defined as

$$R(D) = \frac{\sqrt{\langle \tau_k^2 \rangle - \langle \tau_k \rangle^2}}{\langle \tau_k \rangle}. \quad (30)$$

For (22) with a fixed μ , the latter can be determined from direct numerical simulations. However, inserting for μ the corresponding stochastic averages $\mu^*(D; \eta)$ obtained in the section shows a strong nonlinear dependence both on η and D [see also Figs. 6(a) and 6(c)]. In particular, the strong nonlinear dependence on D for η slightly below the cusp value η_{cu} has a substantial impact on the resonant behavior reflected in the form of $R(D)$. In Fig. 8, we show the $R(D)$ dependence for different values of the control gain η , comparing the numerical results for the fast subsystem (22) with inserted stationary values $\mu^*(D; \eta)$ to numerical simulations of (3) and (4) for $\varepsilon = 0.005$. For $0 < \eta < \eta_{cu}$, one finds that the coherence resonance can be substantially enhanced, cf., for example, the $R(D)$ dependencies for $\eta = 0$ and $\eta = 0.3$. On the other hand, introducing negative values of the control gain η , the resonant effect can be readily suppressed. This implies that the adaptive feedback we employ provides an efficient control of coherence resonance. Such an effect has already been demonstrated in Refs. 40, 41, and 42 by using a delayed feedback control of Pyragas type. However, this control method requires the feedback delay time as an additional control parameter to be well adapted to the maximum resonance frequency.

B. Bursting behavior due to noise-induced switching

For parameter values (η, D) within the bistable region and finite timescale separation $\varepsilon > 0$, the coexisting states of excitable equilibrium and fast oscillations turn into metastable states of full systems (3) and (4). Based on our slow-fast analysis, the corresponding dynamics can be understood as follows. The noisy fluctuations of $\varphi(t)$ around its average distribution, given by the stationary Fokker-Planck Eq. (24), induces fluctuations of $\langle \sin \varphi(t) \rangle_t$, and hence also of μ , around their stationary average values calculated

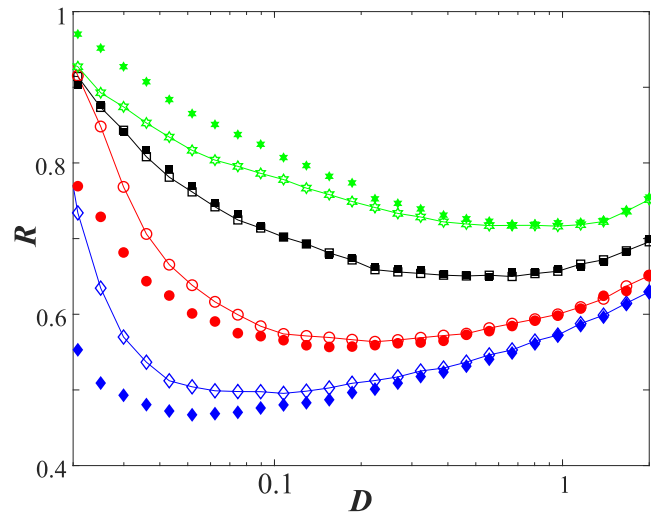


FIG. 8. Enhancement or suppression of coherence resonance by a slowly adapting feedback control. The connected lines with empty symbols refer to $R(D)$ dependencies for full systems (3) and (4) at different values of the control gain: $\eta = -0.2$ (green hexagonals), $\eta = 0$ (black squares), $\eta = 0.2$ (red circles), and $\eta = 0.3$ (blue diamonds), having fixed $I_0 = 0.95, \varepsilon = 0.005$. The unconnected filled symbols indicate the corresponding $R(D)$ dependencies obtained from numerical simulations of the fast subsystem 22 with stationary $\mu^*(D)$.

above. For small ε , the corresponding distribution of μ is centered in narrow peaks at the stable stationary values. However, with increasing ε , the nonlinear filtering induces a strong skewness of each peak in the distribution, and their overlapping indicates the possibility of noise-induced transitions between the two metastable states. Figure 9 shows the distribution for $\varepsilon = 0.005$ and different values of the η within the bistability region. These transitions can be understood in analogy to the Eyring-Kramers process in a double well potential. In the generic case of different energy levels for the two potential wells, transitions in one of the directions occur at a higher rate and the system stays preferably in the state associated with the global minimum of the potential. Such behavior of biased switching is very pronounced closed to the boundaries of the bistability region, where a switching to the state close to the fold has a much lower probability than switching back.

In Fig. 10 are shown the numerical time averages $\langle \mu(T) \rangle$ for varying control gain η . One can see that for most values of η , the long-time behavior is dominated by one of the two metastable states, which indicates a biased switching process. Nevertheless, at an intermediate value of η , we find a balanced switching, where transitions in both directions occur at an almost equal rate. A corresponding time trace is shown in Figs. 11 and 1(b). For $\varepsilon \rightarrow 0$, the switching rate decreases to zero exponentially and the switching bias in the unbalanced regime increases. This leads to the characteristic steplike behavior of the averages observed in Fig. 10 for smaller ε .

The noise-induced switching shown in Figs. 11 and 1(b) resembles the regime of bursting in neuronal systems. Here, it emerges by an interplay of slow adaptation and noise. In the present setup,

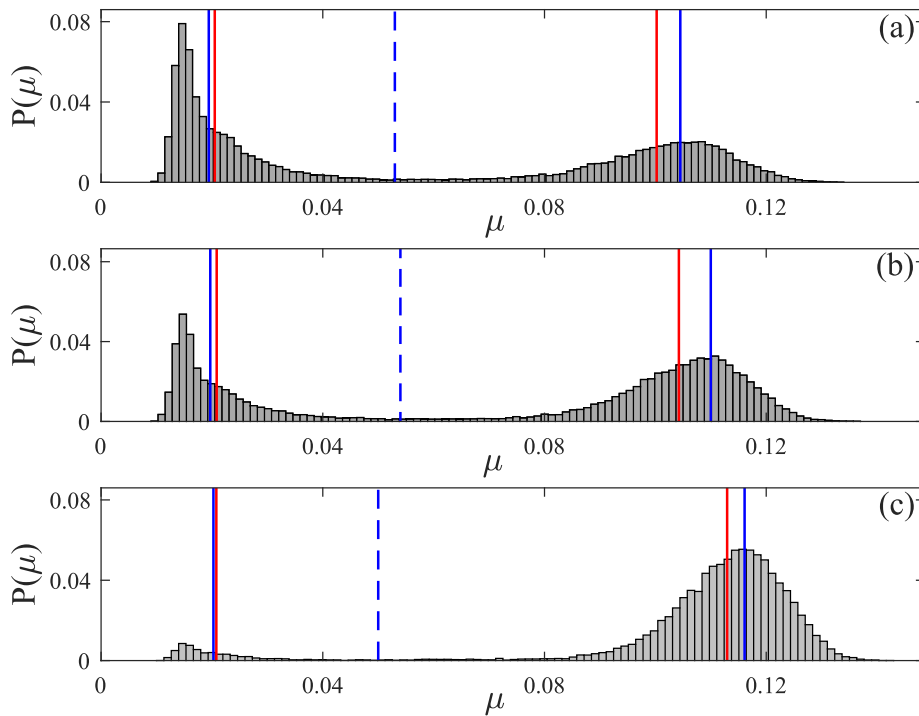


FIG. 9. Stationary distributions $P(\mu)$, sampled from numerical simulations of (3) and (4) with $\varepsilon = 0.005$. Parameters $\eta = 0.37$ in (a), $\eta = 0.373$ in (b) and $\eta = 0.38$ in (c) and fixed noise level $D = 0.009$ lie inside the bistability region from Fig. 6(b). Blue vertical lines indicate the fixed points of μ from the stationary Fokker–Planck Eq. (24) together with the fixed point Eq. (18) of the slow dynamics. Red vertical lines indicate the mean values of all μ in $P(\mu)$ below and of all μ above the unstable fixed point in the middle (dashed blue lines).

the bursts are triggered just by the stochastic fluctuations. However, in regime $\eta > \eta_{cu}$, the system is also quite susceptible to external inputs, which could initiate the bursts even without any intrinsic noise.

V. DISCUSSION AND OUTLOOK

Our model provides a novel perspective on how the dynamics of an excitable system is influenced by the interaction of a slowly adapting feedback and noise. The feedback is taken from a low-pass

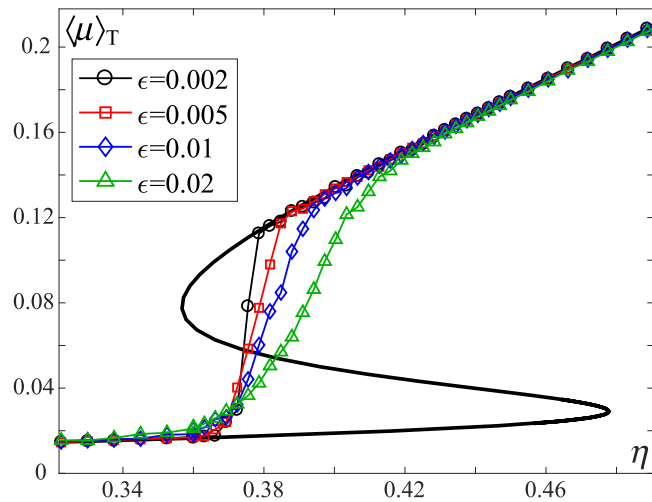


FIG. 10. Long-time averages $\langle \mu \rangle_T$ from numerical simulations of (3) and (4) with fixed noise intensity $D = 0.008$ and varying control gain η at different values of $\varepsilon \in \{0.002, 0.005, 0.01, 0.02\}$. The black curve represents the corresponding result for the infinite timescale separation [cf. Fig. 6(a)].

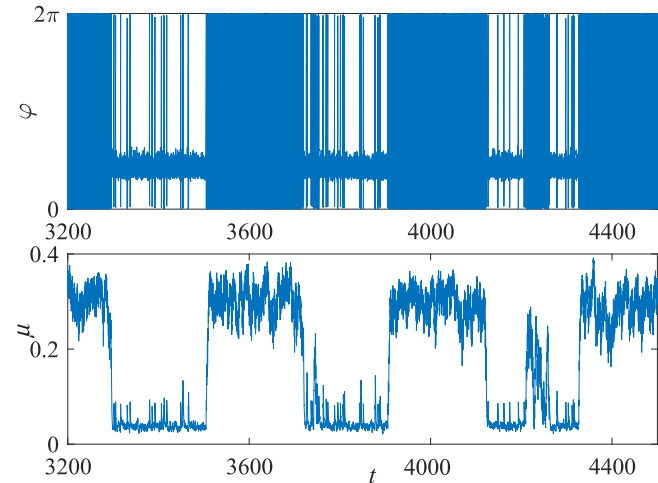


FIG. 11. Time series $\varphi(t)$ (top panel) and $\mu(t)$ (bottom panel) illustrating the regime of balanced switching. The system parameters are $\eta = 0.38$, $D = 0.008$, $l_0 = 0.95$, $\varepsilon = 0.01$.

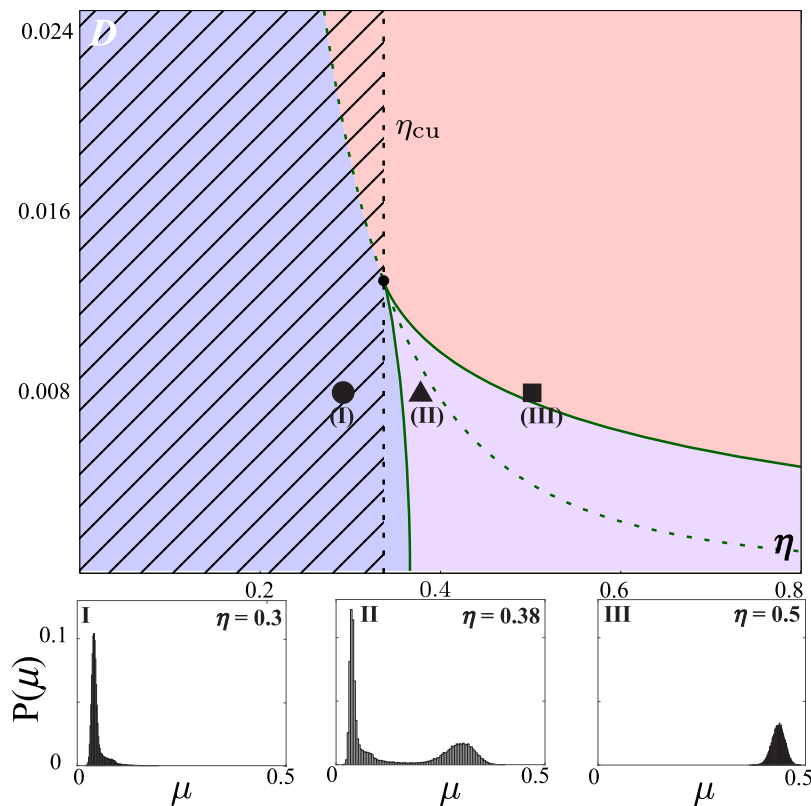


FIG. 12. Upper panel: parameter regions for different dynamical regimes: noise-induced spiking (blue), noise-perturbed oscillations (red), and noise-induced bursting (violet). Enhanced coherence resonance can be found in the hatched region. Symbols indicate the parameter values associated with the histograms $P(\mu)$ shown below. Lower panels: sampled distributions of $\mu(T)$ from numerical solutions with $\varepsilon = 0.005$, $D = 0.008$, and $\eta \in \{0.3, 0.38, 0.5\}$.

filter of a function that gives a positive feedback to the oscillations by pushing the excitability parameter toward the oscillatory regime. Since excitability, feedback, and noise are typical ingredients of neural systems, we believe that the application of our results to a specific neural model would be a next natural step, aiming to gain a deeper understanding of the onset of different dynamical regimes, as well as the means of controlling their properties and the emerging resonant effects. In Fig. 12 are summarized our main results. In particular, the multiple timescale analysis for the limit of infinite timescale separation has allowed us to perform a numerical bifurcation analysis providing the parameter regions for the different dynamical regimes illustrated in Fig. 1. Numerical simulations for finite values of ε (lower panels in Fig. 12) show that the slowly varying control variable $\mu(T)$ is distributed around the stationary values from the limiting problem $\varepsilon = 0$ [see also Fig. 9]. Moreover, we have demonstrated that the filtered feedback in our model provides an efficient control of the effect of coherence resonance, which can be substantially enhanced or suppressed by a corresponding choice of the feedback gain. In the regime where the limiting problem $\varepsilon = 0$ indicates bistability between the equilibrium and a fast oscillation, the stochastic fluctuations at finite values of ε give rise to switching between the associated metastable states. However, our analysis shows that for sufficiently high noise intensity, this bistability vanishes and the two different deterministic states can no longer be distinguished.

From the point of view of the theory of multiscale systems, the deterministic part of the presented model provides one of the simplest examples combining the regimes of stable equilibrium and oscillations within the fast subsystem. A rigorous mathematical treatment of the dynamical transitions between the two regimes and the corresponding reductions by the standard adiabatic elimination and the averaging technique is still missing. Also, our approach to analysis of stochastic dynamics in multiscale systems by introducing a stationary Fokker–Planck equation for the fast dynamics leads to important questions concerning the limiting properties of the trajectories and the specific implications of the fluctuations. Nevertheless, we have considered only the case when the noise acts in the fast variable. An open problem is to study how the obtained results are influenced by the noise in the slow variable, where interesting new effects can be expected.⁴³

ACKNOWLEDGMENTS

I.F. and I.B. acknowledge funding from the Institute of Physics Belgrade through the grant by the Ministry of Education, Science and Technological Development of the Republic of Serbia. S.Y. acknowledges the support from the Deutsche Forschungsgemeinschaft (DFG) under Project No. 411803875. The work of M.W. and S.E. was supported by the Deutsche Forschungsgemeinschaft (DFG, German Research Foundation)—Projektnummer 163436311—SFB 910.

APPENDIX A: MULTISCALE AVERAGING IN THE REGIME OF FAST OSCILLATIONS

In this appendix, we provide a rigorous formal derivation of the slow averaged Eq. (14) for the case of periodic dynamics in the fast layers.

We apply the following general multiscale ansatz:

$$\begin{aligned} \varphi &= \bar{\varphi}(t, \varepsilon t) + \varepsilon \hat{\varphi}(t, \varepsilon t), \\ \mu &= \bar{\mu}(t, \varepsilon t) + \varepsilon \hat{\mu}(t, \varepsilon t). \end{aligned}$$

Substituting this ansatz into (3) and (4), one obtains up to the terms of the order ε ,

$$\begin{aligned} \partial_1 \bar{\varphi} + \varepsilon \partial_2 \bar{\varphi} + \varepsilon \partial_1 \hat{\varphi} &= I_0 - \sin(\bar{\varphi} + \varepsilon \hat{\varphi}) + \bar{\mu} + \varepsilon \hat{\mu}, \\ \partial_1 \bar{\mu} + \varepsilon \partial_2 \bar{\mu} + \varepsilon \partial_1 \hat{\mu} &= \varepsilon(-\bar{\mu} - \varepsilon \hat{\mu} + \eta(1 - \sin(\bar{\varphi} + \varepsilon \hat{\varphi}))), \end{aligned}$$

where subscripts 1 and 2 refer to partial derivatives with respect to t and εt , respectively. Collecting the terms of order $\mathcal{O}(1)$, one finds

$$\partial_1 \bar{\varphi} = I_0 - \sin \bar{\varphi} + \bar{\mu}, \tag{A1}$$

$$\partial_1 \bar{\mu} = 0. \tag{A2}$$

Equation (A2) implies that $\bar{\mu} = \bar{\mu}(\varepsilon t)$ depends only on the slow time and acts as a parameter in (A1). For $\bar{\mu} > 1 - I_0$, Eq. (A1) has the oscillating solution $\bar{\varphi} = \varphi_{\bar{\mu}}(t)$ given by (13). Note that the parameters of this solution can depend on the slow time.

As a next step, we consider the terms of order ε ,

$$\begin{aligned} \partial_2 \bar{\varphi} + \partial_1 \hat{\varphi} &= -\hat{\varphi} \cos \bar{\varphi} + \hat{\mu}, \\ \partial_2 \bar{\mu} + \partial_1 \hat{\mu} &= -\bar{\mu} + \eta(1 - \sin \bar{\varphi}). \end{aligned} \tag{A3}$$

We rewrite Eq. (A3) as

$$\partial_2 \bar{\mu} + \bar{\mu} = -\partial_1 \hat{\mu} + \eta(1 - \sin \bar{\varphi}), \tag{A4}$$

where the left-hand side depends only on the slow time. Hence, the solvability condition for (A4) is the requirement that its right-hand side is independent on the fast time t , i.e.,

$$-\partial_1 \hat{\mu} + \eta(1 - \sin \bar{\varphi}) = u(T), \tag{A5}$$

with some function $u(T)$, where $T = \varepsilon t$ is the slow time. By integrating (A5) with respect to the fast time, we obtain

$$\hat{\mu}(t) = \hat{\mu}(0) + \eta \left(t - \int_0^t \sin \bar{\varphi} dt \right) - tu(T). \tag{A6}$$

The integral in (A6) can be computed using (A1),

$$\int_0^t \sin \bar{\varphi} dt = tI_0 + t\bar{\mu} - \bar{\varphi}(t) + \bar{\varphi}(0),$$

such that

$$\hat{\mu}(t) = \hat{\mu}(0) + t \left[\eta \left(1 - I_0 - \bar{\mu} + \frac{\bar{\varphi}(t) - \bar{\varphi}(0)}{t} \right) - u(T) \right].$$

Taking into account that

$$\frac{\bar{\varphi}(t) - \bar{\varphi}(0)}{t} = \Omega(\bar{\mu}) + \mathcal{O}\left(\frac{1}{t}\right),$$

we obtain the expression for $\hat{\mu}$,

$$\hat{\mu}(t) = \hat{\mu}(0) + t[\eta(1 - I_0 - \bar{\mu} + \Omega(\bar{\mu})) - u(T)] + \mathcal{O}(1),$$

where the linearly growing term must vanish for $\hat{\mu}(t)$ to be bounded. Setting such a secular term to zero (even without computing explicitly $\hat{\mu}$), we have

$$u(T) = \eta(1 - I_0 - \bar{\mu} + \Omega(\bar{\mu}))$$

and, hence, taking into account (A4) and (A5), the equation for the leading order approximation of the slow variable reads

$$\partial_2 \bar{\mu} + \bar{\mu} = \eta(1 - I_0 - \bar{\mu} + \Omega(\bar{\mu})).$$

Since $\bar{\mu}$ is the function of the slow time only, we have $\partial_2 \bar{\mu} = \bar{\mu}'$, which results in the required averaged Eq. (14).

APPENDIX B: EXPLICIT SOLUTION OF THE STATIONARY FOKKER-PLANCK EQUATION

Here, we present the analytic solution of the stationary Fokker-Planck Eqs. (24) and (25). By integrating Eq. (24) once, one obtains

$$\frac{D}{2} \partial_\varphi \rho - (I_0 + \mu - \sin \varphi) \rho = C, \tag{B1}$$

with a constant C to be determined. Solving (B1), and taking into account the normalization (25) and the boundary condition $\rho(0) = \rho(2\pi)$, we arrive at

$$\rho(\varphi; \mu, D) = \frac{1}{g_\Lambda} \Lambda(\varphi),$$

where

$$\begin{aligned} \Lambda(\varphi) &= \int_0^{2\pi} \frac{\Psi(\varphi)}{\Psi(\varphi + \xi)} d\xi, \\ g_\Lambda &= \int_0^{2\pi} \Lambda(\varphi) d\xi, \\ \Psi(\varphi) &= \exp \left\{ \frac{2}{D} [(I_0 + \mu)\varphi + \cos \varphi - 1] \right\}. \end{aligned}$$

DATA AVAILABILITY

The data that support the findings of this study are available from the corresponding author upon reasonable request.

REFERENCES

¹E. M. Izhikevich, *Dynamical Systems in Neuroscience: The Geometry of Excitability and Bursting* (The MIT Press, 2007), ISBN: 9780262090438.
²W. Gerstner, W. M. Kistler, R. Naud, and L. Paninski, *Neuronal Dynamics: From Single Neurons to Networks and Models of Cognition* (Cambridge University Press, 2014), ISBN: 9781107447615.
³L. F. Abbott and P. Dayan, *Theoretical Neuroscience* (The MIT Press, 2005).
⁴C. Clopath, L. Büsing, E. Vasilaki, and W. Gerstner, *Nat. Neurosci.* **13**, 344 (2010).
⁵O. Popovych, S. Yanchuk, and P. A. P. Tass, *Sci. Rep.* **3**, 2926 (2013).
⁶R. Lang and K. Kobayashi, *IEEE J. Quantum Electron.* **16**, 347 (1980).
⁷K. Lüdge, *Nonlinear Laser Dynamics* (Wiley-VCH Verlag GmbH & Co. KGaA, Weinheim, 2011), ISBN: 9783527639823.

- ⁸M. C. Soriano, J. García-Ojalvo, C. R. Mirasso, and I. Fischer, *Rev. Mod. Phys.* **85**, 421 (2013).
- ⁹M. Krupa, B. Sandstede, and P. Szmolyan, *J. Differ. Equ.* **133**, 49 (1997).
- ¹⁰M. Lichtner, M. Wolfrum, and S. Yanchuk, *SIAM J. Math. Anal.* **43**, 788 (2011).
- ¹¹M. Desroches, J. Guckenheimer, B. Krauskopf, C. Kuehn, H. M. Osinga, and M. Wechselberger, *SIAM Rev.* **54**, 211 (2012).
- ¹²C. Kuehn, *Multiple Time Scale Dynamics* (Springer-Verlag GmbH, 2015), Vol. 191, ISBN: 978-3-319-12315-8.
- ¹³H. Jardon-Kojakhmetov and C. Kuehn, arxiv.org/abs/1901.01402 (2019).
- ¹⁴H. Haken, *Advanced Synergetics* (Springer, Berlin, 1985).
- ¹⁵B. Lindner, J. García-Ojalvo, A. Neiman, and L. Schimansky-Geier, *Phys. Rep.* **392**, 321 (2004).
- ¹⁶A. Destexhe and M. Rudolph-Lilith, *Neuronal Noise* (Springer, New York, 2012).
- ¹⁷E. Forgoston and R. O. Moore, *SIAM Rev.* **60**, 969 (2018).
- ¹⁸J. D. Murray, *Mathematical Biology*, Biomathematics Vol. 19 (Springer, New York, 1989), ISBN: 0-387-19460-6 (New York), 3-540-19460-6 (Berlin).
- ¹⁹A. T. Winfree, *The Geometry of Biological Time* (Springer, 2001), Vol. 12, ISBN: 978-1-4419-3196-2
- ²⁰A. S. Pikovsky and J. Kurths, *Phys. Rev. Lett.* **78**, 775 (1997).
- ²¹V.-C. Oriol, M. Ronny, R. Sten, and L. Schimansky-Geier, *Phys. Rev. E* **83**, 036209 (2011).
- ²²G. B. Ermentrout and D. Kleinfeld, *Neuron* **29**, 33 (2001).
- ²³L. Lücken, D. P. Rosin, V. M. Wozniak, and S. Yanchuk, *Chaos* **27**, 13114 (2017).
- ²⁴I. Franović, O. E. Omel'chenko, and M. Wolfrum, *Chaos* **28**, 071105 (2018).
- ²⁵I. Bačić, S. Yanchuk, M. Wolfrum, and I. Franović, *EPJ ST* **227**, 1077 (2018).
- ²⁶I. Franović, K. Todorović, M. Perc, N. Vasović, and N. Burić, *Phys. Rev. E* **92**, 062911 (2015).
- ²⁷I. Franović, M. Perc, K. Todorović, S. Kostić, and N. Burić, *Phys. Rev. E* **92**, 062912 (2015).
- ²⁸S. Yanchuk, S. Ruschel, J. Sieber, and M. Wolfrum, *Phys. Rev. Lett.* **123**, 053901 (2019).
- ²⁹E. M. Izhikevich, *IEEE Trans. Neural Netw.* **15**, 1063 (2004).
- ³⁰S. H. Strogatz, *Nonlinear Dynamics and Chaos: With Applications to Physics, Biology, Chemistry, and Engineering* (Addison-Wesley, 1994).
- ³¹A. Shilnikov and M. Kolomiets, *Int. J. Bifurc. Chaos* **18**, 2141 (2008).
- ³²G. Pavliotis and A. Stuart, *Multiscale Methods: Averaging and Homogenization* (Springer, Berlin, 2008).
- ³³M. Galtier and G. Wainrib, *Phys. Rev. E* **2**, 13 (2012).
- ³⁴L. Lücken, O. V. Popovych, P. A. Tass, and S. Yanchuk, *Phys. Rev. E* **93**, 32210 (2016).
- ³⁵A. I. Neishtadt, *J. Appl. Math. Mech* **48**, 133 (1984).
- ³⁶J. Guckenheimer and P. Holmes, *Nonlinear Oscillations, Dynamical Systems and Bifurcations of Vector Fields* (Springer-Verlag, New York, 1983).
- ³⁷E. J. Doedel, R. C. Paffenroth, A. R. Champneys, T. F. Fairgrieve, Y. A. Kuznetsov, B. Sandstede, and X. Wang, *AUTO-07p: Continuation and Bifurcation Software for Ordinary Differential Equations* (Concordia University, Canada, 2007).
- ³⁸B. Lindner and L. Schimansky-Geier, *Phys. Rev. E* **60**, 7270 (1999).
- ³⁹V. A. Makarov, V. I. Nekorkin, and M. G. Velarde, *Phys. Rev. Lett.* **86**, 3431 (2001).
- ⁴⁰R. Aust, P. Hövel, J. Hizanidis, and E. Schöll, *Eur. Phys. J. Spec. Top.* **187**, 77 (2010).
- ⁴¹N. Kouvaris, L. Schimansky-Geier, and E. Schöll, *Eur. Phys. J. Spec. Top.* **191**, 29 (2010).
- ⁴²N. B. Janson, A. G. Balanov, and E. Schöll, *Phys. Rev. Lett.* **93**, 010601 (2004).
- ⁴³P. H. Dannenberg, J. C. Neu, and S. W. Teitsworth, *Phys. Rev. Lett.* **113**, 020601 (2014).



Contents lists available at ScienceDirect

Chaos, Solitons and Fractals

Nonlinear Science, and Nonequilibrium and Complex Phenomena

journal homepage: www.elsevier.com/locate/chaos

Frontiers

EFFECT of colored noise on the generation of seismic fault MOVEMENT: Analogy with spring-block model DYNAMICS

Srđan Kostić^{a,*}, Nebojša Vasović^b, Kristina Todorović^c, Igor Franović^d^a *Geology Department, Water Institute "Jaroslav Černi", Jaroslava Černog 80, 11226 Belgrade, Serbia*^b *Department of Applied Mathematics, University of Belgrade Faculty of Mining and Geology, Serbia*^c *Department of Physics and Mathematics, University of Belgrade Faculty of Pharmacy, Serbia*^d *Scientific Computing Lab, University of Belgrade, Institute of Physics, Serbia*

ARTICLE INFO

Article history:

Received 27 January 2020

Accepted 2 March 2020

Available online 3 May 2020

Keywords:

Correlated noise

Correspondence with real measurements

Bifurcation

Regimes of fault motion dynamics

ABSTRACT

In present paper authors examined the effect of colored noise on the onset of seismic fault motion. For this purpose, they analyze the dynamics of spring-block model, with 10 all-to-all coupled blocks. This spring-block model is considered as a collection of fault patches (with the increased rock friction), which are separated by the material bridges (more petrified parts of the fault). In the first phase of research, authors confirm the presence of autocorrelation in the background of seismic noise, using the measurement of real fault movement, and the recorded ground shaking before and after an earthquake. In the second stage of the research, authors firstly develop a mean-field model, which accurately enough describes the dynamics of a starting block model, with the introduced delayed interaction among the blocks, while colored noise is assumed to be generated by Ornstein-Uhlenbeck process. The results of the analysis indicate the existence of three different dynamical regimes, which correspond to three regimes of fault motion: steady stationary state, aseismic creep and seismic fault motion. The effect of colored noise lies in the possibility of generating the seismic fault motion even for small values of correlation time. Moreover, it is shown that the tight connection between the blocks, i.e. fault patches prevent the occurrence of seismic fault motion.

© 2020 Elsevier Ltd. All rights reserved.

1. Introduction

Significance of seismic noise study in seismological research lies in the possibility of reliable subsurface tomography using the records on ambient seismic noise [1]. In particular, numerous field studies confirmed that ratio of horizontal to vertical component of ambient noise gives solid data on the subsurface geology in areas with low seismicity or even in aseismic areas [2]. However, none of the previous studies dealt with the effect of noise on the fault movement. Reason for this lies in inaccessibility of the fault zone to direct measurements, both of ambient noise and the fault movement. These measurements are only possible in deep boreholes, near the active fault zones, like in the case of fault movement directly measured at the Driny cave, MaleĀrpaty mts in Slovakia [3], or in the 3 km deep borehole that cuts through the San Andreas fault system within the SAFOD research project [4]. Also, the effect of noise on generation of seismic fault movement is impossi-

ble to prove by the in situ measurements. For these reasons, fault motion is usually examined by modeling in laboratory conditions, whereby simulations are commonly conducted in two ways: either by observing the behavior of an array of blocks (starting from the Burridge-Knopoff model), or by analysis of the motion between the two plates, whose contact is simulated by an assemblage of real or artificial grains. In these conditions, it is possible to simulate movement along the fault, including all the accompanying effects. Nevertheless, as far as authors are aware, effect of noise on fault motion has not been examined in laboratory conditions so far.

However, mathematical expressions which are used to describe the dynamics of such systems allow one to examine different effects, at least from a theoretical viewpoint. Regarding the effect of noise, in our previous work [5] we examined the dynamics of an array of 100 blocks under the effect of random seismic noise. In that case, assumption of random nature of seismic noise came from the two sources. Firstly, we examined the real observed GPS measurements of fault movement at the ground surface at several stations within the San Andreas fault zone, for which we established to have the properties of stochastic time series. Secondly,

* Corresponding author.

E-mail address: srdjan.kostic@jcerni.rs (S. Kostić).

we wanted to examine the effect of permanent background seismic noise, so it was natural to assume its random nature. However, what if the noise along the fault zone or in its immediate vicinity is correlated? Justification for this lies in existence of many potential sources of colored (correlated) noise: reservoir charging/discharging, penetration of sound waves emitted by neighboring fault motion, close earthquakes or explosion, ocean waves and tides, etc. Another source of colored noise could come from the pre-processing of the acquired measurements. In particular, recorded time series could be represented as a combination of a deterministic signal, i.e. convenient combination of sine and cosine wave, with the remaining stochastic residuals, which always have certain level of autocorrelation. All these factors could generate correlated oscillations of small amplitude with respect to the scale of fault motion.

In our previous work on the effect of random noise on the fault motion, we showed that when fault is in inter-seismic stage, near the boundary to the co-seismic regime, even random noise with very small amplitude could generate the transition to co-seismic fault motion. Regarding the possible multiple sources of colored seismic noise, in present paper we want to examine whether correlated noise could be also responsible for earthquake nucleation. For this purpose, we invoke the method of mean-field approximation, which enables us the reduction of large stochastic system to the simple deterministic system which could be further analyzed by applying standard local bifurcation analysis.

Presented research is performed with two main goals. Firstly, we want to show that in situ recorded fault motion is stochastic per se, and that the stochastic part of displacement time series could be treated as colored noise. Secondly, we wish to estimate the impact of colored noise on the generation of instability, i.e. on the occurrence of seismic fault motion. For the former, we invoke the joint deterministic-stochastic approach based on traditional Box-Jenkins method, while for the latter we perform the local bifurcation analysis of the mean-field approximated starting system of 10 blocks in a spring-block array along a single direction.

2. Colored noise in situ

In order to justify the introduction of the colored seismic noise in fault motion model, one needs to confirm the existence of colored noise in real conditions within the Earth's crust. In present case, we analyze the following datasets based on the real measurements:

- (1) Strike-slip fault movement directly measured at the two points in Driny cave, Male Karpaty mts in Slovakia [3] (Fig. 1a),
- (2) Ambient noise measurements before and after the earthquake on 8th September 2015 at the BKS station (Byerly Seismographic Vault, Berkley) (Fig. 1b).

In case (1) we show that once the estimation model of the fault movement is established, estimation error is autocorrelated, indicating the possibility of the existence of the colored noise. In case (2) we show that ambient noise before and after the quake is autocorrelated.

Analysis of the measurement results shown in Fig. 1a indicates that the real observed time series could be well described by the following models in a general form of Fourier series sums of sine and cosine functions:

$$y = a_0 + a_1 \cdot \cos(\omega \cdot t) + b_1 \cdot \sin(\omega \cdot t) + a_2 \cdot \cos(2 \cdot \omega \cdot t) + b_2 \cdot \sin(2 \cdot \omega \cdot t) + \dots \quad (1)$$

where a_i and b_i denote Fourier coefficients, and ω is the average oscillation frequency. Coefficients and frequencies of the resulting models for estimation of displacements at the locations Driny 1 and Driny 3 are given in Table 1.

Using these equations, one could describe the observed horizontal strike-slip motion accurately enough (Fig. 2).

For the present case, properties of the estimation error are of special importance, since the presence of autocorrelation in residuals could indicate the existence of the colored noise in the background of the seismic movement. Indeed, the results of Durbin-Watson statistics indicate the presence of autocorrelation in the recorded noise ($<D_L$), according to recommendations of Savin and White [7] (Table 2).

As for the recorded noise before and after the earthquake on 8th September 2015 at the BKS station (Byerly Seismographic Vault, Berkley), one can simply calculate the autocorrelation function, which, in present case, for both time series (before and after the earthquake) indicates the presence of autocorrelation (Fig. 3). It is clear that there is a significant autocorrelation for the first 8 and 7 lags, for time series before and after the earthquake, respectively, while t-statistics is higher than 2 for the first two lags in both cases.

Concerning the results of the aforementioned analysis, one could reasonably assume that noise in the background of fault movement could be considered as a colored noise.

3. Bifurcation analysis

A new model for seismic fault motion is suggested in a form of a single array spring-block model, described by a deterministic mathematical model with the included effect of colored noise. Analysis of such model is conducted using the standard local bifurcation analysis, which is applied for the analysis of the deterministic mean-field system instead of the starting stochastic model. It is shown that both models display qualitative similar dynamics.

Earthquake fault motion is examined by analysis of dimensionless all-to-all coupled spring-slider model with 10 units, whose dynamics is described by the following set of stochastic delay differential equations (SDDEs):

$$\begin{aligned} \dot{x}_i(t) &= y_i(t) \\ \dot{y}(t) &= -x_i(t) + \Phi(y_i + v) - \Phi(v) \\ &\quad + \frac{K}{N}(x_j(t - \tau) - x_i(t)) + Z_i(t) \\ dZ_i(t) &= -\frac{Z_i}{\varepsilon} dt + \sqrt{\frac{2D}{\varepsilon}} dW_i \end{aligned} \quad (2)$$

where x_i and y_i represent displacement and velocity of the i th block, respectively, K is constant of spring connecting the blocks, Φ stands for the friction force, τ is time delay and v is nondimensional pulling background velocity. $Z_i(t)$ is an Ornstein-Uhlenbeck process, and terms $\sqrt{(2D/\varepsilon)}dW_i$ represent stochastic increments of independent Wiener process, i.e. dW_i satisfy: $E(dW_i)=0$, $E(dW_i dW_j)=\delta_{ij}dt$, where $E(\cdot)$ denotes the expectation over many realizations of the stochastic process. The noise correlation time ε and the intensity of noise D are parameters that can be varied independently. Colored noise generated by Ornstein-Uhlenbeck process with this parametrization is referred to as power-limited colored noise, since the total power of the noise (the integral over the spectral density of the process) is conserved upon varying the noise correlation time.

Friction force Φ is assumed to be only rate-dependent: $\Phi(V) = -(\mu_0 + a \ln(V))$ where V is the general notion for the friction arguments in (2).

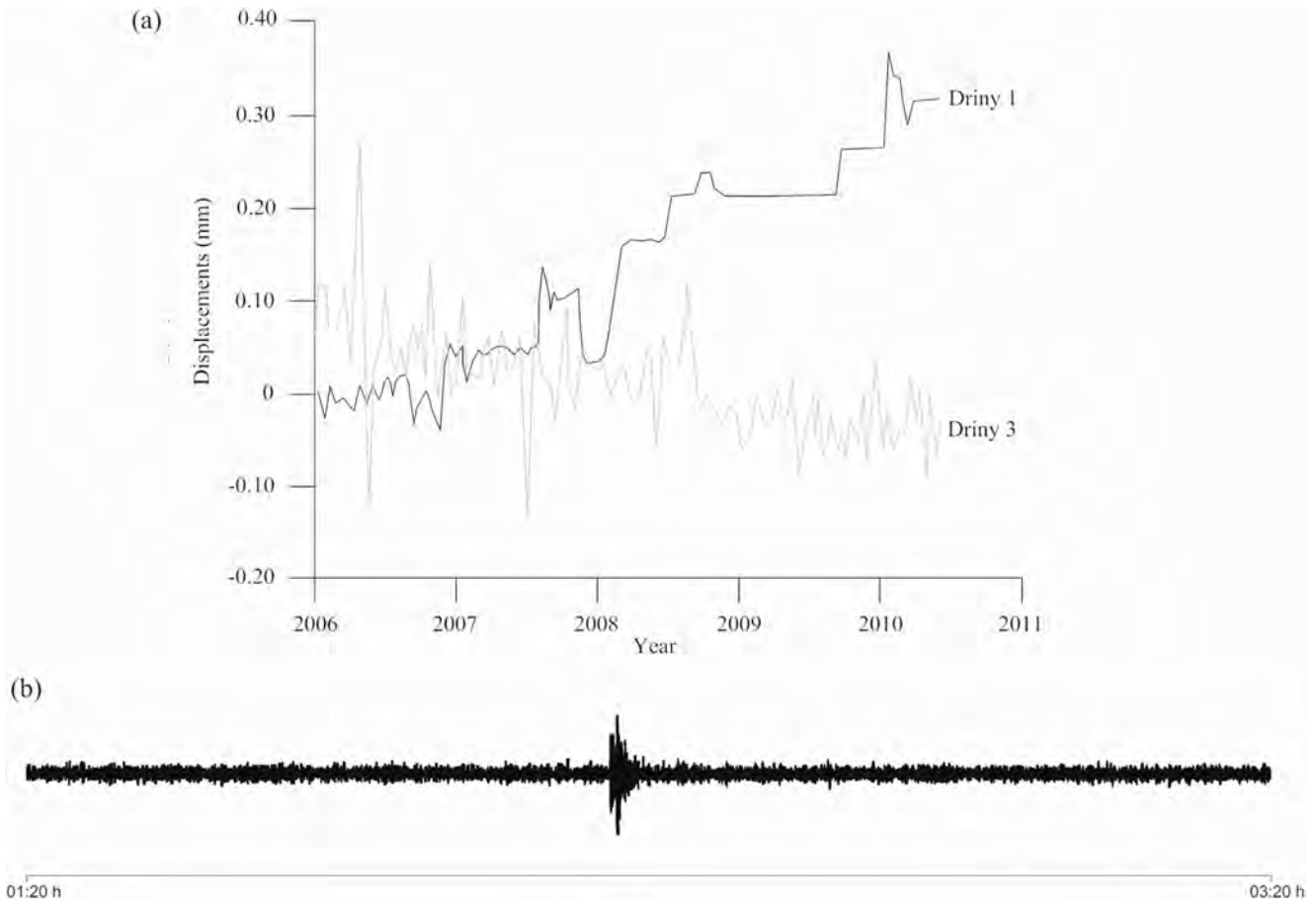


Fig. 1. (a) Horizontal strike-slip displacements along the faults at Driny Cave [3], (b) Permanent noise measurements before and after the earthquake at the Byerly Seismographic Vault, Berkeley [6].

Table 1

Fourier coefficients for deterministic models of fault movement of general form (1) based on the real observations at locations Driny 1 and Driny 3.

Driny 1 ($\omega = 0.108$)		Driny 3 ($\omega = 0.0205$)							
a_0	0.139	a_0	0.012	a_9	-0.002	a_{17}	0.002	a_{25}	-0.004
a_1	0.116	a_1	0.002	b_9	-0.005	b_{17}	-0.002	b_{25}	0.0005
b_1	-0.063	b_1	0.038	a_{10}	0.002	a_{18}	-0.005	a_{26}	0.0003
a_2	0.031	a_2	0.007	b_{10}	0.006	b_{18}	-0.013	b_{26}	-0.0003
b_2	0.033	b_2	0.0280	a_{11}	0.002	a_{19}	0.007	a_{27}	0.0002
a_3	-0.007	a_3	-0.001	b_{11}	-0.009	b_{19}	-0.013	b_{27}	-0.006
b_3	0.048	b_3	-0.0005	a_{12}	0.005	a_{20}	-0.001	a_{28}	-0.009
a_4	-0.005	a_4	0.003	b_{12}	0.011	b_{20}	-0.001	b_{28}	0.008
b_4	0.016	b_4	0.016	a_{13}	0.003	a_{21}	0.009	a_{29}	0.003
a_5	-0.015	a_5	-0.007	b_{13}	0.009	b_{21}	-0.0007	b_{29}	-0.0005
b_5	-0.009	b_5	0.017	a_{14}	0.005	a_{22}	0.002	a_{30}	0.002
a_6	0.001	a_6	-0.006	b_{14}	0.009	b_{22}	0.013	b_{30}	-0.0006
b_6	-0.004	b_6	0.004	a_{15}	-0.011	a_{23}	-0.004	a_{31}	0.0089
a_7	0.008	a_7	-0.009	b_{15}	0.017	b_{23}	0.006	b_{31}	0.002
b_7	-0.006	b_7	0.019	a_{16}	-0.014	a_{24}	-0.004	a_{32}	0.002
a_8	-0.011	a_8	-0.006	b_{16}	-0.011	b_{24}	0.005	b_{32}	0.004
b_8	0.008	b_8	-0.011						

Table 2

Results of Durbin-Watson test for testing the presence of autocorrelation in residuals of the models in general form (1) and with the coefficients given in Table 1.

Recording location	Durbin-Watson statistic	D_L	D_U
Driny 1	0.485	1.696	1.727
Driny 3	0.527	1.807	1.820

In present paper, authors consider this spring-block model as a collection of fault patches mutually separated by the petrified zones (material bridges). This is the modified original model from [8]

Starting from the model (2), one could obtain the following mean-field model, which has qualitatively the same dynamics as

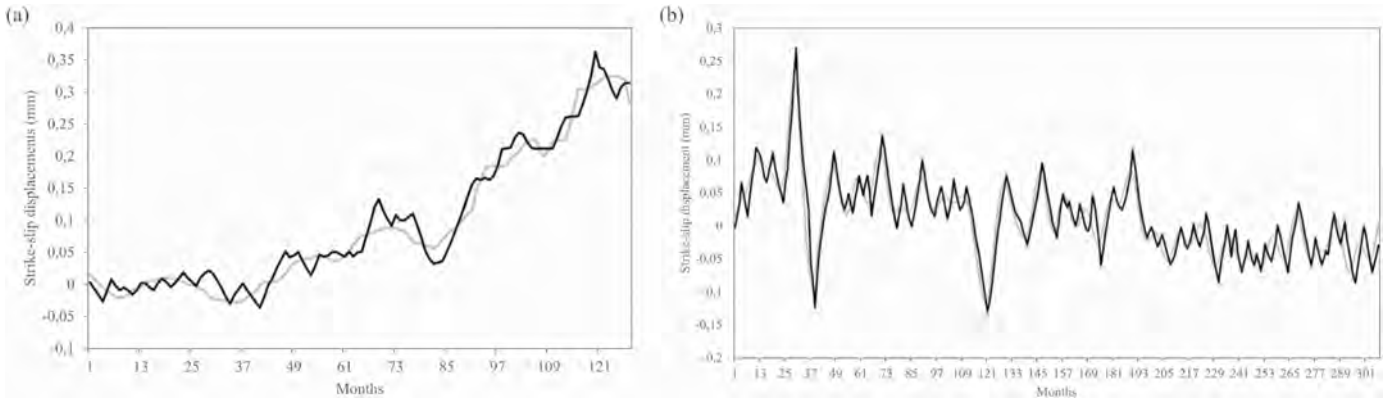


Fig. 2. Comparison of estimated motion and real observed fault movement. Black line stands for the recorded time series, while gray line indicates the result of estimation deterministic model.

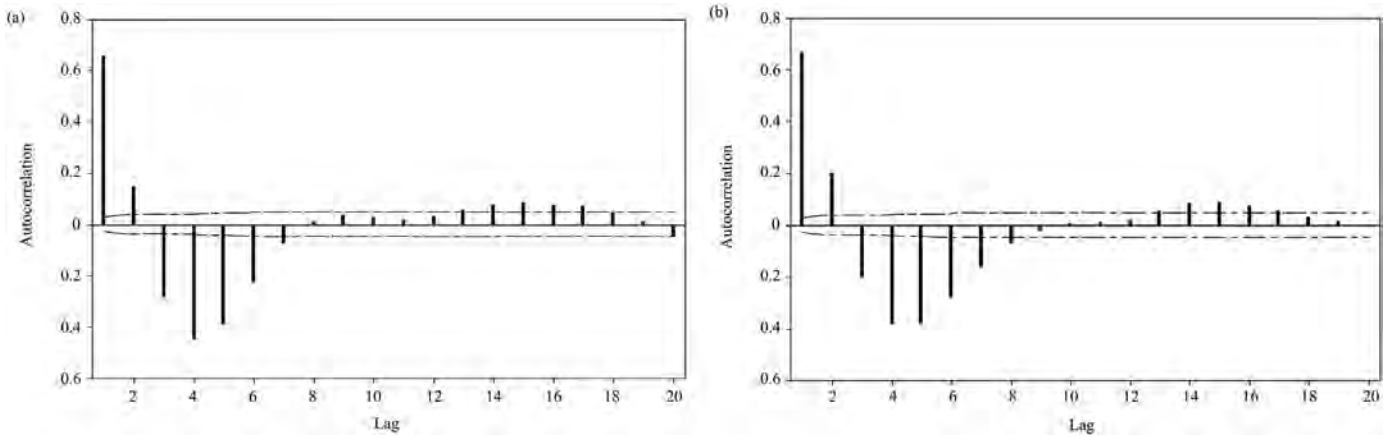


Fig. 3. Autocorrelation function for the time series before (a) and after (b) the earthquake on 8th September 2015 at the BKS station (Byerly Seismographic Vault, Berkley), with the clear indication of the presence of autocorrelation.

the starting model (2):

$$\begin{aligned}
 \dot{m}_x &= m_y \\
 \dot{m}_y &= -m_x - a \ln(m_y + \nu) + a \ln(\nu) + \frac{1}{2} \frac{a}{(m_y + \nu)^2} S_y \\
 &\quad + \frac{3}{4} \frac{a}{(m_y + \nu)^4} S_y^2 + K(m_x(t - \tau) - m_x) + m_z \\
 \dot{m}_z &= -\frac{1}{\varepsilon} m_z \\
 \frac{1}{2} \dot{S}_x &= U_{xy} \\
 \frac{1}{2} \dot{S}_y &= S_y \left[-\frac{a}{m_y + \nu} - \frac{a}{(m_y + \nu)^3} S_y \right] - (K + 1) U_{xy} + U_{yz} \\
 \dot{U}_{xy} &= U_{xy} \left[-\frac{a}{m_y + \nu} - \frac{a}{(m_y + \nu)^3} S_y \right] - (K + 1) S_x + S_y + U_{xz} \\
 \dot{U}_{xz} &= U_{yz} - \frac{1}{\varepsilon} U_{xz} \\
 \dot{U}_{yz} &= -U_{xz} - \frac{a}{m_y + \nu} U_{yz} - \frac{a}{(m_y + \nu)^3} S_y U_{yz} - K U_{xz} + D - \frac{1}{\varepsilon} U_{yz}
 \end{aligned} \tag{3}$$

Detailed derivation of model (3) is given in Appendix.

Results of the numerical analysis of mean-field model (3) indicate the existence of three different dynamical regimes (Fig. 4–6):

- Equilibrium state, which manifests as steady stationary movement (corresponding to the steady regime of fault motion);
- Small-amplitude regular periodic oscillations (corresponding to the creep regime of fault motion);
- High-amplitude irregular oscillations (corresponding to the seismogenic fault motion).

From Fig. 4 one could identify the effect of correlation time ε on the dynamics of mean-field model (2). In particular, with the increase of correlation time, second bifurcation curve vanishes, i.e. there are no high-amplitude oscillations. From the seismolog-

ical point of view, this could indicate that degree of autocorrelation of background seismic noise could directly determine the type of transition from equilibrium state, i.e. creep regime of fault dynamics to low-amplitude oscillations (which could still not induce the seismogenic motion) or to high-amplitude irregular oscillations, whose amplitude progressively increases, which could be considered as the onset of the fault motion which produces the seismic waves responsible for surface soil shaking.

Regarding the effect of coupling strength K , it is clear from Fig. 5 that the increase of coupling strength further increases the impact of both time delay τ and friction a , and excludes the possibility of the occurrence of seismogenic fault motion. In particular, for higher values of K transition from equilibrium state to small amplitude oscillations, i.e. creep regime is possible even for higher values of friction a . From the seismological viewpoint, this means that the stronger interrelations between different patches of fault also induce the stronger role of friction. In the same time, it appears that for higher values of coupling strength, there is no possibility that seismogenic motion occur, since the second bifurcation curve (denoting the transition from creep regime to irregular seismogenic motion) vanishes.

However, this statement is valid only for the lower values of time delay. Indeed, one could see from Fig. 6 that high-amplitude irregular oscillations occur for higher values of time delay, i.e. $\tau > 5$. From the practical viewpoint, this means that the higher delay in interaction between the neighboring patches of fault – the more likely is to expect the onset of seismogenic fault motion. In other words, it seems that without the delay in interaction, or with

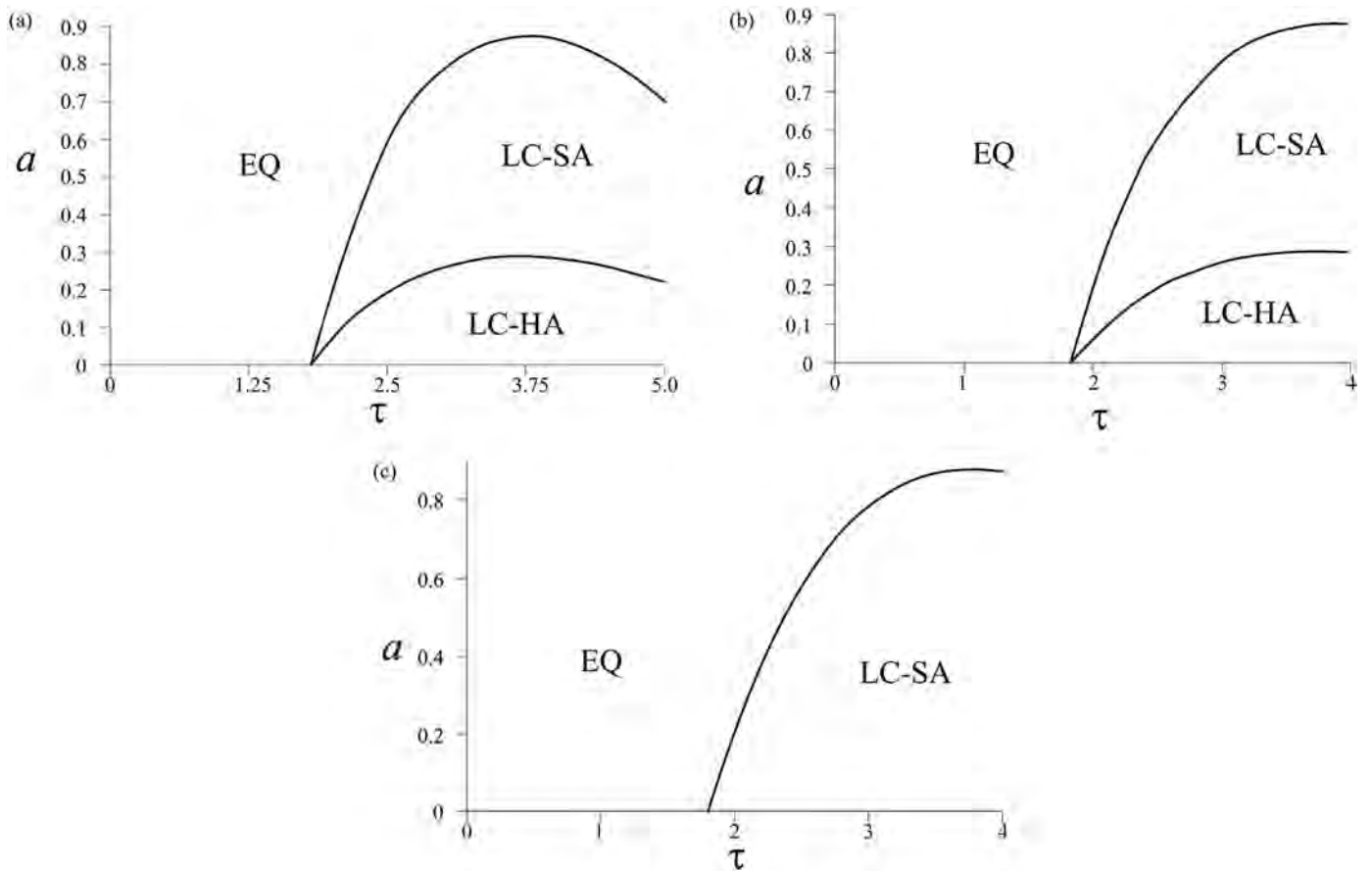


Fig. 4. Andronov-Hopf bifurcation diagram, displaying interaction of friction a and time delay τ , for different values of correlation time ϵ . While friction and delay are being varied, other parameters are being held constant for the mean-field model (3) in equilibrium state: $\mu_0 = 0.1$, $K = 1$, $D = 0.001$, $\nu = 1.2$. (a) $\epsilon = 0.005$, (b) $\epsilon = 0.5$, (c) $\epsilon = 5.0$. EQ denotes the equilibrium state (steady stationary displacement), LC-SA stands for the periodic oscillations of small amplitude, while LC-HA denotes the high-amplitude irregular oscillations.

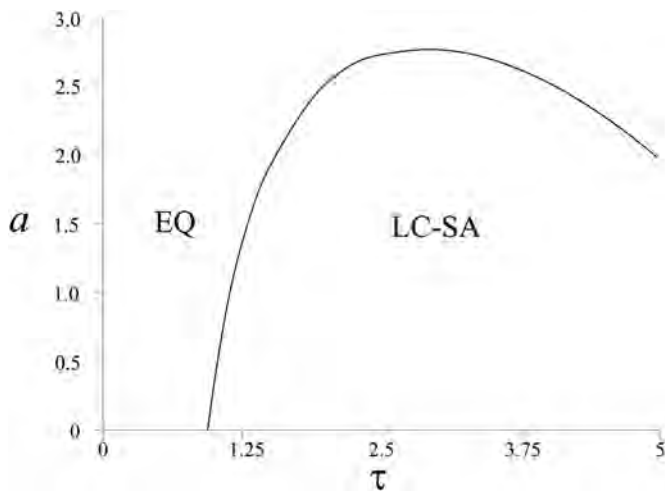


Fig. 5. Effect of coupling strength K on the dynamics of the mean-field model (3). While friction and delay are being varied, other parameters are being held constant for the mean-field model (2) in equilibrium state: $\mu_0 = 0.1$, $D = 0.001$, $\nu = 1.2$, $\epsilon = 0.5$, $K = 5$. EQ denotes the equilibrium state (steady stationary displacement), while LC-SA stands for the periodic oscillations of small amplitude.

4. Discussion and conclusion

In present paper, authors examine the impact of the background colored seismic noise on the dynamics of an active fault. Firstly, authors prove, by analyzing the measurement of the real fault displacement, that background seismic noise could be treated as the colored noise. This is done for the real two examples: (1) strike-slip fault movement directly measured at the two points in Driny cave, Male Karpaty mts in Slovakia [3]; (2) ambient noise measurements before and after the earthquake on 8th September 2015 at the BKS station (Byerly Seismographic Vault, Berkeley). In the second phase of the research, authors investigated the fault dynamics by analyzing the mean-field model of all-to-all coupled blocks, with delayed interaction and with the assumed additive colored noise. The results obtained indicate the existence of three different dynamical regimes, all of which could have its correspondence with the real observed regimes of fault motion: (1) steady stationary state; (2) creep regime and (3) active seismogenic motion. Furthermore, the results indicate interesting effect of correlation time ϵ and coupling strength K on the onset of seismic fault motion. Higher values of correlation time exclude the possibility of seismic fault motion, indicating the affect of strong impact of background seismic noise. Similarly, higher values of coupling strength also make seismic fault motion impossible to occur. In this case, when coupling strength is high, fault patches are interlocked and there is no possibility that irregular motion occur.

the small values of delay, the whole fault acts as a unique block, i.e. the fault patches are locked, preventing the irregular seismogenic motion to occur.

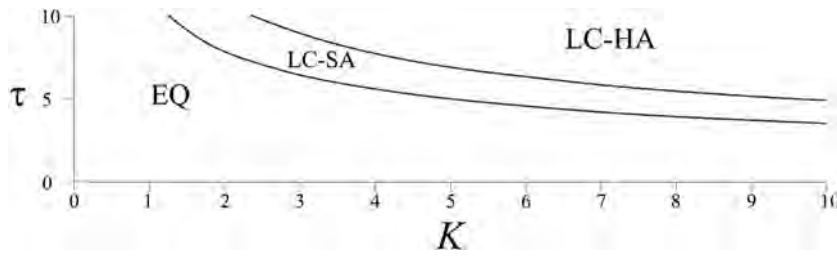


Fig. 6. Andronov-Hopf bifurcation diagram, displaying interaction of coupling strength K and time delay τ . While coupling strength and delay are being varied, other parameters are being held constant for the mean-field model (3) in equilibrium state: $\mu_0 = 0.1$, $D = 0.001$, $\nu = 1.2$, $a = 0.8$, $\varepsilon = 0.5$. EQ denotes the equilibrium state (steady stationary displacement), LC-SA stands for the periodic oscillations of small amplitude, while LC-HA denotes the high-amplitude irregular oscillations.

If one compares the effect of colored seismic noise, analyzed in this paper, and white seismic noise, analyzed in our previous paper [5], the difference lies in the following. For white background seismic noise, seismic fault motions could be expected to occur only in a bi-stable dynamical regime in the vicinity of a bifurcation curve provided that initial conditions along the fault are far from the equilibrium state (the case of active fault). On the other hand, introduction of colored noise brings more rich dynamical behavior, where colored noise with rather small correlation time (Fig. 4a) indicates the onset of seismic fault motion, with the increase of time delay.

Further research on this topic could evaluate the effect of colored noise in case when the interaction of neighboring blocks weakens with the mutual distance of the blocks, which is certainly closer to the real observed scenario.

Declaration of Competing Interest

The authors declare that they have no known competing financial interests or personal relationships that could have appeared to influence the work reported in this paper.

Acknowledgments

This research was partly supported by the Ministry of Education, Science and Technological Development of the Republic of Serbia (Contract nos. 176016 and 171017).

Appendix

By deriving the Taylor expansion of $\Phi(y_i(t)+\nu)$ in the vicinity of the mean values $(x_i, y_i, z_i) = (m_x, m_y, m_z) = (\lim_{N \rightarrow \infty} \frac{1}{N} \sum_{i=1}^N x_i(t), \lim_{N \rightarrow \infty} \frac{1}{N} \sum_{i=1}^N y_i(t), \lim_{N \rightarrow \infty} \frac{1}{N} \sum_{i=1}^N z_i(t))$, system (1) becomes:

$$\begin{aligned} \dot{x}_i(t) &= y_i(t) \\ \dot{y}(t) &= -x_i(t) + \Phi(m_y + \nu) - \Phi(\nu) + \frac{1}{1!} [\Phi'(m_y + \nu)] [y_i(t) - m_y] + \frac{1}{2!} [\Phi''(m_y + \nu)] [y_i(t) - m_y]^2 \\ &\quad + \frac{1}{3!} [\Phi'''(m_y + \nu)] [y_i(t) - m_y]^3 + \frac{1}{4!} [\Phi^{(4)}(m_y + \nu)] [y_i(t) - m_y]^4 + K[m_x(t - \tau) - x_i(t)] + Z_i(t) \\ dZ_i(t) &= -\frac{Z_i(t)}{\varepsilon} dt + \sqrt{\frac{2D}{\varepsilon^2}} dW_i \end{aligned} \quad (1A)$$

In order to derive mean-field approximate dynamical equations for starting system (1), we shall first suppose that: (a) dynamics is such that the distribution of x_i and y_i are Gaussian and (b) for large N the average over local random variables is given by the expectation with respect to the corresponding distribution, as in [9].

The cumulant analysis of a system (2) of above mentioned globally (all-to-all) coupled units shall be performed in the thermodynamic limit of an infinitely large ensemble, $N \rightarrow \infty$.

We introduce deviations from the mean-field: $\langle x(t) \rangle = \lim_{N \rightarrow \infty} \frac{1}{N} \sum_{i=1}^N x_i(t)$, $\langle y(t) \rangle = \lim_{N \rightarrow \infty} \frac{1}{N} \sum_{i=1}^N y_i(t)$, $\langle z(t) \rangle = \lim_{N \rightarrow \infty} \frac{1}{N} \sum_{i=1}^N z_i(t)$, for each element $n_x(t) = \langle x(t) \rangle - x_i(t)$, $n_y(t) = \langle y(t) \rangle - y_i(t)$, $n_z(t) = \langle z(t) \rangle - z_i(t)$.

We assume that these fluctuations are Gaussian and statistically independent in different elements.

There is a set of moments known as cumulants [10,11] or Thiele semi-invariants which have an important property that all of them, for the third order, vanish in the Gaussian case.

Next, we introduce the following notation for the first and the second order cumulants:

- The means: $m_x(t) = \langle x(t) \rangle$, $m_x(t - \tau) = \langle x(t - \tau) \rangle$, $m_y(t) = \langle y(t) \rangle$, $m_z(t) = \langle z(t) \rangle$,
- The mean square deviations: $s_x(t) = \langle n_x^2(t) \rangle$, $s_y(t) = \langle n_y^2(t) \rangle$, $s_z(t) = \langle n_z^2(t) \rangle$,
- The cross-cumulants: $U_{xy}(t) = \langle n_x n_y \rangle$, $U_{xz}(t) = \langle n_x n_z \rangle$, $U_{yz}(t) = \langle n_y n_z \rangle$

By applying Ito's formula (or Ito's chain rule):

$$dX = Fdt + GdW$$

$$Y(t) = U(x, t)$$

$$dY = \frac{\partial U}{\partial t} dt + \frac{\partial U}{\partial x} dX + \frac{1}{2} \frac{\partial^2 U}{\partial x^2} G^2 dt$$

from Eq. (1A), following the procedure described in [9,12] one obtains:

$$\dot{m}_x = m_y \tag{2A}$$

$$\dot{m}_y = -m_x - a \ln(m_y + \nu) + a \ln(\nu) + \frac{1}{2} \frac{a}{(m_y + \nu)^2} s_y + \frac{3}{4} \frac{a}{(m_y + \nu)^4} s_y^2 + K(m_x(t - \tau) - m_x) + m_z \tag{3A}$$

$$\dot{m}_z = -\frac{1}{\varepsilon} m_z \tag{4A}$$

$$\begin{aligned} \dot{s}_x &= \langle \dot{n}_x^2 \rangle = \left\langle \frac{d}{dt} ((x) - x_i)^2 \right\rangle = \left\langle \frac{d}{dt} (m_x^2 - 2m_x x_i + x_i^2) \right\rangle = -\dot{m}_x^2 + \langle \dot{x}_i^2 \rangle = -\dot{m}_x^2 + \langle \dot{x}_i^2 \rangle = -2m_x \dot{m}_x + \langle 2x_i \dot{x}_i \rangle \\ &= -2m_x m_y + \langle 2x_i y_i \rangle = 2U_{xy} \Rightarrow \frac{1}{2} \dot{s}_x = U_{xy} \end{aligned} \tag{5A}$$

$$\begin{aligned} \dot{s}_y &= \langle \dot{n}_y^2 \rangle = \left\langle \frac{d}{dt} ((y) - y_i)^2 \right\rangle = \left\langle \frac{d}{dt} (m_y^2 - 2m_y y_i + y_i^2) \right\rangle = -\dot{m}_y^2 + \langle \dot{y}_i^2 \rangle = -2m_y \dot{m}_y + \langle 2y_i \dot{y}_i \rangle = \\ &= -2m_y \left[-m_x + \Phi(m_y + \nu) - \Phi(\nu) + \frac{1}{2} [\Phi''(m_y + \nu)] s_y + \frac{1}{24} [\Phi^{(4)}(m_y + \nu)] \cdot 3s_y^2 \right. \\ &\quad \left. + K[m_x(t - \tau) - m_x] + m_z \right] + 2 \langle -x_i y_i + y_i \Phi(m_y + \nu) - y_i \Phi(\nu) + [\Phi'(m_y + \nu)] \cdot \\ &\quad \cdot [y_i^2 - m_y y_i] + \frac{1}{2} [\Phi''(m_y + \nu)] \cdot [y_i(y_i^2 - 2y_i m_y + m_y^2)] + \frac{1}{6} [\Phi'''(m_y + \nu)] \cdot \\ &\quad \cdot [y_i(y_i^3 - 3y_i^2 m_y + 3y_i m_y^2 - m_y^3)] + \frac{1}{24} [\Phi^{(4)}(m_y + \nu)] \cdot \\ &\quad \cdot [y_i(y_i^4 - 4y_i^3 m_y + 6y_i^2 m_y^2 - 4y_i m_y^3 + m_y^4)] + K[y_i - m_x(t - \tau) - y_i x_i] + y_i z_i \\ &= -2U_{xy} + 2[\Phi'(m_y + \nu)] s_y + \frac{1}{3} [\Phi'''(m_y + \nu)] 3s_y^2 - 2KU_{xy} + 2U_{yz} \\ &\Rightarrow \frac{1}{2} \dot{s}_y = s_y \left[\Phi'(m_y + \nu) + \frac{1}{2} \Phi'''(m_y + \nu) s_y \right] - (K + 1)U_{xy} + U_{yz} \\ \dot{s}_z &= -\dot{m}_z^2 + \langle \dot{z}_i^2 \rangle + \frac{2D}{\varepsilon^2} = -2m_z \dot{m}_z + \langle 2z_i \dot{z}_i \rangle + \frac{2D}{\varepsilon^2} \\ &= -2m_z \cdot \left(-\frac{1}{\varepsilon} m_z \right) + \left\langle 2z_i \left(-\frac{z_i}{\varepsilon} + \sqrt{\frac{2D}{\varepsilon^2}} dW_i \right) \right\rangle + \frac{2D}{\varepsilon^2} \\ &= -\frac{2}{\varepsilon} s_z + \frac{2D}{\varepsilon^2} \\ &\Rightarrow \frac{1}{2} \dot{s}_z = -\frac{1}{\varepsilon} s_z + \frac{D}{\varepsilon^2} \end{aligned} \tag{6A}$$

Last equation can be solved in order to obtain $s_z = (s_{z0} - \frac{D}{\varepsilon}) e^{-\frac{2}{\varepsilon} t} + \frac{D}{\varepsilon}$, where s_{z0} is an integration constant. It is obvious when $t \rightarrow \infty$, $s_z \rightarrow D/\varepsilon$, and because of that we fix the value for s_z to be exactly D/ε .

$$\begin{aligned} \dot{U}_{xy} &= \left\langle \frac{d}{dt} (\dot{n}_x \dot{n}_y) \right\rangle = \langle (m_x - x_i) \cdot (m_y - y_i) \rangle = \left\langle \frac{d}{dt} (m_x m_y - m_x y_i - x_i m_y + x_i y_i) \right\rangle = -\dot{m}_x \dot{m}_y + \langle \dot{x}_i \dot{y}_i \rangle \\ &= -m_x \dot{m}_y - m_y \dot{m}_x + \langle \dot{x}_i y_i \rangle + \langle x_i \dot{y}_i \rangle \\ &= -m_x \cdot \left[-m_x + \Phi(m_y + \nu) - \Phi(\nu) + \frac{1}{2} \Phi''(m_y + \nu) \cdot s_y + \right. \\ &\quad \left. + \frac{1}{24} \Phi^{(4)}(m_y + \nu) \cdot 3s_y^2 + K \cdot [m_x(t - \tau) - m_x] + m_z \right] - m_y m_x + \langle y_i^2 \rangle \\ &\quad + \left\langle -x_i^2 + x_i \Phi(y_i + \nu) - x_i \Phi(\nu) + \frac{K}{N} \sum_{j=1}^N (x_j(t - \tau) x_i - x_i^2) + x_i z_i \right\rangle \\ &= m_x^2 - m_x \Phi(m_y + \nu) + m_x \Phi(\nu) - m_x \frac{1}{2} \Phi''(m_y + \nu) s_y - \\ &\quad - m_x \frac{1}{24} \Phi^{(4)}(m_y + \nu) \cdot 3s_y^2 - Km_x m_x(t - \tau) + Km_x^2 - m_x m_z - m_y^2 + s_y + m_y^2 - s_x \end{aligned}$$

$$\begin{aligned}
& -m_x^2 + \left\langle m_x \cdot \Phi(m_y + \nu) + \Phi'(m_y + \nu) \cdot (x_i y_i - x_i m_y) + \frac{1}{2} \Phi''(m_y + \nu) \cdot (x_i y_i^2 - 2x_i y_i m_y + x_i m_y^2) \right. \\
& + \frac{1}{6} \Phi'''(m_y + \nu) (x_i y_i^3 - 3x_i y_i^2 m_y + 3x_i y_i m_y^2 - x_i m_y^3) + \frac{1}{24} \Phi^{(4)}(m_y + \nu) (x_i y_i^4 - 4x_i y_i^3 m_y + 6x_i y_i^2 m_y^2 - 4x_i y_i m_y^3 + x_i m_y^4) - m_x \Phi(\nu) \\
& \left. + K m_x m_x(t - \tau) - K s_x - K m_x^2 + U_{xz} + m_x m_z \right\rangle \\
& = s_y - s_x + \Phi'(m_y + \nu) U_{xy} + \frac{1}{6} \Phi'''(m_y + \nu) 3s_y U_{xy} \\
& - K s_x + U_{xz} \Rightarrow \dot{U}_{xy} = U_{xy} \left[\Phi'(m_y + \nu) + \frac{1}{2} \Phi'''(m_y + \nu) s_y \right] - (K + 1) s_x + s_y + U_{xz} \tag{7A}
\end{aligned}$$

$$\begin{aligned}
\dot{U}_{xz} & = \left\langle \dot{\bar{n}_x \bar{n}_z} \right\rangle = \left\langle \dot{(m_x - x_i)(m_z - z_i)} \right\rangle = \left\langle \dot{m_x m_z - m_x z_i - m_z x_i + x_i z_i} \right\rangle = \\
& = \left\langle \dot{m_x m_z} \right\rangle + \left\langle \dot{x_i z_i} \right\rangle = -\dot{m}_x m_z - m_x \dot{m}_z + \langle \dot{x}_i z_i \rangle + \langle x_i \dot{z}_i \rangle = -m_y m_z - \\
& - m_x \left(-\frac{1}{\varepsilon} m_z \right) + \langle y_i z_i \rangle + \left\langle x_i \left(-\frac{z_i}{\varepsilon} \right) + x_i \sqrt{\frac{2D}{\varepsilon^2}} dW_i \right\rangle \\
& \Rightarrow \dot{U}_{xz} = U_{yz} - \frac{1}{\varepsilon} U_{xz} \tag{8A}
\end{aligned}$$

$$\begin{aligned}
\dot{U}_{yz} & = \left\langle \dot{\bar{n}_y \bar{n}_z} \right\rangle = \left\langle \dot{(m_y - y_i)(m_z - z_i)} \right\rangle = \left\langle \dot{m_y m_z - m_y z_i - m_z y_i + y_i z_i} \right\rangle = \\
& = \left\langle \dot{m_y m_z} \right\rangle + \left\langle \dot{y_i z_i} \right\rangle = -\dot{m}_y m_z - m_y \dot{m}_z + \langle \dot{y}_i z_i \rangle + \langle y_i \dot{z}_i \rangle = \\
& - m_z \left[-m_x + \Phi(m_y + \nu) - \Phi(\nu) + \frac{1}{2} \Phi''(m_y + \nu) \cdot s_y + \frac{1}{24} \Phi^{(4)}(m_y + \nu) 3s_y^2 \right. \\
& + K m_x(t - \tau) - K m_x + m_z] - m_y \left(-\frac{1}{\varepsilon} m_z \right) + \left\langle -x_i z_i + z_i \Phi(m_y + \nu) - z_i \Phi(\nu) \right. \\
& + \Phi'(m_y + \nu) (y_i z_i - m_y z_i) + \frac{1}{2} \Phi''(m_y + \nu) (z_i y_i^2 - 2z_i y_i m_y + z_i m_y^2) \\
& + \frac{1}{6} \Phi'''(m_y + \nu) (z_i y_i^3 - 3z_i y_i^2 m_y + 3z_i y_i m_y^2 - z_i m_y^3) + \\
& + \frac{1}{24} \Phi^{(4)}(m_y + \nu) \cdot (z_i y_i^4 - 4z_i y_i^3 m_y + 6z_i y_i^2 m_y^2 - 4z_i y_i m_y^3 + z_i m_y^4) + K z_i m_x(t - \tau) - \\
& \left. - K z_i x_i + z_i^2 \right\rangle + \left\langle y_i \left(-\frac{1}{\varepsilon} z_i \right) + y_i \sqrt{\frac{2D}{\varepsilon^2}} dW_i \right\rangle = -U_{xz} + \Phi'(m_y + \nu) U_{yz} + \frac{1}{6} \Phi'''(m_y + \nu) \cdot 3s_y U_{yz} \\
& - K U_{xz} + s_z - \frac{1}{\varepsilon} U_{yz} \tag{9A}
\end{aligned}$$

Eqs. (2A)–(9A) together compose the mean-field system of equations for earthquake nucleation model with colored noise:

$$\begin{aligned}
\dot{m}_x & = m_y \\
\dot{m}_y & = -m_x - a \ln(m_y + \nu) + a \ln(\nu) + \frac{1}{2} \frac{a}{(m_y + \nu)^2} s_y + \frac{3}{4} \frac{a}{(m_y + \nu)^4} s_y^2 + K(m_x(t - \tau) - m_x) + m_z \\
\dot{m}_z & = -\frac{1}{\varepsilon} m_z \\
\frac{1}{2} \dot{s}_x & = U_{xy} \\
\frac{1}{2} \dot{s}_y & = s_y \left[-\frac{a}{m_y + \nu} - \frac{a}{(m_y + \nu)^3} s_y \right] - (K + 1) U_{xy} + U_{yz} \\
\dot{U}_{xy} & = U_{xy} \left[-\frac{a}{m_y + \nu} - \frac{a}{(m_y + \nu)^3} s_y \right] - (K + 1) s_x + s_y + U_{xz} \\
\dot{U}_{xz} & = U_{yz} - \frac{1}{\varepsilon} U_{xz} \\
\dot{U}_{yz} & = -U_{xz} - \frac{a}{m_y + \nu} U_{yz} - \frac{a}{(m_y + \nu)^3} s_y U_{yz} - K U_{xz} + D - \frac{1}{\varepsilon} U_{yz}
\end{aligned} \tag{10A}$$

which is the Eq. (3) in the main text.

References

- [1] Corela C, Silveira G, Matias L, Schimmel M, Geissler WH. Ambient seismic noise tomography of SW Iberia integrating seafloor-and land-based data. *Tectonophysics* 2017;700-701:131–49.
- [2] Nakamura Y. A method for dynamic characteristics estimation of subsurface using microtremor on the ground surface. *Quarterly Report of RTRI* 1989;25–33.
- [3] Briestensky M, Stemberk J, Michalik J, Bella P, Rowberry M. The use of a karstic cave system in a study of active tectonics: fault movements recorded at Driny Cave, Male Karpaty Mts (Slovakia). *J Cave Karst Stud* 2011;73:114–23.
- [4] Ryberg T, Haberland Ch, Fuis GS, Ellsworth WL, Shelly DR. Locating non-volcanic tremor along the San Andreas Fault using a multiple array source imaging technique. *Geophys J Int* 2010;183:1485–500.
- [5] Vasović N, Kostić S, Franović I, Todorović K. Earthquake nucleation in a stochastic fault model of globally coupled units with interaction delays. *Comm Non Sci Numer Sim* 2016;38:117–29.
- [6] http://seismo.berkeley.edu/station_book/bks.html; 2018. [Accessed July 2018].
- [7] Savin NE, White KJ. The Durbin-Watson test for serial correlation with extreme sample sizes or many regressors. *Econometrica* 1977;45:1989–96.
- [8] De Sousa Vieira M. Chaos and synchronized chaos in an earthquake model. *Phys Rev Lett* 1999;82:201–4.
- [9] Burić N, Ranković D, Todorović K, Vasović N. Mean field approximation for noisy delay coupled excitable neurons. *Physica A* 2010;389:3956–64.
- [10] Lax M, Cai W, Xu M. *Random processes in physics and finance*. New York: Oxford University Press; 2006.
- [11] Gardiner C. *Stochastic methods: a handbook for the natural and social sciences*. Berlin: Springer; 2009.
- [12] Franović I, Todorović KD, Vasović N, Burić N. Stability, bifurcations, and dynamics of global variables of a system of bursting neurons. *Chaos* 2011;21:033109–1-9.

Two paradigmatic scenarios for inverse stochastic resonance

Cite as: Chaos 30, 033123 (2020); doi: 10.1063/1.5139628

Submitted: 22 November 2019 · Accepted: 4 March 2020 ·

Published Online: 16 March 2020



View Online



Export Citation



CrossMark

Iva Bačić and Igor Franović^{a)}

AFFILIATIONS

Scientific Computing Laboratory, Center for the Study of Complex Systems, Institute of Physics Belgrade, University of Belgrade, Pregrevica 118, 11080 Belgrade, Serbia

^{a)}Author to whom correspondence should be addressed: franovic@ipb.ac.rs

ABSTRACT

Inverse stochastic resonance comprises a nonlinear response of an oscillatory system to noise where the frequency of noise-perturbed oscillations becomes minimal at an intermediate noise level. We demonstrate two generic scenarios for inverse stochastic resonance by considering a paradigmatic model of two adaptively coupled stochastic active rotators whose local dynamics is close to a bifurcation threshold. In the first scenario, shown for the two rotators in the excitable regime, inverse stochastic resonance emerges due to a biased switching between the oscillatory and the quasi-stationary metastable states derived from the attractors of the noiseless system. In the second scenario, illustrated for the rotators in the oscillatory regime, inverse stochastic resonance arises due to a trapping effect associated with a noise-enhanced stability of an unstable fixed point. The details of the mechanisms behind the resonant effect are explained in terms of slow-fast analysis of the corresponding noiseless systems.

Published under license by AIP Publishing. <https://doi.org/10.1063/1.5139628>

The effects of noise may generically be classified into two groups: on the one hand, the noise may enhance or suppress certain features of deterministic dynamics by acting on the system states in an inhomogeneous fashion, while on the other hand, it may give rise to novel forms of behavior, associated with crossing of thresholds and separatrices or to a stability of deterministically unstable states. The constructive role of noise has been evinced in a wide range of real-world applications, from neural networks and chemical reactions to lasers and electronic circuits. The classical examples of stochastic facilitation concern the resonant phenomena, including stochastic resonance, where noise of appropriate intensity may induce oscillations in bistable systems that are preferentially locked to a weak periodic forcing, and coherence resonance, where an intermediate level of noise may trigger coherent oscillations in excitable systems. Recently, a novel form of nonlinear response to noise, called inverse stochastic resonance (ISR), has been discovered while studying individual neural oscillators and models of neuronal populations. It has come to light that noise may reduce the intrinsic spiking frequency of neuronal oscillators, transforming the tonic firing into a bursting-like activity or even quenching the oscillations. Within the present study, we demonstrate two paradigmatic mechanisms of inverse stochastic resonance, one based on biased switching

between the metastable states, and the other associated with a noise-enhanced stability of an unstable fixed point. We show that the effect is robust, in a sense that it may emerge in coupled excitable and coupled oscillatory systems, and both in cases of Type I and Type II oscillators.

I. INTRODUCTION

Noise in excitable or multistable systems may fundamentally change their deterministic dynamics, giving rise to qualitatively novel forms of behavior, associated with crossing of thresholds and separatrices, or stabilization of certain unstable structures.^{1,2} The emergent dynamics may involve noise-induced oscillations and stochastic bursting,^{3–5} switching between metastable states,^{6,7} or noise-enhanced stability of metastable and unstable states,^{8–12} to name but a few. In neuronal systems, the phenomena reflecting the constructive role of noise are collected under the notion of stochastic facilitation,^{13–15} which mainly comprises the resonant effects. The most prominent examples concern coherence resonance,^{16–20} where the regularity of noise-induced oscillations becomes maximal at a preferred noise level, and stochastic resonance,^{13,21} where the sensitivity of a system to a subthreshold periodic stimulation becomes

maximal at an intermediate noise level. Recent studies on the impact of noise in neuronal oscillators have revealed that the noise may also give rise to an inhibitory effect, which consists in reducing the intrinsic spiking frequency such that it becomes minimal at an intermediate noise intensity.^{14,22–30} This effect has been called inverse stochastic resonance (ISR), but in contrast to stochastic resonance, it concerns autonomous rather than periodically driven systems. Apart from reports in models of neurons and neuronal populations, ISR has recently been evinced for cerebellar Purkinje cells *in vitro*,²⁸ having shown how the lifetimes of the so-called UP states with elevated spiking activity and the DOWN states of relative quiescence^{7,31–33} depend on the noise intensity.

The studies of the mechanism behind ISR have so far mostly been focused on Type II neural oscillators with bistable dynamics poised close to a subcritical Hopf bifurcation,^{14,23–25} considering Hodgkin–Huxley and Morris–Lecar models. Under the influence of noise, such systems exhibit switching between the two metastable states, derived from the periodic and the stationary attractor of the deterministic dynamics. At an intermediate noise level, one observes that the switching rates become strongly asymmetric, with the system spending substantially more time in a quasi-stationary state. This is reflected in a characteristic non-monotone dependence of the spiking frequency on noise, which is a hallmark of ISR.

Nevertheless, a number of important issues on the mechanism giving rise to ISR have remained unresolved. In particular, is the effect dependent on the type of neuronal excitability? Also, can there be more than a single mechanism of ISR? And finally, how does the effect depend on the form of couplings and whether it can be robust for adaptively changing couplings, typical for neuronal systems?

To address these issues, we invoke a simple, yet paradigmatic model that combines the three typical ingredients of neuronal dynamics, including excitability, noise, and coupling plasticity. In particular, we consider a system of two identical, adaptively coupled active rotators^{6,29,34} influenced by independent Gaussian white noise sources

$$\begin{aligned}\dot{\varphi}_i &= I_0 - \sin \varphi_i + \kappa_i \sin(\varphi_j - \varphi_i) + \sqrt{D}\xi_i(t), \\ \dot{\kappa}_i &= \varepsilon(-\kappa_i + \sin(\varphi_j - \varphi_i + \beta)).\end{aligned}\quad (1)$$

The indices $i, j \in \{1, 2\}$, $i \neq j$ denote the particular units, described by the respective phases $\{\varphi_1, \varphi_2\} \in S^1$, which constitute the fast variables and the slowly varying coupling weights $\{\kappa_1, \kappa_2\} \in \mathcal{R}$. The scale separation between the characteristic timescales is set by the small parameter $\varepsilon \ll 1$ that defines the adaptivity rate. The local dynamics is controlled by the excitability parameter I_0 such that the saddle-node of infinite period (SNIPER) bifurcation at $I_0 = 1$ mediates the transition between the excitable ($I_0 \lesssim 1$) and the oscillatory regimes ($I_0 > 1$). The excitable units may still exhibit oscillations, induced either by the action of the coupling (*emergent* oscillations) and/or evoked by the stochastic terms (noise-induced oscillations). The noiseless coupled system (1) is invariant with respect to exchange of the units' indices such that all the stationary or the periodic solutions always appear in pairs connected by the Z_2 symmetry. Given the similarity between the active rotators and the theta neurons, which also conform to Type I excitability, system (1) may be considered qualitatively analogous to a motif of two adaptively coupled neurons,³⁷ influenced by an external bias current

I_0 and the synaptic noise. Adaptivity is modeled in terms of phase-dependent plasticity^{36,38–40} of coupling weights, having the modality of the plasticity rule adjusted by parameter β . This form of plasticity has already been shown to be capable of qualitatively reproducing the features of some well-known neuronal plasticity rules.^{39,40} In particular, for $\beta = 3\pi/2$, one recovers Hebbian-like learning,⁴¹ where the synaptic potentiation promotes phase synchronization, while for $\beta = \pi$, adaptation acts similarly to spike-timing-dependent plasticity (STDP),^{42–46} whose typical form^{35,45} favors a causal relationship between the pre- and post-synaptic neuron firing times.^{39,40}

II. INVERSE STOCHASTIC RESONANCE DUE TO A BIASED SWITCHING

The first generic scenario for ISR we demonstrate is based on *biased switching* between the metastable states associated with coexisting stationary and periodic attractors of the corresponding deterministic system. As an example, we consider the noise-induced reduction of frequency of emergent oscillations on a motif of two adaptively coupled stochastic active rotators with excitable local dynamics ($I_0 = 0.95$). To elucidate the mechanism behind the effect, we first summarize the details of the noise-free dynamics and then address the switching behavior. A complete bifurcation analysis of the noiseless version of (1) with excitable local dynamics has been carried out in Refs. 6 and 29, having shown (i) how the number and stability of the fixed points depends on the plasticity rule, characterized by β , as well as (ii) how the interplay between β and the adaptivity rate, controlled by the small parameter ε , gives rise to limit cycle attractors. Our focus is on the interval $\beta \in (3.298, 4.495)$, which approximately interpolates between the limiting cases of Hebbian-like and STDP-like plasticity rules. There, the system exhibits two stable equilibria born from the symmetry-breaking pitchfork bifurcation and has four additional unstable fixed points. For the particular case $\beta = 4.2$ analyzed below, the two stable equilibria, given by EQ1: $(\varphi_1^*, \varphi_2^*, \kappa_1^*, \kappa_2^*) = (1.2757, 0.2127, -0.0078, -0.8456)$ and EQ2: $(\varphi_1^*, \varphi_2^*, \kappa_1^*, \kappa_2^*) = (0.2127, 1.2757, -0.8456, -0.0078)$, have been shown to manifest excitable behavior.⁶

The onset of emergent oscillations, as well as the coexistence between the stable stationary and periodic solutions in the noiseless version of (1), is illustrated in Fig. 1. The maximal stability region of the two Z_2 symmetry-related periodic solutions is indicated in Fig. 1(a), which shows the variation of κ_1 variable, $\sigma_{\kappa_1} = \max(\kappa_1(t)) - \min(\kappa_1(t))$, in the (β, ε) parameter plane. The scan was performed by the method of numerical continuation starting from a stable periodic solution such that the initial conditions for an incremented parameter value are given by the final state obtained for the previous iteration step. One finds that for a given β , there exists an interval $\varepsilon \in (\varepsilon_{\min}, \varepsilon_{\max})$ of intermediate scale-separation ratios supporting the oscillations, cf. the highlighted region in Fig. 1(b). In particular, the two Z_2 -symmetry related branches of stable periodic solutions emanate from the fold of cycles bifurcations, denoted by FC in Fig. 1(b) such that the associated threshold scale-separation $\varepsilon_{\min}(\beta)$ decreases with β . The two branches of oscillatory solutions merge around $\varepsilon \approx 0.06$, where the system undergoes an inverse pitchfork bifurcation (PFC) of limit cycles. The incipient stable limit cycle acquires the anti-phase space–time symmetry

$\varphi_1(t) = \varphi_2(t + T_{osc}/2), \kappa_1(t) = \kappa_2(t + T_{osc}/2)$, with T_{osc} denoting the oscillation period.⁶ An example illustrating the basins of stability of stationary and oscillatory solutions for $\varepsilon = 0.1$, obtained by fixing the initial values of phases and varying the initial coupling weights within the range $\kappa_{i,ini} \in (-1, 1)$, is shown in Fig. 1(c). In the presence of noise, the coexisting attractors of the deterministic system turn to metastable states, which are connected by the noise-induced switching.

Inverse stochastic resonance manifests itself as the noise-mediated suppression of oscillations, whereby the frequency of noise-perturbed oscillations becomes minimal at an intermediate noise level. For the motif of two adaptively coupled excitable active rotators, such characteristic non-monotone dependence on noise is generically found for intermediate adaptivity rates supporting multistability between the stationary and the oscillatory solutions. A family of curves illustrating the dependence of the oscillation frequency on noise variance $\langle f \rangle(D)$ for a set of different ε values is shown in Fig. 2(a). The angular brackets $\langle \cdot \rangle$ refer to averaging over an ensemble of a 100 different stochastic realizations, having fixed a set of initial conditions within the basin of attraction of the limit cycle attractor. Nonetheless, qualitatively analogous results are recovered if for each realization of the stochastic process, one selects a set of random initial conditions lying within the stability basin of a periodic solution. In Ref. 29, we have shown that the noise-induced switching gives rise to a bursting-like behavior, where the spiking is interspersed by the quiescent episodes which correspond to the system residing in the vicinity of the quasi-stationary metastable states. Such episodes become prevalent at the noise levels around the minimum of $\langle f \rangle(D)$. For weaker noise $D \lesssim 10^{-3}$, the frequency of emergent oscillations remains close to the deterministic one, whereas for a much stronger noise, it increases above that of unperturbed oscillations. One observes that the suppression effect of noise depends on the adaptivity rate such that it is enhanced for faster adaptivity, see Ref. 29 for a more detailed analysis. In order to illustrate how the ISR effect is reflected at the level of the dynamics

of coupling weights, in Figs. 2(b)–2(d) are shown the stationary distributions $P(\kappa_1)$ for the noise levels below, at, and above the resonant level. To provide a reference to the deterministic case, we have denoted by the dashed-dotted lines the weight levels associated with the two equilibria EQ1 and EQ2, while the blue shading indicates the variation σ_κ of the stable limit cycle. Note that the stable periodic solution is unique because for the considered ε value, the deterministic system lies above the pitchfork of cycles bifurcation, cf. PFC in Fig. 1(b). The stationary distribution $P(\kappa_1)$ at the resonant noise expectedly shows a pronounced peak at one of the quasi-stationary states, while the distributions below or above the resonant noise level indicate a high occupancy of the oscillatory metastable state.

In order to elucidate the mechanism behind ISR, we have calculated how the fraction of the total time spent at the oscillatory metastable states, T_{osc}/T_{tot} , changes with noise. In terms of numerical experiments, the quasi-stationary and the oscillatory metastable states can readily be distinguished by considering the corresponding $\kappa_i(t)$ series, using the fact that the typical distance $|\kappa_1(t) - \kappa_2(t)|$ is much larger for the quasi-stationary than the oscillatory solutions. This has allowed us to employ a simple threshold method to identify the particular system’s states and trace the associated transitions. Figure 3(a) indicates a non-monotone dependence of $T_{osc}/T_{tot}(D)$, implying that the switching process around the resonant noise level becomes strongly biased toward the quasi-stationary state, even more so for a faster adaptivity. The biased switching is facilitated by the geometry of the phase space, featuring an asymmetrical structure with respect to the separatrix between the coexisting attractors such that the limit cycle lies much closer to the separatrix than the stationary states.

The nonlinear response to noise may be understood in terms of the competition between the transition processes from and to the limit cycle attractor. These processes are characterized by the transition rates from the stability basin of the limit cycle attractor to that of the stationary states $\gamma_{LC \rightarrow FP}$ and vice versa, $\gamma_{FP \rightarrow LC}$, which are numerically estimated as the reciprocal values of the corresponding

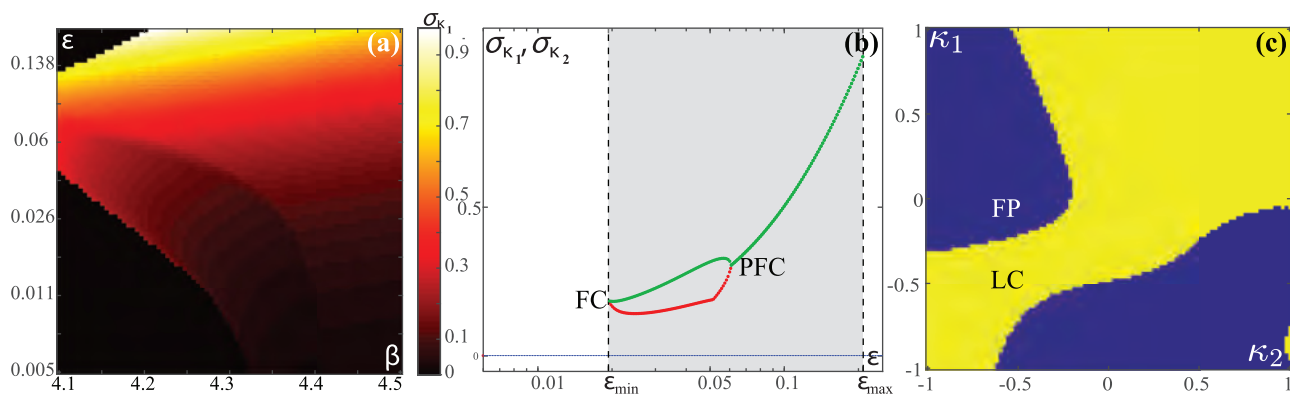


FIG. 1. Emergent oscillations in (1) for $l_0 = 0.95, D = 0$. (a) Variation σ_{κ_1} of the coupling weight κ_1 in the (β, ε) plane. (b) Dependencies $\sigma_{\kappa_i}(\varepsilon), i \in \{1, 2\}$ for the representative stationary (blue) and oscillatory solution (red and green refer to the two units) at fixed $\beta = 4.2$. Shading indicates the ε interval that supports multistability between the two symmetry-related stable equilibria and the limit cycle attractor(s). FC and PFC denote the ε values where the fold of cycles and pitchfork of cycles occur. (c) Basins of stability of the stationary (FP, blue) and oscillatory solutions (LC, yellow) in the (κ_1, κ_2) plane, obtained by fixing the initial phases to $(\varphi_1, \varphi_2) = (1.32, 0.58)$. The remaining parameters are $\beta = 4.2, \varepsilon = 0.1$.

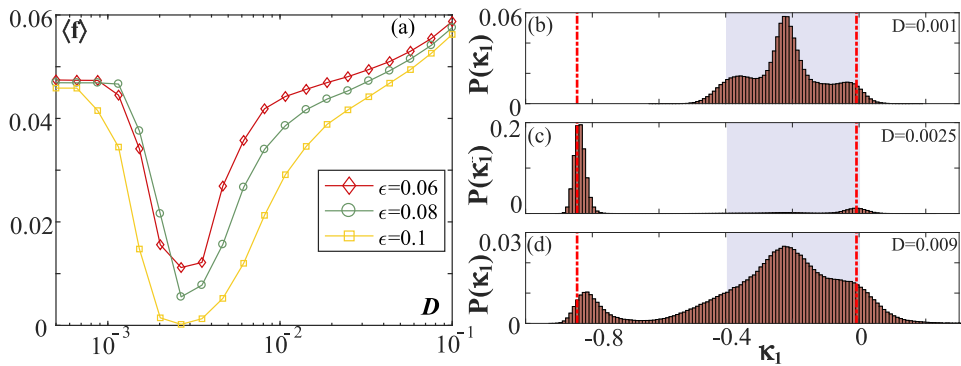


FIG. 2. (a) Dependencies of the mean oscillation frequency on noise for scale separation $\epsilon = 0.06$ (diamonds), $\epsilon = 0.08$ (circles) and $\epsilon = 0.1$ (squares), obtained for fixed $I_0 = 0.95$, $\beta = 4.2$. Averaging has been performed over an ensemble of 100 different stochastic realizations. (b)–(d) show the stationary distributions $P(\kappa_1)$ below ($D = 0.001$), at ($D = 0.0025$), and above ($D = 0.009$) the resonant noise intensity for $\epsilon = 0.1$. The dashed-dotted lines denote the κ_1 levels associated with the two stable equilibria, $\kappa_1^*(EQ1)$ and $\kappa_1^*(EQ2)$, while the blue shaded interval indicates the variation σ_{κ_1} of the unique stable periodic solution.

mean first-passage times.⁴⁷ In Figs. 3(b) and 3(c) is illustrated the qualitative distinction between the noise-dependencies of the transition rates: while $\gamma_{LC \rightarrow FP}$ displays a maximum at the resonant noise level, $\gamma_{FP \rightarrow LC}$ just increases monotonously with noise. For small noise $D \lesssim 10^{-3}$, one observes virtually no switches to the quasi-stationary state, as evinced by the fact that the corresponding oscillation frequency is identical to the deterministic one. For increasing noise, the competition between the two processes is resolved in such a way that at an intermediate/large noise, the impact of $\gamma_{LC \rightarrow FP}/\gamma_{FP \rightarrow LC}$ becomes prevalent. The large values of $\gamma_{FP \rightarrow LC}$ found for quite strong noise $D \gtrsim 0.04$ reflect the point that the system there spends most of the time in the oscillatory metastable state, making only quite short excursions to the quasi-stationary state.

Though ISR is most pronounced for intermediate ϵ , it turns out that an additional subtlety in the mechanism of biased switching may be explained by employing the singular perturbation theory to

the noiseless version of (1). In particular, by combining the critical manifold theory⁴⁸ and the averaging approach,⁴⁹ one may demonstrate the *facilitatory role of plasticity* in enhancing the resonant effect, showing that the adaptation drives the fast flow toward the parameter region where the stationary state is a focus rather than a node.²⁹ The response to noise in multiple timescale systems has already been indicated to qualitatively depend on the character of the stationary states, yielding fundamentally different scaling regimes with respect to noise variance and the scale-separation ratio.^{50–52} Intuitively, one expects that the resonant effects should be associated with the quasi-stationary states derived from the focuses rather than the nodes⁵⁰ because the local dynamics then involves an eigenfrequency.

The fast–slow analysis of (1) for $I_0 = 0.95$ has been carried out in detail in Refs. 6 and 29 such that here we only summarize the main results concerning the associated layer and reduced

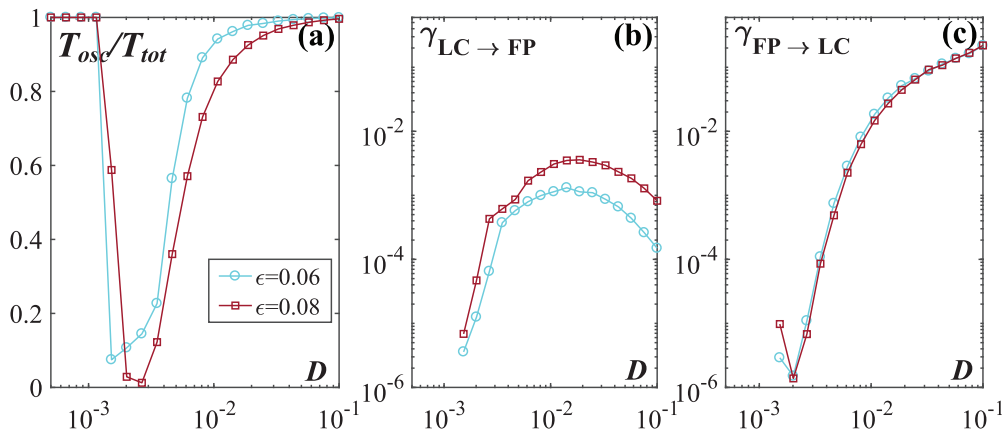


FIG. 3. (a) Fraction of the time spent at the oscillatory metastable state T_{osc}/T_{tot} as a function of noise for $\epsilon = 0.06$ (circles) and $\epsilon = 0.08$ (squares). (b) and (c) Numerically estimated transition rates from the oscillatory to the quasi-stationary metastable states, $\gamma_{LC \rightarrow FP}(D)$ and vice versa, $\gamma_{FP \rightarrow LC}(D)$. The remaining parameters are $I_0 = 0.95$, $\beta = 4.2$.

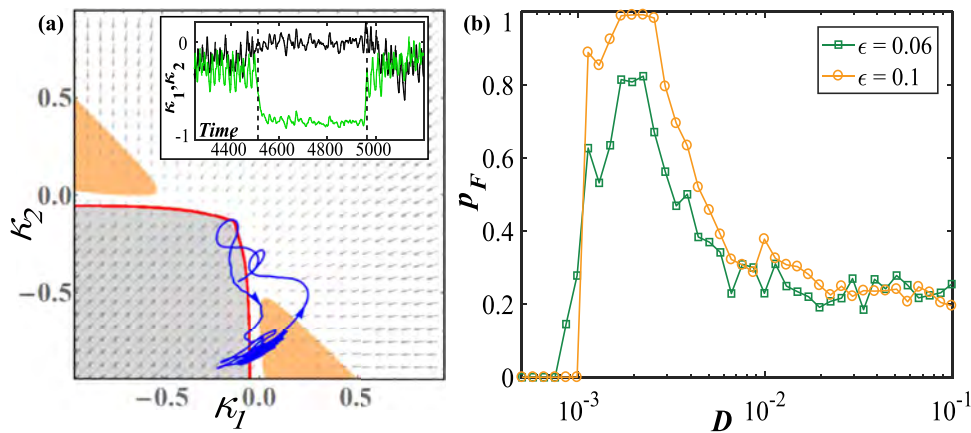


FIG. 4. (a) Fast-slow analysis of (1) for $I_0 = 0.95, D = 0$. The fast flow exhibits a periodic attractor (grey shaded region) and a stable equilibrium (white region), with two branches of SNIPER bifurcations (red lines) outlining the boundary between them. The arrows indicate the vector fields corresponding to the stable sheets of the slow flow. The inset shows $\kappa_i(t)$ series corresponding to a switching episode from the oscillatory to the stationary state and back, obtained for $\epsilon = 0.06, \beta = 4.2$. The corresponding $(\kappa_1(t), \kappa_2(t))$ orbit is indicated by the blue line. Within the two orange regions, the two stable equilibria are focuses rather than the nodes. (b) Conditional probability $p_F(D)$ of having the crossing of SNIPER bifurcation followed by a visit to the orange-shaded region from (a), obtained for $\epsilon = 0.06$ (squares) and $\epsilon = 0.1$ (circles).

problems.⁴⁸ Within the layer problem, the fast flow dynamics

$$\begin{aligned} \dot{\varphi}_1 &= I_0 - \sin \varphi_1 + \kappa_1 \sin(\varphi_2 - \varphi_1), \\ \dot{\varphi}_2 &= I_0 - \sin \varphi_2 + \kappa_2 \sin(\varphi_1 - \varphi_2) \end{aligned} \quad (2)$$

is considered by treating the slow variables $\kappa_1, \kappa_2 \in [-1, 1]$ as additional system parameters. Depending on κ_1 and κ_2 , the fast flow dynamics is found to be almost always *monostable*, exhibiting either a stable equilibrium or a limit cycle attractor, apart from a small region of bistability between the two.^{6,29} The maximal stability region of the oscillatory regime, encompassing both the domain where the oscillatory solution is monostable and where it coexists with a stable equilibrium, is indicated by the gray shading in Fig. 4(a). The latter has been determined by the method of numerical continuation, starting from a periodic solution. The thick red lines outlining the region’s boundaries correspond to the two branches of SNIPER bifurcations.⁶ Note that for each periodic solution above the main diagonal $\kappa_1 = \kappa_2$, there exists a Z_2 symmetry-related counterpart below the diagonal.

By averaging over the different attractors of the fast flow dynamics, we have obtained multiple stable sheets of the slow flow.⁴⁹ The explicit procedure consists in determining the time average $\langle \varphi_2 - \varphi_1 \rangle_t = h(\kappa_1, \kappa_2)$ by iterating (2) for each fixed set (κ_1, κ_2) ^{6,49} and then substituting these averages into the equations of the slow flow

$$\begin{aligned} \kappa_1' &= [-\kappa_1 + \sin(h(\kappa_1, \kappa_2) + \beta)], \\ \kappa_2' &= [-\kappa_2 + \sin(-h(\kappa_1, \kappa_2) + \beta)], \end{aligned} \quad (3)$$

where the prime refers to a derivative over the rescaled time variable $T := t/\epsilon$. The arrows in Fig. 4(a) show the vector fields on the two stable sheets of the slow flow (3) associated with the stationary and the periodic attractors of the fast flow.

The performed fast-slow analysis has allowed us to gain a deeper insight into the facilitatory role of adaptivity within the

ISR. In particular, in the inset of Fig. 4(a) are extracted the time series $(\kappa_1(t), \kappa_2(t))$, which (from left to right) illustrate the switching episode from an oscillatory to the quasi-stationary metastable state. The triggering/termination of this switching event is associated with an inverse/direct SNIPER bifurcation of the fast flow. Note that for (κ_1, κ_2) values immediately after the inverse SNIPER bifurcation, the stable equilibrium of the fast flow is a node. Nevertheless, for the noise levels corresponding to the most pronounced ISR effect, the coupling dynamics guides the system into the triangular orange-shaded regions in Fig. 4(a), where the equilibrium is a stable focus rather than a node. We have verified that this feature is a hallmark of ISR by numerically calculating the conditional probability p_F that the events of crossing the SNIPER bifurcation are followed by the system’s orbit visiting the (κ_1, κ_2) regions with a focus equilibrium. The $p_F(D)$ dependencies for two characteristic ϵ values in Fig. 4(b) indeed show a maximum for the resonant noise levels, corresponding to the minima of the frequency dependencies in Fig. 2(a). The local dynamics around the focus gives rise to a *trapping* effect such that the phase variables remain for a longer time in the associated quasi-stationary states than in case where the metastable states derive from the nodes of the fast flow. Small noise below the resonant values is insufficient to drive the system to the regions featuring focal equilibria, whereas for too strong noise, the stochastic fluctuations completely take over, washing out the quasi-stationary regime. The trapping effect is enhanced for the faster adaptivity rate, as evinced by the fact that the curve $p_F(D)$ for $\epsilon = 0.1$ lies above the one for $\epsilon = 0.06$.

III. INVERSE STOCHASTIC RESONANCE DUE TO A TRAPPING EFFECT

As the second paradigmatic scenario for ISR, we consider the case where the oscillation frequency is reduced due to a noise-induced trapping in the vicinity of an *unstable* fixed point of the

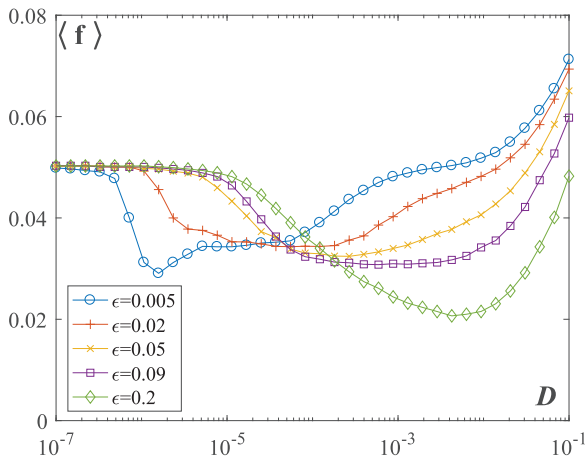


FIG. 5. Family of dependencies $\langle f \rangle(D)$ for scale separations $\epsilon \in \{0.005, 0.02, 0.05, 0.09, 0.2\}$ at fixed $I_0 = 1.05, \beta = \pi$. Stochastic averaging has involved an ensemble of 100 different process realizations.

noiseless system. Such a trapping effect may be interpreted as an example of the phenomenon of *noise-enhanced stability* of an unstable fixed point.⁸⁻¹² This mechanism is distinct from the one based on biased switching because there the quasi-stationary states derive from the *stable* equilibria of the noise-free system such that the noise gives rise to crossing over the separatrix between the oscillatory and the quiescent regime. Nevertheless, in the scenario below, noise induces “tunneling” through the bifurcation threshold, temporarily stabilizing an unstable fixed point of the deterministic system.

In particular, we study an example of a system (1) comprised of two adaptively coupled active rotators in the *oscillatory*, rather than the excitable regime, setting the parameter $I_0 = 1.05$ close to a bifurcation threshold. The plasticity parameter is fixed to $\beta = \pi$ such that the modality of the phase-dependent adaptivity resembles the STDP rule in neuronal systems. One finds that this system exhibits a characteristic non-monotone response to noise, with the oscillation frequency of the phases (f) displaying a minimum at an intermediate noise level (see Fig. 5). In contrast to the mechanism described in Sec. II, the onset of ISR here does not qualitatively depend on the adaptivity rate. One only finds a quantitative dependence of the system’s nonlinear response to noise on ϵ , in a sense that the resonant noise level shifts to larger values with increasing ϵ . Our exhaustive numerical simulations indicate that the ISR effect persists for slow adaptivity rates, cf. the example of the $\langle f(D) \rangle$ for $\epsilon = 0.005$ in Fig. 5, and the results of the fast–slow analysis below will further show that all the ingredients required for the ISR effect remain in the singular perturbation limit $\epsilon \rightarrow 0$. The persistence of the ISR effect has also been numerically confirmed for faster adaptivity rates $\epsilon \sim 0.1$. In this case, we have observed that the minima of the $\langle f(D) \rangle$ curves become deeper with ϵ , suggesting that the ISR becomes more pronounced for higher adaptivity rates.

To elucidate the mechanism behind ISR, we again perform the fast–slow analysis of the corresponding noise-free system. Prior to this, we briefly summarize the results of the numerical bifurcation analysis for the noiseless system in the case of finite scale

separation. First note that selecting a particular plasticity rule $\beta = \pi$ confines the dynamics of the couplings to a symmetry invariant subspace $\kappa_1(t) = -\kappa_2(t) \equiv \kappa(t)$. Due to this, the noiseless version of the original system (1) can be reduced to a three-dimensional form

$$\begin{aligned} \dot{\varphi}_1 &= I_0 - \sin \varphi_1 + \kappa \sin(\varphi_2 - \varphi_1), \\ \dot{\varphi}_2 &= I_0 - \sin \varphi_2 + \kappa \sin(\varphi_2 - \varphi_1), \\ \dot{\kappa} &= \epsilon(-\kappa - \sin(\varphi_2 - \varphi_1)). \end{aligned} \tag{4}$$

By numerically solving the eigenvalue problem, we have verified that (4) possesses no stable fixed points, but rather a pair of saddle nodes and a pair of saddle focuses. Also, we have determined that the maximal real part of the eigenvalues of the focuses displays a power-law dependence on the scale separation, tending to zero in the singular limit $\epsilon \rightarrow 0$. Concerning the oscillatory states, our numerical experiments show that (4) exhibits multistability between three periodic solutions, whereby two of them are characterized by the non-zero couplings and a constant phase-shift between the fast variables, whereas the third solution corresponds to a case of effectively uncoupled units [$\kappa(t) = 0$] and the fast variables synchronized in-phase.

A deeper understanding of the ingredients relevant for the trapping mechanism can be gained within the framework of the fast–slow analysis, considering the layer problem

$$\begin{aligned} \dot{\varphi}_1 &= I_0 - \sin \varphi_1 + \kappa \sin(\varphi_2 - \varphi_1), \\ \dot{\varphi}_2 &= I_0 - \sin \varphi_2 + \kappa \sin(\varphi_2 - \varphi_1). \end{aligned} \tag{5}$$

Treating $\kappa \in [-1, 1]$ as an additional system parameter, we first look for the stationary and periodic attractors of the fast flow. It is convenient to apply the coordinate transformation $(\varphi_1, \varphi_2) \mapsto (\Phi, \delta\varphi) = (\frac{\varphi_1 + \varphi_2}{2}, \frac{\varphi_1 - \varphi_2}{2})$, rewriting (5) as

$$\begin{aligned} \delta\dot{\varphi} &= -\sin \delta\varphi \cos \Phi, \\ \dot{\Phi} &= I_0 - \cos \delta\varphi (\sin \Phi + 2\kappa \sin \delta\varphi). \end{aligned} \tag{6}$$

From the second equation, one readily finds that the fast flow cannot possess any fixed points on the synchronization manifold $\delta\varphi = 0$ because $I_0 > 1$ such that the stationary solutions derive only from the condition $\cos \Phi = 0$. A numerical analysis shows that, depending on κ , the fast flow for $I_0 \gtrsim 1$ can exhibit two or no fixed points. For the particular value $I_0 = 1.05$, one finds that two fixed points, namely, a saddle and a *center*, exist within the interval $\kappa \in [-0.1674, 0.1674]$. The appearance of a center point is associated with the time-reversal symmetry of the fast flow (5). Indeed, one may show that the fast flow is invariant to a symmetry-preserving map R of the form

$$R = \begin{cases} \varphi_1 \rightarrow \pi - \varphi_2, \\ \varphi_2 \rightarrow \pi - \varphi_1, \\ t \rightarrow -t. \end{cases} \tag{7}$$

Note that in case of the finite scale separation, the counterpart of the center point of the fast flow is a weakly unstable focus of the complete system (4).

The structure of the fast flow is organized around the saddle-center bifurcation, which occurs at $\kappa = \kappa_{SC} = -0.1674$. There, the

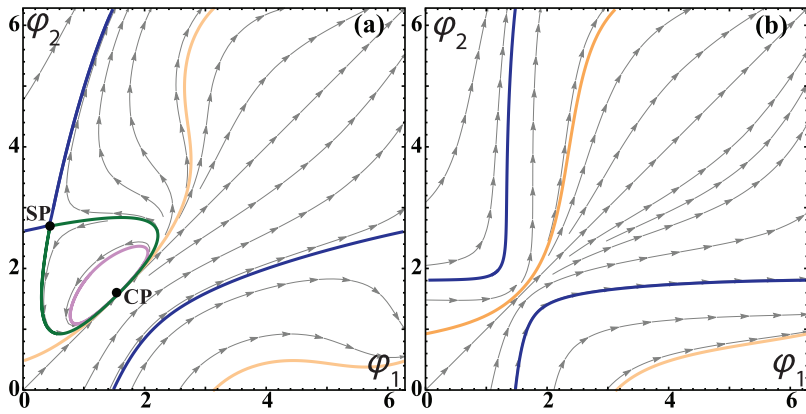


FIG. 6. Typical dynamics of the fast flow (5) for $l_0 = 1.05$ below ($\kappa = -0.8$) and above the saddle-center bifurcation ($\kappa = -0.08$) are illustrated in (a) and (b), respectively. In (a), the system possesses two unstable fixed points, a saddle (SP) and a center (CP), and exhibits three types of closed orbits: a limit cycle attractor (orange), homoclinic connections to SP (blue and green), and subthreshold oscillations around the center (purple). In (b), the system exhibits bistability between two oscillatory states, shown in orange and blue.

two fixed points get annihilated as a homoclinic orbit associated with the saddle collapses onto the center. To gain a complete picture of the dynamics of the fast flow, we have shown in Figs. 6(a) and 6(b) the illustrative examples of the phase portraits and the associated vector fields for $\kappa < \kappa_{SC}$ and $\kappa > \kappa_{SC}$, respectively. For $\kappa \in [-1, \kappa_{SC})$, the fast flow possesses a limit cycle attractor, essentially derived from the local dynamics of the units, cf. the orbit indicated in red in Fig. 6(a). Apart from an attracting periodic orbit, one observes two additional types of closed orbits, namely, the homoclinic connections to the saddle point (SP), shown by blue and

green, as well as the periodic orbits around the center point (CP), an example of which is indicated in orange. For $\kappa > \kappa_{SC}$, the fast flow exhibits bistability between two oscillatory solutions, such that there is a coexistence of a limit cycle inherited from the local dynamics of units and the limit cycle associated with the former homoclinic orbits, cf. Fig. 6(b).

In the presence of noise, the described attractors of the fast flow turn to metastable states. Nevertheless, in contrast to the case of two adaptively coupled excitable units, the slow stochastic fluctuations here do not only involve switching between the metastable

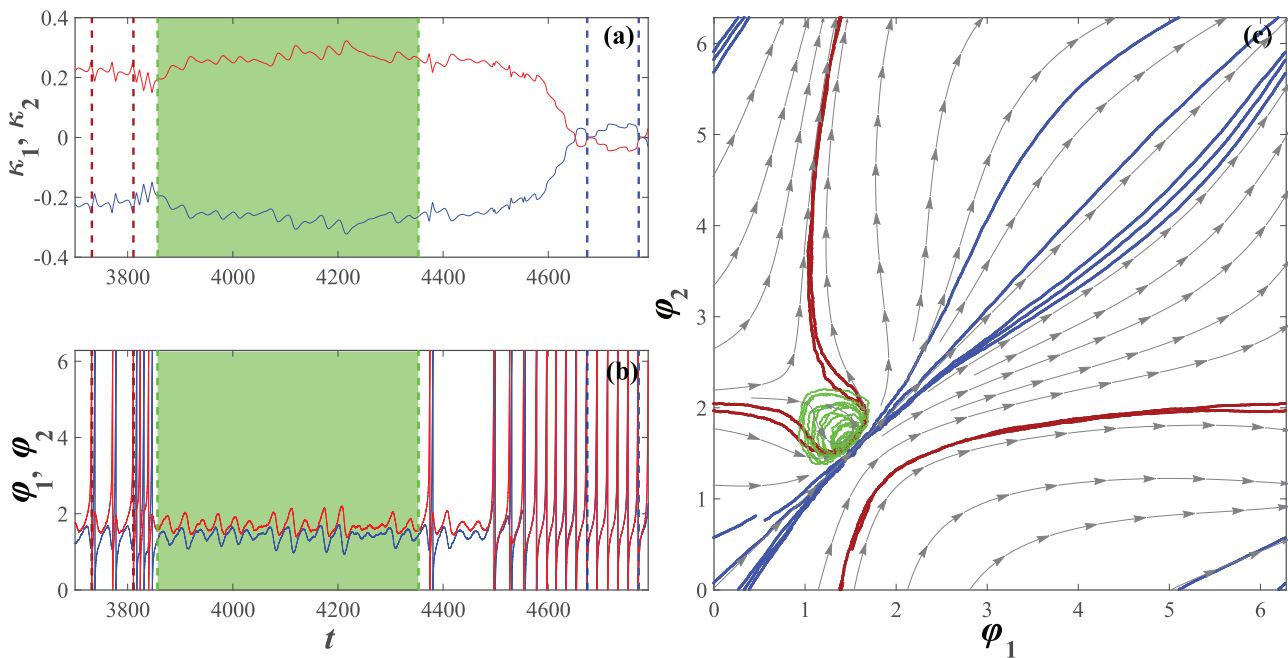


FIG. 7. (a) and (b) show the time traces of $\kappa_i(t)$ and $\varphi_i(t)$, respectively, with an episode where the system remains in the vicinity of an unstable fixed point highlighted in green. The parameters are $l_0 = 1.05$, $\varepsilon = 0.035$, $\beta = \pi$, $D = 10^{-4}$. (c) The orbits conforming to the two metastable states characterized by large-amplitude oscillations of phases are shown in red and blue, whereas the subthreshold oscillations are indicated in green. Superimposed is the vector field of the fast flow, corresponding to the limit $\varepsilon \rightarrow 0$.

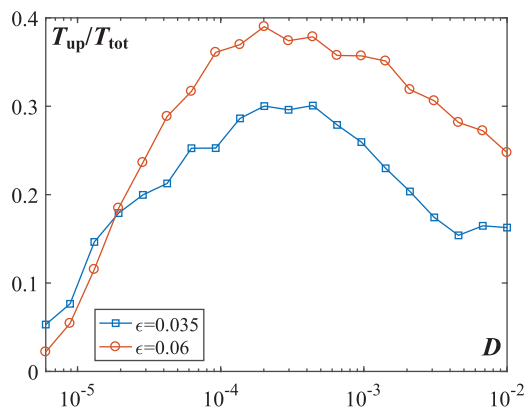


FIG. 8. Numerically estimated fraction of time spent in the vicinity of the unstable fixed point T_{up}/T_{tot} as a function of noise for $\epsilon = 0.035$ (squares) and $\epsilon = 0.06$ (circles). Note that the positions of the maxima coincide with the corresponding resonant noise levels from Fig. 5. Remaining system parameters are $l_0 = 1.05, \beta = \pi$.

states but also comprise the *subthreshold oscillations* derived from the periodic orbits around the center point. These subthreshold oscillations provide for the trapping effect, which effectively leads to a reduced oscillation frequency. An example of the time series $\kappa_i(t)$ and $\varphi_i(t), i \in \{1, 2\}$ obtained for an intermediate $\epsilon = 0.035$ in Figs. 7(a) and 7(b) indeed shows three characteristic episodes, including visits to two distinct oscillatory metastable states and an extended stay in the vicinity of the center, cf. the stochastic orbits

$(\varphi_1(t), \varphi_2(t))$ and the vector field of the fast flow in Fig. 7(c). In the case of finite scale separation, the trapping effect is manifested as the noise-enhanced stability of an unstable fixed point. The prevalence of subthreshold oscillations changes with noise in a non-monotone fashion, see the inset in Fig. 7(c), becoming maximal around the resonant noise level where the frequency dependence on noise exhibits a minimum, cf. Figs. 5 and 8. The fraction of time spent in the metastable state corresponding to subthreshold oscillations has been estimated by the numerical procedure analogous to the one already described in Sec. II.

IV. TWO MECHANISMS OF ISR IN CLASSICAL NEURONAL MODELS

So far, we have demonstrated the two paradigmatic scenarios for ISR considering the examples of coupled Type I units, whose local dynamics is close to a SNIPER bifurcation, be it in the excitable or the oscillatory regime. Nevertheless, the onset of ISR and the specific mechanisms of the phenomenon do not depend on the excitability class of local dynamics. In particular, we have recently demonstrated that a single Type II Fitzhugh–Nagumo relaxation oscillator exhibits qualitatively the same form of non-monotone dependence on noise,³⁰ with the mechanism involving noise-induced subthreshold oscillations that follow the maximal canard of an unstable focus. In that case, it has been established that the trapping effect and the related subthreshold oscillations are triggered due to a phase-sensitive excitability of a limit cycle. Moreover, we have verified that the same model of neuronal dynamics, set to different parameter regimes, may exhibit two different scenarios of ISR. In particular, by an appropriate selection of the system

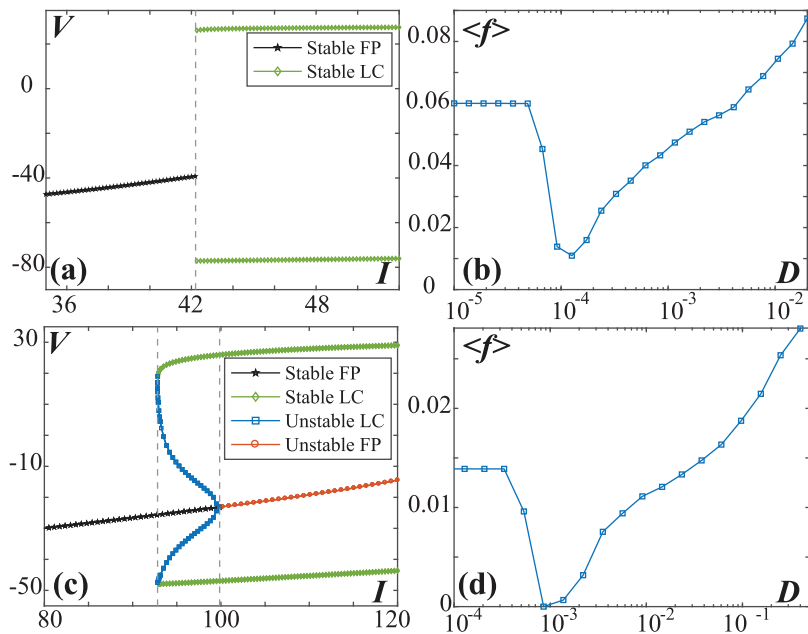


FIG. 9. (a) Bifurcation diagram showing the dependence of the amplitudes of the membrane potential V on the external bias current I for the version of Morris–Lecar model exhibiting a supercritical Hopf bifurcation. (b) illustrates the $\langle f \rangle(D)$ dependence for the Morris–Lecar neural oscillator in close vicinity of the supercritical Hopf bifurcation. (c) $V(I)$ bifurcation diagram for the setup where the Morris–Lecar model displays a subcritical Hopf bifurcation. (d) Characteristic non-monotone dependence $\langle f \rangle(D)$ for the Morris–Lecar model from (c), with the bifurcation parameter $I = 95$ set in the bistable regime. The two sets of parameters putting the Morris–Lecar model in the vicinity of a supercritical or a subcritical Hopf bifurcation are specified in the main text.

parameters, the Morris–Lecar neuron model

$$\begin{aligned}
 C \frac{dv}{dt} &= -g_{fast} m(v)(v - E_{Na}) - g_{slow} W(v - E_K) \\
 &\quad - g_{leak}(v - E_{leak}) + I, \\
 \frac{dv}{dt} &= \phi \frac{W_\infty(v) - W}{\tau(v)}, \\
 m(v) &= 0.5 \left[1 + \tanh \left(\frac{v - \beta_m}{\gamma_m} \right) \right], \\
 W_\infty(v) &= \left[1 + \tanh \left(\frac{v - \beta_w}{\gamma_w} \right) \right], \\
 \tau(v) &= 1 / \cosh \left(\frac{v - \beta_w}{2\gamma_w} \right),
 \end{aligned} \tag{8}$$

where v and W , respectively, denote the membrane potential and the slow recovery variable, can be placed in the vicinity of a supercritical or a subcritical Hopf bifurcation,⁵³ with the external bias current I being the bifurcation parameter. In the first case, obtained for $E_{Na} = 50$ mV, $E_K = -100$ mV, $E_{leak} = -70$ mV, $g_{fast} = 20$ mS/cm², $g_{slow} = 20$ mS/cm², $g_{leak} = 2$ mS/cm², $\phi = 0.15$, $C = 2$ μ F/cm², $\beta_m = -1.2$ mV, $\beta_w = -13$ mV, $\gamma_m = 18$ mV, $\gamma_w = 10$ mV, the model is monostable under the variation of I , and the ISR is observed slightly above the Hopf bifurcation ($I = 43$ μ A/cm²) due to a noise-enhanced stability of an unstable fixed point, cf. Figs. 9(a) and 9(b). In the second case, conforming to the parameter set $E_{Na} = 120$ mV, $E_K = -84$ mV, $E_{leak} = -60$ mV, $g_{fast} = 4.4$ mS/cm², $g_{slow} = 8$ mS/cm², $g_{leak} = 2$ mS/cm², $\phi = 0.04$, $C = 20$ μ F/cm², $\beta_m = -1.2$ mV, $\beta_w = 2$ mV, $\gamma_m = 18$ mV, $\gamma_w = 30$ mV, the model displays bistability between a limit cycle and a stable equilibrium in a range of I just below the Hopf threshold. There, ISR emerges due to a mechanism based on biased switching, see the bifurcation diagram $V(I)$ in Fig. 9(c) and the dependence of the oscillation frequency on noise for $I = 95$ μ A/cm² in Fig. 9(d).

V. DISCUSSION AND OUTLOOK

Considering a model which involves the classical ingredients of neuronal dynamics, such as excitable behavior and coupling plasticity, we have demonstrated two paradigmatic scenarios for inverse stochastic resonance. By one scenario, the phenomenon arises in systems with multistable deterministic dynamics, where at least one of the attractors is a stable equilibrium. Due to the structure of the phase space, and, in particular, the position of the separatrices, the switching dynamics between the associated metastable states becomes biased at an intermediate noise level such that the longevity of the quasi-stationary states substantially increases or they may even turn into absorbing states. In the other scenario, an oscillatory system possesses a weakly unstable fixed point, whose stability is enhanced due to the action of noise. The latter results in a trapping effect such that the system exhibits subthreshold oscillations, whose prevalence is noise-dependent and is found to be maximal at the resonant noise level. Both scenarios involve classical facilitatory effects of noise, such as crossing the separatrices or stochastic mixing across the bifurcation threshold, which should warrant the

ubiquity of ISR. In terms of the robustness of the effect, we have demonstrated that the onset of ISR is independent on the excitability class of local dynamics, and moreover, that the same model of neuronal dynamics, depending on the particular parameters, may display two different scenarios for ISR.

Given that ISR has so far been observed at the level of models of individual neurons,^{23,24,26,30} motifs of units with neuron-like dynamics^{22,29} and neural networks,²⁷ it stands to reason that the phenomenon should be universal to neuronal dynamics, affecting both the emergent oscillations and systems of coupled oscillators. The explained mechanisms appear to be generic and should be expected in other systems comprised of units with local dynamics poised close to a bifurcation threshold. Inverse stochastic resonance should play important functional roles in neuronal systems, including the reduction of spiking frequency in the absence of neuromodulators, the triggering of stochastic bursting, i.e., of on-off tonic spiking activity, the suppression of pathologically long short-term memories,^{14,24,26,28} and most notably, may contribute to generation of UP-DOWN states, characteristic for spontaneous and induced activity in cortical networks.^{31,32}

ACKNOWLEDGMENTS

The authors acknowledge funding from the Institute of Physics Belgrade, through the grant by the Ministry of Education, Science and Technological Development of the Republic of Serbia. The authors would also like to thank Matthias Wolfrum and Serhij Yanchuk for fruitful discussions.

REFERENCES

- ¹B. Lindner, J. García-Ojalvo, A. Neiman, and L. Schimansky-Geier, *Phys. Rep.* **392**, 321 (2004).
- ²E. Forgoston and R. O. Moore, *SIAM Rev.* **60**, 969 (2018).
- ³B. Neiman and D. F. Russell, *Phys. Rev. Lett.* **88**, 138103 (2002).
- ⁴L. Ryashko and E. Slepukhina, *Phys. Rev. E* **96**, 032212 (2017).
- ⁵C. Zheng and A. Pikovsky, *Phys. Rev. E* **98**, 042148 (2018).
- ⁶I. Bačić, S. Yanchuk, M. Wolfrum, and I. Franović, *Eur. Phys. J. Spec. Top.* **227**, 1077 (2018).
- ⁷I. Franović and V. Klinshov, *Chaos* **28**, 023111 (2018).
- ⁸A. Fiasconaro, B. Spagnolo, and S. Boccaletti, *Phys. Rev. E* **72**, 061110 (2005).
- ⁹R. N. Mantegna and B. Spagnolo, *Phys. Rev. Lett.* **76**, 563 (1996).
- ¹⁰S. Ciuchi, F. de Pasquale, and B. Spagnolo, *Phys. Rev. E* **47**, 3915 (1993).
- ¹¹N. V. Agudov, A. A. Dubkov, and B. Spagnolo, *Physica A* **325**, 144 (2003).
- ¹²G. Augello, D. Valentia, and B. Spagnolo, *Eur. Phys. J. B* **78**, 225 (2010).
- ¹³M. D. McDonnell and L. M. Ward, *Nat. Rev. Neurosci.* **12**, 415 (2011).
- ¹⁴B. A. Schmerl and M. D. McDonnell, *Phys. Rev. E* **88**, 052722 (2013).
- ¹⁵A. Destexhe and M. Rudolph-Lilith, *Neuronal Noise* (Springer, New York, 2012).
- ¹⁶A. S. Pikovsky and J. Kurths, *Phys. Rev. Lett.* **78**, 775 (1997).
- ¹⁷B. Lindner and L. Schimansky-Geier, *Phys. Rev. E* **60**, 7270 (1999).
- ¹⁸V. A. Makarov, V. I. Nekorkin, and M. G. Velarde, *Phys. Rev. Lett.* **86**, 3431 (2001).
- ¹⁹A. Zakharova, A. Feoktistov, T. Vadivasova, and E. Schöll, *Eur. Phys. J. Spec. Top.* **222**, 2481 (2013).
- ²⁰N. Semenova, A. Zakharova, V. Anishchenko, and E. Schöll, *Phys. Rev. Lett.* **117**, 014102 (2016).
- ²¹L. H. Gamaitoni, P. Hänggi, P. Jung, and F. Marchesoni, *Rev. Mod. Phys.* **70**, 223 (1998).
- ²²B. S. Gutkin, J. Jost, and H. C. Tuckwell, *Eur. Phys. Lett.* **81**, 20005 (2008).
- ²³H. C. Tuckwell, J. Jost, and B. S. Gutkin, *Phys. Rev. E* **80**, 031907 (2009).

- ²⁴M. Uzuntarla, J. R. Cressman, M. Ozer, and E. Barreto, *Phys. Rev. E* **88**, 042712 (2013).
- ²⁵M. Uzuntarla, *Phys. Lett. A* **377**, 2585 (2013).
- ²⁶M. Uzuntarla, J. J. Torres, P. So, M. Ozer, and E. Barreto, *Phys. Rev. E* **95**, 012404 (2017).
- ²⁷M. Uzuntarla, E. Barreto, and J. J. Torres, *PLoS Comput. Biol.* **13**, e1005646 (2017).
- ²⁸A. Buchin, S. Rieubland, M. Häusser, B. S. Gutkin, and A. Roth, *PLoS Comput. Biol.* **12**, e1005000 (2016).
- ²⁹I. Bačić, V. Klinshov, V. I. Nekorkin, M. Perc, and I. Franović, *Eur. Phys. Lett.* **124**, 40004 (2018).
- ³⁰I. Franović, O. E. Omel'chenko, and M. Wolfrum, *Chaos* **28**, 071105 (2018).
- ³¹T. T. G. Hahn, J. M. McFarland, S. Berberich, B. Sakmann, and M. R. Mehta, *Nat. Neurosci.* **15**, 1531 (2012).
- ³²V. V. Vyazovskiy and K. D. Harris, *Nat. Rev. Neurosci.* **14**, 443 (2013).
- ³³I. Franović and V. Klinshov, *Eur. Phys. Lett.* **116**, 48002 (2016).
- ³⁴J. A. Kromer, R. D. Pinto, B. Lindner, and L. Schimansky-Geier, *Eur. Phys. Lett.* **108**, 20007 (2014).
- ³⁵L. Lücken, O. V. Popovych, P. A. Tass, and S. Yanchuk, *Phys. Rev. E* **93**, 032210 (2016).
- ³⁶D. Kasatkin, S. Yanchuk, E. Schöll, and V. Nekorkin, *Phys. Rev. E* **96**, 062211 (2017).
- ³⁷P. O. Sporns and R. Kotter, *PLoS Biol.* **2**, e369 (2004).
- ³⁸Y. L. Maistrenko, B. Lysyansky, C. Hauptmann, O. Burylko, and P. Tass, *Phys. Rev. E* **75**, 066207 (2007).
- ³⁹T. Aoki and T. Aoyagi, *Phys. Rev. Lett.* **102**, 034101 (2009).
- ⁴⁰T. Aoki and T. Aoyagi, *Phys. Rev. E* **84**, 066109 (2011).
- ⁴¹D. O. Hebb, *The Organization of Behavior: A Neuropsychological Approach* (John Wiley and Sons, New York, 1949).
- ⁴²S. Song, K. D. Miller, and L. F. Abbott, *Nat. Neurosci.* **3**, 919 (2000).
- ⁴³R. C. Froemke and Y. Dan, *Nature* **416**, 433 (2002).
- ⁴⁴H.-X. Wang, R. C. Gerkin, D. W. Nauen, and G.-Q. Bi, *Nat. Neurosci.* **8**, 187 (2005).
- ⁴⁵A. Morrison, M. Diesmann, and W. Gerstner, *Biol. Cybern.* **98**, 459 (2008).
- ⁴⁶O. V. Popovych, S. Yanchuk, and P. A. Tass, *Sci. Rep.* **3**, 2926 (2013).
- ⁴⁷P. Hänggi, P. Talkner, and M. Borkovec, *Rev. Mod. Phys.* **62**, 251 (1990).
- ⁴⁸C. Kuehn, *Multiple Time Scale Dynamics* (Springer International Publishing, Switzerland, 2015).
- ⁴⁹A. Shilnikov, *Int. J. Bifurcat. Chaos* **18**, 2141 (2008).
- ⁵⁰N. Berglund and B. Gentz, *Noise-Induced Phenomena in Slow-Fast Dynamical Systems* (Springer, Berlin, 2006).
- ⁵¹*Stochastic Methods in Neuroscience*, edited by C. Laing and G. J. Lord (Oxford University Press, London, 2009).
- ⁵²J. Touboul and G. Wainrib, *Physica D* **307**, 42 (2015).
- ⁵³H. Wang, L. Wang, L. Yu, and Y. Chen, *Phys. Rev. E* **83**, 021915 (2011).

Two scenarios for the onset and suppression of collective oscillations in heterogeneous populations of active rotators

Vladimir Klinshov*

Institute of Applied Physics of the Russian Academy of Sciences, 46 Ulyanov Street, 603950 Nizhny Novgorod, Russia

Igor Franović[†]

Scientific Computing Laboratory, Center for the Study of Complex Systems, Institute of Physics Belgrade, University of Belgrade, Pregrevica 118, 11080 Belgrade, Serbia



(Received 28 June 2019; revised manuscript received 11 October 2019; published 27 December 2019)

We consider the macroscopic regimes and the scenarios for the onset and the suppression of collective oscillations in a heterogeneous population of active rotators composed of excitable or oscillatory elements. We analyze the system in the continuum limit within the framework of Ott-Antonsen reduction method, determining the states with a constant mean field and their stability boundaries in terms of the characteristics of the rotators' frequency distribution. The system is established to display three macroscopic regimes, namely the *homogeneous stationary state*, where all the units lie at the resting state, the *global oscillatory state*, characterized by the partially synchronized local oscillations, and the *heterogeneous stationary state*, which includes a mixture of resting and asynchronously oscillating units. The transitions between the characteristic domains are found to involve a complex bifurcation structure, organized around three codimension-two bifurcation points: a Bogdanov-Takens point, a cusp point, and a fold-homoclinic point. Apart from the monostable domains, our study also reveals two domains admitting bistable behavior, manifested as coexistence between the two stationary solutions or between a stationary and a periodic solution. It is shown that the collective mode may emerge via two generic scenarios, guided by a saddle-node of infinite period or the Hopf bifurcation, such that the transition from the homogeneous to the heterogeneous stationary state under increasing diversity may follow the classical paradigm, but may also be hysteretic. We demonstrate that the basic bifurcation structure holds qualitatively in the presence of small noise or small coupling delay, with the boundaries of the characteristic domains shifted compared to the noiseless and the delay-free case.

DOI: [10.1103/PhysRevE.100.062211](https://doi.org/10.1103/PhysRevE.100.062211)

I. INTRODUCTION

The onset of a collective mode mediated via a transition to synchrony is a fundamental paradigm of macroscopic behavior in a broad variety of fields, ranging from neuroscience and other biologically inspired models to chemistry, technology, and social science [1,2]. A classical approach within the theory of nonlinear dynamics is to regard populations exhibiting a collective mode as macroscopic oscillators [3–5], which can then interact with other populations or be subjected to external stimuli. In this context, we investigate an important problem of the emergence and the suppression of collective oscillations in populations comprised of units with nonuniform intrinsic parameters, which are drawn from a certain probability distribution. Such nonuniformity is a manifestation of variability [6–9], a ubiquitous feature that often makes it more realistic to consider heterogeneous rather than homogeneous assemblies. Depending on the particular application, variability may alternatively be referred to as diversity, heterogeneity, impurities, or quenched noise. In many cases, the diversity can be large

enough to give rise to qualitative differences in individual dynamics of units, such that some of the active elements within a population may be self-oscillating while the others are excitable.

The classical Kuramoto paradigm [10] addresses the scenario where the diversity is manifested at the quantitative level alone, since all the units are considered to be self-oscillating. There, the continuous transition to synchrony occurs once the coupling between the oscillators becomes strong enough to overcome the effects of diversity [2,11]. Nevertheless, the diversity alone has been shown to be capable, under appropriate conditions, to enhance the response of an assembly to external forcing or to promote synchronization [7,8,12]. Moreover, in the case of heterogeneous assemblies made up of excitable and oscillatory units rather than the oscillators alone, it has been demonstrated that the transition to synchrony with increasing diversity may be classical or reentrant, depending on the particular form of the units frequency distribution [13]. For such a setup, it has also been indicated that the collective firing emerges via a generic mechanism where the entrainment of units is degraded by increasing diversity [8].

In the present paper, we investigate the regimes of macroscopic behavior, as well as the scenarios for the onset and the suppression of collective oscillations in a heterogeneous

*vladimir.klinshov@ipfran.ru

†franovic@ipb.ac.rs

population made up of oscillatory and excitable units, considering a model of active rotators with global sine coupling. Our analysis relies on the Ott-Antonsen reduction method [14,15], based on the ansatz that the long-term macroscopic dynamics of such systems settles on a particular invariant attractive manifold. We first provide an exact description of macroscopic stationary states featuring a *constant mean field* and then determine the bifurcations that outline the stability boundaries of the characteristic domains. While the stationary states and the associated self-consistency equation are obtained for an arbitrary distribution of natural frequencies, the subsequent bifurcation analysis is carried out for a *uniform* frequency distribution on a bounded interval, which has the advantage of allowing for analytical tractability. We establish the complete bifurcation structure and demonstrate two generic scenarios for the emergence and the suppression of the collective mode. While the scenario featuring the successive onset and suppression of oscillations under increasing diversity has earlier been reported to be universal for heterogeneous populations with various distributions of the units' frequencies [12,13], the other scenario, which involves a hysteretic behavior due to existence of bistability regions, is reported here for the first time, as far as we know.

Apart from diversity, the two additional ingredients influencing the dynamics in neuronal and other biophysical systems are coupling delays and noise [16–18]. In particular, realistic models often have to include explicit coupling delays in order to describe the effects of finite velocity of signal propagation or the latency in information processing [17,19–23]. On the other hand, creating coarse-grained models inevitably requires one to incorporate different sources of noise [24–31]. Both coupling delay and noise may play an important role in the collective dynamics of a population. For example, in systems consisting just of excitable units, it is well known that the noise may play a constructive role, contributing to the onset of collective firing via synchronization of local noise-induced oscillations [32–35]. Concerning the effect of coupling delays, the standard Kuramoto model with uniform delays has been shown to exhibit the discontinuous rather than the continuous transition between the incoherent and coherent states, further having the synchronization frequency suppressed by the delay [11,36].

Our study evinces the robustness of the general physical picture, inherited from the noiseless and the delay-free case, in the presence of *small* coupling delay and *small* noise. While the impact of small delay may be analyzed within the local stability approach we developed, the Ott-Antonsen method in principle does not allow one to treat stochastic assemblies. Only quite recently, an approach involving the so-called circular cumulants [37,38] has been developed to incorporate a first-order correction to the Ott-Antonsen theory, which accommodates for the effects of noise. We perform numerical analysis of the system dynamics in presence of small noise and complement it with qualitative arguments.

The paper is organized as follows. In Sec. II, we present the details of the model and provide the continuum limit formulation for the delay- and the noise-free setup, obtaining the Ott-Antonsen equation for the local order parameter. Section III comprises the analytical results on the local structure of the macroscopic stationary states and the related self-consistency

equation, derived for an arbitrary frequency distribution. In Sec. IV, the stability and bifurcation analysis of the stationary states is carried out for a particular distribution of frequencies, comparing the stability boundaries of the characteristic domains to those obtained in numerical experiments. In Sec. V, it is shown that the basic bifurcation scenario persists in presence of small noise or small coupling delay. Section VI contains our concluding remarks.

II. MODEL DYNAMICS AND THE CONTINUUM LIMIT FORMULATION

We consider a heterogeneous assembly of N globally coupled active rotators described by:

$$\dot{\theta}_i(t) = \omega_i - a \sin \theta_i(t) - \frac{K}{N} \sum_j \sin[\theta_i(t) - \theta_j(t - \tau) + \alpha] + \sigma \eta_i(t), \quad i = 1, \dots, N, \quad (1)$$

where the phase variables are $\theta_i \in S^1$ and the local dynamics is governed by the nonisochronicity parameter a and the natural frequency ω_i . Regarding the term “natural frequency,” note that it will be used for convenience to describe the intrinsic parameter involving the quenched randomness, even though some units may exhibit excitable, rather than oscillatory, behavior. The frequencies are distributed according to the probability density function $g(\omega)$ that satisfies $\int_{-\infty}^{\infty} g(\omega) d\omega = 1$ and is characterized by the mean value Ω and the width Δ , which we here explicitly refer to as the *diversity* parameter. The individual unit rotates uniformly with the frequency ω_i for $a = 0$ only, whereas for $a > 0$ its rotation becomes nonuniform, having the rotation direction dependent on the sign of ω_i . The relation between ω_i and the parameter a underlies the excitability feature of autonomous dynamics. In particular, ω_i constitutes the bifurcation parameter, such that for fixed a , an isolated unit lies in the excitable regime if $|\omega_i| < a$. In this case, the unit possesses a stable node, whereas the characteristic nonlinear threshold-like response is mediated by an unstable steady state. At $|\omega_i| = a$, an isolated unit undergoes a saddle-node of infinite period (SNIPER) bifurcation toward the oscillatory regime. The interactions are assumed to be uniform across the population, and are characterized by the coupling strength K , the coupling phase-lag α , and the coupling delay τ . The effect of random fluctuations is represented by the white Gaussian random forces η_i of intensity σ^2 , which act independently on each unit [$\langle \eta_i(t) \rangle = 0$, $\langle \eta_i(t) \eta_j(t) \rangle = \delta_{ij} \delta(t - t)$].

As already indicated, in this and the following section we apply the Ott-Antonsen framework [14,15] to investigate the collective dynamics of an heterogeneous assembly of active rotators in the delay- and the noise-free case $\tau = \sigma = 0$. To this end, let us introduce the Kuramoto complex order parameter, which represents the center of mass of all rotators:

$$R(t) = \rho(t) e^{i\psi(t)} = \frac{1}{N} \sum_j e^{i\theta_j(t)}, \quad (2)$$

such that (1) can be rewritten as

$$\dot{\theta}_i = \omega_i - \frac{a}{2i} (e^{i\theta_i} - e^{-i\theta_i}) + \frac{K}{2i} [R e^{-i(\theta_i + \alpha)} - \bar{R} e^{i(\theta_i + \alpha)}], \quad (3)$$

where the bar denotes the complex conjugate. In the thermodynamic limit $N \rightarrow \infty$, the macroscopic state of the system can be described by the probability density function $f(\theta, \omega, t)$, which, for the considered moment t , gives the relative number of oscillators whose phases and frequencies are $\theta_i(t) \approx \theta$, $\omega_k \approx \omega$. The normalization condition required for the probability density function is $\int_0^{2\pi} f(\theta, \omega, t) d\theta = g(\omega)$. Given the conservation of oscillators, $f(\theta, \omega, t)$ has to fulfill the continuity equation

$$\frac{\partial f}{\partial t} + \frac{\partial}{\partial \theta}(fv) = 0, \quad (4)$$

where the velocity is just

$$v(\theta, \omega, t) = \omega - \frac{a}{2i}(e^{i\theta} - e^{-i\theta}) + \frac{K}{2i}[Re^{-i(\theta+\alpha)} - \bar{R}e^{i(\theta+\alpha)}]. \quad (5)$$

In the last expression, we have used the form of the Kuramoto mean field in the thermodynamic limit $N \rightarrow \infty$,

$$R(t) = \int_{-\infty}^{\infty} d\omega \int_0^{2\pi} f(\theta, \omega, t) e^{i\theta} d\theta, \quad (6)$$

According to the Ott-Antonsen ansatz [14,15], the long-term dynamics of the continuity equation (8) settles on a particular manifold of the form

$$f(\theta, \omega, t) = \frac{g(\omega)}{2\pi} \left\{ 1 + \sum_{n=1}^{\infty} [z^n(\omega, t) e^{in\theta} + z^n(\omega, t) e^{-in\theta}] \right\}, \quad (7)$$

where the complex amplitude $z(\omega, t)$ is such that $|z(\omega, t)| \leq 1$. Introducing the assumption (7) into (4), one finds that $z(\omega, t)$ satisfies the Ott-Antonsen equation

$$\dot{z}(\omega, t) = i\omega z + (1 - z^2) \frac{a}{2} + \frac{K}{2} R e^{-i\alpha} - \frac{K}{2} \bar{R} e^{i\alpha} z^2. \quad (8)$$

Quantity $z(\omega, t)$ should be interpreted as the frequency-dependent *local order parameter*, in the sense that it quantifies the degree of synchrony of oscillators whose intrinsic frequencies ω_i lie within a small interval around the given frequency ω . In the continuum limit, the global and the local order parameter are connected by the self-consistency condition

$$R = \mathcal{G}z = \int_{-\infty}^{\infty} g(\omega) z(\omega) d\omega, \quad (9)$$

which follows from the definition (6) and the ansatz (7). Note that (8) presents a generalization of the corresponding result in Ref. [13] for $a \neq 1$, $\alpha \neq 0$.

III. STATIONARY SOLUTIONS OF THE OTT-ANTONSEN EQUATION

Within this section, our aim is to characterize the microscopic structure of the stationary solutions, finding the means to classify them by applying the self-consistency condition (9). To do so, one first looks for the solutions of the Ott-Antonsen equation (8) for which the Kuramoto mean field $R(t) = \rho(t) e^{i\psi(t)}$ is constant. In particular, we substitute the solution of the form $z(\omega, t) = r(\omega, t) e^{i\varphi(\omega, t)}$ into (8), which

ultimately results in

$$\begin{aligned} \dot{r} &= \frac{B}{2}(1 - r^2) \cos \phi, \\ r\dot{\phi} &= \omega r - \frac{B}{2}(1 + r^2) \sin \phi, \end{aligned} \quad (10)$$

having introduced the notation

$$\begin{aligned} B &= \sqrt{a^2 + K^2 \rho^2 + 2aK\rho \cos(\psi - \alpha)}, \\ \beta &= \arctan \frac{K\rho \sin(\psi - \alpha)}{a + K\rho \cos(\psi - \alpha)}, \\ \phi &= \varphi - \beta. \end{aligned} \quad (11)$$

From the system (10), one infers that the quantity B , which depends only on the coupling strength and the mean field, plays the role of the *macroscopic excitability parameter*. This follows from the fact that the microscopic structure of the stationary state is self-organized in a way that the assembly splits into two groups, according to the relation between the respective natural frequencies ω_i and B . In particular, one group is comprised of rotators in the *excitable regime*, whose intrinsic frequencies satisfy $|\omega| < B$, whereas the other group consists of rotating units, whose intrinsic frequencies satisfy $|\omega| > B$. Another indication on the role of B can be obtained if the definitions of B and β from (11) are applied to transform the original equation for the dynamics of rotators (1) into $\dot{\theta}_i = \omega_i - B \sin(\theta_i - \beta)$, which just conforms to a set of forced active rotators. From the level of single unit's dynamics, B is then classically referred to as the *resistivity parameter* in the sense that it reflects the rotator's ability to modify its natural frequency.

Taking a closer look into the dynamics of the two sub-assemblies following from (10), one finds that for $|\omega| < B$ there exist two steady states, given by

$$r^*(\omega) = 1, \quad \phi^*(\omega) = \arcsin \frac{\omega}{B}, \quad (12)$$

and

$$r^*(\omega) = 1, \quad \phi^*(\omega) = \pi - \arcsin \frac{\omega}{B}, \quad (13)$$

whereby our latter stability analysis will show that only the solution (12) is stable. For the units within the rotating group $|\omega| > B$, the only steady state reads

$$\begin{aligned} r^*(\omega) &= \frac{|\omega|}{B} - \sqrt{\frac{\omega^2}{B^2} - 1} \\ \phi^*(\omega) &= \frac{\pi}{2} \operatorname{sgn} \omega. \end{aligned} \quad (14)$$

In order to fully quantify the stationary solutions of the Ott-Antonsen equation (8), one has to obtain an explicit expression for the macroscopic excitability parameter B . In order to do so, we invoke the self-consistency equation (9). Applying the latter to the stationary state $z^*(\omega) = r^*(\omega) e^{i\phi^*(\omega) + i\beta}$ given by (12) and (14), one obtains

$$\begin{aligned} \rho e^{i(\psi - \beta)} &= \frac{i\Omega}{B} + \int_{|\omega| < B} d\omega g(\omega) \sqrt{1 - \frac{\omega^2}{B^2}} \\ &\quad - \frac{i}{B} \int_{|\omega| > B} d\omega g(\omega) \omega \sqrt{1 - \frac{B^2}{\omega^2}}, \end{aligned} \quad (15)$$

where $\Omega = \int_{-\infty}^{\infty} \omega g(\omega) d\omega$ refers to the mean value of the frequency distribution. Separating for the real and the imaginary part of (15) and after some algebra, one ultimately arrives at the self-consistency equation for B of the form:

$$f(B) = B^2 - a^2 - 2K[f_1(B) \sin \alpha + f_2(B) \cos \alpha] + K^2 \frac{f_1^2(B) + f_2^2(B)}{B^2} = 0, \quad (16)$$

where

$$f_1(B) = \Omega - \int_{|\omega| > B} d\omega g(\omega) \omega \sqrt{1 - \frac{B^2}{\omega^2}},$$

$$f_2(B) = \int_{|\omega| < B} d\omega g(\omega) \sqrt{B^2 - \omega^2}. \quad (17)$$

Note that the analogous expression has been obtained in Ref. [13] but only for the particular case $a = 1$, $\alpha = 0$. The results so far apply for an arbitrary distribution of natural frequencies $g(\omega)$. In order to carry out an explicit analysis on the stability of stationary states, including determining the associated stability boundaries and characterization of the transitions between the different collective regimes, we confine the remainder of the study to a particular case of $g(\omega)$, namely a *uniform* distribution of frequencies on a bounded interval.

IV. STABILITY OF THE STATIONARY SOLUTIONS OF THE OTT-ANTONSEN EQUATION

Within this section, we specify the general results from Sec. III to an example of a uniform distribution of natural frequencies $g(\omega)$ defined on an interval $\omega \in [\omega_1, \omega_2]$:

$$g(\omega) = \begin{cases} 0, & \omega < \omega_1 \\ \gamma, & \omega_1 < \omega < \omega_2, \\ 0, & \omega > \omega_2 \end{cases} \quad (18)$$

where $\gamma = 1/(\omega_2 - \omega_1)$ derives from the normalization condition. The given distribution is characterized by an average $\Omega = \frac{\omega_1 + \omega_2}{2}$ and the width $\Delta = \omega_2 - \omega_1$. The advantage of making such a choice of frequency distribution is that it allows for a full analytical treatment of the self-consistency equation (16) for the macroscopic excitability parameter. In particular, the integrals (17) then read

$$f_1(B) = \begin{cases} \Omega - \gamma[F_1(\omega_2) - F_1(\omega_1)], & B < \omega_1 \\ \Omega - \gamma F_1(\omega_2), & \omega_1 < B < \omega_2, \\ \Omega, & B > \omega_2 \end{cases} \quad (19)$$

where

$$F_1(\omega) = \frac{|\omega|}{2} \sqrt{\omega^2 - B^2} + \frac{B^2}{2} \ln \frac{B}{|\omega| + \sqrt{\omega^2 - B^2}}, \quad (20)$$

and

$$f_2(B) = \begin{cases} 0, & B < \omega_1 \\ \gamma \left[\frac{\pi}{4} B^2 - F_2(\omega_1) \right], & \omega_1 < B < \omega_2, \\ \gamma [F_2(\omega_2) - F_2(\omega_1)], & B > \omega_2 \end{cases} \quad (21)$$

with

$$F_2(\omega) = \frac{|\omega|}{2} \sqrt{B^2 - \omega^2} + \frac{B^2}{2} \arcsin \frac{\omega}{B}. \quad (22)$$

Considering the uniform frequency distribution (18), we have carried out the stability and bifurcation analysis of the Ott-Antonsen equation (8). The main control parameters are the characteristics of $g(\omega)$, namely its mean Ω and the width Δ , while the remaining system parameters a , K , and α are kept fixed. Note that the stability analysis of (8) requires one to rewrite it as a real system in order to eliminate the complex conjugation [39–41]. The analysis *per se* involves linearization of the Ott-Antonsen equation for variations around the stationary solution (12)–(14) and consists in determining how the Lyapunov spectra of the stationary states depend on Ω and Δ . While the technical details of the calculation are elaborated in the Appendix, the analysis we provide below will include characterization of the stationary solutions of the Ott-Antonsen equation (8) and the associated stability domains, as well as the description of the mechanisms behind the onset and the suppression of collective oscillations. The analytical results are corroborated by numerical experiments carried out on a heterogeneous assembly of $N = 10^4$ active rotators.

The microscopic structure of the stationary regimes and the fashion in which their number and stability depend on the characteristics of $g(\omega)$ may conveniently be explained in terms of the solutions of the self-consistency equation (16) for the parameter B . A typical form of the function $f(B)$ for the considered domain of (Ω, Δ) values is illustrated in Fig. 1. The three roots of $f(B)$, denoted by $B_1 > B_2 > B_3$, correspond to the stationary solutions of the Ott-Antonsen equation (8). In particular, the macroscopic regime associated to B_1 presents a global rest state, because the macroscopic excitability parameter is so large that the frequencies of all the units lie below it. Given its microscopic structure, where the local dynamics is solely excitable, this state can also be termed a *homogeneous stationary state*. The corresponding time series $\theta_i(t)$ and the evolution of the modulus of the Kuramoto order parameter $\rho(t) = |R(t)|$ are illustrated in

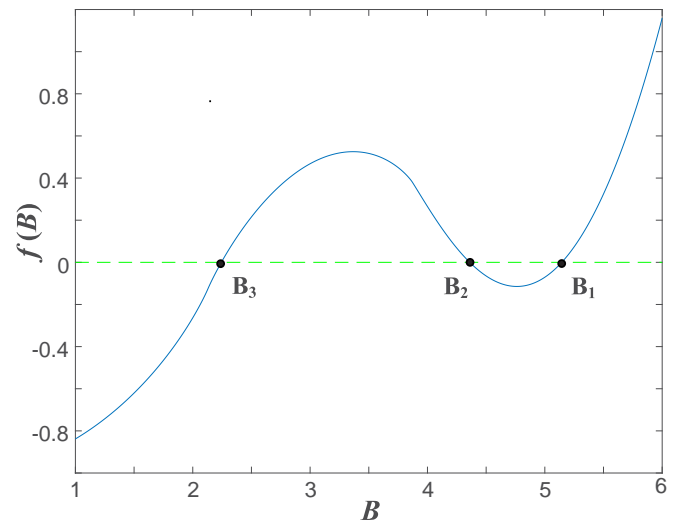


FIG. 1. Typical form of the function $f(B)$ and the three solutions $B_1 > B_2 > B_3$ of the self-consistency equation (16). The system parameters are as follows: $a = 1$, $K = 5$, $\alpha = 0$, $\Omega = 0.87$, and $\Delta = 6$.

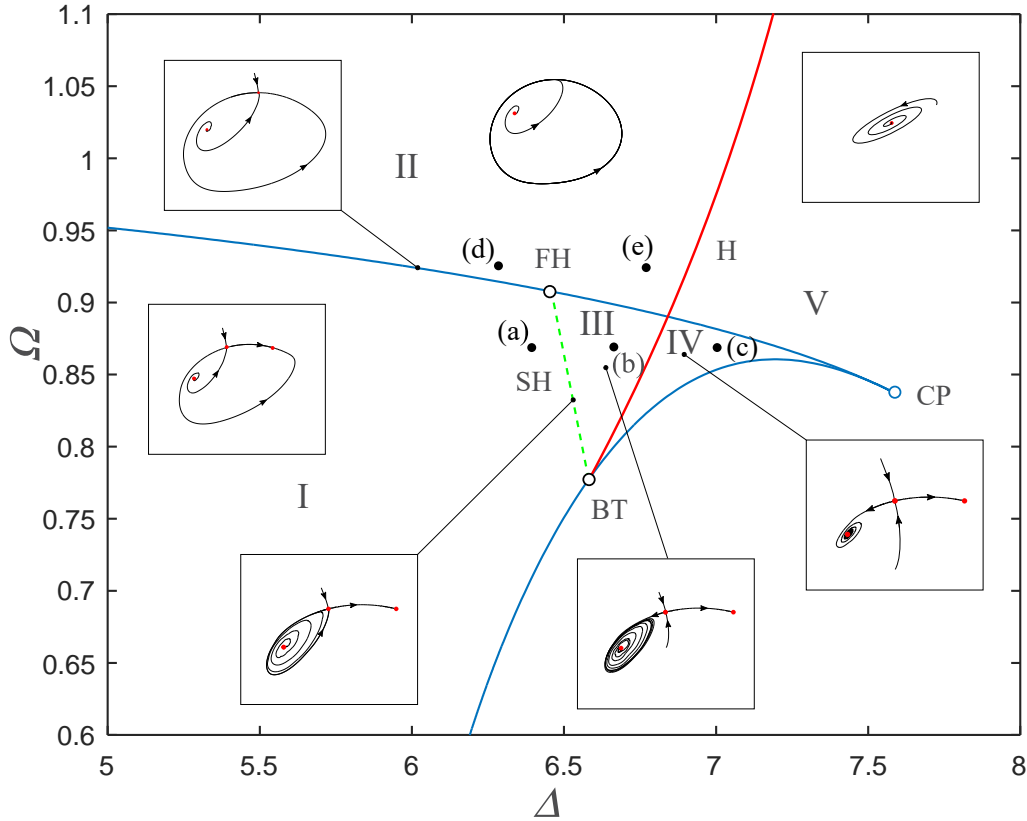


FIG. 2. Bifurcation diagram in the (Ω, Δ) plane, constructed by the method of stability analysis described in the Appendix. The remaining system parameters are fixed to $a = 1, K = 5, \alpha = 0$. The two branches of saddle-node bifurcations (blue solid lines) emanate from the cusp point CP, where the pitchfork bifurcation occurs. From the Bogdanov-Takens point (BT) emanate the Hopf bifurcation curve (H), indicated by the red solid line, and a branch of saddle-homoclinic bifurcations (SH), shown by the green dashed line. The upper branch of folds meets SH at the fold-homoclinic point (FH). The bullets indicate the parameter values associated to the time series in Fig. 4.

Fig. 4(a). We shall demonstrate below that the global rest state may disappear in a fold bifurcation. In contrast to the macroscopic regime given by B_1 , the stationary state corresponding to B_3 is typically a heterogeneous one, involving a subassembly of excitable units ($|\omega_i| < B_3$) and a subassembly of oscillating units ($|\omega_i| > B_3$), see the example of the time series in Fig. 4(c). In Ref. [13], the heterogeneous stationary state is referred to as the asynchronous state, because spiking activity may be observed at the level of single units, but the macroscopic dynamics *per se* does not exhibit a collective mode. The heterogeneous state, as shown in greater detail below, may undergo either a fold or Hopf bifurcation scenario. The stationary state associated to B_2 conforms to a saddle within the relevant (Ω, Δ) domain, undergoing fold bifurcations either with B_1 or B_3 or providing for the separatrices in case of the two observed bistable regimes.

The bifurcation diagram in Fig. 2 shows how the number and stability of the stationary solutions of the Ott-Antonsen equation (8) changes under variation of the parameters of the frequency distribution Ω and Δ . The diagram features five characteristic domains I–V and is organized around three codimension-2 bifurcation points, namely (i) the cusp point (CP), which corresponds to a symmetry-breaking pitchfork bifurcation; (ii) the Bogdanov-Takens point (BT), which unfolds into Hopf (H) and saddle-homoclinic (SH) bifurcation curves; and (iii), the fold-homoclinic point (FH), where a branch of

saddle-node bifurcations meets a curve of homoclinic tangencies of a limit cycle. The upper and the lower branch of folds, which emanate from the cusp, correspond to the coalescence of the state B_2 with B_1 and B_3 , respectively. The former or latter branch has been obtained by solving for the parameters where the local minimum or maximum of the function $f(B)$ crosses the zero level. The Hopf bifurcation curve has been determined by the local stability analysis of the stationary state B_3 . While such local analysis cannot provide for the saddle-homoclinic branch, its existence follows from the general structure of the Bogdanov-Takens bifurcation [42,43].

In the following, we provide a detailed description of the regimes underlying domains I–V, illustrating the associated phase portraits, cf. Fig. 2, and explaining the bifurcations that outline their stability boundaries. At the cusp point CP, the two branches of saddle-node bifurcations coalesce, cf. the two blue solid lines in Fig. 2. In terms of the stationary states B_1 – B_3 from Fig. 1, to the right of CP there exists only a stable fixed point B_2 . Following the pitchfork bifurcation, B_2 becomes a saddle, whereas two stable nodes, B_1 and B_3 , are created. The parameter region admitting only a single stable stationary state, be it B_1, B_2 , or B_3 , is denoted by V in Fig. 2. Decreasing the diversity, the stability of B_1 is influenced only by a fold bifurcation, whereas the character and stability of B_3 are influenced by the fold and Hopf bifurcations, derived from the Bogdanov-Takens point. We have evinced that while

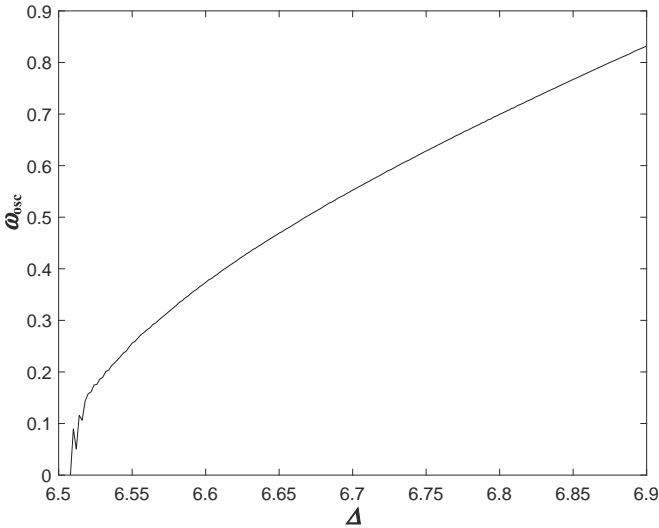


FIG. 3. Oscillation frequency of the periodic solution ω_{osc} in terms of diversity Δ , calculated along the Hopf bifurcation curve. One observes that the frequency tends to zero while approaching the Bogdanov-Takens point. The parameters a , K , and α are the same as in Fig. 2.

approaching BT, the frequency of oscillations ω_{osc} expectedly tends to zero, see Fig. 3. Along the lower branch of folds B_2 and B_3 get annihilated, so that from the right of this curve and to the cusp point, the only stable stationary state of the system is the node B_1 . The Hopf bifurcation curve that emanates from the BT point affects the stability of the stationary state B_3 , such that it becomes unstable for smaller diversities. This implies that within the region IV, bounded by the Hopf curve to the right and the two fold curves on the left, one observes *bistability between two stationary states*, namely the stable node B_1 and the stable focus B_3 , which

are separated by the stable manifold of the saddle B_2 , cf. the corresponding phase portrait in Fig. 2. Reducing diversity, B_3 undergoes a supercritical Hopf bifurcation (H), whereby immediately to the left of the Hopf curve (region III), one finds *bistability between a small limit cycle and the stable node* B_1 , again separated by the stable manifold of the saddle B_2 . The time series illustrating the microscopic and macroscopic dynamics of the oscillatory states born from the Hopf bifurcation for two different parameter sets, $(\Omega_1, \Delta_1) = (0.87, 6.76)$ and $(\Omega_2, \Delta_2) = (0.93, 6.78)$, are provided in Fig. 4(b) and Fig. 4(e).

Consistent with the Bogdanov-Takens scenario, the limit cycle born from the Hopf bifurcation is destabilized via a homoclinic tangency to the saddle B_2 , which is reflected by a branch of saddle-homoclinic bifurcations (SH) emanating from BT, see the green dashed line in Fig. 2. Using the local stability approach described in the Appendix, we are not able to trace the stability of a limit cycle *per se* but have been able to qualitatively verify the disappearance of the limit cycle by numerical means. The SH curve terminates at the fold-homoclinic point (FH), where it meets the upper branch of fold bifurcations. At FH, the stable manifold of the saddle B_2 touches the invariant circle. Decreasing diversity further away from the saddle-homoclinic bifurcation, cf. region I, the system exhibits a stable node B_1 and has two additional unstable fixed points, namely the saddle B_2 and the unstable focus B_3 .

At the upper branch of folds, under increasing diversity, the stable node B_1 and the saddle B_2 collide and disappear. For Δ values less than that of the FH point, the fold takes place on the invariant circle, giving rise to a SNIPER bifurcation. Crossing the SNIPER bifurcation either by increasing Ω or Δ , the collective dynamics of the system exhibits a transition toward the macroscopic oscillatory state. The latter is characterized by synchronous local oscillations of a large period, cf. the

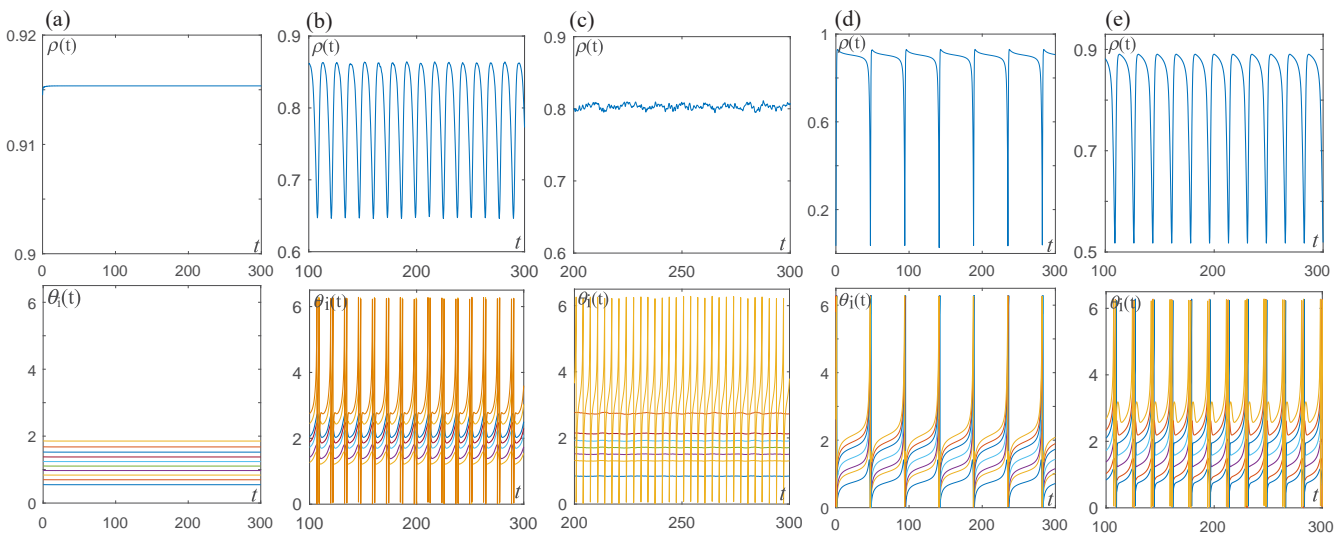


FIG. 4. Local and collective dynamics within the characteristic parameter domains indicated in Fig. 2. In the top row are provided the examples of the time series $\rho(t) = |R(t)|$, while in the bottom row are shown the corresponding local time series $\theta_i(t)$ normalized over 2π . The particular parameter values of the frequency distribution (indicated by bullets in Fig. 2) are $(\Omega, \Delta) = (0.87, 6.64)$ in (a), $(\Omega, \Delta) = (0.87, 6.76)$ in (b), $(\Omega, \Delta) = (0.87, 7)$ in (c), $(\Omega, \Delta) = (0.93, 6.6)$ in (d), and $(\Omega, \Delta) = (0.93, 6.78)$ in (e). The remaining system parameters are the same as in Fig. 2.

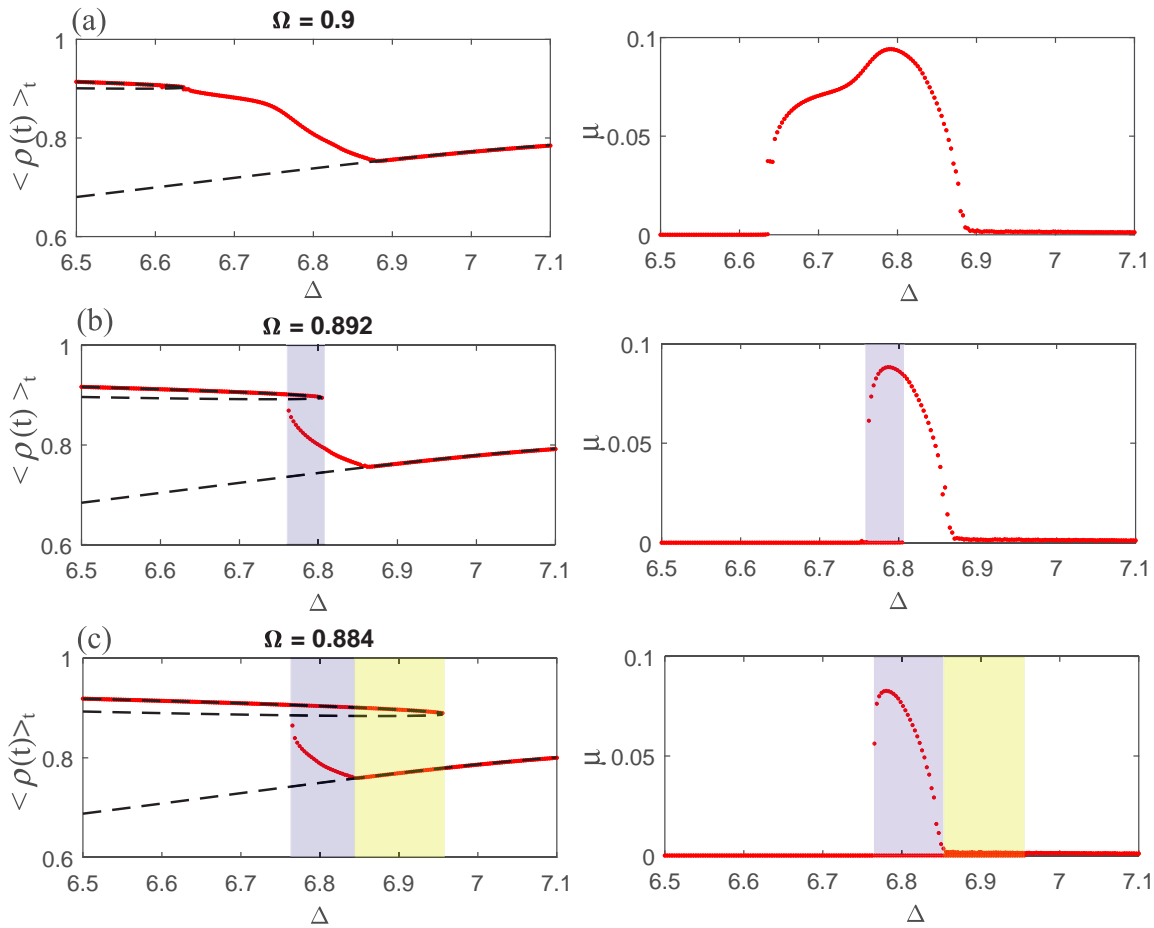


FIG. 5. Characteristic transition sequences between the different macroscopic regimes under increasing diversity for a fixed value of Ω . The states are described by the time-averaged modulus of the Kuramoto order parameter $\langle \rho(t) \rangle_t$ (left column) and the associated variance μ (right column). The mean frequencies are $\Omega = 0.9$ in (a), $\Omega = 0.892$ in (b), and $\Omega = 0.884$ in (c). The classical scenario of transitions is recovered in (a), whereas the two hysteretic scenarios involving passage over one or two bistability regions, indicated by shading in (b) and (c), are reported for the first time as far as we know.

time series in Fig. 4(e). For this reason, it is also called the *synchronous* state in Ref. [13]. For diversities to the right of the FH point, the saddle-node annihilation of B_1 and B_2 no longer occurs on an invariant circle. Thus, the only attractor within region VI corresponds to a small limit cycle emerging from Hopf destabilization of B_3 . For increasing diversity, B_3 gains stability by undergoing the inverse Hopf bifurcation, as already indicated above.

A. Classical and hysteretic transitions between macroscopic regimes

Having characterized all the regimes of macroscopic activity and the associated stability domains, we focus on the scenarios leading to the onset and the suppression of the collective mode in heterogeneous populations, an issue of outstanding importance in the theory of coupled dynamical systems. By the classical paradigm [13], the systematic increase of diversity under fixed mean frequency induces a sequence of transitions between the three regimes of collective dynamics, namely the global rest state, the synchronous state (corresponding to macroscopic oscillations), and the asynchronous

state (a heterogeneous state displaying mixed excitable and oscillatory local dynamics). Our study demonstrates that, apart from this, there exist two novel generic scenarios of transitions involving a *hysteretic behavior*. To gain a deeper insight into this problem, we have plotted how the time-averaged modulus of the Kuramoto mean-field $\rho(t) = |R(t)|$ and the associated variance $\mu = \sqrt{\langle \rho^2 \rangle_t - \langle \rho \rangle_t^2}$ change under variation of the diversity Δ for the three characteristic mean frequencies $\Omega \in \{0.9, 0.892, 0.884\}$, cf. Fig. 5. In order to reveal the potential bistable behavior, we have carried out sweeps in the directions of the increasing and the decreasing Δ applying the method of numerical continuation, where the initial conditions for the system with incremented Δ coincide with the final state at the previous Δ value.

The classical sequence of transitions is indeed recovered for $\Omega = 0.9$, see Fig. 5(a). There the onset of the collective mode is guided by a SNIPER bifurcation, mediating a transition from the homogeneous stationary state B_1 to a periodic solution. The suppression of the collective mode is induced by an inverse Hopf bifurcation that stabilizes the heterogeneous stationary state B_3 , which is analogous to the Kuramoto-type scenario where the system desynchronizes under increasing

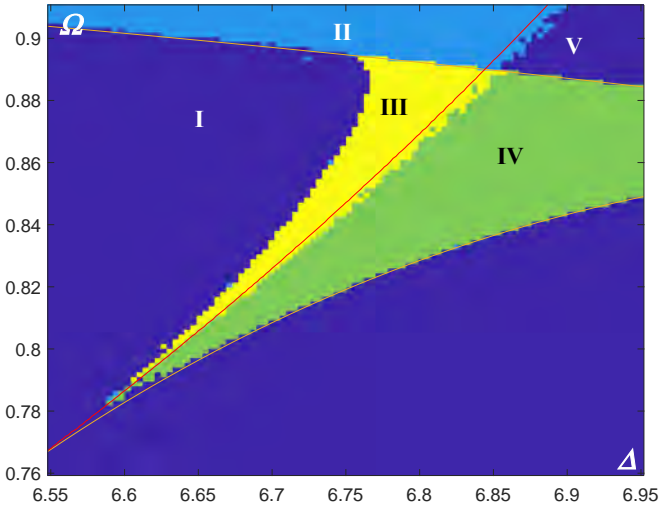


FIG. 6. The (Δ, Ω) parameter plane divided into regions with different macroscopic dynamics: the monostable stationary state (dark blue, regions I and V), monostable limit cycle (light blue, region II), bistability with two coexisting stationary states (green, region IV), and bistability between a stationary state and a limit cycle (yellow, region III). The parameter values are the same as in Fig. 2. Superimposed are the corresponding bifurcation curves obtained analytically within the Ott-Antonsen framework.

disorder. For $\Omega = 0.892$, we have established a hysteretic transition scenario, emerging due to a passage through a bistability region III from Fig. 2, which admits coexistence between the homogeneous stationary state B_1 and the periodic solution created from B_3 , cf. Fig. 5(b). In this case, the onset of a collective mode is induced by a Hopf bifurcation, while its suppression is controlled by the homoclinic tangency of the limit cycle. For $\Omega = 0.884$, the sequence of transitions remains hysteretic but becomes more complex, see Fig. 5(c). In particular, by increasing the diversity, one traverses over two bistability regions, denoted by III and IV in Fig. 2. While the first one is qualitatively the same as for $\Omega = 0.892$, the second one supports two coexisting stationary states, associated to B_1 and B_3 . Nevertheless, the onset and the suppression of the collective mode *per se* follow the same scenario as the one described in Fig. 5(b). Note that the described transition sequences are observed if the mean frequency Ω is sufficiently large.

In order to evince the generic character of the described scenarios and confirm the theoretical predictions regarding the parameter domains supporting the collective oscillations, we have carried out an extensive numerical study of the system's dynamics in terms of the parameters Δ and Ω , see Fig. 7. In particular, using numerical continuation, we have performed bidirectional sweeps over the (Ω, Δ) plane, keeping one of the parameters fixed while the other one was varied, in analogy to the method already described in relation to Fig. 6. This allowed us to partition the (Ω, Δ) plane into different regions according to the number and the type of the supported attractors. Comparison of the boundaries of these regions with the bifurcation curves from Fig. 2, which are shown overlaid, corroborates an excellent agreement between the theory and the numerical results.

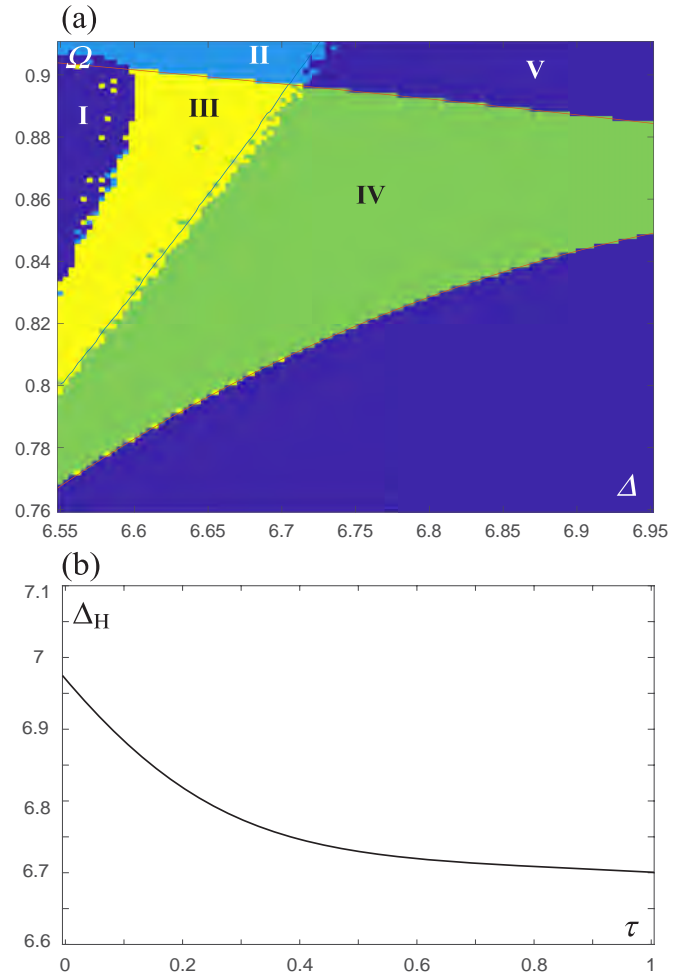


FIG. 7. (a) Characteristic domains of macroscopic behavior in the (Ω, Δ) plane for coupling delay $\tau = 0.3$. Color coding, as well as the remaining system parameters, are the same as in Fig. 6. Superimposed are the bifurcation curves obtained by the local stability approach described in the Appendix. (b) Critical diversity Δ_H corresponding to the Hopf destabilization of the state B_3 in dependence of τ for fixed $\Omega = 0.88$.

We have also examined whether the qualitative picture described so far persists under variation of the coupling strength K . It turns out that the general bifurcation structure holds qualitatively, which indicates the robustness of the scenarios underlying the transitions between the different collective regimes. Still, one notes that under increasing coupling strength, the cusp point and the Hopf bifurcation curve shift to a larger diversity (not shown).

V. IMPACT OF SMALL COUPLING DELAY AND SMALL NOISE

In this section, the goal is to demonstrate that the physical picture described so far for the noiseless and the delay-free case qualitatively also holds in presence of *small* noise or *small* coupling delay. The small-noise scenario concerns a range of noise levels where the applied perturbation typically cannot give rise to noise-induced oscillations but may rather evoke only rare spikes, so that the prevalent fraction

of units within the excitable subassembly remains at the quasistationary state. The small-delay scenario refers to delay values which are significantly less than the typical period of local oscillations, such that no delay-induced oscillations or multistability can emerge [44–46]. Essentially, our intention is not to perform an exhaustive exploration of the effects of noise or coupling delay but rather to confine the analysis to the cases where these two ingredients cannot evoke qualitatively new forms of collective behavior compared to the noiseless and delay-free case. We have carried out extensive numerical simulations to establish how the boundaries of the five characteristic domains in the (Ω, Δ) plane are modified due to the action of small noise or small coupling delay.

A. Effects of small coupling delay

The effects of small coupling delay are illustrated in Fig. 7(a), which shows the characteristic domains of macroscopic behavior in the (Ω, Δ) plane for the delay $\tau = 0.3$. One observes an excellent agreement between the bifurcation curves, obtained analytically by the local stability approach described in the Appendix, and the associated stability boundaries of the domains. In particular, introducing the coupling delay does not affect the very coordinates of the stationary states of the Ott-Antonsen equation (8), meaning that the branches of fold bifurcations remain unchanged relative to the delay-free case. Nevertheless, the key effect of the delay is that the Hopf bifurcation of the state B_3 , which underlies one of the scenarios for the onset of the collective mode, shifts to a smaller diversity compared to the delay-free case. This implies that the delay promotes multistable behavior, in the sense that the bistability domain IV, characterized by the coexistence between the stable stationary states B_1 and B_3 , becomes broader due to the impact of delay, cf. the green highlighted region in Fig. 7(a). From another point of view, the latter also suggests that the coupling delay promotes the onset of the collective mode via Hopf destabilization of the stationary state B_3 but suppresses the scenario where B_1 and B_2 undergo the SNIPER bifurcation. In Fig. 7(b) it is explicitly shown how the critical diversity Δ_H associated to Hopf bifurcation decreases with τ when Ω is kept fixed.

B. Effects of small noise

In contrast to the impact of coupling delay, the small noise is found to influence the effective positions of both the fold and the Hopf bifurcation curves, cf. Fig. 8(a), where the five characteristic domains for the noise level $\sigma = 0.3$ are shown together with the analytical curves for the *noiseless* case. The primary effect of small noise is to promote the onset of the collective mode mediated via the SNIPER bifurcation, in the sense that for a fixed mean frequency Ω , macroscopic oscillations can be observed for the diversity Δ smaller than those in the noiseless case. As a consequence, one observes that the critical diversity Δ_{SN} at which the fold between the states B_1 and B_2 takes place reduces under increasing σ , as indeed shown in Fig. 8(b) for the fixed $\Omega = 0.88$. Nonetheless, noise also shifts the location of the Hopf bifurcation relevant for the stability of the state B_3 , see Fig. 8(a). This may be interpreted as a disordering effect of noise, in the sense

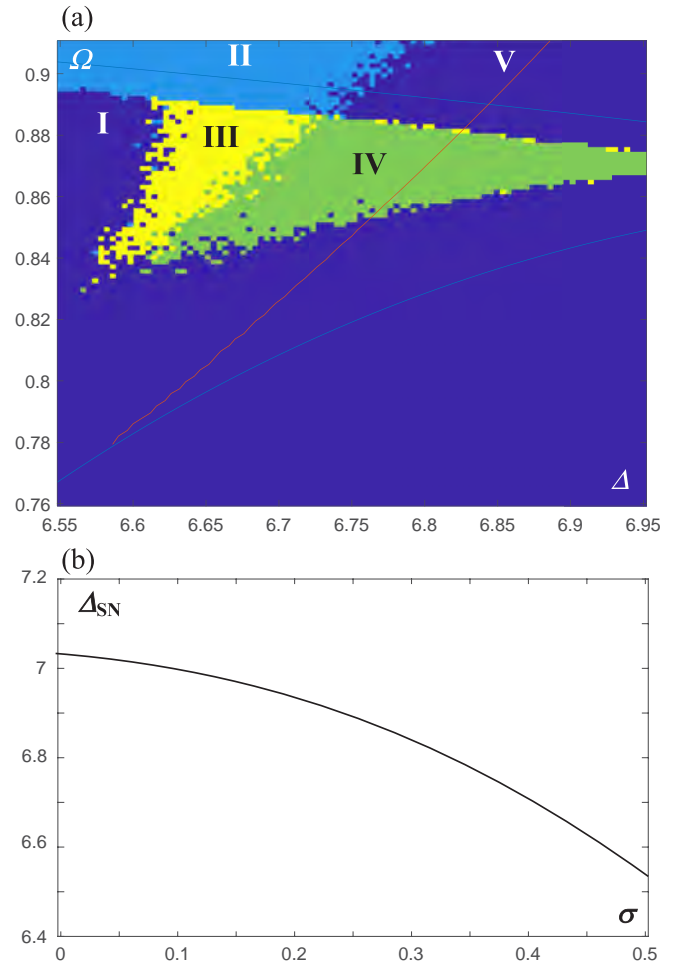


FIG. 8. (a) Characteristic domains of macroscopic dynamics in the (Ω, Δ) plane for the noise level $\sigma = 0.3$. The color coding and the remaining system parameters are the same as in Fig. 6. Superimposed are the bifurcation curves obtained analytically for the *noise-free* case $\sigma = 0$. (b) Decrease of the critical diversity Δ_{SN} with σ , corresponding to the saddle-node annihilation of the states B_1 and B_2 for fixed $\Omega = 0.88$.

that the transition from the regime of macroscopic oscillations (domain II) to the asynchronous regime (domain V) occurs at the diversity smaller than that for the noise-free case. Also note that the bistability regions III and IV shrink as compared to the noiseless case.

In principle, one observes that the structure of the characteristic domains is qualitatively preserved with introduction of small noise, but the associated stability boundaries shift to the left with respect to the noiseless case. This can be understood by the following qualitative reasoning. The impact of small noise on the local dynamics of the nodes can roughly be interpreted as a perturbation of the intrinsic frequency ω_i . To corroborate this, in Fig. 9 we illustrate how the *effective* oscillation frequencies of single units $\omega_{\text{eff},i}$, calculated numerically as the inverse of the respective mean oscillation periods, change in the presence of noise $\sigma = 0.3$. One finds that a certain fraction of units whose intrinsic frequencies ω_i lie closest to the excitability threshold $\omega = 1$ acquire a nonzero effective frequency, i.e., manifest noise-induced oscillations,

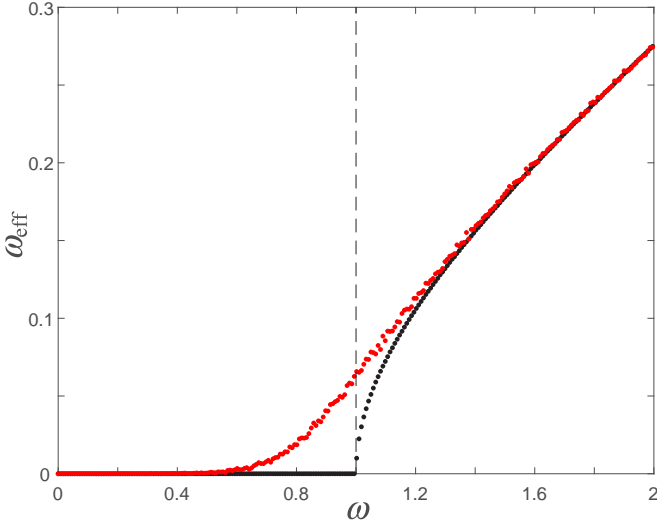


FIG. 9. Effective oscillation frequencies of uncoupled units ω_{eff} for the noiseless case (black dots) and under noise intensity $\sigma^2 = 0.09$ (red dots) as a function of the intrinsic parameters ω_i . The dashed line indicates the excitability threshold $\omega = 1$. The frequency distribution $g(\omega)$ is characterized by $\Omega = 2$, $\Delta = 4$.

while the excitable units further away from the threshold remain quasistationary. Nonetheless, the impact of noise on the self-oscillating units is reflected as a small increase of their effective frequency. Thus, in qualitative terms, the effect of small noise amounts to enhancing the effective frequency of the units near the threshold $\omega = 1$. Since this effect is symmetrical for positive and negative ω , the average assembly frequency Ω remains unchanged, whereas the variance of the associated distribution increases proportionally to the noise intensity. Therefore the introduction of small noise should lead to similar effects as the increase of diversity Δ .

VI. SUMMARY AND CONCLUSION

Considering a heterogeneous assembly of active rotators displaying excitable or oscillatory local dynamics, we have classified the associated macroscopic regimes and have demonstrated the generic scenarios for the onset and the suppression of collective oscillations. The analytical part of the study has been carried out within the framework of Ott-Antonsen theory applied for the delay- and noise-free system in the continuum limit, which enabled us to determine the three macroscopic stationary states in case of an arbitrary distribution of natural frequencies. The main qualitative insight into the microscopic structure of stationary states is that the population may in principle split into the excitable and the rotating subassembly, with the division depending on the relationship between the respective natural frequency of a rotator and the macroscopic excitability parameter. In this context, we have identified a homogeneous equilibrium where the units typically lie at rest, as well as a heterogeneous (mixed) collective stationary state, composed of units either in the excitable regime or the oscillatory regime. The local approach to stability and bifurcation analysis of the stationary states we have derived allowed us to address both the delay-free case and the case where the system's behavior is

influenced by coupling delay. The analysis has been specified to the particular case of a uniform frequency distribution on a bounded interval. While the stationary states have been determined earlier for a similar, but a less general model [13], the stability analysis, as presented here, has been carried out for the first time.

We have demonstrated that the complex bifurcation structure underlying the stability boundaries of the different macroscopic regimes is organized by three codimension-two bifurcation points, including the Bogdanov-Takens point, the cusp point, and the fold-homoclinic point. Our analysis has revealed the existence of five characteristic domains, three of which support the monostable collective behavior, while two admit bistability, involving either the coexistence between two stable stationary states or the coexistence between a stationary and a periodic solution. We have found that, depending on the mean frequency, the onset and the suppression of the collective mode may emerge via two qualitatively different scenarios under variation of diversity. In particular, for a smaller mean frequency, the onset of collective oscillations under decreasing diversity occurs due to a Hopf destabilization of a stationary state, whereas the oscillations are terminated via a saddle-homoclinic bifurcation. Nevertheless, for a sufficiently large mean frequency, increasing the diversity gives rise to collective oscillations in a SNIPER bifurcation, while the suppression of oscillations is due to an inverse Hopf bifurcation.

The classical paradigm concerning the sequence of transitions between the collective regimes in heterogeneous systems under increasing diversity involves three characteristic states, namely the global rest state; the synchronous state, characterized by macroscopic oscillations; and the asynchronous state, based on mixed excitable and oscillatory local dynamics [13]. In addition to this paradigm, our analysis has revealed two novel scenarios, which are hysteretic and involve a passage through one or two bistable domains. By the first scenario, the transition from the global rest state to the asynchronous state occurs via two bistable regimes, the first involving a coexistence between a periodic solution and the rest state and the second one featuring coexistence between the rest state and the asynchronous state. The second hysteretic scenario is similar, but the intermediate stage involves only the coexistence between the homogeneous and the oscillatory state.

Combining theoretical methods and numerical experiments, we have shown that the basic bifurcation structure from the delay- and noiseless case persists in the presence of small noise or small coupling delay. Nevertheless, these two ingredients are found to modify the stability boundaries of the five characteristic domains. In particular, due to coupling delay, the position of the Hopf bifurcation curve is shifted toward the smaller diversity, which effectively promotes the Hopf-mediated onset of macroscopic oscillations and also enhances the parameter domain supporting bistability. Noise is seen to affect both the fold and the Hopf bifurcations, whereby the effective position of the fold or Hopf curve is shifted to smaller mean frequency or smaller diversity. At the level of macroscopic behavior, this is reflected as the promotion or suppression of the onset of macroscopic oscillations via SNIPER or Hopf bifurcation scenario, contributing in

addition to a reduction of the two bistability domains. While the described bifurcation structure appears to be generic for the considered type of frequency distribution, remaining qualitatively similar under the influence of small noise or small coupling delay, it would be interesting to examine whether and how it is modified for a substantially different form of a frequency distribution, such as a bimodal one.

ACKNOWLEDGMENTS

The work on Secs. III and IV was supported by the Russian Foundation for Basic Research under Project No. 17-02-00904. The work on Sec. V was supported by the Russian Foundation for Basic Research under Project No. 19-52-10004. The numerical simulations were supported by the Russian Science Foundation under Project No. 19-72-10114. I.F. acknowledges the support from the Ministry of Education, Science and Technological Development of the Republic of Serbia under Project No. 171017. The authors thank Matthias Wolfrum for fruitful discussions during the various stages of the study.

APPENDIX: CALCULATION OF THE STABILITY OF THE STATIONARY SOLUTION OF THE OTT-ANTONSEN EQUATION

Here we elaborate on the method applied to calculate the stability of the stationary solutions of the Ott-Antonsen equation (8). In particular, we first introduce the expressions $z(\omega, t) = x(\omega, t) + iy(\omega, t)$ and $R(\omega, t) = X(\omega, t) + iY(\omega, t)$ for the local and the global order parameters, respectively, transforming (8) to

$$\begin{aligned} \dot{x} = F(x, y, X, Y) = & \frac{a}{2}(y^2 - x^2 + 1) - \omega y \\ & - Kxy(Y \cos \alpha - X \sin \alpha) - \frac{K}{2}(X \cos \alpha + Y \sin \alpha) \\ & \times (x^2 - y^2) + \frac{K}{2}(X \cos \alpha + Y \sin \alpha) \end{aligned}$$

$$\begin{aligned} \dot{y} = G(x, y, X, Y) = & -axy + \omega x - Kxy(Y \sin \alpha + X \cos \alpha) \\ & + \frac{K}{2}(Y \cos \alpha - X \sin \alpha)(x^2 - y^2) \\ & + \frac{K}{2}(Y \cos \alpha - X \sin \alpha). \end{aligned} \quad (\text{A1})$$

The linearization of Ott-Antonsen equation (8) for variations $\xi = (\delta x, \delta y)^T$, $\Xi = (\delta X, \delta Y)^T$ of the stationary solution (x_0, y_0) can then succinctly be written in the matrix form as

$$\frac{d\xi(\omega, t)}{dt} = A(\omega)\xi(\omega, t) + B(\omega)\Xi(t), \quad (\text{A2})$$

where the matrices of derivatives are

$$A(\omega) = \begin{pmatrix} \frac{\partial F}{\partial x} & \frac{\partial F}{\partial y} \\ \frac{\partial G}{\partial x} & \frac{\partial G}{\partial y} \end{pmatrix}, \quad B(\omega) = \begin{pmatrix} \frac{\partial F}{\partial X} & \frac{\partial F}{\partial Y} \\ \frac{\partial G}{\partial X} & \frac{\partial G}{\partial Y} \end{pmatrix}. \quad (\text{A3})$$

Assuming that the variation $\xi(\omega, t)$ satisfies the ansatz $\xi(\omega, t) = \xi(\omega)e^{\lambda t}$, and similarly $\Xi(t) = \Xi e^{\lambda t}$, (A2) becomes

$$[A(\omega) - \lambda I]\xi(\omega) + B(\omega)\Xi = 0, \quad (\text{A4})$$

where I denotes the identity matrix. As shown in Ref. [40], the continuous Lyapunov spectrum consists of the eigenvalues of the matrix $B(\omega)$ for all $\omega \in [\omega_1, \omega_2]$. In our case, the continuous spectrum turns out to be always stable or marginally stable, such that the stability of the stationary solutions is determined by the discrete spectrum. In order to obtain the discrete spectrum, we multiply (A4) from the left by $g(\omega)[A(\omega) - \lambda I]^{-1}$ and integrate over ω obtaining $C(\lambda)\Xi = 0$, where

$$C(\lambda) = I + \int_{-\infty}^{\infty} d\omega g(\omega)[A(\omega) - \lambda I]^{-1}B(\omega). \quad (\text{A5})$$

The discrete Lyapunov spectrum can then be calculated by numerically solving the system $\det C(\lambda) = 0$.

In the case of nonzero coupling delay, the same type of analysis remains valid, while one has to replace X and Y in the r-hand side of (A1) by their delayed counterparts $X(t - \tau)$ and $Y(t - \tau)$. This leads to the same matrix $C(\lambda)$ as in (A5), with the only difference being the substitution of $B(\omega)$ by $B(\omega)e^{-\lambda\tau}$.

-
- [1] A. Pikovsky, M. Rosenblum, and J. Kurths, *Synchronization: A Universal Concept in Nonlinear Sciences* (Cambridge University Press, Cambridge, 2003).
- [2] J. A. Acebrón, L. L. Bonilla, C. J. P. Vicente, F. Ritort, and R. Spigler, *Rev. Mod. Phys.* **77**, 137 (2005).
- [3] Y. Baibolatov, M. Rosenblum, Z. Z. Zhanabaev, M. Kyzgarina, and A. Pikovsky, *Phys. Rev. E* **80**, 046211 (2009).
- [4] I. Franović, K. Todorović, N. Vasović, and N. Burić, *Phys. Rev. E* **87**, 012922 (2013).
- [5] S. Olmi, R. Livi, A. Politi, and A. Torcini, *Phys. Rev. E* **81**, 046119 (2010).
- [6] S. Strogatz, *Physica D (Amsterdam)* **143**, 1 (2000).
- [7] N. Komin and R. Toral, *Phys. Rev. E* **82**, 051127 (2010).
- [8] C. J. Tessone, A. Scirè, R. Toral, and P. Colet, *Phys. Rev. E* **75**, 016203 (2007).
- [9] D. Pazo and E. Montbrió, *Phys. Rev. E* **73**, 055202(R) (2006).
- [10] Y. Kuramoto, *Chemical Oscillations, Waves, and Turbulence* (Springer-Verlag, Berlin, 1984).
- [11] F. A. Rodrigues, T. K. DM. Peron, P. Ji, and J. Kurths, *Phys. Rep.* **610**, 1 (2016).
- [12] C. J. Tessone, C. R. Mirasso, R. Toral, and J. D. Gunton, *Phys. Rev. Lett.* **97**, 194101 (2006).
- [13] L. F. Lafuerza, P. Colet, and R. Toral, *Phys. Rev. Lett.* **105**, 084101 (2010).
- [14] E. Ott and T. M. Antonsen, *Chaos* **18**, 037113 (2008).
- [15] E. Ott and T. M. Antonsen, *Chaos* **19**, 023117 (2009).
- [16] L. S. Tsimring and A. Pikovsky, *Phys. Rev. Lett.* **87**, 250602 (2001).
- [17] A. Pototsky and N. B. Janson, *Phys. Rev. E* **77**, 031113 (2008).

- [18] A. Zakharova, S. A. M. Loos, J. Siebert, A. Gjurchinovski, J. C. Claussen, and E. Schöll, Controlling chimera patterns in networks: Interplay of structure, noise, and delay, in *Control of Self-Organizing Nonlinear Systems*, edited by E. Schöll, S. H. L. Klapp, and P. Hövel (Springer International Publishing, Cham, Switzerland, 2016).
- [19] F. M. Atay (ed.), *Complex Time-Delay Systems: Theory and Applications* (Springer, Berlin, 2010).
- [20] E. Schöll, G. Hiller, P. Hovel, and M. A. Dahlem, *Philos. Trans. R. Soc. Lond. A* **367**, 1079 (2009).
- [21] A. Takamatsu, T. Fujii, and I. Endo, *Phys. Rev. Lett.* **85**, 2026 (2000).
- [22] M. G. Rosenblum and A. S. Pikovsky, *Phys. Rev. Lett.* **92**, 114102 (2004).
- [23] P. Perlikowski, S. Yanchuk, O. V. Popovych, and P. A. Tass, *Phys. Rev. E* **82**, 036208 (2010).
- [24] B. Lindner, J. García-Ojalvo, A. Neiman, and L. Schimansky-Geier, *Phys. Rep.* **392**, 321 (2004).
- [25] V. Klinshov and I. Franović, *Phys. Rev. E* **92**, 062813 (2015).
- [26] I. Franović and V. Klinshov, *Chaos* **28**, 023111 (2018).
- [27] I. Franović and V. Klinshov, *Europhys. Lett.* **116**, 48002 (2016).
- [28] I. Franovic and V. Klinshov, *Eur. Phys. J.- Spec. Top.* **227**, 1063 (2018).
- [29] I. Franović, K. Todorović, M. Perc, N. Vasović, and N. Burić, *Phys. Rev. E* **92**, 062911 (2015).
- [30] I. Franović, M. Perc, K. Todorović, S. Kostić, and N. Burić, *Phys. Rev. E* **92**, 062912 (2015).
- [31] I. Bačić, V. Klinshov, V. I. Nekorkin, M. Perc, and I. Franović, *Europhys. Lett.* **124**, 40004 (2018).
- [32] S. Kadar, J. Wang, and K. Showalter, *Nat. Lond.* **391**, 770 (1998).
- [33] S. Alonso, I. Sendina-Nadal, V. Perez-Munuzuri, J. M. Sancho, and F. Sagues, *Phys. Rev. Lett.* **87**, 078302 (2001).
- [34] D. E. Postnov, S. K. Han, T. G. Yim, and O. V. Sosnovtseva, *Phys. Rev. E* **59**, R3791 (1999).
- [35] M. A. Zaks, A. B. Neiman, S. Feistel, and L. Schimansky-Geier, *Phys. Rev. E* **68**, 066206 (2003).
- [36] M. Y. Choi, H. J. Kim, D. Kim, and H. Hong, *Phys. Rev. E* **61**, 371 (2000).
- [37] I. V. Tyulkina, D. S. Goldobin, L. S. Klimenko, and A. Pikovsky, *Phys. Rev. Lett.* **120**, 264101 (2018).
- [38] D. S. Goldobin, I. V. Tyulkina, L. S. Klimenko, and A. Pikovsky, *Chaos* **28**, 101101 (2018).
- [39] M. Wolfrum, S. V. Gurevich, and O. E. Omel'chenko, *Nonlinearity* **29**, 257 (2016).
- [40] O. E. Omel'chenko, and M. Wolfrum, *Physica D (Amsterdam)* **263**, 74 (2013).
- [41] O. E. Omel'chenko and M. Wolfrum, *Phys. Rev. Lett.* **109**, 164101 (2012).
- [42] H. Sakaguchi, S. Shinomoto, and Y. Kuramoto, *Prog. Theor. Phys.* **79**, 600 (1988).
- [43] B. Sonnenschein, M. A. Zaks, A. B. Neiman, and L. Schimansky-Geier, *Eur. Phys. J. Spec. Top.* **222**, 2517 (2013).
- [44] S. Yanchuk and P. Perlikowski, *Phys. Rev. E* **79**, 046221 (2009).
- [45] V. Klinshov, L. Lüicken, D. Shchapin, V. Nekorkin, and S. Yanchuk, *Phys. Rev. Lett.* **114**, 178103 (2015).
- [46] M. Wolfrum, S. Yanchuk, P. Hövel, and E. Schöll, *Eur. Phys. J. Spec. Top.* **191**, 91 (2010).

Leap-frog patterns in systems of two coupled FitzHugh-Nagumo units

Sebastian Eydam,^{1,*} Igor Franović,² and Matthias Wolfrum¹

¹Weierstrass Institute for Applied Analysis and Stochastic, Mohrenstrasse 39, 10117 Berlin, Germany

²Scientific Computing Laboratory, Center for the Study of Complex Systems, Institute of Physics Belgrade, University of Belgrade, Pregrevica 118, 11080 Belgrade, Serbia



(Received 17 January 2019; published 12 April 2019)

We study a system of two identical FitzHugh-Nagumo units with a mutual linear coupling in the fast variables. While an attractive coupling always leads to synchronous behavior, a repulsive coupling can give rise to dynamical regimes with alternating spiking order, called leap-frogging. We analyze various types of periodic and chaotic leap-frogging regimes, using numerical path-following methods to investigate their emergence and stability, as well as to obtain the complex bifurcation scenario which organizes their appearance in parameter space. In particular, we show that the stability region of the simplest periodic leap-frog pattern has the shape of a locking cone pointing to the canard transition of the uncoupled system. We also discuss the role of the timescale separation in the coupled FitzHugh-Nagumo system and the relation of the leap-frog solutions to the theory of mixed-mode oscillations in multiple timescale systems.

DOI: [10.1103/PhysRevE.99.042207](https://doi.org/10.1103/PhysRevE.99.042207)

I. INTRODUCTION

The FitzHugh-Nagumo system is a classical model of neuronal dynamics. As the simplest, yet paradigmatic example of a coupled neuronal system, we investigate here a pair of two identical FitzHugh-Nagumo units with a weak mutual coupling. Such a network motif of two coupled neurons has been considered as a basic building block of central pattern generators [1] and the complex neural networks of the cortex [2–5]. The dynamics of such systems has typically been investigated in the framework of the synchronization paradigm [6–8], focusing on the stability of states with phase-locked firing and their potential role in rhythmogenesis [9]. Nevertheless, a remarkable property of these simple circuits is that they are also able to generate complex activity patterns where the interspike intervals show complex dynamics. A typical example of such patterns is the so-called leap-frog dynamics [10], sometimes also called leader-switching dynamics [11], where the units exchange their order of firing within each oscillation cycle. Such a regime has so far been associated exclusively to class I neural oscillators coupled via strong synapses with complex nonlinear dynamics [12–16]. In the present paper, we investigate the emergence of leap-frogging dynamics in a system of two classical FitzHugh-Nagumo units interacting only via a small linear coupling. The emerging complex dynamical patterns can be explained as a result of the timescale separation between the activator and the recovery variable. For a single unit, the timescale separation is crucial for the mechanism inducing the rapid change in the amplitude from small subthreshold oscillations to large relaxation oscillations. Introducing a repulsive coupling in the

fast variables, the leap-frog patterns emerge in locking cones generated by a complex bifurcation scenario immediately at this transition. The alternation in the spiking order of the units arises from trajectories containing both the small-amplitude subthreshold oscillations and the large-amplitude relaxation oscillations. Such a behavior involving interspersed small- and large-amplitude oscillations, called *mixed-mode oscillations* [17–20], is a typical phenomenon in slow-fast systems with at least two slow variables and has been studied extensively by geometric singular perturbation methods for the limit of infinite timescale separation. In particular, a three-dimensional version of the FitzHugh-Nagumo system has been used as a classical example for mixed-mode oscillations, see, e.g., Ref. [20] and references therein. Singular perturbation techniques have been also applied to coupled nonidentical mixed-mode oscillators [21] and for the synchronization of weakly coupled slow-fast oscillations [22].

Coupled systems of two identical oscillators have specific symmetry properties, which at vanishing coupling induce an additional degeneracy. First numerical studies of coupled slow-fast oscillators can already be found in Refs. [23,24], where a detailed exposition of the four-dimensional slow-fast structure is given. Due to the symmetry-induced degeneracy, for such systems the existing theoretical results for mixed-mode oscillations do not apply directly. We will present here a first numerical exploration of a system of two identical FitzHugh-Nagumo units with symmetric mutual coupling. Our approach will be a detailed bifurcation analysis using path-following methods at finite values of the timescale separation. We perform this both for the degenerate case of small coupling, where we find an essentially new dynamical scenario, and for larger coupling, where the leap-frog dynamics is organized in a way that conforms to the general results on mixed-mode oscillations.

*sebastian.eydam@wias-berlin.de

The dynamics of the considered system of two identical FitzHugh-Nagumo units is given by

$$\begin{aligned}\frac{dv_{1,2}}{dt} &= v_{1,2} - v_{1,2}^3/3 - w_{1,2} + c(v_{2,1} - v_{1,2}), \\ \frac{dw_{1,2}}{dt} &= \varepsilon(v_{1,2} + b),\end{aligned}\quad (1)$$

where the symmetric linear coupling acts in the fast variables $v_{1,2}$. The small parameter ε facilitates the timescale separation between the fast variables v_i and the slow variables w_i . In the context of neuroscience, the former represent the neuronal membrane potentials, whereas the latter correspond to the coarse-grained activities of the membrane ion-gating channels. For a single unit, the parameter b mediates the transition from the quiescent regime for $b > 1$ to the oscillatory regime for $-1 < b < 1$. Due to the timescale separation, this is accompanied by a *canard transition* from small-amplitude subthreshold oscillations to the large-amplitude relaxation oscillations. We invoke some basic results derived from singular perturbation theory about the slow-fast structure of the uncoupled FitzHugh-Nagumo unit in Sec. II.

Since the parameters b and ε are taken to be identical for both units, system Eq. (1) possesses a \mathbb{Z}_2 -symmetry, being equivariant with respect to exchanging the indices by

$$\sigma : (v_1, w_1, v_2, w_2) \mapsto (v_2, w_2, v_1, w_1).$$

This leads to the appearance of solutions with different symmetry types, reflecting the different states of in-phase and anti-phase synchronization, which will be discussed in Sec. II which concerns the basic types of solutions bifurcating from the stationary regime. Close to the canard transition of the uncoupled system, there appear various types of periodic and chaotic leap-frog patterns in the system with repulsive coupling. Using the software package AUTO [25] for numerical bifurcation analysis by continuation methods, in Sec. III we investigate in detail the complex bifurcation scenarios responsible for the onset of the different types of leap-frogging dynamics. We conclude the paper with an outlook in Sec. IV, discussing the relation of our results to earlier findings on leap-frog dynamics in models of neuronal systems.

II. BASIC DYNAMICAL REGIMES

We begin our investigation of system Eq. (1) by collecting simple stationary and periodic solutions together with their stability and symmetry properties. In the symmetric regime

$$v_1 = v_2 \quad \text{and} \quad w_1 = w_2, \quad (2)$$

the coupling term vanishes and the dynamics Eq. (1) is governed by a single FitzHugh-Nagumo system, where the units display simultaneously the well-known transition from the quiescent regime with a unique stable equilibrium for $b > 1$ to the oscillatory regime for $b < 1$, mediated by a supercritical Hopf bifurcation at $b = 1$. Due to the timescale separation $0 < \varepsilon \ll 1$, the bifurcating branch of periodic solutions displays a characteristic transition from small-amplitude harmonic oscillations of period $O(1/\sqrt{\varepsilon})$ to large-amplitude relaxation oscillations of period $O(1/\varepsilon)$, called a *canard transition*. This scenario has been extensively studied within the framework of singular perturbation theory, viz. in the

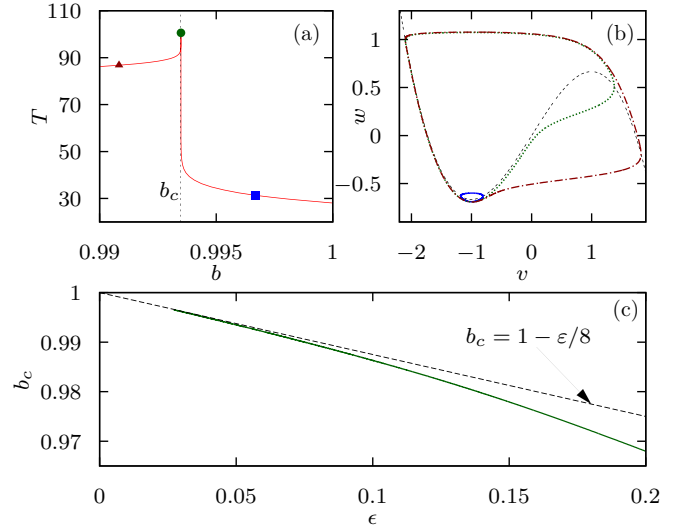


FIG. 1. (a) Variation of the period T along the branch of synchronous periodic solutions for varying b and fixed $\varepsilon = 0.05$. (b) Phase portraits of selected periodic solutions: a subthreshold oscillation for $b_c < b < b_H$ (blue solid), the canard trajectory $b_c = b$ (green dotted), a relaxation oscillations with $b_c > b$ (red dotted-dashed), corresponding to the square, the triangle, and the disk, in (a) respectively, and the cubic nullcline (dashed black). The corresponding values of b are indicated by the colored dots in (a). (c) Location of the canard transition b_c for varying ε . Numerical path-following of the periodic solution with maximal period (green line) is compared to asymptotic formula Eq. (3), shown dashed.

limit $\varepsilon \rightarrow 0$; see, e.g., Ref. [18] for a recent overview. In Fig. 1 we illustrate the canard transition in the symmetric regime, showing numerical results obtained by path-following methods [25]. In Fig. 1(a) we have fixed $\varepsilon = 0.05$, displaying the varying period along the branch of periodic orbits emerging from the Hopf-bifurcation at $b = b_H = 1$. Note the nearly vertical transition from small to large periods at the canard transition $b = b_c$. The phase portraits of the three orbits shown in Fig. 1(b), selected before, after, and immediately at the transition, indicate that the change in the period is accompanied by a transition from small to large amplitudes via *canard trajectories* that follow the unstable part of the slow manifold, which is close to the critical manifold $w = v - v^3/3$. From the neuroscience perspective, this corresponds to a transition route from the quiescent state to the spiking regime via subthreshold oscillations. A detailed asymptotic analysis reveals that the leading order approximation for the location b_c of the canard transition is given by

$$b_c \approx (1 - \varepsilon/8), \quad (3)$$

see Ref. [26]. In Fig. 1(c) we show that for small $\varepsilon > 0$ this expression (dashed line) provides indeed a good approximation for the actual location of the canard transition (solid green line), which we obtained numerically by path-following in ε the trajectory of maximal period, sometimes called *maximal canard* [green curve in Fig. 1(b)]. Recall that both the regimes of stable equilibrium and of subthreshold oscillations are excitable [27,28] in a sense that a strong enough perturbation

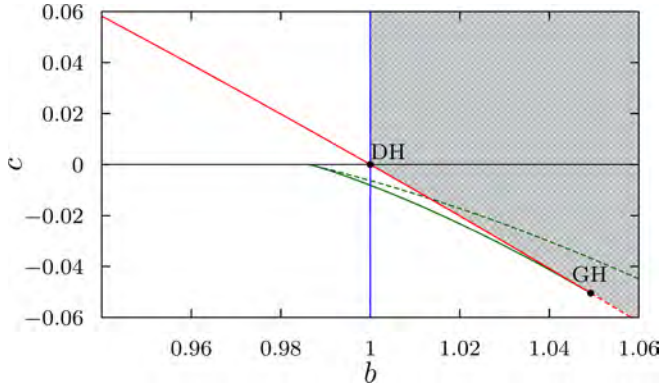


FIG. 2. Stability region (checkered pattern) of the symmetric equilibrium Eq. (5) in the (b, c) plane, bounded by in-phase Hopf instability (vertical blue line) and antiphase Hopf instability (diagonal red line). The antiphase Hopf bifurcation changes from supercritical to subcritical in a generalized Hopf point (GH), where a fold curve of the antiphase synchronous limit cycles emerges (green line). DH denotes the resonant double Hopf point for the decoupled system at $(b, c) = (1, 0)$.

may elicit a large excursion in phase space, i.e., a spiking response in the form of a single relaxation oscillation.

The full system Eq. (1), which can be rewritten in coordinates longitudinal and transversal to the symmetry subspace Eq. (2),

$$v_{L,T} = v_1 \pm v_2, \quad w_{L,T} = w_1 \pm w_2, \quad (4)$$

has a slow-fast structure with two fast and two slow variables. For small coupling c , the corresponding critical manifolds and fast fibers are given trivially as a direct sum of the corresponding objects for each of the units. It can be easily seen that the only stationary state of Eq. (1) is the symmetric equilibrium

$$(v_1, w_1, v_2, w_2) = (-b, -b + b^3/3, -b, -b + b^3/3), \quad (5)$$

obtained from the single FitzHugh-Nagumo unit. While the symmetry-preserving Hopf bifurcation at $b = 1$ in the coupled system is analogous to the Hopf bifurcation of the single FitzHugh-Nagumo unit and does not depend on the coupling parameter c , in the coupled system the symmetric equilibrium may also undergo symmetry-breaking bifurcations. In particular, it may become unstable via a Hopf bifurcation to antiphase synchronized periodic solutions of the form

$$v_1(t) = v_2\left(t + \frac{T}{2}\right), \quad w_1(t) = w_2\left(t + \frac{T}{2}\right), \quad (6)$$

where $T > 0$ is the period. Using the longitudinal and transversal coordinates Eq. (4) one obtains the condition

$$c = \frac{1 - b^2}{2} \quad (7)$$

for this antiphase Hopf instability of the synchronous equilibrium Eq. (5). In Fig. 2, the associated bifurcation curve is shown in the (b, c) plane together with the in-phase Hopf instability at $b = 1$. For attractive coupling $c > 0$, the stability region (checkered pattern) of the symmetric equilibrium Eq. (5) is bounded by the in-phase Hopf instability, shown by

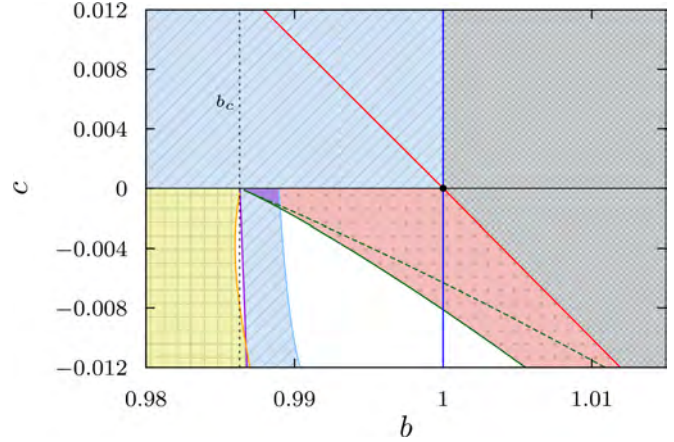


FIG. 3. Stability regions of basic periodic solutions in the (b, c) plane for $\varepsilon = 0.1$: in-phase synchronous oscillations (blue diagonal stripes); antiphase synchronous subthreshold oscillations (red dotted); coexistence of in-phase and antiphase subthreshold oscillations (purple filled); asynchronous oscillations—successive spiking (yellow squared). Bifurcation curves delineating the stability boundaries: in-phase Hopf instability (vertical blue line); antiphase Hopf instability (diagonal red line); fold of antiphase synchronous limit cycles (left boundary of the lower dotted region, green); subcritical period doubling of in-phase subthreshold oscillations (left boundary of the lower striped region, purple); subcritical symmetry breaking pitchfork of in-phase subthreshold oscillations (right boundary of the lower striped region, light blue); supercritical period doubling of asynchronous oscillations (boundary of the squared region, orange). Canard transition at $b = b_c$ (black dashed); see Fig. 1.

the blue line, while for repulsive coupling $c < 0$, the stability boundary is given by the antiphase Hopf Eq. (7). For larger negative values of c , this bifurcation is subcritical, such that no stable branch of antiphase synchronized oscillations emerges. The criticality changes in a generalized Hopf (Bautin) point, labeled as GH in Fig. 2. From this point emanates a curve of folds of limit cycles, shown by the green line in Fig. 2. The two Hopf bifurcation curves intersect in the resonant double Hopf point (DH) located at $(b, c) = (1, 0)$. Note that this point belongs to the line $c = 0$ where the system decouples, thus behaving neutral with respect to all symmetry-breaking perturbations.

Figure 3 shows the stability regions and the associated stability boundaries of the periodic solutions. For attractive coupling $c > 0$, all synchronous oscillations are stable (blue diagonal striped region), undergoing at $b = b_c$ the canard transition from small- to large-amplitude oscillations as in the case of a single unit; cf. Fig. 1. For repulsive coupling $c < 0$, the situation is more complicated. There is a small region (red dotted in Fig. 3) above the generalized Hopf point and the emanating fold of limit cycles (green curve) where one finds stable antiphase synchronized oscillations. Note that after a secondary bifurcation, the fold of limit cycles (green curve) is no longer a stability boundary of the antiphase synchronized oscillations (dashed part of the curve). Surprisingly, there are also stable in-phase synchronized solutions for repulsive coupling $c < 0$. They are confined to a narrow region immediately below the canard transition, which is bounded by a curve of period doubling (left, purple line) and

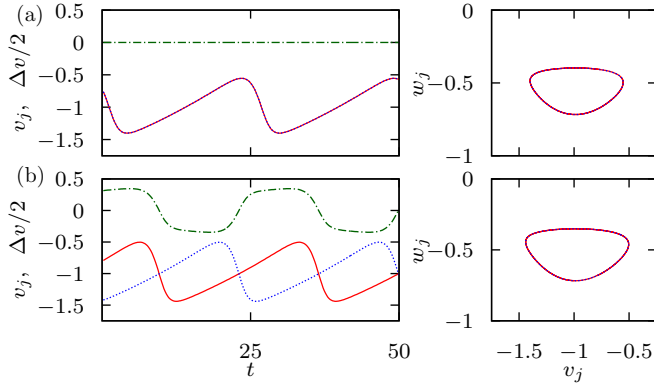


FIG. 4. Time traces and phase portraits of stable coexisting in-phase synchronous (a) and antiphase synchronous (b) subthreshold oscillations. Parameters $(\varepsilon, b, c) = (0.1, 0.9885, -0.0005)$ belong to the coexistence region (purple in Fig. 3). Variables $v_{1,2}(t)$ are shown in red (solid) and blue (dotted), whereas the coupling term $\Delta v = c(v_2 - v_1)$ is indicated in green color (dash-dotted).

a curve of symmetry-breaking pitchfork bifurcations (right, light blue line). In particular, for small negative coupling, one encounters a region of bistability, where both the in-phase and antiphase synchronized oscillations are stable (purple-shaded region in Fig. 3). Figure 4 illustrates coexisting stable in-phase and antiphase synchronous solutions computed for the parameters $(\varepsilon, b, c) = (0.1, 0.9885, -0.0005)$ from this region. Note that the coexistence region is confined to subthreshold oscillations prior to the canard transition at $b = b_c$.

Apart from the in-phase and antiphase synchronous regimes, there may also appear periodic solutions without any symmetry. For repulsive coupling $c < 0$ and beyond the canard transition, i.e., $b < b_c$, there is a large parameter region admitting a stable regime of *successive spiking*, with both units performing relaxation oscillations shifted in phase. The stability region of this successive spiking, shown in yellow (square pattern) in Fig. 3, is bounded by a curve of supercritical period doubling (right, orange line). Figures 5(a) and 5(b) provide the time traces and phase portraits for the regime of

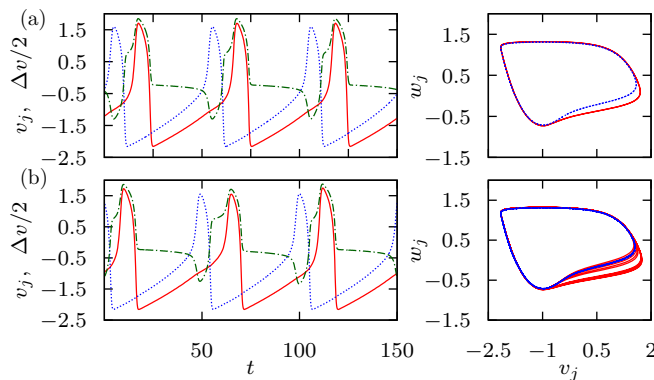


FIG. 5. Time traces and phase portraits of stable asymmetric successive spiking: (a) before period doubling ($b = 0.98625$) and (b) after several period doubling bifurcations ($b = 0.98692$). The remaining parameters are $(c, \varepsilon) = (-0.01, 0.1)$. Colors and line styles are as described in the caption of Fig. 4.

successive spiking before period doubling and after several period doubling bifurcations, respectively. Note that in Fig. 3 several bifurcation curves point toward the canard transition, thus creating a complex scenario where the different dynamical regimes with different symmetry properties bifurcate and interchange their stability. This indicates that a detailed study of the limit $\varepsilon \rightarrow 0, c \rightarrow 0$ could reveal the dependence of all these bifurcations on ε and in this way explain the whole scenario by an unfolding of the corresponding singularity.

Moreover, there is a region, indicated in white in Fig. 3, where none of the periodic solutions described above is stable. We demonstrate below that in this region the system exhibits several periodic or chaotic regimes characterized by the fact that the trajectory of each unit comprises large relaxation oscillation loops as well as smaller loops of a size comparable to that of subthreshold oscillations. This phenomenon of such so called mixed-mode oscillations has been extensively studied using geometric singular perturbation methods for the limit $\varepsilon \rightarrow 0$. They are known to arise generically in slow-fast systems with two slow variables and a folded node singularity. Let us very briefly recall the corresponding slow-fast geometry of system Eq. (1), see also Ref. [24]. Following the classical approach (see, e.g., Ref. [18]), we find the fold condition for the two-dimensional critical manifold as

$$(1 - v_1^2)(1 - v_2^2) = c(2 - v_1^2 - v_2^2).$$

For $c = 0$, this provides two lines of folds, intersecting at the point $v_1 = v_2 = -1$. At $b = 1$, the symmetric equilibrium Eq. (5) passes through this intersection of folds (DH point in Fig. 2). At the same time, the slow flow across the folds vanishes along the whole pair of intersecting lines of folds and hence violates also the usual genericity assumption on a folded singularity. An unfolding at small $c \neq 0$ of this degenerate situation involves the interplay of two small quantities. As a first step, we will explore these mixed-mode type dynamics without invoking the singular limit where these two quantities tend to zero. Instead, we use simulations and numerical path-following techniques to describe the bifurcation scenario for finite values of ε . Comparing the results of the numerical bifurcation analysis for different values of ε will also provide some information about possible scalings between the two small quantities.

III. COMPLEX DYNAMICAL REGIMES AT THE CANARD TRANSITION

To numerically examine the different types of solutions of system Eq. (1), we have performed a parameter sweep with respect to b at fixed $c = -0.01$ and $\varepsilon = 0.1$; see Fig. 6. The scan is performed by a numerical continuation according to the following procedure: after each increment in the sweeping parameter b , we use the final state of the preceding simulation as an initial condition, then discard a transient, and sample the return times T_n between consecutive crossings of the Poincaré section $w_1 = -2/3$. The robustness of the numerical results has been verified for different simulation step sizes of the fourth-order Runge-Kutta scheme, which has been used in all of our simulations. Sweeping has been carried out in forward (increasing b , red points) and backward direction (decreasing b , black points), allowing us to detect potential coexisting

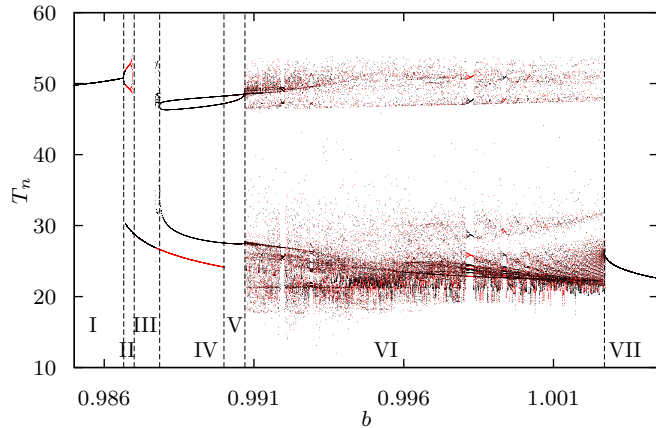


FIG. 6. Sampled return times T_n between consecutive crossings of the hyperplane $w_1 = -2/3$ for varying b and $(c, \varepsilon) = (-0.01, 0.1)$. Red and black points correspond to different sweeping directions in b .

stable regimes. Note that the return times $T_n \approx 50$ correspond to a single round trip of the unit $j = 1$ along the relaxation oscillation orbit, while the return times $T_n < 30$ correspond to a round trip following a subthreshold oscillation orbit. In Fig. 6, one can identify the regime of successive spiking in regions I and II, the in-phase subthreshold oscillations in regions II–IV, and the antiphase subthreshold oscillations in region VII. In addition, we find the periodic regime displayed in Fig. 7(a), which is the only attractor in region V and coexists with the in-phase subthreshold oscillations in region IV. Note that due to the space-time symmetry Eq. (6), the phase portraits of the trajectories of both units in the (v, w)

plane coincide. This periodic regime can be characterized as follows. Within one period, each unit performs two round trips along the relaxation oscillation orbit and one round trip along a subthreshold oscillation orbit. The spikes of the two units again occur with a phase shift as in the successive spiking regime. However, as a result of the inlaid subthreshold oscillations, the spiking order gets reversed for every pair of successive relaxation oscillations. This regime of alternating spiking order with a single subthreshold oscillation performed between each pair of successive spikes is referred to as *simple leap-frogging*. We shall discuss the underlying bifurcation scenario and its dependence on the slow-fast structure of the system in the following section.

In region VI, one observes chaotic behavior, interrupted by some small parameter intervals of more complicated periodic behavior. Chaotic mixed-mode oscillations have already been numerically observed in Ref. [29] for a periodically forced slow-fast oscillator. Examples of chaotic orbits are shown in Figs. 7(e) and 7(f). More complicated periodic orbits from some of the periodic windows in region VI are provided in Figs. 7(b)–7(d). The periodic orbits in Figs. 7(b) and 7(d) carry the space-time symmetry Eq. (6), which leads to a similar exchange in the spiking order as the leap-frog orbit in Fig. 7(a). The periodic solution in Fig. 7(c) is asymmetric, displaying successive spikes with fixed spiking order similar to Fig. 4(a), but interspersed with several almost antiphase subthreshold oscillations.

A. Simple leap-frogging

The dynamical regime of leap-frogging illustrated in Fig. 7(a) is a periodic regime where successive spikes occur with an alternating spiking order. The alternation is induced

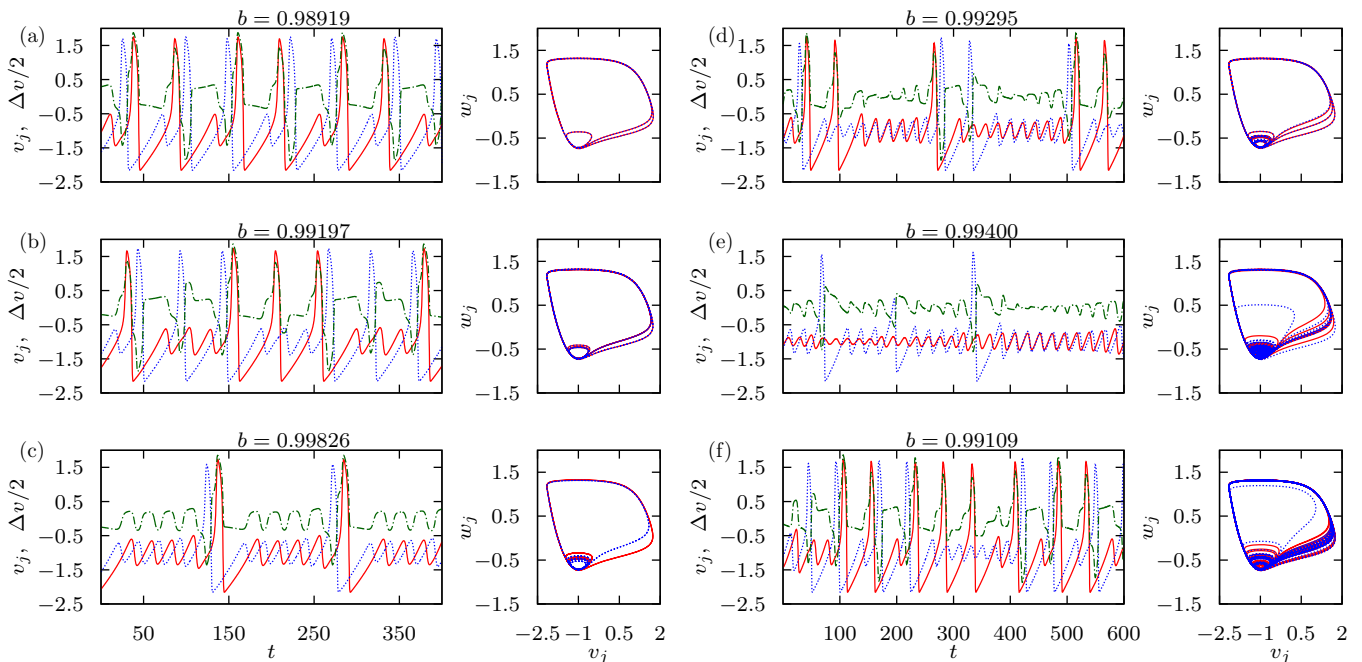


FIG. 7. Time traces and phase portraits of selected trajectories from regions V and VI in Fig. 6: Simple leap frogging in (a); periodic orbits with space-time symmetry in (b) and (d); asymmetric periodic orbit with several subthreshold oscillations in between successive spikes in (c); chaotic regimes in (e) and (f). Other parameters and colors and line styles are as described in the caption of Fig. 4.

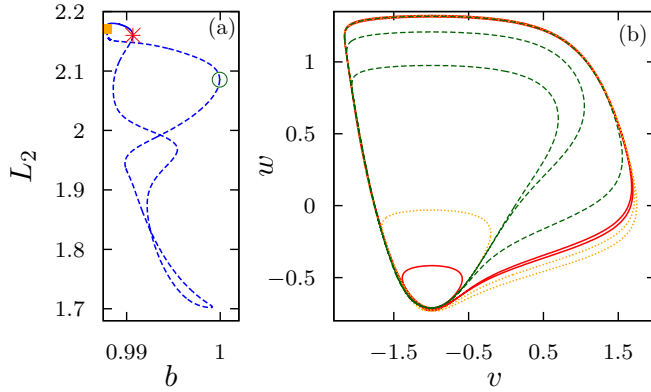


FIG. 8. (a) Branch of simple leap-frog solutions for varying b and fixed $c = -0.01$, $\varepsilon = 0.1$. The stability region (solid curve) is bounded by two folds of limit cycles (yellow square and red cross). At all other folds (e.g., green circle) both branches are unstable (dashed curves). (b) Phase portraits of limit cycles at the folds from panel (a), square (dotted), cross (solid), and circle (dashed).

by a subthreshold oscillation of the leading unit, whereby the lagging unit, passing without such a small loop, can overtake the current leader and spike the next time first. During the next spiking event, the units follow an analogous scenario but with interchanged roles, which results in the space-time symmetry Eq. (6). Figure 8(a) provides the branch of leap-frogging solutions for varying b and fixed $(c, \varepsilon) = (-0.01, 0.1)$. The branch has the shape of a closed curve and is stable only within a small region bounded by two folds of limit cycles. A continuation of these folds in the two parameters (b, c) , shown as black curves, provides the purple stability region shown in Fig. 9(a). The latter has the shape of a linear cone and points to the canard transition of the uncoupled periodic regime at $(b, c) = (b_c, 0)$. However, for the chosen value of $\varepsilon = 0.1$, the exact bifurcation structure in the vicinity of this point could not be reliably resolved numerically. Therefore, to gain a better understanding of the bifurcation structure at the tip of the stability cone, we increased the value of ε . Figure 9(b) shows the associated stability region in the (b, ε) plane. For the fixed values of $\varepsilon = 0.15$ and $\varepsilon = 0.2$, we calculated again the stability cones in the (b, c) plane, see the green and blue regions in Fig. 9(a). For these larger values of ε , it becomes apparent that the cones are clearly detached from the line $c = 0$, and that the sharp tip of the cone is actually formed by a single smooth curve of fold bifurcations. However, there is a codimension-two point close to the tip where a curve of symmetry-breaking pitchfork bifurcations crosses through the fold and becomes the stability boundary of the leap-frogging regime. The pitchfork curves are plotted in red in Fig. 9. For larger $\varepsilon = 0.15$ [see the green stability cone in Fig. 9(a)], we observe another cusp point where the branch of stable leap-frogging folds over, such that its stability region is again delineated by a fold (black curves in Fig. 9).

For $\varepsilon = 0.2$ we were able to completely resolve the bifurcation scenario in the vicinity of the tip; see Fig. 10. At small coupling $c = -0.00195$ the branch of leap-frogging solutions emerges as a small bubble [panel (I)]. For stronger coupling, this closed branch folds over and a further pair of folds

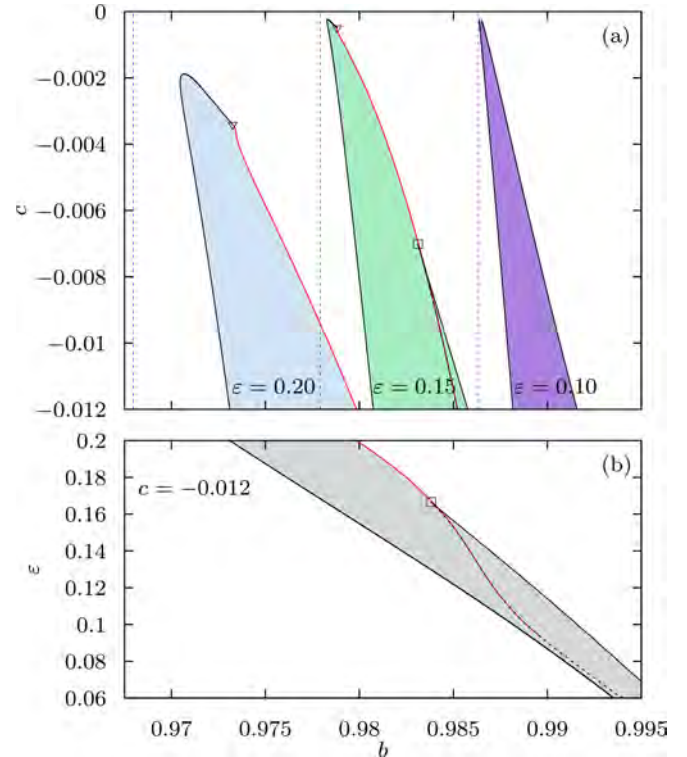


FIG. 9. (a) Stability regions of the simple leap-frog solutions in the (b, c) plane for fixed $\varepsilon \in \{0.2, 0.15, 0.1\}$ are shown in blue, green, and purple, respectively. The vertical dashed lines of corresponding color indicate the location $b_c(\varepsilon)$ of the canard transition of the synchronous oscillations. (b) Stability regions of the simple leap-frog solutions in the (b, ε) plane for fixed $c = -0.012$. In both panels, the stability regions are bounded by curves of fold bifurcations (solid black lines) and curves of pitchfork bifurcations (shown by red color). Triangles and squares indicate pitchfork-fold interaction and cusp points.

emanates from a cusp point. Moreover, through symmetry-breaking pitchfork bifurcations, there appears a branch of *asymmetric* leap-frogging solutions, which is also folded in an increasingly complex fashion, sometimes even featuring a small region of stability [see panel (II)]. Another type of codimension-two bifurcation points are 1:1 resonances, which give rise to branches of torus bifurcations. Figure 9 shows that for smaller ε , this complicated bifurcation scenario is contracted to a small vicinity of the canard transition of the uncoupled periodic regime at $(b, c) = (b_c, 0)$. The presumably exponential scaling of this contraction would clarify why already for $\varepsilon = 0.1$ the bifurcations at the tip of the cone could not be reliably resolved by our numerics.

B. Multiple leap-frogging

We have observed that the stable simple leap-frog solutions emerge already at very weak negative coupling and are accompanied with a regime of complicated or chaotic mixed-mode oscillations. However, for stronger negative coupling, one finds a different scenario. In Fig. 11 we show different dynamical regimes for varying parameter b , now with $c = -0.1$, while ε is fixed again to 0.1. Similar to Fig. 6, we

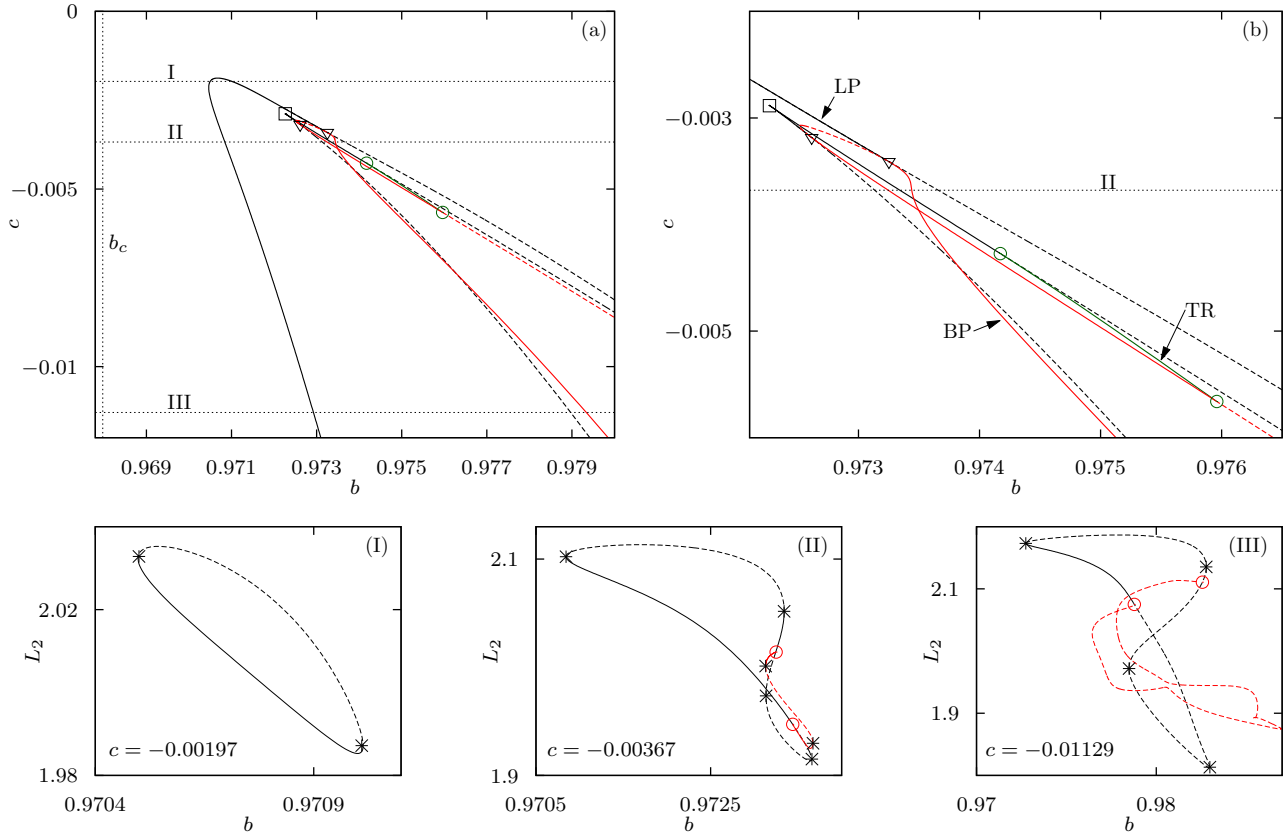


FIG. 10. (a) Bifurcations of the simple leap-frogging solutions in the (b, c) plane for $\varepsilon = 0.2$. (b) Enlarged view of the region where the complexity of the bubble increases. Bifurcation curves: folds of limit cycles (black), pitchfork bifurcations (red), torus bifurcations (green), also indicated by the labels LP, BP, and TR in panel (b), respectively. Solid curves indicate bifurcations delimiting the stability region; Dashed bifurcation curves involve only unstable states. Codimension-two bifurcations: cusps of limit cycles (squares), pitchfork-fold (triangles), torus (green circles). (I)–(III) Solid curves indicate stable branches of leap-frogging solutions with folds points (stars) and pitchfork bifurcations (circles), dashed curves indicate unstable branches. Asymmetric branches emerging from pitchfork bifurcations (red circles) are shown in red. The chosen values of c are indicated in panels (a) and (b).

have for each b value sampled the return times between consecutive Poincaré events where one of the units crosses $v_j = -b$ in increasing direction. For this stronger repulsive coupling we find a sequence of periodic patterns with a

gradually increasing number of subthreshold oscillations between two subsequent relaxation oscillations. Beginning from the regime of successive spiking at the left edge of the diagram, the system switches to the simple leap-frogging regime, characterized by two slightly different return times $T_n \approx 50$ corresponding to round trips along the relaxation oscillation orbit and a single return time $T_n < 30$ corresponding to the subthreshold oscillation following only after every second spike. Due to the symmetry Eq. (6) and the alternating spiking order, the units leave an identical trace in the respective return times. The time traces typical for the subsequent dynamical regime at larger b are shown in Fig. 12(a). Here, the subthreshold oscillations follow after each spike, which results in an asymmetric solution with fixed leader and laggard unit, distinguished by slightly different return times for the small loop and the relaxation oscillation. Note that the subthreshold oscillations, performed almost in antiphase, allow for the units to interchange the leadership twice. This is why we call this regime *double leap-frogging*. Increasing b further, we find another regime, again with the space-time symmetry Eq. (6) and an alternating spiking order, now caused by a triple interchange of leadership while performing the small loops; see Fig. 12(b). The following periodic regimes for larger b exhibit a further increasing number of subthreshold oscillations and

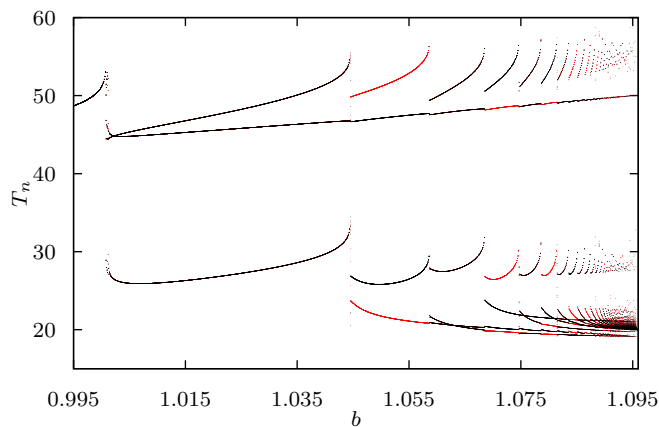


FIG. 11. Sampled return times between consecutive Poincaré events of $v_1 = -b$ (red) or $v_2 = -b$ (black) for varying b and fixed $(c, \varepsilon) = (-0.1, 0.1)$.

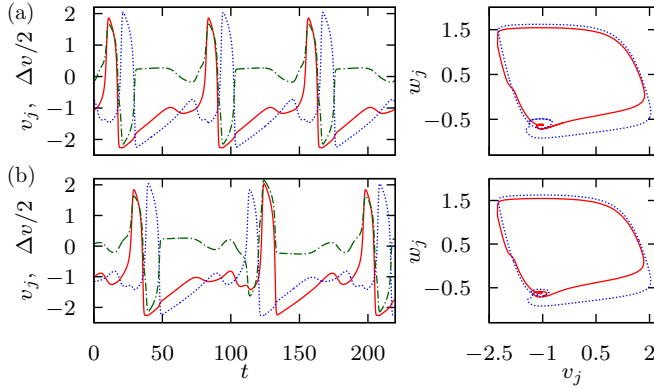


FIG. 12. Time traces and phase portraits of double leap-frogging at $b = 1.05$ (a) and triple leap-frogging at $b = 1.065$ (b). Other parameters are $(c, \varepsilon) = (-0.1, 0.1)$. Colors and line styles are as described in the caption of Fig. 4.

are successively either of the asymmetric type with fixed spiking order or of the type with the space-time symmetry and an alternating order of spiking, characterized by an even and odd number of leadership exchanges, respectively.

We have examined the stability regions of the double leap-frogging regime for varying c and different values of ε ; see Fig. 13. In contrast to the case of simple leap-frogging, these regions do not extend to a close vicinity of the degeneracy at $c = 0$. Under varying ε , their position with respect to the parameter b does not adapt to the canard transition $b_c(\varepsilon)$ of the symmetric oscillations (vertical dashed lines), as in case of the simple leap-frogging. The stability boundaries are outlined

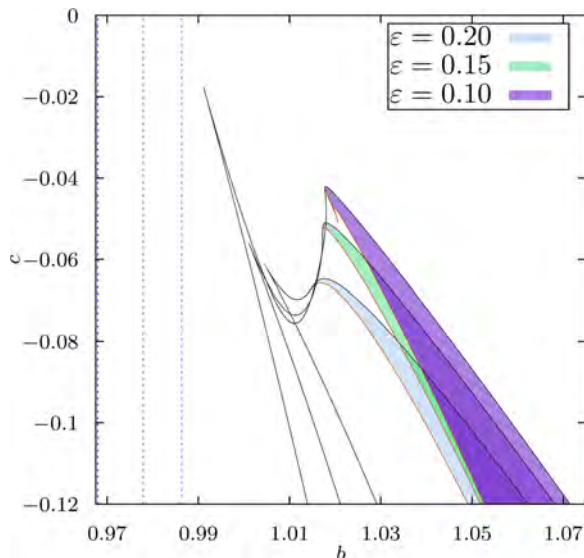


FIG. 13. Stability regions of the double leap-frog solutions in the (b, c) plane for fixed $\varepsilon \in \{0.2, 0.15, 0.1\}$ are presented in blue (bottom), green (middle), and purple (top), respectively. The left boundary of each region is given by a curve of period doubling bifurcations (orange), whereas the right one is provided by a fold curve (black). The vertical dashed lines of corresponding color indicate the location $b_c(\varepsilon)$ of the canard transition of the synchronous oscillations.

by curves of period doubling (orange) and curves of fold bifurcations (black) and do not involve any codimension-two bifurcations. This scenario for larger negative coupling, which is characterized by subsequent periodic patterns with different numbers of large relaxation oscillations and small loops, conforms, except for the different symmetry types, to the results of the asymptotic theory of mixed-mode oscillations at a folded node singularity.

IV. DISCUSSION AND OUTLOOK

In the present study, we have demonstrated that a variety of complex leap-frog patterns may emerge in a simple system comprised of two FitzHugh-Nagumo units with linear repulsive coupling in the fast variables. This complex dynamical scenario appears for parameter values in a vicinity of the canard transition of the uncoupled system and involves periodic solutions of different symmetry types. For larger repulsive coupling we obtain periodic regimes combining different numbers of small subthreshold and large relaxation oscillations, which resemble the general results for mixed-mode oscillations in slow-fast systems. For almost vanishing coupling, where the system gains an additional degeneracy, the situation is different. The stability region of the regime of simple leap frogging has the shape similar to a locking cone that approaches extremely close to the canard transition at vanishing coupling. Close to the tip of the cone, we have found a complex bifurcation scenario, which for decreasing ε is contracted to a close vicinity of the degenerate canard at $c = 0$. This contraction happens at a very fast and presumably exponential rate, such that already for moderately small values of ε a reliable numerical treatment became unfeasible and it would be a challenging task to perform an analytical study of this scenario in the singular limit $\varepsilon \rightarrow 0$.

Qualitatively, the onset of the leap-frog patterns may be explained as a result of a strong sensitivity to perturbations of the relaxation oscillation of a single FitzHugh-Nagumo unit just above the canard transition. There, already very small perturbations applied during the passage near the fold singularity of the slow manifold can deviate the trajectory away from the relaxation oscillation, giving rise to one or several loops conforming to subthreshold oscillations. Such a behavior of phase-sensitive excitability and the resulting response to excitations by noise of a single FitzHugh-Nagumo unit has been studied in Ref. [30]. Similar phenomena where the excitations arise from interactions in more complex networks have been studied in Ref. [31].

So far, the conditions relevant for the emergence of leap-frog patterns have mostly been considered within the context of neuroscience, especially in terms of relation to synchronized states. It has been known that such patterns cannot be obtained within the framework of weak-coupling theory for a pair of phase oscillators, because alternating order of firing cannot be described by reduction to an autonomous flow on the corresponding torus [32–34]. Thus, it was first believed that to observe the leap-frog solutions, one has to complement the phase oscillator dynamics by a complex synaptic coupling involving a finite synaptic time constant [12]. The suggested alternative has been to augment the simple phase dynamics by an additional negative phase branch

corresponding to strong hyperpolarization after the spiking event, as in case of the quadratic integrate-and-fire neuron model [12]. With regard to relaxation oscillators, the leap-frog patterns have first been observed as near-synchronous states where the complete phase synchronization is perturbed by *strong* inhibitory or excitatory coupling [13,14]. Later research focused on class I neural oscillators represented by Wang-Buzsáki [15] or Morris-Lecar model [12,35]. In both instances, it has been found that the appropriate inhibitory noninstantaneous synaptic dynamics is crucial for the onset of leap-frog dynamics. In particular, in the case of Morris-Lecar oscillators, such patterns are facilitated by the fact that the strong coupling causes the neurons to become transiently trapped in the subthreshold (excitable) state during a certain interval of the oscillation cycle, which allows for the exchange of the spiking order between the units [12]. In contrast to the above studies, we do not suggest a specific physiological mechanism, but discuss the general case of a system of *weakly*

coupled *excitable* units and show how the mechanism behind the exchange of leadership involves subthreshold oscillations, typically observed in class II neural oscillators [17,18,20]. In this sense our small negative linear coupling term can be seen as the essence of how qualitatively a local linearization of a more complicated functional dependence has to act to induce the leap-frog patterns.

ACKNOWLEDGMENTS

This work was supported by the Ministry of Education, Science, and Technological Development of Republic of Serbia under Project No. 171017, the DAAD Serbia-Germany Bilateral Project “Emergent Dynamics in Systems of Coupled Excitable Units,” as well as the DFG within the framework of Collaborative Research Center SFB 910. The authors thank O. E. Omel’chenko and N. Semenova for fruitful discussions.

-
- [1] R. C. Elson, A. I. Selverston, R. Huerta, N. F. Rulkov, M. I. Rabinovich, and H. D. I. Abarbanel, *Phys. Rev. Lett.* **81**, 5692 (1998).
- [2] R. Milo, S. Shen-Orr, S. Itzkovitz, N. Kashtan, D. Chklovskii, and U. Alon, *Science* **298**, 824 (2002).
- [3] E. Bullmore and O. Sporns, *Nat. Rev. Neurosci.* **10**, 186 (2009).
- [4] O. Sporns, *Networks of the Brain* (MIT Press, Cambridge, MA, 2011).
- [5] S. Song, P. J. Sjöström, M. Reigl, S. Nelson, and D. B. Chklovskii, *PLoS Biol.* **3**, e68 (2005).
- [6] A. Pikovsky, M. Rosenblum, and J. Kurths, *Synchronization, a Universal Concept in Nonlinear Science* (Cambridge University Press, Cambridge, UK, 2003).
- [7] E. M. Izhikevich, *Dynamical Systems in Neuroscience: The Geometry of Excitability and Bursting* (MIT Press, Cambridge, MA, 2007).
- [8] D. Terman, E. Lee, J. Rinzel, and T. Bem, *SIAM J. Appl. Dynam. Syst.* **10**, 1127 (2011).
- [9] G. Buzsáki, *Rhythms of the Brain* (Oxford University Press, Oxford, 2009).
- [10] P. Goel and G. B. Ermentrout, *Physica D (Amsterdam)* **163**, 191 (2002).
- [11] C. D. Acker, N. Kopell, and J. A. White, *J. Comp. Neurosci.* **15**, 71 (2003).
- [12] M. Oh and V. Matveev, *J. Comput. Neurosci.* **26**, 303 (2009).
- [13] A. Bose, N. Kopell, and D. Terman, *Physica D (Amsterdam)* **140**, 69 (2000).
- [14] Y. D. Sato and M. Shiino, *Phys. Rev. E* **75**, 011909 (2007).
- [15] S. K. Maran and C. C. Canavier, *J. Comput. Neurosci.* **24**, 37 (2008).
- [16] D. Terman, J. E. Rubin, and C. O. Diekmann, *Chaos* **23**, 046110 (2013).
- [17] M. Desroches, J. Guckenheimer, B. Krauskopf, C. Kuehn, H. M. Osinga, and M. Wechselberger, *SIAM Rev.* **54**, 211 (2012).
- [18] C. Kuehn, *Multiple Time Scale Dynamics* (Springer International Publishing, Switzerland, 2015).
- [19] E. N. Davison, Z. Aminzare, B. Dey, and N. E. Leonard, *Chaos* **29**, 033105 (2019).
- [20] M. Desroches, B. Krauskopf, and H. M. Osinga, *Chaos* **18**, 015107 (2008).
- [21] M. Krupa, B. Ambrosio, and M. A. Aziz-Alaoui, *Nonlinearity* **27**, 1555 (2014).
- [22] E. Köksal Ersöz, M. Desroches, and M. Krupa, *Physica D (Amsterdam)* **349**, 46 (2017).
- [23] M. N. Stolyarov, V. A. Romanov, and E. I. Volkov, *Phys. Rev. E* **54**, 163 (1996).
- [24] J. Guckenheimer, K. Hoffman, and W. Weckesser, *Int. J. Bifurcat. Chaos* **10**, 2669 (2000).
- [25] E. J. Doedel, and B. E. Oldeman, *AUTO-07P: Continuation and Bifurcation Software for Ordinary Differential Equations* (Concordia University, Montreal, 2012).
- [26] S. M. Baer and T. Erneux, *SIAM J. Appl. Math.* **46**, 721 (1986).
- [27] V. A. Makarov, V. I. Nekorkin, and M. G. Velarde, *Phys. Rev. Lett.* **86**, 3431 (2001).
- [28] B. Lindner, J. Garcia-Ojalvo, A. Neiman, and L. Schimansky-Geier, *Phys. Rep.* **392**, 321 (2004).
- [29] K. Shimizu, Y. Saito, M. Sekikawa, and N. Inaba, *Physica D (Amsterdam)* **241**, 1518 (2012).
- [30] I. Franović, O. E. Omel’chenko, and M. Wolfrum, *Chaos* **28**, 071105 (2018).
- [31] G. Ansmann, K. Lehnertz, and U. Feudel, *Phys. Rev. X* **6**, 011030 (2016).
- [32] M. Golubitsky, K. Josic, and E. Shea-Brown, *J. Nonlin. Sci.* **16**, 201 (2006).
- [33] E. M. Izhikevich, and Y. Kuramoto, *Weakly coupled oscillators, Encycl. Math. Phys.* **5**, 448 (2006).
- [34] F. C. Hoppensteadt and E. M. Izhikevich, *Weakly Connected Neural Networks* (Springer, New York, 1997).
- [35] *Frontiers of Applied and Computational Mathematics*, edited by D. Blackmore, A. Bose, and P. Petropoulos (World Scientific, Singapore, 2008).

Inverse stochastic resonance in a system of excitable active rotators with adaptive coupling

IVA BAČIĆ¹, VLADIMIR KLINSHOV², VLADIMIR NEKORKIN², MATJAŽ PERC³ and IGOR FRANOVIĆ^{1(a)}

¹ *Scientific Computing Laboratory, Center for the Study of Complex Systems, Institute of Physics Belgrade, University of Belgrade - Pregrevica 118, 11080 Belgrade, Serbia*

² *Institute of Applied Physics of the Russian Academy of Sciences - 46 Ulyanov Street, 603950 Nizhny Novgorod, Russia*

³ *Faculty of Natural Sciences and Mathematics, University of Maribor - Koroška cesta 160, SI-2000 Maribor, Slovenia*

received 17 September 2018; accepted in final form 8 November 2018

published online 11 December 2018

PACS 05.40.Ca – Noise

PACS 87.19.1n – Oscillations and resonance

Abstract – Inverse stochastic resonance is a phenomenon where an oscillating system influenced by noise exhibits a minimal oscillation frequency at an intermediate noise level. We demonstrate a novel generic scenario for such an effect in a multi-timescale system, considering an example of emergent oscillations in two adaptively coupled active rotators with excitable local dynamics. The impact of plasticity turns out to be twofold. First, at the level of multiscale dynamics, one finds a range of intermediate adaptivity rates that give rise to multistability between the limit cycle attractors and the stable equilibria, a condition necessary for the onset of the effect. Second, applying the fast-slow analysis, we show that the plasticity also plays a facilitatory role on a more subtle level, guiding the fast flow dynamics to parameter domains where the stable equilibria become focuses rather than nodes, which effectively enhances the influence of noise. The described scenario persists for different plasticity rules, underlying its robustness in the light of potential applications to neuroscience and other types of cell dynamics.

Copyright © EPLA, 2018

Introduction. – Noise in coupled excitable or bistable systems may induce two types of generic effects [1]. On the one hand, it can modify the deterministic behavior by acting non-uniformly on different states of the system, thus amplifying or suppressing some of its features. On the other hand, noise may give rise to completely novel forms of behavior, typically based on crossing the thresholds or separatrices, or involving enhanced stability of deterministically unstable structures. In neuronal systems, the constructive role of noise at different stages of information processing, referred to as “stochastic facilitation” [2,3], mainly comprises resonant phenomena. A classical example is the stochastic resonance [4], which allows for the detection of weak subthreshold periodic signals. A more recent development concerns the effect of inverse stochastic resonance (ISR) [3,5–12], where noise selectively reduces the spiking frequency of neuronal oscillators, converting the tonic firing into intermittent bursting-like activity or a short-lived transient followed

by a long period of quiescence. The name of the effect should be taken *cum grano salis*, because in contrast to stochastic resonance, it involves no additional external signal: one rather observes a non-monotonous dependence of the spiking rate on noise variance, whereby the oscillation frequency becomes minimal at a preferred noise level. Such an inhibitory effect of noise has recently been shown for cerebellar Purkinje cells [11], having explicitly demonstrated how the lifetimes of the spiking (“up”) and the silent (“down”) states [13–15] are affected by the noise variance. ISR has been indicated to play important functional roles in neuronal systems, including the reduction of spiking frequency in the absence of neuromodulators, suppression of pathologically long short-term memories, triggering of on-off tonic spiking activity and even optimization of information transfer along the signal propagation pathways [3,7,9,11].

So far, theoretical studies on ISR have mostly concerned the scenario where a single neuron exhibits bistable deterministic dynamics, featuring coexistence between a limit cycle and a stable equilibrium. Such bistability is

^(a)E-mail: franovic@ipb.ac.rs

typical for Type-II neurons below the subcritical Hopf bifurcation, *e.g.*, classical Hodgkin-Huxley and Morris-Lecar models [3,6–8]. There, applying noise induces switching between the metastable states, but at an intermediate noise level, one surprisingly finds a strong asymmetry of the associated switching rates, which makes the periods spent in the vicinity of equilibrium much longer than the periods of spiking activity.

An important open problem concerns conditions giving rise to ISR in coupled excitable systems, where noise influences the emergent oscillations. Here we address in detail this issue, as it may be crucial to understanding the prevalence of the effect in neural networks, whose activity depends on the interplay of excitability, coupling properties and noise. Synaptic dynamics typically involves the plasticity feature, which makes self-organization in neuronal systems a multi-timescale process: the short-term spiking activity unfolds on a quasi-static coupling configuration, while the slow adjustment of coupling weights depends on the time-averaged evolution of units.

Motivated by the findings in neuroscience, we focus on the onset of ISR in a simplified, yet paradigmatic system of two adaptively coupled stochastic active rotators with excitable local dynamics. Active rotators are canonical for Type-I excitability and may be seen as equivalent to the theta-neuron model. Adaptivity is introduced in a way that allows continuous interpolation between a spectrum of plasticity rules, including Hebbian learning and spike-time-dependent plasticity (STDP) [16–18].

We demonstrate a generic scenario for the plasticity-induced ISR, where the system’s multiscale structure, defined by the adaptivity rate, plays a crucial role. On a basic level, plasticity gives rise to multistable behavior involving coexisting stationary and oscillatory regimes. An additional subtlety, which we show by the fast-slow analysis, is that the plasticity promotes the resonant effect by guiding the fast flow toward the parameter region where the stable fixed points are focuses rather than nodes.

The paper is organized as follows. In the next section the details of the model and the numerical bifurcation analysis of the deterministic dynamics are presented. The third section contains the results on the ISR effect and the supporting conditions. In the fourth section the fast-slow analysis is applied to explain the mechanism by which plasticity enhances the system’s non-linear response to noise. Apart from providing a brief summary, in the last section we also discuss the prevalence of the observed effect.

Model and bifurcation analysis of deterministic dynamics. – Our model involves two stochastic active rotators interacting by adaptive couplings [19–22],

$$\begin{aligned}\dot{\varphi}_1 &= I_0 - \sin \varphi_1 + \kappa_1 \sin(\varphi_2 - \varphi_1) + \sqrt{D}\xi_1(t), \\ \dot{\varphi}_2 &= I_0 - \sin \varphi_2 + \kappa_2 \sin(\varphi_1 - \varphi_2) + \sqrt{D}\xi_2(t), \\ \dot{\kappa}_1 &= \epsilon(-\kappa_1 + \sin(\varphi_2 - \varphi_1 + \beta)), \\ \dot{\kappa}_2 &= \epsilon(-\kappa_2 + \sin(\varphi_1 - \varphi_2 + \beta)),\end{aligned}\quad (1)$$

where the phases $\{\varphi_1, \varphi_2\} \in S^1$, while the coupling weights $\{\kappa_1, \kappa_2\}$ are real variables.

The excitability parameters I_0 , which one may interpret as external bias currents in the context of neuroscience, are assumed to be identical for both units. For such a setup, the deterministic version of (1) possesses a Z_2 symmetry, being invariant to the exchange of units’ indices. The uncoupled units undergo a SNIPER bifurcation at $I_0 = 1$, with the values $I_0 < 1$ ($I_0 > 1$) corresponding to the excitable (oscillatory) regime. We consider the case of excitable local dynamics, keeping $I_0 = 0.95$ fixed throughout the paper, such that the oscillations may emerge only due to the coupling terms and/or noise. The scale separation between the fast dynamics of the phases and the slow dynamics of adaptation is adjusted by the parameter $\epsilon \ll 1$. The fast variables are influenced by independent white noise of variance D such that $\xi_i(t)\xi_j(t') = \delta_{ij}\delta(t-t')$ for $i, j \in \{1, 2\}$. Conceptually, adding stochastic input to the fast variables embodies the action of synaptic noise in neuronal systems [23].

The modality of the plasticity rule is specified by the parameter β , whose role may be understood by invoking the qualitative analogy between the adaptation dynamics in classical neuronal systems and the systems of coupled phase oscillators. This issue has first been addressed in [24–26], and a deeper analysis of the correspondence between the phase-dependent plasticity rules and the STDP has been carried out in [19]. In particular, it has been shown that the plasticity dynamics for $\beta = 3\pi/2$, where the stationary weights between the oscillators with smaller/larger phase differences increase/decrease, qualitatively resembles the Hebbian learning rule [25,26]. Nevertheless, when $\beta = \pi$, the coupling weights encode a causal relationship between the spiking of oscillators by changing in the opposite directions, in analogy to an STDP-like plasticity rule. Our interest lies with the β interval interpolating between these two limiting cases.

Using bifurcation analysis of the deterministic dynamics of (1), we first show how the modality of the plasticity rule influences the number of stationary states, and then explain how the onset of oscillations depends on adaptivity rate. The bifurcation diagram in fig. 1 indicates that the number and the stability of fixed points of (1) change with β in such a way that the system may possess two, four or six fixed points. Due to invariance to Z_2 symmetry, one always finds pairs of solutions sharing the same stability features. We consider the plasticity rules described by $\beta \in (3.298, 4.495)$, cf. the shaded region in fig. 1, where the system has two stable fixed points lying off the synchronization manifold $\varphi_1 = \varphi_2$, as well as four unstable fixed points. The bifurcations occurring at the boundaries of the relevant β interval are as follows. At $\beta = 3.298$, the system undergoes a supercritical symmetry-breaking pitchfork bifurcation giving rise to a pair of stable fixed points off the synchronization manifold. For $\beta = 4.495$, this pair of stable fixed points collides with a pair of unstable fixed points off

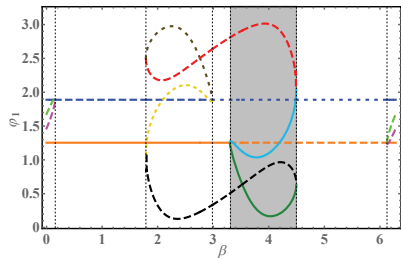


Fig. 1: (Color online) Bifurcation diagram for the fixed points of (1) with $D = 0$ under variation of β . Solid lines refer to stable fixed points, while dashed and dotted lines correspond to saddles of unstable dimension 1 and 2, respectively. Shading indicates the considered range of plasticity rules. The two fixed points independent on β belong to the synchronization manifold. The remaining parameters are $I_0 = 0.95, \epsilon = 0.05$.

the synchronization manifold, getting annihilated in two symmetry-related inverse fold bifurcations. Note that the weight levels typical for the two stable stationary states support effective unidirectional interaction, in a sense that one unit exerts a much stronger impact on the dynamics of the other unit than vice versa. When illustrating the effect of ISR, we shall mainly refer to the case $\beta = 4.2$. For this β , the two stable focuses of (1) at $D = 0$ are given by $(\varphi_1, \varphi_2, \kappa_1, \kappa_2) = (1.177, 0.175, 0.032, -0.92)$ and $(\varphi_1, \varphi_2, \kappa_1, \kappa_2) = (0.175, 1.177, -0.92, 0.032)$. Within the considered β interval, the two stable fixed points of the coupled system exhibit excitable behavior, responding to external perturbation by generating either the successive spikes or synchronized spikes [21].

The onset of oscillations for the deterministic version of (1) relies on the interplay between the plasticity rule, controlled by β , and the adaptation rate, characterized by ϵ . In fig. 2(a) are shown the results of parameter sweep indicating the variation of κ_1 variable, $\sigma_{\kappa_1} = \max(\kappa_1(t)) - \min(\kappa_1(t))$, within the (β, ϵ) parameter plane. The sweep indicates the maximal stability region of the two emerging periodic solutions, related by the exchange symmetry of units indices. The data are obtained by numerical continuation starting from a stable periodic solution, such that the final state reached for the given parameter set is used as initial conditions of the system dynamics for incremented parameter values. One observes that for fixed β , there exists an interval of timescale separation ratios $\epsilon \in (\epsilon_{min}, \epsilon_{max})$ admitting oscillations, see fig. 2(b). Within the given ϵ range, the system exhibits multistability where periodic solutions coexist with the two symmetry-related stable stationary states. The lower threshold for oscillations, ϵ_{min} , reduces with β , whereas the upper boundary value, ϵ_{max} , is found to grow as β is enhanced. Note that the waveform of oscillations also changes as ϵ is increased under fixed β . In particular, for smaller ϵ , the waveforms corresponding to the two units are rather different. Nevertheless, around $\epsilon \approx 0.06$ the system undergoes a pitchfork bifurcation of limit cycles, such that

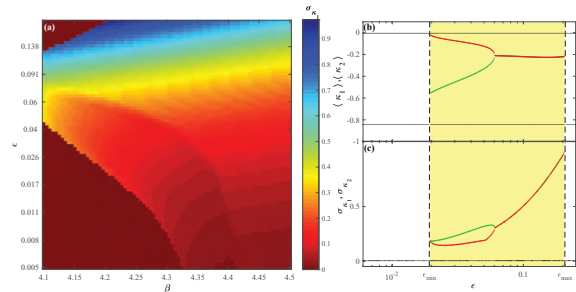


Fig. 2: (Color online) Onset of oscillations in (1) for $D = 0$. (a) Variation σ_{κ_1} of the coupling weight κ_1 in the (β, ϵ) -plane. (b) Mean coupling weights $\langle \kappa_1 \rangle(\epsilon)$ and $\langle \kappa_2 \rangle(\epsilon)$ for oscillatory (thick lines) and stationary states (thin lines) at $\beta = 4.2$. (c) Variation $\sigma_{\kappa_1}(\epsilon)$ and $\sigma_{\kappa_2}(\epsilon)$, presented as in (b). Shading in (b) and (c) indicates the ϵ interval admitting the stable periodic solutions.

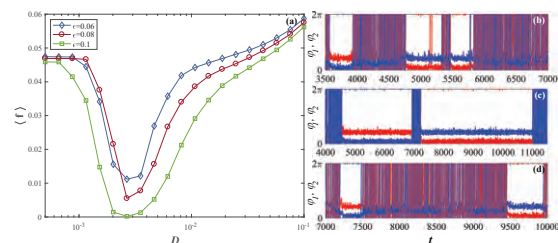


Fig. 3: (Color online) (a) Mean spiking rate $\langle f \rangle$ in terms of D for $\epsilon \in \{0.06, 0.08, 0.1\}$. The curves exhibit a characteristic minimum at an intermediate noise level. (b)–(d) Time traces $\varphi_1(t)$ and $\varphi_2(t)$ for noise levels below, at and above the resonant value. The remaining parameters are $I_0 = 0.95, \beta = 4.2, \epsilon = 0.06$.

the oscillatory solution gains the anti-phase space-time symmetry $\varphi_1(t) = \varphi_2(t + T/2), \kappa_1(t) = \kappa_2(t + T/2)$, where T denotes the oscillation period [21].

Numerical results on ISR. – Inverse stochastic resonance manifests itself as noise-mediated suppression of oscillations, whereby the frequency of noise-perturbed oscillations becomes minimal at a preferred noise level. For system (1), we find such an effect to occur generically for intermediate adaptivity rates, supporting multistability between the stationary and the oscillatory solutions, as described in the previous section. A family of curves describing the dependence of the oscillation frequency on noise variance $\langle f \rangle(D)$ for different ϵ values is shown in fig. 3. All the curves corresponding to $\epsilon \geq \epsilon_{min}(\beta)$ show a characteristic non-monotonous behavior, displaying a minimum at the optimal noise intensity. For weaker noise, the oscillation frequency remains close to the deterministic one, whereas for much stronger noise, the frequency increases above that of unperturbed oscillations. The displayed results are obtained by averaging over an ensemble of 1000 different stochastic realizations, having excluded the transient behavior, and having fixed a single set of initial conditions within the basin of attraction of the limit cycle attractor. Nevertheless, we have verified that the

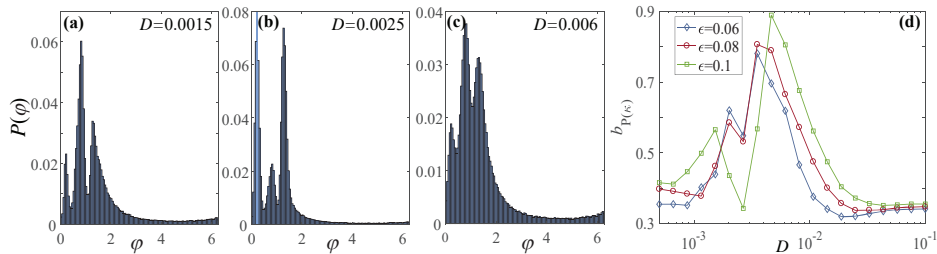


Fig. 4: (Color online) (a)–(c) Stationary distribution $P(\varphi_1)$ for the noise levels below, at and above the resonant value. System parameters are $I_0 = 0.95$, $\beta = 4.2$ and $\epsilon = 0.06$. From the three observable peaks, the middle one, prevalent in (a) and (c), refers to the metastable state associated to the oscillatory mode of (1) for $D = 0$. The two lateral peaks, dominant in (b), correspond to quasi-stationary states derived from the stable equilibria of the deterministic version of (1). (d) Bimodality coefficient for the stationary distribution of κ_1 , $b_{P(\kappa_1)}$, as a function of D . The three curves refer to $\epsilon = 0.06$ (diamonds), $\epsilon = 0.08$ (circles) and $\epsilon = 0.1$ (squares).

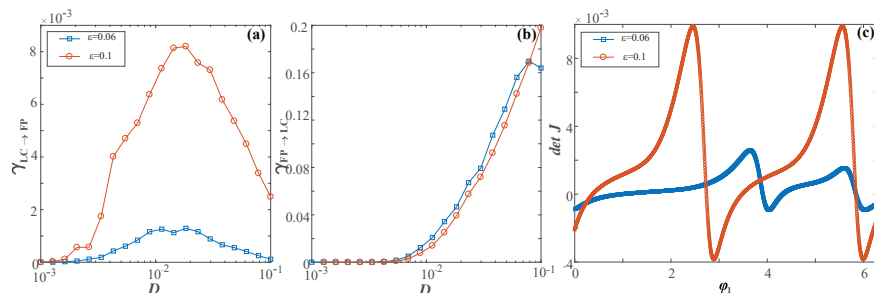


Fig. 5: (Color online) (a) and (b): transition rates from the stability basin of the limit cycle to the fixed point, $\gamma_{LC \rightarrow FP}(D)$ and vice versa, $\gamma_{FP \rightarrow LC}(D)$, numerically obtained for $\epsilon = 0.06$ (squares) and $\epsilon = 0.1$ (circles). The remaining parameters are $I_0 = 0.95$, $\beta = 4.2$. (c) Determinant of the Jacobian calculated along the limit cycle orbit as a function of the phase variable. The quantity provides an indication of the sensitivity of certain sections of the orbit to external perturbation. Blue and red colors correspond to $\epsilon = 0.06$ and $\epsilon = 0.1$, respectively.

qualitatively analogous results are obtained if for each realization of stochastic process one selects a set of random initial conditions lying within the stability basin of the periodic solution. The suppression effect of noise depends on the adaptivity rate, and is found to be more pronounced for faster adaptivity. Indeed, for smaller ϵ , $\varphi(t)$ series corresponding to the noise levels around the minimum of $\langle f \rangle(D)$ exhibit bursting-like behavior, whereas for larger ϵ , noise is capable of effectively quenching the oscillations, such that the minimal observed frequency approaches zero.

The core of the described effect concerns switching dynamics between the metastable states associated to coexisting attractors of the deterministic version of system (1). To illustrate this, in fig. 4 we have considered the stationary distributions of one of the phase variables, $P(\varphi)$, for the noise levels below, at and above the minimum of the $\langle f \rangle(D)$, having fixed the remaining parameters to $(\beta, \epsilon) = (4.2, 0.06)$. The distribution $P(\varphi)$ is characterized by two lateral peaks, reflecting the two symmetry-related quasi-stationary states, and the area around the central peak, corresponding to the oscillatory mode. For small noise $D = 0.0015$, see fig. 4(a), and very large noise $D = 0.006$, cf. fig. 4(c), the central peak of $P(\varphi)$ is expectedly prevalent compared to the two lateral peaks. Nevertheless, the switching dynamics for

$D = 0.0025$, the noise level about the minimum of $\langle f \rangle(D)$, is fundamentally different, and the corresponding distribution $P(\varphi)$ in fig. 4(b) shows that the system spends much more time in the quasi-stationary states than performing the oscillations. The onset of ISR in the dynamics of fast variables is accompanied by the increased bimodality of the stationary distribution of the couplings, see fig. 4(d).

In order to observe the non-monotonous response of the system's frequency to noise, the geometry of the phase space has to be asymmetrical with respect to the separatrix between the coexisting attractors in such a way that the limit cycle attractor lies much closer to the separatrix than the stationary states. Such structure of phase space gives rise to asymmetry in switching dynamics, whereby at the preferred noise level around the minimum of $\langle f \rangle(D)$, the transition rate from the stability basin of the limit cycle attractor to that of stationary states $\gamma_{LC \rightarrow FP}$ becomes much larger than the transition rate in the inverse direction, $\gamma_{FP \rightarrow LC}$. Figures 5(a) and (b) corroborate that the dependences $\gamma_{LC \rightarrow FP}(D)$ and $\gamma_{FP \rightarrow LC}(D)$ are qualitatively distinct: the former displays a maximum at the resonant noise level, whereas the latter just increases monotonously with noise. The fact that ISR is more pronounced for higher adaptivity rates is reflected in that the curve $\gamma_{LC \rightarrow FP}(D)$ for $\epsilon = 0.1$ lies substantially above that for $\epsilon = 0.06$, see fig. 5(a).

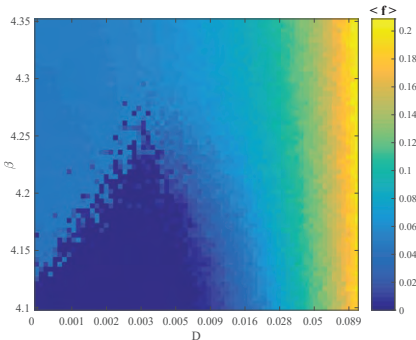


Fig. 6: (Color online) Mean spiking rate $\langle f \rangle$ as a function of β and D for fixed $\epsilon = 0.05$. The results evince the robustness of the ISR effect with respect to different plasticity rules.

To understand why the interplay of adaptivity rate and noise yields a stronger resonant effect for larger ϵ , we have investigated the susceptibility of the limit cycle attractor to external perturbation. In particular, fig. 5(c) shows how the determinant of the Jacobian calculated along the limit cycle orbit change for $\epsilon = 0.06$ (blue line) and $\epsilon = 0.1$ (red line), respectively. For smaller ϵ , one may identify two particular points where the determinant of the Jacobian is the largest, *i.e.*, where the impact of external perturbation is felt the strongest. This implies that noise is most likely to drive the systems trajectory away from the limit cycle attractor around these two sections of the orbit, which should lie closest to the boundary to the stability basins of the stationary states. Such a physical picture is maintained for larger ϵ , but one should stress that the sensitivity of limit cycle attractor to external perturbation substantially increases along the entire orbit, cf. fig. 5(c). In other words, faster adaptivity enhances the impact of noise, contributing to a more pronounced ISR effect. This point is addressed from another perspective in the next section.

We also examine the robustness of ISR to different modalities of the plasticity rule specified by β . Figure 6 shows how the average oscillation frequency changes with β and D for fixed $\epsilon = 0.05$. The non-linear response to noise, conforming to a resonant effect with a minimum of oscillation frequency at an intermediate noise level, persists in a wide range of β , essentially interpolating between the Hebbian-like and the STDP-like adaptive dynamics.

Fast-slow analysis: role of plasticity in the resonant effect. – Though ISR is observed for intermediate ϵ , here we show that the fast-slow analysis may still be applied to demonstrate a peculiar feature of the mechanism behind the resonant effect. In particular, we find that the plasticity enhances the resonant effect by driving the fast flow dynamics toward the parameter domain where the stationary state is a focus rather than a node. It is well known that the response to noise in multi-timescale systems qualitatively depends on the character of stationary states. Indeed, by using the sample-paths approach and other advanced techniques, it has already been shown

that such systems may exhibit fundamentally different scaling regimes with respect to noise variance and the scale-separation ratio [27,28]. Moreover, the resonant effects may typically be expected in the case in which quasi-stationary states are focuses [27], essentially because the local dynamics around the stationary state then involves an eigenfrequency.

Within the standard fast-slow analysis, one may either consider the layer problem, defined on the fast timescale, or the reduced problem, concerning the slow timescale [29]. For the layer problem, the fast flow dynamics $\varphi_1(t; \kappa_1, \kappa_2), \varphi_2(t; \kappa_1, \kappa_2)$ is obtained by treating the slow variables κ_1 and κ_2 as system parameters, whereas in the case of the reduced problem, determining the dynamics of the slow flow $(\kappa_1(t), \kappa_2(t))$ involves time-averaging over the stable regimes of the fast flow of the layer problem. The fast flow can in principle exhibit several attractors, which means that multiple stable sheets of the slow flow may emerge from the averaged dynamics on the different attractors of the fast flow. Our key point concerns the dynamics of the slow flow, which requires us to first classify the attractors of the fast flow.

The fast flow dynamics is given by

$$\begin{aligned}\dot{\varphi}_1 &= I_0 - \sin \varphi_1 + \kappa_1 \sin(\varphi_2 - \varphi_1), \\ \dot{\varphi}_2 &= I_0 - \sin \varphi_2 + \kappa_2 \sin(\varphi_1 - \varphi_2),\end{aligned}\quad (2)$$

where $\kappa_1, \kappa_2 \in [-1, 1]$ are considered as additional system parameters. One may formally obtain (2) by setting $\epsilon = 0$ in (1) with $D = 0$. We find that the fast flow is monostable for most of the (κ_1, κ_2) values, exhibiting either a stable equilibrium or a limit cycle attractor, see fig. 7(a). In general, the fast flow admits either two or four fixed points, and a more detailed physical picture, including the associated bifurcations, is presented in [21]. The stability region of the oscillatory regime, outlined by the red color, has been calculated by numerical continuation starting from a stable periodic solution. Bistability between a stable fixed point and a limit cycle is observed only in a small area near the main diagonal $\kappa_1 = \kappa_2$. Within the region featuring oscillatory regime, each periodic solution obtained for (κ_1, κ_2) above the main diagonal has a Z_2 symmetry-related counterpart below the diagonal. Typically, the periodic solutions emanate from SNIPER bifurcations, which make up two branches where either κ_1 or κ_2 are almost constant and close to zero.

Using the results from the analysis of the layer problem, our goal is to determine the vector fields corresponding to the stable sheets of the slow flow. We have numerically obtained the dynamics of the slow flow by a standard two-step approach [19,30]. First, for fixed values (κ_1, κ_2) , we have determined the time-averaged dynamics of the fast flow (2), $\langle \varphi_2 - \varphi_1 \rangle_t = h(\kappa_1, \kappa_2)$, whereby the averaging $\langle \cdot \rangle_t$ is carried out over a sufficiently long time interval, having excluded the transient behavior. As already indicated, such an average depends on the attractor of the fast flow for the given (κ_1, κ_2) . If the fast flow possesses

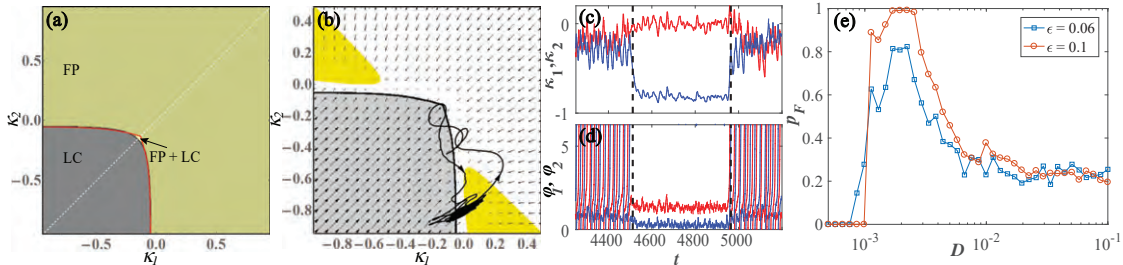


Fig. 7: (Color online) (a) Attractors of the fast flow (2) in terms of κ_1 and κ_2 , now treated as free parameters. The fast flow is typically monostable, admitting either a stable fixed point (FP) or a stable limit cycle (LC), apart from a small region of bistability (FP+LC) around the main diagonal. (b) Vector field of the slow flow (3) determined by considering only the stable regimes of the fast flow for $\beta = 4.2, I_0 = 0.95$. Within the yellow-highlighted regions, the stable fixed point of the fast flow is a focus rather than the node. The displayed orbit $(\kappa_1(t), \kappa_2(t))$ corresponds to a switching episode from the oscillatory state to the quasi-stationary state and back (evolution direction indicated by arrows). Panels (c) and (d) show the time traces of phases and couplings during the switching episode. (e) Conditional probability $p_F(D)$ for $\epsilon = 0.06$ (blue squares) and $\epsilon = 0.1$ (red circles).

a stable fixed point, then $\langle \varphi_2 - \varphi_1 \rangle_t = \varphi_2^* - \varphi_1^*$, which corresponds to the slow critical manifold of the system. For (κ_1, κ_2) where the attractor of the fast flow is a periodic solution, $\langle \varphi_2 - \varphi_1 \rangle_t$ amounts to the time average over the period. Averaging over a periodic attractor of the fast flow is a standard approximation [30], quite natural when describing the influence of oscillations in the fast flow to the dynamics of the slow flow.

As the second step, the obtained time averages are substituted into the coupling dynamics

$$\begin{aligned} \dot{\kappa}_1 &= \epsilon[-\kappa_1 + \sin(h(\kappa_1, \kappa_2) + \beta)], \\ \dot{\kappa}_2 &= \epsilon[-\kappa_2 + \sin(-h(\kappa_1, \kappa_2) + \beta)]. \end{aligned} \quad (3)$$

The system (3) allows one to determine the vector fields on the stable sheets of the slow flow, which correspond to the attractors of the fast flow. In fig. 7(b), the vector fields associated to each of the attractors (fixed point or limit cycle) are presented within its respective (κ_1, κ_2) stability region. In the small region of the (κ_1, κ_2) -plane supporting coexisting stable solutions of the fast flow, the corresponding vector field of the slow flow is given on multiple overlapping sheets, since the value of the average $f(\kappa_1, \kappa_2)$ depends on the initial conditions.

Within the above framework, one is able to explain a subtle influence of adaptivity on the mechanism behind the ISR. To this end, in fig. 7(b) we have projected a typical example of the $(\kappa_1(t), \kappa_2(t))$ trajectory of the full system (1) corresponding to a switching episode between the metastable states associated to a limit cycle attractor and a stable equilibrium of the deterministic system, see the time traces in figs. 7(c), (d). One observes that for the oscillating regime, the coupling dynamics always remains close to the SNIPER bifurcation of the fast flow, cf. fig. 7(a), which makes the oscillations quite susceptible to noise. Recall that the fast flow is typically monostable. Thus, switching events in the full system are naturally associated to the fast flow undergoing the SNIPER bifurcation: either a direct one, leading from the oscillatory to the stationary regime, or the inverse one, unfolding in the

opposite direction. For (κ_1, κ_2) values immediately after the SNIPER bifurcation toward the quiescent state, the stable equilibrium of the fast flow is a node. Nevertheless, for the noise levels where the effect of ISR is most pronounced, we find that the coupling dynamics guides the system into the region where the equilibrium is a stable focus rather than a node, see the yellow highlighted region in fig. 7(b). We have verified that this feature is a hallmark of the resonant effect by numerically calculating the conditional probability p_F that the events of crossing the SNIPER bifurcation are followed by the system's orbit visiting the (κ_1, κ_2) region where the stable equilibrium is a focus. The $p_F(D)$ dependences for two characteristic ϵ values at fixed $\beta = 4.2$ are plotted in fig. 7(e). One learns that $p_F(D)$ has a maximum for the resonant noise levels, where the corresponding curve $f(D)$ displays a minimum. In other words, the fact that the coupling dynamics drives the fast flow to the focus-associated regions of the (κ_1, κ_2) -plane results in trapping the phase variables for a longer time in the quasi-stationary (quiescent) state. Small noise below the resonant values is insufficient to drive the system to this region, whereas for too large a noise, the stochastic fluctuations completely take over, washing out the quasi-stationary regime. Note that for the faster adaptivity rate, the facilitatory role of coupling becomes more pronounced, as evinced by the fact that the curve $p_F(D)$ for $\epsilon = 0.1$ lies above the one for $\epsilon = 0.06$.

Discussion. – In the present paper, we have demonstrated a novel generic scenario for the onset of ISR, which involves an interplay between the local excitability feature and the adaptive dynamics of the couplings. For the example of two active rotators with coupling plasticity, we have shown that the spiking frequency corresponding to emergent oscillations varies non-monotonously with noise, displaying a minimum at a preferred noise level. Though the model *per se* is simplified, the underlying paradigm is relevant for combining the two core features of typical neuronal systems. The effect derives from the multi-timescale structure of the system, whereby the scale

separation between the local and the weight dynamics is tuned via adaptivity rate. Within a range of intermediate adaptivity rates, the deterministic dynamics of the full system exhibits multistability between the limit cycle attractors and the stable equilibria, each appearing in pairs due to the systems invariance to Z_2 symmetry. Applying the standard fast-slow analysis, we have shown that the resonant effect with noise is in fact plasticity-enhanced: plasticity promotes the impact of noise by guiding the fast flow toward the parameter domain where the stable equilibria become focuses instead of nodes. This mechanism increases the trapping efficiency by which the noise is able to deviate the systems trajectory from the metastable oscillatory states to the non-spiking regime. For faster adaptivity, the resonant effect is found to be more pronounced in a sense that the frequency dependence on noise shows deeper minima. Our scenario has proven to persist in a wide range of plasticity rules, interpolating between the cases analogous to Hebbian learning and STDP.

In earlier studies, observation of ISR has mostly been confined to Type-II neurons with intrinsic bistable dynamics, as in case of Hodgkin-Huxley or Morris-Lecar neurons near the subcritical Hopf bifurcation [3,6–9]. Even in case of networks, the macroscopic ISR effect has been linked to dynamical features of single units, only being modulated by the details of synaptic dynamics and the network topology [10]. In contrast to that, our results show that ISR may not rely on bistability of local dynamics, but may rather emerge due to the facilitatory role of coupling, here reflected in the interplay of multiscale dynamics and plasticity. Another distinction from most of the previous studies is that our scenario concerns Type-I units. For this class of systems, it is known that the dependence of the oscillating frequency of a single unit with noise is just monotonous [3,12], so that the resonant effect can only be observed in case of coupled units. So far, the latter case has been analyzed only once [5], but the underlying scenario is different from ours insofar as it involves static, rather than the adaptive couplings, and the effect *per se* is confined to a narrow region of the parameter space.

Quite recently, the onset of ISR has been reported for a single Fitzhugh-Nagumo oscillator [12], which is the first observation of the effect for Type-II neuron model in the vicinity of the supercritical Hopf bifurcation. Similar to the scenario we elaborated, ISR there also derives from the multiscale structure of the system. However, the actual mechanism behind the effect is associated to phase-sensitive (non-uniform) excitability of a limit cycle orbit conforming to relaxation oscillations [12]. These findings and the results here suggest that ISR may indeed provide a generic means of controlling and optimizing the firing rate in multi-timescale systems, which can be applied to neuronal activity, calcium signaling and other types of cell dynamics.

IF and IB would like to thank M. WOLFRUM and S. YANCHUK for useful discussions. The work of VK on

the third section was supported by the Russian Science Foundation, grant No. 16-42-01043. The work of VN on the fourth section was supported by the Russian Science Foundation, grant No. 14-12-01358.

REFERENCES

- [1] LINDNER B., GARCIA-OJALVO J., NEIMAN A. and SCHIMANSKY-GEIER L., *Phys. Rep.*, **392** (2004) 321.
- [2] McDONNELL M. D. and WARD L. M., *Nat. Rev. Neurosci.*, **12** (2011) 415.
- [3] SCHMERL B. A. and McDONNELL M. D., *Phys. Rev. E*, **88** (2013) 052722.
- [4] GAMMAITONI L., HÄNGGI P., JUNG P. and MARCHESONI F., *Rev. Mod. Phys.*, **70** (1998) 223.
- [5] GUTKIN B. S., JOST J. and TUCKWELL H. C., *EPL*, **81** (2008) 20005.
- [6] TUCKWELL H. C., JOST J. and GUTKIN B. S., *Phys. Rev. E*, **80** (2009) 031907.
- [7] UZUNTARLA M., CRESSMAN J. R., OZER M. and BARRETO E., *Phys. Rev. E*, **88** (2013) 042712.
- [8] UZUNTARLA M., *Phys. Lett. A*, **377** (2013) 2585.
- [9] UZUNTARLA M., TORRES J. J., SO P., OZER M. and BARRETO E., *Phys. Rev. E*, **95** (2017) 012404.
- [10] UZUNTARLA M., BARRETO E. and TORRES J. J., *PLoS Comput. Biol.*, **13** (2017) e1005646.
- [11] BUCHIN A., RIEUBLAND S., HÄUSSER M., GUTKIN B. S. and ROTH A., *PLoS Comput. Biol.*, **12** (2016) e1005000.
- [12] FRANOVIĆ I., OMEL'CHENKO O. E. and WOLFRUM M., *Chaos*, **28** (2018) 071105.
- [13] HAHN T. T. G., MCFARLAND J. M., BERBERICH S., SAKMANN B. and MEHTA M. R., *Nat. Neurosci.*, **15** (2012) 1531.
- [14] FRANOVIĆ I. and KLINSHOV V., *Chaos*, **28** (2018) 023111.
- [15] FRANOVIĆ I. and KLINSHOV V., *EPL*, **116** (2016) 48002.
- [16] SONG S., MILLER K. D. and ABBOTT L. F., *Nat. Neurosci.*, **3** (2000) 919.
- [17] FROMKE R. C. and DAN Y., *Nature*, **416** (2002) 433.
- [18] WANG H.-X., GERKIN R. C., NAUEN D. W. and BI G.-Q., *Nat. Neurosci.*, **8** (2005) 187.
- [19] LÜCKEN L., POPOVYCH O. V., TASS P. A. and YANCHUK S., *Phys. Rev. E*, **93** (2016) 032210.
- [20] KASATKIN D. V. and NEKORKIN V. I., *Radiophys. Quantum Electron.*, **58** (2016) 877.
- [21] BAČIĆ I., YANCHUK S., WOLFRUM M. and FRANOVIĆ I., *Eur. Phys. J. ST*, **227** (2018) 1077.
- [22] KASATKIN D., YANCHUK S., SCHÖLL E. and NEKORKIN V., *Phys. Rev. E*, **96** (2017) 062211.
- [23] DESTEXHE A. and RUDOLPH-LILITH M., *Neuronal Noise* (Springer, New York) 2012.
- [24] MAISTRENKO Y. L., LYSYANSKY B., HAUPTMANN C., BURLYKO O. and TASS P., *Phys. Rev. E*, **75** (2007) 066207.
- [25] AOKI T. and AOYAGI T., *Phys. Rev. Lett.*, **102** (2009) 034101.
- [26] AOKI T. and AOYAGI T., *Phys. Rev. E*, **84** (2011) 066109.
- [27] BERGLUND N. and GENTZ B., *Noise-Induced Phenomena in Slow-Fast Dynamical Systems* (Springer, Berlin) 2006.
- [28] LAING C. and LORD G. J. (Editors), *Stochastic Methods in Neuroscience* (Oxford University Press, London) 2009.
- [29] KUEHN C., *Multiple Time Scale Dynamics* (Springer International Publishing, Switzerland) 2015.
- [30] SHILNIKOV A., *Int. J. Bifurcat. Chaos*, **18** (2008) 2141.

Stimulus-evoked activity in clustered networks of stochastic rate-based neurons

Igor Franović^{1,a} and Vladimir Klinshov^{2,b}

¹ Scientific Computing Laboratory, Center for the Study of Complex Systems, Institute of Physics Belgrade, University of Belgrade, Pregrevica 118, 11080 Belgrade, Serbia

² Institute of Applied Physics of the Russian Academy of Sciences, 46 Ulyanov Street, 603950 Nizhny Novgorod, Russia

Received 29 April 2018 / Received in final form 22 June 2018

Published online 12 December 2018

Abstract. Understanding the effect of network connectivity patterns on the relation between the spontaneous and the stimulus-evoked network activity has become one of the outstanding issues in neuroscience. We address this problem by considering a clustered network of stochastic rate-based neurons influenced by external and intrinsic noise. The bifurcation analysis of an effective model of network dynamics, comprised of coupled mean-field models representing each of the clusters, is used to gain insight into the structure of metastable states characterizing the spontaneous and the induced dynamics. We show that the induced dynamics strongly depends on whether the excitation is aimed at a certain cluster or the same fraction of randomly selected units, whereby the targeted stimulation reduces macroscopic variability by biasing the network toward a particular collective state. The immediate effect of clustering on the induced dynamics is established by comparing the excitation rates of a clustered and a homogeneous random network.

1 Introduction

Characterizing the structure of spontaneous emergent activity in neuronal populations, and the fashion in which it is modulated by the sensory stimuli, is fundamental to understanding the principles of information processing in the cortex. The generic patterns of spontaneous cortical dynamics, called slow rate fluctuations or UP–DOWN states, involve switching between the episodes of elevated neuronal and synaptic activity, and the stages of relative quiescence [1–3]. Alternation between UP and DOWN states is orchestrated by coherent action of individual neurons, with the observed rates typically lying in the range from 0.1 to 2 Hz [3]. Slow rate fluctuations give rise to macroscopic variability in the cortex [4,5], underlying in vivo activity during quiet wakefulness, sleep or under anesthesia [1,6,7], and even featuring in various in vitro preparations [8,9]. Our paper focuses on the open issues concerning the ingredients that affect the relationship between the stimulus-evoked and the ongoing

^a e-mail: franovic@ipb.ac.rs

^b e-mail: vladimir.klinshov@ipfran.ru

dynamics of neural assemblies, as well as the way the induced activity depends on the stimulus.

The research on induced patterns in sensory cortical areas has surprisingly shown that regardless of the type of stimuli, these patterns exhibit remarkable similarity to those of the idling activity [10–13]. In fact, the onset of UP–DOWN states has been recorded while performing perceptual tasks, but has also been found crucial to pyramidal neurons of neocortex, where it facilitates certain forms of learning and memory consolidation [1,14–17]. Such data evince that typical evoked activity patterns are drawn from a limited “vocabulary” already present within the spontaneous dynamics [10], whereby the sampling ability is pinned by the form of sensory stimuli. The striking similarity between the ongoing and the induced cortical activity is now considered as a generic feature of cortical dynamics, verified at increasing levels of structural complexity [18]. Certain experimental studies have linked the similarity to nontrivial properties of cortical connectivity, suggesting that it confines the pool of potential activity patterns [18]. By this paradigm, the structure of patterns reflects the modular (clustered) architecture of cortical networks, whereby certain patterns are activated by stimulating particular local subcircuits, known as the leader sites [19]. Conceptually, investigating the impact of clustered topology on different aspects of collective dynamics is biologically plausible [5,20], as recent research indicates strong prevalence of clustered over the homogeneous connectivity in cortical networks [21–24]. Clustering has already been shown to enable task-specialization, maintaining of high levels of neuronal activity, or adaptation to certain types of stimuli [25,26].

Here, we examine how the interplay of modular network architecture and noise influences the relation between the spontaneous and induced macroscopic activity, as well as how the macroscopic variability is affected by the different types of network stimulation. We analyze a model of a clustered network of noisy rate-based neurons [27–29], employing a second-order effective model of collective dynamics to gain insight into the structure of network’s metastable states. While the spontaneous activity consists of noise-induced fluctuations between the metastable states, we show that the specific type of stimulation, targeted at a certain cluster, biases the network toward a particular state, thereby reducing the macroscopic variability.

The origin of macroscopic variability, as an emergent network phenomenon, has so far been treated within two different frameworks, one associating slow rate fluctuations to deterministic networks, where balanced massive excitation and inhibition render the collective dynamics highly sensitive to fluctuations, and the other, which ties the slow rate fluctuations to multistability in attractor model networks, such that switching between coexisting states emerges due to noise, whose action amounts to a finite-size effect. In our recent paper [27], we have applied the latter approach, comparing the switching dynamics in clustered networks relative to random (statistically uniform) networks with the same average connectivity, having shown that clustering promotes multistability, thereby enhancing the switching phenomenon and its robustness. Here, the use of effective model of collective dynamics derived in [27] is extended to capture the response of random and clustered networks to external stimuli. In case of clustered networks, we compare the effects of two different stimulation protocols, including (i) the targeted stimulation, where an increased bias current is introduced only to units in a certain cluster, and (ii) the distributed stimulation, where the same fraction of randomly selected neurons is excited. It is found that due to modular architecture, the two stimulation scenarios may give rise to fundamentally different responses of the network.

The paper is organized as follows. In Section 2, we introduce the model of network dynamics and present the effective model of its macroscopic behavior. Section 3 contains the bifurcation analysis of the effective model of a clustered network in

the thermodynamic limit, applying it to anticipate the induced dynamics of the network. In Section 4, we compare the numerical results to the predictions of the mean-field model. Section 5 provides a brief summary and discussion on the obtained results.

2 Network dynamics: full and the effective model

We consider an m -cluster network comprised of N neurons, assuming random connectivity both within and between the clusters. The intra-cluster connectivity, specified by connectedness probability p_{in} , is more dense than the cross-connectivity p_{out} , whereby the degree of topological heterogeneity is characterized by the clustering parameter $g = p_{\text{in}}/p_{\text{out}}$. Larger g implies stronger clustering, such that the limiting case $g = 1$ describes the non-clustered (homogeneous random) network, while the case $g \rightarrow \infty$ corresponds to a network of uncoupled clusters. The clustering algorithm involves rewiring of a sparse random network, and thus preserves the average connectedness probability, set to a biologically plausible level $p = 0.2$. The parameters p_{in} and p_{out} can be linked to p via $p_{\text{in}} = \frac{gm}{m-1+g}p$ and $p_{\text{out}} = \frac{m}{m-1+g}p$, which allows one to explicitly compare the relevant parameter domains between the homogeneous and the clustered network.

The local dynamics follows a stochastic rate model [27–31]

$$\frac{dr_{Xi}}{dt} = -\lambda_X r_{Xi} + H(v_{Xi}) + \sqrt{2D}\xi_{Xi}(t), \tag{1}$$

where r_{Xi} is the firing rate of neuron i from cluster X , λ_X defines the rates relaxation time, and H is the nonlinear gain function, whose argument is the total input to a neuron v_{Xi} . The latter is given by $v_{Xi} = u_{Xi} + I_X + \sqrt{2B}\eta_{Xi}(t)$, where u_{Xi} is the synaptic input $u_{Xi} = \kappa \sum_Y \sum_j a_{YXji} r_{Yj}$ and I_X denotes the external bias current. The coupling scheme is specified by the adjacency matrix $a_{YXji} \in \{0, 1\}$, such that a_{YXji} stands for the link projecting from neuron j in cluster Y to neuron i in cluster X . Coupling weights are assumed to be homogeneous and scale with the network size as $\kappa = K_{YX}/N$. The random perturbations in the microscopic dynamics derive from two distinct sources of noise. In particular, the external noise, characterized by B , and the intrinsic noise, described by D , are introduced to account for the action of synaptic and ion-channel noise, respectively. All the associated fluctuations are independent and are given by Gaussian white noise.

Note that the form (1) is quite general, in a sense that by choosing different H , one may interpolate between different classes of models, including Wilson–Cowan or Hopfield model. From a broader perspective, a plausible gain function should meet three simple requirements: it should drop to zero for sufficiently small input, exhibit saturation for large enough input, and just be monotonous for intermediate input values. Here, the form of H

$$\mathcal{H}(U) = \begin{cases} 0, & U \leq 0, \\ 3U^2 - 2U^3, & 0 < U < 1, \\ 1, & U \geq 1. \end{cases} \tag{2}$$

is selected to make the analysis of macroscopic dynamics analytically tractable [27–29]. Note that the qualitative physical picture associated to the collective multi-stable behavior in assemblies of neurons with rate-based dynamics does not depend

on the particular choice of the gain function. This point has been extensively elaborated in [30], and we have also numerically verified that the results presented here persist for the Heaviside-like gain function.

2.1 Effective model of clustered network dynamics

The effective model of network dynamics is comprised of coupled mean-field models representing the activities of particular clusters. Typically, the effective models of network behavior concern either the case of random sparse connectivity or the case of full connectivity. In this context, our model can be seen as interpolating between the two standard scenarios, featuring dense intra-cluster connectivity and sparse inter-cluster connections. The applied mean-field approach involves a Gaussian closure hypothesis [32–35], such that the collective dynamics of each cluster X is described by the mean-rate R_X and the associated variance S_X

$$R_X = \frac{1}{N_X} \sum_i r_{Xi} \equiv \langle r_{Xi} \rangle S_X = \langle r_{Xi}^2 \rangle - R_X^2, \quad (3)$$

where $\langle \cdot \rangle$ denotes averaging over the neurons within the given cluster. For each of the clusters, we use the bottom-up approach to obtain the second-order stochastic equations of macroscopic behavior. With the detailed derivation of the effective model already provided in [27], here we only briefly outline the two main steps necessary to carry out the appropriate averaging over the microscopic dynamics, namely the Ansatz on local variables and the Taylor expansion of \mathcal{H} function.

The Ansatz on local variables consists in writing r_{Xi} as $r_{Xi} = R_X + \sqrt{S_X} \rho_{Xi}$ [36], where $\{\rho_{Xi}\}$ is a set of variables satisfying $\langle \rho_{Xi} \rangle = 0$, $\langle \rho_{Xi}^2 \rangle = 1$, as readily follows from definition (3). The introduced Ansatz is applied to rewrite the total input to a neuron as $v_{xi} = U_X + \delta v_{Xi}$, where

$$U_X = I_X + \kappa \sum_Y p_{YX} N_Y R_Y \quad (4)$$

presents the assembly-averaged input to cluster X , p_{YX} denotes the connectedness probability from cluster Y to cluster X , and N_Y is the size of cluster Y . The deviation δv_{Xi} from the average input U_X consists of two terms:

$$\delta v_{Xi} = \kappa \sum_Y R_Y \nu_{YXi} + \kappa \sum_Y \sqrt{S_Y} \sigma_{YXi}. \quad (5)$$

The first term accounts for the topological effect associated to the deviation $\nu_{YXi} = \sum_j a_{YXji} - p_{YX} N_Y$ from the average number of connections $p_{YX} N_Y$, whereas the second term captures the effect of local rate fluctuations, contained within the factor $\sigma_{YXi} = \sum_j a_{YXji} \rho_{Yj}$. Equations (4) and (5) allow one to average the terms containing the gain function by developing $H(v_{Xi})$ about U_X up to second order. This leads to $H(v_{Xi}) = H_{0X} + H_{1X} \delta v_{Xi} + H_{2X} \delta v_{Xi}^2$, having introduced notation $H_{0X} \equiv H(U_X)$, $H_{1X} = \frac{dH}{dv_{Xi}}(U_X)$, $H_{2X} = \frac{1}{2} \frac{d^2H}{dv_{Xi}^2}(U_X)$.

Following a number of intermediate steps elaborated in [27], one arrives at the effective model of network dynamics stated in terms of interacting finite-size mean-field models describing the cluster dynamics. The effective model is given by

$$\begin{aligned} \frac{dR_X}{dt} &= -\lambda_X R_X + H_{0X} + 2B_X H_{2X} + H_{2X} \sum_Y K_{YX}^2 p_{YX} N_Y (R_Y^2 + S_Y) / N^2 \\ &\quad + \sqrt{\Psi_X} \beta(t) + \sqrt{\Omega_X} \eta, \\ \frac{dS_X}{dt} &= -2\lambda_X S_X + 2B_X H_{1X}^2 + 2D_X, \end{aligned} \tag{6}$$

and involves three types of finite-size effects, including the small deterministic correction term, the effective “macroscopic” noise of intensity Ψ_X , as well as the quenched randomness, accounting for the fact that each particular network realization features distinct deviations from the average connectivity degree. The macroscopic noise is multiplicative

$$\Psi_X = \frac{1}{N} (2D_X + 2B_X H_{1X}^2) + \frac{1}{N} H_{1X}^2 \sum_Y K_{YX}^2 p_{YX} \frac{N_Y}{N_X} S_Y, \tag{7}$$

and incorporates three terms: the first two describe how the local external and intrinsic noise are translated to macroscopic level, whereas the third one reflects the impact of local fluctuations in the input arriving to each neuron in the cluster. At variance with the time-varying stochastic term featuring $\beta(t)$, the effect of quenched randomness in (6) is characterized by a constant random term of magnitude $\Omega_X = \frac{1}{N} H_{1X}^2 \sum_Y K_{YX}^2 p_{YX} \frac{N_Y}{N_X} R_Y^2$, with η being just a constant random number $\mathcal{N}(0, 1)$.

In the S_X dynamics, for simplicity we omit all the finite-size effects, including the deterministic correction and the stochastic terms. One may do so because the variance S_X only affects the $\mathcal{O}(1/N)$ terms in the dynamics of R_X .

3 Bifurcation analysis of the effective model in the thermodynamic limit

In this section, we carry out the bifurcation analysis of the system (6) in the limit $N \rightarrow \infty$ to characterize the response of a clustered network to external stimuli. Our focus is on the scenario of targeted stimulation, where an increased bias current is applied to a certain cluster, while the rest of the network remains unperturbed. The stimulation is provided in the form of a rectangular pulse, whose duration Δ is sufficiently long such that the network is allowed to reach the new metastable state. Our analysis will address the issues of why the evoked states of the network are similar to those occurring within the spontaneous activity, and how the stimulus biases the network dynamics to a particular collective state. Note that the system (6) holds for networks of an arbitrary number of clusters of arbitrary sizes, but for simplicity we consider the case of m equal clusters of size $N_c = N/m$.

In our previous study, the model (6) has been analyzed in case where the entire network receives homogeneous external current I . Here, we deal with inhomogeneous stimulation, conforming to a paradigm with l clusters delivered the current I_A , whereas the remaining ones are influenced by I_B . One is interested into solutions where the mean activity of the unperturbed clusters equals R_B , whereas the state of

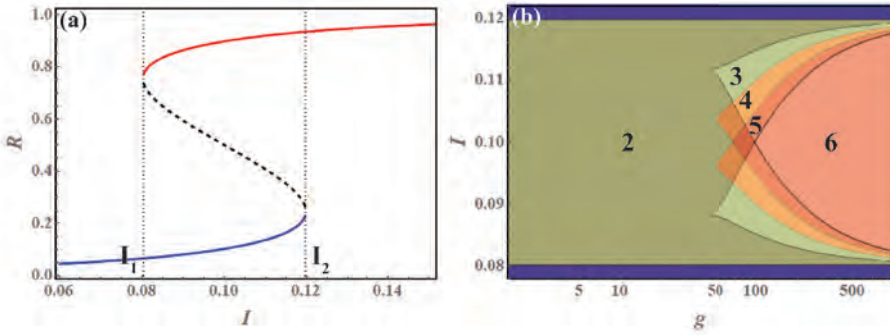


Fig. 1. (a) Bifurcation diagram $R(I)$ for the non-clustered network subjected to homogeneous stimulation. The network parameters are $\alpha = 0.8$, $B = 0.004$, $D = 0.02$ and $g = 1$. (b) Bifurcation diagram for the clustered network $m = 5$ influenced by the homogeneous stimulation: bias current I against logarithm of the clustering coefficient g . The numbers indicate how many coexisting attractors exist within the given region.

the excited clusters R_A may be different. Neglecting the finite-size effects $\mathcal{O}(1/N)$, it follows that the network dynamics is given by

$$\begin{aligned} \frac{dR_A}{dt} &= -R_A - 2U_A(R_A, R_B)^3 + 3U_A(R_A, R_B)^2 + 6B(1 - 2U_A(R_A, R_B)) \\ \frac{dR_B}{dt} &= -R_B - 2U_B(R_A, R_B)^3 + 3U_B(R_A, R_B)^2 + 6B(1 - 2U_B(R_A, R_B)), \end{aligned} \quad (8)$$

where the average input to the two subsets of clusters reads

$$\begin{aligned} U_A(R_A, R_B) &= I_A + \frac{\alpha}{m-1+g} \left[(g+l-1)R_A + (m-l)R_B \right] \\ U_B(R_A, R_B) &= I_B + \frac{\alpha}{m-1+g} \left[lR_A + (g+m-l-1)R_B \right], \end{aligned} \quad (9)$$

having $\alpha = Kp$ denote the network coupling parameter.

Prior to analyzing the induced dynamics of the network, let us briefly consider the spontaneous activity, which is in this framework represented by a setup with homogeneous bias currents $I_A = I_B = I$. In case of a non-clustered network ($g = 1$), one observes bistability in a certain interval $I \in [I_1, I_2]$ [29], provided the coupling parameter α is sufficiently large. The corresponding bifurcation diagram $R(\alpha)$ in Figure 1a contains two stable branches associated to the UP and DOWN states of the network. Introducing sufficiently strong clustering promotes multistability, giving rise to network states which do not exist in the non-clustered case. The increased number of network levels derives from the states with broken symmetry, where subsets of clusters may lie in their respective high or low states [27]. For such inhomogeneous collective states, the system symmetry is reduced from the permutation group Σ_m (permutation of all cluster indices), to a subgroup of the type $\Sigma_l \otimes \Sigma_{m-l}$, where $l \in \{1, 2, \dots, m-1\}$. Given that each cluster may either lie in the low or the high state, the maximal multistability of a network comprised of m clusters is $m+1$. To provide an example, in Figure 1b is shown a bifurcation diagram in the (g, I) plane for a modular network $m = 5$. There, one observes that maximal multistability is facilitated by the clustering parameter $g \gtrsim 100$.

Note that the external noise B acts in (8) as a bifurcation parameter, influencing the number and position of stationary states in the thermodynamic limit. Figure 2a

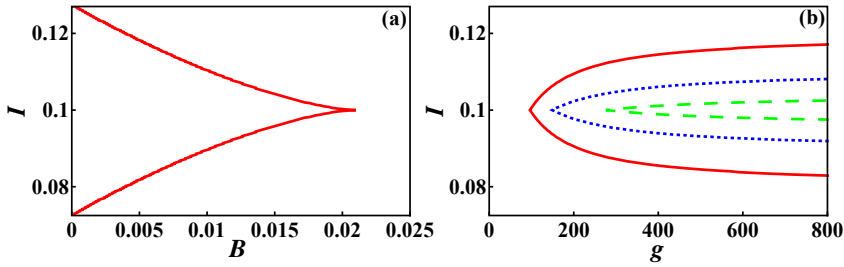


Fig. 2. (a) Bifurcation diagram in the (B, I) for the non-clustered network subjected to homogeneous stimulation. The remaining parameters are $\alpha = 0.8$, $D = 0.02$ and $g = 1$. (b) Shift of the maximal multistability region in the (g, I) plane for a clustered network $m = 5$. The red solid lines outline the maximal multistability domain for noise level $B = 0.004$, whereas the blue dotted lines and the green dashed lines correspond to $B = 0.01$ and $B = 0.015$, respectively.

shows the bifurcation diagram referring to spontaneous activity of the non-clustered network in the (B, I) plane, obtained under fixed connectivity $\alpha = 0.8$. The bistability region again lies between two branches of fold bifurcations (red curves) that meet at the cusp point, where a pitchfork bifurcation occurs. One finds that for fixed I , there always exists a B value above which a non-clustered network can no longer support bistable behavior. For the spontaneous dynamics of a clustered network, it can be shown that the region of maximal multistability in the (g, I) plane, bounded by two curves of fold bifurcations intersecting at the pitchfork bifurcation, reduces and shifts toward stronger clustering under increasing B , cf. Figure 2b. In other words, for higher external noise, one requires larger clustering in order to observe maximal multistability in the network.

To investigate the scenario of a targeted stimulation, we analyze the network’s response by looking into solutions of (8) for $l = 1$, such that the stimulated cluster occupies the state different from the remaining clusters. The clustering coefficient g and the stimulation current I_A are considered as control parameters, while the remaining parameters $\alpha = 0.8$, $B = 0.004$, and $I_B = 0.1$ are such that the spontaneous dynamics of the associated homogeneous random network with $I = I_B$ pertains to bistability region in Figure 1a. The (g, I_A) bifurcation diagram explaining the action of targeted stimulation is plotted in Figure 3a. For $I_A \approx I_B$ and strong enough clustering, the network possesses four stable steady states, which can readily be traced in the limit of ultimate clustering $g \rightarrow \infty$. Indeed, suppose that a network is decomposed into a set of non-interacting clusters, and that I_A and I_B lie within the interval $[I_1, I_2]$ from Figure 1a. Then, each of the clusters is bistable, which gives exactly four stable steady states in the full system (8). The area of maximal multistability, where both the stimulated cluster and the resting network may either occupy the low or the high state, extends to moderate clustering $g \sim 100$. In Figure 3b, the four stable steady states of the effective model are denoted by O_{LL} , O_{LH} , O_{HL} and O_{HH} . Note that the first and second index refer to states of the stimulated cluster and the rest of the network, respectively, whereby L/H indicates the low/high level, and U denotes the unstable state.

As the stimulation I_A increases, the system undergoes a saddle-node bifurcation in which the states O_{LH} and O_{UH} are annihilated, see the curve C_1 in Figure 3a. Then the system passes to the area with 3 stable steady states, with the corresponding phase portrait shown in Figure 3c. Further growth of I_A causes the states O_{LL} and O_{UL} to collide, cf. the curve C_2 in Figure 3a, such that the system becomes bistable, as corroborated by the phase portrait in Figure 3d. For small g , very strong simulation I_A leads to a collision and disappearance of the steady states O_{HL}

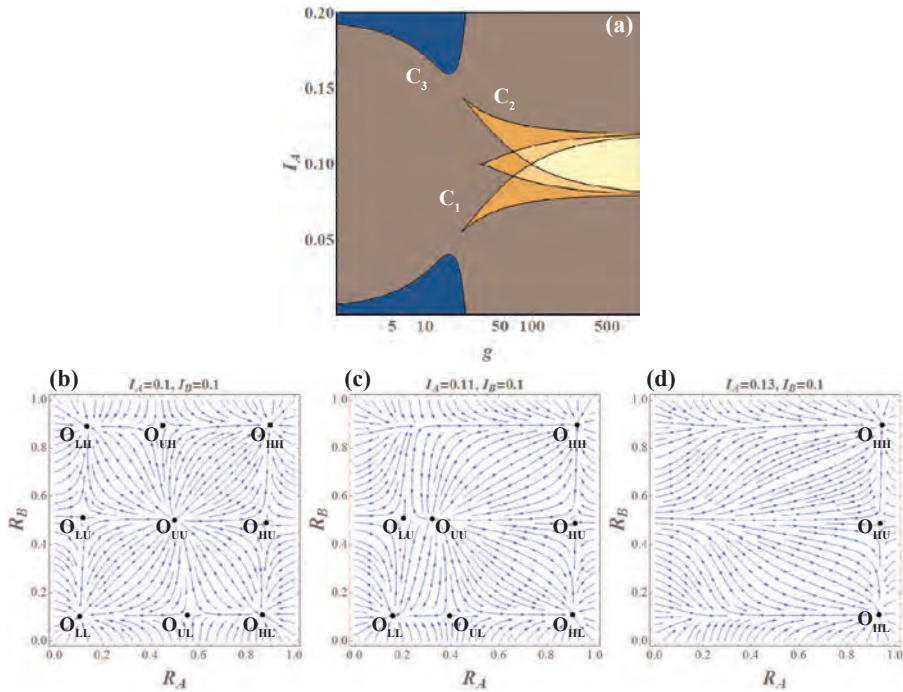


Fig. 3. (a) Bifurcation diagram $I_A(g)$ of system (8), with the number of coexisting solutions indicated for particular regions. The remaining parameters are fixed to $\alpha = 0.8$, $B = 0.004$, $D = 0.02$, $m = 5$ and $I_B = 0.1$. (b–d) Phase portraits associated to system (8) under increasing I_A .

and O_{HU} , see the curve C_3 in Figure 3a, whereby the system becomes monostable. Note that the decrease of I_A (targeted inhibition) gives rise to a similar scenario. When I_A is systematically reduced, the system first becomes tristable with coexisting states O_{LL} , O_{LH} and O_{HH} , then bistable and eventually passes to monostability domains.

4 Numerical results: targeted vs. distributed stimulation

In this section, our aim is to first explicitly demonstrate that the effective model (8) can successfully predict the response of a clustered network in case of targeted stimulation. Nevertheless, we shall also show an interesting effect evincing that the response of modular networks to external stimulation is strongly dependent on the character of stimulation, i.e. the fashion in which it is distributed to neurons within the network.

In Figure 4, the response of a clustered network $m = 5$ to a targeted stimulation is compared against the induced dynamics of the effective model analyzed in Section 3. Note that the numerical experiments concerning the full system (1) have been carried out on a relatively small network comprised of $N = 300$ neurons, which corresponds to only 60 neurons per cluster, having fixed the noise levels to $D = 0.02$ and $B = 0.004$. Given the relatively small cluster size, one would expect strong fluctuations in the network dynamics. Nevertheless, it will be shown that even under such conditions, the mean-field analysis performed in case of thermodynamic limit still remains qualitatively valid, in a sense of being able to qualitatively capture the induced behavior of the network.

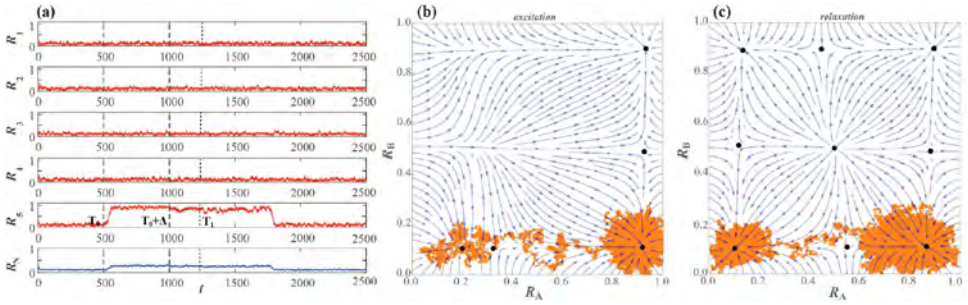


Fig. 4. (a) Response of a clustered network ($m = 5$) to a stimulus of intensity I_A and duration Δ introduced to cluster 5 at the moment T_0 . Notation $R_i, i \in [1, 5]$ refers to mean-rates of particular clusters, whereas R_N stands for the collective network activity. Panels (b) and (c) show excitation and relaxation processes of the network in the (R_A, R_B) plane, respectively. The system’s orbit is superimposed on the vector field of the effective model (8), obtained for $(I_A, I_B) = (0.12, 0.1)$ in (b) and $I_A = I_B = 0.1$ in (c). The remaining parameters are $g = 250, B = 0.004, D = 0.02$.

The scenario of targeted stimulation unfolds in such a way that before introducing the stimulation, all the clusters occupy the low state and are influenced by the same current $I_A = I_B = 0.1$. Then, at the moment $T_0 = 500$, a rectangular pulse of elevated bias current $I_A = 0.12$ is introduced solely to cluster 5. The pulse is maintained for a sufficiently long time $\Delta = 500$, such that the network is allowed to reach the new metastable state. Note that during the stimulation, I_A lies very close to the bifurcation curve C_2 from Figure 3a. Therefore the state O_{LL} is weakly stable, and the finite-size fluctuations may easily drive the system away from it, as indicated by the time traces in Figure 4a. In Figure 4b, we have plotted the excitation orbit of the network in the (R_A, R_B) plane in order to demonstrate that the system switches between the metastable states anticipated by the effective model (8). In particular, the vector field provided in the background presents the flow of system (8) for $(I_A, I_B) = (0.12, 0.1)$. One observes that the network rapidly leaves the vicinity of the state O_{LL} and switches to O_{HL} , conforming to the path where a single cluster, described by R_A , is perturbed by the stimulation, whereas the remaining clusters, associated to R_B , remain unaffected.

We have also examined the relaxation process of the network after the termination of the stimulus at $t = T_0 + \Delta$. In Figure 4c, the relaxation orbit is plotted against the vector field of the system (8) for $I_A = I_B = 0.1$. As predicted by the effective model, the state O_{HL} lies far from bifurcations, which makes it relatively stable, in a sense that the network may spend quite a long time in its vicinity. However, the fluctuations induced by the finite-size effect eventually drive the network back to the homogeneous DOWN state O_{LL} .

The dependence of the networks response on the stimulation magnitude I_A is illustrated in Figure 5. The response is characterized by the "excitation rate" γ , defined as the average fraction of excited neurons at the moment $T_0 + \Delta$ just after the stimulus has ceased, having performed averaging over an ensemble of 80 stochastic realizations. Since the targeted stimulation may only give rise to excitation of a single cluster, γ in this case is merely the probability of cluster excitation. The response function $\gamma(I_A)$ exhibits threshold-like behavior, with the rising stage triggered at $I_A \approx 0.11$ and completed at $I_A \approx 0.12$, cf. the blue solid line with empty circles. Note that the latter value is in perfect agreement with the prediction of the bifurcation diagram in Figure 3a. For large I_A , the excitation rate saturates at $\gamma = 1/m = 0.2$, which implies that only a single cluster is excited regardless of how large I_A becomes.

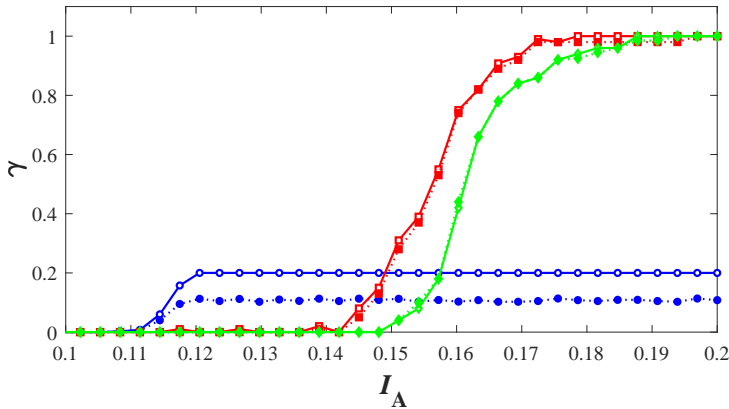


Fig. 5. Excitation rate, i.e. fraction of excited clusters γ in terms of I_A for the different stimulation scenarios. The circles and squares refer to targeted and distributed stimulation of a clustered network ($m = 5, g = 250$), respectively, whereas the diamonds indicate the response of a homogeneous random network ($g = 1$). The empty symbols connected by solid lines denote γ values at the moment $T_0 + \Delta$ when the stimulation is terminated. The solid symbols connected by the dotted lines show γ at the moment T_1 after the stimulation has ceased, cf. Figure 4a. The remaining network parameters are $B = 0.004$, $D = 0.02$ and $I_B = 0.1$.

In general, the persistence of the elevated state does not depend on the applied stimulation magnitude I_A , but is rather determined by the relaxation speed of the state the network occupies at the moment $T_0 + \Delta$ when the stimulation is terminated. In order to analyze the features of the relaxation process, we have measured the excitation rate γ at a later moment $T_1 = 1250$, sufficiently long after the excitation pulse has ceased, cf. the blue dotted line connecting the filled circles in Figure 5. Since in the case of targeted stimulation one always encounters the same excited state with only a single cluster perturbed, it is natural to expect proportionality between the excitation rate immediately after the stimulation (moment $T_0 + \Delta$) and at a later moment T_1 . Our results corroborate that the elevated state may indeed persist considerably longer than the triggering pulse.

As already announced, we also report on an interesting finding that the induced dynamics of modular networks strongly depends on the applied stimulation protocol. In particular, suppose that instead of a targeted stimulation, one introduces an elevated bias current to the same fraction of neurons as in a single cluster, but just randomly distributed over the network. We refer to such a scenario as “distributed stimulation”. In this instance, for sufficiently large stimulation I_A , the network may reach states where substantially more than a single cluster is elicited, in spite of relatively large clustering coefficient g .

The network excitation rate as a function of I_A for the case of distributed stimulation is indicated by the solid red line with empty squares in Figure 5. One immediately realizes that the impact of the distributed stimulation is quite distinct from that of the targeted one in two aspects: (i) the I_A threshold where it starts to excite a single cluster is significantly larger than for the targeted stimulation and (ii) for sufficiently strong stimulation I_A , all the clusters may cross to high state.

To gain a deeper insight into how the network’s response is shaped by clustering, we consider an additional scenario, where a certain fraction of neurons is stimulated in a homogeneous random network $g = 1$. To allow the comparison, we have perturbed the same fraction of units as in the clustered network, but here one cannot distinguish between the targeted and the distributed stimulation protocols

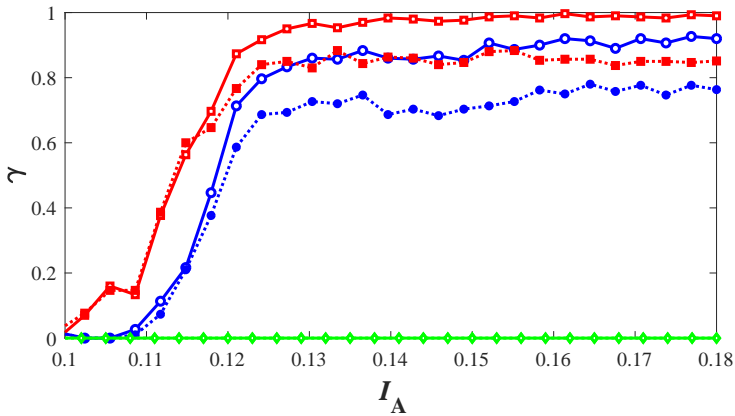


Fig. 6. Dependence of excitation rate γ on the applied current I_A for levels of external noise B where the network cannot exhibit maximal multistability. The green diamonds concern the response of a homogeneous random network $g = 1$ in case where the effective model exhibits only the DOWN state ($B = 0.028, D = 0.02, I_B = 0.1$). The blue circles and the red squares refer cases of a targeted and distributed stimulation of a clustered network $m = 5$, respectively. In the thermodynamic limit, the parameters of the clustered network facilitate bistable dynamics between the homogeneous UP and DOWN states ($B = 0.018, D = 0.02, g = 60, I_B = 0.1$). The solid/empty symbols are used the same way as in Figure 5.

because any subset of units is equivalent. The ensuing excitation rate, plotted in Figure 5 by the solid green line, indicates a response substantially distinct from that of a clustered network in case of targeted stimulation, but reminiscent of the induced dynamics typical for the distributed stimulation. This is so because the homogeneous network possesses only two metastable states, namely the homogeneous DOWN and UP states, which implies that one cannot excite only a certain fraction of units, but can rather excite the entire network. As the DOWN state vanishes at the bifurcation curve C_3 in Figure 3a, the guaranteed excitation of the network is observed only if I_A lies sufficiently close to this curve. The associated threshold current corresponds to the saturation of the excitation rate observed at $I_A \approx 0.19$ in Figure 5.

As already indicated, the external noise influences the multistable dynamics of both the homogeneous and the clustered networks. In Figure 6, it is examined how the excitation rate changes if the level of external noise B is increased such that the network can no longer exhibit maximal multistability in the thermodynamic limit. For the non-clustered network, we have considered the case where the deterministic dynamics is monostable, admitting only the DOWN state. As expected, stimulating a fraction of neurons with arbitrary strong external current cannot switch the network to the UP state, cf. the green diamonds in Figure 6. For the clustered network $m = 5$, the external noise B and the clustering coefficient g have been set such that the deterministic dynamics exhibits only bistability between the homogeneous UP and DOWN states. For both the scenarios of the targeted and distributed stimulation protocols, the excitation rate exhibits a threshold-like behavior, ultimately reaching the network-wide UP state for a sufficiently strong stimulation. As predicted by the effective model, the targeted stimulation can no longer bring the network to a heterogeneous state where only a single cluster is excited.

5 Summary and discussion

In the present paper, we have analyzed the induced dynamics of a clustered network subjected to two types of stimulation protocols, the targeted stimulation and the distributed stimulation. In the former case, it has explicitly been demonstrated that the effective model, describing the macroscopic dynamics in terms of coupled mean-field models associated to each of the clusters, may accurately capture the networks response, predicting the metastable state reached by the network.

An interesting finding is that the response of a clustered network strongly depends on the applied stimulation protocol. In particular, in case of a targeted stimulation, under sufficiently strong clustering, one typically observes that only the targeted cluster is activated, whereas the remaining clusters are unaffected by the perturbation. Nevertheless, for the distributed stimulation, applying a sufficiently strong excitation may result in much richer dynamics, where different forms of elevated states, including a network-wide high state, may be reached.

Concerning the immediate impact of the modular network architecture, we have established that the response of a clustered network is drastically different from that of a statistically homogeneous one even if the same number of randomly selected units is stimulated. In particular, given the same stimulation magnitude, the excitation rate of the homogeneous random network turns out to be substantially lower than that of a clustered network. This distinction derives from the fact that a non-clustered network cannot exhibit heterogeneous states. As expected, the differences in behavior of the non-clustered and clustered networks vanish for sufficiently strong stimuli, where the network-wide excitation becomes the prevalent scenario regardless of the network structure. In case of a non-clustered network, the reduced model has been shown to provide a good estimate of the threshold current that guarantees reaching the elevated state.

The external noise has been found to play a nontrivial role with respect to the excitation process, because it affects the features of the network's multistable behavior in the thermodynamic limit. This is a consequence of the fact that the macroscopic noise derived from the local external noise is multiplicative [37]. The associated changes in the multistability have been shown to substantially influence the excitation rates in clustered networks for both the stimulation protocols, as well as in the scenario where the stimulus acts on a certain fraction of neurons in a non-clustered network.

For the particular stimulation protocol, the properties of the relaxation process are found not to be determined by the intensity of excitation, but rather by the state of the network at the moment the stimulation is terminated. One should note that instances of prolonged relaxation have been observed, especially in the case of distributed stimulation under higher intensities of the applied current, which facilitate excitation to the homogeneous UP state. The lifetimes of the metastable states are also influenced by the level of the external noise, and the underlying effects provide an interesting topic for future studies. In particular, the impact of multistability on the relaxation process may consist in inducing nonlinear dependencies of relaxation times on the noise level, which can manifest as noise-enhanced stability of metastable states [38,39].

Within the present study, we have explained by the effective model, and corroborated numerically, why the induced dynamics of a clustered network resembles the spontaneous one, further demonstrating how the stimulation biases the network toward a particular collective state. Recent experimental research indicates that the external stimulation reduces both the macroscopic and the microscopic neuronal variability [10,40,41], the latter being associated to randomness in local dynamics, viz. the spiking series of individual units. While our results may indeed account for the stimulation-induced decrease of macroscopic variability, one cannot

infer anything regarding the microscopic variability, since we apply a rate-based neuron model. In this context, it would be of interest to consider in detail the induced dynamics of a clustered network of spiking neurons via an effective model, especially given that the numerical results in [5,13,20] already link the stimulated activity with reduction of both the macroscopic and microscopic neuronal variability.

This work is supported by the Ministry of Education, Science and Technological Development of Republic of Serbia under project No. 171017, by the Russian Foundation for Basic Research under project No. 17-02-00904, and by the Russian Science Foundation under project No. 16-42-01043.

References

1. T.T.G. Hahn, J.M. McFarland, S. Berberich, B. Sakmann, M.R. Mehta, *Nat. Neurosci.* **15**, 1531 (2012)
2. G. Buzsáki, C.A. Anastassiou, C. Koch, *Nat. Rev. Neurosci.* **13**, 407 (2012)
3. V.V. Vyazovskiy, K.D. Harris, *Nat. Rev. Neurosci.* **14**, 443 (2013)
4. M.R. Cohen, A. Kohn, *Nat. Neurosci.* **14**, 811 (2011)
5. A. Litwin-Kumar, B. Doiron, *Nat. Neurosci.* **15**, 1498 (2012)
6. C.C.H. Petersen, T.T.G. Hahn, M. Mehta, A. Grinvald, B. Sakmann, *Proc. Natl. Acad. Sci. U.S.A.* **100**, 13638 (2003)
7. D. Millman, S. Mihalas, A. Kirkwood, E. Niebur, *Nat. Phys.* **6**, 801 (2010)
8. J. Anderson et al., *Nat. Neurosci.* **3**, 617 (2000)
9. R. Cossart, D. Aronov, R. Yuste, *Nature* **423**, 283 (2003)
10. A. Luczak, P. Barthó, K.D. Harris, *Neuron* **62**, 413 (2009)
11. A. Luczak, P. Barthó, K.D. Harris, *J. Neurosci.* **33**, 1684 (2013)
12. D.L. Ringach, *Curr. Opin. Neurobiol.* **19**, 439 (2009)
13. G. Deco, E. Hugues, *PLoS Comput. Biol.* **8**, e1002395 (2012)
14. D. Ji, M.A. Wilson, *Nat. Neurosci.* **10**, 100 (2007)
15. S. Diekelmann, J. Born, *Nat. Rev. Neurosci.* **11**, 114 (2010)
16. D. Miyamoto et al., *Science* **352**, 1315 (2016)
17. G. Rothschild, E. Eban, L.M. Frank, *Nat. Neurosci.* **20**, 251 (2017)
18. J.L. Vincent et al. *Nature* **447**, 83 (2007)
19. V. Pasquale, S. Martinoia, M. Chiappalone, *Sci. Rep.* **7**, 9080 (2017)
20. B. Doiron, A. Litwin-Kumar, *Front. Comput. Neurosci.* **8**, 56 (2014)
21. S. Song, P. Sjöström, M. Reigl, S. Nelson, D. Chklovskii, *PLoS Biol.* **3**, e68 (2005)
22. S. Lefort, C. Tamm, J.-C.F. Sarria, C.C.H. Petersen, J.C. Floyd Sarria, C.C.H. Petersen, *Neuron* **61**, 301 (2009)
23. R. Perin, M. Telefont, H. Markram, *Front. Neuroanat.* **7**, 1 (2013)
24. V.V. Klinshov, J.N. Teramae, V.I. Nekorkin, T. Fukai, *PLoS One* **9**, e94292 (2014)
25. S.B. Hofer, H. Ko, B. Pichler, J. Vogelstein, H. Ros et al., *Nat. Neurosci.* **14**, 1045 (2011)
26. H. Ko, S.B. Hofer, B. Pichler, K.A. Buchanan, P.J. Sjöström, T.D. Mrsic-Flogel, *Nature* **473**, 87 (2011)
27. I. Franović, V. Klinshov, *Chaos* **28**, 023111 (2018)
28. I. Franović, V. Klinshov, *Europhys. Lett.* **116**, 48002 (2016)
29. V. Klinshov, I. Franović, *Phys. Rev. E* **92**, 062813 (2015)
30. H. Hasegawa, *Phys. Rev. E* **75**, 051904 (2007)
31. R.A. Anderson, S. Musallam, B. Pesaran, *Curr. Opin. Neurobiol.* **14**, 720 (2004)
32. B. Lindner, J. Garcia-Ojalvo, A. Neiman, L. Schimansky-Geier, *Phys. Rep.* **392**, 321 (2004)
33. M.A. Zaks, X. Sailer, L. Schimansky-Geier, A.B. Neiman, *Chaos* **15**, 026117 (2005)
34. I. Franović, K. Todorović, N. Vasović, N. Burić, *Phys. Rev. E* **87**, 012922 (2013)

35. I. Franović, K. Todorović, N. Vasović, N. Burić, *Phys. Rev. E* **89**, 022926 (2014)
36. A.N. Burkitt, *Biol. Cybern.* **95**, 1 (2006)
37. S. Ciuchi, F. de Pasquale, B. Spagnolo, *Phys. Rev. E* **47**, 3915 (1993)
38. N.V. Agudov, A.A. Dubkov, B. Spagnolo, *Physica A* **325**, 144 (2003)
39. G. Augello, D. Valentia, B. Spagnolo, *Eur. Phys. J. B* **78**, 225 (2010)
40. L. Mazzucato, A. Fontanini, G. La Camera, *J. Neurosci.* **35**, 8214 (2015)
41. I.-C. Lin, M. Okun, M. Carandini, K.D. Harris, *Neuron* **87**, 644 (2015)

Noise-induced switching in two adaptively coupled excitable systems

Iva Bačić¹, Serhiy Yanchuk², Matthias Wolfrum³, and Igor Franović^{1,a}

¹ Scientific Computing Laboratory, Center for the Study of Complex Systems, Institute of Physics Belgrade, University of Belgrade, Pregrevica 118, 11080 Belgrade, Serbia

² Institute of Mathematics, Technische Universität Berlin, Straße des 17. Juni 136, 10623 Berlin, Germany

³ Weierstrass Institute, Mohrenstrasse 39, 10117 Berlin, Germany

Received 30 April 2018 / Received in final form 19 June 2018
Published online 12 December 2018

Abstract. We demonstrate that the interplay of noise and plasticity gives rise to slow stochastic fluctuations in a system of two adaptively coupled active rotators with excitable local dynamics. Depending on the adaptation rate, two qualitatively different types of switching behavior are observed. For slower adaptation, one finds alternation between two modes of noise-induced oscillations, whereby the modes are distinguished by the different order of spiking between the units. In case of faster adaptation, the system switches between the metastable states derived from coexisting attractors of the corresponding deterministic system, whereby the phases exhibit a bursting-like behavior. The qualitative features of the switching dynamics are analyzed within the framework of fast-slow analysis.

1 Introduction

In many complex systems, ranging from biology, physics and chemistry to social sciences and engineering, the interaction patterns are not static, but are rather affected by the states of constituent units [1–4]. This gives rise to complex feedback mechanisms, where the coupling weights adapt to dynamical processes at the units, which in turn influences the evolution of units itself. Modeling of such systems is based on the paradigm of adaptive networks, where self-organization unfolds both at the level of coupling weights and the collective states of the units, typically involving a separation of characteristic timescales. The faster and the slower timescales are naturally associated to the dynamics of units and couplings, respectively, such that the short-term evolution of the units occurs on a quasi-static network, whereas the slow changes in coupling weights depend on the time-averaged dynamics of the units. An important example of adaptive connectivity is provided by neuronal systems, where the strength of synaptic couplings is adjusted to the underlying spiking activity via spike-time-dependent plasticity (STDP), a temporally asymmetric form of Hebbian learning [5],

^a e-mail: franovic@ipb.ac.rs

promoting causal relationship between the spikes of pre- and postsynaptic neurons [6–8].

Motivated by the research on neuronal systems, in the present paper we study a simplified model which incorporates the basic ingredients of neurodynamics, such as excitability, plasticity and noise. The considered system consists of two adaptively coupled active rotators, whose intrinsic dynamics is set to excitable regime and subjected to noise. The plasticity rule is introduced in such a way that one may continuously interpolate between the coupling dynamics characteristic to Hebbian learning and STDP. We demonstrate that the interplay of plasticity and noise may facilitate two qualitatively different forms of slow stochastic fluctuations, depending on the adaptation rate. While for slower adaptation the self-organized dynamics consists of switching between the two modes of noise-induced oscillations, in case of faster adaptation, the switching dynamics comprises metastable states associated to attractors of the deterministic system.

In the context of neuroscience, one may compare the considered system to a binary neuron motif. It is well known that the same structural motif, defined at the level of anatomy, can support multiple functional motifs [9–12], characterized by different weight configurations and potentially distinct directions of information flow. In these terms, our study will show that the co-effect of plasticity and noise may (i) contribute to the emergence of different functional motifs on top of the given structural one and (ii) trigger slow alternation between the functional motifs.

So far, the co-effects of noise and the STDP plasticity rule have been analyzed in systems of two coupled neural oscillators, as well as in networks of oscillators. In case of two units, multistability between different weight configurations has been found, surprisingly indicating that noise may stabilize configurations of strong bidirectional coupling absent in the deterministic system [13]. At variance with this, our study concerns excitable local dynamics and explicitly addresses the slow stochastic fluctuations between metastable states. For networks of adaptively coupled neural or phase oscillators, the previous research has mainly focused on the impact of plasticity on the synchronization behavior. In the absence of noise, several generic forms of macroscopic dynamics have been identified, including desynchronized or partially synchronized states with weak couplings, as well as cluster states [14–18]. In presence of noise, an interesting effect of self-organized noise resistance to desynchronization has been reported in the case of a network of neural oscillators [19]. In networks of excitable units, the STDP rule has been shown to give rise to oscillating coupling configurations that facilitate switching between strongly and weakly synchronized states [20–22].

The paper is organized as follows. The details of the model are introduced in Section 2. An overview of the underlying deterministic dynamics, characterizing the impact of plasticity on the stationary states and the onset of emergent oscillations, is provided in Section 3. Section 4 is dedicated to a fast–slow analysis of the deterministic dynamics, whereas in Section 5 are explained the features of the two generic types of switching behavior. In Section 6 we provide a summary of our main results.

2 Model

We consider a system of two stochastic active rotators interacting by adaptive couplings, where the dynamics of the phases $\{\varphi_1(t), \varphi_2(t)\}$ and the coupling weights $\{\kappa_1(t), \kappa_2(t)\}$ is given by

$$\begin{aligned}
 \dot{\varphi}_1 &= I_0 - \sin \varphi_1 + \kappa_1 \sin(\varphi_2 - \varphi_1) + \sqrt{D}\xi_1 \\
 \dot{\varphi}_2 &= I_0 - \sin \varphi_2 + \kappa_2 \sin(\varphi_1 - \varphi_2) + \sqrt{D}\xi_2 \\
 \dot{\kappa}_1 &= \epsilon(-\kappa_1 + \sin(\varphi_2 - \varphi_1 + \beta)) \\
 \dot{\kappa}_2 &= \epsilon(-\kappa_2 + \sin(\varphi_1 - \varphi_2 + \beta)),
 \end{aligned} \tag{1}$$

where $\varphi_1, \varphi_2 \in S^1$, while κ_1 and κ_2 are real variables. The rotators are assumed to be identical, having their local dynamics governed by the excitability parameter I_0 , which gives rise to a SNIPER bifurcation at $I_0 = 1$. We focus on the excitable regime, such that $I_0 = 0.95$ is kept fixed throughout the paper. In this case, the uncoupled system always converges to a steady state, whereas the collective dynamics emerges due to interaction and noise. The parameter $\epsilon \ll 1$ defines the scale separation between the fast dynamics of the phases and the slow dynamics of adaptation. White noise of variance D acts only within the subspace of fast variables, whereby the terms $\xi_1(t)$ and $\xi_2(t)$ are independent ($\xi_i(t)\xi_j(t') = \delta_{ij}\delta(t-t')$ for $i, j \in \{1, 2\}$). In the context of neuroscience, I_0 can be interpreted as external bias current, whereas the impact of stochastic terms is analogous to that of synaptic noise. Note that the deterministic version of (1) is symmetric with respect to the exchange of indices $1 \leftrightarrow 2$.

The plasticity rule is controlled by the parameter β , which allows one to interpolate between the different adaptation modalities. The analogy between the adaptivity dynamics in classical neuronal systems and the systems of coupled phase oscillators has been addressed in [14,23,24], whereas a deeper analysis of the correspondence between the phase-dependent plasticity rules and the STDP has been provided in [13]. From these studies, it follows that the scenario found for $\beta = 3\pi/2$, where the stationary weights increase for smaller phase differences and decrease for larger ones (“like-and-like” form of behavior), qualitatively resembles the Hebbian learning rule [23,24]. Nevertheless, in the case $\beta = \pi$, the two coupling weights always change in opposite directions, which may be interpreted as promoting an STDP-like plasticity rule. In the present paper, we are interested in the β interval between these two limit cases, since it admits two coexisting excitable fixed points.

3 Deterministic dynamics of the full system

In this section, we analyze the details of the *deterministic* dynamics of the full system (1), considering first the stationary states and the associated excitability feature, and then focusing on the scenario that gives rise to emergent oscillations.

3.1 Stationary states and excitable dynamics

Fixed points $(\varphi_1^*, \varphi_2^*, \kappa_1^*, \kappa_2^*)$ of the complete system (1) for $D = 0$ are given by the solutions of the following set of equations:

$$\begin{aligned} \sin \varphi_1^* - \sin(\varphi_2^* - \varphi_1^* + \beta) \sin(\varphi_2^* - \varphi_1^*) &= I_0, \\ \sin \varphi_2^* - \sin(\varphi_1^* - \varphi_2^* + \beta) \sin(\varphi_1^* - \varphi_2^*) &= I_0, \end{aligned} \tag{2}$$

with

$$\begin{aligned} \kappa_1^* &= \sin(\varphi_2^* - \varphi_1^* + \beta), \\ \kappa_2^* &= \sin(\varphi_1^* - \varphi_2^* + \beta). \end{aligned} \tag{3}$$

Equation (2) can be solved numerically for any fixed parameter set, or numerical path-following can be applied in order to study the dependence of the fixed points on the parameters.

The bifurcation diagram in Figure 1 shows how the number and stability of fixed points of the full system change with β . In particular, depending on β , there may be two, four or six fixed points. Due to symmetry, the solutions always appear in pairs of points sharing the same stability features. Since our study concerns plasticity rules which support excitable fixed points, we have confined the analysis to the interval $\beta \in (3.298, 4.495)$, where the system has *two stable* fixed points, which lie off the synchronization manifold $\varphi_1 = \varphi_2$. Apart from that, there are also four unstable

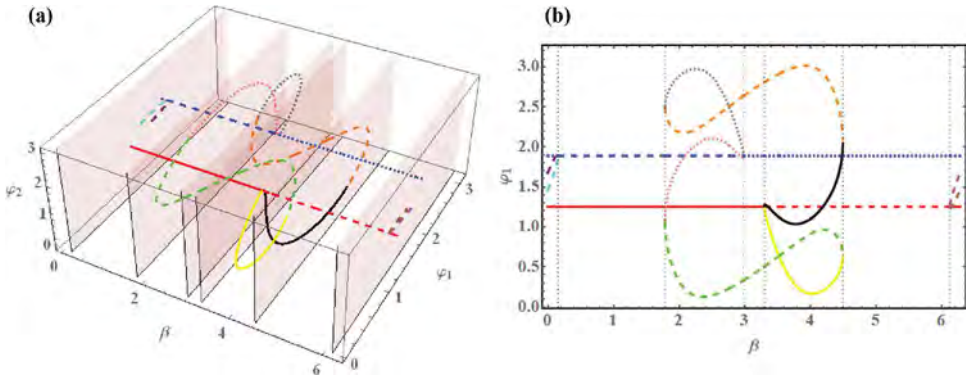


Fig. 1. (a) Bifurcation diagram for the fixed points of system (1) with $D = 0$ in the $(\beta, \varphi_1, \varphi_2)$ space. (b) Projection of the bifurcation diagram to (β, φ_1) plane. The two fixed points independent on β belong to the synchronization manifold: the red (blue) one is always longitudinally stable (unstable). The solid lines denote stable fixed points, whereas the dashed and dotted lines denote saddles of unstable dimension 1 and 2, respectively.

fixed points. The bifurcations associated to the boundaries of the given β interval are as follows: at $\beta = 3.298$ the system undergoes a supercritical symmetry-breaking pitchfork bifurcation where a symmetry related pair of two stable fixed points off the synchronization manifold is created, whereas at $\beta = 4.495$, this pair meets another pair of unstable fixed points off the synchronization manifold such that both are annihilated in symmetry related inverse saddle-node bifurcations. For instance, at $\beta = 4.1$, one finds the symmetry related pair of stable foci given by $(\varphi_1, \varphi_2, \kappa_1, \kappa_2) = (1.177, 0.175, 0.032, -0.92)$ and $(\varphi_1, \varphi_2, \kappa_1, \kappa_2) = (0.175, 1.177, -0.92, 0.032)$. Note that these weight levels support effective master-slave configurations, where one unit exerts a much stronger influence on the other unit than vice versa.

The two stable asymmetric fixed points in the interval $\beta \in (3.298, 4.495)$ are excitable, and may exhibit several different types of response to external perturbations, see the classification in Figure 2. Introducing the perturbations by setting different initial conditions, we plot in Figure 2 the phase dynamics in the fast subspace while keeping the weights (κ_1, κ_2) fixed. Note that in the case where both units respond with a single spike, the order of firing is such that the unit with larger initial phase $\varphi_i(0), i \in \{1, 2\}$ fires first.

3.2 Onset of oscillations

The onset of emergent oscillations in system (1) with $D = 0$ depends on the interplay between the plasticity rule, specified by β , and the speed of adaptation, characterized by ϵ . A parameter scan indicating the variation of κ_1 , $A_{\kappa_1} = \max(\kappa_1(t)) - \min(\kappa_1(t))$ in terms of (β, ϵ) is shown in Figure 3a. The results are obtained by numerical continuation beginning from a stable periodic solution, such that the final state reached for a certain set of (β, ϵ) values provides the initial conditions for the simulation of the system at incremented parameter values. By this method, we have determined the maximal stability region of the periodic solution.

One finds that for a fixed β , there actually exists an interval of timescales separation $\epsilon \in (\epsilon_{min}, \epsilon_{max})$ admitting oscillations, cf. Figure 3b. The periodic solutions in this interval coexist with the two symmetry-related stable stationary states. One observes that the threshold ϵ_{min} reduces with β , whereas the upper boundary value ϵ_{max} grows with increasing β . The detailed bifurcation mechanisms behind the onset

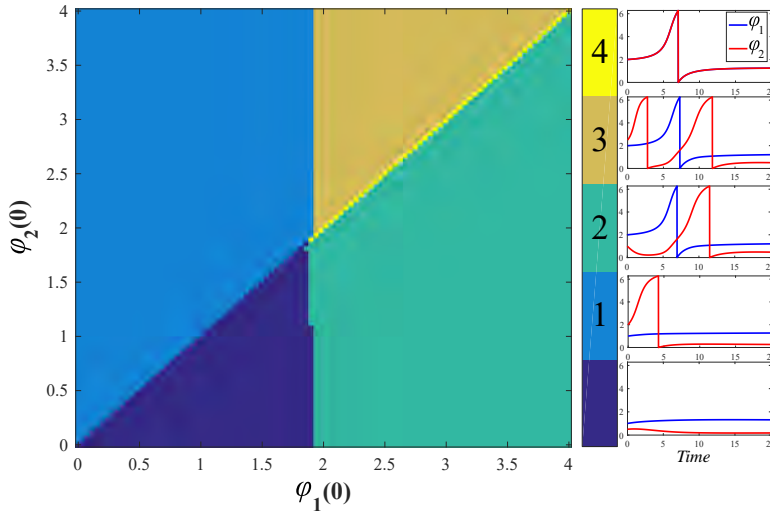


Fig. 2. Modalities of the response to external perturbation for system (1) with $D = 0$. The system parameters are $I_0 = 0.95$, $\epsilon = 0.01$ and $\beta = 4.212$, whereas the initial conditions for the coupling weights are set to $\kappa_1(0) = -0.0077$, $\kappa_2(0) = -0.846$. Depending on the initial phases $(\varphi_1(0), \varphi_2(0))$, one may observe the following regimes: (0) no spikes; (1) the unit with larger $\varphi(0)$ emits one spike and the other does not; (2) both units emit a single spike, with the unit with larger $\varphi(0)$ firing first; (3) the unit with larger $\varphi(0)$ emits two spikes and the other unit emits one; (4) both units spike synchronously.

of oscillations and multistability are beyond the scope of this paper, and essentially involve an interplay between the fast and slow variables.

Enhancing ϵ under fixed β gives rise to a supercritical symmetry-breaking pitchfork bifurcation of limit cycles, indicated by PFL in Figure 3b. Below the bifurcation, the phases $\varphi_1(t)$ and $\varphi_2(t)$ maintain a small phase-shift, while the oscillation profiles $\kappa_i(t), i \in \{1, 2\}$ are rather different, see Figures 3d and 3e, respectively. Above the bifurcation, the system gains the anti-phase space-time symmetry $\varphi_1(t) = \varphi_2(t + T/2), \kappa_1(t) = \kappa_2(t + T/2)$ where T denotes the oscillation period, cf. the associated waveforms in Figures 3g and 3f.

4 Slow-fast analysis of the deterministic dynamics

The deterministic dynamics in case of slow adaptation, corresponding to a strong timescale separation between the fast and slow variables, may be analyzed within the framework of standard fast-slow analysis. In general, one may either consider the layer problem, defined on the fast timescale, or the reduced problem, which concerns the slow timescale. Within the layer problem, the aim is to determine the fast flow dynamics $\varphi_1(t; \kappa_1, \kappa_2), \varphi_2(t; \kappa_1, \kappa_2)$ by treating the slow variables κ_1 and κ_2 as parameters, whereas the reduced problem consists in determining the dynamics of the slow flow $(\kappa_1(t), \kappa_2(t))$ (reduced flow) assuming that the fast flow of the layer problem is either at a stable equilibrium or at the averaged value of a stable regime.

In this section, we first investigate the fast layer problems. Depending on the values of the slow variables (κ_1, κ_2) , the fast flow can exhibit several attractors, such that multiple sheets of the slow flow emerge from the averaged dynamics on the different attractors of the fast flow.

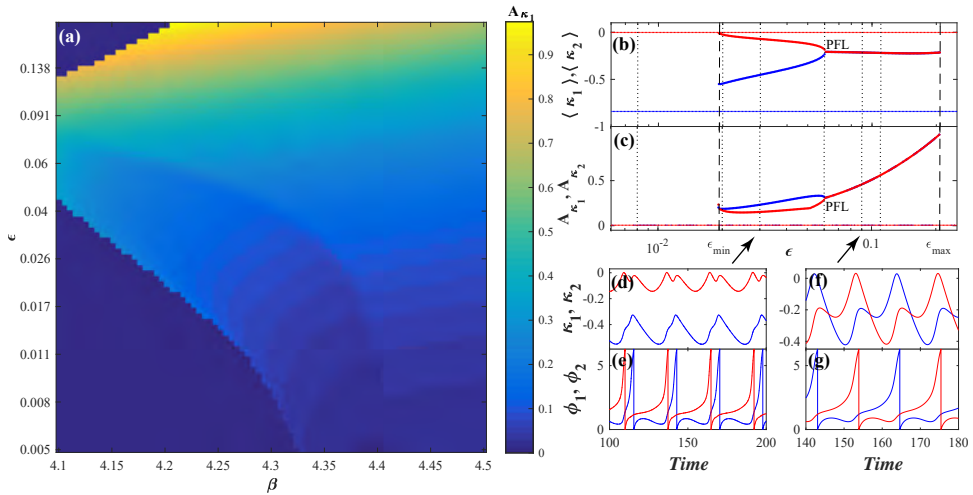


Fig. 3. Onset of oscillations in the full system (1) for $D = 0$. In panel (a) is shown how the variation A_{κ_1} of coupling weight κ_1 changes in the (β, ϵ) plane. Panel (b) shows how the mean coupling weights $\langle \kappa_1 \rangle$ and $\langle \kappa_2 \rangle$ of oscillatory states (thick lines) change with ϵ under fixed $\beta = 4.212$. The thin solid lines indicate the stationary state. In panel (c) are plotted the analogous dependencies for variation of the oscillation. The dotted lines in (b) and (c) indicate the ϵ values corresponding to the time traces in Figure 7, whereas the dashed lines indicate the boundaries of the ϵ region supporting the stable periodic solutions. The symmetry-breaking pitchfork bifurcation of limit cycles is denoted by PFL. In panels (d)–(g) are shown the waveforms of periodic solutions without and with the anti-phase space-time symmetry, obtained for $\epsilon = 0.03$ and $\epsilon = 0.09$, respectively (see the arrows). The excitability parameter is fixed to $I_0 = 0.95$.

4.1 Dynamics of the fast flow

Within the layer problem, one studies the dynamics of the fast variables

$$\begin{aligned}\dot{\varphi}_1 &= I_0 - \sin \varphi_1 + \kappa_1 \sin(\varphi_2 - \varphi_1) \\ \dot{\varphi}_2 &= I_0 - \sin \varphi_2 + \kappa_2 \sin(\varphi_1 - \varphi_2),\end{aligned}\quad (4)$$

where $\kappa_1, \kappa_2 \in [-1, 1]$ are considered as additional system parameters. Formally, system (4) is obtained by setting $\varepsilon = 0$ in (1) for $D = 0$.

The numerically obtained bifurcation diagram in Figure 4a shows that the fast flow is monostable for most of the (κ_1, κ_2) values, possessing either an equilibrium or a limit cycle attractor. The stability boundary of the periodic solution (red curves) has been obtained by the method of numerical continuation where, beginning from a stable periodic solution, the initial conditions for incremented parameter values are given by the final state reached for the previous set of (β, ϵ) values. The coexistence between a stable fixed point, lying on the synchronization manifold, and a limit cycle is found within a small region near the diagonal, see Figure 4a. Let us first classify the fixed points of the fast flow and then examine the scenarios that give rise to oscillations.

It can be shown that the fast flow admits either two or four fixed points, with the associated regions indicated in Figure 4b. In particular, two fixed points FP1 and FP2 on the synchronization manifold are *independent* on κ_1 and κ_2 . They are given by $(\varphi_1^*, \varphi_2^*) = (\arcsin I_0, \arcsin I_0)$ and $(\varphi_1^*, \varphi_2^*) = (\pi - \arcsin I_0, \pi - \arcsin I_0)$. One may also find two additional fixed points off the synchronization manifold, referred

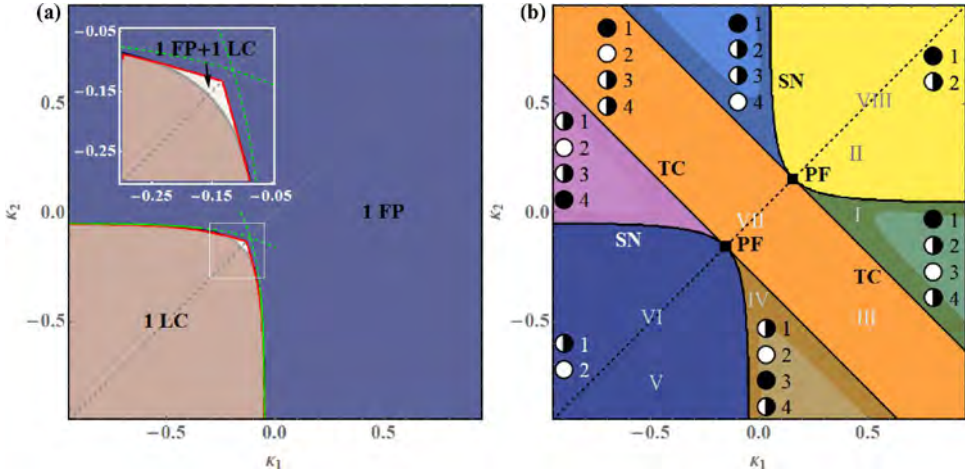


Fig. 4. (a) Attractors of the fast flow (4) in terms of κ_1 and κ_2 , now considered as parameters. The fast flow is typically monostable, supporting either a stable fixed point (FP) or a stable limit cycle (LC), apart from a small region around the main diagonal, where it exhibits bistable behavior. The green dashed curves indicate approximations of two branches of SNIPER bifurcations, obtained by the method described in the text. The red lines correspond to the numerically determined stability boundaries of the oscillatory solution. (b) Classification of the fixed points of the fast flow (4). The fixed points are labeled the same way as in the main text, with their stability indicated as follows: full circles denote stable fixed points, semi-full circles represent saddle points and white circles correspond to doubly unstable fixed points. Within the four light-shaded triangular-shaped regions, the doubly unstable fixed point is a focus, rather than a node. The notation I–VIII refers to parameter values corresponding to the phase portraits in Figure 5.

to as FP3 and FP4 in Figure 4b. The bifurcations affecting the number and stability of the fixed points, beginning from the lower left region of the (κ_1, κ_2) plane, can be summarized as follows. Along the main diagonal $\kappa_1 = \kappa_2$, we find two points of supercritical pitchfork bifurcations (PF), where from the symmetric fixed points the saddles FP3 and FP4 appear and disappear. Off the main diagonal, the pitchforks are unfolded into curves of saddle-node (SN) and transcritical bifurcations (TC), see Figure 4b.

The (κ_1, κ_2) region featuring stable oscillations almost completely matches the lower left domain admitting two unstable fixed points. Within this region, each periodic solution obtained for (κ_1, κ_2) above the main diagonal $\kappa_1 = \kappa_2$ has a counterpart in the domain below the main diagonal, related to it by the exchange symmetry of units indices. Typically, the periodic solutions emerge via SNIPER bifurcations, comprising two branches where either κ_1 or κ_2 remain almost constant and close to zero. In both cases, the two fixed points that collide and disappear are FP3 and FP4. Nevertheless, such scenarios cannot be maintained in the small (κ_1, κ_2) region admitting coexistence between a fixed point and a limit cycle, because the SNIPER bifurcation is accompanied by a change in the number of fixed points. Our findings suggest that near the main diagonal, the limit cycle emerges via a heteroclinic bifurcation, where an orbit connects two saddles lying off the synchronization manifold (not shown). Note that the orbit of the limit cycle follows the unstable manifold of the saddle point FP2 on the synchronization manifold. To the left or the right of the main diagonal, instead of a heteroclinic bifurcation, one finds homoclinic bifurcations, whereby a saddle point, either FP3 or FP4, touches the limit cycle orbit. The schematic phase portraits indicating the stable and unstable manifolds of the fixed points and the limit

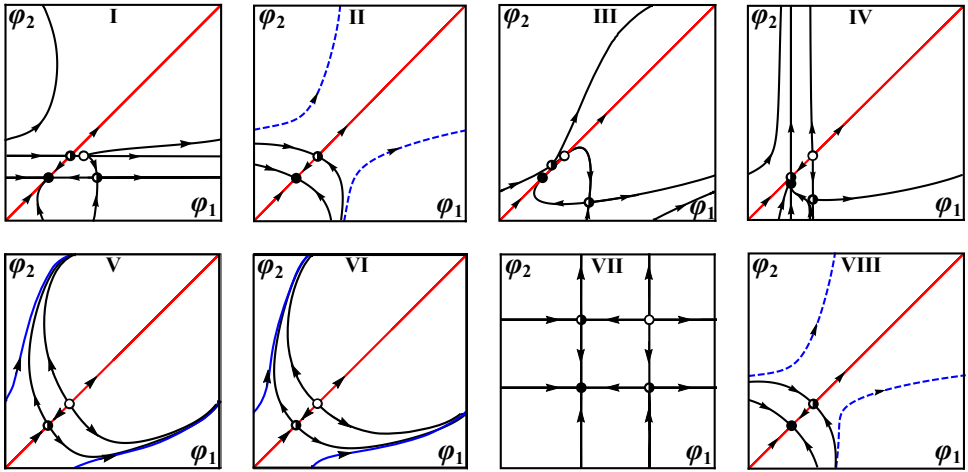


Fig. 5. Schematic phase portraits corresponding to the characteristic regimes of the fast flow. The panels I–VIII refer to representative parameter values indicated in Figure 4b. Also, the stability of fixed points is presented the same way as in Figure 4b. The invariant synchronization manifold is denoted by the red color, whereas the orbit of a stable/unstable limit cycle is indicated by the solid/dashed blue lines.

cycle for the characteristic regimes of the fast flow, denoted by I–VIII in Figure 4b, are illustrated in Figure 5.

The two branches of SNIPER bifurcations may readily be approximated for small values of κ_1 and κ_2 by a simple scheme, which amounts to reducing the fast flow to a normal form of saddle-node bifurcation. Suppose first that $\kappa_1 \ll 1$ and $I_0 - 1 \ll 1$. More specifically, let $\xi \ll 1$ be a small parameter such that $I_0 - 1 = \xi$ (close to the threshold) and $\kappa_1 = \gamma\xi$, i.e. γ is a rescaling parameter of κ_1 , allowing for a zoom in the neighborhood of zero. Then, the steady states are given by the system

$$\begin{aligned} 1 + \xi - \sin \varphi_1 + \xi\gamma \sin(\varphi_2 - \varphi_1) &= 0, \\ 1 + \xi - \sin \varphi_2 + \kappa_2 \sin(\varphi_1 - \varphi_2) &= 0. \end{aligned} \tag{5}$$

The first equation in the zeroth order approximation leads to $\varphi_1 = \pi/2$. Hence, using the perturbation approach, we have

$$\varphi_1^* = \frac{\pi}{2} + \sqrt{\xi}\Psi_1 + \dots; \quad \varphi_2^* = \Psi_2 + \dots, \tag{6}$$

where the $\sqrt{\xi}$ scaling follows from the Taylor expansion of the function $\sin \varphi_1$ at $\pi/2$. Inserting (6) into (5), one obtains the system of equations for Ψ_1 and Ψ_2

$$\begin{aligned} 1 + \frac{1}{2}\Psi_1^2 - \gamma \cos \Psi_2 &= 0, \\ 1 - \sin \Psi_2 + \kappa_2 \cos \Psi_2 &= 0. \end{aligned} \tag{7}$$

From system (7), it is not difficult to see that the saddle-node bifurcation takes place if the condition $1 - \gamma \cos \Psi_2 = 0$ is satisfied. This leads to the parametric representation $\kappa_1 = \xi\gamma = \frac{I_0 - 1}{\cos \Psi_2}$, $\kappa_2 = \frac{\sin \Psi_2 - 1}{\cos \Psi_2}$, of the saddle-node curve for small κ_1 values, where Ψ_2 plays the role of the parameter along the curve. An analogous approach may be used to capture the second branch of saddle-node bifurcations, cf. the green dashed lines in Figure 4a.

4.2 Dynamics of the slow flow

We have numerically obtained the dynamics of the slow flow by applying a two-step approach. First, for fixed values (κ_1, κ_2) , we determine the time-averaged dynamics of the fast flow (4), $\langle \varphi_2 - \varphi_1 \rangle_t = f(\kappa_1, \kappa_2)$. Here, the averaging $\langle \cdot \rangle_t$ is performed over a sufficiently large time interval, having eliminated a transient. Hence, this average depends on the attractor of the fast flow for the given (κ_1, κ_2) . In particular, if the fast flow possesses a stable fixed point, then $\langle \varphi_2 - \varphi_1 \rangle_t = \varphi_2^* - \varphi_1^*$, where $(\varphi_1^*, \varphi_2^*)$ is a solution of

$$\begin{aligned} I_0 - \sin \varphi_1^* + \kappa_1 \sin (\varphi_2^* - \varphi_1^*) &= 0 \\ I_0 - \sin \varphi_2^* + \kappa_2 \sin (\varphi_1^* - \varphi_2^*) &= 0. \end{aligned} \tag{8}$$

This procedure just results in determining the slow critical manifold of the system. In case when the attractor of the fast flow is periodic, $\langle \varphi_2 - \varphi_1 \rangle_t$ presents the time average over the period. Averaging approximation in case of a periodic attractor of the fast flow constitutes a standard approach [13,25], rather natural for describing the influence of oscillations in the fast flow on the dynamics of the slow flow. At the second stage, the obtained time-averages are substituted into the dynamics of the weights

$$\begin{aligned} \dot{\kappa}_1 &= \epsilon[-\kappa_1 + \sin(f(\kappa_1, \kappa_2) + \beta)] \\ \dot{\kappa}_2 &= \epsilon[-\kappa_2 + \sin(-f(\kappa_1, \kappa_2) + \beta)]. \end{aligned} \tag{9}$$

The system (9) is used to determine the vector field of the slow flow by taking into account only the attractors of the fast flow, such that the vector field associated to each attractor is plotted within its respective stability region, cf. Figure 6.

In regions of the (κ_1, κ_2) plane where there are coexisting stable solutions of the fast flow, the corresponding vector field of the slow flow is given on multiple overlapping sheets, since the value of the average $f(\kappa_1, \kappa_2)$ depends on the initial conditions. In our case, this occurs only in a small region of coexistence between an equilibrium and a stable limit cycle.

One should single out two important features of the slow flow: (i) it exhibits two symmetry-related fixed points in the green and blue regions in Figure 6, and (ii) the slow vector field is pointed in opposite directions close to the boundary between the fast oscillatory regime (orange region) and the steady states of the fast flow (blue, green and white regions). The latter in particular implies that interesting effects occur close to the border of the oscillatory and the steady state regime of the fast flow. Moreover, adding noise gives rise to fluctuations around this boundary, which leads to switching between the quasi-stationary and the fast spiking dynamics. Such effects are studied in more detail within the next section.

5 Switching dynamics

Our main observation in this section is that the interplay of plasticity and noise induces slow stochastic fluctuations (switching dynamics), mediating two qualitatively different scenarios depending on the speed of adaptation. The latter include (i) switching between two modes of *noise-induced* oscillations for slower adaptation (small $\epsilon \simeq 0.01$) and (ii) switching between multiple coexisting attractors of the deterministic dynamics for faster adaptation (intermediate $\epsilon \simeq 0.05$).

In case (i), the impact of noise is twofold: on a short timescale, it gives rise to spiking dynamics, whereas on a long time scale, it induces random transitions between

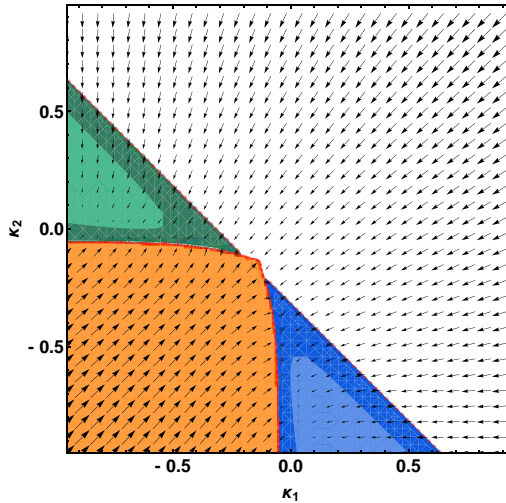


Fig. 6. Vector field of the slow flow obtained by taking into account only stable attractors of the fast flow for $\beta = 4.212$, $I_0 = 0.95$. The color coding is as follows: orange color denotes the region associated to the stable limit cycle of the fast flow, white stands for the stable fixed point of the fast flow FP1, whereas blue and green color correspond to the two stable fixed points FP3 and FP4. Within the light-shaded regions, FP3 and FP4 are foci rather than nodes, cf. Figure 4b.

the two oscillatory modes. In case (ii), the switching dynamics comprises metastable states derived from two fixed points, as well as two limit cycles associated to emergent oscillations of the corresponding deterministic system. The key difference between the effects (i) and (ii) is that for slower adaptation, the system switches between the oscillatory modes that do not exist as deterministic attractors. Moreover, the two generic types of switching are characterized by distinct phase dynamics: for slower adaptation, one finds alternation of patterns with different order of spiking between the units, whereas for faster adaptation, the phases effectively exhibit bursting behavior, involving a succession between episodes of spiking and relative quiescence. An overview on how the typical dynamics of couplings changes with ϵ at fixed β is provided in Figure 7. Note that the difference between the average coupling weights of the stable periodic solutions of the deterministic system are much smaller than a typical distance between the coupling levels for the stationary states. The prevalence of metastable states is affected by ϵ so that intermediate adaptation favors oscillatory modes, whereas the fast adaptation apparently promotes the two quasi-stationary states. In the next two subsections, we provide further insight into the mechanisms behind the switching dynamics using the results of the fast-slow analysis.

5.1 Switching dynamics under slow adaptation

As already indicated, ϵ is here taken sufficiently small, such that it cannot facilitate emergent oscillations in the full system (1). For $\epsilon \simeq 0.01$ and under appropriate noise levels, one observes noise-induced oscillations [26]. The latter arise via a scenario involving a multiple-timescale stochastic bifurcation, whereby noise acts only within the fast subsystem of (1). The onset of oscillations under increasing D occurs in two stages. In the first stage, the phase dynamics gradually exhibits more induced spikes,

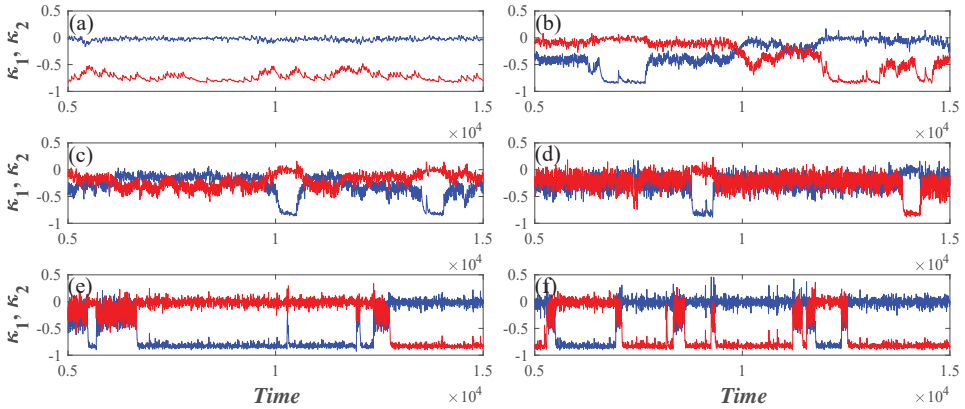


Fig. 7. Switching dynamics under variation of ϵ . The time traces $(\kappa_1(t), \kappa_2(t))$ are obtained for fixed $I_0 = 0.95$, $D = 0.006$, $\beta = 4.212$, whereas ϵ assumes the following values: (a) $\epsilon = 0.008$, (b) $\epsilon = 0.02$, (c) $\epsilon = 0.03$, (d) $\epsilon = 0.06$, (e) $\epsilon = 0.09$, (f) $\epsilon = 0.11$.

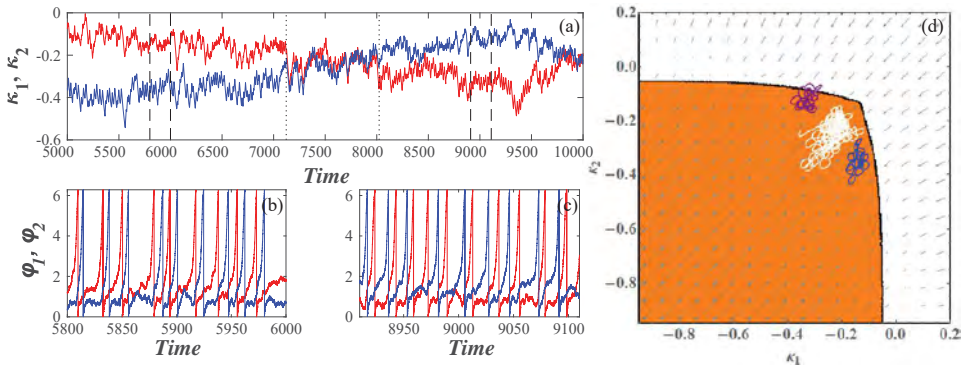


Fig. 8. Switching dynamics between the two modes of noise-induced oscillations. Time traces of the weights are shown in panel (a), whereas panel (b) and (c) display the corresponding time traces of the phases during the intervals between the dashed lines in panel (a). In panel (d), the $(\kappa_1(t), \kappa_2(t))$ projections of the orbits associated to each of the two modes (blue color), as well as the switching episode, shown in white, are superimposed to the vector field of the slow flow from Figure 6. The shaded area corresponds to the stable limit cycle. The system parameters are $I_0 = 0.95$, $\beta = 4.212$, $\epsilon = 0.01$, $D = 0.009$.

such that the stationary distributions of phases eventually acquire a longer tail reflecting the occurrence of spikes (not shown). Nevertheless, the stationary distributions $P(\kappa_i)$ change appreciably only at the second stage, which takes place for sufficiently large D . Such a change accompanies the emergence of coupling oscillations. Note that the system (1) actually exhibits *two modes* of noise-induced oscillations, characterized by the different order of firing between the two units, cf. the time traces of phase dynamics and the associated evolution of couplings in Figure 8a.

It is interesting to examine whether the vector field of the slow flow from Section 4.2 can be used to explain the slow stochastic fluctuations of the coupling weights. To this end, we have superimposed the $(\kappa_1(t), \kappa_2(t))$ orbits of the two noise-induced modes, as well as a switching episode, to a vector field of the slow flow from Figure 6. Note that the orbits typically lie close to the boundary outlining the transition between the two attractors of the fast flow, featuring non-negligible coupling weights. Moreover, the two modes are confined to small areas of the (κ_1, κ_2) plane

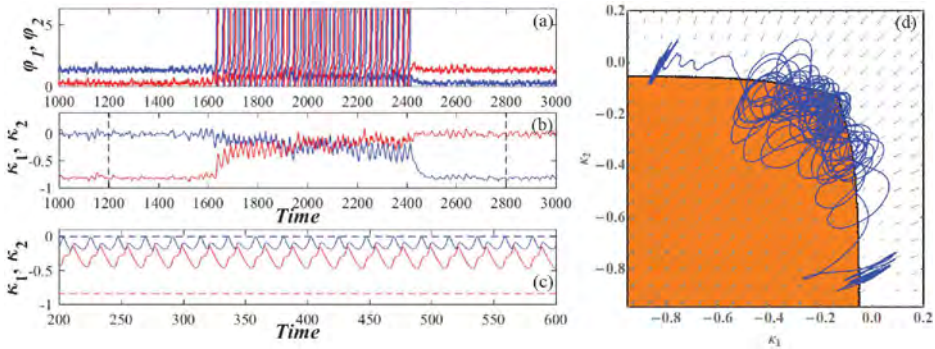


Fig. 9. Time traces of the phases (a) and weights (b) associated to noise-induced switching between the coexisting attractors of the deterministic system. The results are obtained for $I_0 = 0.95$, $\beta = 4.212$, $\epsilon = 0.05$, $D = 0.004$. In panel (c) is provided the deterministic dynamics of weights obtained for the same parameter values. In panel (d), the $(\kappa_1(t), \kappa_2(t))$ orbit corresponding to the interval between the dashed lines in (b) is super-imposed on the vector field of the slow flow cf. Figure 6.

symmetrical with respect to the main diagonal $\kappa_1 = \kappa_2$, whereas the switching episode virtually takes place on the diagonal. Apparently, the noise-induced modes occupy regions where the oscillations in the fast flow emerge via homoclinic bifurcations, rather than the SNIPER scenario. Nonetheless, the switching episode seems to involve the domain featuring coexistence of the two stable sheets of the slow vector field. Within these sheets, which correspond to two attractors of the fast flow (a stable node and a stable limit cycle), the vector fields are oriented in opposite directions, thereby contributing to switching.

5.2 Switching dynamics for faster adaptation

In case of faster adaptation associated to intermediate ϵ , the switching dynamics involves four metastable states, derived from the attractors of the deterministic system. The deterministic multistable behavior includes two symmetry-related stationary states, as well as two symmetry-related limit cycles. Note that while the two stable steady states exist for arbitrary small ϵ and are therefore visible in the slow flow in Figure 6, the oscillatory solutions disappear for small ϵ and hence cannot be observed in the slow flow. The two oscillatory regimes are characterized by the same phase shift, but the reverse order of firing between the two units. Influenced by noise, the phases effectively engage in bursting behavior, manifesting slow stochastic fluctuations between episodes of intensive spiking activity and periods of relative quiescence, see Figure 9a. For a fixed noise level, the prevalence of metastable states, defined by transition probabilities between them, changes with adaptation speed. One observes that for $\epsilon \simeq 0.05$, the oscillatory dynamics is preferred, whereas for $\epsilon \simeq 0.1$, the quasi-stationary states are more ubiquitous.

A comparison of the (κ_1, κ_2) orbits displaying switching dynamics and the vector field of the slow flow from Figure 6 again shows that the former is confined to the criticality region at the boundary between the stationary and oscillatory regimes in the fast flow, cf. Figure 9. One should remark on how the transitions between the different metastable states take place. In particular, from Figure 9b, it is clear that there can be no direct transitions between the two quasi-stationary states, but they rather have to be mediated by the system passing through the oscillatory states. Also, the transition from oscillatory to quasi-stationary states typically occurs

once the couplings approach a master-slave-like configuration, where the coupling in one direction is much stronger than the other one. This scenario coincides with the SNIPER bifurcation of the fast flow described in Section 4.1. The scenario of transition between the two metastable oscillatory states resembles closely the one from Section 5.2.

6 Summary

In the present study, we have analyzed a system of two adaptively coupled active rotators with excitable intrinsic dynamics, demonstrating that the interplay of plasticity and noise may give rise to slow stochastic fluctuations. Two qualitatively different types of self-organized behavior have been identified, depending on the adaptation speed. For slower adaptation, the switching dynamics consists of an alternation between two modes of noise-induced oscillations, associated to a preferred order of spiking between the two units. In this case, noise plays a twofold role: on one hand, it perturbs the excitable local dynamics giving rise to oscillations on a short timescale, whereas on the other hand, it elicits the alternation between the two oscillatory states on a long timescale. The underlying phase dynamics shows slow switching between two patterns distinguished by the different order in which the units are spiking. In case of faster adaptation, the coupling becomes capable of eliciting emergent oscillations in the deterministic system [27]. The latter then exhibits complex multistable behavior, involving two stationary and two oscillatory regimes. Under the influence of noise, the system undergoes switching between these four different metastable states, whose prevalence at fixed noise level depends on the speed of adaptation. The deterministic attractors associated to metastable states are related by the Z_2 symmetry. Thus, a mismatch in excitability parameters would lead to symmetry-breaking, whereby a small mismatch would induce a bias in switching dynamics, whereas a larger mismatch, corresponding to a scenario with one excitable and one oscillatory unit, would completely alter the observed dynamics.

Though the underlying phenomena are not found in the singular limit of infinite scale separation, the fast-slow analysis we have applied still allows one to explain the qualitative features of both considered types of switching behavior. Studying the layer problem, and in particular the vector field of the slow flow, has enabled us to gain insight into the metastable states and the transitions between them. It has been demonstrated that the coupling dynamics is always in a state of “criticality”, being confined to the boundary between the stationary and oscillatory regimes of the fast flow.

Given that excitability, plasticity and noise are inherent ingredients of neuronal systems, the obtained results can be interpreted in the context of neuroscience. It is well known that the backbone of neural networks is made up of binary and ternary neuron motifs, whereby the structural motifs typically support multiple functional motifs, essentially characterized by the weight configuration and the underlying direction of the information flow. With this in mind, the scenario of switching under slow adaptation may be important, because it implies that a binary motif can display slow alternation between two effectively unidirectional weight configurations, promoting opposite direction of information flow. For faster adaptation, one finds multistability between unidirectional coupling and bidirectional coupling of moderate strength. Nonetheless, the underlying phase dynamics, if extended to networks, may be considered as a paradigm for UP-DOWN states, typical for cortical dynamics [28,29]. Thus, it would be of interest to examine the impact of plasticity in networks of noisy excitable units, where one may expect different types of emergent behavior, such as cluster, non-synchronized and partially synchronized states, depending on the frustration of local dynamics and the impact of noise.

We thank S. Eydam for useful discussions. This work was supported by the Ministry of Education, Science and Technological Development of Republic of Serbia under project No. 171017, the DAAD Serbia-Germany Bilateral Project “Emergent Dynamics in Systems of Coupled Excitable Units”, as well as the DFG within the framework of Collaborative Research Center SFB 910.

Author contribution statement

I.F. and S.Y. conceived the model and defined the analysis of noise-induced switching as the main goal of the research. S.Y. and M.W. developed the general framework to investigating the deterministic fast-slow problem and the bifurcation analysis of the associated reduced systems. I.B. obtained all the numerical results, whereas I.B. and I.F. carried out the bifurcation analysis, identified the two types of noise-induced switching behavior and made the main contribution to writing the manuscript. All the authors discussed the findings and participated in interpretation of the results.

References

1. F. Sorrentino, E. Ott, Phys. Rev. Lett. **100**, 114101 (2008)
2. F. Vazquez, V.M. Eguiluz, M.S. Miguel, Phys. Rev. Lett. **100**, 108702 (2008)
3. N. Caporale, Y. Dan, Ann. Rev. Neurosci. **31**, 25 (2008)
4. C. Furusawa, K. Kaneko, Phys. Rev. Lett. **90**, 088102 (2003)
5. D.O. Hebb, *The Organization of Behavior: a Neuropsychological Approach* (John Wiley & Sons, New York, 1949)
6. S. Song, K.D. Miller, L.F. Abbott, Nat. Neurosci. **3**, 919 (2000)
7. R.C. Froemke, Y. Dan, Nature (London) **416**, 433 (2002)
8. H.-X. Wang, R.C. Gerkin, D.W. Nauen, G.-Q. Bi, Nat. Neurosci. **8**, 187 (2005)
9. O. Sporns, R. Kotter, PLoS Biol. **2**, e369 (2004)
10. I. Franović, V. Miljković, Chaos Soliton. Fract. **44**, 122 (2011)
11. I. Franović, V. Miljković, Chaos Soliton. Fract. **45**, 527 (2012)
12. I. Franović, V. Miljković, EPL **92**, 68007 (2011)
13. L. Lüchen, O.V. Popovych, P.A. Tass, S. Yanchuk, Phys. Rev. E **93**, 032210 (2016)
14. Y.L. Maistrenko, B. Lysyansky, C. Hauptmann, O. Burylko, P.A. Tass, Phys. Rev. E **75**, 066207 (2007)
15. P. Seliger, S.C. Young, L.S. Tsimring, Phys. Rev. E **65**, 041906 (2002)
16. M. Li, S. Guan, C.-H. Lai, New J. Phys. **12**, 103032 (2010)
17. P.S. Skardal, D. Taylor, J.G. Restrepo, Physica D **267**, 27 (2014)
18. D. Kasatkin, S. Yanchuk, E. Schöll, V. Nekorkin, Phys. Rev. E **96**, 062211 (2017)
19. O.V. Popovych, S. Yanchuk, P.A. Tass, Sci. Rep. **3**, 2926 (2013)
20. K. Mikkelsen, A. Imparato, A. Torcini, Phys. Rev. Lett. **110**, 208101 (2013)
21. D. Millman, S. Mihalas, A. Kirkwood, E. Niebur, Nat. Phys. **6**, 801 (2010)
22. A. Levina, J.M. Herrmann, T. Geisel, Phys. Rev. Lett. **102**, 118110 (2009)
23. T. Aoki, T. Aoyagi, Phys. Rev. Lett. **102**, 034101 (2009)
24. T. Aoki, T. Aoyagi, Phys. Rev. E **84**, 066109 (2011)
25. A. Shilnikov, Int. J. Bifurc. Chaos **18**, 2141 (2008)
26. S.-J. Wang, G. Ouyang, J. Guang, M. Zhang, Phys. Rev. Lett. **116**, 018101 (2016)
27. Q. Ren, K.M. Kolwankar, A. Samal, J. Jost, Phys. Rev. E **86**, 056103 (2012)
28. T.T.G. Hahn, J.M. McFarland, S. Berberich, B. Sakmann, M.R. Mehta, Nat. Neurosci. **15**, 1531 (2012)
29. V.V. Vyazovskiy, K.D. Harris, Nat. Rev. Neurosci. **14**, 443 (2013)

Phase-sensitive excitability of a limit cycle

Igor Franović, Oleh E. Omel'chenko, and Matthias Wolfrum

Citation: *Chaos* **28**, 071105 (2018); doi: 10.1063/1.5045179

View online: <https://doi.org/10.1063/1.5045179>

View Table of Contents: <http://aip.scitation.org/toc/cha/28/7>

Published by the [American Institute of Physics](#)



Chaos

An Interdisciplinary Journal of Nonlinear Science

Fast Track Your Research. *Submit Today!*

Phase-sensitive excitability of a limit cycle

Igor Franović,^{1,a)} Oleh E. Omel'chenko,^{2,b)} and Matthias Wolfrum^{2,c)}

¹Scientific Computing Laboratory, Center for the Study of Complex Systems, Institute of Physics Belgrade, University of Belgrade, Pregrevica 118, 11080 Belgrade, Serbia

²Weierstrass Institute, Mohrenstrasse 39, 10117 Berlin, Germany

(Received 18 June 2018; accepted 6 July 2018; published online 27 July 2018)

The classical notion of excitability refers to an equilibrium state that shows under the influence of perturbations a nonlinear threshold-like behavior. Here, we extend this concept by demonstrating how periodic orbits can exhibit a specific form of excitable behavior where the nonlinear threshold-like response appears only after perturbations applied within a certain part of the periodic orbit, i.e., the excitability happens to be phase-sensitive. As a paradigmatic example of this concept, we employ the classical FitzHugh-Nagumo system. The relaxation oscillations, appearing in the oscillatory regime of this system, turn out to exhibit a phase-sensitive nonlinear threshold-like response to perturbations, which can be explained by the nonlinear behavior in the vicinity of the canard trajectory. Triggering the phase-sensitive excitability of the relaxation oscillations by noise, we find a characteristic non-monotone dependence of the mean spiking rate of the relaxation oscillation on the noise level. We explain this non-monotone dependence as a result of an interplay of two competing effects of the increasing noise: the growing efficiency of the excitation and the degradation of the nonlinear response. *Published by AIP Publishing.* <https://doi.org/10.1063/1.5045179>

The classical concept of excitability refers to a specific non-linear response of a system to perturbations of its rest state. While for small perturbations the system reacts only with a linear relaxation directly back to the rest state, for larger perturbations above a certain threshold it reacts with a large non-linear response, called excitation. Such a behavior can be observed, for example, when a neuron in the quiescent state receives a presynaptic impulse and reacts with the emission of a spike. Until the non-linear response has terminated, the system is not susceptible to further excitations. Only after the system has again reached the rest state, can it be excited again. We study here the case where the rest state is not a stationary state but a stable periodic orbit. Then, the response of the system to perturbations may be nonuniform along the orbit. Of particular interest is the case where the non-linear response to perturbations above threshold appears only in a certain part of the periodic orbit. We call this situation *phase-sensitive excitability* and demonstrate that the oscillatory regime of the FitzHugh-Nagumo system can serve as an example for this type of behavior. It is well known that for other parameter values, the FitzHugh-Nagumo system has an excitable equilibrium. In this case, a perturbation above threshold induces a response in the form of a single spike. We present a completely different scenario. Perturbations are now applied to the regime of periodic spiking. If these perturbations act close to the passage near the unstable equilibrium, they may evoke a response in the form of a subthreshold oscillation and in this way prevent the system for a certain time from spiking. There are many cases where the triggering of an excitable system by noise can result in a characteristic non-monotone

dependence of the system behavior on the noise intensity. This also holds for our example of the oscillatory regime of the FitzHugh-Nagumo system, where we can demonstrate that the spiking frequency becomes minimal at an intermediate noise level.

I. INTRODUCTION

In their groundbreaking work from 1946, Wiener and Rosenblueth,¹ having observed propagating contractions in the cardiac muscle, developed the fundamental concept of an excitable system: exciting a state of rest by perturbations above a certain threshold, the system reacts with a non-linear response. Subsequently, the system needs a certain time, called the refractory period, until it can be excited again. This concept provided an extremely successful framework for understanding a large variety of real-life systems.² Beginning from biological systems, where it describes not only cardiac tissue³ but also certain functionalities of organisms,^{4,5} and behavioral aspects of individuals, or of whole populations,^{6,7} it has been translated to gene regulatory networks,⁸ chemical reactions,⁹ laser systems,¹⁰ and semiconductors,¹¹ and last but not least, it has become one of the key principles of theoretical neuroscience.^{12–16}

We extend the concept of excitability by considering as the rest state of the system a stable periodic orbit rather than an equilibrium. In this case, the nonlinear threshold-like response may additionally depend on the phase of the oscillation at which the impulse acts such that an excitation may occur only if a super-threshold perturbation is applied within a certain part of the periodic orbit. We shall use the regime of relaxation oscillations in the FitzHugh-Nagumo system as an example

^{a)}Electronic mail: franovic@ipb.ac.rs

^{b)}Electronic mail: omelchen@wias-berlin.de

^{c)}Electronic mail: wolfrum@wias-berlin.de

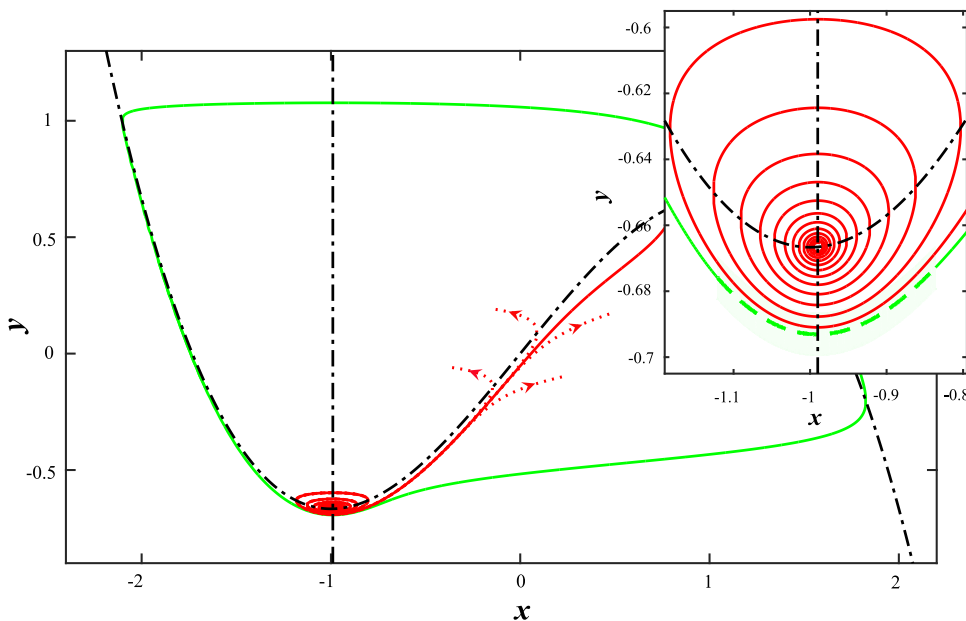


FIG. 1. Phase plane for (1) with $b = 0.99$, $\epsilon = 0.05$, $I(t) = 0$: relaxation oscillation orbit (green), maximal canard (red), and nullclines (dash-dotted). Inset: region close to the unstable equilibrium. In the region of phase-sensitive excitability (green stripe), the maximal canard passes close to the relaxation oscillation orbit such that small perturbations may deviate a solution to make an extra round trip around the unstable equilibrium.

of this general concept of phase-sensitive excitability. In the context of neuroscience, this spiking regime can already be considered as the “excited state” of a neuron. Nevertheless, here we shall consider this periodic regime as the “rest state” in the sense of Refs. 1 and 2 and shall study its nonlinear threshold-like response to perturbations, which in this case manifests as a reduced spiking activity. Note that in Ref. 17 a similar model was considered but with the rest state given by the subthreshold oscillations and with the excited state associated to the large-amplitude oscillations. Using multi-scale techniques and the canard trajectories, we shall analyze in detail the specific mechanism realizing the non-linear excitations in our system.

In Ref. 18, it has been pointed out that excitable systems can respond to noise in a specific way, showing a characteristic non-monotone dependence on the noise level. Such effects have been studied extensively and the FitzHugh-Nagumo system in the regime of an excitable equilibrium represents one of the classical examples.^{18–20} There, it is the mean spiking regularity of *noise-induced* oscillations that shows a characteristic maximum, called coherence resonance, at an intermediate noise level. Our study of the FitzHugh-Nagumo system in the oscillatory regime will demonstrate that also the relaxation oscillation shows a non-monotone response to noise: here, however, it is the mean spiking rate that shows a characteristic minimum at an intermediate noise level. This effect is most pronounced for intermediate values of the time-scale separation ($\epsilon \approx 0.05$), while in the singular limit $\epsilon \rightarrow 0$, the effect disappears. This is the reason why the effect has not been observed in the detailed study of Muratov and Vanden-Eijnden,²¹ where the behavior of the FitzHugh-Nagumo system under the influence of noise has been investigated by singular perturbation techniques. We believe that our parameter regime can be adequate in the context of neuroscience and that the effect of phase-sensitive excitability may be of importance both for deterministic inputs in coupled network systems and for the case of stochastic input signals.

II. THE FITZHUGH-NAGUMO OSCILLATOR

Our basic example for the mechanism of phase-sensitive excitability is the FitzHugh-Nagumo system

$$\begin{aligned}\epsilon \dot{x} &= x - x^3/3 - y, \\ \dot{y} &= x + b + I(t).\end{aligned}\quad (1)$$

In the context of neuroscience, x and y correspond to the neuronal membrane potential and the ion-gating channels, respectively. The time-dependent input signal $I(t)$ can be used to resemble intrinsic noise in the opening of the ion-channels.²² The smallness of the parameter ϵ reflects the time-scale separation between the dynamics of x and y . The system has been extensively studied as a slow-fast system, using the singular limit $\epsilon \rightarrow 0$, cf. Ref. 23 for an overview on the deterministic case and Refs. 2, 19, 20, and 24–26 for different scenarios with noise. Classical results for the case without input signal $I(t)$ show that system (1) undergoes a supercritical Hopf bifurcation at $b = 1$ such that for decreasing b a branch of small-amplitude oscillations of period $\mathcal{O}(\sqrt{\epsilon})$ appears. Then, for $b = b_c \approx 1 - \epsilon/8$, there is a rapid transition to large-amplitude relaxation oscillations of period $\mathcal{O}(1)$.²⁷ From the neuroscience point of view, this corresponds to the transition from the quiescent state to the spiking regime via subthreshold oscillations. In order to explain the mechanism of phase-sensitive excitability, we consider the slow-fast structures in the phase space for the relaxation oscillations at $b < b_c$ in the system (1). Figure 1 shows the relaxation oscillation orbit together with the nullclines of the vector field. During the passage close to the unstable equilibrium, located at the intersection of the nullclines, the relaxation oscillation orbit is excitable in the following sense: there is an exponentially thin layer of trajectories, called *maximal canard*, such that any perturbation large enough to elevate the state from the periodic orbit to a point above these trajectories will cause the system to make at least one loop around the unstable equilibrium before proceeding again along the relaxation oscillation orbit. Smaller perturbations or perturbations in directions below

the relaxation oscillation orbit will not give rise to such a response.

The maximal canard trajectories are characterized by the fact that they follow the whole unstable branch of the slow manifold, which in first approximation is given by the part of the nullcline $y = x - x^3/3$ lying in between the two folds, cf. Ref. 28. Already exponentially small deviations from the maximal canard cause the solutions to rapidly depart from it, traveling in either direction towards one of the stable branches of the slow manifold (dotted curves in Fig. 1). A maximal canard trajectory can readily be determined numerically by selecting an initial condition closely below the upper fold $(x, y) = (1, 2/3)$, and from there integrating backward in time. Following one of the canard trajectories in this way, one finds a region where it passes extremely close to the relaxation oscillation orbit. Along this part of the relaxation oscillation orbit, the maximal canard acts as a threshold for perturbations such that super-threshold perturbations cause a nonlinear response with an extra excitation loop around the unstable equilibrium.

III. RESPONSE TO NOISE

Having understood the response of the system to single impact perturbations of different size, we examine now the response to Gaussian white noise

$$I(t) = D\xi(t),$$

of varying amplitude D . Figure 2 shows typical realizations of trajectories for three different levels of noise. The plots show that for low noise level (a), the noise-induced excitation loops occur rarely and are well confined by the spiral structure of the maximal canard. For increasing noise level (b), they become more frequent, but at the same time they get increasingly blurred by the noise. For the largest noise level (c), the prevalence of the small excitation loops decreases again since the efficiency of the confinement by the deterministic maximal canard is reduced.

To study this process in more detail, we introduce a Poincaré section at

$$x = x_0 = -0.99, \quad y < x_0 - x_0^3/3, \quad (2)$$

i.e., we record passages through a vertical line extending below the unstable fixed point. In Fig. 3(a), we show the sampled return times ΔT between successive crossing events, obtained for the same noise levels as used in Fig. 2. The histograms show that for all three noise levels one can clearly distinguish between return times $\Delta T \approx T_R$ corresponding to relaxation oscillation cycles and those corresponding to excitation loops $\Delta T \approx T_E$. For the time trace shown in Fig. 3(b), we have shaded the corresponding time intervals accordingly. Panel (c) shows the corresponding variances $\sigma_{R,E}$ for each of the two separate peaks of the return time distribution, and panel (d) shows their relative size for varying noise level D . One can observe that there is a prevalence of excitation loops for intermediate values of the noise level $D \approx 10^{-2}$. Above this value, the variances for each of the peaks start to increase, indicating an increasing degradation of the nonlinear response by noise. The excitation loops delay the

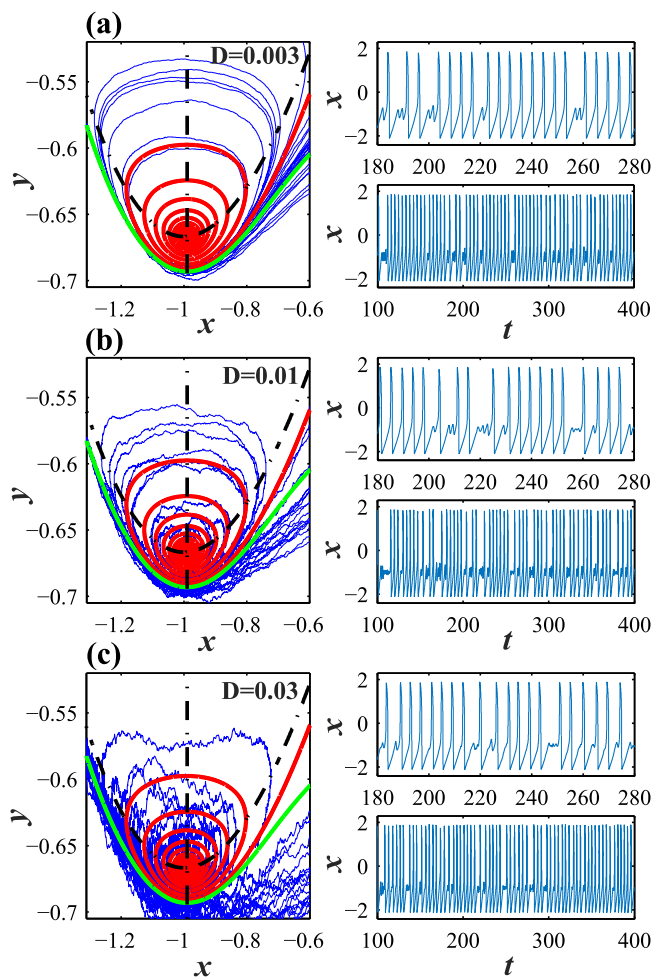


FIG. 2. Response of the relaxation oscillation to different levels of noise: (a) $D = 0.003$, (b) $D = 0.01$, and (c) $D = 0.03$. Left panels: noisy trajectories in the phase plane together with the deterministic relaxation oscillation orbit and maximal canard. Top panels: corresponding time traces $x(t)$ from the panels above. Bottom panels: longer time traces indicating the prevalence of noise induced small excitation loops for the middle noise level $D = 0.01$.

occurrence of the next spike and thus affect the mean spiking rate of the system $\langle R \rangle$, measured as the average number of large-amplitude oscillations per time. Figure 4 shows that the spiking rate exhibits a non-monotone dependence with increasing noise level D , where the minimum of $\langle R \rangle$ coincides with the maximal fraction of small excitation loops shown in Fig. 3(d).

Note that this effect is most pronounced for intermediate values $\varepsilon \approx 0.05$ of the time-scale separation. This is due to the fact that the duration of the excitation loop, given to the leading order by the linearization at the unstable equilibrium, which is a weakly undamped center, scales like $\mathcal{O}(\sqrt{\varepsilon})$. Hence, the delaying effect on the spikes and the consequent decrease of the spiking rate become small in the singular limit.

IV. EXCITATION EFFICIENCY AND DEGRADATION

The non-monotone dependence of the spiking rate $\langle R \rangle(\sigma)$ can be explained as the result of two competing effects of the increasing noise: the increasing efficiency of the excitation and the degradation of the nonlinear response. To study this competition in more detail, we consider the return times

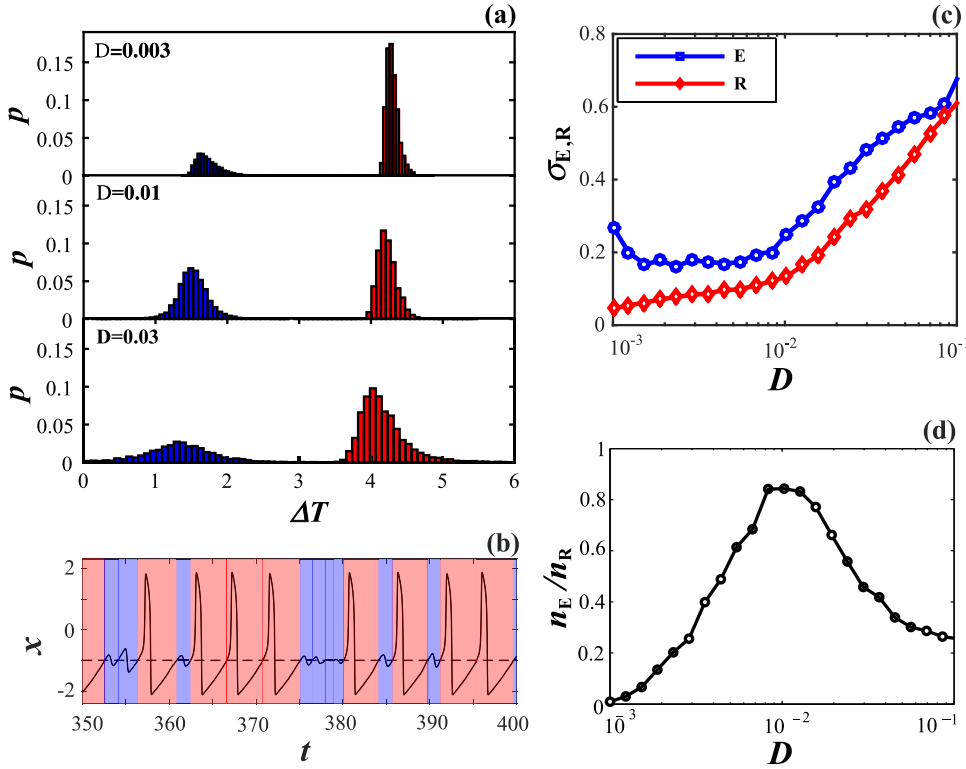


FIG. 3. (a) Sampled return times ΔT between subsequent crossings of the Poincaré section (2) for different noise levels. The two peaks in the distributions correspond to relaxation oscillations $\Delta T \approx T_R$ (red) and noise-induced excitation loops $\Delta T \approx T_E$ (blue). (b) Time trace for $D = 0.01$ with respective time intervals ΔT colored accordingly. [(c) and (d)] Variances $\sigma_{R,E}$ and relative size n_E/n_R from the two separate peaks of the return time distributions for varying noise level.

$\Delta \tilde{T}$, associated to the Poincaré section (2) with $x_0 = -0.2$. In this case, the excitation loops do not lead to additional crossing events and the corresponding return time $\Delta \tilde{T}$ measures the round trip time of each relaxation oscillation together with the included excitation loops. For small noise, the corresponding histograms in Fig. 5(a) show distributions with well separated peaks centered around $\Delta \tilde{T} \approx T_R + kT_E$, where $k \in \{0, 1, 2, 3, \dots\}$ counts the number of excitation loops between two successive Poincaré events. We observe that for $D < 10^{-2}$ there is not only an increasing number of such excitation loops, cf. Fig. 3(d) but also an increasing number of multiple successive excitation loops. This can be seen from the corresponding probabilities of successive loops for varying noise intensity D given in Fig. 5(b). It underlines the increasing efficiency of the excitation process, driven by

noise in the subcritical range $D < 10^{-2}$. Above this value, the degradation effect takes over, which consists in the loss of correlation between the number of included excitation loops and the total duration of the corresponding relaxation oscillation cycle.

In order to quantify the degradation effect, we have calculated the noise-dependence of the correlation coefficient δ between the number k of small loops the unit performs between the two successive passages of the Poincaré cross-section, and the first return time $\Delta \tilde{T}$ being in the corresponding interval $[T_R + (k - \frac{1}{2})T_E, T_R + (k + \frac{1}{2})T_E]$. Evaluating numerically this correlation coefficient, we see the onset of a strong decay above the critical noise level of $D \approx 10^{-2}$, indicating the degradation of the nonlinear response, see Fig. 5(c). Similar effects have been described in Refs. 29 and 30 as noise-induced linearization.

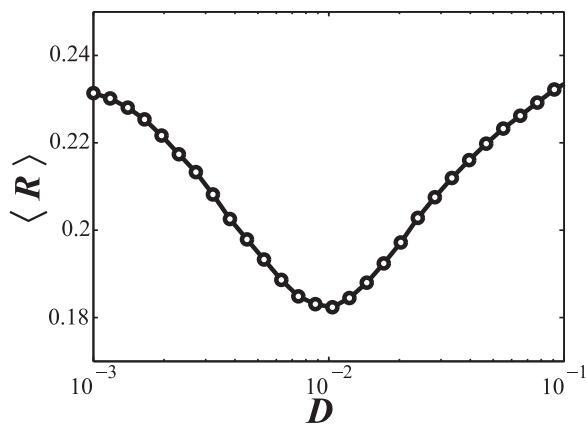


FIG. 4. Non-monotone response to noise of a phase-sensitive excitable periodic orbit: mean spiking rate $\langle R \rangle$ of the relaxation oscillations of (1) shows a characteristic minimum at an intermediate noise level $D \approx 10^{-2}$.

V. DISCUSSION AND OUTLOOK

It is important to remark that a periodic orbit emerging in a transition from an excitable equilibrium, as it happens in the FitzHugh-Nagumo system, does not necessarily inherit phase-sensitive excitability from the excitability of the preceding equilibrium. This can be seen, e.g., for the active rotator

$$\dot{\theta} = 1 + b - \sin \theta + D\xi(t), \quad \theta \in \mathbb{R}/2\pi\mathbb{Z}, \quad (3)$$

where a saddle-node infinite period (SNIPER) bifurcation at $b = 0$ mediates a transition from excitable to oscillatory behavior. However, the periodic solution at $b = 0.02$ shows no phase-sensitive excitability, and the dependence of the spiking rate on the noise level is monotone, cf. Fig. 6(a). On the other hand, for the FitzHugh-Nagumo system with a noise term $\sqrt{D/\varepsilon}\xi(t)$ added to the fast variable x so to resemble the

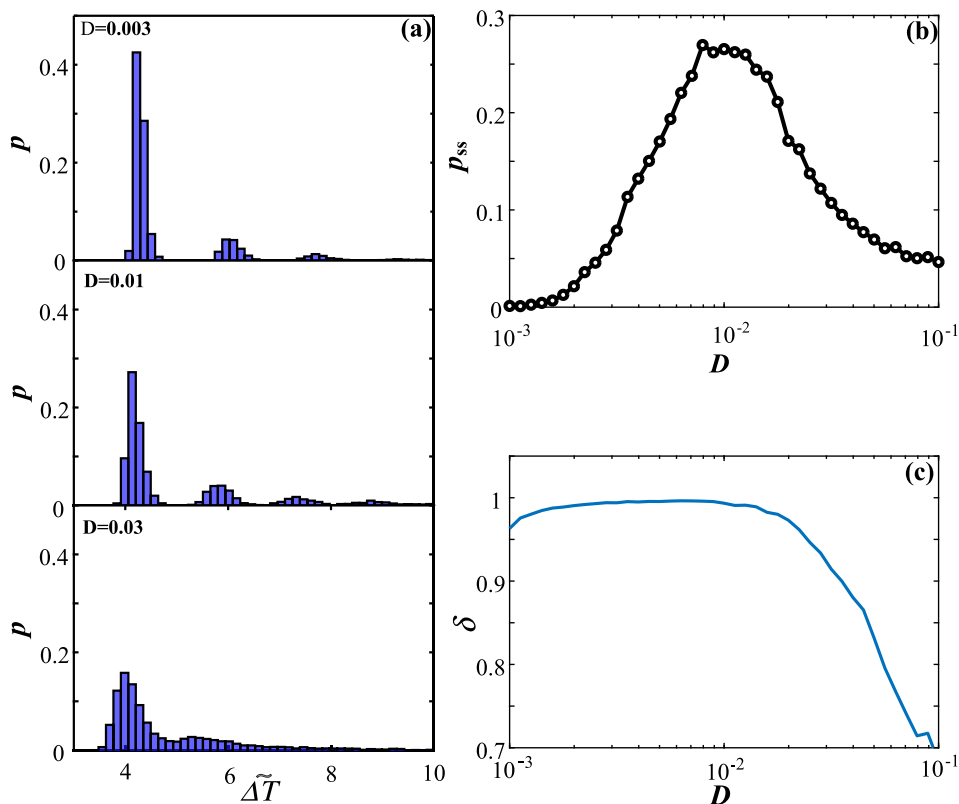


FIG. 5. (a) Histograms of first return times $\Delta\tilde{T}$ to a Poincaré section (2) with $x_0 = -0.2$. (b) Relative frequency of two successive excitation loops. (c) Correlation coefficient between the number of excitation loops in a relaxation oscillation cycle and its duration $\Delta\tilde{T}$.

action of synaptic noise,²² the excitable behavior and the non-monotone dependence can be observed in a similar way, cf. Figs. 4 and 6(b).

The presented concept of phase-sensitive excitability establishes a natural extension of the classical concept of excitability of equilibria to periodic orbits, offering a general framework for describing certain nonlinear effects in driven or interacting oscillatory systems. It resembles the main properties of the classical case:

- (i) nonlinear threshold-like response to perturbation impulses and
- (ii) non-monotone response to noisy inputs of increasing amplitude.

The nature of the non-monotone dependence on the noise level for phase-sensitive excitability in the regime of relaxation oscillations of the FitzHugh-Nagumo system is qualitatively distinct from the two classical cases concerning the FitzHugh-Nagumo model where the rest state is given by an excitable equilibrium or conforms to the regime of subthreshold oscillations before the canard explosion ($b > b_c \approx 1 - \epsilon/8$). In both the classical examples, the excited state conforms to a relaxation oscillation (spike), and the applied noise affects the *regularity* of noise-induced oscillations such that it becomes maximal for the optimal noise intensity.^{17–20} The qualitative similarity between these two cases is to be expected because the subthreshold oscillations become indistinguishable from an equilibrium in the

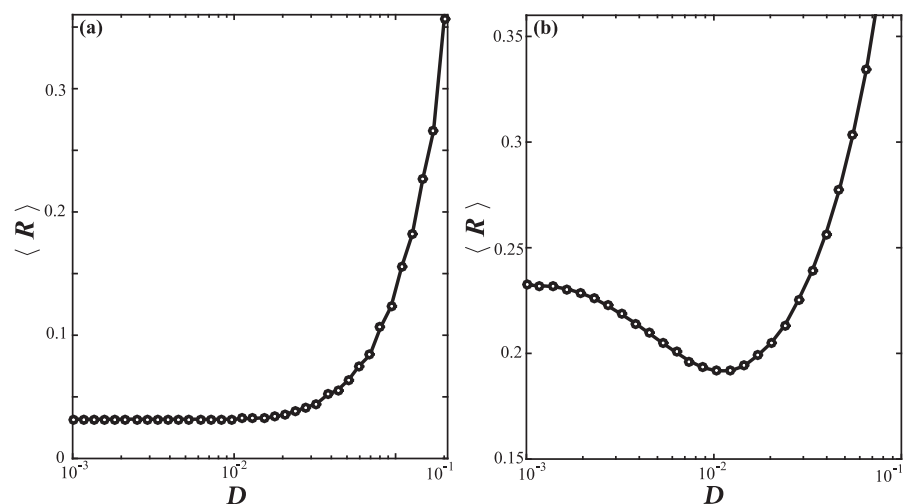


FIG. 6. (a) Monotone mean spiking rate $\langle R \rangle$ of the active rotator (3). (b) Non-monotone mean spiking rate of the relaxation oscillations of (1) with $I(t) = 0$ and adding instead noise of varying levels to the fast variable.

singular limit $\epsilon \rightarrow 0$. As opposed to that, our scenario of phase-sensitive excitability involves the regime of relaxation oscillations as the rest state, the subthreshold oscillations conform to the excited state, and the applied noise affects the *mean spiking frequency* such that it becomes minimal at an intermediate noise level.

In the context of neuroscience, the resonant effect consisting in a reduction of the spiking frequency of neural oscillators within a certain range of intermediate noise levels has been referred to as *inverse stochastic resonance*. Such an inhibitory action of noise has been observed experimentally³¹ and has also been discussed in several model studies, concerning the impact of external or intrinsic noise on single^{32–34} or coupled neurons.^{35,36} The effect has been suggested as a potential paradigm for computational tasks that either require reducing the neuronal spiking frequency without chemical neuro-modulation or involve generating episodes of bursting activity in neurons that are not endogenously bursting. The generic mechanism behind the effect has typically been linked to *bistability* of the underlying deterministic dynamics, which exhibits coexistence between an equilibrium and a stable limit cycle. For such a scenario, the noise induces a switching between the corresponding metastable states, with the spiking frequency decreasing at a certain range of intermediate noise levels where the transition rate from the quasi-stationary to oscillatory state becomes much smaller than the one in the opposite direction. The noise-driven effect reported here is based on a qualitatively distinct mechanism, because the deterministic dynamics is monostable, and the excitations off the limit cycle emerge due to phase-sensitive excitability of the associated orbit, derived from the multi-scale structure of the system.

Revisiting earlier work on coupled oscillator systems, one can find instances where effects that could be explained as a result of phase-sensitive excitability have been reported. Indeed, some of the results in Ref. 37 about space-time patterns in a coupled network of FitzHugh-Nagumo oscillators seem to be based on the phase-sensitive excitability of the relaxation oscillations. Also, the alternating behavior reported in Ref. 38 could possibly be an effect of phase-sensitive excitability. These examples may underline the importance of the abstract concept as such, offering a general framework and a unifying view for a variety of closely related phenomena.

ACKNOWLEDGMENTS

This work was supported by the Ministry of Education, Science and Technological Development of Republic of Serbia under Project No. 171017, the DAAD Serbia-Germany Bilateral Project “Emergent Dynamics in Systems of Coupled Excitable Units,” and the Deutsche Forschungsgemeinschaft (DFG) within the framework of Collaborative Research Center SFB 910.

- ¹N. Wiener and A. Rosenblueth, Arch. Inst. Cardiol. Mex. **16**, 205 (1946), available at <https://www.ncbi.nlm.nih.gov/pubmed/20245817>.
- ²B. Lindner, J. Garcia-Ojalvo, A. Neiman, and L. Schimansky-Geier, *Phys. Rep.* **392**, 321 (2004).
- ³S. Alonso and M. Bär, *Phys. Rev. Lett.* **110**, 158101 (2013).
- ⁴J. D. Murray, *Mathematical Biology* (Springer, Berlin, Heidelberg, New York, 1993).
- ⁵J. P. Keener and J. Sneyd, *Mathematical Physiology* (Springer, New York, 2009).
- ⁶I. Farkas, D. Helbing, and T. Vicsek, *Nature* **419**, 131 (2002).
- ⁷S. P. Borgatti, A. Mehra, D. J. Brass, and G. Labianca, *Science* **323**, 892 (2009).
- ⁸Y. Chen, J. K. Kim, A. J. Hirring, K. Josić, and M. R. Bennett, *Science* **349**, 986 (2015).
- ⁹A. S. Mikhailov and K. Showalter, *Phys. Rep.* **425**, 79 (2006).
- ¹⁰S. Wiecek, B. Krauskopf, T. B. Simpson, and D. Lenstra, *Phys. Rep.* **416**, 1 (2005).
- ¹¹A. M. Yacomotti, P. Monnier, F. Raineri, B. B. Bakir, C. Seassal, R. Raj, and J. A. Levenson, *Phys. Rev. Lett.* **97**, 143904 (2006).
- ¹²E. M. Izhikevich, *Dynamical Systems in Neuroscience: The Geometry of Excitability and Bursting* (MIT Press, Cambridge, 2007).
- ¹³J. White, J. Rubinstein, and A. Kay, *Trends Neurosci.* **23**, 131 (2000).
- ¹⁴I. Franović, K. Todorović, N. Vasović, and N. Burić, *Phys. Rev. E* **87**, 012922 (2013).
- ¹⁵I. Franović, K. Todorović, N. Vasović, and N. Burić, *Phys. Rev. Lett.* **108**, 094101 (2012).
- ¹⁶I. Franović, K. Todorović, N. Vasović, and N. Burić, *Chaos* **22**, 033147 (2012).
- ¹⁷V. A. Makarov, V. I. Nekorkin, and M. G. Velarde, *Phys. Rev. Lett.* **86**, 3431 (2001).
- ¹⁸A. S. Pikovsky and J. Kurths, *Phys. Rev. Lett.* **78**, 775 (1997).
- ¹⁹R. E. Lee De Ville, E. Vanden-Eijnden, and C. B. Muratov, *Phys. Rev. E* **72**, 031105 (2005).
- ²⁰C. B. Muratov, E. Vanden-Eijnden, and E. Weinan, *Physica D* **210**, 227 (2005).
- ²¹C. B. Muratov and E. Vanden-Eijnden, *Chaos* **18**, 015111 (2008).
- ²²A. Destexhe and M. Rudolph-Lilith, *Neuronal Noise* (Springer, New York, 2012).
- ²³C. Kuehn, *Multiple Time Scale Dynamics*, (Springer International Publishing, Switzerland, 2015).
- ²⁴I. Franović, K. Todorović, M. Perc, N. Vasović, and N. Burić, *Phys. Rev. E* **92**, 062911 (2015).
- ²⁵J. M. Newby and M. A. Schwemmer, *Phys. Rev. Lett.* **112**, 114101 (2014).
- ²⁶N. Berglund and D. Landon, *Nonlinearity* **25**, 2303 (2012).
- ²⁷S. M. Baer and T. Erneux, *SIAM J. Appl. Math.* **46**, 721 (1986).
- ²⁸M. Krupa and P. Szmolyan, *SIAM J. Math. Anal.* **33**, 286 (2001).
- ²⁹N. G. Stocks, N. D. Stein, H. E. Short, R. Mannella, D. G. Luchinsky, and P. V. E. McClintock, in *Fluctuations and Order: The New Synthesis* (Springer, Berlin, 1996), pp. 53–67.
- ³⁰E. Hunsberger, M. Scott, and C. Eliasmith, *Neural Comput.* **26**, 1600 (2014).
- ³¹D. Paydarfar, D. B. Forger, and J. R. Clay, *J. Neurophysiol.* **96**, 3338 (2006).
- ³²H. C. Tuckwell, J. Jost, and B. S. Gutkin, *Phys. Rev. E* **80**, 031907 (2009).
- ³³M. Uzuntarla, J. R. Cressman, M. Ozer, and E. Barreto, *Phys. Rev. E* **88**, 042712 (2013).
- ³⁴M. Uzuntarla, J. J. Torres, P. So, M. Ozer, and E. Barreto, *Phys. Rev. E* **95**, 012404 (2017).
- ³⁵B. S. Gutkin, J. Jost, and H. C. Tuckwell, *Europhys. Lett.* **81**, 20005 (2008).
- ³⁶M. Uzuntarla, E. Barreto, and J. J. Torres, *PLoS Comput. Biol.* **13**, e1005646 (2017).
- ³⁷G. Ansmann, K. Lehnertz, and U. Feudel, *Phys. Rev. X* **6**, 011030 (2016).
- ³⁸N. Semenova, A. Zakharova, V. Anishchenko, and E. Schöll, *Phys. Rev. Lett.* **117**(1), 014102 (2016).



Collective Activity Bursting in a Population of Excitable Units Adaptively Coupled to a Pool of Resources

Igor Franović^{1*}, Sebastian Eydam^{2*}, Serhiy Yanchuk^{3,4,5} and Rico Berner^{6,7*}

¹Scientific Computing Laboratory, Center for the Study of Complex Systems, Institute of Physics Belgrade, University of Belgrade, Belgrade, Serbia, ²Neural Circuits and Computations Unit, RIKEN Center for Brain Science, Wako, Japan, ³Institut für Mathematik, Technische Universität Berlin, Berlin, Germany, ⁴Potsdam Institute for Climate Impact Research, Potsdam, Germany, ⁵Institut für Mathematik, Humboldt-Universität zu Berlin, Berlin, Germany, ⁶Institut für Physik, Humboldt-Universität zu Berlin, Berlin, Germany, ⁷Institut für Theoretische Physik, Technische Universität Berlin, Berlin, Germany

We study the collective dynamics in a population of excitable units (neurons) adaptively interacting with a pool of resources. The resource pool is influenced by the average activity of the population, whereas the feedback from the resources to the population is comprised of components acting homogeneously or inhomogeneously on individual units of the population. Moreover, the resource pool dynamics is assumed to be slow and has an oscillatory degree of freedom. We show that the feedback loop between the population and the resources can give rise to collective activity bursting in the population. To explain the mechanisms behind this emergent phenomenon, we combine the Ott-Antonsen reduction for the collective dynamics of the population and singular perturbation theory to obtain a reduced system describing the interaction between the population mean field and the resources.

Keywords: local and collective excitability, heterogeneous neural populations, metabolic resources, collective bursting, adaptive coupling, switching dynamics, multiscale dynamics, multistability

1 INTRODUCTION

Complex dynamical networks are indispensable for modeling many processes in nature, technology, and social sciences (Strogatz, 2001; Boccaletti et al., 2006; Arenas et al., 2008; Yanchuk et al., 2021). In realistic situations, collective dynamics in such networks is affected by the constraints on available resources from the environment (Roberts et al., 2014; Kroma-Wiley et al., 2021), resulting in complex dynamical phenomena, especially if the systems are self-organized to operate close to criticality (Levina et al., 2007). Often, additional resource dynamics gives rise to adaptive mechanisms such as frequency adaptation (Fuhrmann et al., 2002; Taylor et al., 2010; Ha and Cheong, 2017; Kroma-Wiley et al., 2021), delay adaptation (Fields, 2015; Park and Lefebvre, 2020), or various forms of homeostatic plasticity in neuronal systems (Zierenberg et al., 2018).

Compared with other somatic cells, neurons have a very high energy consumption (Attwell and Laughlin, 2001) and are highly sensitive to energy limitations affecting their cellular metabolic processes. Hence, the availability of metabolic resources, their dynamics and their interplay with the neuronal activity are important factors for the overall performance of neural networks and their homeostasis (Vergara et al., 2019). Dynamical networks with resource constraints have been in the focus of recent studies (Taylor et al., 2010; Roberts et al., 2014; Virkar et al., 2016; Nicosia et al., 2017;

OPEN ACCESS

Edited by:

Wei Lin,
Fudan University, China

Reviewed by:

Xiyun Zhang,
Jinan University, China
Fabrizio Lombardi,
ETH Zürich, Switzerland

*Correspondence:

Rico Berner
rico.berner@physik.hu-berlin.de
Igor Franović
franovic@ipb.ac.rs
Sebastian Eydam
richard.eydam@riken.jp

Specialty section:

This article was submitted to
Networks of Dynamical Systems,
a section of the journal
Frontiers in Network Physiology

Received: 22 December 2021

Accepted: 16 February 2022

Published: 28 March 2022

Citation:

Franović I, Eydam S, Yanchuk S and
Berner R (2022) Collective Activity
Bursting in a Population of Excitable
Units Adaptively Coupled to a Pool
of Resources.
Front. Netw. Physiol. 2:841829.
doi: 10.3389/fnetp.2022.841829

Song et al., 2020; Kroma-Wiley et al., 2021). In particular, in (Song et al., 2020) it has been investigated how phase synchronization between the mutually uncoupled system elements depends on the interaction with the environment. A mini-review (Roberts et al., 2014) has highlighted the importance of reciprocal coupling between neuronal activity and metabolic resources in self-organizing and maintaining neuronal operation near criticality, and has also presented a general slow-fast formulation for the case where resources change slowly relative to neural activity. In (Virkar et al., 2016), a discrete two-layer model has been proposed to describe a mechanism by which metabolic resources are distributed to neurons via glial cells. An example of frequency adaptation in Kuramoto model was provided in (Taylor et al., 2010), reproducing certain phenomena that are not qualitatively accounted for the classical Kuramoto model, such as long waiting times before reaching synchronization. In (Nicosia et al., 2017), neuronal dynamics and nutrient transport were assumed to be bidirectionally coupled, such that the allocation of the transport process at one layer depends on the degree of synchronization in the other and vice versa. In (Kroma-Wiley et al., 2021), a system of coupled Kuramoto oscillators that consume or produce resources depending on their oscillation frequency was considered.

Inspired by the mechanisms for the interaction of a neuronal network with a population of glial cells, the studies (Fields, 2015; Lücken et al., 2017; Park and Lefebvre, 2020) introduced models of networks with adaptive time-delays.

Of particular interest are adaptive networks in which connectivity changes are related to intrinsic nodal dynamics (Gross and Blasius, 2008; Berner, 2021). For example, these types of networks can model synaptic neuronal plasticity (Meisel and Gross, 2009; Markram et al., 2011), chemical (Jain and Krishna, 2001; Kuehn, 2019), epidemic (Gross et al., 2006), biological, and social systems (Horstmeyer and Kuehn, 2020). A paradigmatic example of adaptively coupled phase oscillators gained considerable interest recently (Gutiérrez et al., 2011; Kasatkin et al., 2017; Berner et al., 2019a; Berner et al., 2019b; Berner et al., 2020; Feketa et al., 2020; Berner et al., 2021). This type of phase oscillator models seems to be useful for predicting and describing phenomena in more realistic and detailed models (Popovych et al., 2015; Lücken et al., 2016; Röhr et al., 2019) as well as for the understanding of collective phenomena such as multicluster states (Berner et al., 2019a; Berner et al., 2019b) or recurrent synchronization (Thiele et al., 2022).

In the present paper, we consider coupled excitable units (Lindner et al., 2004; Izhikevich, 2007), characterized by a linearly stable rest state susceptible to finite-amplitude perturbations. Excitable systems act as nonlinear threshold-like elements, such that applying a sufficiently small perturbation gives rise to a small-amplitude linear response, while a perturbation exceeding a certain threshold may trigger a large-amplitude nonlinear response. A classical example for the excitability feature are neurons (Ermentrout and Kopell, 1986; Izhikevich, 2007) which respond to a supra-threshold stimulation by emitting a spike. Apart from neuronal systems, excitability is important for other living cells (Sciolla et al., 2021), lasers

(Yanchuk et al., 2019; Terrien et al., 2021), chemical reactions (Chigwada et al., 2006), machine learning (Ceni et al., 2019), and many other fields. A variety of phenomena, including resonances, oscillations, patterns and waves, are caused by the interplay of excitability and noise (Pikovsky and Kurths, 1997; Neiman et al., 1999; Pototsky and Janson, 2008; Franović et al., 2015; Bačić et al., 2018a; Bačić et al., 2018b; Franović et al., 2018; Zheng and Pikovsky, 2018; Bačić and Franović, 2020; Franović et al., 2020) or time-delay (Brandstetter et al., 2010; Klinshov et al., 2016).

As a prototype of excitable local dynamics, we consider active rotators, paradigmatic for type I excitability (Shinomoto and Kuramoto, 1986; Park and Kim, 1996; Lindner et al., 2004; Osipov et al., 2007; Dolmatova et al., 2017; Franović et al., 2020; Klinshov et al., 2021). Active rotators have been used to study interacting excitable systems with noise (Lindner et al., 2004), synchronization in the presence of noise (Shinomoto and Kuramoto, 1986; Park and Kim, 1996; Dolmatova et al., 2017; Klinshov et al., 2021), the interplay of noise and an adaptive feedback (Franović et al., 2020), effects of an adaptive network structure (Thamizharasan et al., 2021), co-effects of noise, coupling, and adaptive feedback (Bačić et al., 2018b; Song et al., 2020) or delayed feedback (Yanchuk et al., 2019) and the impact of higher-order Fourier modes (Ronge and Zaks, 2021), to name but a few.

An important ingredient of our model is the multiscale structure of the dynamics, whereby the processes at the pool of resources are assumed to occur much slower than the dynamics of excitable units at the nodes. Utilizing this feature, we apply the methods of singular perturbation theory (Desroches et al., 2012; Kuehn, 2015) to first study the fast dynamics (layer dynamics) for fixed resource levels with the Ott-Antonsen approach, and then reduce the problem to the slow dynamics of resources.

Our main result consists in demonstrating how the adaptive interaction between a population of excitable units with a pool of resources gives rise to collective activity bursting. Such emergent dynamics is characterized by alternating episodes of stationary and oscillating behavior of the macroscopic order parameter. We describe the mechanisms behind the activity bursting and indicate parameter regions where this phenomenon can be reliably observed. So far, collective bursting phenomena have been considered to emerge due to time-varying neuronal inputs (Stoop et al., 2002), the interplay of external input and homeostatic plasticity (Zierenberg et al., 2018), or synaptic short-term plasticity (Gast et al., 2020). In these studies, possible implications for healthy and diseased brain states have been drawn. Moreover, the important role of bursting phenomena for the understanding of brain-organ interactions have been highlighted in the perspectives article (Ivanov, 2021). Our study complements recent research on emergent bursting dynamics in brain and organ systems by providing a simple and analytically tractable model generating collective activity bursting.

Our paper is organized as follows. In **Section 2** we lay out the model of a heterogeneous population of excitable units adaptively coupled to a pool of resources, while in **Section 3** we introduce the main phenomenon of collective activity bursting. **Section 4**

and **Section 5** concern the analysis of the system’s multiscale dynamics within the framework of singular perturbation theory, first elaborating on the layer problem and then using the reduced problem to explain the mechanism of collective bursting and the origin of multistability in the full system. **Section 6** proposes two different approaches to induce switches between the coexisting collective regimes, whereas **Section 7** provides our concluding remarks and outlook.

2 MODEL

We consider a system of N coupled active rotators (Strogatz, 1994) with a Kuramoto-type coupling given by,

$$\dot{\phi}_k = I_k(\mathbf{r}) - \sin \phi_k + \frac{\sigma}{N} \sum_{j=1}^N \sin(\phi_j - \phi_k), \quad (1)$$

where $\phi_k \in [0, 2\pi)$, $k = 1, \dots, N$ are the local phase variables, and σ is the coupling strength. While providing a simplified description of local dynamics, active rotators manifest the excitability feature crucial to neuronal activity (Strogatz, 1994; Izhikevich, 2007), and are similar to the model of theta neurons (Luke et al., 2013; Laing, 2014) paradigmatic for type I neural excitability. Note that more detailed models of neuronal dynamics, such as those of Morris-Lecar (Morris and Lecar, 1981) and Wang-Buzsáki (Wang and Buzsáki, 1996), also belong to this excitability class. External inputs $I_k(\mathbf{r}(t)) = r_1(t) + r_2(t) \nu_k$ received by each unit comprise of a *homogeneous* component $r_1(t)$, acting identically at all the units, and a *heterogeneous* component, where the variability is due to parameters ν_k drawn from a normalized Gaussian distribution $\nu_k \in \mathcal{N}(0, 1)$. Recall that in models of coupled active rotators, terms I_k are classically interpreted as local bifurcation parameters describing individual oscillation frequencies. Nevertheless, here $I_k(t)$ at each moment follow a Gaussian distribution $g(I) = \mathcal{N}(r_1, r_2^2)$, such that the local velocities of the units are modulated by coupling to r_1 and r_2 . The latter modulation can be seen as describing an interaction with the *resources* from the environment (Song et al., 2020; Kroma-Wiley et al., 2021) summarized within the two-component resource variable $\mathbf{r} = (r_1, r_2)$. In the context of neuroscience such modulation of local velocities is reminiscent of frequency adaptation of neuronal spiking (Fuhrmann et al., 2002; Ha and Cheong, 2017) due to a limited amount of metabolic resources affecting e.g. neurotransmitters.

Adaptation of spiking activity is a slow process compared to spike emission (Ha and Cheong, 2017), which should be reflected in the dynamics of metabolic resources $\mathbf{r}(t)$. In fact, a model involving such a separation of time scales has recently been proposed to describe the interplay of energy consumption and activity in neuronal populations (Roberts et al., 2014). Here we introduce a simple model of dynamical resources based on the Hopf normal form. We consider \mathbf{r} as a complex variable, i. e. $\mathbf{r} = r_1 + ir_2$, which satisfies the dynamical equation

$$\dot{\mathbf{r}} = \epsilon f(\mathbf{r} - \mathbf{s}, \lambda), \quad (2)$$

$$\dot{\lambda} = -\epsilon'(\lambda - \lambda_0 - \gamma A(t)), \quad (3)$$

with activity

$$A(t) := \frac{1}{N} \sum_{j=1}^N \dot{\phi}_j, \quad (4)$$

The metabolism describing function given by $f(\mathbf{r}, \lambda) = \mathbf{r}(\lambda + i\omega - |\mathbf{r}|^2)$, the frequency ω and the resource base level given by $\mathbf{s} = s_1 + is_2$. Small parameters $\epsilon \ll 1$ and $\epsilon' \ll 1$ are introduced to account for the scale separation between the fast spiking dynamics of units and the slowly adapting dynamics of the resources. Note that we consider the case $\epsilon' = \epsilon$ throughout the paper.

System **Eq. 2, 3** that describes the interaction between the two resources undergoes a supercritical Hopf bifurcation at $\lambda = 0$. This allows for the interpretation of the resource dynamics as being *inactive* if $\lambda < 0$, when it possesses a stable focus at \mathbf{s} , or as *active* if $\lambda > 0$, when it displays a stable limit cycle. In other words, in the inactive states, the resource dynamics lies stationary at the resource base level $\mathbf{s} = s_1 + is_2$, while for active states, the resource dynamics is attracted to a periodic orbit that encircles the resource base level. We further assume that the dynamics of metabolic resources adapts to the activity $A(t)$ of the population, see **Eq. 4**. In particular, the adaptation dynamics **Eq. 3** can be regarded as a feedback mechanism whereby due to a feedback loop, an activated neuronal population may activate the pool of resources which in turn may further activate or even deactivate the neuronal population. The adaptation strength is described by parameter γ which controls the impact of the population’s dynamics on the dynamics of resources. Throughout the paper, we keep $\gamma = 0.5$. In case of no spiking activity, i.e., if $A(t) = 0$ or $\gamma = 0$, the resource dynamics is inactive and the corresponding resource activity variable λ settles to the rest level λ_0 . In the remainder, the level $\lambda_0 = -0.05$ is assumed to correspond to a stable steady state at \mathbf{s} . Due to the dynamical interplay between the metabolic resources and the neuronal population, the activity variable $\lambda(t)$ may change in time. Accordingly, the state of the resources may change between active (periodic attractor) and inactive (stationary state). To describe the coherence of the population dynamics, we use the complex order parameter Z defined by

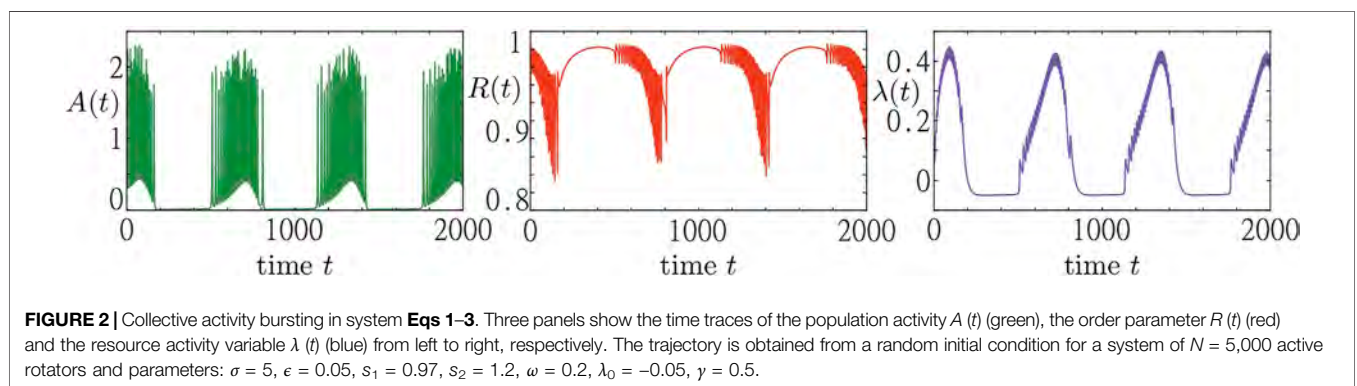
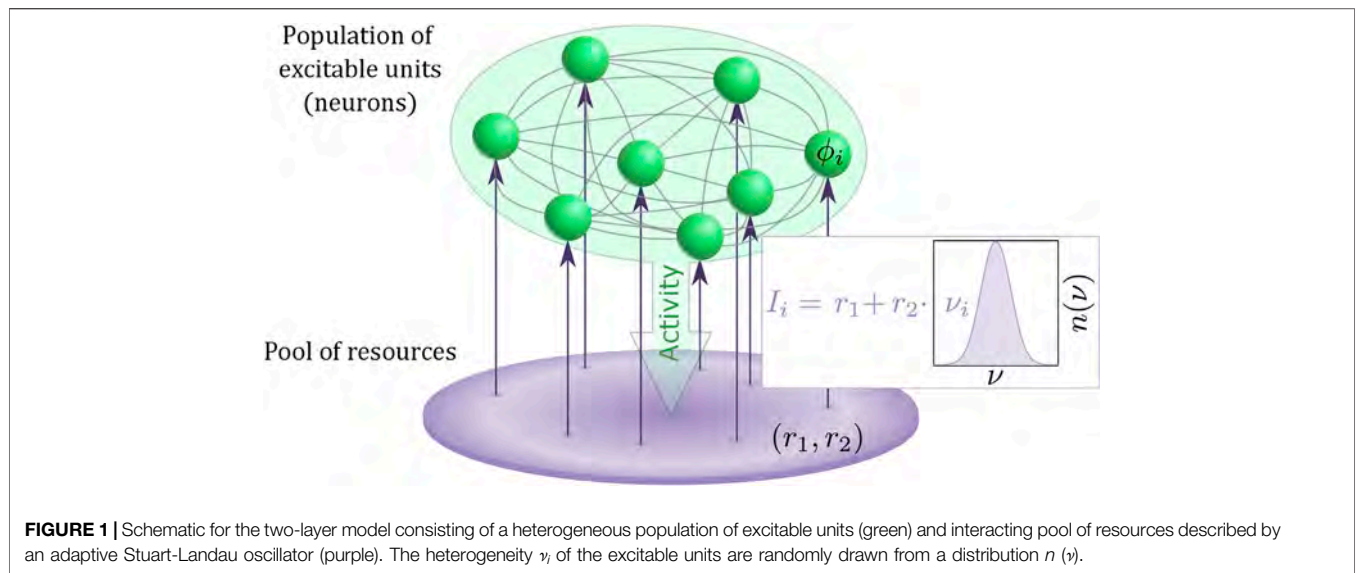
$$Z(\phi(t)) = \frac{1}{N} \sum_{j=1}^N e^{i\phi_j(t)} = R(\phi(t))e^{i\Theta(\phi(t))}, \quad (5)$$

where R is the Kuramoto order parameter, and Θ is the mean phase (Bick et al., 2020).

Summarizing, we have proposed a multiscale model of a heterogeneous population of active rotators, featuring local excitability and spike frequency adaptation as two important ingredients of typical neuronal activity, coupled to a pool of resources that slowly adjusts its dynamics to the activity of the population. **Figure 1** provides an illustration of our model.

3 COLLECTIVE ACTIVITY BURSTING

In this section, we briefly introduce the phenomenon of collective activity bursting induced by an adaptive coupling to resources. A



more detailed analysis of the phenomenon will be performed in the subsequent sections.

In **Figure 2**, we show a simulation result of a system consisting of $N = 5,000$ active rotators adaptively coupled to a pool of resources as described by **Eqs 1–3**. The emergent collective dynamics within the population is represented by the macroscopic variables $A(t)$ and $R(t)$. The dynamics within the resource pool is characterized by the activity variable $\lambda(t)$. We observe that the population of active rotators displays a recurrent temporal formation of bursts in the macroscopic activity $A(t)$ followed by periods of inactivity. Such episodes of macroscopic activity and inactivity correspond to episodes of a rapidly and slowly varying order parameter $R(t)$, respectively. Switching between the different regimes is equally well visible in the evolution of the resource variable $\lambda(t)$ showing the pattern of recurrent activation ($\lambda > 0$) and deactivation ($\lambda < 0$).

We note that this recurrent switching between macroscopic activity and inactivity is due to the adaptive feedback provided by the dynamical resources and can not be observed in a system of active rotators alone. In fact, active rotators are a paradigmatic model for excitable systems, supporting regimes of either activity

$\dot{\phi}_i > 0$ or inactivity $\dot{\phi}_i = 0$ depending on parameters such as the input currents I_i , see e.g. (Franović et al., 2020) for more details. The slow adaptation of the input currents caused by the resource dynamics, however, provides a mechanism to switch between the two regimes. In the following sections, we systematically describe the emergence of collective activity bursting by making use of the separation of timescales between the dynamics of the population and the resources. The slow-fast analysis within singular perturbation theory, see e.g. (De Maesschalck and Wechselberger, 2015; Kuehn, 2015), allows for a splitting of multiscale dynamics into a so-called layer dynamics of the fast variables and an averaged dynamics for the slow variables.

The layer dynamics of system **Eqs 1–3** consists of a population of actively coupled rotators with input currents drawn for a Gaussian distribution $\mathcal{N}(r_1, r_2^2)$. The subsequent analysis of the layer equation in **Section 4** provides us with a clear mapping for the regimes of population activity and inactivity. Building on this, we analyse the full system **Eqs 1–3** and show that the collective activity bursting emerge close to criticality, i.e., the boundary between activity and inactivity of the layer dynamics. We also describe regimes of multistability between activity

bursting and inactivity, and provide insights into perturbations that give rise to transitions between different states.

4 LAYER DYNAMICS: HETEROGENEOUS POPULATION OF ACTIVE ROTATORS

The fast subsystem, describing the evolution of the original slow-fast problem Eqs 1–3 on the fast timescale, comprises of a heterogeneous assembly of N globally coupled active rotators

$$\dot{\phi}_k = r_1 + r_2 \nu_k - \sin \phi_k + \frac{\sigma}{N} \sum_{j=1}^N \sin(\phi_j - \phi_k). \tag{6}$$

In the absence of adaptation of the resource variables r_1 and r_2 , the local dynamics $\dot{\phi}_k = I_k - \sin \phi_k$ depends on external input $I_k = r_1 + r_2 \nu_k$ which may be seen as an effective bifurcation parameter mediating the transition between an excitable ($I_k \leq 1$) and oscillatory regime ($I_k > 1$) via a SNIPER (saddle-node infinite period) bifurcation at $|I_k| = 1$. In the singular limit $\epsilon \rightarrow 0$, system (Eq. 6) defines the layer problem, where r_1 and r_2 are treated as additional system parameters.

According to classical singular perturbation theory (De Maesschalck and Wechselberger, 2015; Kuehn, 2015), the layer problem describes solutions of the multiscale system Eqs 1–3 on a timescale much shorter than $1/\epsilon$, where the variables r_1 and r_2 do not change significantly. In particular, it can describe fast (rapidly changing) segments of the solutions.

4.1 Ott-Antonsen Approach for the Layer Dynamics

We analyze the layer problem by determining the stability of stationary solutions of the layer dynamics and their bifurcations within the framework of Ott-Antonsen theory (Ott and Antonsen, 2008; Ott and Antonsen, 2009). We start by rewriting the layer dynamics in terms of complex order parameter (Eq. 5), which leads to

$$\dot{\phi}_k = I_k - \sin \phi_k + \sigma \text{Im}(Z(t)e^{-i\phi_k}). \tag{7}$$

In the thermodynamic limit $N \rightarrow \infty$, the state of the population can be described by the probability density $h(\phi, I, t)$, which satisfies the normalization condition $\int_0^{2\pi} h(\phi, I, t) d\phi = g(I)$, see e.g. (Omel'chenko and Wolfrum, 2012; Omel'chenko and Wolfrum, 2013). The continuity equation for $h(\phi, I, t)$ then reads

$$\frac{\partial h}{\partial t} + \frac{\partial}{\partial \phi}(h\nu) = 0, \tag{8}$$

where the velocity is given by $\nu = I - \sin \phi + \sigma \text{Im}(Z(t)e^{-i\phi})$. According to Ott-Antonsen ansatz (Ott and Antonsen, 2008; Ott and Antonsen, 2009), the long-term dynamics of Eq. 8 settles onto an invariant manifold of the form

$$h(\phi, I, t) = \frac{g(I)}{2\pi} \left\{ 1 + \sum_{n=1}^{\infty} [\bar{z}^n(I, t)e^{in\phi} + z^n(I, t)e^{-in\phi}] \right\}, \tag{9}$$

where $z(I, t)$ is the local order parameter, connected with the global complex order parameter (Eq. 5) via

$$Z(t) = \int_{-\infty}^{\infty} g(I)z(I, t)dI. \tag{10}$$

Inserting Eq. 9 into Eq. 8, one obtains the Ott-Antonsen equation for the layer dynamics

$$\dot{z} = \frac{1}{2}(1 - z^2) + iIz + \frac{\sigma}{2}Z - \frac{\sigma}{2}\bar{Z}z^2, \tag{11}$$

where bar denotes the complex conjugate.

4.2 Stationary Solutions of the Layer Dynamics

To find stationary solutions of Eqs 10, 11, we first write the local order parameter in polar form $z(I, t) = \rho(I, t)e^{i\Theta(I, t)}$. Separating for the real and imaginary parts, Eq. 11 becomes

$$\begin{aligned} \dot{\rho} &= \frac{1}{2}(1 - \rho^2)B \cos \Phi, \\ \rho\dot{\Phi} &= I\rho - \frac{1}{2}(1 + \rho^2)B \sin \Phi, \end{aligned} \tag{12}$$

where the new variables B , β and Φ are given by

$$\begin{aligned} B(t)e^{i\beta(t)} &= 1 + \sigma R(t)e^{i\Theta(t)}, \\ \Phi &= \vartheta - \beta. \end{aligned} \tag{13}$$

From Eq. 13, it follows that B and β are related with the macroscopic order parameter Eq. 5 via

$$\begin{aligned} B &= \sqrt{1 + \sigma^2 R^2 + 2\sigma R \cos \Theta}, \\ \tan \beta &= \frac{\sigma R \sin \Theta}{1 + \sigma R \cos \Theta}. \end{aligned} \tag{14}$$

Note that the local dynamics can be rewritten in terms of B as $\dot{\phi}_k = I_k - B \sin(\phi_k - \beta)$, suggesting that B may be understood as an effective excitability parameter that describes how local excitability is changed by the impact of interactions. As a consequence, the structure of stationary solutions of the Ott-Antonsen system Eq. 12 depends on the relation between $|I_k|$ and B , such that a population splits into two groups comprised of excitable ($|I| < B$) or oscillating units ($|I| > B$). In particular, the stationary solutions (ρ^* , Φ^*) are given by

$$\begin{aligned} (\rho^*, \Phi^*) &= \left(1, \arcsin \frac{I}{B}\right), \\ (\rho^*, \Phi^*) &= \left(1, \pi - \arcsin \frac{I}{B}\right), \end{aligned} \tag{15}$$

for the excitable (inactive) group, and

$$(\rho^*, \Phi^*) = \left(\frac{|I| - \sqrt{I^2 - B^2}}{B}, \frac{\pi}{2} \text{sign}(I)\right) \tag{16}$$

for the oscillating (active) group. An explicit expression for B can be obtained by invoking the self-consistency relation between the global and local order parameter (Eq. 10). Inserting the results for the stationary local and global order parameter [using Eq. 10,

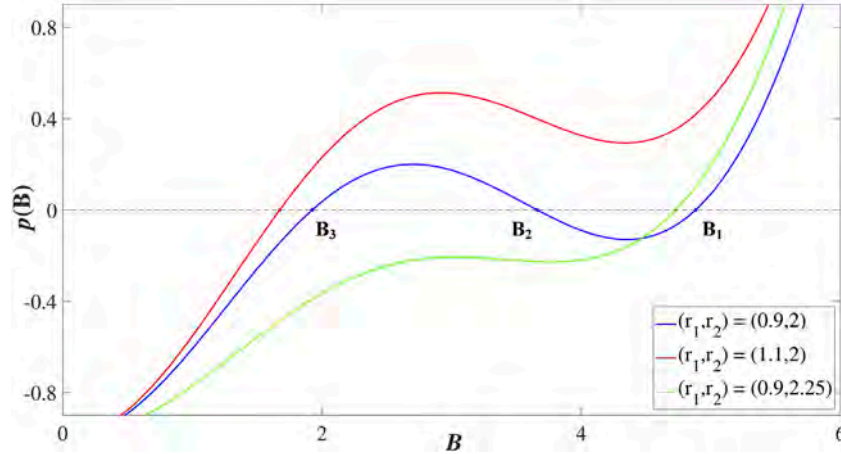


FIGURE 3 | Changes in form and the number of roots of the function $p(B)$ given by Eq. 17 under variation of r_1 and r_2 for fixed $\sigma = 5$. The function $p(B)$ has three roots for $(r_1, r_2) = (0.9, 2)$ (blue line; roots indicated by letters) and a single root for $(r_1, r_2) = (1.1, 2)$ (red) and $(r_1, r_2) = (0.9, 2.25)$ (green).

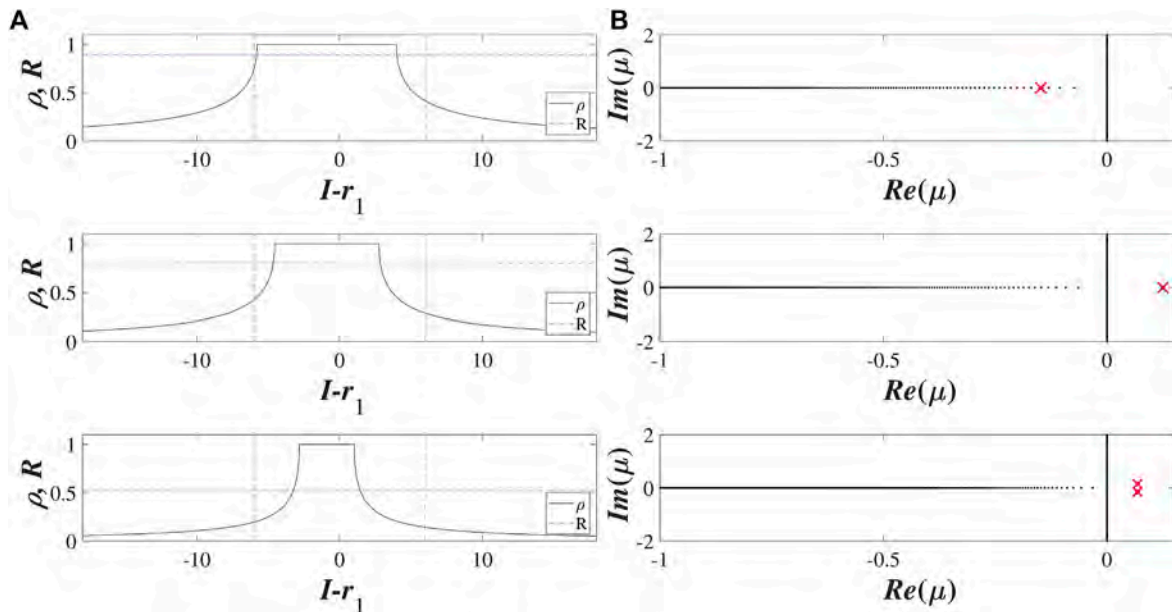


FIGURE 4 | Local structure and spectra of stationary solutions B_1 (a), B_2 (b) and B_3 (c) of Ott-Antonsen equation Eq. 11 for $\sigma = 5$ and $(r_1, r_2) = (0.9, 2)$. (A) shows the dependencies of the local order parameter on the input $z(l)$ (black solid lines) and the corresponding Kuramoto order parameter R (blue dash-dotted lines) for the three stationary solutions. Red dashed lines indicate the interval $(r_1 - 3r_2, r_1 + 3r_2)$ relevant for the distribution of external inputs. (B) shows the continuous (black dots) and the discrete spectra (red crosses) for the stationary solutions: B_1 and B_2 are stable and unstable nodes, respectively, while B_3 is an unstable focus.

Eq. 15, Eq. 16, and the first equation from Eq. 13] and separating for the real and imaginary parts, one ultimately arrives at a self-consistency equation for B (Lafuerza et al., 2010; Klinshov and Franović, 2019)

$$p(B) = B^2 - 2\sigma p_2(B) + \frac{\sigma^2}{B^2} (p_1^2(B) + p_2^2(B)) - 1 = 0, \quad (17)$$

where $p_1(B)$ and $p_2(B)$ are given by

$$\begin{aligned} p_1(B) &= r_1 - \int_{|I|>B} I g(I - r_1) \sqrt{1 - \left(\frac{B}{I}\right)^2} dI, \\ p_2(B) &= \int_{|I|<B} g(I - r_1) \sqrt{B^2 - I^2} dI. \end{aligned} \quad (18)$$

Having determined B , the stationary local and global order parameters can be obtained using the relations

$R = \sqrt{p_1^2 + p_2^2}/B$ and $\Theta = \arctan(p_1/(p_2 - \sigma R^2))$, which follow from Eqs 10–14.

For a fixed coupling strength σ , the function $p(B)$ may have from one to three roots, depending on the mean value r_1 and the standard deviation r_2 of the distribution of intrinsic parameters I_k . The examples in Figure 3 illustrate how the number of solutions of Eq. 17 changes between one and three for fixed $\sigma = 5$, $r_1 = 0.97$ under increasing r_2 . We refer to the stationary solutions by the corresponding B values, which we arrange in decreasing order $B_1 > B_2 > B_3$. Recalling the arguments above, one sees that the larger B value implies a prevalence of excitable over oscillating units within the local structure of the stationary state. This is evinced by the left column of Figure 4 which shows the dependence of the local order parameter $z(I)$. Typically, the state B_1 comprises of a clear majority of excitable units, corresponding to a coherent domain $z = 1$, and may thus be referred to as a *homogeneous* stationary state. The two remaining stationary states B_2 and B_3 are *heterogeneous* in the sense that they involve a mixture of excitable and asynchronously oscillating units.

4.3 Stability and Bifurcation Analysis of Stationary Solutions

Given that Ott-Antonsen equation Eq. 11 contains both the global order parameter and its complex conjugate, stability and bifurcation analysis of the stationary solutions (Omel'chenko and Wolfrum, 2013; Klinshov and Franović, 2019) can be carried out by writing the local and global order parameters as $z(I, t) = x(I, t) + iy(I, t)$, $Z(t) = X(t) + iY(t)$ and separating for the real and imaginary parts. This results in the system

$$\begin{aligned} \dot{x} &= F(x, y, X, Y) = \frac{1}{2}(1 - x^2 + y^2) - Iy + \frac{\sigma}{2}X - \frac{\sigma}{2}X(x^2 - y^2) - \sigma xyY, \\ \dot{y} &= G(x, y, X, Y) = -xy + Ix + \frac{\sigma}{2}Y - \sigma xyX + \frac{\sigma}{2}Y(x^2 - y^2), \end{aligned} \tag{19}$$

which can be linearized for variations $\xi = (\delta x, \delta y)^T$, $\Xi = (\delta X, \delta Y)^T$ around the stationary solution (x_0, y_0, X_0, Y_0) , ultimately arriving at

$$\frac{d\xi}{dt} = \hat{P}(I)\xi(I, t) + \hat{Q}(I)\Xi(t), \tag{20}$$

where \hat{P} and \hat{Q} are the corresponding Jacobian matrices

$$\hat{P} = \begin{pmatrix} \frac{\partial F}{\partial x} & \frac{\partial F}{\partial y} \\ \frac{\partial G}{\partial x} & \frac{\partial G}{\partial y} \end{pmatrix}, \hat{Q} = \begin{pmatrix} \frac{\partial F}{\partial X} & \frac{\partial F}{\partial Y} \\ \frac{\partial G}{\partial X} & \frac{\partial G}{\partial Y} \end{pmatrix}.$$

Eq. 20 is augmented by the variational equation for Eq. 10:

$$\Xi(t) = \int_{-\infty}^{\infty} g(I)\xi(I, t) dI. \tag{21}$$

Assuming that the variations $\xi(I, t)$ and $\Xi(t)$ satisfy $\xi(I, t) = \xi_0(I)e^{\mu t}$, $\Xi(t) = \Xi_0 e^{\mu t}$, systems Eq. 20 and Eq. 21 transform into

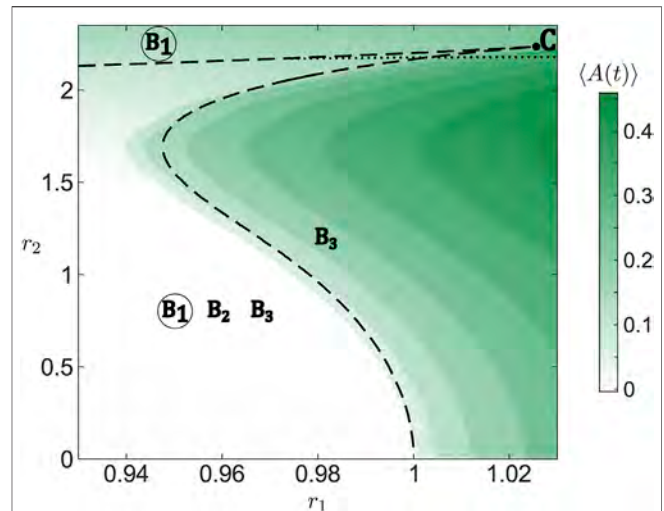


FIGURE 5 | Bifurcation diagram for the system of active rotators Eq. 1 in dependence on resource levels r_1 and r_2 . For the simulation, we have chosen one set of random initial conditions for the phases and one set of parameters ν_k randomly drawn from a normalized Gaussian distribution $\mathcal{N}(0, 1)$. Simulations comprise of 200 time units with activity averaged over the last 100 time units. Fold bifurcations involving stationary solutions B_1 and B_2 (lower branch) and B_2 and B_3 (upper branch) obtained from Eq. 17 are shown by black dashed lines that give rise to a cusp point marked with C. Existence of particular solutions and their stability, derived from the discrete spectrum of Eq. 23, are indicated by their corresponding letters and a circle, respectively, whereby the circle indicates a stable solution. Along the black dotted line, stationary solution B_3 changes its stability in a Hopf-like bifurcation. Other parameters: $N = 5,000$, $\sigma = 5$.

$$(\hat{P}(I) - \mu \hat{\mathbb{I}})\xi_0(I) + Q(I)\Xi_0 = 0, \quad \Xi_0 = \int_{-\infty}^{\infty} g(I)\xi_0 dI, \tag{22}$$

where $\hat{\mathbb{I}}$ denotes the identity operator. From the general spectrum theory of linear operators (Omel'chenko and Wolfrum, 2013; Mirollo and Strogatz, 2007), it follows that the Lyapunov spectrum of Eq. 22 consists of a continuous and a discrete part. Here, the continuous spectrum turns out to be always stable or marginally stable, such that the stability of stationary solutions depends on the discrete spectrum. The latter can be determined by rewriting Eq. 22 in the form $\hat{C}(\mu)\Xi_0 = 0$, where

$$\hat{C}(\mu) = \hat{\mathbb{I}} + \int_{-\infty}^{\infty} g(I)(\hat{P}(I) - \mu \hat{\mathbb{I}})^{-1} Q(I) dI. \tag{23}$$

The discrete spectrum is then obtained by solving the characteristic equation $\det \hat{C}(\mu) = 0$ (Klinshov and Franović, 2019). An example of the discrete and continuous spectra calculated for the stationary states B_1, B_2 and B_3 at $(r_1, r_2) = (0.9, 2)$ is provided in the right column of Figure 4.

4.4 Comparison Between Analysis and Numerics

The previous analysis allows for an analytic description of the existence and stability of stationary solutions in the limit of large

populations ($N \rightarrow \infty$). In particular, the bifurcation diagram for the Ott-Antonsen equation of the layer dynamics **Eq. 11** in the (r_1, r_2) plane is organized around a co-dimension two cusp point, indicated by C in **Figure 5** where the two branches of folds meet (black dashed lines). Both branches of folds are calculated by numerical continuation of the solutions of **Eq. 17** using the software package BifurcationKit.jl (Veltz, 2020). The lower branch of folds which folds over for larger r_2 corresponds to annihilation and reemergence of a pair of equilibria, B_1 and B_2 , whereby the former (latter) is always stable (unstable). For smaller r_2 , crossing this branch either by enhancing r_1 or r_2 gives rise to long-period collective oscillations as a stable equilibrium B_1 vanishes by colliding with an unstable equilibrium B_2 . The divergence of the oscillation period when approaching the curve indicates that it corresponds to a SNIPER bifurcation of the full system. For larger r_2 , as the branch folds over, one observes the reappearance of a stable stationary state B_1 , emerging in an inverse fold bifurcation together with an unstable equilibrium B_2 . The upper branch of folds involves stationary states B_2 and B_3 , such that they collide and disappear above the curve, where B_1 remains the only stable stationary state, cf. **Figure 5**.

Note that apart from the fold bifurcation, the stability of B_3 is also affected by a Hopf-like bifurcation (black dotted line). Above the given curve, stability of B_3 is determined by a pair of complex conjugate eigenvalues which have the smallest negative real parts. However, crossing the curve, these eigenvalues merge with the imaginary axis and remain neutrally stable immediately below the curve, implying that the central manifold theorem associated to Hopf bifurcation cannot immediately be applied. Still, in close vicinity below the curve, starting from an initial condition corresponding to B_3 results in oscillations similar to a genuine scenario of Hopf bifurcation.

Using numerical continuation, we have verified that the described structure of bifurcation diagram for the layer dynamics remains qualitatively the same under variation of coupling strength σ . One only notes that for increasing σ , the branches of folds shift toward larger r_2 , which corresponds to a higher diversity of external inputs.

Figure 5 further shows a comparison of the existence and stability conditions for the collective stationary states derived from Ott-Antonsen approach for the limit $N \rightarrow \infty$ with simulations for a finite population of $N = 5,000$ active rotators with fixed resources r_1 and r_2 . One observes that simulation results agree well with the fold bifurcation lines separating parameter regimes of low and high collective activity. The differences can be attributed to the finite size of assemblies considered in the simulations.

With **Figure 6** we complement the analysis of the layer equation. In particular, we show how the dynamical regimes change in a wide range of parameters r_1 and r_2 , and indicate the boundary (black dashed line) that separate parameter regions supporting stable stationary states from those admitting oscillatory states. We illustrate three different trajectories corresponding to qualitatively different collective regimes found by numerical analysis. For parameter pairs a and b , we observe the emergence of stationary states in accordance with the

bifurcation analysis shown in **Figure 5**. In both cases, activity $A(t)$ and the coherence measure $R(t)$ settle to a constant value. We observe that with increasing r_2 (b to a) the activity level rises while the coherence level declines. For the parameter set c , there is no stable stationary state and we observe stable oscillations. The activity shows a regular, tonic-like spiking shape corresponding to an increase in the average activity. Meanwhile, variation of the order parameter causes its average value to decrease. In order to quantify the temporal variations of the order parameter, we also plot the difference $\max R(t) - \min R(t)$ for the considered average time interval. We observe that even though the activity level might be high, e.g. for $r_1 > 1$ close to $r_2 = 0$, the coherence within the population is not necessarily strongly varying. However, there are also regimes, e.g. for $r_1 > 1$ and $r_2 > 2$, where the order parameter varies strongly and covers almost the entire interval from 0 to 1. In this section, we have illustrated the stability regions of macroscopic stationary states in a heterogeneous population of active rotators. Numerically, we have also determined the values of resource parameters r_1 and r_2 where no stable stationary solutions exist. Using these insights, we are now able to qualitatively describe the phenomena in systems with a slow adaptation of the resources and the resource-dependent dynamics. The next section is devoted to explaining the emerging states of collective activity bursting.

5 (SLOW) RESOURCE DYNAMICS AND THE EMERGENCE OF MULTISTABILITY

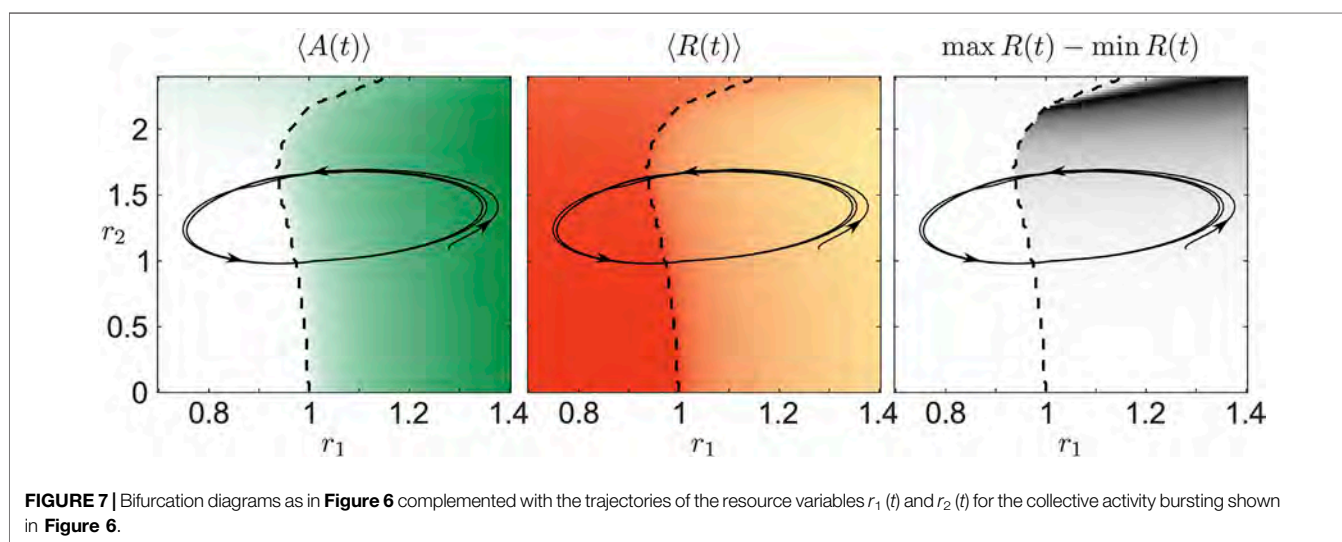
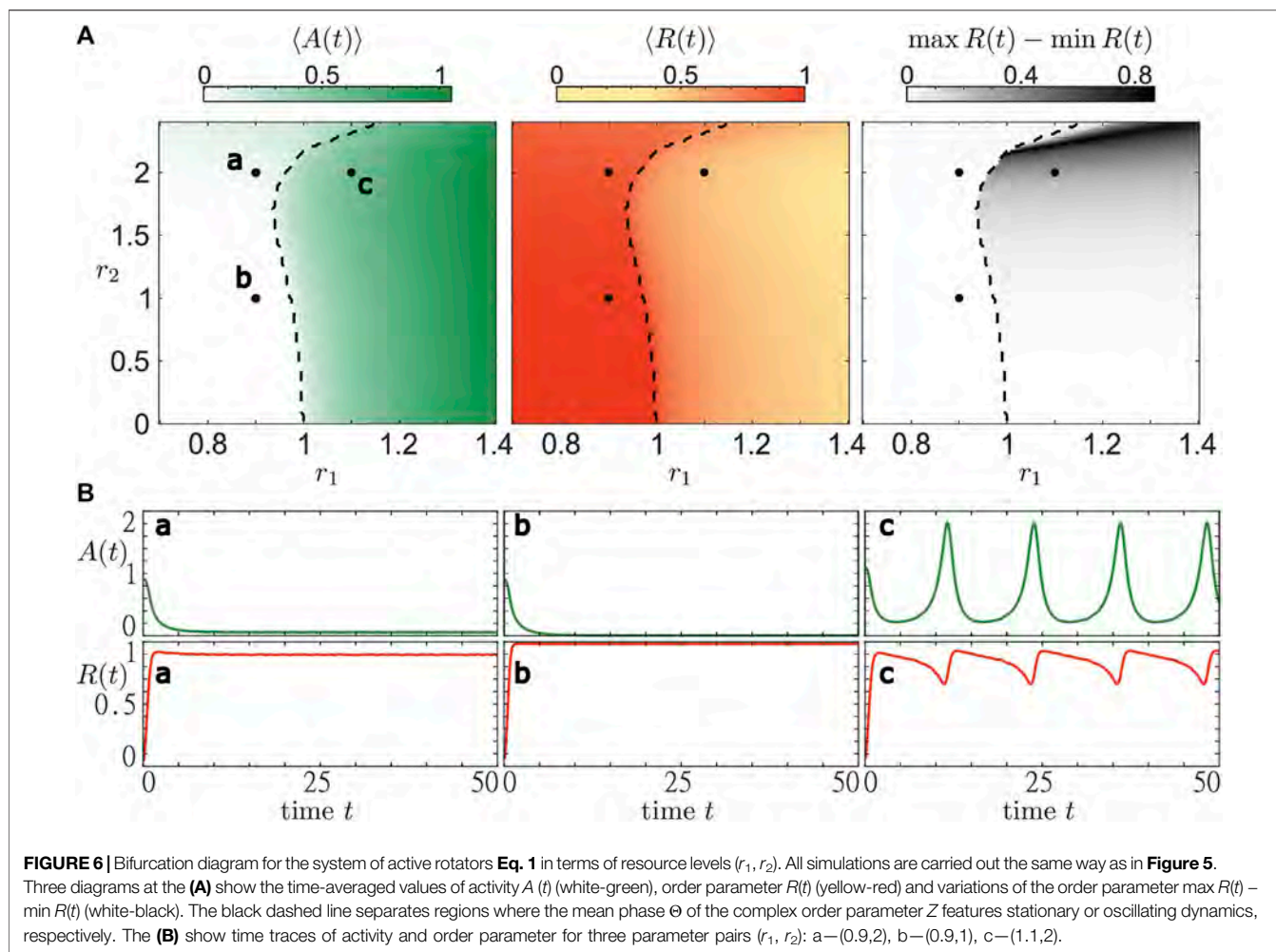
The analysis of the layer dynamics in **Section 4** provides insight on how the system evolves for constant resources r_1 and r_2 . Due to the different timescales of the population (fast dynamics) and the pool of resources (slow dynamics), we can average (Sanders et al., 2007; Franović et al., 2020) the system **Eqs 2, 3** as

$$\dot{\mathbf{r}} = \mathbf{f}(\mathbf{r} - \mathbf{s}, \lambda), \tag{24}$$

$$\dot{\lambda} = -\lambda + \lambda_0 + \rho \langle A \rangle, \tag{25}$$

where $\langle A \rangle = \frac{1}{T} \int_0^T A(s) ds$. Here we also assume $e' = \epsilon$ and rescale time $t_{\text{new}} = \epsilon t_{\text{old}}$. Note that the average activity shown in **Figure 6** depends on the resource variables \mathbf{r} , since the definition **Eq. 4** implies $A = r_1 - \text{Im}(Z)$. Hence, the system **Eqs 24, 25** describes an effective three-dimensional coupled dynamics for the slow subsystem. A further analytical analysis of this system is beyond the scope of our study. However, we directly use the insight that the slow dynamics follows the average activity of the fast system to understand the emergence of collective activity bursting.

Figure 7 shows the trajectories of the resource variables $r_1(t)$ and $r_2(t)$ for the collective bursting presented in **Figure 6** along with the averaged values of population activity and the order parameter. We clearly see that the asymptotic orbit passes through both the regimes of an active and inactive population which explains the episodes of high and low activity in **Figure 2A**. Also the segments of increasing and decreasing average activity visible in **Figure 2A** can be explained by **Figure 7**. Here, the average activity shows the same pattern along the trajectory (r_1



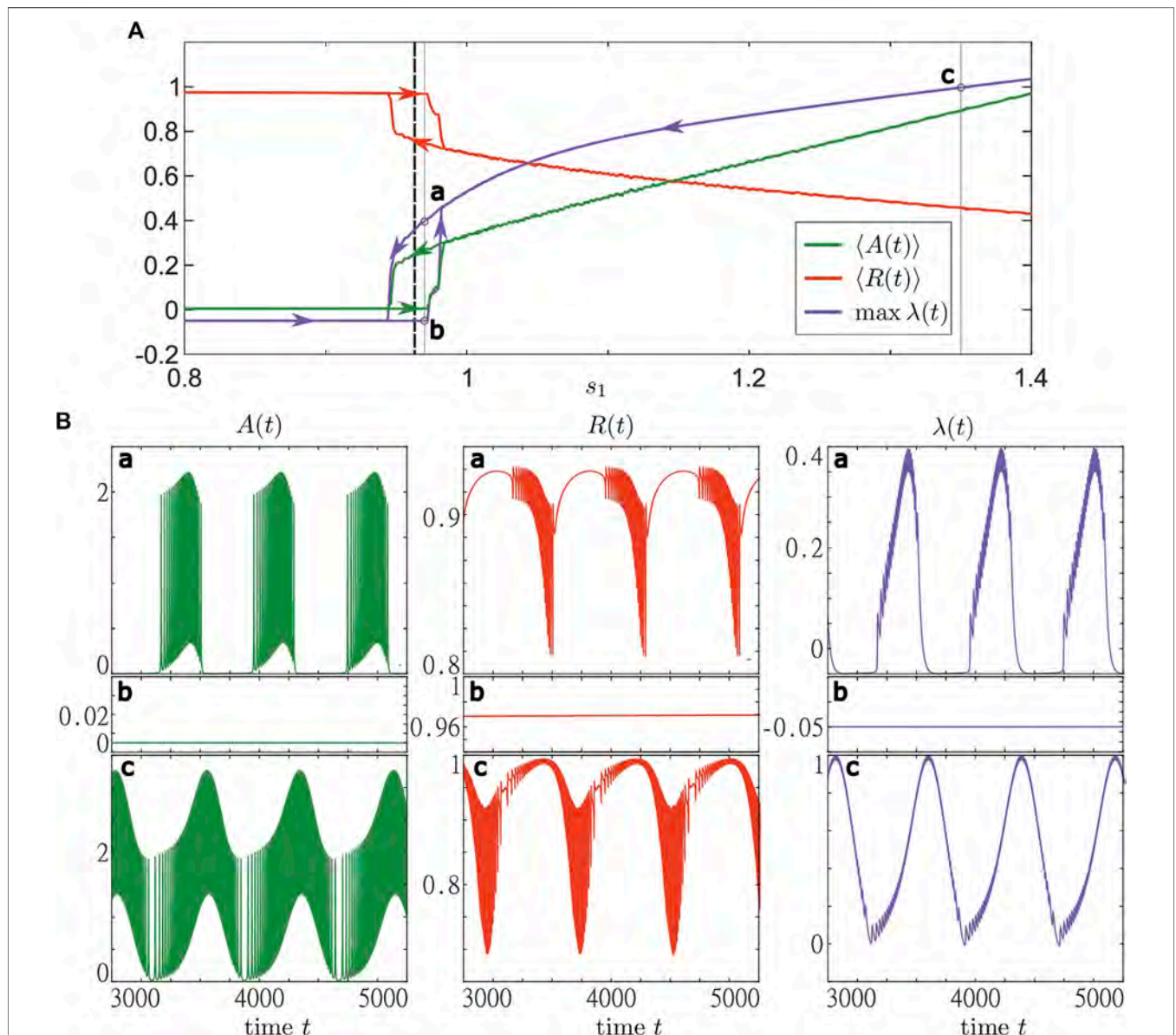
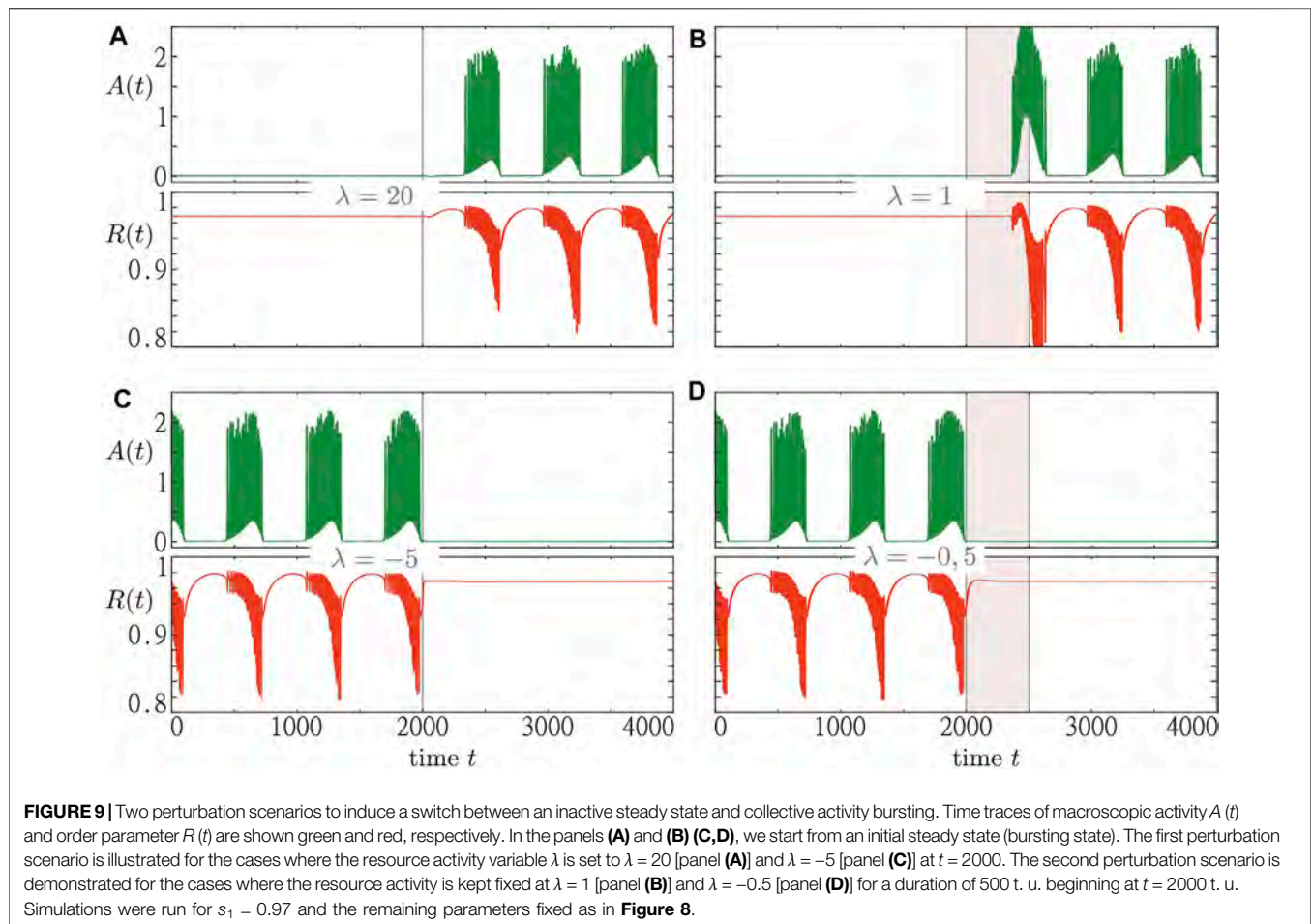


FIGURE 8 | Bifurcation diagram with respect to the resource base level s_1 for a system of active rotators with adaptive resource interaction **Eqs 1–3**. The **(A)** shows the results from two adiabatic continuations with step size $\Delta s_1 = 0.002$ from $s_1 = 0.8$ to $s_1 = 1.4$ (sweep up) and vice versa (sweep down). Sweeps up and down start from a stable stationary and a stable oscillatory state, respectively. For both sweeps are shown the average activity $\langle A(t) \rangle$ (green), average order parameter $\langle R(t) \rangle$ (red) and maximal resource activity λ (blue). The branches corresponding to the two sweeps are marked by arrows. The black dashed lines indicate the value ($s_1 \approx 0.963$) of the critical line shown in **Figure 6**. Three trajectories represented by the activity (green, first column), order parameter (red, middle column) and the resource activity (blue, last column) are shown in the **(B)** for (a,b) $s_1 = 0.97$ and (c) $s_1 = 1.35$. The panels in (a) and (b) represent the states found along the sweeps down and up, respectively. The simulations were performed using the same values of ν_k as in **Figure 5**. Parameters: $N = 5,000$, $\sigma = 5$, $\epsilon = 0.05$, $s_2 = 1.2$, $\omega = 0.2$, $\gamma = 0.5$.

(t) , $r_2(t)$). The same also holds for the average values of the order parameter and even its variations if we compare **Figure 2B** with **Figure 7**. Therefore, the splitting of the fast from the slow subsystem provides a very good qualitative explanation for the observed phenomenon. To understand the emergence of the full periodic orbit shown in **Figure 7**, we first note that without any population activity, i.e., $\langle A \rangle = 0$ and $\lambda_0 = -0.05$, the resource dynamics possess a stable focus close to the critical line (black

dashed line in **Figure 7**) describing the transition from stationary to oscillatory dynamics of the mean phase Θ . During the stationary phase, r_1 and r_2 tend to $s_1 = 0.97$ and $s_2 = 1.2$, respectively. As in **Figure 7**, the trajectory $(r_1(t), r_2(t))$ may start in the active region, i.e., oscillatory mean phase dynamics. Due to the positive average value of activity, the variable $\lambda(t)$ characterizing the resource activity increases according to **(Eq. 25)** and becomes positive, see **Figure 2C**. Hence, the resources



become activated and $(r_1(t), r_2(t))$ follows the limit cycle solution of the resource dynamics revolving around (s_1, s_2) . Note that the resources obey the Hopf normal form with a Hopf bifurcation at $\lambda = 0$, see **Eq. 2**. After passing the critical line, the average activity immediately drops to $\langle A \rangle \approx 0$ which causes λ to tend to λ_0 , see **Figure 2C**. After λ falls below zero, the dynamics of the resources $(r_1(t), r_2(t))$ is described by a spiral towards (s_1, s_2) . This spiral, however, enters the active region by passing the critical line which ultimately leads to the recurrent phenomenon observed in **Figure 2**. As we have seen, the emergence of collective activity bursting relies on the subtle interplay between activation and deactivation of resources and the population. Furthermore, the need for the spiraling dynamics towards a stable focus explains well the necessity for the resource basis levels (s_1, s_2) to be close to the critical line separating the population active and inactive regimes.

With regards to the above description of the collective activity bursting, one might ask for the coexistence of a stable steady state in the system **Eqs 1–3** as long as (s_1, s_2) lie in the inactive regime. This state might have a small basin of attraction such that the spiral towards the steady state cannot reach the active regime.

In order to get insights into the different stable states that exist in **Eqs 1–3**, we use the numerical method of adiabatic continuation. To do so, we fix the base level $s_2 = 1.2$ and gradually vary s_1 from 0.8 to 1.4 (sweep up) and from 1.4 to

0.8 (sweep down). For each value of s_1 , we run the simulation starting from the final state of the previous simulation. In **Figure 8**, we show the results of both sweeps. We observe the existence of stable steady and stable oscillating states for various values of s_1 . As expected, close to the boundary between active and inactive states of layer dynamics, we also find an interval of coexistence between collective activity bursting and stable steady states, see panels for (a) and (b) in **Figure 8**, respectively. For larger s_2 , only the oscillatory state can be observed, which does not enter the inactive regime above a certain s_1 , see panel (c) in **Figure 8**. Note that the character of the solution can be deduced from the maximal value of $\lambda(t)$ on the averaging time interval. In particular, there is a stationary state only if $\max \lambda(t) < 0$. In all other cases, there are time intervals where the trajectory of r diverges from the base level s and follows the periodic solution of **Eq. 24**.

From the arguments laid out in this section, we have seen that the mutual activation and deactivation between the neural population and the pool of resources close to criticality of layer dynamics induces a rich dynamical behavior. It is believed, particularly, that the human brain operates close to criticality (Chialvo, 2010; Haimovici et al., 2013; Yu et al., 2013; Cocchi et al., 2017; Wilting and Priesemann, 2019). Therefore, it is of major importance to understand the dynamics of neural populations in this regimes including the interaction with its

environment. In the next section, we propose a simple mechanism which can induce a switch between coexisting macroscopic regimes.

6 POPULATION SWITCHING DYNAMICS INDUCED BY RESOURCE ACTIVATION AND INACTIVATION

In the vicinity of the transition between the population inactivity and activity, we have observed collective activity bursting induced by an adaptive dynamical pool of resources. Moreover, this phenomenon emerges in a stable coexistence with a steady state. In this section, we consider two simple perturbation approaches that can induce a switch between these two functionally different states.

Figure 9 shows the results for two different perturbation approaches to system **Eqs. 1–3**. The first approach aims to induce a switch in population dynamics by an instantaneous resetting of the resource activity λ . In the second approach, we induce such a transition by maintaining the resource activity at a certain level for a certain period of time. The first approach works well for large resetting values of λ , see **Figures 9A,C**. Small values, however, would not be sufficient to induce the macroscopic regime switch. Furthermore, in case of an initial bursting state, eliciting the switch to a steady state depends on the moment at which the perturbation is applied. However, in our numerical simulations (not shown), we have always been able to induce a switching for sufficiently large resetting values of λ .

Due to the functionally very different nature of the two stable states, there might be reasons to favor one over the other in light of potential applications in medicine. Therefore, it is of great interest to understand simple mechanisms that would induce a switch to the desired state. While the first perturbation approach provides such a mechanism, it still requires strong perturbations which might be undesirable for certain medical reasons, e.g. side effects. Therefore, we have proposed another perturbation approach that leads to a switch while keeping the reset level lower. For this approach, we have also been able to induce switches between a steady state and a bursting state in one or the other direction, see **Figures 9B,D**, with the advantage of having the resetting level of the resource activity much lower than for the first method.

In this section, we have proposed two simple perturbation approaches to induce a switch between the two functionally different macroscopic states of the full system which emerge near the transition in layer dynamics between the population activity and inactivity and due to an adaptive dynamical pool of resources. We note that the approaches we proposed are not the only way to induce macroscopic regime shifts. One might also think of perturbing the resource variables (r_1 , r_2) or even the whole population. Thus, perturbation of the resource activity variable is perhaps the simplest but not the only approach possible.

7 CONCLUSION

We have investigated collective dynamics in a system of interacting excitable units coupled to a pool of resources with

nontrivial dynamics. The feedback of the resources to the population of coupled excitable units has been realized by an adaptation of the individual units' inputs, whereas in turn, the excitable population is capable of activating or deactivating the pool of resources depending on the population's own activity. As a prototype of excitable local dynamics, we have considered active rotators. Following the ideas outlined by Roberts et al. (Roberts et al., 2014), we have assumed the processes at the pool of resources to occur much slower than the local dynamics of excitable units. As a consequence, we have ended up with a system featuring multiscale dynamics, allowing us to use the methods from singular perturbation theory (Desroches et al., 2012; Kuehn, 2015).

As our most important finding, we have reported on the phenomenon of collective activity bursting. The phenomenon is characterized by a recurrent switching between episodes of quiescence and episodes of activity bursts in the population of active rotators. To gain a better understanding of the emergence of collective activity bursting, we have made use of the explicit slow-fast timescale separation. In particular, we have divided the system dynamics into the fast layer dynamics of the population and the slow average dynamics of the resources.

Using the Ott-Antonsen approach, we have analyzed the stability and bifurcations of the stationary solutions of layer dynamics in the thermodynamic limit. For the population of active rotators with a heterogeneity given by a Gaussian distribution, we have derived a bifurcation diagram for the steady state solutions. The bifurcations of layer dynamics depending on the mean and the width of the Gaussian distribution have been corroborated by numerical simulations of a large ensemble of rotators. Doing so, we have determined the parameter regions admitting high or low (or even no) population activity and have obtained the critical lines separating these regions.

Taking the analysis of the layer problem into account, we have further analyzed how the slow averaged dynamics of the resources gives rise to a slow variation of the mean and width of the Gaussian distribution. We have observed the onset of collective activity bursting close to criticality where the population of active rotators undergoes a transition from an inactive to an active state. The emergence of collective bursting is due to a subtle interplay of co-activation and co-deactivation of the dynamical population of rotators and the pool of resources.

We have further found a region of bistability between collective activity bursting and an inactive steady state close to criticality of the layer dynamics. A similar observation has been also discussed in the context of collective bursting induced by synaptic short-term plasticity (Gast et al., 2020). Moreover, we have proposed two different perturbation methods that can trigger switches between coexisting macroscopic regimes. In particular, we have demonstrated that the regime shifts can be induced either by using instantaneous large perturbations or persistent perturbations of the resource activity.

In terms of theory, an important extension of our work could concern a further analytical study of the reduced slow-fast system governing the collective dynamics of the ensemble of excitable

units and its interaction with the resources. For convenience, we summarize the reduced system here

$$\begin{aligned}\dot{z}(I, t) &= \frac{1}{2}(1 - z^2(I, t)) + iIz(I, t) + \frac{\sigma}{2}Z(t) - \frac{\sigma}{2}\bar{Z}(t)z^2(I, t), \\ \dot{\mathbf{r}}(t) &= \epsilon f(\mathbf{r}(t) - \mathbf{s}, \lambda(t)), \\ \dot{\lambda}(t) &= -\epsilon[\lambda(t) - \lambda_0 - \rho(r_1 - \text{Im}(Z(t)))],\end{aligned}$$

with

$$Z(t) = \int g(I)z(I, t) dI.$$

In a broader context, we have proposed a simple paradigmatic model to study the emergence of complex collective phenomena induced by a dynamically co-evolving pool of resources. The research on the impact of resource constraints on the dynamical regimes of populations of neurons or neuron-like units from the dynamical network perspective (Nicosia et al., 2017; Kroma-Wiley et al., 2021) has begun only recently. In our study, we have shown that even a simple model that includes nontrivial dynamical resources gives rise to the emergence of collective activity bursting close to criticality in a population of neuron-like excitable units. Our study underlines the potentially important role of resource constraints in the operating of the human brain that is often hypothesized to operate close to criticality. We have further shown that the collective activity bursting may stably coexist with a steady state. Either one of these regimes could be desirable or undesirable, which makes understanding of the control mechanisms to switch between the regimes highly important (Tang and Bassett, 2018). In this context, we have discussed two simple approaches that can successfully induce such regime shifts. Both approaches impose perturbations to the single activity variable of the resource pool and can thus be

generalized to systems with even more complex dynamical resource pools.

DATA AVAILABILITY STATEMENT

The original contributions presented in the study are included in the article/Supplementary Material, further inquiries can be directed to the corresponding authors.

AUTHOR CONTRIBUTIONS

All authors listed have made a substantial, direct, and intellectual contribution to the work and approved it for submission.

FUNDING

The work of RB and SY was supported by the German Research Foundation DFG, Project Nos 411803875 and 440145547.

ACKNOWLEDGMENTS

IF acknowledges funding from the Institute of Physics Belgrade through the grant by the Ministry of Education, Science and Technological Development of the Republic of Serbia. We acknowledge support by the German Research Foundation (DFG) and the Open Access Publication Fund of Humboldt-Universität zu Berlin.

REFERENCES

- Arenas, A., Díaz-Guilera, A., Kurths, J., Moreno, Y., and Zhou, C. (2008). Synchronization in Complex Networks. *Phys. Rep.* 469, 93–153. doi:10.1016/j.physrep.2008.09.002
- Attwell, D., and Laughlin, S. B. (2001). An Energy Budget for Signaling in the Grey Matter of the Brain. *J. Cereb. Blood Flow Metab.* 21, 1133–1145. doi:10.1097/00004647-200110000-00001
- Bačić, I., and Franović, I. (2020). Two Paradigmatic Scenarios for Inverse Stochastic Resonance. *Chaos* 30, 033123. doi:10.1063/1.5139628
- Bačić, I., Klinshov, V. V., Nekorkin, V. I., Perc, M., and Franović, I. (2018a). Inverse Stochastic Resonance in a System of Excitable Active Rotators with Adaptive Coupling. *EPL* 124, 40004. doi:10.1209/0295-5075/124/40004
- Bačić, I., Yanchuk, S., Wolfrum, M., and Franović, I. (2018b). Noise-induced Switching in Two Adaptively Coupled Excitable Systems. *Eur. Phys. J. Spec. Top.* 227, 1077–1090. doi:10.1140/epjst/e2018-800084-6
- Berner, R., Sawicki, J., and Schöll, E. (2020). Birth and Stabilization of Phase Clusters by Multiplexing of Adaptive Networks. *Phys. Rev. Lett.* 124, 088301. doi:10.1103/PhysRevLett.124.088301
- Berner, R., Vock, S., Schöll, E., and Yanchuk, S. (2021). Desynchronization Transitions in Adaptive Networks. *Phys. Rev. Lett.* 126, 028301. doi:10.1103/PhysRevLett.126.028301
- Berner, R., Schöll, E., and Yanchuk, S. (2019a). Multiclusters in Networks of Adaptively Coupled Phase Oscillators. *SIAM J. Appl. Dyn. Syst.* 18, 2227–2266. doi:10.1137/18m1210150
- Berner, R., Fialkowski, J., Kasatkin, D., Nekorkin, V., Yanchuk, S., and Schöll, E. (2019b). Hierarchical Frequency Clusters in Adaptive Networks of Phase Oscillators. *Chaos* 29, 103134. doi:10.1063/1.5097835
- Berner, R. (2021). *Patterns of Synchrony in Complex Networks of Adaptively Coupled Oscillators* (Cham: Springer). Springer Theses.
- Bick, C., Goodfellow, M., Laing, C. R., and Martens, E. A. (2020). Understanding the Dynamics of Biological and Neural Oscillator Networks through Exact Mean-Field Reductions: a Review. *J. Math. Neurosci.* 10, 9. doi:10.1186/s13408-020-00086-9
- Boccaletti, S., Latora, V., Moreno, Y., Chavez, M., and Hwang, D. (2006). Complex Networks: Structure and Dynamics. *Phys. Rep.* 424, 175–308. doi:10.1016/j.physrep.2005.10.009
- Brandstetter, S., Dahlem, M. A., and Schöll, E. (2010). Interplay of Time-Delayed Feedback Control and Temporally Correlated Noise in Excitable Systems. *Phil. Trans. R. Soc. A* 368, 391–421. doi:10.1098/rsta.2009.0233
- Ceni, A., Ashwin, P., and Livi, L. (2019). Interpreting Recurrent Neural Networks Behaviour via Excitable Network Attractors. *Cogn. Comput.* 12, 330–356. doi:10.1007/s12559-019-09634-2
- Chialvo, D. R. (2010). *Emergent Complex Neural Dynamics*. *Nat. Phys* 6, 744–750. doi:10.1038/nphys1803
- Chigwada, T. R., Parmananda, P., and Showalter, K. (2006). Resonance Pacemakers in Excitable media. *Phys. Rev. Lett.* 96, 244101. doi:10.1103/physrevlett.96.244101
- Cocchi, L., Gollo, L. L., Zalesky, A., and Breakspear, M. (2017). Criticality in the Brain: A Synthesis of Neurobiology, Models and Cognition. *Prog. Neurobiol.* 158, 132–152. doi:10.1016/j.pneurobio.2017.07.002

- De Maesschalck, P., and Wechselberger, M. (2015). Neural Excitability and Singular Bifurcations. *J. Math. Neurosci.* 5, 16. doi:10.1186/s13408-015-0029-2
- Desroches, M., Guckenheimer, J., Krauskopf, B., Kuehn, C., Osinga, H. M., and Wechselberger, M. (2012). Mixed-mode Oscillations with Multiple Time Scales. *SIAM Rev.* 54, 211–288. doi:10.1137/100791233
- Dolmatova, A. V., Goldobin, D. S., and Pikovsky, A. (2017). Synchronization of Coupled Active Rotators by Common Noise. *Phys. Rev. E* 96, 062204. doi:10.1103/PhysRevE.96.062204
- Ermentrout, G. B., and Kopell, N. (1986). Parabolic Bursting in an Excitable System Coupled with a Slow Oscillation. *SIAM J. Appl. Math.* 46, 233–253. doi:10.1137/0146017
- Feketa, P., Schaum, A., and Meurer, T. (2020). Synchronization and Multi-Cluster Capabilities of Oscillatory Networks with Adaptive Coupling. *IEEE Trans. Autom. Control.* 66, 3084.
- Fields, R. D. (2015). A New Mechanism of Nervous System Plasticity: Activity-dependent Myelination. *Nat. Rev. Neurosci.* 16, 756–767. doi:10.1038/nrn4023
- Franović, I., Omel'chenko, O. E., and Wolfrum, M. (2018). Phase-sensitive Excitability of a Limit Cycle. *Chaos* 28, 071105. doi:10.1063/1.5045179
- Franović, I., Yanchuk, S., Eydam, S., Bačić, I., and Wolfrum, M. (2020). Dynamics of a Stochastic Excitable System with Slowly Adapting Feedback. *Chaos* 30, 083109. doi:10.1063/1.5145176
- Franović, I., Perc, M., Todorović, K., Kostić, S., and Burić, N. (2015). Activation Process in Excitable Systems with Multiple Noise Sources: Large Number of Units. *Phys. Rev. E* 92, 062912. doi:10.1103/physreve.92.062912
- Fuhrmann, G., Markram, H., and Tsodyks, M. (2002). Spike Frequency Adaptation and Neocortical Rhythms. *J. Neurophysiol.* 88, 761–770. doi:10.1152/jn.2002.88.2.761
- Gast, R., Schmidt, H., and Knösche, T. R. (2020). A Mean-Field Description of Bursting Dynamics in Spiking Neural Networks with Short-Term Adaptation. *Neural Comput.* 32, 1615–1634. doi:10.1162/neco_a_01300
- Gross, T., and Blasius, B. (2008). Adaptive Coevolutionary Networks: a Review. *J. R. Soc. Interf.* 5, 259–271. doi:10.1098/rsif.2007.1229
- Gross, T., D'Lima, C. J. D., and Blasius, B. (2006). Epidemic Dynamics on an Adaptive Network. *Phys. Rev. Lett.* 96, 208701. doi:10.1103/physrevlett.96.208701
- Gutiérrez, R., Amann, A., Assenza, S., Gómez-Gardeñes, J., Latora, V., and Boccaletti, S. (2011). Emerging Meso- and Macroscales from Synchronization of Adaptive Networks. *Phys. Rev. Lett.* 107, 234103. doi:10.1103/physrevlett.107.234103
- Ha, G. E., and Cheong, E. (2017). Spike Frequency Adaptation in Neurons of the central Nervous System. *Exp. Neurobiol.* 26, 179–185. doi:10.5607/en.2017.26.4.179
- Haimovici, A., Tagliazucchi, E., Balenzuela, P., and Chialvo, D. R. (2013). Brain Organization into Resting State Networks Emerges at Criticality on a Model of the Human Connectome. *Phys. Rev. Lett.* 110, 178101. doi:10.1103/physrevlett.110.178101
- Horstmeyer, L., and Kuehn, C. (2020). Adaptive Voter Model on Simplicial Complexes. *Phys. Rev. E* 101, 022305. doi:10.1103/PhysRevE.101.022305
- Ivanov, P. C. (2021). *The New Field of Network Physiology: Building The Human Physiome*. *Front. Net. Physiol.* 1, 1. doi:10.3389/fnetp.2021.711778
- Izhikevich, E. M. (2007). *Dynamical Systems in Neuroscience*. Cambridge, MA: MIT Press.
- Jain, S., and Krishna, S. (2001). A Model for the Emergence of Cooperation, Interdependence, and Structure in Evolving Networks. *Proc. Natl. Acad. Sci.* 98, 543–547. doi:10.1073/pnas.98.2.543
- Kasatkina, D. V., Yanchuk, S., Schöll, E., and Nekorkin, V. I. (2017). Self-organized Emergence of Multilayer Structure and Chimera States in Dynamical Networks with Adaptive Couplings. *Phys. Rev. E* 96, 062211. doi:10.1103/PhysRevE.96.062211
- Klinshov, V., and Franović, I. (2019). Two Scenarios for the Onset and Suppression of Collective Oscillations in Heterogeneous Populations of Active Rotators. *Phys. Rev. E* 100, 062211. doi:10.1103/PhysRevE.100.062211
- Klinshov, V. V., Shchapin, D. S., Lücken, L., Yanchuk, S., and Nekorkin, V. I. (2016). Experimental Study of Jittering Chimeras in a Ring of Excitable Units. *AIP Conf. Proc.* 1738, 210007. doi:10.1063/1.4951990
- Klinshov, V. V., Zlobin, D. A., Maryshev, B. S., and Goldobin, D. S. (2021). Effect of Noise on the Collective Dynamics of a Heterogeneous Population of Active Rotators. *Chaos* 31, 043101. doi:10.1063/5.0030266
- Kroma-Wiley, K. A., Mucha, P. J., and Bassett, D. S. (2021). Synchronization of Coupled Kuramoto Oscillators under Resource Constraints. *Phys. Rev. E* 104, 014211. doi:10.1103/PhysRevE.104.014211
- Kuehn, C. (2015). *Multiple Time Scale Dynamics*. Cham: Springer.
- Kuehn, C. (2019). Multiscale Dynamics of an Adaptive Catalytic Network. *Math. Model. Nat. Phenom.* 14, 402. doi:10.1051/mmnp/2019015
- Lafuerza, L. F., Colet, P., and Toral, R. (2010). Nonuniversal Results Induced by Diversity Distribution in Coupled Excitable Systems. *Phys. Rev. Lett.* 105, 084101. doi:10.1103/PhysRevLett.105.084101
- Laing, C. R. (2014). *Derivation Of a Neural Field Model from a Network of Theta Neurons*. *Phys. Rev. E Stat. Nonlin Soft Matter Phys.* 90, 010901. doi:10.1103/PhysRevE.90.010901
- Levina, A., Herrmann, J. M., and Geisel, T. (2007). Dynamical Synapses Causing Self-Organized Criticality in Neural Networks. *Nat. Phys.* 3, 857–860. doi:10.1038/nphys758
- Lindner, B., García-Ojalvo, J., Neiman, A. B., and Schimansky-Geier, L. (2004). Effects of Noise in Excitable Systems. *Phys. Rep.* 392, 321–424. doi:10.1016/j.physrep.2003.10.015
- Lücken, L., Popovych, O. V., Tass, P. A., and Yanchuk, S. (2016). Noise-enhanced Coupling between Two Oscillators with Long-Term Plasticity. *Phys. Rev. E* 93, 032210. doi:10.1103/PhysRevE.93.032210
- Lücken, L., Rosin, D. P., Worlitzer, V. M., and Yanchuk, S. (2017). Pattern Reverberation in Networks of Excitable Systems with Connection Delays. *Chaos* 27, 013114. doi:10.1063/1.4971971
- Luke, T. B., Barreto, E., and So, P. (2013). Complete Classification of the Macroscopic Behavior of a Heterogeneous Network of Theta Neurons. *Neural Comput.* 25, 3207–3234. doi:10.1162/neco_a_00525
- Markram, H., Gerstner, W., and Sjöström, P. J. (2011). A History of Spike-timing-dependent Plasticity. *Front. Synaptic Neurosci.* 3, 4. doi:10.3389/fnsyn.2011.00004
- Meisel, C., and Gross, T. (2009). Adaptive Self-Organization in a Realistic Neural Network Model. *Phys. Rev. E Stat. Nonlin Soft Matter Phys.* 80, 061917. doi:10.1103/PhysRevE.80.061917
- Mirollo, R., and Strogatz, S. H. (2007). The Spectrum of the Partially Locked State for the Kuramoto Model. *J. Nonlinear Sci.* 17, 309–347. doi:10.1007/s00332-006-0806-x
- Morris, C., and Lecar, H. (1981). Voltage Oscillations in the Barnacle Giant Muscle Fiber. *Biophysical J.* 35, 193–213. doi:10.1016/s0006-3495(81)84782-0
- Neiman, A., Schimansky-Geier, L., Cornell-Bell, A., and Moss, F. (1999). Noise-enhanced Phase Synchronization in Excitable media. *Phys. Rev. Lett.* 83, 4896–4899. doi:10.1103/physrevlett.83.4896
- Nicosia, V., Skardal, P. S., Arenas, A., and Latora, V. (2017). Collective Phenomena Emerging from the Interactions between Dynamical Processes in Multiplex Networks. *Phys. Rev. Lett.* 118, 138302. doi:10.1103/physrevlett.118.138302
- Omel'chenko, O. E., and Wolfrum, M. (2013). Bifurcations in the Sakaguchi-Kuramoto Model. *Physica D* 263, 74. doi:10.1016/j.physd.2013.08.004
- Omel'chenko, O. E., and Wolfrum, M. (2012). Nonuniversal Transitions to Synchrony in the Sakaguchi-Kuramoto Model. *Phys. Rev. Lett.* 109, 164101.
- Osipov, G. V., Kurths, J., and Zhou, C. (2007). *Synchronization in Oscillatory Networks*. Berlin, Heidelberg: Springer.
- Ott, E., and Antonsen, T. M. (2009). Long Time Evolution of Phase Oscillator Systems. *Chaos* 19, 023117. doi:10.1063/1.3136851
- Ott, E., and Antonsen, T. M. (2008). Low Dimensional Behavior of Large Systems of Globally Coupled Oscillators. *Chaos* 18, 037113. doi:10.1063/1.2930766
- Park, S. H., and Kim, S. (1996). Noise-induced Phase Transitions in Globally Coupled Active Rotators. *Phys. Rev. E* 53, 3425–3430. doi:10.1103/physreve.53.3425
- Park, S. H., and Lefebvre, J. (2020). Synchronization and Resilience in the Kuramoto white Matter Network Model with Adaptive State-dependent Delays. *J. Math. Neurosci.* 10, 16. doi:10.1186/s13408-020-00091-y
- Pikovsky, A. S., and Kurths, J. (1997). Coherence Resonance in a Noise-Driven Excitable System. *Phys. Rev. Lett.* 78, 775–778. doi:10.1103/physrevlett.78.775
- Popovych, O. V., Xenakis, M. N., and Tass, P. A. (2015). The Spacing Principle for Unlearning Abnormal Neuronal Synchrony. *PLoS ONE* 10, e0117205. doi:10.1371/journal.pone.0117205
- Pototsky, A., and Janson, N. (2008). Excitable Systems with Noise and Delay, with Applications to Control: Renewal Theory Approach. *Phys. Rev. E Stat. Nonlin Soft Matter Phys.* 77, 031113. doi:10.1103/PhysRevE.77.031113

- Roberts, J. A., Iyer, K. K., Vanhatalo, S., and Breakspear, M. (2014). Critical Role for Resource Constraints in Neural Models. *Front. Syst. Neurosci.* 8, 154. doi:10.3389/fnsys.2014.00154
- Röhr, V., Berner, R., Lameu, E. L., Popovych, O. V., and Yanchuk, S. (2019). Frequency Cluster Formation and Slow Oscillations in Neural Populations with Plasticity. *PLoS ONE* 14, e0225094. doi:10.1371/journal.pone.0225094
- Ronge, R., and Zaks, M. A. (2021). Emergence and Stability of Periodic Two-Cluster States for Ensembles of Excitable Units. *Phys. Rev. E* 103, 012206. doi:10.1103/PhysRevE.103.012206
- Sanders, J. A., Verhulst, F., and Murdock, J. (2007). *Averaging Methods in Nonlinear Dynamical Systems*. New York, NY: Springer.
- Sciaglia, S., Loppini, A., Patriarca, M., and Heinsalu, E. (2021). Hubs, Diversity, and Synchronization in FitzHugh-Nagumo Oscillator Networks: Resonance Effects and Biophysical Implications. *Phys. Rev. E* 103, 052211. doi:10.1103/PhysRevE.103.052211
- Shinomoto, S., and Kuramoto, Y. (1986). Phase Transitions in Active Rotator Systems. *Prog. Theor. Phys.* 75, 1105–1110. doi:10.1143/ptp.75.1105
- Song, T., Kim, H., Son, S. W., and Jo, J. (2020). Synchronization of Active Rotators Interacting with Environment. *Phys. Rev. E* 101, 022613. doi:10.1103/PhysRevE.101.022613
- Stoop, R., Blank, D., Kern, A., v.d. Vyver, J.-J., Christen, M., Lecchini, S., et al. (2002). Collective Bursting in Layer IV. *Cogn. Brain Res.* 13, 293–304. doi:10.1016/s0926-6410(01)00123-9
- Strogatz, S. H. (1994). *Nonlinear Dynamics and Chaos*. 1st ed. Cambridge, MA: Perseus Books.
- Strogatz, S. H. (2001). *Exploring Complex Networks*. *Nature* 410, 268–276. doi:10.1038/35065725
- Tang, E., and Bassett, D. S. (2018). *Colloquium: Control Of Dynamics in Brain Networks*. *Rev. Mod. Phys.* 90, 031003. doi:10.1103/revmodphys.90.031003
- Taylor, D., Ott, E., and Restrepo, J. G. (2010). Spontaneous Synchronization of Coupled Oscillator Systems with Frequency Adaptation. *Phys. Rev. E Stat. Nonlin Soft Matter Phys.* 81, 046214. doi:10.1103/PhysRevE.81.046214
- Terrien, S., Pammi, V. A., Krauskopf, B., Broderick, N. G. R., and Barbay, S. (2021). Pulse-timing Symmetry Breaking in an Excitable Optical System with Delay. *Phys. Rev. E* 103, 012210. doi:10.1103/PhysRevE.103.012210
- Thamizharasan, S., Chandrasekar, V. K., Senthilvelan, M., Berner, R., Schöll, E., and Senthilkumar, D. V. (2021). Exotic States Induced by Co-evolving Connection Weights and Phases, arXiv:2111.09861
- Thiele, M., Berner, R., Tass, P. A., Schöll, E., and Yanchuk, S. (2022). Asymmetric Adaptivity Induces Recurrent Synchronization in Complex Networks, arXiv:2112.08697. submitted
- Veltz, R. (2020). BifurcationKit.jl. URL <https://hal.archives-ouvertes.fr/hal-02902346>.
- Vergara, R. C., Jaramillo-Riveri, S., Luarte, A., Moënné-Loccoz, C., Fuentes, R., Couve, A., et al. (2019). The Energy Homeostasis Principle: Neuronal Energy Regulation Drives Local Network Dynamics Generating Behavior. *Front. Comput. Neurosci.* 13, 49. doi:10.3389/fncom.2019.00049
- Virkar, Y. S., Shew, W. L., Restrepo, J. G., and Ott, E. (2016). Feedback Control Stabilization of Critical Dynamics via Resource Transport on Multilayer Networks: How Glia Enable Learning Dynamics in the Brain. *Phys. Rev. E* 94, 042310. doi:10.1103/PhysRevE.94.042310
- Wang, X.-J., and Buzsáki, G. (1996). Gamma Oscillation by Synaptic Inhibition in a Hippocampal Interneuron Network Model. *J. Neurosci.* 16, 6402–6413. doi:10.1523/jneurosci.16-20-06402.1996
- Wilting, J., and Priesemann, V. (2019). 25 Years of Criticality in Neuroscience - Established Results, Open Controversies, Novel Concepts. *Curr. Opin. Neurobiol.* 58, 105–111. doi:10.1016/j.conb.2019.08.002
- Yanchuk, S., Ruschel, S., Sieber, J., and Wolfrum, M. (2019). Temporal Dissipative Solitons in Time-Delay Feedback Systems. *Phys. Rev. Lett.* 123, 053901. doi:10.1103/PhysRevLett.123.053901
- Yanchuk, S., Roque, A. C., Macau, E. E. N., and Kurths, J. (2021). Dynamical Phenomena in Complex Networks: Fundamentals and Applications. *Eur. Phys. J. Spec. Top.* 230, 2711–2716. doi:10.1140/epjs/s11734-021-00282-y
- Yu, S., Yang, H., Shriki, O., and Plenz, D. (2013). Universal Organization of Resting Brain Activity at the Thermodynamic Critical point. *Front. Syst. Neurosci.* 7, 42. doi:10.3389/fnsys.2013.00042
- Zheng, C., and Pikovsky, A. (2018). Delay-induced Stochastic Bursting in Excitable Noisy Systems. *Phys. Rev. E* 98, 042148. doi:10.1103/physreve.98.042148
- Zierenberg, J., Wilting, J., and Priesemann, V. (2018). Homeostatic Plasticity and External Input Shape Neural Network Dynamics. *Phys. Rev. X* 8, 031018. doi:10.1103/physrevx.8.031018

Conflict of Interest: The authors declare that the research was conducted in the absence of any commercial or financial relationships that could be construed as a potential conflict of interest.

Publisher's Note: All claims expressed in this article are solely those of the authors and do not necessarily represent those of their affiliated organizations, or those of the publisher, the editors and the reviewers. Any product that may be evaluated in this article, or claim that may be made by its manufacturer, is not guaranteed or endorsed by the publisher.

Copyright © 2022 Franović, Eydam, Yanchuk and Berner. This is an open-access article distributed under the terms of the Creative Commons Attribution License (CC BY). The use, distribution or reproduction in other forums is permitted, provided the original author(s) and the copyright owner(s) are credited and that the original publication in this journal is cited, in accordance with accepted academic practice. No use, distribution or reproduction is permitted which does not comply with these terms.

Chapter 4

Generic Mechanisms of Inverse Stochastic Resonance

Igor Franović*

Institute of Physics Belgrade, University of Belgrade, Serbia

Abstract

Two decades since the discovery of stochastic resonance, it has first been shown that the oscillating systems may also display a characteristic non-monotone response to noise, reflected in that their average oscillation frequency becomes minimal at an intermediate noise level. This came as a surprise because it was a common intuition that the frequency of noise-perturbed oscillations should just increase monotonously with noise. The new phenomenon, called inverse stochastic resonance for manifesting a suppression instead of an enhancing type of a response to noise, bears some resemblance to a classical stochastic resonance, such as the existence of a threshold-like behavior in deterministic dynamics. Nevertheless, the deterministic dynamics itself has a limit cycle attractor, and the system is not exposed to a subthreshold periodic forcing.

Inverse stochastic resonance readily shows that the response of an oscillating system to noise actually depends on the structure of the rest of the system's phase space and can in certain instances become non-trivial. In this chapter, I demonstrate two generic scenarios for the onset of inverse stochastic resonance: one where the deterministic system is multistable and the noise induces a biased switching between stationary and oscillatory metastable states, and the other, where the noise enhances the stability of an unstable equilibrium of the unperturbed system. In both instances, there is an intermediate noise level where the mean lifetime of

* Corresponding Author's Email: franovic@ipb.ac.rs.

a quasi-stationary state becomes maximal, such that the perturbed oscillating system displays a bursting-like activity with long episodes of quiescence interspersed with rare clusters of spikes, or the oscillations may even become completely quenched by noise. I show that the effect of inverse stochastic resonance occurs both in systems of intrinsic oscillators and systems where oscillations emerge due to coupling. Moreover, it may not only appear at the level of individual units but at the level of assemblies of units alike. Though most of the studies of inverse stochastic resonance have been associated with neuronal systems, both in terms of theoretical framework and applications, the robustness of the indicated mechanisms warrant the prominence of the effect in diverse fields, including the recently shown applications to nematic liquid crystals and dynamics of ecosystems. Despite that the impact of inverse stochastic resonance in neuronal systems may at first appear inhibitory, it may actually be cast to a corpus of stochastic facilitation phenomena, having the noise play a constructive functional role with respect to reducing neuronal spiking frequency in the absence of neuromodulators, turning spiking into stochastic bursting, or to generating UP-DOWN states characteristic for spontaneous and evoked activity in cortical networks.

PACS: 05.40.Ca, 87.19.In.

Keywords: resonant phenomena, noise-perturbed oscillations, multistability and noise, stochastic multiscale dynamics, noise-induced switching, noise-enhanced stability

1. Introduction

While the influence of noise has initially been seen as a nuisance, being likely detrimental for the unperturbed dynamics of the system, it has long since been understood that the noise may also modify or qualitatively change the deterministic dynamics in a function-wise favorable way. The tipping point that led to this change of paradigm was the discovery of stochastic resonance [1, 2, 3, 4, 5], the phenomenon where the optimal level of noise effectively enhances the systems sensitivity, or rather its ability to detect a weak (subthreshold) periodic forcing acting upon the system. It is now established that the impact of noise on deterministic dynamics of the system may be twofold [6, 7]: on the one hand, it may just be quantitative, in the sense of enhancing or suppressing some al-

ready existing features of deterministic dynamics; at the other hand, it may also be qualitative, such that the noise introduces novel forms of behavior absent in the deterministic dynamics of the system. The latter case is typically associated with noise-induced crossing of thresholds or separatrices, or noise-induced stabilization of certain deterministically unstable structures. Some of the most important examples of such effects include resonant phenomena, such as coherence and stochastic resonance [8], then noise-induced switching between coexisting metastable states [7, 9, 10], noise-induced preference of attractors [11, 12], the emergence of stochastic oscillations (spiking or bursting) [13], or stochastic stabilization of unstable equilibria [14, 15]. In neuronal media, all these phenomena witnessing the constructive role of noise are abundant and have become known by the umbrella term of stochastic facilitation [16, 17].

This chapter is intended to highlight how some of the above mentioned forms of noise-induced behavior contribute to the onset of a recently discovered resonant phenomenon, called inverse stochastic resonance [15, 18, 19, 20, 21, 22]. The latter can be described as a stochastic suppression of oscillations present in the unperturbed system, whereby the average frequency of noise-perturbed oscillations becomes minimal at an intermediate level of noise. Just like other resonant phenomena, inverse stochastic resonance also involves a non-monotone dependence on noise, but in contrast to the stochastic resonance, the signal-to-noise ratio has a characteristic minimum rather than the maximum. Historically, it was precisely this counter-analogy that inspired coining of the term inverse stochastic resonance. Nevertheless, one should immediately caution against overexploiting either analogies or counter-analogies to the effect of stochastic resonance. Primarily, one should be aware of the major difference between the two effects: stochastic resonance occurs in *periodically forced* systems with typically stationary unperturbed dynamics, while inverse stochastic resonance concerns *autonomous* systems where the unperturbed dynamics has a limit cycle attractor. Note that the latter may be intrinsic to an isolated systems dynamics or the oscillations may emerge in coupled systems as a result of interactions. The second point where one should caution against potential overstretching the analogy between the phenomena of stochastic resonance and inverse stochastic resonance concerns their onset mechanisms. Namely, initially it has been claimed that in order to observe inverse stochastic resonance, the underlying deterministic dynamics necessarily has to feature bistability between a stable limit cy-

cle and a stable equilibrium. This likely appeared as conveniently similar with the classical setting for stochastic resonance, which has been known for some time. There, the isolated deterministic dynamics of the system is bistable, with two coexisting stable equilibria (though more exotic scenarios with coexisting periodic or chaotic attractors are also possible), much like a particle in a double-well potential; the system is further subjected to a subthreshold periodic forcing, which may elicit only small excitations around either of the equilibria, without being able to induce hopping over the potential barrier between them. Then, the stochastic resonance arises by adapting the noise intensity such that the corresponding Kramers switching rate of the particle between the potential wells becomes commensurate with the frequency of external periodic forcing [5].

This chapter aims to portray a similar paradigmatic physical picture for the effect of inverse stochastic resonance. Nevertheless, in this case, instead of just one, it turns out that there are two such paradigmatic pictures [15]. By the first scenario, which I call *trapping scenario*, along with a stable limit cycle, the deterministic system features an additional unstable equilibrium, whose stability is enhanced by the influence of noise, such that at certain intermediate noise levels, stochastic trajectories show strong deviations away from the oscillatory metastable state, i.e., the system effectively becomes trapped for increased periods of time by the quasi-stationary metastable state. By the second scenario, that I call *biased switching scenario*, the unperturbed dynamics shows a coexistence between a stable limit cycle and a stable equilibrium, such that the noise induces switching between the corresponding states, whereby the switching process becomes strongly biased toward a quasi-stationary state at an intermediate noise level. In the following, I will elucidate these two generic scenarios by providing several illustrative examples. Apart from underlying the generic features intended to corroborate on the expected ubiquity of the effect of inverse stochastic resonance, I will also address certain problems more specific to the application in neuroscience, where the effect has been first observed. In particular, I will consider the problem of the robustness of the effect under the conditions associated with neuronal dynamics, like its persistence in coupled excitable systems, the potential influence of the type of units excitability, as well as the dependence on the multiscale dynamics of the units and their interactions.

The Chapter is organized as follows. In Section 2. I provide two illustrative examples for the trapping scenario, while in Section 3. I do the same for the

biased switching scenario. In Section 3.2., apart from the summary of the main findings, I also provide an outlook concerning the prevalence of the effect of inverse stochastic resonance.

2. Trapping Scenario

In this Section, I will explain in detail the trapping scenario for inverse stochastic resonance by providing two paradigmatic examples, mostly inspired by the applications in neuroscience. The first example concerns the stochastic suppression of relaxation oscillations in the case of a single FitzHugh-Nagumo unit, and the other involves a pair of active rotators with excitable local dynamics, where the noise depresses emergent oscillations induced by interactions. Apart from illustrating the particular scenario, these examples are also intended to explicitly demonstrate that inverse stochastic resonance may emerge both in self-oscillatory systems (endogenous oscillators) and systems with emergent oscillations.

2.1. Trapping Scenario for a Single FitzHugh-Nagumo Unit

FitzHugh-Nagumo model [23] is a multiple timescale model originally classically derived to describe neuronal dynamics both in the excitable and the oscillatory regimes, but its application has permeated to various fields beyond theoretical neuroscience, such as cell biology, e.g. when modeling the activity of cardiac cells [24] or pancreatic β -cells [25], and chemistry, e.g. in relation to autocatalytic chemical reactions [26]. The dynamics of a FitzHugh-Nagumo system influenced by noise is given by

$$\begin{aligned}\varepsilon\dot{u} &= u - u^3/3 - v + \sqrt{\varepsilon}\sigma_u\zeta(t) \\ \dot{v} &= u + b + \sigma_v\xi(t),\end{aligned}\tag{1}$$

where u and v denote the activator (fast) and the recovery (slow) variable, respectively, and the slow-fast structure is due to a small parameter $\varepsilon \ll 1$, here fixed to $\varepsilon = 0.05$, which provides for the timescale separation. From the neuroscience point of view, fast variable is interpreted as analogous to neuronal membrane potential, whereas the slow variable stands for the cumulative action of membrane ion-gating channels. The deterministic system (1) with $\sigma_u = \sigma_v = 0$ has been extensively studied within the framework of singular perturbation theory considering the singular limit $\varepsilon \rightarrow 0$ [28]. The classical result states that a

stable equilibrium $(u^*, v^*) = (-b, -b + b^3/3)$ undergoes a supercritical Hopf bifurcation at $b = 1$, such that a branch of small-amplitude harmonic oscillations of period $\mathcal{O}(\sqrt{\varepsilon})$ emanates for decreasing b . At $b = b_c \approx 1 - \varepsilon/8$, one observes a so-called canard transition, which corresponds to a rapid transition to large-amplitude relaxation oscillations of period $\mathcal{O}(1)$ [27]. In terms of neuronal dynamics, the described sequence of transitions under increasing b corresponds to the regime shift from quiescence to spiking via subthreshold oscillations. The system is assumed to be influenced by two independent Gaussian white noise sources, whereby the noise acting on the fast variable is classically interpreted as an external synaptic noise derived from interaction with the embedding environment, whereas the noise acting on the slow variable is seen as intrinsic ion-channel noise coming from the random opening of the ion-gating channels [16].

In the following, I consider the impact of noise on the FitzHugh-Nagumo system in the regime of relaxation oscillations, having set the bifurcation parameter $b = 0.99$ beyond the canard transition. For convenience, I will first confine the analysis to the case where only the intrinsic noise is present ($\sigma_u = 0, \sigma_v > 0$), but later it will also be shown that qualitatively the same effect occurs under the action of noise in the fast variable. It turns out that the stochastic dynamics of the system is strongly influenced by the presence of an unstable fixed point (u^*, v^*) , and that there exists a threshold manifold associated with it, such that the impact of noise, i.e., the way it perturbs the relaxation oscillations, depends on the type of fluctuations it induces in vicinity of the threshold. This may be understood in analogy to the concept of excitability, though it classically concerns the nonlinear threshold-like response of a system possessing a stable equilibrium, such as system (1) for $b \gtrsim 1$. There, a small perturbation elicits a linear, small-amplitude response such that the perturbed system remains in close vicinity of equilibrium and rapidly regains the rest state. Nevertheless, a strong enough perturbation is capable of inducing a large loop in phase space, such that the system returns to equilibrium after having performed a large-amplitude relaxation oscillation. Similar to this, the response to noise of FitzHugh-Nagumo system in the regime of relaxation oscillations can be described as *phase-sensitive excitability of a periodic orbit* [32]. Namely, depending on the strength of perturbation, noise may induce only marginal fluctuations around the relaxation oscillation orbit, or may cause a considerable deviation from the orbit, manifested as one or more successive small-amplitude (subthreshold) oscillations around the unstable equilibrium at

(u^*, v^*) . The term phase-sensitive underlies that the response of the system to perturbation is not uniform over the orbit of relaxation oscillations: the system is in fact most susceptible to perturbation during the passage of the orbit in vicinity of the unstable fixed point.

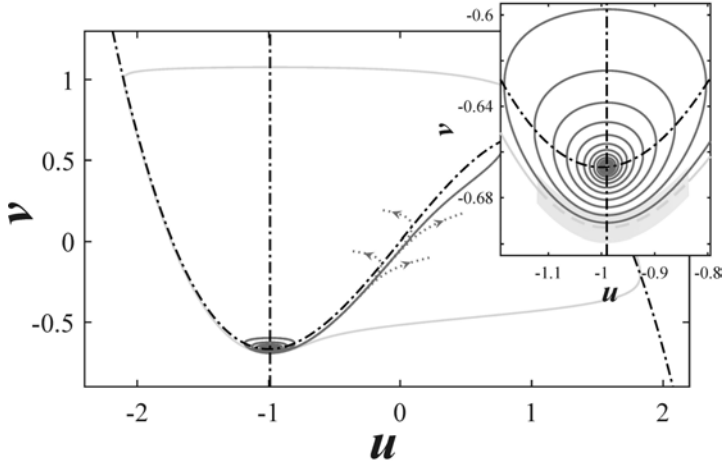


Figure 1. Phase plane for the noise-free system (1) with $b = 0.99$, $\varepsilon = 0.05$: Inset: region close to the unstable equilibrium. Shaded stripe indicates the region of phase-sensitive excitability, where the maximal canard acts as a threshold for the nonlinear response to perturbation in the form of a small-amplitude excitation loop.

The particular structure of the threshold manifold is given by a thin layer of close-by trajectories forming the so-called *maximal canard*, see Fig. 1, which may be explained in more detail within the framework of singular perturbation theory [28]. The latter classically involves considering the layer problem and the reduced problem, defined on the fast and the slow timescale, respectively, which are complementary in the sense that the reduced/layer problem describes slow/fast segments of solutions of a multiple timescale system. By setting $\varepsilon = 0$ for the deterministic dynamics of (1), one precisely obtains the reduced problem for the FitzHugh-Nagumo system. Then, the slow (critical) manifold $v = u - u^3/3$ is comprised of three branches of fixed points of the fast subsystem, with the two outer ones being stable, and the one in the middle being unstable. Most importantly, the slow manifold has two folded node singularities at the points where stable and unstable branches meet, which is closely associated with the

existence of canard trajectories. In the singular limit, the maximal canard is the trajectory that follows the whole unstable (middle) branch of the slow manifold [28, 29, 30]. Beyond the singular limit, i.e., for a small but finite ε , maximal canard foliates into a thin layer of exponentially close trajectories that follow the unstable branch for a long time relative to the slow timescale. In practice, maximal canard trajectories can be obtained from initial conditions set close to the upper fold $(u, v) = (1, 2/3)$ of the critical manifold and then running a backward integration in time. Such folded-node canard trajectories provide the threshold manifold for the phase-sensitive excitability of the orbit of relaxation oscillations in the following sense: perturbations deviating the systems orbit above the maximal canard induce a nonlinear type of response where the system generates one or several successive small loops around the unstable equilibrium; subthreshold perturbations or perturbations acting away from the threshold do not invoke such a response. The paradigm above explains the systems response to an arbitrary perturbation, depending on its direction and magnitude, and also provides the basis for explaining the impact of noise as a continuous random perturbation.

In particular, in Fig. 2 are illustrated typical stochastic trajectories of the system (1) under the influence of intrinsic noise for three different noise levels. For small noise, the excitations conforming to small-amplitude oscillations around the unstable equilibrium are relatively rare and are closely confined by the spiraling structure of the maximal canard. For intermediate noise, the noise-induced excitations become more frequent, but their spiraling structure also get partially smeared by fluctuations. Further increasing noise, the small-amplitude excitations are again suppressed as the threshold structure gets washed out by stochasticity, which reflects the effect of noise-induced linearization [31]. To resolve the recurrence of small excitation loops with noise, one may introduce a Poincaré section at $u = u_0 = -0.99, v < u_0 - u_0^3/3$ to record passages through a vertical line extending below the unstable fixed point. In Fig. 3(a) are shown the return times ΔT between successive crossings of the section for the three noise levels from Fig. 2. In all three cases, one readily distinguishes between return times $\Delta T \approx T_R$ corresponding to relaxation oscillations and the return times corresponding to excitation loops $\Delta T \approx T_E$. The corresponding episodes are indicated by the appropriate shading in the time trace in Fig. 3(b). The corresponding variances $\sigma_{R,E}$ for each of the two separate peaks of the return time distribution are shown in Fig. 3(c), whereas in Fig. 3(d) are provided their relative sizes with varying noise level σ_v . The largest prevalence

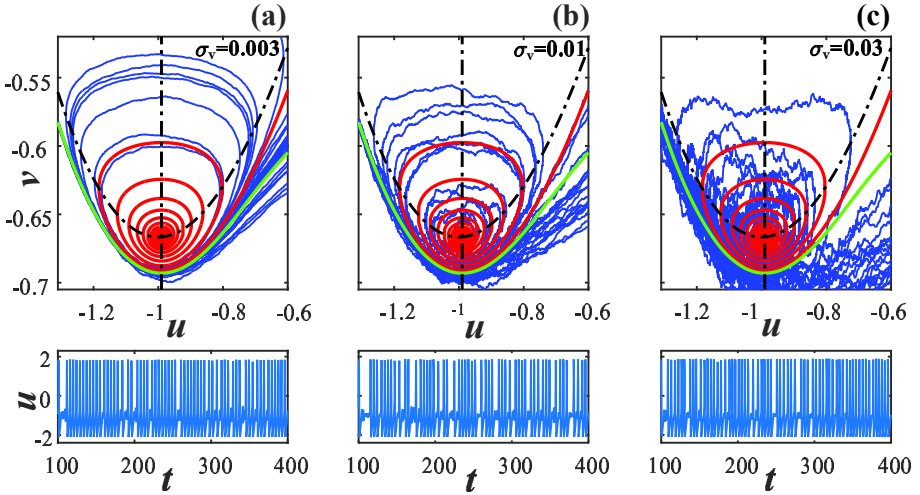


Figure 2. Stochastic trajectories for different levels of noise: (a) $\sigma_v = 0.003$, (b) $\sigma_v = 0.01$, and (c) $\sigma_v = 0.03$. Top panels: orbits $(u(t), v(t))$ in the phase plane together with the unperturbed relaxation oscillation orbit and maximal canard. Bottom panels: time traces $u(t)$ indicating the prevalence of small excitation loops for intermediate noise level $\sigma_v = 0.01$.

of small-amplitude excitation loops is clearly observed for intermediate noise levels $\sigma_v \approx 10^{-2}$. Above this value, the variances corresponding to each of the peaks start growing as the nonlinear threshold-like response becomes smoothed by noise.

The prevalence of small-amplitude excitation loops with noise affects the average spiking rate $\langle f \rangle$, calculated as the number of large-amplitude relaxation oscillations per time averaged over a sufficiently long time interval. The particular impact of small-amplitude excitation loops consists in delaying the next spiking event, which effectively reduces the systems average spiking rate. As the prevalence of excitation loops changes non-monotonously with noise, so the average spiking rate exhibits a non-monotone noise dependence, see Fig. 4, displaying the minimum for an intermediate noise level where the fraction of small-amplitude excitation loops in Fig. 3(d) is maximal.

As any resonant effect, the non-monotone noise-dependence of the spiking rate $\langle f \rangle(\sigma)$ can be explained as the result of two competing effects. In this case, the two competing effects are the increasing efficiency of excitation and

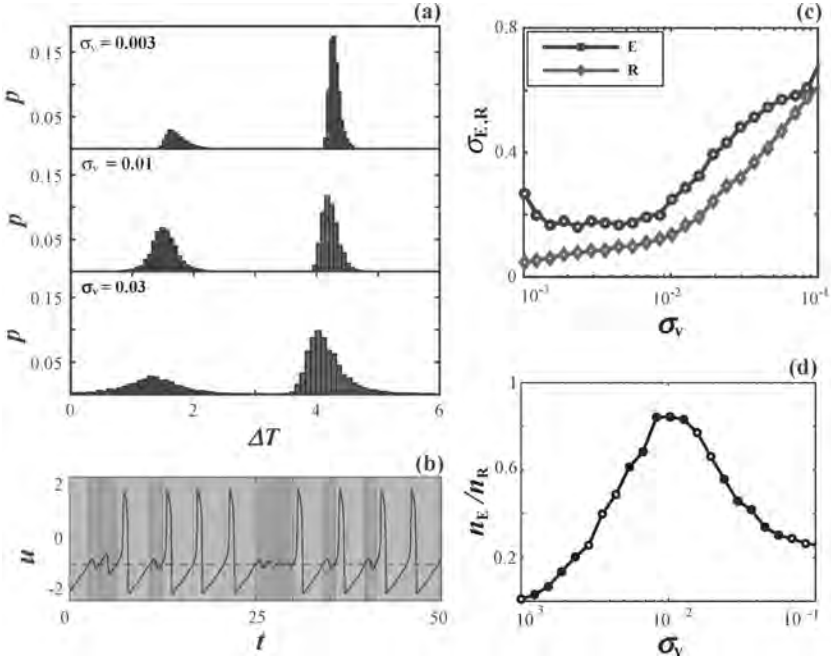


Figure 3. (a) Return times ΔT between successive crossings of the Poincaré section $u = u_0 = -0.99, v < u_0 - u_0^3/3$ for different noise levels. The two peaks correspond to relaxation oscillations $\Delta T \approx T_R$ (right peaks) and noise-induced excitation loops $\Delta T \approx T_E$ (left peaks); (b) Time trace for $\sigma_v = 0.01$ with respective time intervals ΔT shaded dark (left peaks in (a)) and light gray (right peaks in (a)); (c), (d) Noise-dependencies of variances $\sigma_{R,E}$ and relative sizes n_E/n_R for the two separate peaks of the return time distributions.

the degradation of the nonlinear threshold-like response [32]. A better insight into this competition can be gained by inspecting the return times $\Delta \tilde{T}$ associated with the Poincaré section $u = u_0 = -0.2, v < u_0 - u_0^3/3$. In this case, small-amplitude excitation loops are not recorded as individual Poincaré crossing events but rather contribute cumulatively to the return time $\Delta \tilde{T}$ for the round trip of each relaxation oscillation. For small noise, the corresponding histograms in Fig. 5(a) show multiple well separated peaks centered around $\Delta \tilde{T} \approx T_R + kT_E$, where $k \in \{0, 1, 2, 3, \dots\}$ denotes the number of recurring excitation loops between two successive Poincaré crossing events. This

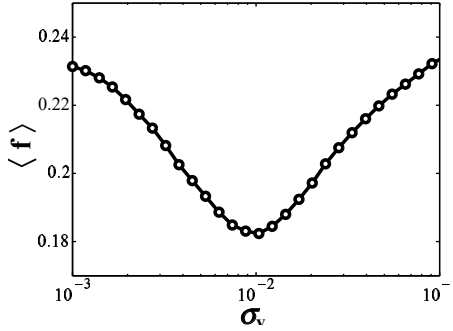


Figure 4. Noise-dependence of average spiking frequency $\langle f \rangle$ of relaxation oscillations shows a characteristic minimum at an intermediate noise level $\sigma_v \approx 10^{-2}$.

reveals that for $\sigma_v < 10^{-2}$, it is not only that the excitation loops become more abundant, as implied by Fig. 3(d), but they also tend to cluster as multiple successive events, cf. the noise-dependence of the corresponding probabilities of successive loops in Fig. 5(b). Such increasing recurrence tendency of excitation loops for $\sigma_v < 10^{-2}$ underlies the growing efficiency of the excitation process, or rather the growing ability of noise to trap the system within the spiraling structure of the maximal canard. Above the optimum noise range, the threshold behavior is gradually smoothed out giving way to noise degradation effect, which qualitatively implies spoiling of the additive contribution of the small-amplitude excitation loops to the total duration of the cycle of relaxation oscillation. Quantitatively, this may be expressed by the noise-dependence of the correlation coefficient δ between the number k of small excitation loops the unit performs between two successive passages through the Poincaré cross-section $u = u_0 = -0.2, v < u_0 - u_0^3/3$, and having the first return time $\Delta \tilde{T}$ within the corresponding interval $[T_R + (k - \frac{1}{2})T_E, T_R + (k + \frac{1}{2})T_E]$. The numerically evaluated noise-dependence of this correlation coefficient in Fig. 5(c) shows a strong decay above the critical level $\sigma_v < \approx 10^{-2}$, coinciding with the onset of the noise-induced degradation of the systems nonlinear threshold-like response.

Note that while the analysis so far has been confined to the impact of intrinsic noise, which may be seen as a parametric perturbation that does not affect the systems slow-fast structure, or rather the critical manifold, it is important

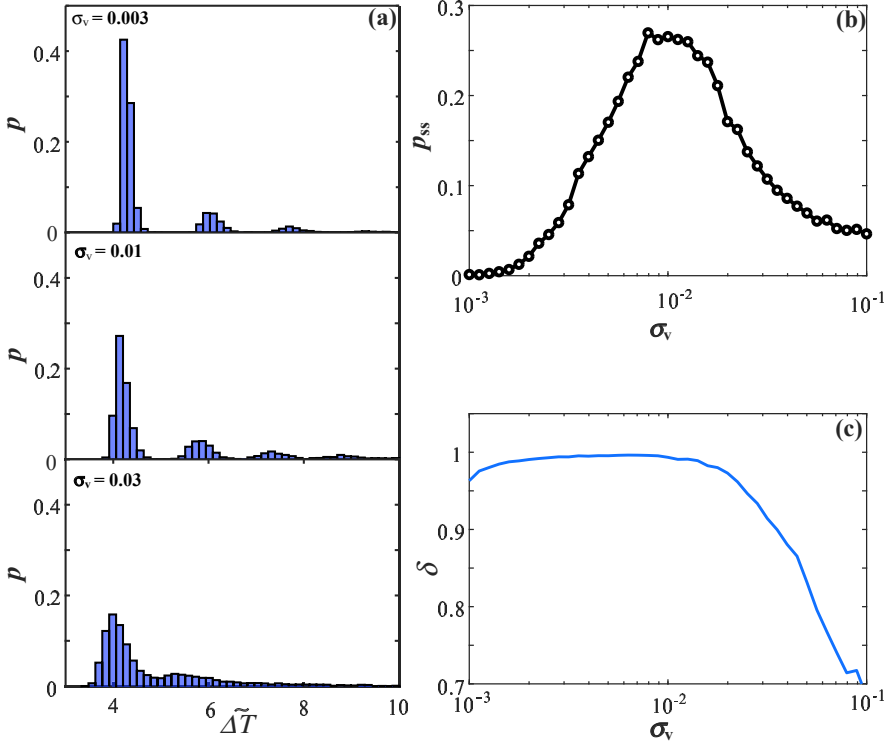


Figure 5. (a) Histograms of first return times $\Delta\tilde{T}$ to the Poincaré section $u = u_0 = -0.2, v < u_0 - u_0^3/3$. (b) Relative frequency of two successive excitation loops. (c) Correlation coefficient δ between number of small-amplitude excitation loops in a relaxation oscillation cycle and the cycles duration $\Delta\tilde{T}$.

to stress that qualitatively the same type of stochastic suppression of oscillation frequency is obtained under the influence of external noise, i.e., when the noise is added to the fast subsystem, see Fig. 6. However, the way in which the effect of inverse stochastic resonance is expressed for the stochastically perturbed relaxation oscillations of the FitzHugh-Nagumo system qualitatively depends on the separation of timescales, and is in fact most pronounced for intermediate values $\varepsilon \approx 0.05$. The effect itself vanishes for infinite scale separation, as evinced by its absence in [33], where the stochastic FitzHugh-Nagumo system has been analytically investigated by singular perturbation techniques addressing the limiting case $\varepsilon \rightarrow 0$. The reason for such a behavior with diminishing ε

can be explained as follows. The duration of the small-amplitude excitation loop scales like $\mathcal{O}(\sqrt{\varepsilon})$, i.e., it is described to the leading order by the linearization at the unstable equilibrium, which is a weakly undamped focus. Consequently, the delaying effect on the spiking events and the associated decrease of the average spiking rate become small in the singular limit.

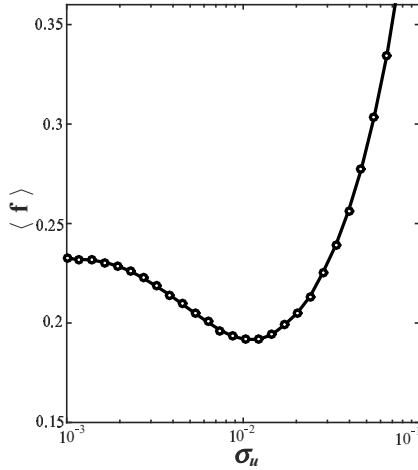


Figure 6. Non-monotone noise-dependence of the mean spiking rate of relaxation oscillations for noise acting in the fast subsystem (external or synaptic noise).

2.2. Trapping Scenario for a Motif of Two Coupled Oscillators

Having shown how the noise-induced trapping effect leads to a suppression of intrinsic relaxation oscillations of the FitzHugh-Nagumo system, I turn to a more complex example concerning a motif of two coupled oscillators with multiple timescale dynamics. This example is also partially intended to show that the effect of inverse stochastic resonance may not always qualitatively depend on the scale separation in multiscale systems, i.e., that there are indeed cases where it also persists in the singular limit.

The paradigmatic model I consider is to a certain extent inspired by neuroscience, comprising two identical stochastic active rotators with slowly varying

adaptive couplings [9, 34, 35]. The model reads

$$\begin{aligned}\dot{\varphi}_i &= I_0 - \sin \varphi_i + \kappa_i \sin(\varphi_j - \varphi_i) + \sqrt{\sigma} \xi_i(t) \\ \dot{\kappa}_i &= \varepsilon(-\kappa_i + \sin(\varphi_j - \varphi_i + \beta)),\end{aligned}\tag{2}$$

where $i, j \in \{1, 2\}$, $i \neq j$ denote individual units. The local dynamics is described by the phase variables $\{\varphi_1, \varphi_2\} \in S^1$, evolving on the fast timescale, while the phase interactions involve standard first Fourier components and are characterized by the slowly varying coupling weights $\{\kappa_1, \kappa_2\} \in \mathcal{R}$. The dynamics of an isolated (non-interacting noise-free) unit is controlled by the excitability parameter I_0 , whose role may be compared to that of an external bias current in neuronal systems. An isolated unit undergoes the transition between the excitable ($I_0 \lesssim 1$) and oscillatory regime ($I_0 > 1$) via the saddle-node of infinite period (SNIPER) bifurcation at $I_0 = 1$. Here, I consider the case where the units are self-oscillatory ($I_0 = 1.05$). Phase variables are influenced by independent Gaussian white noise sources, whose action may be compared to that of synaptic noise in neuronal systems. Scale separation derives from the smallness of the parameter $\varepsilon \ll 1$, which here controls the rate of adaptation process. Adaptation of coupling strengths is a part of a feedback loop often encountered in neuronal systems, where the activity of neurons impacts the coupling strengths between them, reflecting different forms of synaptic plasticity, while such changes in synaptic strength in turn modify the neuronal activity. Adaptive dynamics given by the second equation in (2) conforms to the so-called phase-dependent plasticity [36, 37, 38], whose modality can be adjusted by the parameter β . In particular, depending on β , phase-dependent plasticity can qualitatively reproduce the features of several well-known synaptic plasticity rules [37, 38]. For example, choosing $\beta = 3\pi/2$ is known to promote phase synchronization between the units, similar to the Hebbian learning rule [39], while setting $\beta = \pi$ favors a causal relationship between the pre- and post-synaptic units firing times [37, 38], resembling the effect of spike-timing-dependent plasticity (STDP) [40, 41, 42, 43]. In what follows, I will focus on the latter scenario. The model of active rotators itself is quite similar to theta neurons, which are paradigmatic for type I neuronal excitability. In line with that analogy, the whole system (2) can be seen as a simplified model of a motif of adaptively coupled neuronal oscillators subjected to synaptic noise. In terms of the underlying dynamics, it is important to note that the noise-free system (2) is equivariant to exchange of units' indices, which brings up an additional degeneracy such that all the stationary or periodic solutions appear as Z_2 symmetry-connected twins.

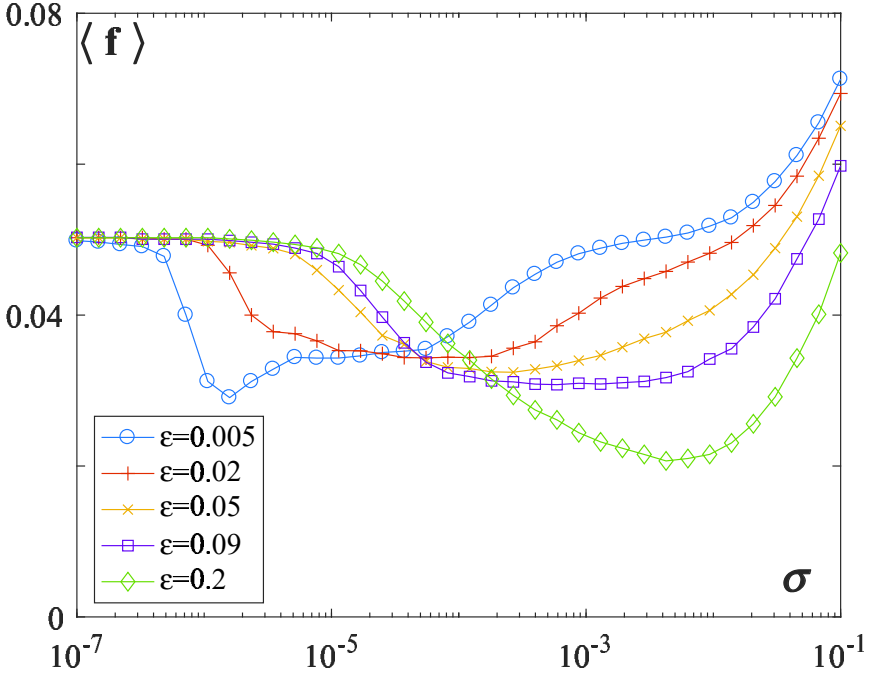


Figure 7. Average oscillation frequencies in terms of noise $\langle f \rangle(\sigma)$ for a set of scale separations $\varepsilon \in \{0.005, 0.02, 0.05, 0.09, 0.2\}$ and fixed $I_0 = 1.05, \beta = \pi$.

For $I_0 = 1.05$ and $\beta = \pi$, the system (2) exhibits a characteristic non-monotone response to noise conforming to inverse stochastic resonance, where the average oscillation frequency of phases $\langle f \rangle$ displays a minimum at an intermediate noise level, see Fig. 7. In contrast to the scenario from Sec. 2.1., the onset of inverse stochastic resonance here does not qualitatively depend on the scale separation ε , i.e., the adaptation rate. There is only a quantitative dependence on ε , in the sense that the resonant noise level shifts to larger values with increasing ε . The numerical simulations corroborate that the resonant effect persists for very slow adaptation, as demonstrated in Fig. 7 for $\varepsilon = 0.005$. The below analysis within the framework of singular perturbation theory [28, 44] will further show that all the necessary ingredients giving rise to inverse stochastic resonance persist in the singular limit of infinite scale separation $\varepsilon \rightarrow 0$. At the other hand, the robustness of inverse stochastic resonance has also been numerically confirmed for faster adaptation, e.g. in case $\varepsilon \sim 0.1$, cf. Fig. 7. One

further observes that the minima of $\langle f \rangle(\sigma)$ dependencies become deeper with ε , indicating that the noise-suppression effect becomes more pronounced for higher adaptation rates.

To gain insight into the mechanism underpinning inverse stochastic resonance, I will turn to the slow-fast analysis [28] of the noise-free system (2). Before that, it is important to briefly summarize the results of numerical bifurcation analysis for the noise-free system (2) for the case of finite scale separation. First note that selecting the STDP-like plasticity rule $\beta = \pi$ confines the coupling dynamics to the symmetry invariant subspace $\kappa_1(t) = -\kappa_2(t) \equiv \kappa(t)$. Due to this, the noise-free system (2) can be reduced to

$$\begin{aligned}\dot{\varphi}_1 &= I_0 - \sin \varphi_1 + \kappa \sin(\varphi_2 - \varphi_1) \\ \dot{\varphi}_2 &= I_0 - \sin \varphi_2 + \kappa \sin(\varphi_2 - \varphi_1) \\ \dot{\kappa} &= \varepsilon(-\kappa - \sin(\varphi_2 - \varphi_1)).\end{aligned}\tag{3}$$

By numerically solving the eigenvalue problem, one can verify that system (3) possesses no stable fixed points, but rather a pair of saddle nodes and a pair of saddle focuses. Also, the maximal real part of the eigenvalues of the focuses display a power-law dependence on ε , tending to zero in the singular limit $\varepsilon \rightarrow 0$. Concerning the oscillatory states, the numerical experiments indicate that (3) displays multistability between three periodic solutions: two of them involve non-zero coupling strengths and a constant phase-shift between the phase variables, whereas the third solution corresponds to effectively uncoupled units ($\kappa(t) = 0$) and the phase variables synchronized in-phase.

Next I will demonstrate how the classical slow-fast analysis [28] can be employed to better understand the trapping mechanism facilitating the onset of inverse stochastic resonance. To this end, I consider the layer problem

$$\begin{aligned}\dot{\varphi}_1 &= I_0 - \sin \varphi_1 + \kappa \sin(\varphi_2 - \varphi_1) \\ \dot{\varphi}_2 &= I_0 - \sin \varphi_2 + \kappa \sin(\varphi_2 - \varphi_1).\end{aligned}\tag{4}$$

Treating the slow variable $\kappa \in [-1, 1]$ as an additional system parameter, one first looks for the stable stationary and periodic solutions of the fast flow. It is convenient to apply the coordinate transformation $(\varphi_1, \varphi_2) \mapsto (\Phi, \delta\varphi) = (\frac{\varphi_1 + \varphi_2}{2}, \frac{\varphi_1 - \varphi_2}{2})$, so that (4) can be rewritten as

$$\begin{aligned}\delta\dot{\varphi} &= -\sin \delta\varphi \cos \Phi \\ \dot{\Phi} &= I_0 - \cos \delta\varphi (\sin \Phi + 2\kappa \sin \delta\varphi).\end{aligned}\tag{5}$$

The second equation indicates that the fast flow cannot possess any fixed points on the synchronization manifold $\delta\varphi = 0$ because $I_0 > 1$, implying that the stationary solutions can emerge only from the condition $\cos \Phi = 0$. Depending on κ , the fast flow for $I_0 \gtrsim 1$ can actually exhibit two or no fixed points. For the value of excitability parameter fixed in our case ($I_0 = 1.05$), one can readily find numerically that two fixed points, namely a saddle and a *center*, exist within the interval $\kappa \in [-0.1674, 0.1674]$. It may be shown that the existence of a center point is associated with the time-reversal symmetry of the fast flow (4). Indeed, the fast flow is invariant to a symmetry-preserving map R of the form

$$R = \begin{cases} \varphi_1 \rightarrow \pi - \varphi_2, \\ \varphi_2 \rightarrow \pi - \varphi_1, \\ t \rightarrow -t \end{cases} \quad (6)$$

In the case of finite scale separation, the counterpart of the center point of the fast flow is a weakly unstable focus of the complete system (3).

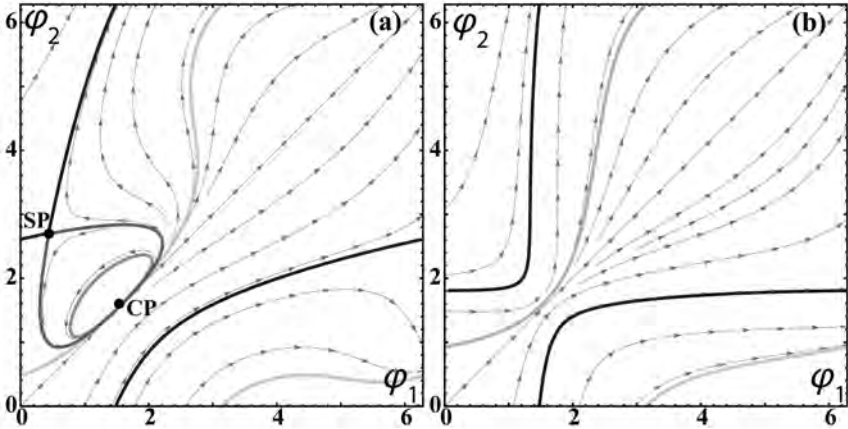


Figure 8. Dynamics of fast flow (4) for $I_0 = 1.05$ (a) below ($\kappa = -0.8$) and (b) above the saddle-center bifurcation ($\kappa = -0.08$). In (a), the system possesses two unstable fixed points: saddle (SP) and a center (CP), and has three types of closed orbits: a limit cycle attractor (light gray), homoclinic connections to SP (black and dark gray), and subthreshold oscillations around the center (medium gray). In (b), the system exhibits bistability between two oscillatory states (light gray and black).

The structure of the fast flow is organized around the saddle-center bifurcation, which happens for $\kappa = \kappa_{SC} = -0.1674$ [15]. Within this scenario, two fixed points get annihilated as a homoclinic orbit connecting stable and unstable manifolds of the saddle collapses onto the center. In Fig. 8(a) and Fig. 8(b) are shown the illustrative examples of the phase portraits and the associated vector fields for $\kappa < \kappa_{SC}$ and $\kappa > \kappa_{SC}$, respectively. For $\kappa \in [-1, \kappa_{SC})$, the fast flow has a limit cycle attractor, essentially reflecting the local dynamics of the units, see the orbit indicated in red in Fig. 8(a). Apart from the periodic attractor, there are two additional types of closed orbits, namely the homoclinic connections to the saddle point (SP), shown by blue and green, and the periodic orbits around the center point (CP), an example of which is indicated in orange. For $\kappa > \kappa_{SC}$, the fast flow displays bistability between two oscillatory solutions: a limit cycle inherited from the local dynamics of units and the limit cycle associated with the former homoclinic orbits, cf. Fig. 8(b).

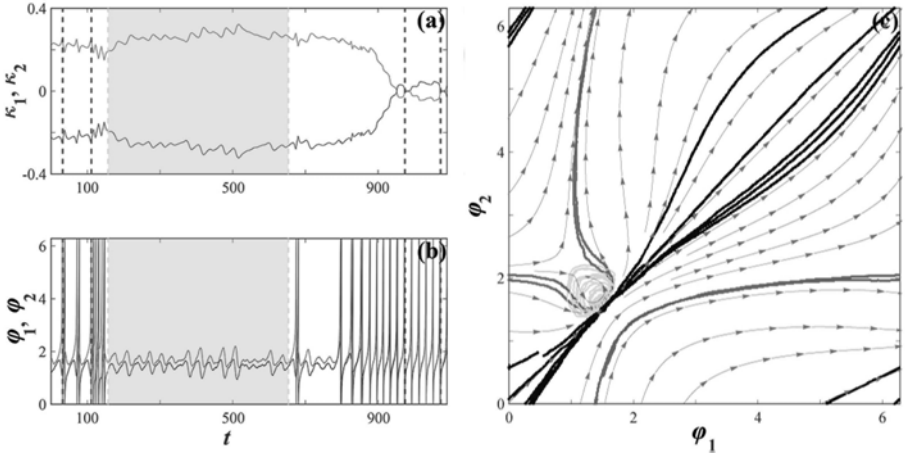


Figure 9. Time traces (a) $\kappa_i(t)$ and (b) $\phi_i(t)$, with the episode of circling in vicinity of unstable fixed point shown shaded. (c) black and dark gray: orbits associated with two metastable states featuring large-amplitude oscillations of phases, light gray: subthreshold oscillations. Superimposed is the vector field of the fast flow. Parameters are: $I_0 = 1.05$, $\varepsilon = 0.035$, $\beta = \pi$, $\sigma = 10^{-4}$.

Under the influence of noise, the attractors of the fast flow become metastable states. Apart from the noise-induced switching between the metastable states, the emerging slow stochastic fluctuations also involve

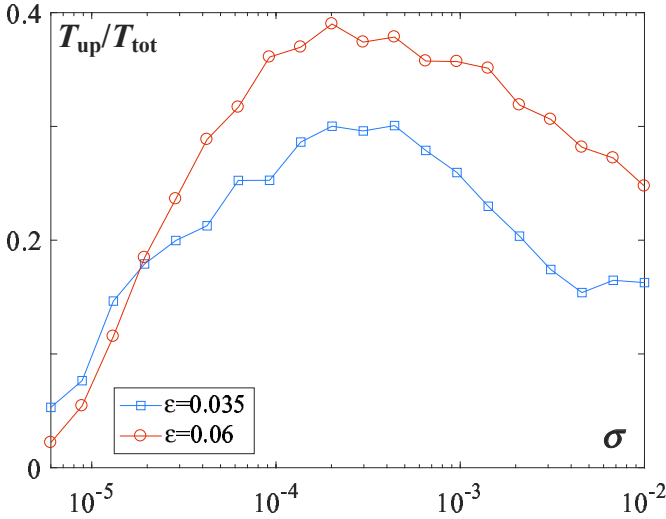


Figure 10. Relative fraction of time spent in vicinity of unstable fixed point T_{up}/T_{tot} as a function of noise for $\epsilon = 0.035$ (squares) and $\epsilon = 0.06$ (circles). Remaining parameters are $I_0 = 1.05$, $\beta = \pi$.

subthreshold oscillations derived from the periodic orbits around the center point. It is precisely these subthreshold oscillations that provide for the trapping effect responsible for the stochastic suppression of the oscillation frequency. An example of the time traces $\kappa_i(t)$ and $\varphi_i(t)$, $i \in \{1, 2\}$ for an intermediate $\epsilon = 0.035$ in Fig. 9(a)-(b) clearly illustrates three characteristic episodes, including those where the system explores two distinct oscillatory metastable states and an extended episode localized around the center, see the stochastic orbits $(\varphi_1(t), \varphi_2(t))$ and the fast flow vector field in Fig. 9(c). For a finite scale separation, the described trapping effect is manifested as the noise-enhanced stability of an unstable fixed point [14]. The prevalence of subthreshold oscillations varies non-monotonously with noise, see Fig. 10, becoming maximal around the resonant noise level where the frequency dependence on noise shows a minimum value, cf. Fig. 10 and Fig. 7.

3. Biased Switching Scenario

In this Section, I provide two paradigmatic examples for the scenario where inverse stochastic resonance emerges due to noise-induced switching between oscillatory and quasi-stationary metastable states, such that the latter become most prevalent for intermediate noise levels facilitating the strongest suppression of oscillations. I first briefly consider a simple example of a single stochastic Morris-Lecar neuron, and then consider the case of two adaptively coupled stochastic active rotators with excitable rather than self-oscillatory local dynamics, such that the noise suppresses emergent oscillations.

3.1. Biased Switching for a Single Morris-Lecar Neuron

Morris-Lecar model is one of the classical multiscale models of neuronal dynamics, capable of reproducing a wide spectrum of neuronal behaviors [23, 45]. It is given by

$$\begin{aligned}
 C \frac{dv}{dt} &= -g_{fast}m(v)(v - E_{Na}) - g_{slow}W(v - E_K) - \\
 &\quad - g_{leak}(v - E_{leak}) + I \\
 \frac{dv}{dt} &= \phi \frac{W_\infty(v) - W}{\tau(v)} \\
 m(v) &= 0.5[1 + \tanh(\frac{v - \beta_m}{\gamma_m})] \\
 W_\infty(v) &= [1 + \tanh(\frac{v - \beta_w}{\gamma_w})] \\
 \tau(v) &= 1 / \cosh(\frac{v - \beta_w}{2\gamma_w}), \tag{7}
 \end{aligned}$$

where the fast variable v and the slow variable W respectively accommodate for the dynamics of neuronal membrane potential and the normalized K^+ ion conductance. Depending on the bifurcation parameter I , which can be interpreted as an external bias current, the model can be poised in vicinity of a subcritical or a supercritical Hopf bifurcation [46], i.e., it may display Type I or Type II neuronal excitability. The current focus is on the former case, which may be realized by selecting the following parameter set: $E_{Na} = 120$ mV, $E_K = -84$ mV, $E_{leak} = -60$ mV, $g_{fast} = 4.4$ mS/cm², $g_{slow} = 8$ mS/cm², $g_{leak} = 2$ mS/cm², $\phi = 0.04$, $C = 20$ μF/cm², $\beta_m = -1.2$ mV, $\beta_w = 2$ mV, $\gamma_m = 18$ mV, $\gamma_w = 30$ mV. Then, for a range of

I values just below the threshold of a subcritical Hopf bifurcation, the Morris-Lecar neuron displays bistability between a stable equilibrium and a stable limit cycle, see the bifurcation diagram $V(I)$ in Fig. 11(a).

The noise immediately transforms the attractors of deterministic dynamics into metastable states, namely a quasi-stationary and an oscillatory one, causing the system to switch between the two different regimes. For an intermediate noise level, the switching process becomes extremely biased, such that the system spends much more time fluctuating around the quasi-stationary state than performing the noise-perturbed oscillations. This effect reduces the oscillation frequency, and is ultimately even capable of completely quenching the oscillations at the resonant noise level, so that the system escapes from the attraction basin of the oscillatory metastable state and is absorbed by the quasi-stationary state, see the noise dependence of oscillation frequency for $I = 95 \mu A/cm^2$ in Fig. 11(b).

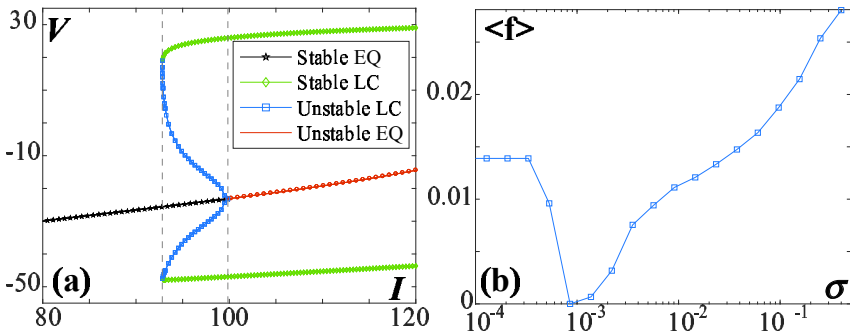


Figure 11. (a) Bifurcation diagram $V(I)$ for the Morris-Lecar model in vicinity of a subcritical Hopf bifurcation; (b) Noise-dependence of average spiking frequency $\langle f \rangle(\sigma)$ for the Morris-Lecar model from (a), with bifurcation parameter $I = 95 \mu A/cm^2$ set to bistable regime.

3.2. Biased Switching for Emergent Oscillations in Two Adaptively Coupled Active Rotators

In this Subsection, I consider the stochastic suppression of emergent oscillations in a motif of two adaptively coupled active rotators in the excitable regime. Motif dynamics is described by (2), but in contrast to the parameter selection in Sec. 2.2., the local bifurcation parameter here is set to $I_0 = 0.95$,

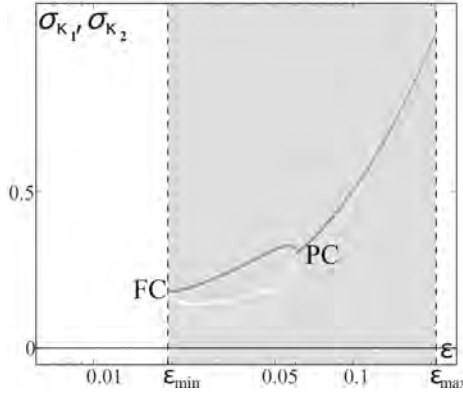


Figure 12. Emergence of oscillations in noise-free system (2) with $I_0 = 0.95$. Dependencies $\sigma_{\kappa_i}(\varepsilon)$, $i \in \{1, 2\}$ for illustrative stationary (black) and oscillatory solution (gray and white refer to different units) for $\beta = 4.2$. Shading indicates ε interval that admits multistability between the two symmetry-related stable equilibria and limit cycle attractor(s). FC and PC denote ε values where fold of cycles and pitchfork of cycles take place.

and the plasticity parameter β lies within the range $\beta \in (3.298, 4.495)$, which approximately interpolates between the Hebbian-like and STDP-like plasticity rules. For such parameters, system (2) possesses two stable equilibria born from the symmetry-breaking pitchfork bifurcation, and has four additional unstable fixed points. Recall that due to exchange symmetry, all the solutions appear in pairs as symmetry-related twins. For the particular plasticity parameter $\beta = 4.2$ employed in the analysis below, the two stable equilibria, given by EQ1:= $(\varphi_1^*, \varphi_2^*, \kappa_1^*, \kappa_2^*) = (1.2757, 0.2127, -0.0078, -0.8456)$ and EQ2:= $(\varphi_1^*, \varphi_2^*, \kappa_1^*, \kappa_2^*) = (0.2127, 1.2757, -0.8456, -0.0078)$, have been shown to manifest excitable behavior [9].

In the following, I first consider the numerical bifurcation diagram for the noise-free system (2) with finite scale separation and the rest of parameters selected as indicated above, see Fig. 12. This is intended to disclose the mechanism by which emergent oscillations are born and to highlight the parameter region supporting bistability between the stable stationary and stable periodic solutions. Note that the scale separation parameter ε , i.e., the adaptation rate, plays an important part in shaping the systems dynamics. The maximal stability region of the two symmetry-related periodic solutions in the (β, ε) parameter

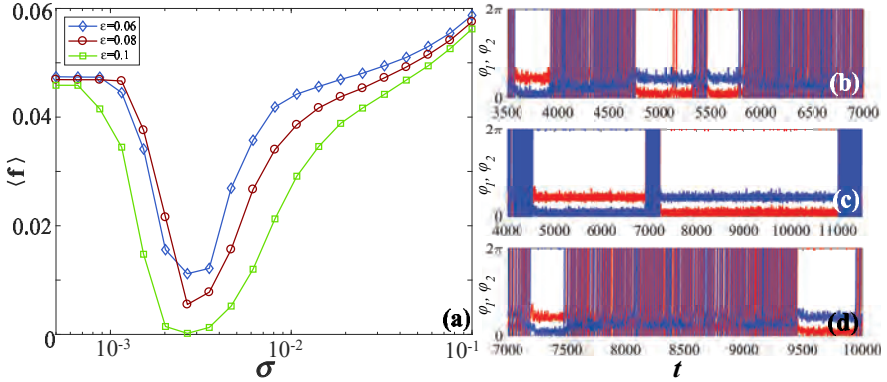


Figure 13. (a) Noise-dependence of average spiking frequency $\langle f \rangle$ for scale separations $\varepsilon \in \{0.06, 0.08, 0.1\}$. (b)-(d) Time traces $\varphi_1(t)$ and $\varphi_2(t)$ for noise levels below, at and above the resonant value. Parameters are: $I_0 = 0.95$, $\beta = 4.2$, $\varepsilon = 0.06$.

plane can be found in [15, 35]. Here I just mention that for the given plasticity parameter β , there exists an interval $\varepsilon \in (\varepsilon_{min}, \varepsilon_{max})$ of intermediate scale separation ratios supporting the oscillations, cf. the highlighted region in Fig. 12. Two Z_2 -symmetry related branches of stable periodic solutions emanate from the fold of cycles bifurcations, denoted by FC in Fig. 12, whereby the associated threshold scale separation $\varepsilon_{min}(\beta)$ decreases with β . Two branches of oscillatory solutions merge around $\varepsilon \approx 0.06$, which is the locus of an inverse pitchfork bifurcation of limit cycles (PC). As in my previous example, the impact of noise is such that the coexisting attractors of the deterministic system turn to metastable states connected by the noise-induced switching.

For the motif of two adaptively coupled excitable active rotators, the non-monotone dependence of average oscillation frequency with noise characteristic for inverse stochastic resonance is generically found for intermediate ε supporting the multistability between the stationary and the oscillatory solutions. A family of noise-dependencies of average oscillation frequency $\langle f \rangle(\sigma)$ for different scale separation ε is shown in Fig. 13(a). The angular brackets $\langle \cdot \rangle$ refer to averaging over an ensemble of a 100 different stochastic realizations, with the initial conditions fixed within the basin of attraction of the limit cycle. Qualitatively the same results are also obtained if for each realization of the stochastic process, one selects a set of random initial conditions from the stability basin of

the periodic solution.

The noise-induced switching between quasi-stationary and oscillatory metastable states gives rise to a bursting-like behavior [35], where the spikes, appearing in clusters, are interspersed by the quiescent episodes, see Fig. 13(b). The latter dominate the phases time series at the noise levels where the corresponding dependence $\langle f \rangle(\sigma)$ exhibits a minimum. For the weaker noise $\sigma \lesssim 10^{-3}$, the frequency of emergent oscillations remains close to the unperturbed one, while beyond the resonant noise levels, it increases above the frequency of unperturbed oscillations. The efficiency of the stochastic suppression of oscillations depends on the scale separation ε , i.e., the adaptation rate, in the sense that it increases for a faster adaptation process (larger ε) [35]. To illustrate how the inverse stochastic resonance is reflected at the slower timescale of the dynamics of the coupling weights, in Fig. 14(a)-(c) are shown the typical stationary distributions $P(\kappa_1)$ for the noise levels below, at and above the resonance. As a reference to the unperturbed dynamics, the dash-dotted lines indicate the weight levels associated with the two equilibria EQ1 and EQ2, while the blue shading denotes the variation σ_κ of the stable limit cycle. Note that here the stable periodic solution is unique because the scale separation ε value lies above the pitchfork of cycles bifurcation, cf. PC in Fig. 12(b). The stationary distribution $P(\kappa_1)$ around the resonant noise level shows a pronounced peak at one of the quasi-stationary states, while instead the distributions below or above the resonant noise feature high occupancies of the oscillatory metastable state. This is corroborated by looking into how the fraction of the total time spent at the oscillatory metastable states, T_{osc}/T_{tot} , changes with noise, see Fig. 15(a). The non-monotone dependence $T_{osc}/T_{tot}(D)$ indeed shows that the switching process around the resonant noise level becomes strongly biased toward the quasi-stationary state, and that the effect becomes stronger for a faster adaptation. Such biased switching is facilitated by the geometry of the systems phase space, where the boundary between the basins of attraction of two stationary states and the limit cycle is shifted much closer toward the limit cycle.

The switching process, manifested as slow stochastic fluctuations between the available metastable states, can be quantified by looking separately into competing transition processes from and to the oscillatory state [15]. In particular, the transition rates from the stability basin of the limit cycle attractor to those of the stationary states and vice versa, $r_{LC \rightarrow FP}$ and $r_{FP \rightarrow LC}$, can be numerically estimated as the reciprocal values of the corresponding mean first-passage (escape) times [47], see Fig. 15(b)-(c). The noise-dependencies of the two transition rates are indeed qualitatively different: while $r_{LC \rightarrow FP}$ dis-

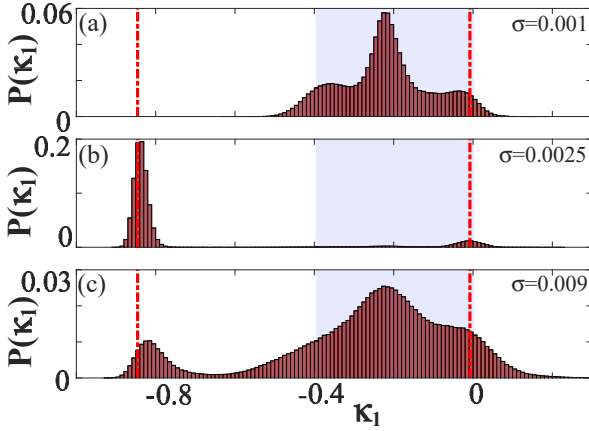


Figure 14. Stationary distributions $P(\kappa_1)$ (a) below ($\sigma = 0.001$), (b) at ($\sigma = 0.0025$) and (c) above ($\sigma = 0.009$) the resonant noise level for $\varepsilon = 0.1$; dash-dotted lines: κ_1 levels associated with two stable equilibria, $\kappa_1^*(EQ1)$ and $\kappa_1^*(EQ2)$; light shaded interval: variation σ_{κ_1} of the unique stable periodic solution.

plays a maximum at the resonant noise level and a subsequent decay with noise, $r_{FP \rightarrow LC}$ just increases monotonously. For very small noise $\sigma \lesssim 10^{-3}$, there are virtually no switches to the quasi-stationary states. However, for intermediate noise levels, the transition rate $r_{LC \rightarrow FP}$ dominates, whereas under further increase of noise $r_{FP \rightarrow LC}$ takes over.

An additional subtlety for the current example of inverse stochastic resonance is that the adaptation plays a facilitatory role by enhancing the resonant effect. By combining two multiscale methods, namely the critical manifold theory and the averaging approach, one may show that the adaptation drives the fast flow toward the part of the (κ_1, κ_2) parameter plane where the stationary state changes character, turning from a stable node to a stable focus [35]. In general, path-following techniques have already been applied to show that the response to noise in multiple timescale systems qualitatively depends on the character of stationary states, recovering fundamentally different scaling regimes with respect to noise and the scale-separation ratio [48, 49, 50]. Intuitively, one may expect more resonant effects to be associated with focuses rather than nodes [48], because in the former case, the post-perturbation process of relaxation to equilibrium features an eigenfrequency.

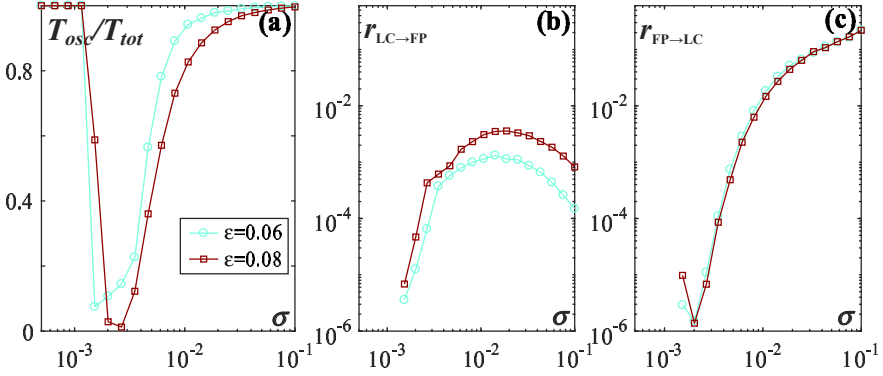


Figure 15. (a) Fraction of time spent at the oscillatory metastable state T_{osc}/T_{tot} in terms of noise for $\epsilon = 0.06$ (circles) and $\epsilon = 0.08$ (squares). Transition rate from (b) oscillatory to quasi-stationary metastable states, $r_{LC \rightarrow FP}(\sigma)$ and (c) *vice versa*, $r_{FP \rightarrow LC}(\sigma)$. Remaining parameters: $I_0 = 0.95$, $\beta = 4.2$.

To explain the role of adaptation in enhancing the resonant effect, I will invoke the results concerning the slow-fast analysis of (2) for $I_0 = 0.95$ [9, 35]. In particular, the layer problem

$$\begin{aligned}\dot{\varphi}_1 &= I_0 - \sin \varphi_1 + \kappa_1 \sin(\varphi_2 - \varphi_1) \\ \dot{\varphi}_2 &= I_0 - \sin \varphi_2 + \kappa_2 \sin(\varphi_1 - \varphi_2),\end{aligned}\tag{8}$$

is considered by treating the slow variables $\kappa_1, \kappa_2 \in [-1, 1]$ as the additional system parameters. Depending on κ_1 and κ_2 , one finds that the fast flow dynamics is typically *monostable*, exhibiting either a stable stationary or periodic solution, apart from a small bistability region [9, 35]. The numerically obtained maximal stability domain of the oscillatory solution, including both the domain where it is the only attractor and the domain where it coexists with a stable equilibrium, is denoted by gray shading in Fig. 16(a). The thick lines outlining the stability domain of the periodic solution are given by the two branches of SNIPER bifurcations [9]. Within the domain, each periodic solution above the main diagonal $\kappa_1 = \kappa_2$ has a Z_2 symmetry-related twin below the diagonal.

Now, the above results of the multiple timescale dynamics can be used to gain insight into how the slow adaptation process is capable of modifying the suppression effect of noise on emergent oscillations. Let us consider the time traces $(\kappa_1(t), \kappa_2(t))$ in the inset of Fig. 16(a) which (from left to right) show the

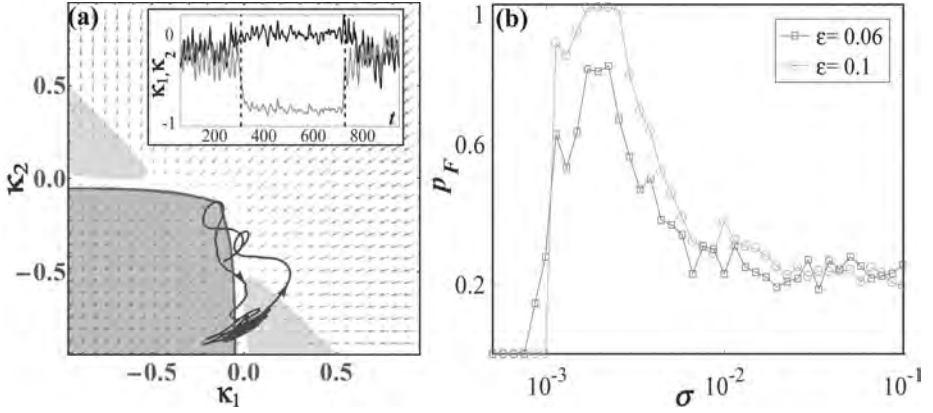


Figure 16. (a) Slow-fast analysis of (2) for $I_0 = 0.95, \sigma = 0$. Fast flow possesses a periodic attractor (medium gray shaded region) and a stable equilibrium (white region), with two branches of SNIPER bifurcations (dark gray) outlining the boundary between them. Arrows indicate vector fields corresponding to stable sheets of the slow flow. Inset: $\kappa_i(t)$ series show a switching episode from oscillatory to stationary state and back ($\varepsilon = 0.06, \beta = 4.2$); Corresponding $(\kappa_1(t), \kappa_2(t))$ orbit is indicated in black; light gray regions: domains where two stable equilibria are focuses rather than nodes. (b) Conditional probability $p_F(\sigma)$ to have the crossing of SNIPER bifurcation followed by a passage through the light gray region from (a), obtained for $\varepsilon = 0.06$ (squares) and $\varepsilon = 0.1$ (circles).

switching episode from an oscillatory to the quasi-stationary metastable state. The onset and termination of the switching event are associated with an inverse and direct SNIPER bifurcation of the fast flow, respectively. Within the narrow (κ_1, κ_2) regions immediately beyond the SNIPER bifurcation, the fast flow possesses a stable node. However, in the close vicinity, there are triangular-shaped domains, highlighted in orange in Fig. 16(a), where the equilibria of fast flow are focuses rather than the nodes. It turns out that precisely for the resonant noise levels, the coupling dynamics $(\kappa_1(t), \kappa_2(t))$ fluctuates within the triangular region, so that the corresponding equilibrium of the fast flow is a focus. In order to explicitly show that this feature is a signature of the resonant effect, one may numerically calculate the conditional probability p_F that the events of crossing the SNIPER bifurcation are followed by the system visiting

the triangular-shaped (κ_1, κ_2) regions with a focus equilibrium of the fast flow [15, 35]. The $p_F(\sigma)$ dependencies for two different ε values in Fig. 16(b) indeed show a maximum for the resonant noise levels associated with the minima of the frequency dependencies in Fig. 13(a). In other words, it is the resonant noise levels that are capable of confining the coupling dynamics within the regions where the fast flow has stable focuses instead of nodes. Smaller noise is incapable of driving the system toward regions supporting focal equilibria, whereas too large a noise just washes out the quasi-stationary regime. The enhancement of inverse stochastic resonance is more efficient for larger ε , i.e., for faster adaptation, as evinced by the vertical order of curves $p_F(\sigma)$ for $\varepsilon = 0.1$ and $\varepsilon = 0.06$.

Conclusion and Outlook

This chapter has been aimed at highlighting inverse stochastic resonance, a recent development in understanding of the impact of noise on oscillating dynamics. The effect is to a certain extent unexpected, in the sense of showing that the noise may selectively suppress the oscillations instead of just contributing to the monotonous increase of oscillation frequency compared to the unperturbed system. My particular goal has been to portray paradigmatic physical picture for the dynamics of systems manifesting inverse stochastic resonance, similar to the well-known picture of a stochastic over-damped particle in a double-well potential subjected to a weak periodic forcing in the case of stochastic resonance [5]. Instead of showing a single paradigm, it turned out that inverse stochastic resonance may occur by two generic scenarios [15], based on the two classical effects of noise, namely either on the noise-enhanced stabilization of deterministically unstable equilibria or the noise-induced crossing of boundaries between the basins of attraction of coexisting stable limit cycles and stable equilibria. By the first scenario, an oscillatory system possesses a weakly unstable fixed point, whose stability is enhanced due to the action of noise. The latter results in a trapping effect, such that the system exhibits subthreshold oscillations, whose prevalence is noise-dependent and is maximal for the resonant noise level. By the second scenario, inverse stochastic resonance emerges in systems with multistable deterministic dynamics, where at least one of the attractors is a stable equilibrium. Due to the asymmetric structure of the phase space, and in particular the relative proximity (far distance) of the limit cycle (stable equilibrium) to the basin boundary [51], the noise-induced switching between the associ-

ated metastable states becomes biased at an intermediate noise level, where the lifetime of quasi-stationary states becomes substantially longer than that of oscillatory state, or the quasi-stationary states may even become absorbing.

In terms of the robustness of inverse stochastic resonance, I have shown that it may occur as a stochastic suppression of intrinsic and emergent oscillations alike. Also, in contrast to the impression created by the pioneering work [18, 20, 21, 22], the effect is not dependent on the type of bifurcation giving rise to oscillations in the sense that it may occur both for subcritical and supercritical bifurcation scenarios. However, one should note that at variance with other resonant phenomena, including stochastic resonance, inverse stochastic resonance is partly sensitive to the choice of initial conditions. Such sensitivity refers to the scenario based on biased switching, where the effect may not be captured if the initial conditions are set only within the basin of attraction of the stationary state.

An important aspect of inverse stochastic resonance not directly covered by this chapter concerns the underlying adjustment of timescales between the stochastic and deterministic dynamics. Namely, in order to observe stochastic resonance, it is well known that one needs to adapt the noise so that the emerging Kramers switching rate [47] matches the oscillation frequency of the external forcing. In the case of inverse stochastic resonance, it is actually the matching between the characteristic timescale of noise-induced boundary crossing and the period of limit cycle that facilitates the resonant effect. For an explicit treatment of this problem in the framework of large deviations theory, I refer the reader to [19].

So far, inverse stochastic resonance has most often been reported in models of neuronal dynamics, both at the level of individual units [19, 20, 21, 22, 32], motifs of units with neuron-like dynamics [18, 35] and neural networks [52]. It can be cast as a stochastic facilitation effect because it is believed to play important functional roles in neuronal systems, such as facilitating the reduction of spiking frequency in the absence of neuromodulators, then triggering of stochastic bursting, i.e., on-off tonic spiking activity, the suppression of pathologically long short-term memories [17, 21, 22, 53], and most notably, may contribute to generation of UP-DOWN states, characteristic for spontaneous and induced activity in cortical networks [54, 55]. The first experimental verification of the inverse stochastic resonance actually came in relation to the latter scenario when considering the in-vitro preparation of cerebellar Purkinje cells [53]. Purkinje neurons are fundamental to cerebellar computations, mostly re-

sponsible for motor control and motor learning [56], since they provide the sole output of cerebellar cortex [57, 58]. It has been found that depending on the level of noise, Purkinje cells can operate in two different regimes: the linear filter regime, where the noise level is close to optimal for inverse stochastic resonance such that it may terminate the UP state, and the all-or-none toggle regime, where the noise is not optimal for inverse stochastic resonance, such that switches between the UP and DOWN states emerge due to the external signals.

Given the robustness of the scenarios underpinning inverse stochastic resonance, it is to be expected that the effect should be ubiquitous to many different fields beyond neuroscience. In fact, inverse stochastic resonance has recently been demonstrated in two substantially different contexts. In one case, the effect has been observed in an experimental study on nematic liquid crystals in relation to ac-driven electroconvection under the influence of colored noise [59]. In the other case, inverse stochastic resonance has been reported in the dynamics of ecosystems, in particular for changing savanna landscapes [60], where the intermediate environmental variability may cause a reduction of oscillation frequency in the vegetation landscape, ultimately leading to the establishment of a stable forest landscape.

An interesting new direction of research concerns the potential relation between stochastic resonance and inverse stochastic resonance. In particular, it has recently been reported that the two effects may coexist in a single system, namely a motif of two quadratic integrate and fire neurons [61], and that moreover, the two effects promote each other in the sense that tuning the noise level to the preferred value for the inverse stochastic resonance is also optimal for the transmission of information between the neurons when the motif is subjected to an external periodic stimulation.

References

- [1] Benzi R, Sutera A, Vulpiani A. The mechanism of stochastic resonance. *J. Phys. A* (1981) 14:L453-L457
- [2] Benzi R, Parisi G, Sutera A, Vulpiani A, Stochastic resonance in climate change. *Tellus* (1982) 34:10-16.
- [3] Nicolis C. Solar variability and stochastic effects on climate. *Sol. Phys.* (1981) 74:473-478.

- [4] Nicolis C. Stochastic aspects of climatic transitions-response to a periodic forcing. *Tellus* (1982) 34:1-9.
- [5] Gammaitoni L, Hänggi P, Jung P. and Marchesoni F. Stochastic Resonance. *Rev. Mod. Phys.* (1998) 70:223-287.
- [6] Lindner B, Garcia-Ojalvo J, Neiman A, Schimansky-Geier L. Effects of noise in excitable systems. *Phys. Rep.* (2004) 392:321.
- [7] Forgoston E, Moore RO, A primer on noise-induced transitions in applied dynamical systems. *SIAM Rev.* (2018) 60:969.
- [8] Pikovsky A, Kurths J. Coherence Resonance in a Noise-Driven Excitable System. *Phys. Rev. Lett.* (1997) 78:775.
- [9] Bačić I, Yanchuk S, Wolfrum M, Franović I. Noise-induced Switching in Two Adaptively Coupled Excitable Systems. *Eur. Phys. J. Spec. Top.* (2018) 227:1077.
- [10] Franović I, Klinshov V. Clustering Promotes Switching Dynamics in Networks of Noisy Neurons. *Chaos* (2018) 28:023111.
- [11] Pisarchik AN, Feudel U. Control of multistability. *Phys. Rep.* (2014) 540:167.
- [12] Franović I, Eydam SR, Semenova N, Zakharova A. Unbalanced Clustering and Solitary States in Coupled Excitable Systems. *Chaos* (2022) 32:011104.
- [13] Franović I, Yanchuk S, Eydam S, Bačić I, Wolfrum M. Dynamics of a Stochastic Excitable System with Slowly Adapting Feedback. *Chaos*(2020) 30:083109.
- [14] Fiasconaro A, Spagnolo B, Boccaletti S. Signatures of noise-enhanced stability in metastable states. *Phys. Rev. E* (2005) 72:061110.
- [15] Bačić I, Franović I. Two paradigmatic scenarios for inverse stochastic resonance. *Chaos* (2020) 30:033123.
- [16] Destexhe A, Rudolph-Lilith M. *Neuronal Noise*. New York: Springer; 2012.

- [17] Schmerl BA, McDonnell MD. Channel-noise-induced stochastic facilitation in an auditory brainstem neuron model. *Phys. Rev. E* (2013) 88:052722.
- [18] Gutkin BS, Jost J, Tuckwell HC. Transient termination of spiking by noise in coupled neurons. *EPL* (2008) 81:20005.
- [19] Zhu J. Unified mechanism of inverse stochastic resonance for monostability and bistability in HindmarshRose neuron. *Chaos* (2021) 31:033119.
- [20] Tuckwell HC, Jost J, Gutkin BS, Inhibition and modulation of rhythmic neuronal spiking by noise. *Phys. Rev. E* (2009) 80:031907.
- [21] Uzuntarla M, Cressman JR, Ozer M, Barreto E. Dynamical structure underlying inverse stochastic resonance and its implications. *Phys. Rev. E* (2013) 88:042712.
- [22] Uzuntarla M, Torres JJ, So P, Ozer M, Barreto E. Double inverse stochastic resonance with dynamic synapses. *Phys. Rev. E* (2017) 95:012404.
- [23] Izhikevich EM. *Dynamical Systems in Neuroscience: The Geometry of Excitability and Bursting*. Cambridge MA: MIT Press; 2007.
- [24] Chiang W.-Y, Lai P.-Y, Chan CK. Frequency enhancement in coupled noisy excitable elements. *Phys. Rev. Lett.* (2011) 106:254102.
- [25] Scialla S, Loppini A, Patriarca M, Heinsalu E. Hubs, diversity, and synchronization in FitzHugh-Nagumo oscillator networks: resonance effects and biophysical implications. *Phys. Rev. E* (2021) 103:052211.
- [26] Alonso S, Bär M, Kapral R. Complex wave patterns in an effective reaction-diffusion model for chemical reactions in microemulsions. *J. Chem. Phys.* (2009) 134:214102.
- [27] S. M. Baer, T. Erneux, Singular Hopf bifurcation to relaxation oscillations. *SIAM J. Appl. Math.* (1986) 46:721.
- [28] Kuehn C. *Multiple Time Scale Dynamics*. Switzerland: Springer International Publishing; 2015.

- [29] Wechselberger M, Mitry J, Rinzel J. Canard theory and excitability. In: Kloeden P, Poetzsche C, editors. *Nonautonomous Dynamical Systems in the Life Sciences*. Switzerland: Springer International Publishing; 2013.
- [30] Vo T, Wechselberger M. Canards of Folded Saddle-Node Type I. *SIAM J. Math. Anal.* (2015) 47:3235-3283.
- [31] Hunsberger E, Scott M, Eliasmith C. The competing benefits of noise and heterogeneity in neural coding. *Neural Comput.* (2014) 26:1600.
- [32] Franović I, Omel'chenko OE, Wolfrum M, Phase-sensitive excitability of a limit cycle. *Chaos* (2018) 28:071105.
- [33] Muratov CB, Vanden-Eijnden E. Noise-induced mixed-mode oscillations in a relaxation oscillator near the onset of a limit cycle. *Chaos* (2008) 18:015111.
- [34] Kromer JA, Pinto RD, Lindner B, Schimansky-Geier L. Noise-controlled bistability in an excitable system with positive feedback. *EPL* (2014) 108:20007.
- [35] Bačić I, Klinshov V, Nekorkin VI, Perc M, Franović I, Inverse stochastic resonance in a system of excitable active rotators with adaptive coupling. *EPL* (2018) 124:40004.
- [36] Maistrenko YL, Lysyansky B, Hauptmann C, Burylko O, Tass P. Multistability in the Kuramoto model with synaptic plasticity. *Phys. Rev. E* (2007) 75:066207.
- [37] Aoki T, Aoyagi T. Co-evolution of phases and connection strengths in a network of phase oscillators. *Phys. Rev. Lett.* (2009) 102:034101.
- [38] Aoki T, Aoyagi T. Self-organized network of phase oscillators coupled by activity-dependent interactions. *Phys. Rev. E* (2011) 84:066109.
- [39] Hebb DO. *The Organization of Behavior: a Neuropsychological Approach*. New York: John Wiley and Sons; 1949.
- [40] Song S, Miller KD, Abbott LF. Competitive Hebbian learning through spike-timing-dependent synaptic plasticity. *Nat. Neurosci.* (2000) 3:919.

- [41] Froemke RC, Dan Y. Spike-timing-dependent synaptic modification induced by natural spike trains. *Nature* (2002) 416:433.
- [42] Wang H.-X, Gerkin RC, Nauen DW, Bi G.-Q. Coactivation and timing-dependent integration of synaptic potentiation and depression. *Nat. Neurosci.* (2005) 8:187.
- [43] Lücken L, Popovych OV, Tass PA, Yanchuk S, Noise-enhanced coupling between two oscillators with long-term plasticity. *Phys. Rev. E* (2016) 93:032210.
- [44] De Maesschalck P, Wechselberger M. Neural excitability and singular bifurcations. *J. Math. Neurosci.* (2015) 5:16.
- [45] Morris C, Lecar, H. Voltage oscillations in the barnacle giant muscle fiber. *Biophys. J.* (1981) 35: 193 – 213.
- [46] Wang H, Wang L, Yu L, Chen Y, Response of Morris-Lecar neurons to various stimuli. *Phys. Rev. E*(2011) 83:021915.
- [47] Hänggi P, Talkner P, Borkovec M. Reaction-rate theory: fifty years after Kramers. *Rev. Mod. Phys.*(1990) 62:251.
- [48] Berglund N, Gentz B. *Noise-Induced Phenomena in Slow-Fast Dynamical Systems*. Berlin: Springer; 2006.
- [49] Laing C, Lord GJ, editors. *Stochastic Methods in Neuroscience*. London: Oxford University Press; 2009.
- [50] Touboul J, Wainrib G. Dynamics and absorption properties of stochastic equations with Hölder diffusion coefficients. *Physica D* (2015) 307:42.
- [51] Torres JJ, Uzuntarla M, Marro J. A theoretical description of inverse stochastic resonance in nature. *Commun. Nonlinear Sci. Numer. Simulat.* (2020) 80:104975
- [52] Uzuntarla M, Barreto E, Torres JJ. Inverse stochastic resonance in networks of spiking neurons. *PLoS Comput. Biol.* (2017) 13:e1005646.
- [53] Buchin A, Rieubland S, Häusser M, Gutkin BS, Roth A. Inverse stochastic resonance in cerebellar Purkinje cells. *PLoS Comput. Biol.* (2016) 12(8):e1005000.

- [54] Hahn TTG, McFarland JM, Berberich S, Sakmann B, Mehta MR. Spontaneous persistent activity in entorhinal cortex modulates cortico-hippocampal interaction in vivo. *Nat. Neurosci.* (2012) 15:1531.
- [55] Vyazovskiy VV, Harris KD. Sleep and the single neuron: the role of global slow oscillations in individual cell rest. *Nat. Rev. Neurosci.* (2013) 14:443.
- [56] Raymond JL, Lisberger SG, Mauk MD. The cerebellum: a neuronal learning machine? *Science* (1996) 272:11261131.
- [57] Fernandez FR, Engbers JDT, Turner RW. Firing dynamics of cerebellar purkinje cells. *J. Neurophysiol.* (2007) 98(1):27894.
- [58] Kano M, Watanabe M. Cerebellar circuits. In: Rubenstein J, Rakic P, editors. *Neural Circuit and Cognitive Development*. Academic Press; 2020.
- [59] Huh JH. Inverse stochastic resonance in electroconvection by multiplicative colored noise. *Phys. Rev. E* (2016) 94:052702.
- [60] Touboul JD, Staver AC, Levin SA. On the complex dynamics of savanna landscapes. *PNAS* (2018) 115(7):E1336-E1345
- [61] Zamani A, Novikov N, Gutkin B. Concomitance of inverse stochastic resonance and stochastic resonance in a minimal bistable spiking neural circuit. *Commun. Nonlinear Sci. Numer. Simulat.* (2020) 82:105024